

# **Metal Complexes of Dioxolene and Iminonitroxyl Radical Ligands**

Sam Creatorex

Submitted in accordance with the requirements for the degree of

Doctor of Philosophy

The University of Leeds

School of Chemistry

July 2018

---

The candidate confirms that the work submitted is his/her own, except where work which has formed part of jointly-authored publications has been included. The contribution of the candidate and the other authors to this work has been explicitly indicated below. The candidate confirms that appropriate credit has been given within the thesis where reference has been made to the work of others. The reference for the jointly authored paper is stated below:

S. Greateorex, M. A. Halcrow, *Cryst. Eng. Comm.*, **2016**, *18*, 4695-4698.

This copy has been supplied on the understanding that it is copyright material and that no quotation from the thesis may be published without proper acknowledgement.

The right of Sam Greateorex to be identified as Author of this work has been asserted by him in accordance with the Copyright, Designs and Patents Act 1988.

---

In memory of Jack Everson

---

## Acknowledgements

EPR measurements were carried out in collaboration with Dr. Amgalanbaatar Baldansuren and the University of Manchester. SEC measurements were carried out in collaboration with Dr. Kevin Vincent, Dr. Nathan Patmore and the University of Huddersfield. Chapter 5 was made possible by the help of Prof. Viktor Ovcharenko and the International Tomography Centre, Novosibirsk. TGA measurements were carried out by Dr. Algy Kazlaucunas. Elemental Analyses were performed by Stephen Boyer of London Metropolitan University.

First and foremost I would like to thank Prof. Halcrow and Prof Hardie for all of their help, guidance, and support throughout this project. I could not have asked for a better supervisor than Malcolm, who has always gone above and beyond the call of duty to help me along the way. I consider myself very fortunate to have been given the opportunity to attend several international conferences and collaborations, as these were some of the highlights of the Ph.D and left me with memories that I will always look back on fondly. I would also like to thank Dr. Chris Pask for his help with crystallography and for keeping the service running smoothly.

Thank you to my friends Kane Maskell, Jaike Belgrave and Olly Bourne for keeping me sane, and to Dan Moon, Steven Chowney, Nikki Cookson, James Green, Sam Oldknow, Blue Jenkins, and Jonny Fowler for being friendly faces around the department. Thank you to Ed Britton, Matt Allinson, Ahmed Ahmed, and Izar Capel for supporting me through hard times.

Finally, and most importantly, I would like to thank my parents for their constant encouragement.

---

## Abstract

This thesis focuses on the design, synthesis and analysis of multinuclear mixed-valent dioxolene complexes and Cu(II) nitroxyl complexes.

Chapter 1 contains a review of the relevant literature for the field of mixed-valent dioxolene complexes and molecular magnetism in nitroxyl complexes.

Chapter 2 reports the synthesis and crystallographic analysis of a series of novel highly porous solvent-supported supramolecular assemblies of triptycene derivatives.

Chapter 3 reports the complexation and characterisation of triptycene derivatives and related multi-dioxolene ligands with Pt(II).

Chapter 4 reports the synthesis, complexation and characterisation of a rigid *tris*(dioxolene) CTC derivative with Pt(II). It also describes the attempted synthesis of coordination polymers containing multi-dioxolene ligands.

Chapter 5 reports the synthesis and characterisation of a series of Cu(II) complexes containing the biradical ligand bisimpy.

Chapter 6 contains a description of all synthetic procedures undertaken during this work.

---

<b>Acknowledgements</b> .....	<b>iv</b>
<b>Abstract</b> .....	<b>v</b>
<b>Table of Contents</b> .....	<b>vi</b>
<b>List of Abbreviations</b> .....	<b>xi</b>
<b>Chapter 1</b> .....	<b>1</b>
1.1 Intramolecular Electron Transfer (IET) .....	1
1.2 Valence Tautomerism .....	1
1.3 Mixed Valency .....	1
1.4 Introduction to Dioxolenes and Tetraoxolenes .....	3
1.4.1 Dioxolenes .....	3
1.4.2 Tetraoxolenes .....	4
1.5 Transition Metal Dioxolene Complexes: Periodic Trends .....	6
1.5.1 Ti, Zr, and Hf .....	7
1.5.2 V, Nb and Ta .....	8
1.5.2.1 Catechol Oxidation .....	9
1.5.3 Cr, Mo, and W .....	10
1.5.3.1 Molybdenum Oligomers .....	11
1.5.4 Mn, Tc and Re .....	18
1.5.5 Fe, Ru, and Os .....	19
1.5.6 Co, Rh and Ir .....	21
1.5.6.1 Mononuclear Cobalt Dioxolene Complexes .....	21
1.5.6.2 Dinuclear Cobalt Dioxolene Complexes .....	27
1.5.6.3 Dinuclear Cobalt Tetraoxolene Complexes .....	30
1.5.6.3.1 Redox Induced Electron Transfer .....	31
1.5.6.4 Oligomers of Cobalt Dioxolenes .....	32
1.5.6.5 Hydrogen Bonded Networks .....	33
1.5.6.6 Coordination Polymers of Cobalt Dioxolenes .....	35
1.5.6.6.1 Ditopic Pyridyl Linking Groups .....	35
1.5.6.6.2 Ditopic Dioxolene Linking Groups .....	39
1.5.6.6.3 Bifunctional Linking Groups .....	41
1.5.6.6.4 Nanoparticles .....	41

---

1.5.6.6.5 Self-assembled VT Nanoparticle Monolayers .....	43
1.5.6.7 Rh and Ir .....	45
1.5.6.7.1 H-bond Networks .....	45
1.5.6.7.2 Iridium .....	47
1.5.7 Ni, Pd and Pt .....	48
1.5.8 Cu, Ag and Au .....	51
1.5.9 Zn, Cd and Hg .....	54
1.5.10 Summary of Periodic Trends .....	55
1.6 Nitronyl nitroxides .....	56
1.6.1 Coordination Through the Oxygen Atom .....	57
1.6.2 Coordination Through the Nitrogen Atom .....	58
1.6.3 Geometry of the Nitroxyl .....	58
1.6.4 Effect of the Counter-ion .....	58
1.6.5 The Bisimpy Ligand .....	60
1.7 Project Aims .....	65
1.7.1 Porous Crystalline Clathrates of Triptycene Derivatives .....	65
1.7.2 Multinuclear Mixed-Valent Dioxolene Complexes .....	65
1.7.3 Copper(II) Complexes of a Bis-Nitroxyl Chelate Ligand .....	66
1.8 References .....	67
<b>Chapter 2 .....</b>	<b>76</b>
2.1 Introduction .....	76
2.2 Results and Discussion .....	77
2.2.1 Synthesis .....	77
2.2.2 Single Crystal X-Ray Structural Determination of Crystalline Clathrates and Platinum Complexes of Triptycene .....	82
2.2.3 Thermogravimetric Analysis (TGA) of Crystalline Clathrates of Triptycene .....	97
2.3 Conclusions and Future Work .....	99
2.4 References .....	100
<b>Chapter 3 .....</b>	<b>103</b>
3.1 Introduction .....	103

---

3.2.1 Results and Discussion .....	105
3.2.1 [{"(dppe)Pt"} <sub>2</sub> ( <b>2.18</b> )] ( <b>3.1</b> ) and [{"(dppb)Pt"} <sub>2</sub> ( <b>2.18</b> )] ( <b>3.2</b> ) .....	105
3.2.1.1 Synthesis and Characterisation .....	105
3.2.1.2 X-ray Crystal Structure Refinement of <b>3.2</b> .....	109
3.2.1.3 Electrochemical Analysis of Complexes <b>3.1</b> and <b>3.2</b> .....	111
3.2.1.4 Spectroelectrochemical analysis of <b>3.1</b> .....	117
3.2.1.5 UV-vis-NIR Oxidative Titrations .....	122
3.2.1.6 EPR Measurements of Chemically Oxidised Mixed-Valent Radical Cations of <b>3.1</b> and <b>3.2</b> .....	123
3.2.2 [{"(dppe)Pt"} <sub>3</sub> ( <b>2.5</b> )] ( <b>3.3</b> ) and [{"(dppb)Pt"} <sub>3</sub> ( <b>2.5</b> )] ( <b>3.4</b> ) .....	126
3.2.2.1 Synthesis and Characterisation .....	126
3.2.2.2 X-ray Crystal Structure Refinement of <b>3.3</b> .....	128
3.2.2.3 Electrochemical Analysis of Complexes <b>3.3</b> and <b>3.4</b> .....	131
3.2.2.4 UV-vis/NIR Oxidative Titrations with [FeCp <sub>2</sub> ]PF <sub>6</sub> .....	136
3.2.2.5 EPR Measurements of Chemically Oxidised Mixed-Valent Radical Cations of <b>3.3</b> and <b>3.4</b> .....	141
3.2.2.6 Spectroelectrochemical Analysis of <b>3.4</b> .....	143
3.2.3 [{"(dppe)Pt"} <sub>2</sub> ( <b>3.9</b> )] and [{"(dppb)Pt"} <sub>2</sub> ( <b>3.9</b> )] .....	144
3.2.3.1 Synthesis of Complexes <b>3.5</b> and <b>3.6</b> .....	144
3.2.3.2 X-ray Crystal Structure Refinement of <b>3.6</b> .....	148
3.2.3.3 Electrochemical Analysis of Complexes <b>3.5</b> and <b>3.6</b> .....	149
3.2.3.4 UV-vis/NIR Oxidative Titrations of <b>3.5</b> and <b>3.6</b> .....	154
3.2.3.5 Spectroelectrochemical Analysis of <b>3.6</b> .....	158
3.2.3.6 EPR Measurements of Chemically Oxidised Mixed-Valent Radical Cations of <b>3.5</b> and <b>3.6</b> .....	159
3.3 Summary, Trends and Conclusions .....	161
3.4 References .....	165
<b>Chapter 4</b> .....	<b>166</b>
4.1 Introduction .....	166
4.2 Results and Discussion .....	167
4.2.1 Synthesis of the Ligand .....	167

---

---

4.2.2 Characterisation of <b>4.1</b> , [ $\{(\text{dppe})\text{Pt}\}_3(\mathbf{4.1})$ ] ( <b>4.14</b> ) and [ $\{(\text{dppb})\text{Pt}\}_3(\mathbf{4.1})$ ] ( <b>4.15</b> ) .....	172
4.2.3 Electrochemical Analysis of <b>4.14</b> and <b>4.15</b> .....	177
4.2.4 UV-vis-NIR Oxidative Titrations .....	184
4.2.5 Spectroelectrochemical Analysis of <b>4.14</b> .....	189
4.2.6 EPR Measurements of Chemically Oxidised Mixed-Valent Radical Cations of <b>4.14</b> and <b>4.15</b> .....	192
4.3 Summary, Trends, Conclusions and Future Work .....	195
4.4 Towards Coordination Polymers .....	196
4.4.1 Introduction .....	196
4.4.2 Synthesis .....	201
4.4.3 Coordination Polymers – Conclusions and Future Work .....	209
4.5 References .....	211
<b>Chapter 5</b> .....	<b>213</b>
5.1 Introduction .....	213
5.1.1 Coordination through the oxygen atom .....	214
5.1.2 Coordination through the nitrogen atom .....	215
5.1.3 Geometry of the nitroxyl .....	215
5.1.4 Effect of the counter-ion .....	216
5.1.5 The bisimpy ligand .....	217
5.2 Synthesis .....	220
5.3 Crystallography .....	228
5.4 Magnetic Measurements .....	234
5.5 Conclusions and Future Work .....	242
5.6 References .....	244
<b>Chapter 6</b> .....	<b>246</b>
6.1 Methods and Instrumentation .....	246
6.1.1 NMR Spectroscopy .....	246
6.1.2 Mass Spectrometry .....	246
6.1.3 Elemental Analysis .....	246
6.1.4 X-ray Crystallography .....	246

---

6.1.5 Infrared Spectroscopy .....	247
6.1.6 Electronic Absorbance (UV/vis/NIR) Spectroscopy .....	247
6.1.7 Electrochemical Analysis .....	247
6.1.8 Magnetic Susceptibility Measurements .....	247
6.1.9 Thermogravimetric Analysis .....	248
6.1.10 Electron Paramagnetic Resonance .....	248
6.1.11 Spectroelectrochemical Analysis .....	248
6.2 Experimental Details .....	249
6.3 Crystallographic Data Tables .....	277
6.4 References .....	283

---

## List of Abbreviations

biscat	9,10-dimethyl-2, 3,6,7-tetrahydroxy-9,10-[1',2']benzenoanthracene
bispicen	N,N'-bis(2-pyridylmethyl)-1,2-ethanediamine)
BQ	benzoquinone
Bz	benzyl
Cat	catechol
cth	( <i>dl</i> )-5,7,7,12,14,14-hexamethyl-1,4,8,11-tetraazacyclotetradecane
CV	cyclic voltammetry
DBCat	3,6-di- <i>tert</i> -butylcatechol
DBQ	3,6-di- <i>tert</i> -butylbenzoquinone
DBSQ	3,6-di- <i>tert</i> -butyl-1,2-benzosemiquinonate
DCM	dichloromethane
DFT	density functional theory
dhBQ	dihydroxybenzoquinone
diox	dioxolene
DMF	dimethylformamide
dpqa	di(2-pyridylmethyl)-N-(quinolin-2-ylmethyl)amine
EPR	electron paramagnetic resonance
[Fc]	[Fe(Cp) <sub>2</sub> ] <sup>+</sup>
H <sub>6</sub> CTC	2,3,7,8,12,13-Hexahydroxy-10,15-dihydro-5 <i>H</i> -tribenzo[a,d,g][9]annulene
H <sub>4</sub> thea	2,3,6,7-tetrahydroxy-9,10-dimethyl-9,10-dihydro-9,10-ethanoanthracene
HS	high spin
LIESST	light induced excited spin state transition
LS	low spin
Me	methyl
NIR	near infrared
Ph	phenyl
pmea	bis[(2-pyridyl)methyl]-2-(2-pyridyl)ethylamine

---

pmm	4,6-di-2'-pyridylpyrimidine
py	pyridine
py <sub>2</sub> O	<i>bis</i> (pyridyl)ether
RIET	redox induced electron transfer
SCO	spin crossover
SEC	spectroelectrochemistry
spiro	3,3,3',3'-tetramethyl-5,5',6,6'-tetrahydroxy-1,1'-spiro <i>bis</i> (indane)
SQ	semiquinone
tbtq	2,3,6,7,10,11-Hexahydroxy-12d-methyl-4b,8b,12b,12d-tetrahydrodibenzo[2,3:4,5]pentaleno[1,6- <i>ab</i> ]indene-4b,8b,12b(12d <i>H</i> )-triol
tpa	<i>tris</i> (2-pyridylmethyl)amine
tpom	<i>tetrakis</i> (4-pyridyloxymethylene)methane
triscat	9,10-dimethyl-2,3,6,7,14,15-hexahydroxy-9,10-[1',2']benzenoanthracene
UV-vis	ultraviolet-visible
VT	valence tautomerism

---

# Chapter 1

## Introduction

### 1.1 Intramolecular Electron Transfer (IET)

The development of functional molecular materials capable of switching between electronic states is of importance for the future development of data storage, sensors, and optical devices. Several molecular systems which are capable of switching electronic states are known of, including spin crossover (SCO) complexes,<sup>[1-2]</sup> light induced excited spin state trapping (LIESST) complexes, and valence tautomeric (VT) transition complexes.<sup>[3-10]</sup> SCO and LIESST involve a change in spin state for a metal centre, whereas VT transitions involve electron transfer on a redox-active ligand. Both processes can be promoted by a change in an external stimulus such as temperature, pressure, magnetic/electric fields or irradiation with light.

### 1.2 Valence Tautomerism

Valence tautomers are constitutional isomers of a compound within which bonds are rapidly formed and broken without the migration of atoms. VT transitions are observed in a wide variety of coordination complexes, including but not limited to those of cobalt, iron, nickel, ruthenium, manganese and platinum. Ligands which may be isolated in a variety of different oxidation states are described as being redox active or non-innocent,<sup>[11-12]</sup> and are themselves of interest to catalysis,<sup>[13]</sup> bioinorganic chemistry<sup>[14]</sup> and molecular materials.<sup>[15]</sup> Redox-active ligands have been used to create a wide variety of coordination complexes which undergo VT transitions, typically with ligands such as *o*-dioxolenes,<sup>[10]</sup> *o*-diimines,<sup>[16]</sup> dithiolenes,<sup>[17]</sup> porphyrins,<sup>[18]</sup> *o*-aminophenolates<sup>[17]</sup> and phenoxy radicals.<sup>[19]</sup>

### 1.3 Mixed Valency

Mixed valent compounds contain an element in more than one oxidation state.<sup>[20]</sup> This property may exist in both organic and inorganic compounds, however this thesis will focus primarily on examples pertaining to metal complexes. Perhaps the most well-

known mixed valent complex is Prussian blue. However, while it was discovered over 300 years ago, the electronic structure of Prussian blue was not elucidated until much more recently. An idealised solid state sample of Prussian blue has the formula  $\text{Fe}_7(\text{CN})_{18} \cdot x\text{H}_2\text{O}$ , with a 1:1 ratio of low-spin (LS) Fe(II) and high-spin (HS) Fe(III) ions bridged by cyanide ligands.<sup>[21]</sup>

Although compounds like Prussian blue have been known for a long time, the field of mixed valency had its proper genesis with the synthesis of the  $[(\text{NH}_3)_5\text{Ru}]\text{L}(\text{Ru}(\text{NH}_3)_5)^{5+}$  family of dinuclear ruthenium complexes in the 1970s.<sup>[22]</sup> When L = pyrazine this is known as the Creutz-Taube ion (**Figure 1.1**), and electronic delocalization takes place between the Ru(II) and Ru(III) centres to give a formal ruthenium oxidation state of +2.5. Follow-up work by Hush *et al.* showed that it is possible to localise the valent electron on one ruthenium centre by increasing the distance between the two metal atoms using vinyl spacers. The amount of electronic coupling between metals decreases exponentially with distance.<sup>[23]</sup>

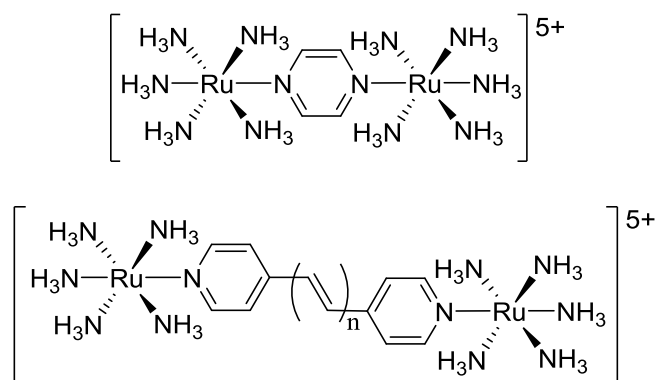


**Figure 1.1.** Top: Creutz-Taube ion. Bottom: Creutz-Taube ion with vinyl spacers.

As more examples of mixed valent compounds were discovered, efforts were made to form a unified and systematic description of the different types of complexes that had been found. Robin and Day proposed that symmetric mixed valent complexes can be assigned to one of three possible categories, based on the extent of electronic mixing between different oxidation states.<sup>[24]</sup> Class I complexes are those in which two substantially different metal-ligand sites are present, preventing interconversion between the two sites. Class III complexes are those in which the two metal sites are

identical, and experience a large degree of mixing between the two electronic states. Class II complexes are the intermediate between these two extremes, where the metal sites are similar but not identical, leading to partial mixing of the two oxidation states (**Figure 1.2**).

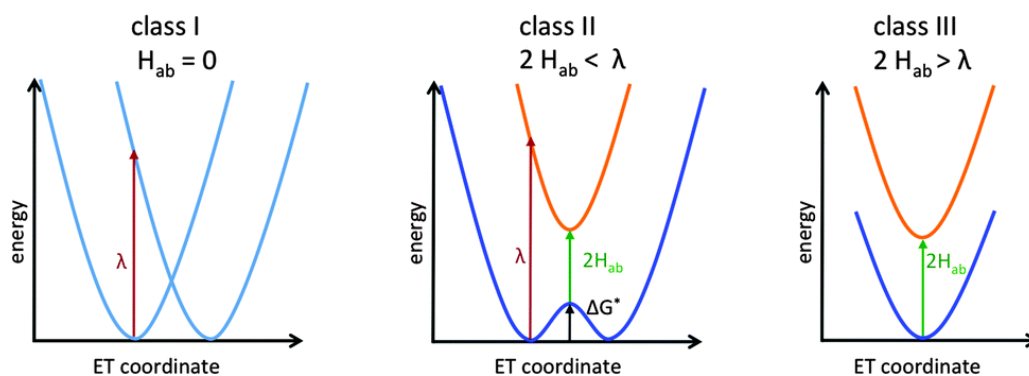
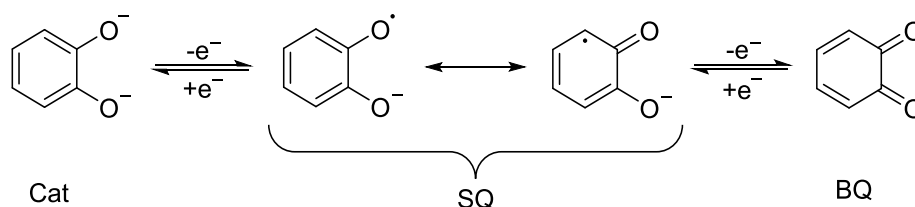


**Figure 1.2.** Potential energy surfaces for the three Robin-Day electron transfer classes.  $H_{ab}$  is the electronic coupling and  $\lambda$  is the reorganisation energy. Reproduced from Kaupp *et al.*<sup>[25]</sup>

## 1.4 Introduction to Dioxolenes and Tetraoxolenes

### 1.4.1 Dioxolenes

Dioxolenes are redox-active and may exist in one of three possible oxidation states, depending on a variety of factors. From most reduced to most oxidised, they are named catechol (Cat), semiquinone (SQ) and quinone (BQ). These redox forms are illustrated in **Scheme 1.1** below for 1,2-dimethoxybenzene (catechol), the simplest possible dioxolene.



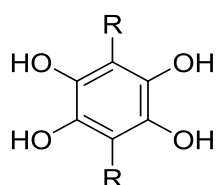
**Scheme 1.1.** Catechol, semiquinonate and benzoquinone forms of catechol.

---

Ligands containing this functional group are hence non-innocent, and reports of coordination complexes containing dioxolenes in all three oxidation states have been reported.<sup>[26]</sup> The applications of dioxolenes are wide, but usually involve exploiting their electron rich nature and affinity for certain metals. They are also biologically relevant, being involved in catechol dioxygenase enzymes which catalyse the cleavage of catechol with O<sub>2</sub>, which has been a subject of research interest.<sup>[27]</sup> As well as this, metal dioxolene complexes have been suggested as candidates for new catalysts, due to the ability of the dioxolene to reversibly cycle between oxidation states while acting as an electron reservoir.<sup>[28]</sup>

#### 1.4.2 Tetraoxolenes

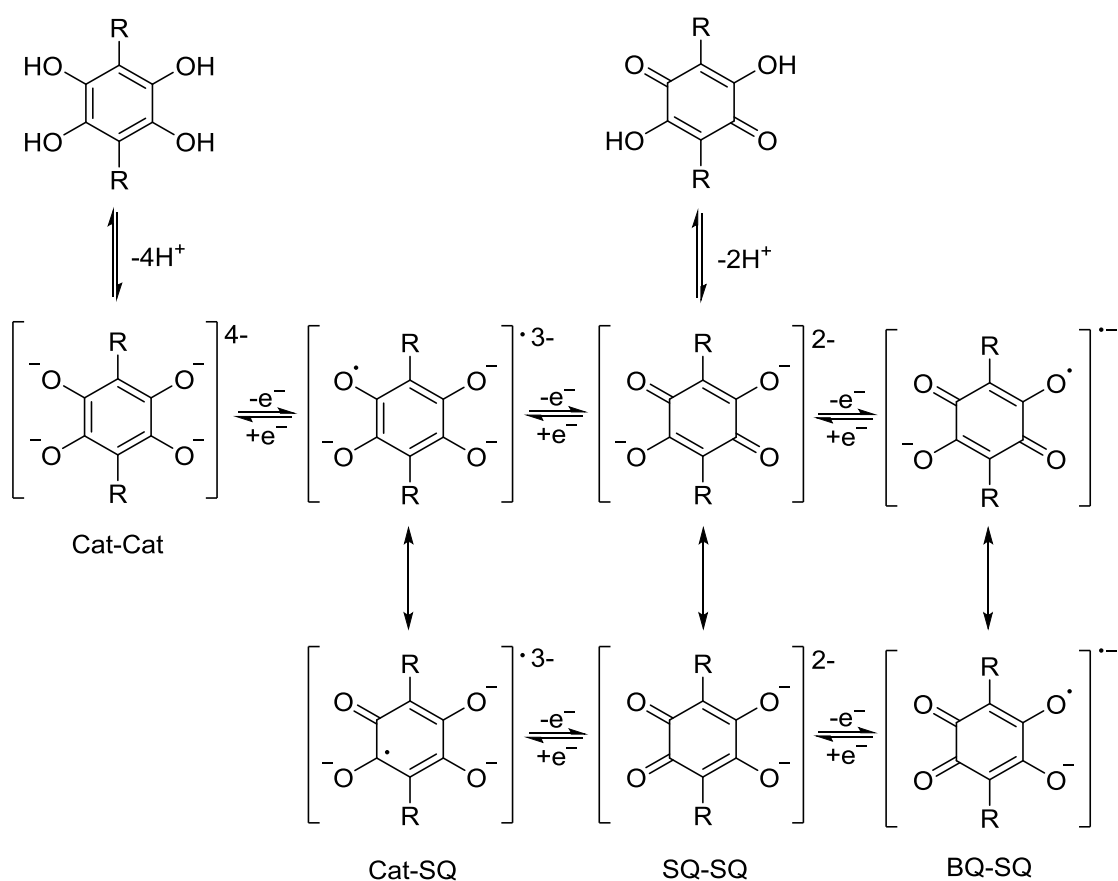
Tetraoxolenes are closely related to dioxolenes, bearing hydroxy groups at the 1,2,4,5 positions of benzene rather than just the 1,2 positions, and they too are redox-active. 1,2,4,5-Tetrahydroxybenzene is the simplest example of a redox-active tetraoxolene ligand (**Figure 1.3**).<sup>[29]</sup>



R = H, Cl, Br, <sup>t</sup>Bu

**Figure 1.3.** Prototypical tetraoxolene ligand 1,2,4,5-tetrahydroxybenzene with R groups.

1,2,4,5-Tetrahydroxybenzene may be converted between four possible oxidation states, from the fully reduced *bis*(Cat) form to the most oxidised BQ-SQ form. The various redox forms and their resonance structures are displayed in **Scheme 1.2**.



**Scheme 1.2.** The four redox forms of 1,2,4,5-tetrahydroxybenzene, with resonance structures.

Ligands of this type may coordinate to form mononuclear complexes of several tetraoxolenes around a single metal atom, or they may act as bridging ligands in di- or polynuclear complexes.

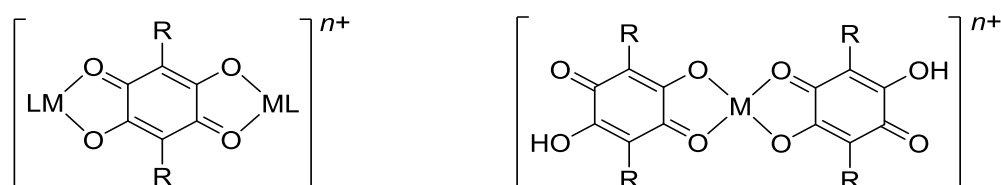


**Figure 1.4.** Generic mononuclear and dinuclear tetraoxolene complexes. L is any ancilliary ligand.

---

## 1.5 Transition Metal Dioxolene Complexes: Periodic Trends

Dioxolene ligands and their complexes have a host of special properties which set them apart from other classes of coordination compounds. They are similar to oxo ligands in terms of their charge and ability to coordinate as  $\pi$  donors with electron deficient metals. The energy separation between the quinone  $\pi^*$  orbitals and the transition metal  $d$  orbitals is small. In the case of analogous complexes containing 1,2-diimines and oxidized 1,2-dithiolene ligands, there is a high degree of electronic delocalisation between the metal and ligand. This is in contrast to the properties of dioxolene ligands, which instead are best described as being charge-localised in either the quinone, semiquinone or catecholate form. In several cases, the electronic energy similarity between metal and quinone orbitals can lead to valence tautomeric equilibria due to direct charge transfer between the two states.

The degree of electron delocalisation can be determined by electron paramagnetic resonance (EPR) measurements. In the case of  $V(\text{bpy})_3$  and  $V(\text{S}_2\text{C}_2\text{Ph}_2)_3$ , hyperfine coupling to the  $^{51}\text{V}$  nucleus is weak (83 and 62 G).<sup>[30-31]</sup> In the isoelectronic complex  $V^{\text{III}}(\text{SQ})_2$ , hyperfine coupling is generally less than 5 G.<sup>[32]</sup> Hence, there is a larger degree of charge-localisation in quinone complexes than with corresponding N and S donor ligands, which is reflected in aspects of their structure such as bond lengths. Crystal structures of a wide variety of dioxolene complexes show that the C-O and C-C bond lengths can be diagnostic of which charge state the ligand is in, and magnetic measurements often show antiferromagnetic or ferromagnetic M-SQ and/or SQ-SQ exchange.<sup>[26,33]</sup> Redox processes may be carried out both chemically and electrochemically on these complexes, opening up possibilities for applications such as dioxygen activation, which is posited to occur through reaction with either the nucleophilic metal (as in extradiol catechol dioxygenase oxidations) or the catecholate ligand (as in intradiol dioxygenase enzymes).<sup>[34-35]</sup>

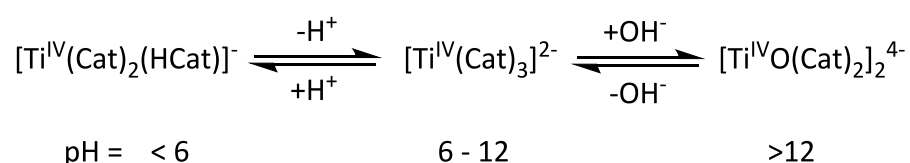
When a paramagnetic metal ion coordinates a semiquinone radical, the metal-SQ superexchange is usually antiferromagnetic with a spin-coupled ground state. In extreme cases such as that of the tetranuclear complex  $\text{Fe}_4(\text{DBSQ})_4(\text{DBCat})_4$ , (DBSQ = 3,5-di-*tert*-butyl-*o*-semiquinone and DBCat = 3,5-di-*tert*-butylcatechol) the

superexchange is strong enough that the compound is almost completely diamagnetic at low temperatures. SQ ligands may also experience superexchange with one another, and antiferromagnetic coupling is observed between SQ ligands even in complexes where the metal itself is diamagnetic (e.g.  $\text{Co}^{\text{III}}(\text{3,6-DBSQ})_3$ ). Quantitatively, cooling this complex from ambient temperature to 5 K results in a drop in magnetic moment from 3.0  $\mu\text{B}$  to 2.1  $\mu\text{B}$ , providing evidence that the three initially non-interacting  $S = \frac{1}{2}$  centres begin to couple as the temperature is lowered.

The chemistry of metal catecholate complexes can be rationalised by periodic trends arising from differences in metal orbital energies across the d-block. Henceforth, a literature review of each d-block group will be discussed in the context of its dioxolene complexes and their properties.

### 1.5.1 Ti, Zr, and Hf

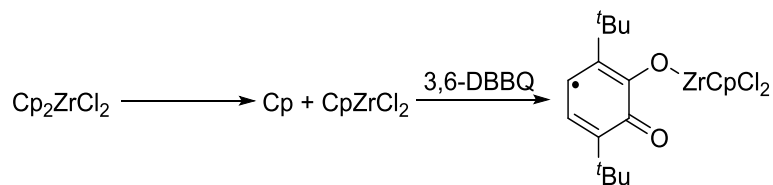
Complexes of these metals demonstrate the general property of catecholate ligands to stabilise strong Lewis acid metals with high oxidation states. Despite the tendency for quinone ligands to give rise to ambiguous charge distribution, the chemistry of this metal series is largely dominated by simple Lewis acid-base chemistry. The complex  $[\text{Ti}(\text{Cat})_3]^{2-}$  has attracted interest as a polymerisation catalyst, and is remarkably stable to changes in pH, with an equilibrium existing between the following three species (**Scheme 1.3**).<sup>[36-37]</sup>



**Scheme 1.3.** Three forms of Ti(IV) dioxolene complexes and their pH dependence.

While typically bidentate, there are also examples of quinone ligands bonding to this group in a monodentate way. Vlcek *et al.* synthesised  $[\text{Ti}(\text{Cp})\text{Cl}_2(\text{3,5-DBSQ})]$  through a photochemical radical reaction, in which the semiquinone ligand is coordinated

through a single oxygen atom (**Scheme 1.4**).<sup>[38]</sup> A zirconium analogue of this complex can also be prepared.<sup>[39]</sup>

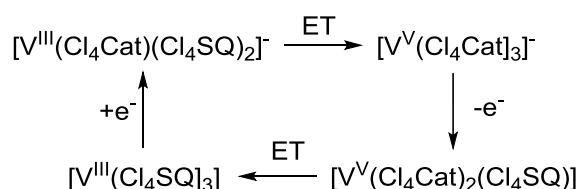


**Scheme 1.4.** Photochemical synthesis of  $\text{Ti}(\text{Cp})\text{Cl}_2(3,5\text{-DBSQ})$ .

The Hf(IV) ion, with its large atomic radius, is able to coordinate four quinone ligands (as in  $[\text{Hf}(\text{Cat})_4]^{4-}$ ). It has been structurally characterised, but thus far has not found further applications.<sup>[40]</sup>

### 1.5.2 V, Nb and Ta

Many dioxolene complexes of this group (such as  $\text{V}(\text{DBSQ})_3$ ) are not stable in air, however by perchlorinating the dioxolene to make it more electron withdrawing ( $\text{V}(\text{Cl}_4\text{SQ})$ ) increases the reduction potential by  $\sim 0.5$  V compared to the *tris*(DBSQ) complex, which is hence far more stable in air.<sup>[32, 41]</sup> As a result, the  $\text{V}^{\text{III}}(\text{Cl}_4\text{SQ})_3 / [\text{V}^{\text{V}}(\text{Cl}_4\text{Cat})_3]^-$  redox couple can be studied (**Scheme 1.5**).



**Scheme 1.5.** Redox cycle of a *tris*(dioxolene) complex of vanadium.

The electron transfer steps of this cycle are important, as the ability for dioxolene ligands to act as electron reservoirs which can reduce/oxidise the metal by way of interconversion between the Cat/SQ forms is a characteristic property of these ligands.

The biological role of dioxolene complexes of vanadium has also been a well explored area of study, particularly in regards to marine organisms known as tunicates. Tunicate blood cells contain up to 0.1 M concentrations of vanadium, which is  $10^8$

---

times greater than in the surrounding seawater they inhabit. The vanadium in these organisms is understood to be bound to a class of naturally occurring “tunichromes”, which are *tris*(Cat) ligands ideal for chelating V(III) ions (**Figure 1.5**).<sup>[42-43]</sup>

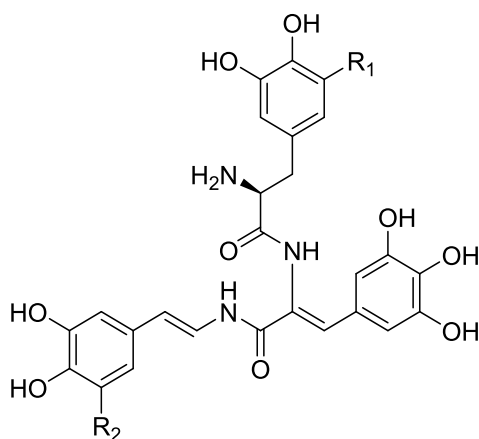


**Figure 1.5.** *Ascidia nigra* tunichromes: An-1,  $R_1 = R_2 = \text{OH}$ ; An-2,  $R_1 = \text{H}$ ,  $R_2 = \text{OH}$ ; An-r,  $R_1 = R_2 = \text{H}$ .

The synthetic ligand TRENCAM is structurally related to these tunicates, and Raymond et. al. have studied  $[\text{V}^{\text{III}}(\text{TRENCAM})]^{3-}$  as a model for this biological system.<sup>[44]</sup>

### 1.5.2.1 Catechol Oxidation

The catalytic oxidation of catechol can be achieved with a large number of metal ions, with vanadium demonstrating particularly good activity. Complexes such as  $[\text{VO}(\text{acac})(\text{Cat})]$ ,  $[\text{VO}(\text{acac})_2]$ ,  $[\text{VO}(\text{salen})]$ , and  $[\text{VO}(\text{acac})(\mu\text{-OMe})_2]$  may use  $\text{O}_2$  or  $\text{H}_2\text{O}_2$  as an oxidising agent to form a mixture of oxidised products including the corresponding benzoquinone, muconic acid anhydride, and pyrone (**Figure 1.6**).<sup>[45]</sup>

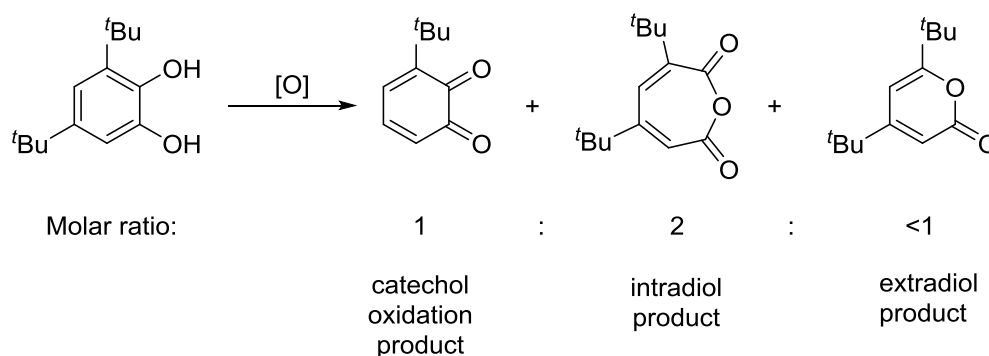
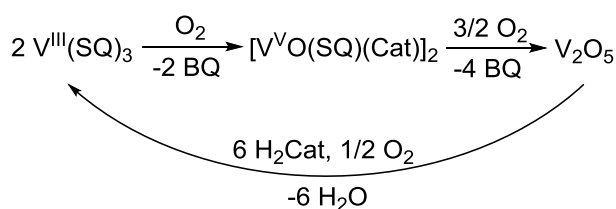


**Figure 1.6.** Products of the catalytic oxidation of DBCat by vanadium.

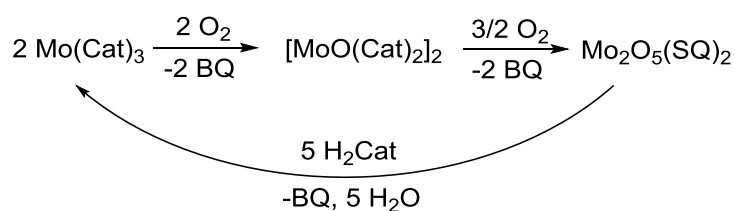
Another catalytic cycle for the oxidation of catechol is based around the complex  $[\text{VO}(\text{DBCat})_2]^{2-}$ , which upon oxidation with one equivalent of  $\text{O}_2$  forms  $[\text{VO}(\text{DBSQ})(\text{DBCat})]_2$ . This is then further oxidised with  $\text{O}_2$  to give  $\text{V}_2\text{O}_5$  and the product benzoquinone, 3,5-DBBQ. Free  $\text{H}_2\text{DBCat}$  may then reduce the  $\text{V}_2\text{O}_5$  back to  $[\text{VO}(\text{DBSQ})(\text{DBCat})]_2$ , completing the cycle (**Scheme 1.7**).<sup>[46]</sup>



**Scheme 1.7.** Catalytic cycle for the oxidation of catechol with vanadium.

### 1.5.3 Cr, Mo, and W

The dioxolene complexes of this group share many similarities with the group 5 metals. Generally these compounds are reported to be synthesised by the addition of the reduced metal (e.g.  $\text{Mo}(\text{CO})_6$ ) with the benzoquinone.<sup>[47]</sup> The dimeric products of these reactions, such as  $[\text{M}(\text{Cl}_4\text{Cat})_3]_2$  show three distinct two-electron reduction steps in their electrochemistry, demonstrating a clear example of ligand-centred reduction.<sup>[48-50]</sup> Oxidation of catechol to benzoquinone in the complex  $[\text{Mo}(\text{Cat})_3]$  follows a similar catalytic cycle to the analogous vanadium complex, forming  $[\text{MoO}(\text{Cat})_2]_2$  and  $[\text{Mo}_2\text{O}_5(\text{SQ})_2]$  by sequential oxidation steps before being reduced back to the parent compound by  $\text{H}_2\text{Cat}$  (**Scheme 1.8**).<sup>[50]</sup>



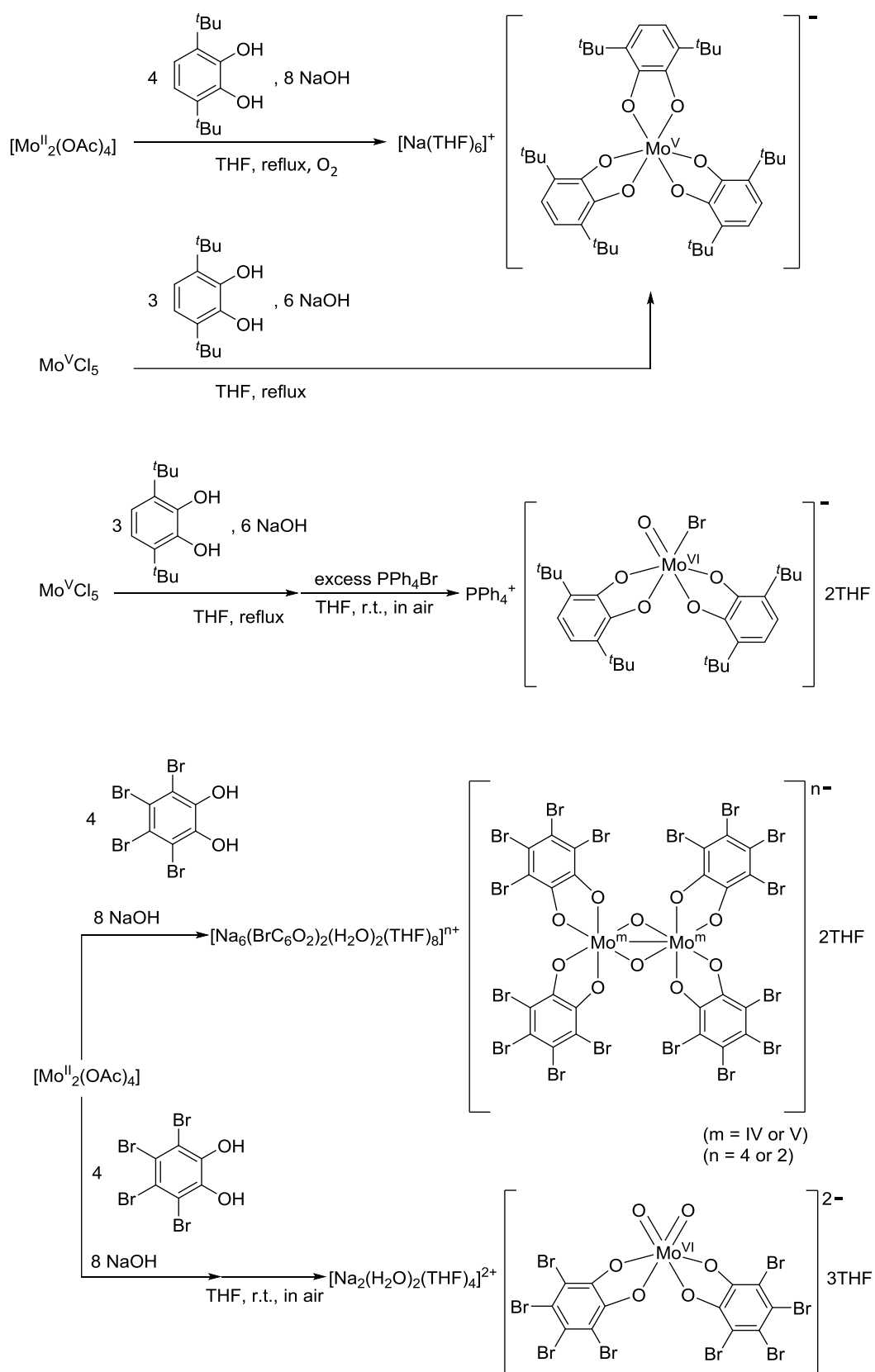
**Scheme 1.8.** Catalytic cycle for the oxidation of catechol with molybdenum.

Chromium complexes of 3,5-DBBQ,<sup>[51]</sup> 3,6-DBBQ<sup>[52]</sup> and 9,10-PhenBQ<sup>[51]</sup> undergo one-electron oxidation and reduction to produce paramagnetic cations/anions that are characterised by EPR measurements as  $[\text{Cr}^{\text{III}}(\text{BQ})(\text{SQ})_2]^+$  and  $[\text{Cr}^{\text{III}}(\text{SQ})_2(\text{Cat})]^-$ . In the previous section it was shown that  $[\text{V}^{\text{III}}(\text{SQ})_3]$  complexes exhibit strong antiferromagnetic coupling between the metal  $S = 1$  spin state and the ligand  $S = 1/2$  spin state, leading to a ligand-localised  $S = 1/2$  ground state. A similar picture exists for Cr dioxolene complexes in the  $[\text{Cr}(\text{BQ})(\text{SQ})_2]$  level, whose  $S = 3/2$  metal ion and two  $S = 1/2$  radical ligands leave a metal localised spin.<sup>[53]</sup>

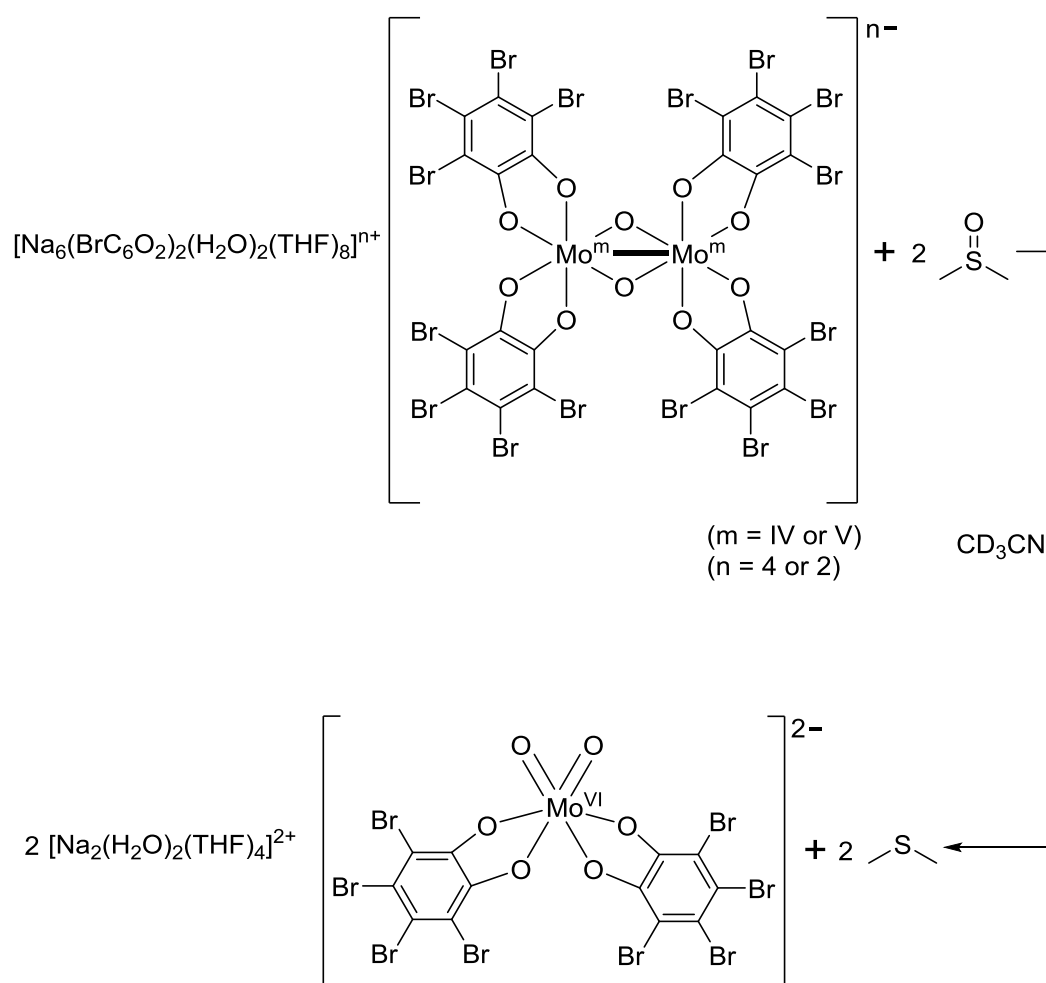
An important consideration in the synthesis of these compounds is their tendency towards being sensitive to oxygen exposure. The reaction of  $\text{Mo}(\text{CO})_6$  and 3,5-DBBQ in the presence of oxygen gives  $[\text{MoO}(\text{DBCat})_2]_2$ , but under strictly oxygen free conditions the terminal oxygen ligand is not present, with  $[\text{Mo}(\text{DBCat})_3]$  being formed instead.<sup>[54]</sup> Many different terminal and bridging oxo forms of these complexes are accessible, which often leads to a mixture of structurally related products.

### 1.5.3.1 Molybdenum Oligomers

Chang *et al.* have synthesised a variety of mono and dinuclear molybdenum dioxolene complexes. The oxophilic nature of molybdenum leads to the possibility of several bridging/terminal oxo forms of these complexes, making the synthesis of a single stoichiometrically defined product challenging. These complexes possess a high degree of oxophilicity due to their electron-deficient nature, and will readily perform O-atom abstraction from molecular  $\text{O}_2$  or oxygenated solvents such as DMSO. Some of the complexes will even reduce DMSO to DMS, as shown in **Scheme 1.9** and **1.10**.<sup>[55]</sup>

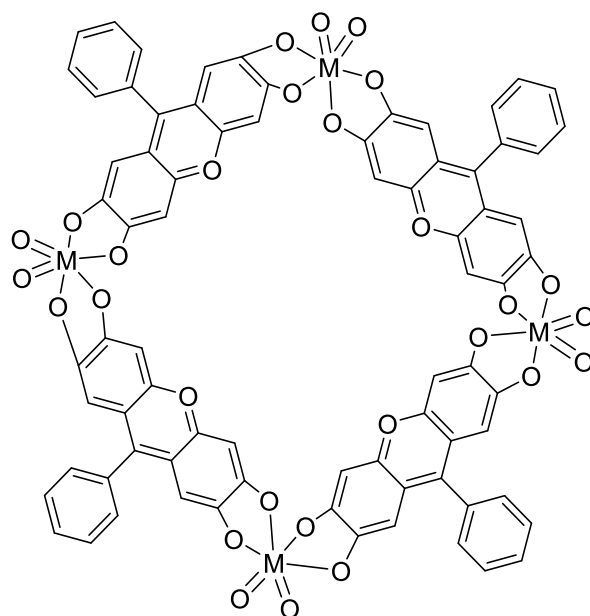


**Scheme 1.9.** Synthetic route to a variety of molybdenum dioxolenes.



**Scheme 1.10.** Catalytic reduction of DMSO with a dimolybdenum catecholate complex.

A pair of distorted square {4 + 4} metallocycles containing Mo or W have been produced by Robson *et al.* (**Figure 1.7**). These are capable of encapsulating various cations in the pore, the structures of which are displayed in **Figure 1.8**.<sup>[56]</sup>



M = Mo, W

**Figure 1.7.** Distorted square {4 + 4} metallocycle of Mo or W.

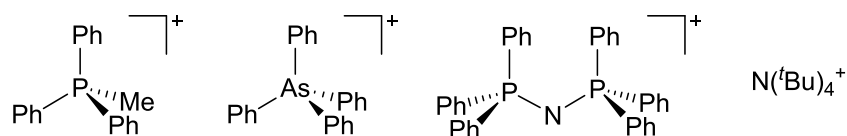


**Figure 1.8.** Guest cations which can be encapsulated in the pore.

Xu has reported a Mo catecholate dimer which has a structure consisting of hydrogen-bonded 1D chains mediated by crystalline water molecules, and further hydrogen bonding through a 2-methylbenzimidazole cation leading to a quasi-2D structure (**Figure 1.9**).<sup>[57]</sup>

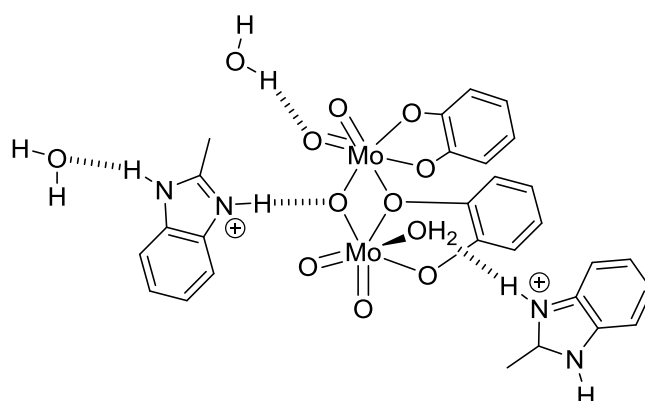


**Figure 1.9.** 1D chain structure and hydrogen bond connectivity of a molybdenum catecholate dimer.

A chiral tetramer has been reported by Pierpont *et al.* (**Figure 1.10**). This structure forms due to the placement of sterically bulky *tert*-butyl groups at the 3 and 6 positions on the dioxolene ring, preventing the formation of a bridging structure as seen in complexes such as  $[\text{MoO}(\text{3,5-DBCat})_2]_2$ .<sup>[58]</sup>

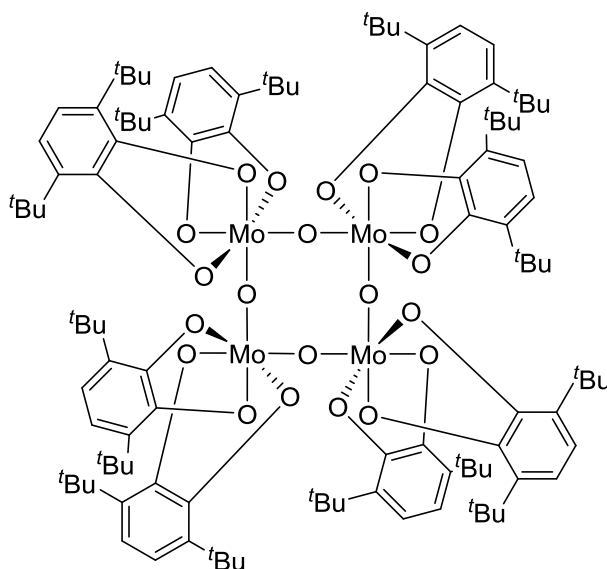
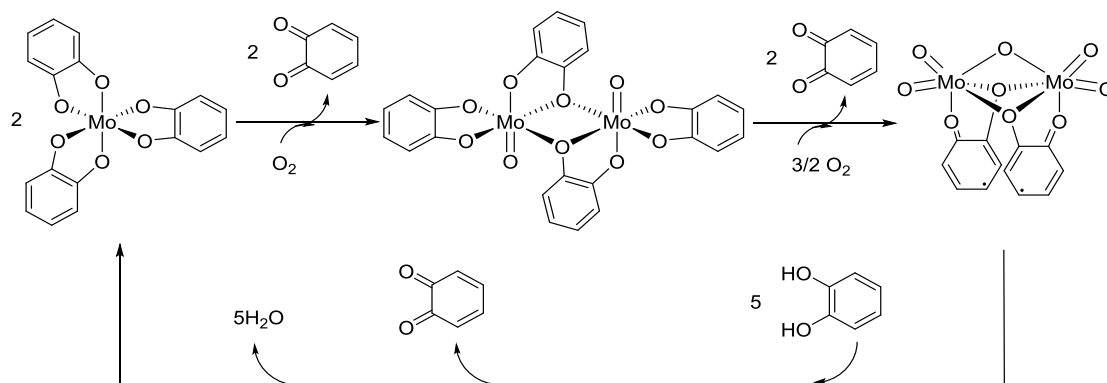


**Figure 1.10.** Chiral molybdenum catecholate tetramer.

The same group also report that Mo dioxolene complexes readily undergo interconversion between different products upon exposure to atmospheric  $\text{O}_2$ . Starting from the monomeric  $[\text{Mo}(\text{Cat})_3]$ , the addition of one equivalent of  $\text{O}_2$  results in the

oxidation of two catechols to benzoquinone and the formation of a dimeric intermediate bridged by two catechol ligands. An additional  $3/2$  equivalents of  $O_2$  can then oxidise two further catechol ligands to afford a *bis*(SQ) dimer containing four terminal oxo groups and one bridging oxo group. Supplying excess catechol leads to an overall catalytic cycle that converts catechol into benzoquinone (**Scheme 1.11**).<sup>[59]</sup>



**Scheme 1.11.** Catalytic oxidation of catechol with  $[Mo(Cat)_3]$ .

Cotton *et al.* synthesised a family of tetramolybdenum complexes, consisting of two quadruply bonded Mo-Mo dimers bridged by a tetraoxolene bearing H, Cl or  $NO_2$  groups at the 3 and 6 positions (**Figure 1.11**). Oxidation of these complexes can be achieved by addition of excess  $[FeCp_2]PF_6$  or  $AgBF_4$ . Cyclic voltammetry reveals three reversible one-electron oxidations (-1.115, -0.940, and -0.872 mV respectively), corresponding to the  $Cat \rightarrow SQ$  ligand oxidation and two metal based oxidations. The  $\Delta E_{1/2}$  values for the two Mo centred redox steps (763-816 mV depending on R substituent) are large, giving comproportionation constants of an order of  $10^{13}$ , indicating a high degree of delocalisation and essentially pure class III Robin-Day character.<sup>[60]</sup>

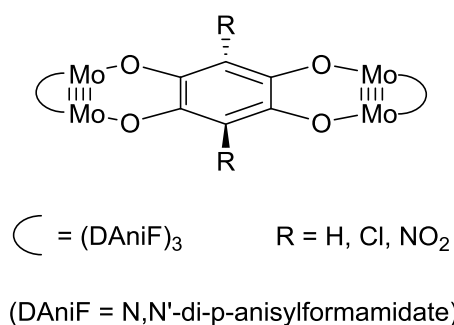
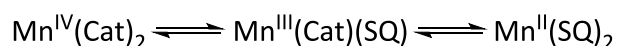


**Figure 1.11.** Tetramolybdenum tetraoxolene complex.

### 1.5.4 Mn, Tc and Re

Manganese, like cobalt, is an inherently suitable metal for the study of valence tautomerism. This is due to its wide number of available oxidation states, and the fact that the vibrational contribution to the entropy is larger in Mn(II) complexes, providing a thermodynamic driving force for thermal VT transition.<sup>[3]</sup> Manganese differs from cobalt in *bis*(dioxolene) complexes because both dioxolenes undergo electron transfer, cycling the metal through three oxidation states instead of two. There is also no change in spin state as would be expected with cobalt, thus its general VT behaviour can be summarised in **Scheme 1.12**:

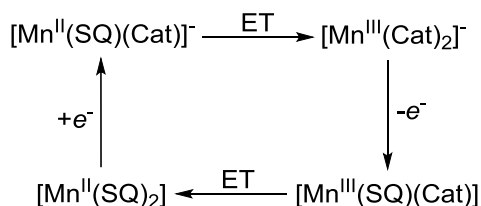


**Scheme 1.12.** Valence tautomeric transitions of Mn(Cat)<sub>2</sub>.

Thermal VT transitions have been reported for the complex [Mn(cth)(3,5-DBdiox)]<sup>+</sup> (cth = (*dl*)-5,7,7,12,14,14-hexamethyl-1,4,8,11-tetraazacyclotetradecane).<sup>[61]</sup> As with other complexes, the solvent used in the reaction has a large effect on which tautomer is formed, with highly polar solvents favouring [Mn<sup>III</sup>(cth)(DBCat)] and weakly polar solvents favouring [Mn<sup>II</sup>(cth)(DBSQ)]. This is due to polar solvents favouring the formation of the most polar form of the complex (in this case the Mn(III) form).

This group shares many of the same properties as the previous one, such as the first row metal often having different electrochemical properties to the metals below it. Mn typically has a lower oxidation state, and the separation between the metal and

dioxolene frontier orbitals is narrower. When  $M = \text{Mn}$  in the complex  $[\text{M}^{\text{IV}}(\text{DBCat})_3]^{2-}$  electrochemical oxidation occurs irreversibly on the catechol ligand to produce  $[\text{M}^{\text{III}}(\text{DBCat})_2]^-$  and DBBQ. However when  $M = \text{Tc}$  or  $\text{Re}$ , a reversible metal based  $\text{M}(\text{IV})/\text{M}(\text{V})$  couple exists, allowing  $[\text{M}^{\text{V}}(\text{DBCat})_3]^-$  to be accessed. Further oxidation of the Mn complex leads to a similar redox cycle to the case of vanadium (**Scheme 1.13**).<sup>[62-64]</sup>



**Scheme 1.13.** Redox cycle of a *bis*(dioxolene) complex of manganese.

The intramolecular electron transfer steps observed here imply that the metal/ligand electronic levels are discrete, with little delocalisation between the constituent orbitals. This gives complexes of this type an inherent bistability between tautomeric forms differing in charge distribution.

Manganese analogues of cobalt coordination polymers have also been explored,<sup>[65]</sup> leading to the synthesis of one dimensional Mn polymers with a dinuclear repeat unit, such as  $[\text{Mn}_2(\text{NLN})(\text{Cl}_4\text{-diox})_2]_n$  (**Figure 1.12**).<sup>[66]</sup>

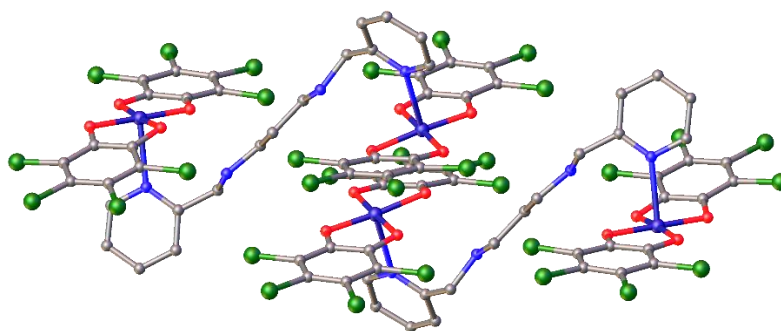
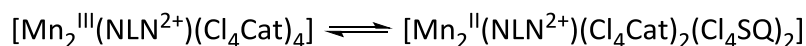


**Figure 1.12.** Single crystal X-ray structure of  $[\text{Mn}_2(\text{NLN})(\text{Cl}_4\text{-diox})_2]_n$  at 180 K. Image reproduced from Banerjee *et al.*<sup>[66]</sup>

---

This 1D coordination polymer also undergoes thermal VT transition in the temperature range of 298-338 K, described by **Scheme 1.14**:



**Scheme 1.14.** Thermal VT transition of  $[\text{Mn}_2(\text{NLN})(\text{diox})_4]$ .

### 1.5.5 Fe, Ru, and Os

The metals located further to the right side of the d block have more varied dioxolene chemistry, and the electrochemical properties of these complexes can be complicated by the emergence of competing valence tautomeric forms of the same complex.

Until the work of Banerjee in 2004,<sup>[67]</sup> it was thought that VT transitions could not occur in complexes of iron, because the entropic driving force for the reaction is considerably weaker than for cobalt.<sup>[68]</sup> Support for this argument comes from the fact that there is little difference in Fe-O bond distances in high spin Fe(II) and Fe(III) complexes (0.03 Å) when compared to the difference between low spin Co(III) and high spin Co(II) (0.2 Å). Antiferromagnetic coupling between high spin Fe(II) centres and the semiquinonate ligands does not lead to an increase in spin degeneracy accompanying the VT transition as it does in the cobalt case, resulting in a smaller electronic contribution to the entropy as well.

However, the observation of isosbestic points in the visible and near IR electronic absorption spectra of  $[\text{Fe}(\text{bispicen})(\text{Cl}_4\text{SQ})(\text{Cl}_4\text{Cat})]$  at 298-338 K provides evidence of thermally induced VT in this Fe complex. Magnetic susceptibility between 50-300 K shows an  $S = 2$  temperature independent ground state assigned to a high spin Fe(III) centre antiferromagnetically coupled to a semiquinonate ligand. It is notable that the perchlorinated dioxolene ligand of the complex is highly electron withdrawing, in contrast to the electron donating dioxolenes used to facilitate oxidation to the semiquinonate form for VT cobalt systems.

$[\text{Fe}(\text{tpa})(\text{diox})](\text{BPh}_4)$  is also notable because its crystal structure contains two distinct sites which have been observed to undergo a thermal transition in a two-step manner. Density functional calculations suggest that both HS and LS forms of this complex

---

exist as a mixture of Fe(III)-Cat and Fe(II)-SQ, therefore while SCO does occur there lacks evidence for a VT transition.<sup>[69]</sup>

The study of Fe catechol complexes has also often had a focus on the biological role of these molecules. Many microorganisms employ chelating catechol-derived siderophores to bind, dissolve and transport Fe(III). The siderophore known as enterobactin is the strongest binding ligand for Fe(III) that is currently known, with a  $K_f$  of  $10^{49}$  (**Figure 1.12**).<sup>[70-71]</sup>

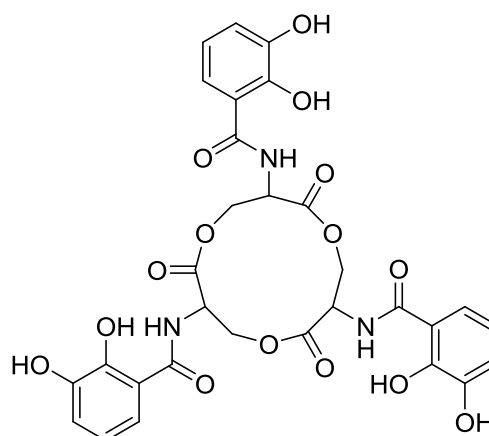


**Figure 1.12.** Enterobactin structure, containing three catechol groups.

Much of this affinity arises from the preference of Fe(III) for hard O ligands, however other related chelating *tris*(Cat) ligands such as TRENCAM (*N,N,N'*-(nitrilotri-2,1-ethanediyl)tris[2,3-dihydroxybenzamide]) have lower ( $10^{43.6}$ ) formation constants,<sup>[71-72]</sup> suggesting there may be a steric or conformational driving force at play too. This hypothesis has been investigated, with protein studies showing that the natural  $\Delta$ -*cis* form of enterobactin binds more strongly to receptors than its enantiomer.<sup>[73]</sup> *In silico* molecular mechanics studies also show that this  $\Delta$ -*cis* conformation contains important structural hydrogen bonds between the N-H protons and the catechol O donor atoms, increasing the stability of the complex.<sup>[74]</sup> Crystallographic studies have shown that the TRENCAM ligand adopts a distorted octahedral geometry around the Fe(III) centre, due to it being slightly too small.<sup>[74]</sup> Enterobactin on the other hand has a large enough central ring to adopt the preferred rigorously octahedral geometry

---

around the metal ion. It is a combination of these factors that ultimately lead to the extremely strong binding affinity of enterobactin to Fe(III).

Several examples of VT transitions in ruthenium 9,10-phenanthrenequinone complexes have been reported.<sup>[75-76]</sup> Ruthenium differs from other metals in this group as it has tendency for the dioxolene to coordinate as the benzoquinonate form rather than the catecholate.

Other developments in this area include the study of  $[\text{Ru}(\text{NH}_3)_4(3,5\text{-dbdiox})](\text{PF}_6)_2 \cdot \text{H}_2\text{O}$  and  $[\text{Ru}(\text{NH}_3)_4(\text{diox})](\text{BPh}_4)_2 \cdot \text{H}_2\text{O}$ , which show a mixture of the LS-Ru(II)-BQ and LS-Ru(III)-SQ forms in the solid state, without temperature dependence.<sup>[77]</sup> As with other VT complexes, this system is highly sensitive to solvents, with the LS-Ru(II)-BQ tautomer favoured by solvents with smaller donor number, and LS-Ru(III)-SQ favoured by larger donor number.

## 1.5.6 Co, Rh and Ir

### 1.5.6.1 Mononuclear Cobalt Dioxolene Complexes

Co has been one of the most well explored metals in the context of dioxolene chemistry, and all three metals in this group have been shown to display dioxolene-centred redox activity when coordinated by a single dioxolene ligand. Cobalt is intrinsically a good candidate metal to study because it undergoes spin transition from low spin to high spin when a thermal VT transition occurs, enhancing the vibrational and electronic components of the entropy associated with the Gibbs free energy.

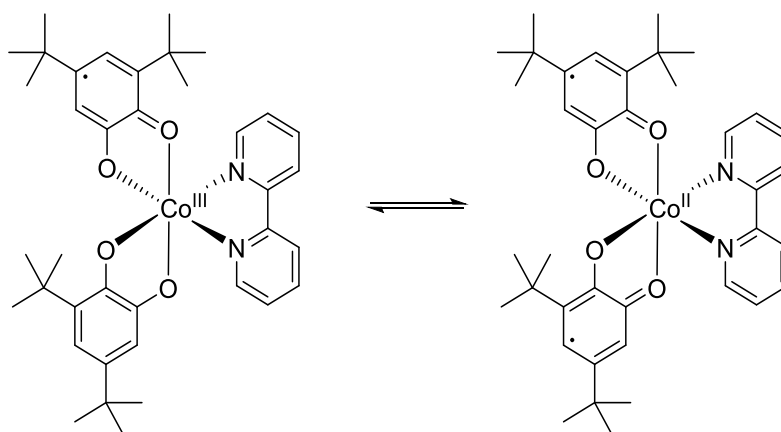
A wide range of N and S-donor co-ligands are tolerated, e.g. in the case of  $[\text{Co}(\text{trien})(\text{DBSQ})]^{2+}$  which shows a characteristic SQ radical EPR spectrum with weak coupling to the  $^{59}\text{Co}$  ( $I = 7/2$ ) nucleus.<sup>[78]</sup> Divalent Rh/Ir complexes are also accessible but are less stable than their Co analogues. One such example is that of  $[\text{Rh}_2(\mu\text{-S})(\mu\text{-dmp})_2(\text{CO})_2]$ , which may undergo oxidative addition of  $\text{Cl}_4\text{BQ}$  to give  $[\text{Rh}_2(\text{Cl}_4\text{Cat})(\mu\text{-S})(\mu\text{-dmp})_2(\mu\text{-CO})(\text{CO})]$ , a mixed-valent Rh(III)-Rh(I) compound.<sup>[79]</sup>

These metals have also shown great promise in the development of VT, and provide the first reported example of a tautomeric equilibrium wherein oxidation of the

---

dioxolene leads to reduction of the metal (and *vice versa*).<sup>[80]</sup> As with the earlier metal series discussed, the key property that ultimately causes the complexes to show this behaviour is the similarity between the orbitals energies of the dioxolene and metal.<sup>[81]</sup>

The first example of a valence tautomeric dioxolene complex was discovered by Pierpont in 1980.<sup>[81]</sup> In toluene solution  $[\text{Co}(2,2'\text{-bpy})(3,5\text{-DBSQ})(3,5\text{-DBdiox})]$  exists in an equilibrium with  $[\text{Co}(2,2'\text{-bpy})(3,5\text{-DBSQ})_2]$ , undergoing rapid conversion between these two forms (**Scheme 1.15**).



**Scheme 1.15.** Two valence tautomeric forms of  $[\text{Co}(2,2'\text{-bpy})(3,5\text{-DBSQ})(3,5\text{-DBdiox})]$ .

Of important note is that the central cobalt ion undergoes metal-ligand electron transfer during this process, either accepting an electron from the catecholate or donating an electron to the semiquinone. A spin transition accompanies this electron transfer, with the Cat-SQ form occupying a low spin configuration and the  $(\text{SQ})_2$  form occupying a high spin configuration (**Figure 1.13**).



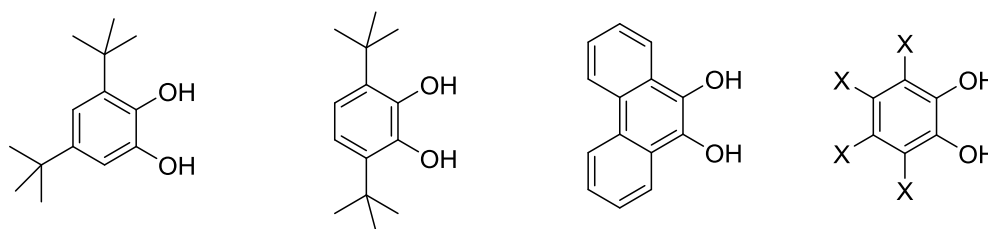
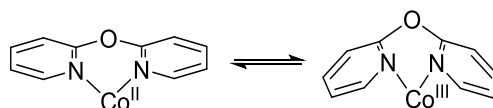


**Figure 1.14.** Commonly used dioxolene ligands for VT Co complexes. Left to right; 3,5-di-*tert*-butyl-CatH<sub>2</sub>, 3,6-di-*tert*-butyl-CatH<sub>2</sub>, phenCatH<sub>2</sub> and X<sub>4</sub>CatH<sub>2</sub> (X = Cl, Br).

VT transitions in cobalt dioxolene complexes can be induced thermally. This is primarily an entropically driven process due to a higher density of vibrational states and spin state degeneracy in the HS (SQ) tautomer.<sup>[9]</sup> VT transition can also be induced by application of pressure, magnetic field, or by irradiation with visible light or soft X-rays.

Solvent incorporation into the crystal lattice has been shown to be very influential over VT behaviour in the solid state.<sup>[86-87]</sup> The first example of a two-step VT transition was in [Co(Me<sub>2</sub>tpa)(3,5-dbdiox)]PF<sub>6</sub>·toluene which contains two crystallographically distinct complex environments which undergo thermal transition at different temperatures.<sup>[88]</sup> So-called “chemical pressure” from solvent molecules in the lattice can be responsible for the inhibition of VT transition in similar complexes, due to steric clashing preventing a bond length increase associated with the transition.<sup>[89]</sup>

Another factor that can influence the ability of a complex to undergo VT transition is cooperativity. Cooperativity describes situations where structural features such as ancillary ligands or changes in adjacent complexes in the crystal lattice can enhance the VT behaviour of a complex. The first reported example of this was for [Co(py<sub>2</sub>O)(3,6-DBSQ)(3,6-DBdiox)], which has a wide thermal VT transition hysteresis (100-330 K) which is the result of the py<sub>2</sub>O ligands undergoing conformational change when VT transition occurs.<sup>[90]</sup> In the Co(II) form, the py<sub>2</sub>O ligand is planar, but in the Co(III) form it is folded to encapsulate the smaller ion (Scheme 1.16).



**Scheme 1.16.** Change in geometry of a py<sub>2</sub>O ligand as a result of a VT transition.

Shultz *et al.* have also demonstrated strong cooperativity effects in their study of *trans*-[Co(4-CNpy)<sub>2</sub>(3,5-DBSQ)(3,5-DBdiox)] and related complexes. When quenched from 298 K to 10 K, thermal trapping of the HS-Co(II)-SQ tautomer occurs due to intramolecular hydrogen bonding between metal centres stabilising the Co(II) form.<sup>[91-92]</sup> This thermally trapped state can be prevented from forming by disrupting this hydrogen bonding with solvent intercalation of toluene, referred to as “lattice softening”. The group has explored the inclusion of several different solvents, confirming that this unusual VT behaviour only occurs when the complex molecules are directly hydrogen bonded to one another. It has been theorised that both tautomers are stabilised by this hydrogen bonding, with the activation energy for elongation of the Co-O/N bonds being lowered.

This complex is also of interest because the HS-Co(II)-SQ tautomer can be photogenerated at 10 K, and does not return to the LS-Co(III)-SQ state until the temperature is raised past 90 K. When the complex is continuously irradiated while the temperature is varied, a light-induced thermal hysteresis loop is observed. Below 50 K, the HS-Co(II)-SQ tautomer has a considerably lower relaxation rate than any other VT complex reported to date.

VT transitions can also be tuned by modifying the ancillary ligand used. A representative example of this can be shown with macrocyclic ligands such as cth, cyclam or tpa derivatives. Macrocycles have been demonstrated to grant additional stability to one of the tautomers,<sup>[93]</sup> and small changes to the ancillary ligand such as methylation (in the case of tpa) can lead to steric crowding which in turn affects the charge distribution on the dioxolene ligand. This line of investigation has been expanded upon more recently with the synthesis of complexes containing ligands of the form Pz<sub>n</sub>Py<sub>3-n</sub> (**Figure 1.15**).<sup>[94]</sup>

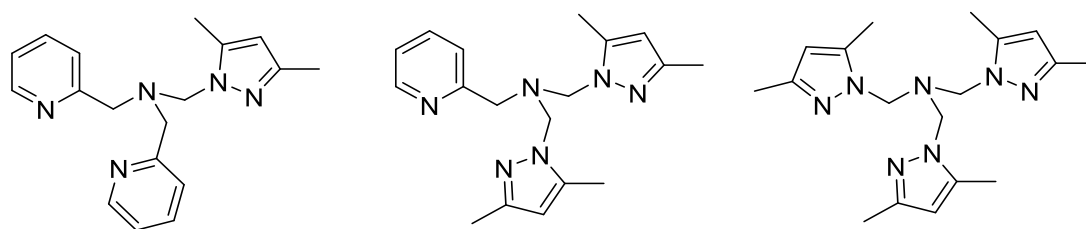


**Figure 1.15.** Left to right; PzPy<sub>2</sub>, Pz<sub>2</sub>Py, and Py<sub>3</sub>.

Similarly to the case with methyl substituted tpa derivatives, introducing more methyl groups in the form of pz moieties leads to increased steric hindrance on the dioxolene ligand, affecting the electronic state of the complex. The PzPy<sub>2</sub> form stabilises the LS-Co(III)-Cat tautomer, while Pz<sub>2</sub>Py and Pz<sub>3</sub> stabilise the HS-Co(II)-SQ tautomer.

When highly electron withdrawing dioxolenes have also been studied in complexes such as [Co(Me<sub>3</sub>tpa)(Cl<sub>4</sub>-diox)]<sup>+</sup>, it was predicted that any fewer than 3 methyl groups would lead to a loss of VT behaviour, and this was later confirmed experimentally. Panja *et al.* have investigated perbromodioxolene complexes of cobalt, finding that the use of 8-aminoquinolene and pyrimidine ancillary ligands in complexes of the form [CoL(Br<sub>4</sub>-diox)]<sup>+</sup> results in redox activity, but use of other ancillary ligands such as phen and en renders the complexes redox inactive.<sup>[95]</sup>

In 2010, Krüger *et al.* reported the complex shown in **Figure 1.16**. When R = <sup>t</sup>Bu, the Co ion remains in the +2 oxidation state at all temperatures, making this is the first reported Co dioxolene that undergoes VT without undergoing SCO transition. The analogous complex with R = Me has markedly different properties, because it remains in the diamagnetic LS Co(III) catechol state at all temperatures. This difference is due to steric considerations, as the bulkier <sup>t</sup>Bu groups clash with the dioxolene ligand leading to increased Co-N bond length, weakening the ability for the dioxolene to donate electron density to the metal and reducing the ligand field strength of the macrocycle.<sup>[96]</sup>

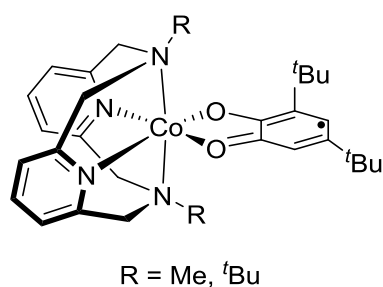


**Figure 1.16.** Cobalt semiquinonate complex which undergoes SCO without VT transition.

### 1.5.6.2 Dinuclear Cobalt Dioxolene Complexes

The development and study of dinuclear dioxolene complexes is an important advancement to the field and allows for a greater array of accessible VT transitions. In the simplest case, a dinuclear complex may exist in three states; HS-HS, HS-LS or LS-LS. Complexes of this type also open up the possibility for intramolecular electron transfer, which in practice can play a large role in the electronic behaviour.

Broadly speaking there have been two approaches to synthesising dinuclear complexes. One of these is to use a bidentate bipyridyl or imidazolyl ancillary ligand (**Figure 1.17**), while the other is to use a bidentate redox-active dioxolene.

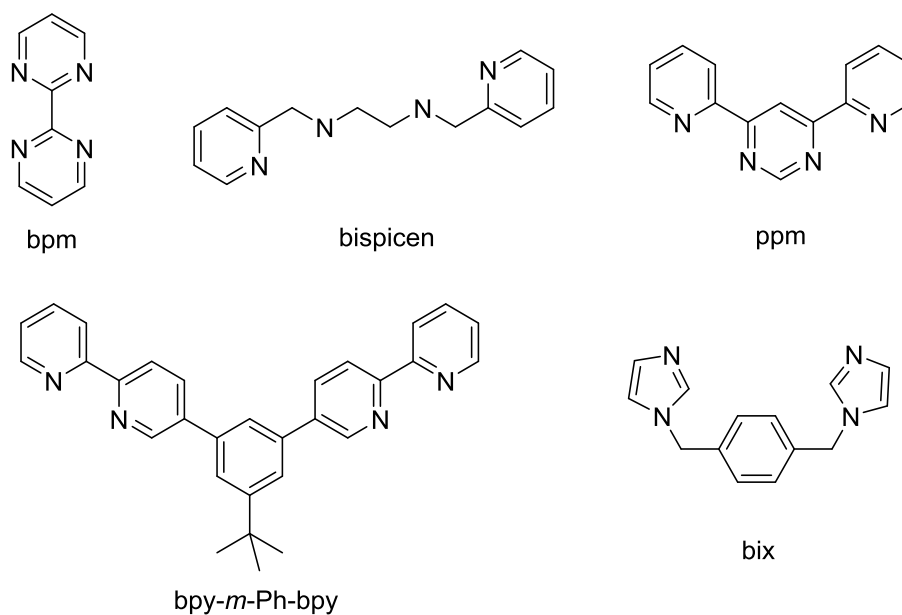


**Figure 1.17.** Bidentate bipyridyl/imidazolyl ancillary ligands.

Complexes of cobalt with bidentate *para*- and *meta*-phenylene bridged 2,2'-bipyridine linkers and 3,5-DBdiox ligands have been synthesised, and while they undergo VT transitions from the III to II oxidation state, these occur in a one-step rather than two-step fashion.<sup>[97]</sup>

[(Co(3,5-DBSQ)ppm(3,5(DBdiox)))] displays the more interesting property of undergoing a two-step transition across the temperature range of 88-428 K, with an intermediate mixed-valent state as shown by near infrared spectroscopy (**Figure 1.18**).<sup>[98]</sup>

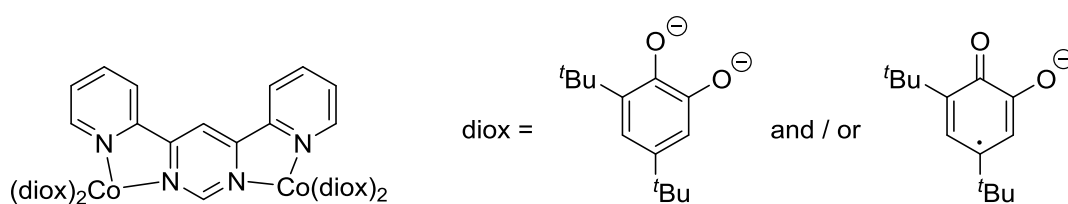


**Figure 1.18.** Two-step VT transition of [(Co(3,5-DBSQ)ppm(3,5(DBdiox)))].

It should be noted that at 88 K the transition to the (Cat)<sub>2</sub> state is incomplete.<sup>[99]</sup>

The other way to produce dinuclear complexes is through the use of bidentate *bis*(dioxolene) or tetraoxolene ligands. Some of the more well studied examples are shown in **Figure 1.19**.

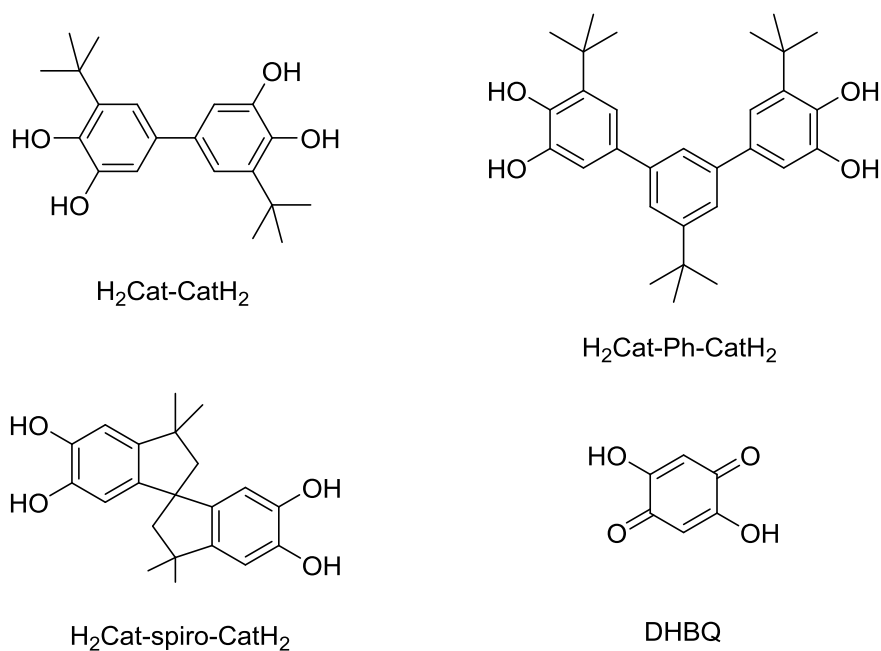


**Figure 1.19.** Bidentate *bis*(dioxolene) or tetraoxoelene ligands.

A major breakthrough was made with the synthesis of Co complexes of the spiroconjugated ligand H<sub>2</sub>Cat-spiro-CatH<sub>2</sub> (**Figure 1.20**).

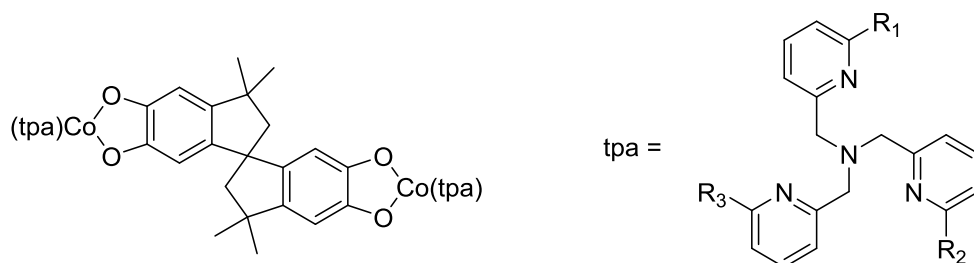


**Figure 1.20.** Cobalt complex with a spiroconjugated dioxolene ligand. R = Me or H.

These complexes provided the first example of a two-step (thermal) VT transition in the solution phase (butyronitrile) when R<sub>1</sub> and R<sub>2</sub> = Me and R<sub>3</sub> = H. The authors proposed that the two-step transition is a result of spiroconjugation of the *bis*(dioxolene) mediating thermally activated coupling between the two Co centres.<sup>[100]</sup>

### 1.5.6.3 Dinuclear Cobalt Tetraoxolene Complexes

The *bis*-bidentate tetraoxolene ligand DHBQ has been employed as a bridging ligand for dinuclear complexes of cobalt, with *cth*, *tpa* and *dpqa* ancillary ligands.<sup>[101]</sup> The most significant of these compounds is  $[(\text{Co}(\text{tpa}))_2(\text{DHBQ})](\text{PF}_6)_3$  which has a wide thermally induced VT transition hysteresis at room temperature (310 K for heating, 297 K for cooling, **Figure 1.21**).<sup>[102]</sup>

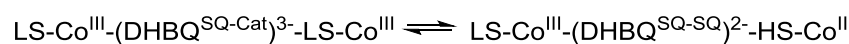
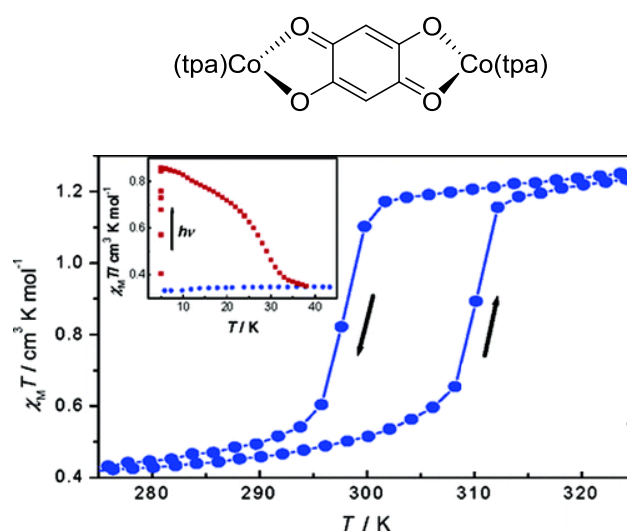


**Figure 1.21.** Structure and thermal VT transition hysteresis of  $[(\text{Co}(\text{tpa}))_2(\text{DHBQ})](\text{PF}_6)_3$ . Graph reproduced from Tao *et al.*<sup>[102]</sup>

The crystal structure of this complex shows molecular stacking such that the complexes are aligned head-to-waist in two dimensional sheets separated by  $\text{PF}_6$  counterions. This head-to-waist stacking offsets  $\pi$ - $\pi$  interactions between the pyridyl rings of the ancillary ligand and the tetraoxolene, which contributes to producing the observed hysteresis (**Figure 1.22**).

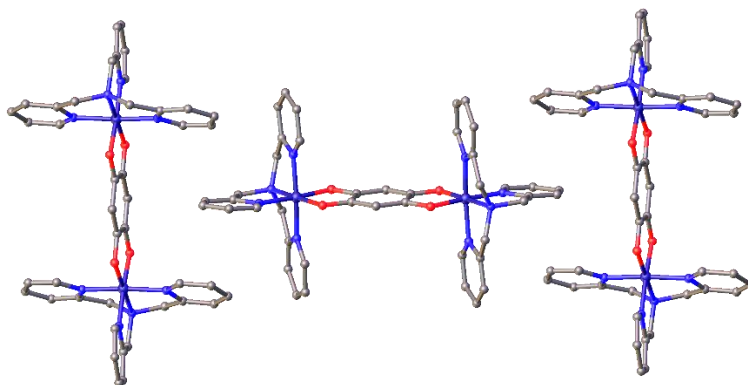
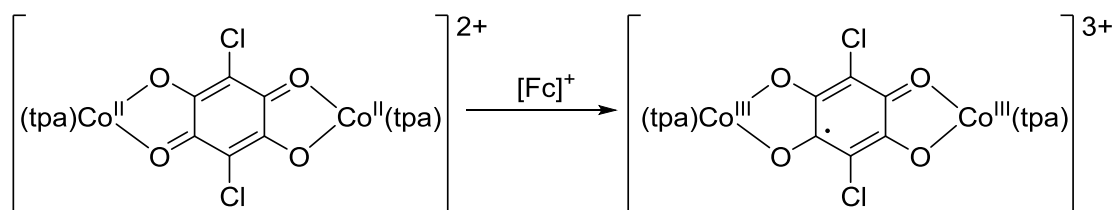


**Figure 1.22.** Single crystal X-ray structure of  $[(\text{Co}(\text{tpa}))_2(\text{DHBQ})](\text{PF}_6)_3$  showing head-to-waist packing.

This system is highly sensitive to changes in the counterion and ancillary ligands, with transition temperature and hysteresis width exhibiting a large degree of variability.<sup>[87, 103-104]</sup> In particular,  $[(\text{Co}(\text{pmea}))_2(\text{DHBQ})](\text{BF}_4)$  is mixed-valent with well defined HS-Co(II) and LS-Co(III) centres (as shown by crystallographic bond lengths) at temperatures above 173 K.<sup>[105]</sup> Below this temperature, the complex exists in the LS-Co(III)-(DHBQ-SQ-Cat)<sup>3-</sup>-LS-Co(II) form as previously described in the analogous complex.

#### 1.5.6.3.1 Redox Induced Electron Transfer

Redox induced electron transfer (RIET) describes a process whereby an oxidation or reduction leads to a subsequent electronic redistribution inside the molecule.<sup>[29]</sup> An example of RIET can be seen in the one-electron oxidation of one cobalt centre in the dinuclear complex  $[(\text{Co}(\text{tpa})_2)\text{tetoxCl}_2]^{2+}$  with ferrocenium. This oxidation leads to a second one-electron oxidation on the opposite Co centre and a one-electron reduction of the bridging tetraoxolene ligand (**Scheme 1.17**).<sup>[29, 106]</sup>

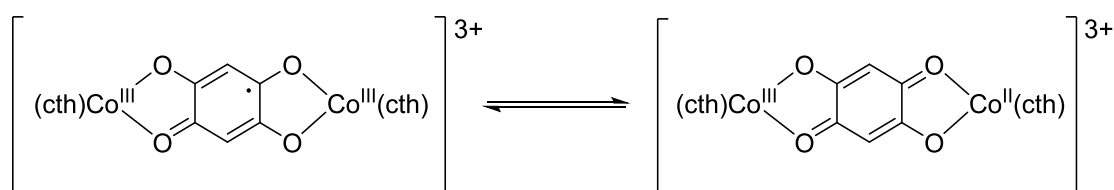


**Scheme 1.17.** RIET of  $[(\text{Co}^{\text{II}}(\text{tpa}))_2\text{tetoxCl}_2]^{2+}$  to form  $[(\text{Co}^{\text{III}}(\text{tpa}))_2\text{tetoxCl}_2]^{3+}$ .

---

An analogous RIET is observed when Co(II) is replaced with Fe(II) and H-substituted tetraoxolene is used as the bridging ligand, with cth ancillary ligands.<sup>[99]</sup>

Valence tautomeric transitions have also been shown to accompany RIET. In the dinuclear cobalt complex  $[(\text{Co}(\text{cth}))_2\text{tetox}]^{3+}$ , temperature dependent magnetic susceptibility shows that below 175 K it exists in its ground state as two Co(III) centres. Heating above 175 K leads to a hysteretic valence tautomeric spin transition to form the mixed-valent complex  $[(\text{cth})\text{Co}^{\text{III}}(\text{tetox})\text{Co}^{\text{II}}(\text{cth})]^{3+}$  (**Scheme 1.18**).<sup>[101]</sup>



**Scheme 1.18.** VT transition by RIET to form a mixed valent complex.

$[(\text{Co}(\text{cth}))_2\text{tetox}]^{3+}$  also undergoes reversible photoexcitation with 647 nm light.

#### 1.5.6.4 Oligomers of Cobalt Dioxolenes

Rentschler *et al.* published the first example of oligomeric Co dioxolene complex,  $[\text{Co}_3(3,5\text{-DBSQ})_2(\text{tBuCOO})_4(\text{NEt}_3)_2]$  (**Figure 1.23**), which shows no evidence of VT or spin crossover between the temperature range of 8-200 K. All three Co atoms are assigned as high-spin Co(II) due to their crystallographic bond lengths. The semiquinone ligands are thus acting in an innocent manner in this complex. The  $\chi_{\text{MT}}$  decreases non-linearly from  $12 \text{ cm}^3 \text{ K mol}^{-1}$  at 300 K down to  $1.1 \text{ cm}^3 \text{ K mol}^{-1}$  at 8 K. This decrease in  $\chi_{\text{MT}}$  can be rationalised by a combination of antiferromagnetic coupling and quenching of orbital angular momentum.<sup>[107]</sup>

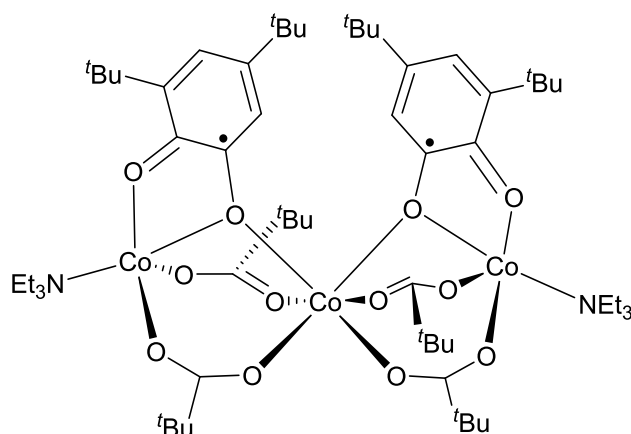


**Figure 1.23.** First reported oligomeric Co dioxolene complex.

The exchange can be described with a simplified model which includes a zig-zag chain of three  $S = 3/2$  and  $L = 1$  Co ions connected by  $S = 1/2$  O atoms, with four  $J$  values, as shown in **Figure 1.24**.

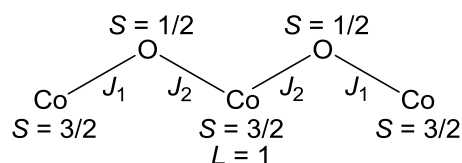
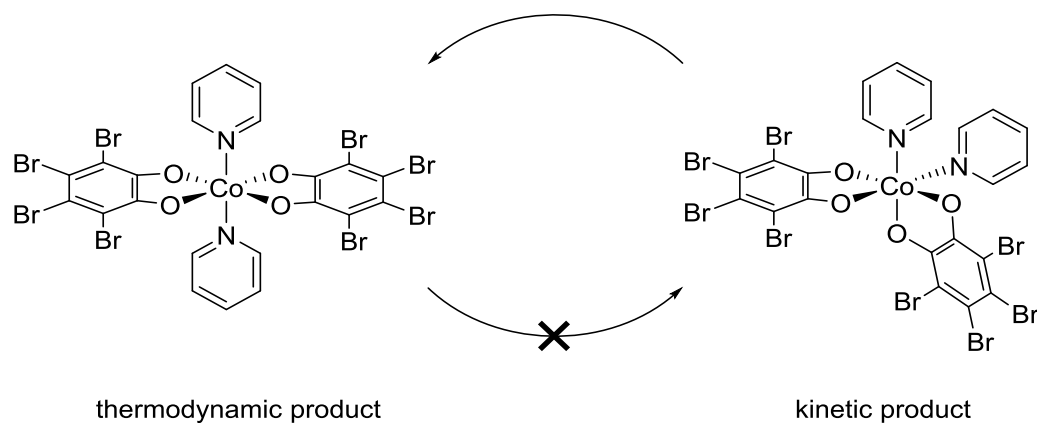


**Figure 1.24.** Model used to describe electronic exchange in the complex.

### 1.5.6.5 Hydrogen bonded networks

Recently published work by Mathonière *et al.* demonstrates the importance of the solvent choice in the formation of VT complexes which can potentially have network structures based on hydrogen bonding. Two Co(III) dioxolene complexes were discussed, the kinetic (*cis*) product is formed by crystallisation from methanol (polar protic solvent), whereas the thermodynamic (*trans*) product is formed by crystallisation from acetone (less polar aprotic solvent). The *cis* product undergoes slow conversion over time to the *trans* product in DMF solution (**Scheme 1.19**). Both complexes undergo thermal VT transition, however it is irreversible due to loss of solvent from the lattice.<sup>[108]</sup>



**Scheme 1.19.** Interconversion between the kinetic and thermodynamic product.

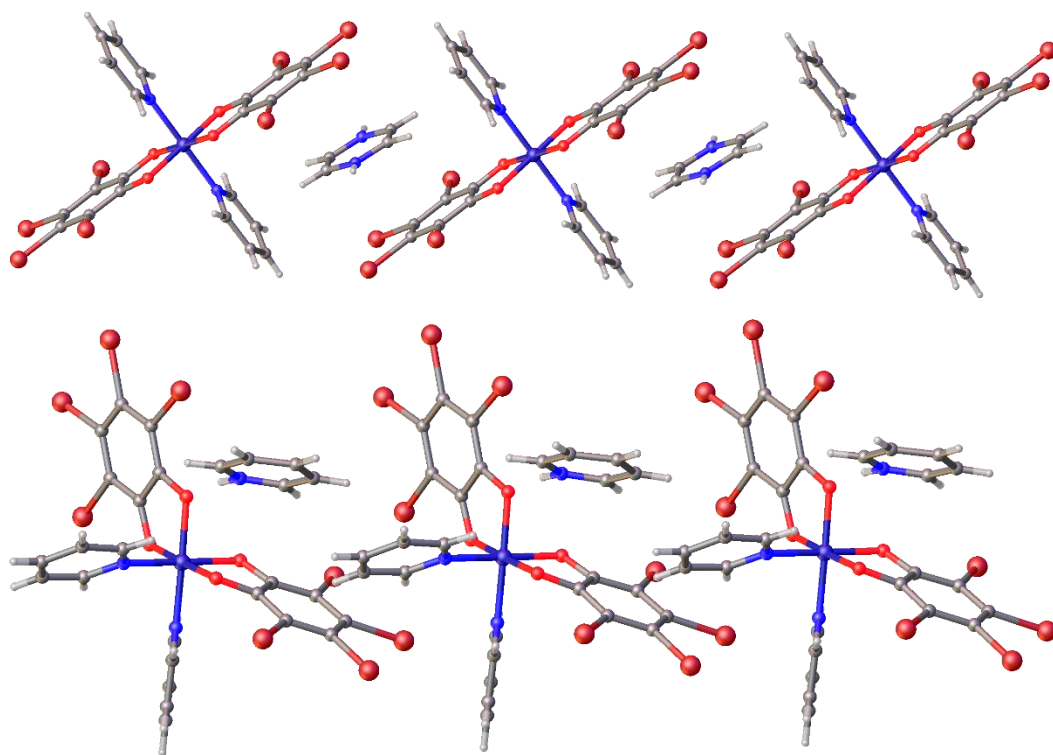


**Figure 1.25.** Comparison in the crystal packing between *trans* and *cis* forms of the same complex.

X-ray structures of the two isomers show 1D hydrogen bond networks through the pyridinium (**Figure 1.25**). In the *cis* structure the pyridinium has a  $\pi$ -stacking interaction to one complex and an edge-to-face interaction to the adjacent complex.

---

In the *trans* structure, the pyridinium has two  $\pi$ -stacking interactions between two adjacent complexes.

### 1.5.6.6 Coordination Polymers of Cobalt Dioxolenes

#### 1.5.6.6.1 Ditopic pyridyl linking groups

Inoue *et al.* reported the first example of a SCO Co coordination polymer  $[\text{Co}(\text{pyterpy})\text{Cl}_2]\text{MeOH}$  (**Figure 1.26**). It is a 1D chain with either methanol or water solvent molecules in the lattice. The structure includes intermolecular  $\pi$ - $\pi$  stacking to produce a pseudo-3D structure. Solvate choice is important as the methanol solvate always exists in the HS-Co(II) form, whereas the water solvate undergoes SCO with a  $T_{1/2}$  of 223 K.<sup>[109]</sup>

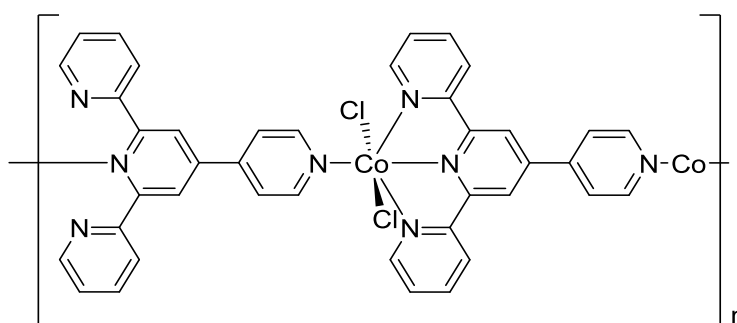


**Figure 1.26.** First reported example of a SCO Co coordination polymer.

While the direction of much research on VT complexes has involved increasing the number of metal centres from mononuclear to di/trinuclear complexes for the purpose of enhancing intramolecular cooperativity, more recently the interest in increasing the number of metal centres has led to the synthesis of VT coordination polymers. SCO coordination polymers are fairly well explored, with classical examples based on Prussian blue,<sup>[1]</sup> but valence tautomeric coordination polymers are rarer. The first reported 1D VT coordination polymer of Co was  $[\text{Co}(\text{pyz})(3,6\text{-DBSQ})(3,6\text{-DBdiox})]_n$  which is formed individual chains of repeating metal-pyrazine units, with equatorial dioxolenes (**Figure 1.27**).<sup>[110]</sup>

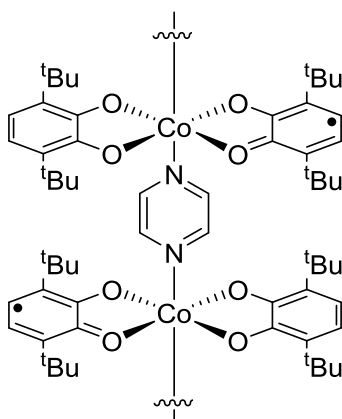


**Figure 1.27.** A section of repeating structure of  $[\text{Co}(\text{pyz})(3,6\text{-DBSQ})(3,6\text{-DBdiox})]_n$ .

This polymer undergoes VT transition from HS-Co(II)-SQ to LS-Co(III)-Cat between 350-5 K. Coordination polymers of this type (variations typically involve placement of the tertiary butyl groups on the dioxolene ring) undergo thermal VT transition between  $(\text{LS-Co(III)-Cat})_n$  and  $(\text{HS-Co(II)-SQ})_n$  without hysteresis. Upon irradiation with light a reversible photomechanical distortion occurs as a consequence of VT transition, leading to a 6% change in polymer length as a consequence of change in Co-N bond length.

Following this, subsequent 1D coordination polymers were found using similar synthetic methods. Replacing the pyrazine linker with one of a variety of ditopic *bis*(pyridyl) moieties. These all display thermal VT transition above 100 K. Linear pyridyl linkers lead to straight 1D chains, whereas bent linkers such as dpq (1,2-di-4-pyridinyl-1,2-ethanediol) lead to 1D zig-zag chains (**Figure 1.31**).

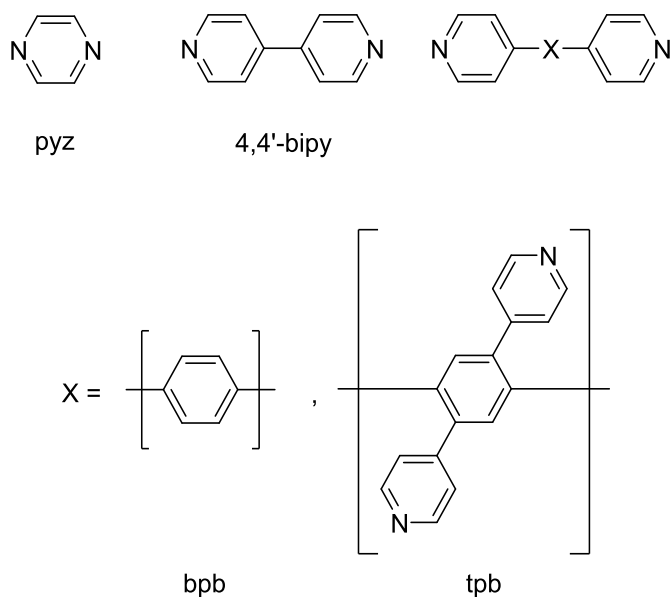


**Figure 1.28.** Ditopic aromatic pyridyl linking ligands for coordination polymers.

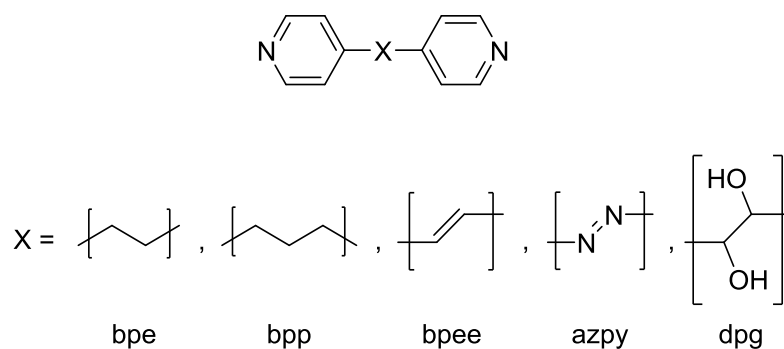


**Figure 1.29.** Ditopic pyridyl linking ligands for coordination polymers.

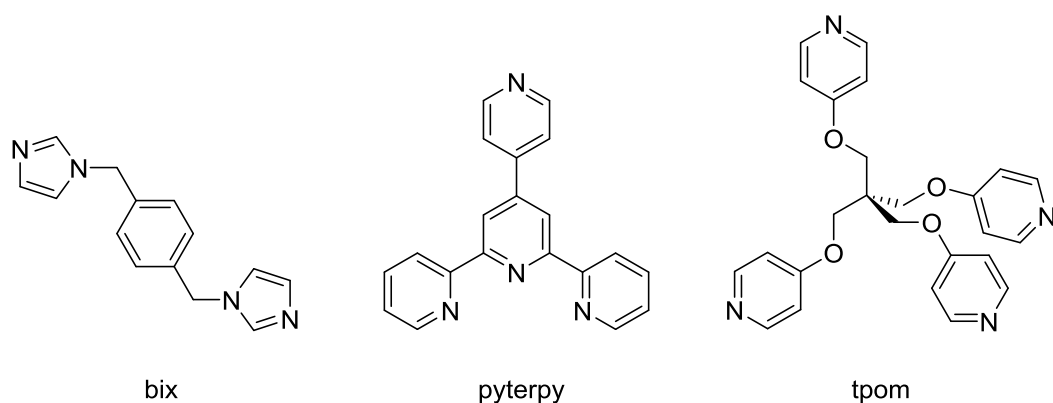


**Figure 1.30.** Other linking ligands for coordination polymers.

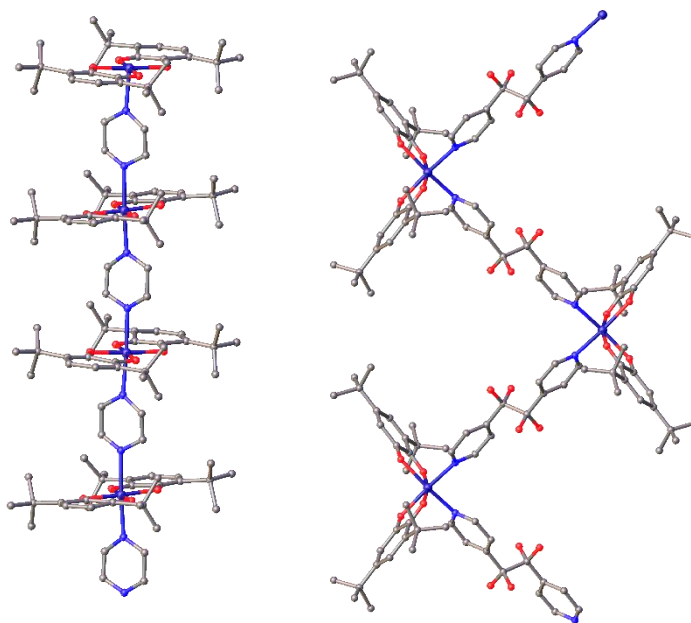


**Figure 1.31.** Crystal structures of a linear and zig-zag Co dioxolene coordination polymers.

Only one example of a two dimensional VT coordination polymer has been reported, that being  $[\text{Co}(\text{tpom})(3,5\text{-DBSQ})(3,5\text{-DBdiox})]_n$ .<sup>[111]</sup>

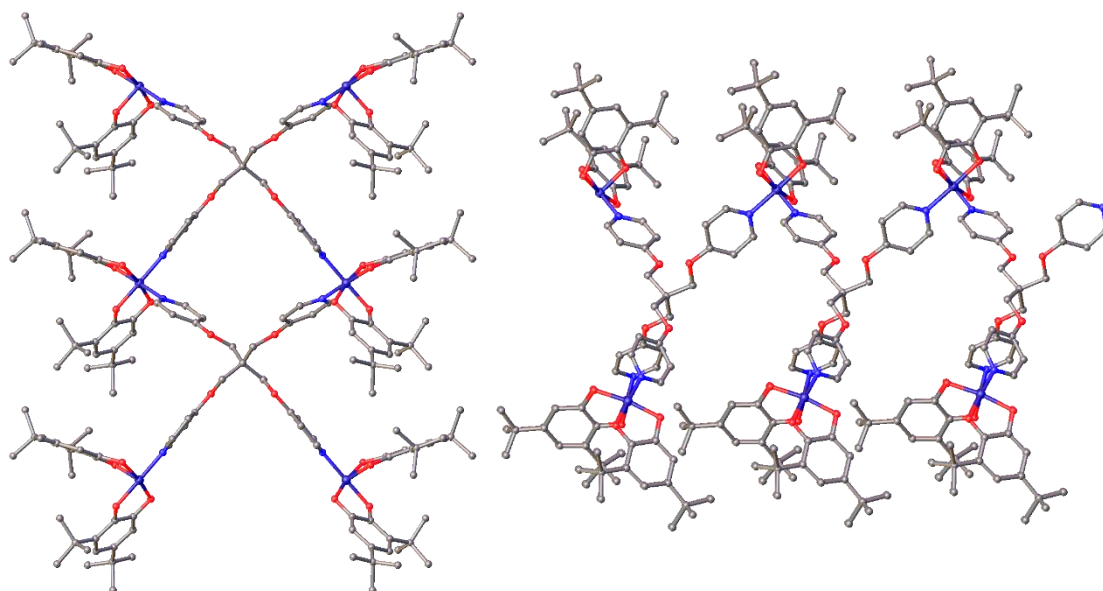


**Figure 1.32.** Crystal structure of  $[\text{Co}(\text{tpom})(3,5\text{-DBSQ})(3,5\text{-DBdiox})]_n$  showing its two dimensional structure from two angles.<sup>[111]</sup>

---

[Co(tpom)(3,5-DBSQ)(3,5-DBdiox)]<sub>n</sub> may undergo a thermal and photo-induced VT transition, although in the thermal case it is observed that solvent molecules incorporated within the structure are lost upon heating, leading to a very gradual profile. The ancillary ligand is flexible about the ether moiety, and hence there is little evidence of cooperativity.

#### 1.5.6.6.2 Ditopic dioxolene linking groups

Further to his investigation into coordination polymer nanoparticles, Ruiz-Molina has also developed a *bis*(Cat) ligand with imine linker (**Figure 1.33**). When coordinated to Co, the coordination polymer particle (CPP) product shows a pH-dependent spin transition. The imine bond can be hydrolysed by exposure to acidic conditions (pH 5), leading to a breakdown of the spherical nanoparticles into agglomerates. Hydrolysis of the imine bond leads to a different spin transition, providing a potential application as a molecular sensor (**Figure 1.34**).<sup>[112]</sup>

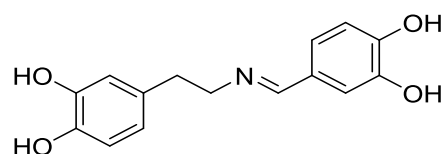


**Figure 1.33.** Ditopic dioxolene linking ligand for coordination polymers.

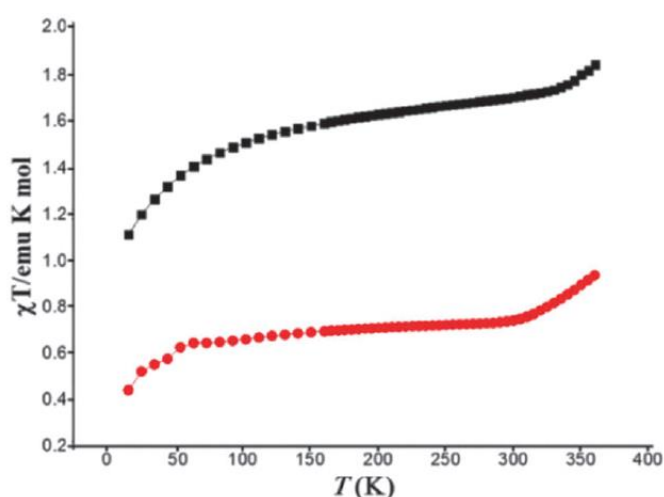


**Figure 1.34.** Black squares = before addition of acid. Red circles = after acidic (pH 5) treatment for 14 h. Reproduced from Ruiz-Molina *et al.*<sup>[112]</sup>

Dei *et al.* report a coordination polymer containing the bifunctional H<sub>2</sub>-Cat-spiro-Cat-H<sub>2</sub> ligand as a crosslinker, with the remaining Co coordination sites filled with chelating bipyridyl based ligands (**Figure 1.36**).<sup>[113]</sup>

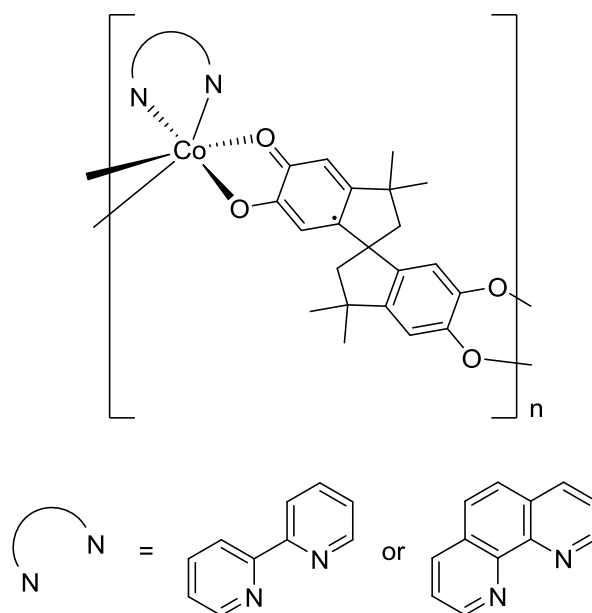


**Figure 1.36.** Co coordination polymer with a spiroconjugated *bis*(dioxolene) ligand.

As is common in these coordination polymers, the product is insoluble and amorphous, with the structure (only) being assigned by elemental microanalysis. The  $\chi_{MT}$  curve is dominated by antiferromagnetic coupling at temperatures  $>25$  K, and by a temperature induced VT transition from the Co(III)-Cat-SQ-Co(III) form to the Co(II)-(SQ)<sub>2</sub>-Co(II) form between 210 and 320 K. The mixed valency is assigned as class I due to the poor orbital overlap between the orthogonal dioxolene groups on the ligand.

The low temperature magnetic susceptibility can be fitted to the following Bleaney-Bowers equation.

$$\chi T = \frac{Ng^2\beta^2}{k} \left[ \frac{1}{3 + \exp\left(\frac{J}{kT}\right)} \right] (1 - \rho) + \rho \frac{Ng^2\beta^2}{2k}$$

**Equation 1.1.** Bleaney-Bowers equation for the complex.

---

Where  $\rho$  accounts for a small fraction of paramagnetic impurity (suggested to be HS-Co(II)) and  $J$  is the isotropic exchange Hamiltonian  $\mathbf{H}_{HDVV} = JS_1S_2$ , with  $g = 1.998$ ,  $J = 12.5$  and  $\rho = 0.113$ .

#### 1.5.6.6.3 Bifunctional linking groups

Thus far, all of the coordination polymers discussed fall into one of two structural categories. Either they contain one or more mono-dioxolene ligands and a linking group consisting of two or more pyridyl or pyrazolyl moieties, or they contain a *bis*(dioxolene) linker with additional pyridyl ligands occupying the remaining metal coordination sites. Ruiz-Molina *et al.* have worked towards developing a different strategy, namely to produce a linking group which contains both catechol and pyridyl functionalities connected by an alkyl chain (pbdH<sub>2</sub>, **Figure 1.29**).

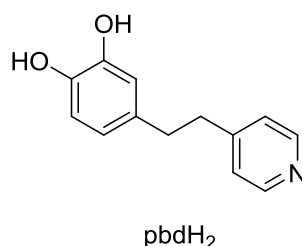


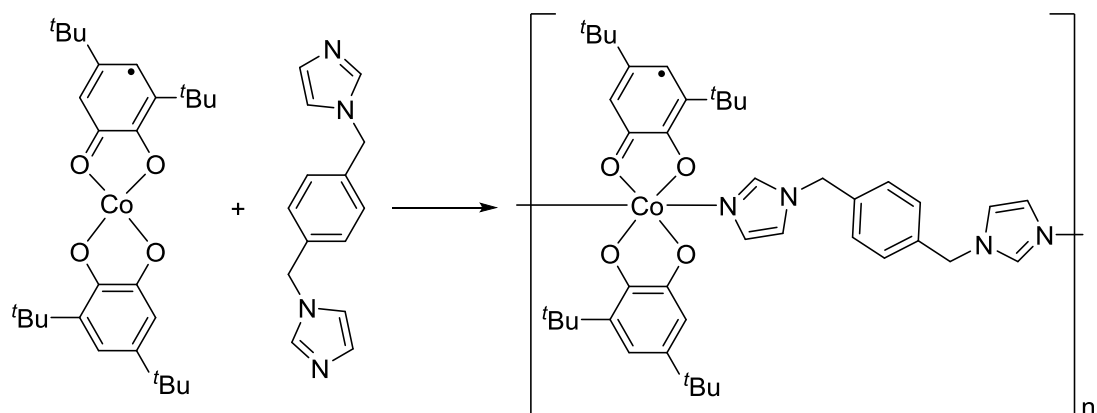
**Figure 1.37.** Bifunctional ligand used by Ruiz-Molina *et al.*

The reaction of this ligand with Co(II) results in a darkly coloured insoluble amorphous nanoparticulate product (average particle diameter of 110 nm). The complex undergoes VT over the temperature range of 35-370 K, with a 12 K hysteresis.<sup>[114]</sup>

#### 1.5.6.6.4 Nanoparticles

Ruiz-Molina has also reported the first example of a (spherical) nanoparticle VT 1D coordination polymer (**Scheme 1.20**). The particles have a  $76-204 \pm 9-13$  nm diameter depending on the rate of precipitation by addition of water. The product is amorphous, which precludes crystallographic characterisation, however energy-dispersive X-ray spectroscopy (EDX) shows that it contains Co, C, O and N atoms, and elemental

microanalysis corroborates the predicted structure. The IR spectrum contains bands at 1480 and 1446  $\text{cm}^{-1}$  which correspond to Co-O bonds.<sup>[115]</sup>



**Scheme 1.20.** Reaction to form 1D Co dioxolene coordination polymer nanoparticles.

At 5 K the  $\chi_{\text{MT}} = 0.4 \text{ emu K mol}^{-1}$  (LS-Co(III) with 1 unpaired electron on the semiquinone), and this value increases slowly and linearly up to 275 K where it reaches  $0.6 \text{ emu K mol}^{-1}$ . Between 275 and 350 K, there is a sharp transition up to a maximum  $\chi_{\text{MT}}$  value of  $2.6 \text{ emu K mol}^{-1}$  corresponding to HS-Co(II) with 5 unpaired electrons in total, 3 centred on the metal and 2 on the semiquinone radicals.

([Co(DBCat)(DBSQ)(4,4'-bipy)]) can be synthesised in both single-crystal and nanoparticle form. There are two different nanoparticle polymorphs that can arise based on the conditions of the reaction (concentration, temperature, solvent, and surfactant). The single-crystal and nanoparticle polymorphs all exhibit different VT behaviour, demonstrating that the VT transition has a high dependence on the surrounding matrix. At low concentrations of metal salt (0.01 M) the  $\alpha$ -phase is formed in agreement with single crystal X-ray structural determination (sponge-like morphology). At higher concentrations ( $>0.04 \text{ M}$ ) the  $\beta$ -phase is formed, which has a different crystal morphology (rods) and gives a different powder pattern. This change is largely due to an increased number of nucleation sites. The phase which is formed also depends on temperature; at  $0 \text{ }^\circ\text{C}$  only the  $\alpha$ -phase is present, but at  $70 \text{ }^\circ\text{C}$  the  $\beta$ -

---

phase dominates. Upon addition of a surfactant (polymeric polyvinylpyrrolidone (PVP) or sodium dodecyl sulfate (SDS) <5%), at low concentrations of metal salt the  $\alpha$ -phase remains unchanged, however at higher metal salt concentrations the  $\beta$ -phase is formed with much larger rod-like crystals, due to the surfactant preventing seed crystal aggregation and thus enhancing single crystal growth. Solvent choice also has an effect, with THF giving only the  $\beta$ -phase at all temperatures and metal salt concentrations, whereas DMF behaves similarly to ethanol with the phase depending on metal salt concentration and temperature.<sup>[116]</sup> The  $\alpha$ -phase has a VT transition starting at 275 K with a maximum value of  $\mu_{\text{eff}} = 5.3 \mu_{\text{B}}$  reached at 380 K. The  $\beta$ -phase exhibits a  $T_{\text{c}}$  shift by more than +50 K with maximum value of  $\mu_{\text{eff}} = 3.5 \mu_{\text{B}}$ .

#### 1.5.6.6.5 Self-assembled VT nanoparticle monolayers

In order to produce novel hybrid interfaces capable of undergoing VT transition, Ruiz-Molina functionalised a dioxolene with a 2-propenoic acid (caffeic acid) group, allowing for the corresponding nanoparticulate product (130 nm diameter) to be attached to a gold surface decorated with amino-terminated alkyl groups, thus forming a self-assembled monolayer of VT nanoparticles (**Figure 1.38-1.40**). The monolayer produced is uniform (85-90% coverage). The VT transition is hard to monitor, however XPS measurements show that as the temperature is increased from 80 to 393 K, there is some conversion from the LS-Co(III) form to the HS-Co(II) form.<sup>[117]</sup>

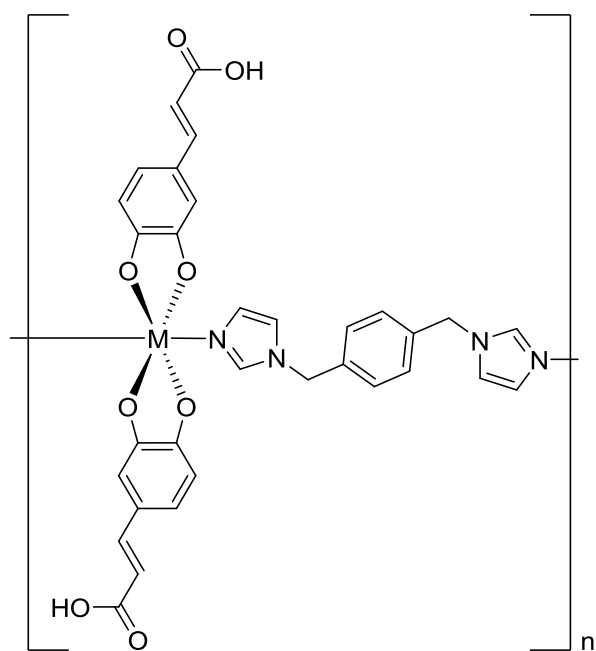


**Figure 1.38.** Structure of the complex used to form coordination polymer particles with pendant carboxylate groups.

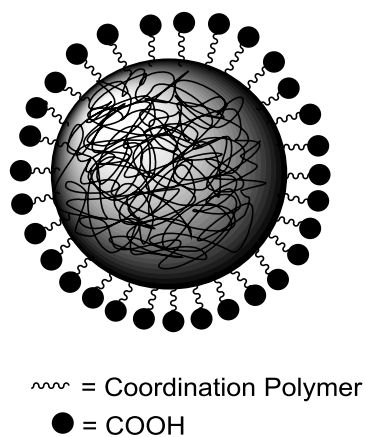


**Figure 1.39.** Simplified model of the resultant coordination polymer nanoparticles.

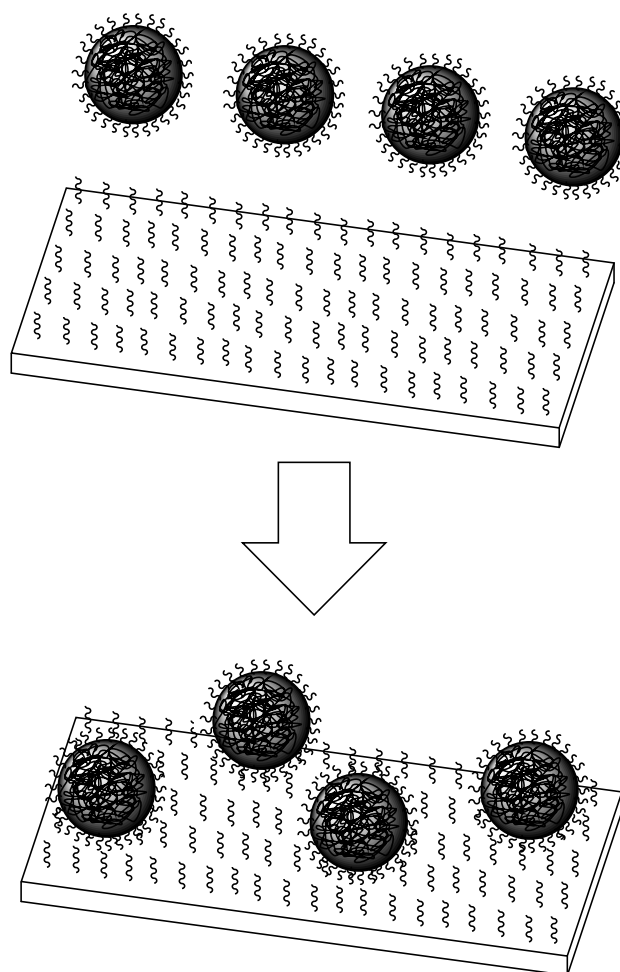


**Figure 1.40.** Simplified drawing of a Au surface before and after the coordination polymer particles have been appended to the surface.

### 1.5.6.7 Rh and Ir

#### 1.5.6.7.1 H-bond networks

Other examples of photophysical phenomena have been observed in group 9, particularly with Rh. The most striking of these is seen with the complex  $\text{Rh}(\text{CO})_2(3,6\text{-DBSQ})$  (**Figure 1.41**).<sup>[118]</sup> Single crystals of this complex bend reversibly when irradiated with 1400-1500 nm light or when cooled. The unit cell is triclinic and the crystals take the form of long needles with the Rh centres stacked on

---

top of one another. The Rh-Rh separation is large (3.27 Å) but there is still significant orbital overlap between the metal ions.

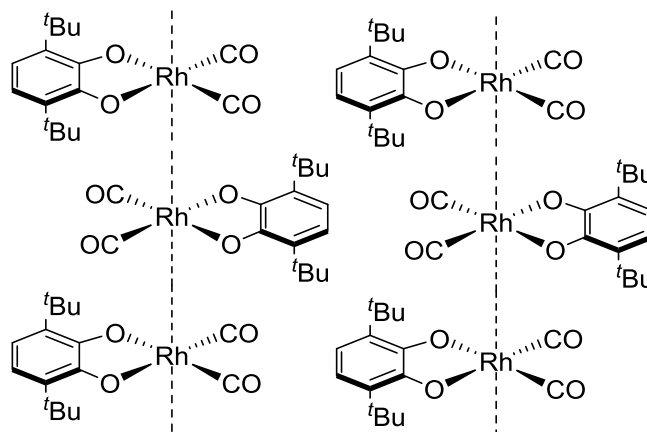


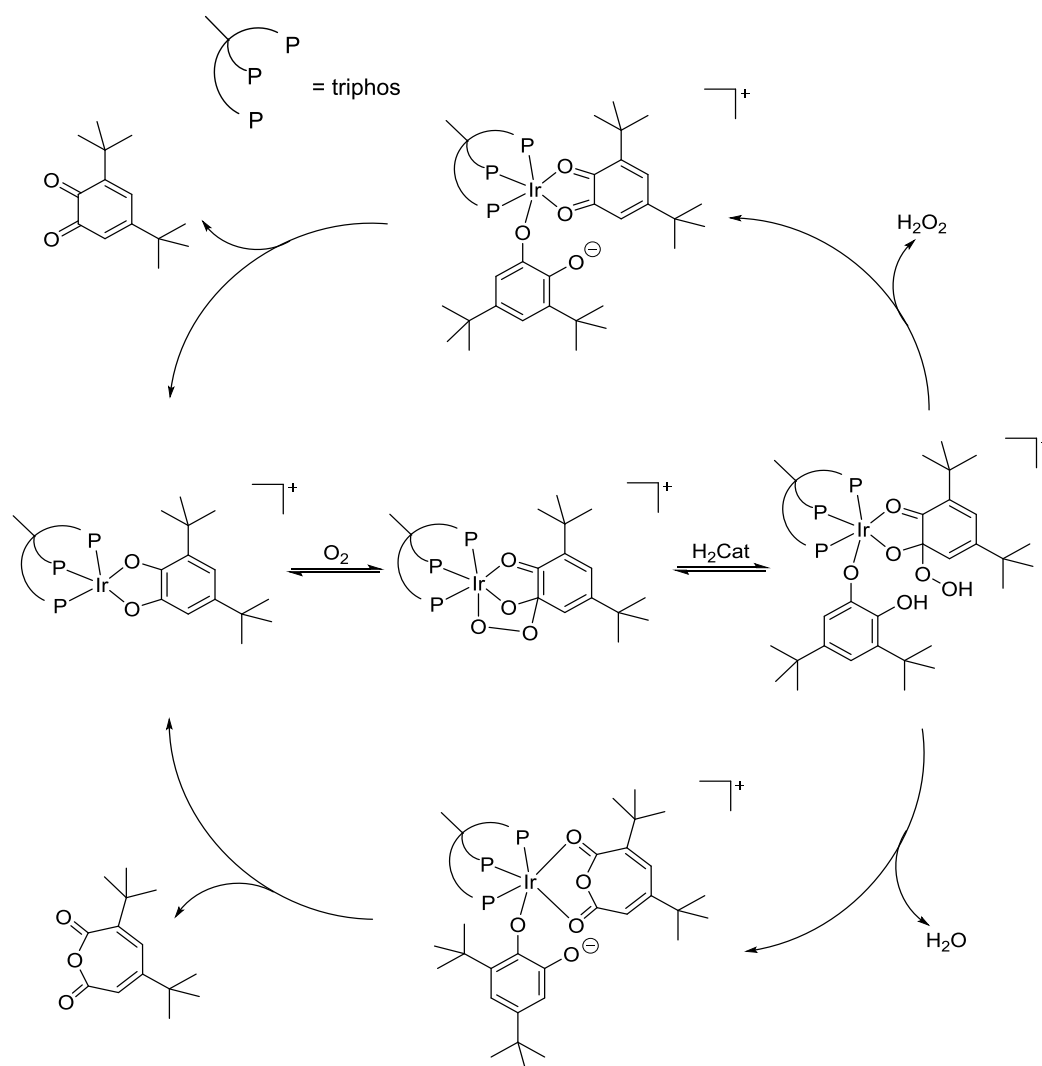
**Figure 1.41.** Coordination polymer of a rhodium dioxolene complex, showing linear stacks of Rh-Rh bonds.

In solution, the electronic spectra of this complex between 150 and 250 K suggest that Rh-Rh linked oligomers form as a function of temperature. As the number of stacked complexes increases, out-of-plane metal orbitals overlap to form filled bonding/antibonding energy levels, with an energy separation between the filled antibonding level and the quinone  $\pi^*$  level that decreases as the number of complexes in the oligomer increases. Hence, as the solution is cooled, individual peaks begin to appear at close energies to one another, each of which corresponds to an aggregate containing a different number of monomers. At the limit of this polymerisation (i.e. an infinite stack), a new electronic band is formed from the interacting metal energy levels, and this band may undergo charge transfer to the aforementioned quinone  $\pi^*$  level, seen at 1500 nm. Population of this level increases the  $\text{Rh}^{\text{II}}(\text{DBCat})$  character of the complexes, shortening the Rh-Rh interaction. When all of these observations are considered, a picture of what is happening on a molecular level to cause this photo/thermal bending begins to emerge. Upon irradiation, one face of the needle is exposed to more light than the other, leading to an anisotropic bending of that side of the crystal, causing it to bend in the direction of light source.

---

### 1.5.6.7.2 Iridium

Iridium has been used as a catalyst for catechol oxidation, but the catalytic cycle has remained elusive. There are several ways in which the Ir ion may facilitate oxidation, such as the outer-sphere reduction of O<sub>2</sub> accompanied by oxidation of catechol,<sup>[119]</sup> or the co-coordination of O<sub>2</sub> followed by inner-sphere electron transfer to a coordinated catechol,<sup>[120]</sup> or even through a peroxosemiquinone rearrangement.<sup>[121]</sup> The latter mechanism has proved to be promising, as a crystal structure of the peroxo intermediate species [Ir(triphos)(O<sub>2</sub>PhenSQ)]<sup>+</sup> has been obtained.<sup>[122]</sup> A catalytic cycle has been proposed to rationalise this intermediate, which contains a bimolecular transition state and is zero order with respect to O<sub>2</sub> and first order with respect to the catalyst (**Scheme 1.21**). The cycle branches as is able to follow two possible routes back to the starting point, with either BQ (and H<sub>2</sub>O<sub>2</sub>) or muconic anhydride (and water) being formed.



**Scheme 1.21.** Proposed catalytic cycle for the oxidation of catechol by iridium.

### 1.5.7 Ni, Pd and Pt

Nickel dioxolene complexes have rarely been studied, but recent findings in the area highlight the dramatic effect that relatively small changes that ancillary ligands or solvents can have on VT transition. Tanaka *et al.* have prepared the complexes  $[\text{Ni}^{\text{II}}(\text{PyBz}_2)(3,5\text{-DBSQ})]^+$  ( $\text{Py}(\text{Bz})_2 = \text{N,N-bis}(\text{benzyl})\text{-N}-(2\text{-pyridyl})\text{methylamine}$ ) and  $[\text{Ni}^{\text{III}}(\text{MePy}(\text{Bz})_2)(3,5\text{-DBCat})]^+$  ( $\text{MePy}(\text{Bz})_2 = \text{N,N-bis}(\text{benzyl})\text{-}i\text{-}[(6\text{-methyl-2-pyridyl})\text{methylamine}]$ ), which exist in markedly different electronic states caused by the *o*-methyl group weakening the pyridine-nickel bond due to steric clashing. This leads to the dioxolene ligand coordinating the nickel more strongly which in turn results in displacement of electron density to favour the catechol form over the semiquinone.<sup>[123]</sup>

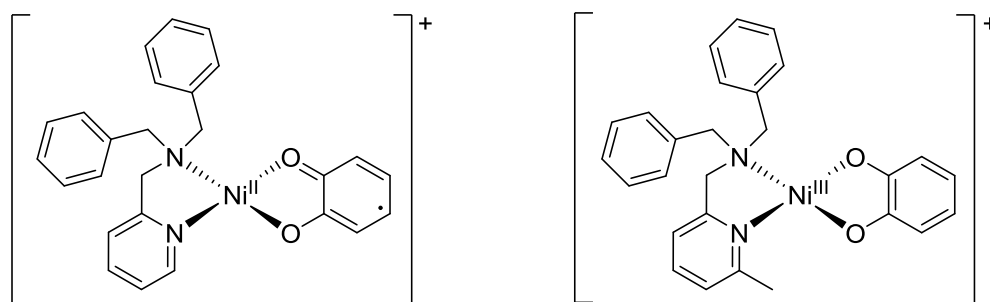


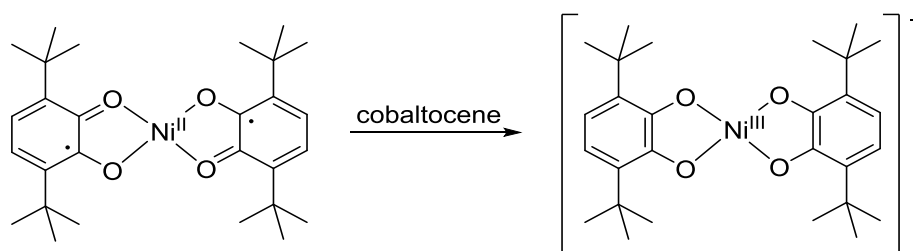
**Figure 1.42.** Left: non-methylated complex in SQ form. Right: methylated complex in Cat form.

In non-coordinating solvents such as  $\text{CH}_2\text{Cl}_2$ ,  $[\text{Ni}^{\text{II}}(\text{PyBz}_2)(3,5\text{-DBSQ})]^+$  and  $[\text{Ni}^{\text{III}}(\text{MePy}(\text{Bz})_2)(3,5\text{-DBCat})]^+$  are blue and brown respectively. Addition of a coordinating solvent such as DMF produces a colour change to light green, which electron absorption spectroscopy reveals is the result of two solvent molecules coordinating with the metal to form an octahedral complex with a corresponding change in spin state from low spin Ni(II)-SQ or Ni(III)-Cat forms to the HS-SQ form.<sup>[124]</sup> Varying the amount of DMF added to a solution of the methylated complex in  $\text{CH}_2\text{Cl}_2$  allows for the observation of a thermally induced VT transition between the four and six coordinate complexes, described by the following equilibrium:



**Scheme 1.22.** Thermally induced VT transition of  $[\text{Ni}^{\text{II}}(\text{MePy}(\text{Bz})_2)(\text{DMF})_2(3,5\text{-DBSQ})]^+$ .

Another example of RIET leading to a mixed valent product is the *bis*(dioxolene) complex  $[\text{Ni}(3,6\text{-DBSQ})_2]$ . It has been shown that when one of the DBSQ ligands undergoes one-electron reduction by addition of cobaltocene, the other DBSQ ligand is also one-electron reduced while the metal is oxidised from Ni(II) to Ni(III) to form the complex  $[\text{Ni}^{\text{II}}(\text{dbdiox})_2]^-$ .



**Scheme 1.23.** VT transition induced by RIET after oxidation with cobaltocene.

Recent work in the Halcrow group has explored the redox activity of Pt complexes of the dioxolene ligand H<sub>4</sub>thea (H<sub>4</sub>thea = 2,3,6,7-tetrahydro-9,10-dimethyl-9,10-dihydro-9,10-ethanoanthracene).<sup>[125]</sup>

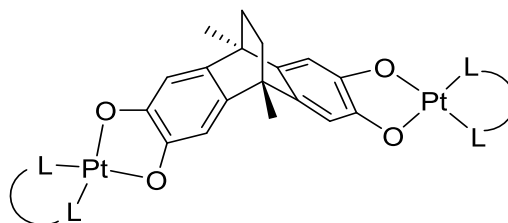


**Figure 1.43.** General structure of a dinuclear platinum complex of thea.

This ligand is of curiosity because while the two dioxolene moieties are not formally conjugated they reside only a short distance from one another in the complex and thus exhibit electron transfer between the dioxolene rings on the EPR timescale in the mixed Cat/SQ level (as seen in 3,3,3',3'-tetramethyl-1,1'-spiro-bis-(5,6-dihydroxyindane) and other examples). Cyclic voltammetry shows that it undergoes two-step reversible low-potential oxidation at -0.37 and -0.11 V versus [FeCp<sub>2</sub>]/[FeCp<sub>2</sub>]<sup>+</sup> corresponding to the  $\text{cat}/\text{cat} \rightleftharpoons \text{cat}/\text{sq} \rightleftharpoons \text{sq}/\text{sq}$  transitions. Further irreversible oxidation to the SQ/BQ and (BQ)<sub>2</sub> states is also observed. Structural determination by X-ray crystallography reveals that the singly oxidised salt [Pt<sub>2</sub>(thea)(L-L)<sub>2</sub>](PF<sub>6</sub>) forms nested dimers, which may be charge-transfer assemblies.

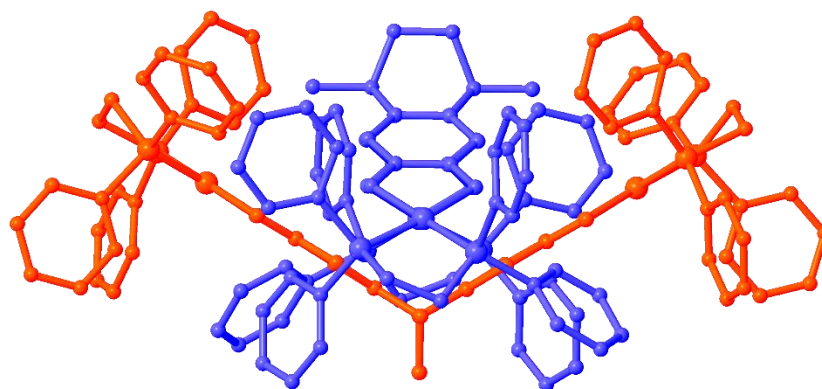


**Figure 1.44.** Nested dimer of radical cations salt  $[\text{Pt}_2(\text{thea})(\text{L-L})_2]^+$ . Adapted from Halcrow *et al.*<sup>[125]</sup>

There is also a rare example in this group of a semiquinone complex in which the metal is facially bonded  $\pi$ -bonded to the ring in a classic sandwich complex. The complex is isolated as a low-yield side product from the reaction of 3,5-DBBQ and  $\text{Pd}_2(\text{DBA})_3$ .<sup>[126]</sup>

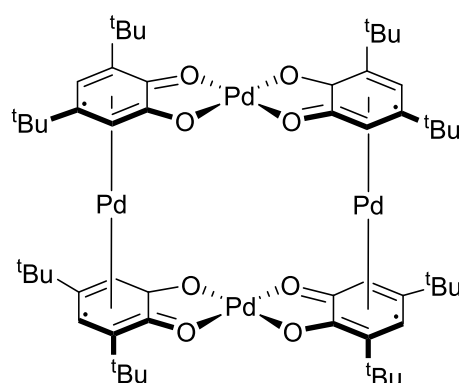


**Figure 1.45.** Tetranuclear palladium dioxolene complex, with two Pd atoms bonded facially to the aromatic rings.

### 1.5.8 Cu, Ag and Au

A large number of VT copper dioxolene complexes have been synthesised. It is generally the case that for complexes of the form  $[(\text{L-L})\text{Cu}(\text{diox})]$ , the dioxolene will exist in the catecholate form when L-L is a hard ligand, and the semiquinonate form when L-L is a soft ligand. Kaim *et al.* have been heavily involved in the study of

---

copper dioxolenes, showing particular interest in the biological significance of such complexes.<sup>[127]</sup> [(mmb)Cu(diox)] (mmb = 1-methyl-2-(methylthiomethyl)-1*H*-benzimidazole) undergoes thermal VT transition above 250 K to convert from the catecholate form to the semiquinone form.<sup>[128]</sup>

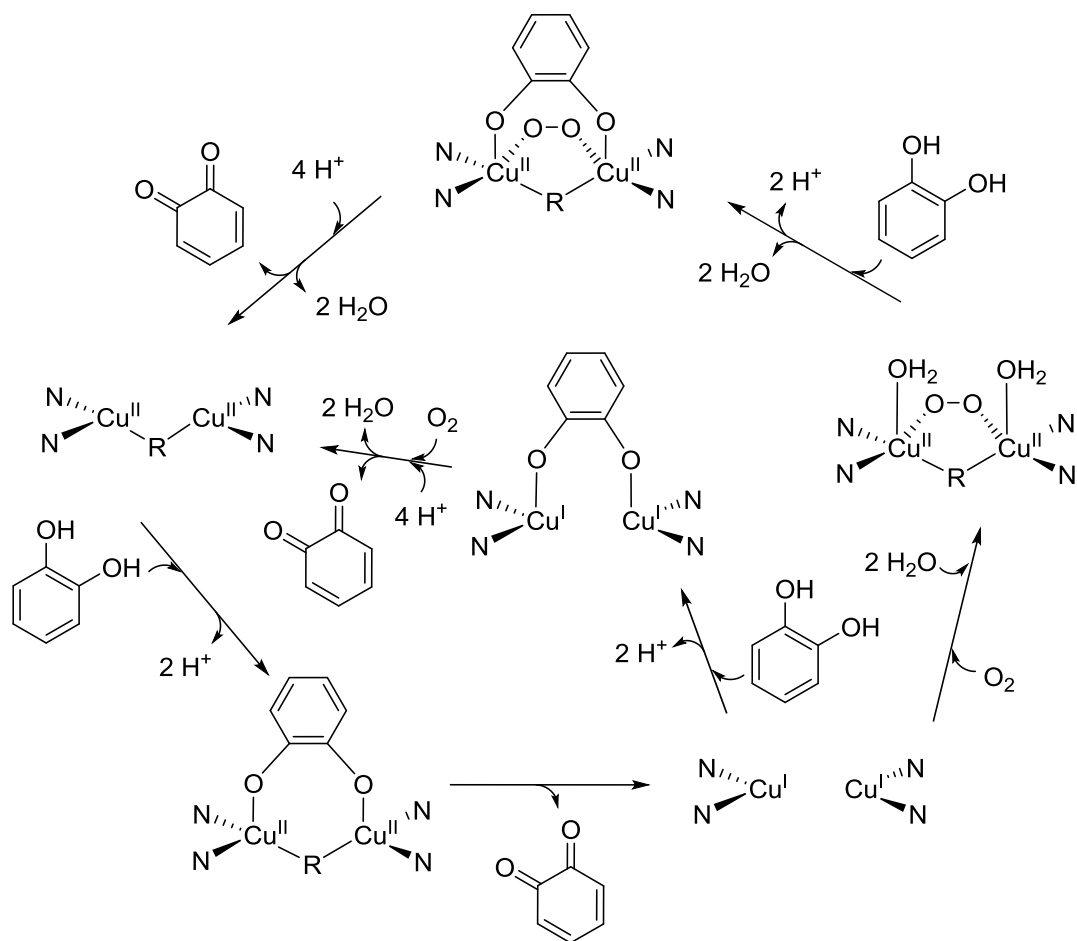
Examples of copper dioxolenes have also been reported within the context of their role in oxio-reductive enzymes.<sup>[129]</sup> In a copper containing amine oxidase enzyme, the following VT transition is observed:



**Scheme 1.24.** VT transition of a copper dioxolene complex.

The enzymes in question are involved in growth regulation and tissue maturation. Oxidation of primary amines by these enzymes is accomplished through a two-electron reduction of O<sub>2</sub> to H<sub>2</sub>O<sub>2</sub>, which requires circumvention of spin conservation problems by converting the initial Cu(II)-Cat form to the Cu(I)-SQ form by intramolecular electron transfer. The evidence for this Cu(I) intermediate comes from differences in *g* factor and hyperfine coupling constants in the EPR spectrum.

The biological role of copper containing enzymes which oxidise catechol has been well researched.<sup>[130]</sup> The tyrosinase enzyme contains two antiferromagnetically coupled Cu centres in close proximity to one another, and is capable of ortho-hydroxylating tyrosine to produce 1,2-benzoquinone.<sup>[131]</sup> The catalytic cycle involves a resting Cu(I) step, which is oxidised to Cu(II) by the binding of a bridging O<sub>2</sub> molecule. Phenol may then coordinate to the metals, reducing them back to the Cu(I) stage and being released as the benzoquinone product (**Scheme 1.25**).<sup>[131-132]</sup>



**Scheme 1.25.** Catalytic cycle for the oxidation of catechol by copper. R = endogenous phenolate, alkoxide or hydroxide.

The Cu can therefore be seen as serving the function of transferring charge from catecholate to  $O_2$ . This mechanism has been investigated as a process which could be mimicked synthetically, and complexes such as  $[Cu(HB(3,5-Me_2pz)_3)]_2(\mu-\eta^2:\eta^2 O_2)$  have been shown to produce 3,5-DBBQ from  $H_2(3,5-DBCat)$ .<sup>[133]</sup>

Catechol derivatives containing additional N-donor moieties have been synthesised by Latour *et al.* as a route towards multinuclear complexes (**Figure 1.46**).<sup>[134]</sup>

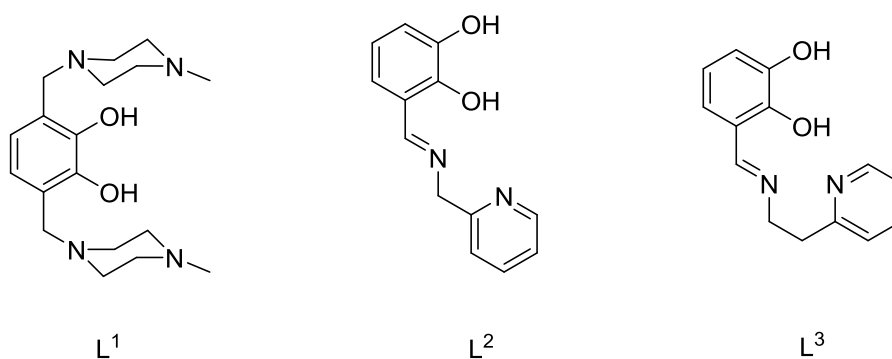


**Figure 1.46.** Catechol ligands containing N-donor moieties.

Reaction of  $L^1$  forms the pentanuclear complex  $Cu_5(OH)_2(L^1)_2(NO_3)_4$  containing a catechol-coordinated Cu ion, with the remaining four Cu ions being N-coordinated. Tetranuclear  $[Cu(HL^2)(NO_3)]_4$  has also been formed, which contains a  $Cu_4O_4$  cubane structure.<sup>[135]</sup> Finally, ligand  $L^3$  also forms a tetranuclear complex  $[Cu_2(L^2)(OAc)_2]_2$  with the two inner metals occupying square pyramidal geometry and the two outer ones being trigonal bipyramidal.<sup>[136]</sup>

Hupp *et al.* have pursued a coordination polymer which contains a  $[bis(Cat)salen]Mn(III)$  catechol functionality as a crosslinking group (**Figure 1.47**). The product, isolated as an amorphous and insoluble powder, can effectively catalyse epoxidation reactions via the Mn centre.<sup>[137]</sup>

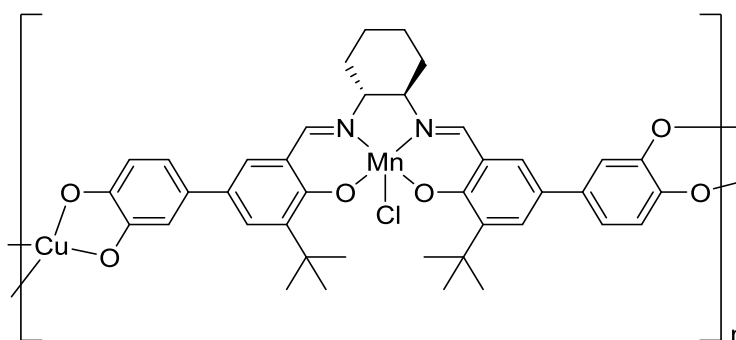


**Figure 1.47.** Dioxolene coordination polymer with Cu and Mn.

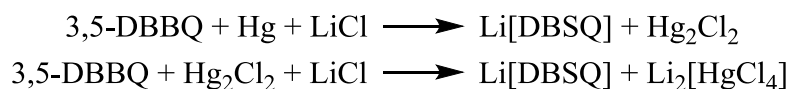
### 1.5.9 Zn, Cd and Hg

Group 12 is less well explored due to the often extreme air sensitivity of the resulting complexes. The  $Zn(3,5-DBSQ)_2$  complex undergoes reduction at  $-0.37$  which helps

---

to explain the high reactivity.<sup>[138]</sup> Despite this, a few examples have been characterised, such as  $M(3,6\text{-DBSQ})_2$  ( $M = \text{Zr}$  or  $\text{Cd}$ ), and these may be chemically reduced to give  $[M(3,6\text{-DBSQ})(3,6\text{-DBCat})]^-$  which gives a characteristic SQ radical EPR spectrum showing hyperfine coupling to the  $^{111}\text{Cd}$  or  $^{113}\text{Cd}$  nucleus.<sup>[139]</sup>

Catecholate complexes of Hg have rarely been reported in the literature, as the Hg tends to reduce the benzoquinone without coordinating it. It is possible to reduce 3,5-DBBQ in the presence of LiCl via the following reactions.<sup>[140]</sup>



**Scheme 1.26.** Outer-sphere reduction of 3,5-DBBQ with mercury.

Hg/DBBQ have therefore attracted attention as radical traps for use in reactions involving the photolytic cleavage of Hg-Pt bonds, such as those in  $(\text{CF}_3)\text{HgPt}(\text{PPh}_3)_2(\text{CF}_3)$ .<sup>[141]</sup> This strategy can be used to form  $(3,6\text{-DBSQ})\text{Hg}(\text{B}_{10}\text{C}_2\text{H}_{11})$  from the di(carboran-9-yl)mercury starting material.<sup>[142]</sup>

### 1.5.10 Summary of Periodic Trends

The following diagram (**Figure 1.48**) shows a simplified picture of the dominant energetic factors that lead to the characteristic charge distributions observed in metal quinone complexes. When the metal orbital energy level ( $M$ ) is high compared to the  $\pi$ -orbital energy level ( $\pi_Q$ ), the ligand exists in the catecholate form. A charge transition occurs with decreasing the metal orbital energy such that metals with a lower orbital energy lead to the ligand adopting the semiquinonate form and donating electron density to metal-centred levels.

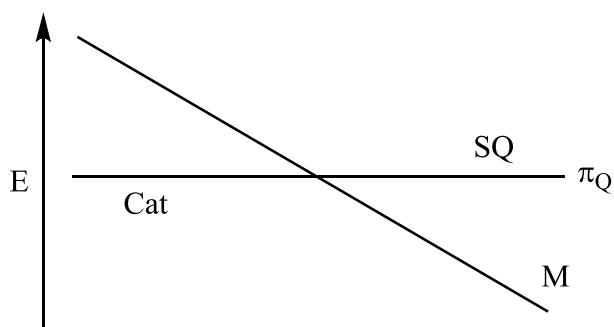


**Figure 1.48.** Simplified graph of the comparative energies of the Cat, SQ,  $\pi_Q$  and metal orbitals.

Metal orbital energy increases down the group, and it is typical to see the 3d elements adopt the  $M^{III}(SQ)_3$  form, but the analogous 5d element adopt the  $M^{VI}(Cat)_3$  form. While the  $M/\pi_Q$  orbital energy separation is the dominant factor in determining charge distribution, in borderline cases where the energies are very close to one another (such as in Cu), co-ligand effects begin to have a meaningful impact and their contribution cannot be neglected.

At energies close to the intersection shown in **Figure 1.48**, equilibria are commonly observed between the different valence tautomeric forms of the complexes. This bistability has been reported mainly in Co chemistry, but there are also less common examples for Mn, Fe, Cu, Ni, Rh, Ir and Pt. The reduction potential for  $O_2$  is close to the potential of benzoquinones, which has led to many examples where metal catecholate complexes can act as a template for the oxidation of catechol to benzoquinone or muconic anhydride using  $O_2$ .

There are literature examples of all four types of magnetic exchange that are theoretically accessible for metal-SQ and SQ-SQ interactions.  $Fe^{III}(SQ)_3$  shows antiferromagnetic exchange between the spin 5/2 metal and the three spin 1/2 SQ radicals (giving  $S = 1$  overall spin). In contrast, the orbitals in  $Ni^{II}(BQ)(SQ)_2$  are orthogonal and thus give rise to ferromagnetic exchange. When the metal is diamagnetic such as in  $Co(3,6-DBSQ)_3$  there is a through-metal antiferromagnetic interaction between the spins of the individual SQ ligands. Replacing Co with Ga

---

provides an example of the opposite effect, where the SQ-SQ exchange is now ferromagnetic.

## 1.6 Nitronyl nitroxides

Nitronyl nitroxide ligands are in many ways analogous to dioxolenes. They have been a subject of research interest due to their ease of functionalisation, ability to exist as stable free radicals, and ability to coordinate to a metal by several different modes.<sup>[143-144]</sup> The synthetic route towards nitroxyl radicals involves synthesis of a hydroxylamine followed by oxidation with  $\text{NaNO}_2$  to form the radical. The 4 and 5 positions on the imidazole ring are typically functionalised with methyl groups to enhance steric protection. The magnetic orbitals in nitronyl nitroxides have  $\pi^*$  symmetry as displayed in **Figure 1.49**.

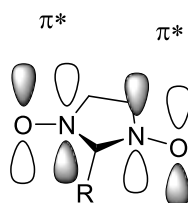


**Figure 1.49.** Magnetic orbitals in nitronyl nitroxides.<sup>[145]</sup>

The nitrogen and oxygen atoms carry large positive spin densities, whereas the  $\text{sp}^2$  carbon atom carries negative spin density.<sup>[146-147]</sup> The unpaired electron occupies a  $\pi^*$  molecular orbital and can be represented as the following Lewis structure (**Figure 1.50**).

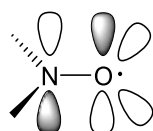


**Figure 1.50.** Lewis representation of the nitroxyl group.

---

### 1.6.1 Coordination through the oxygen atom

Orbital overlap between the nitroxyl magnetic orbital and the metal magnetic orbital(s) is highly dependent on the number of unpaired electrons present on the metal. In the case of Cu(II) nitroxyl complexes, the single unpaired d electron occupies a half filled d-orbital and thus different coordination geometries can lead to substantially altered orbital overlap between the metal and ligand. Transition metals with several half-filled d orbitals are more flexible due to the multitude of potential magnetic orbital overlaps available.<sup>[148-149]</sup>

Antiferromagnetic coupling is observed when the orbital overlap takes place along the M-O bond, whereas ferromagnetic coupling is observed in the case of Cu(II) complexes where the nitroxyl is bound axially, due to the orthogonality of the ligand  $\pi$  and metal  $d_{x^2-y^2}$  orbitals. The magnitude of the interaction varies from +100  $\text{cm}^{-1}$  in rigorously octahedral complexes, to smaller values of 10-30  $\text{cm}^{-1}$  in distorted octahedral complexes.<sup>[148-149]</sup>

### 1.6.2 Coordination through the nitrogen atom

The nitrogen lone pair that is donated to the metal is orthogonal to the  $\pi^*$  magnetic orbital. Orbital overlap is disfavoured and coupling is therefore ferromagnetic. For Cu(II) and Ni(II) complexes, the strength of the interaction is in the region of 300-400  $\text{cm}^{-1}$  and  $>100 \text{ cm}^{-1}$  respectively.

### 1.6.3 Geometry of the nitroxyl

There is no method of predicting whether the nitroxyl will bond in an axial or equatorial geometry with absolute certainty, due to the subtle interplay of steric and electronic factors. However, some general trends have been observed; in octahedral complexes, bulky nitroxyls favour axial coordination due to the concomitant

---

reduction in steric clashing. This effect is magnified in Jahn-Teller elongated complexes due to the increased axial bond lengths providing additional space to accommodate the ligand. Conversely, nitroxyls which contain only a single coordinating group and a small steric bulk tend to favour the equatorial coordination mode. Careful consideration of the structural design of the nitroxyl (and ancillary ligands if present) can be used to influence which coordination geometry will ultimately be obtained.

#### 1.6.4 Effect of the counter-ion

The choice of counter-ion in Cu nitroxyl complexes can have a marked effect on magnetic behaviour. Yoshioka *et al.* synthesised a family of bidentate nitronyl nitroxide and imino nitroxyl ligands functionalised with either pyridyl or pyrazolyl moieties (**Figure 1.51**).<sup>[150]</sup>

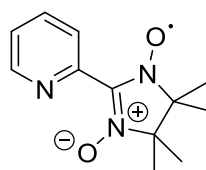


**Figure 1.51.** 4,5-dihydro-4,4,5,5-tetramethyl-2-(2-pyridinyl)-1*H*-imidazol-1-yloxy-3-oxide ligand.

When this ligand is complexed with Cu with chloride co-ligands ions, the resultant Jahn-Teller elongated complex has the chlorides coordinated in the axial positions. At 300 K the complex shows magnetic behaviour indicative of three non-interacting spins (1.16 emu), however at temperatures lower than 75 K the value of  $\chi_m T$  rises due to ferromagnetic coupling. In contrast, when the same complex is formed with perchlorate counter ions, the 300 K  $\chi_m T$  is lower (0.65 emu) and a drop in  $\chi_m T$  is observed as the complex is cooled, indicative of antiferromagnetic coupling (**Figures 1.52 and 1.53**).

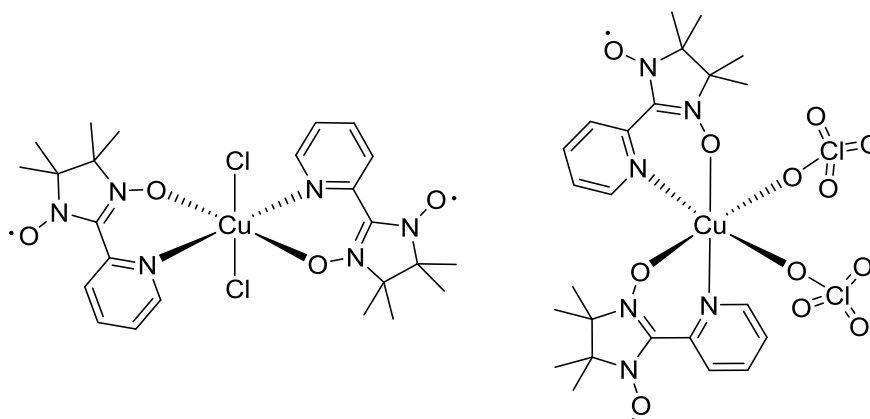


**Figure 1.52.** Two Cu complexes which can be formed based on which co-ligand is used.

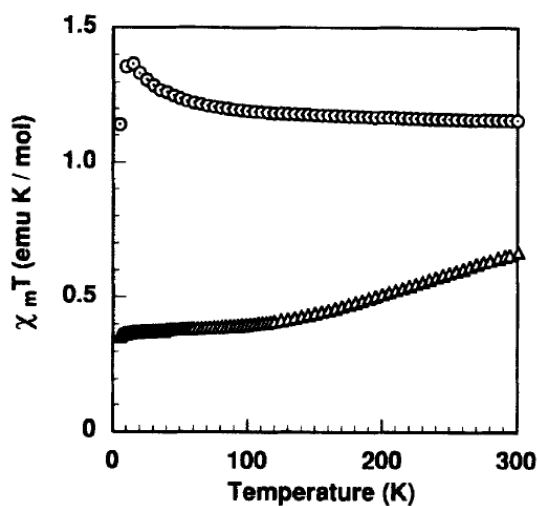


**Figure 1.53.**  $\chi_m T$  vs  $T$  for the two Cu complexes. Circles = chloride complex, triangles = perchlorate complex.<sup>[150]</sup>

The chloride complex contains an NO group coordinated axially to the Cu, giving rise to the observed ferromagnetic coupling, however the perchlorate complex is coordinated equatorially, hence antiferromagnetic coupling occurs. This demonstrates that a small variation in the counter ion can lead to a markedly different magnetic behaviour.<sup>[150]</sup>

### 1.6.5 The bisimpy ligand

The bisimpy (2,2'-(2,6-pyridinediyl)bis[4,5-dihydro-4,4,5,5-tetramethyl]-1H-imidazol-1-yloxy) ligand has been the subject of recent studies in the literature. Zhou *et al.* synthesised a variety of complexes where the bisimpy was present as a biradical complexed to Mn and Co with hfac co-ligands (**Figure 1.54**).<sup>[151]</sup>

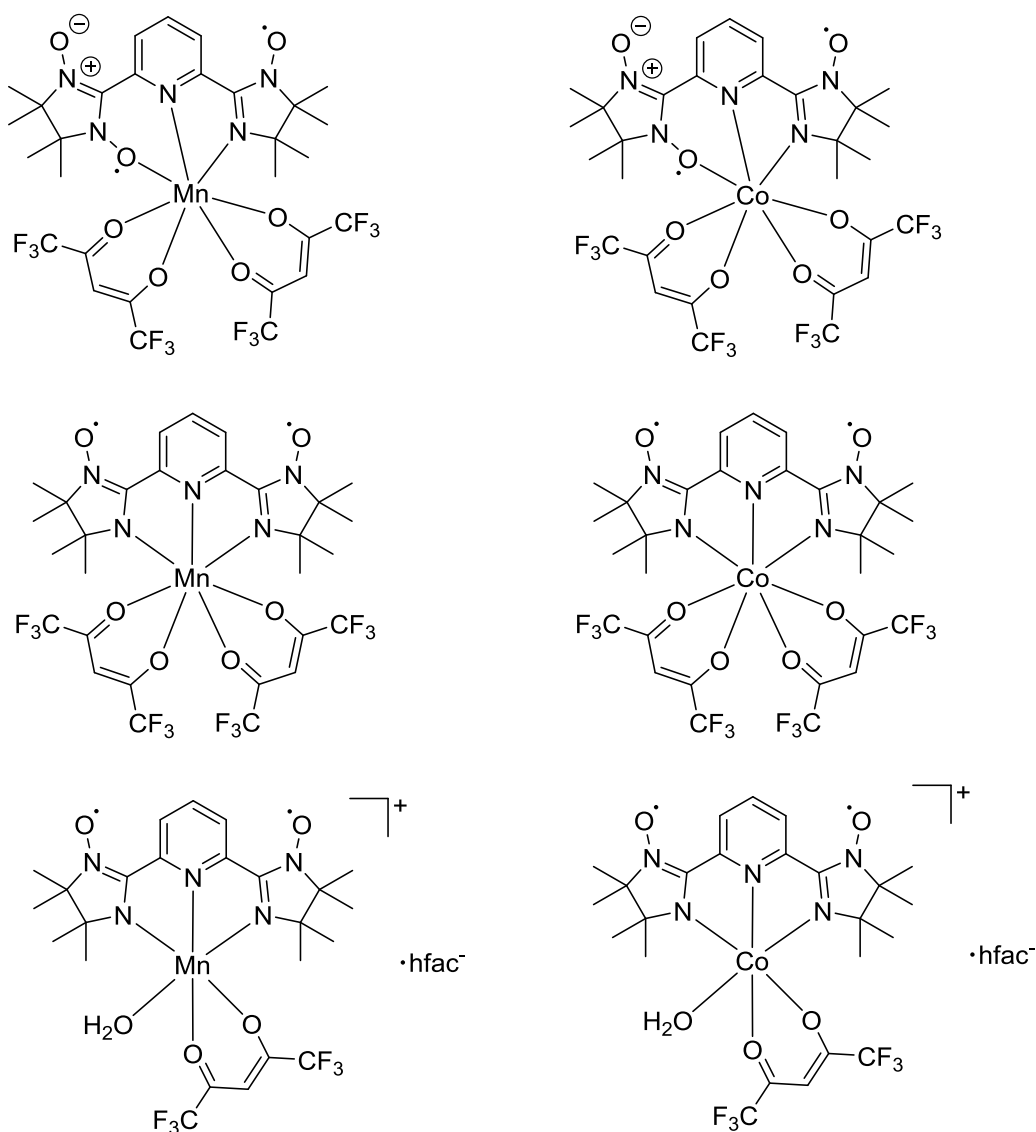


**Figure 1.54.** Six complexes reported by Zhou *et al.*

At high temperature all of the complexes show antiferromagnetic coupling, however several different magnetic behaviours are exhibited upon cooling. [Mn(bisimp<sup>-</sup>)(hfac)<sub>2</sub>] has a room temperature  $\chi_m T$  of 3.27 cm<sup>3</sup> K mol<sup>-1</sup>, which is less than the theoretical value for a totally uncorrelated spin system. The  $\chi_m T$  increases linearly upon cooling, until a temperature of 15 K is reached, at which point the  $\chi_m T$  rapidly decreases until reaching a minimum of 0.84 cm<sup>3</sup> K mol<sup>-1</sup>, indicating strong antiferromagnetism. The authors model the magnetic exchange as a scalene triangle of three spins (one spin  $S = 5/2$  Mn(II) ion and two  $S = 1/2$  ligands, **Figure 1.54**), which has the following spin Hamiltonian (**Equation 1.2**).

$$\hat{H} = -2J_1\hat{S}_{Mn}\hat{S}_{rad1} - 2J_2\hat{S}_{Mn}\hat{S}_{rad2}$$

**Equation 1.2.** Spin Hamiltonian for a scalene triangle of spins.

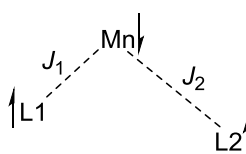


**Figure 1.55.** Model of the antiferromagnetic coupling between the three spins in the complex.

[Mn(bisimp<sup>-</sup>)(hfac)(H<sub>2</sub>O)] has a room temperature  $\chi_m T$  of 3.96 cm<sup>3</sup> K mol<sup>-1</sup>, which is lower than the predicted value of 5.12 cm<sup>3</sup> K mol<sup>-1</sup>, indicating some degree of antiferromagnetism. The  $\chi_m T$  decreases linearly as the temperature is reduced to 35 K, reaching a minimum of 2.10 cm<sup>3</sup> K mol<sup>-1</sup>. Upon cooling below this temperature to 2 K the  $\chi_m T$  rises to a maximum of 2.87 cm<sup>3</sup> K mol<sup>-1</sup>, due to intermolecular radical-radical ferromagnetic coupling.

The magnetic susceptibility of [Mn(bisimp<sup>-</sup>)(hfac)<sub>2</sub>] and [Mn(bisimp<sup>-</sup>)(hfac)(H<sub>2</sub>O)] were modelled as an isosceles triangle of spins (**Figure 1.56**) with the following spin Hamiltonian (**Equation 1.3**):

$$\hat{H} = -2J(\hat{S}_{Mn}\hat{S}_{rad1} + \hat{S}_{Mn}\hat{S}_{rad2}) - 2J' \hat{S}_{rad1}\hat{S}_{rad2}$$

**Equation 1.3.** Spin Hamiltonian for an isosceles triangle of spins.

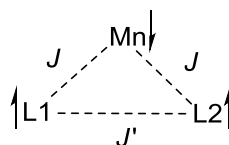


**Figure 1.56.** Model of the antiferromagnetic coupling between the three spins in the complex.

The resulting Bleaney-Bowers equation and magnetic susceptibility was derived (Equations 1.4 and 1.5).

$$\chi = \frac{N\beta^2 g^2}{4kT} \times \frac{84 + 35 \exp\left(\frac{-7J}{kT}\right) + 10 \exp\left(\frac{-12J}{kT}\right) + 35 \exp\left(\frac{-5J-2J'}{kT}\right)}{4 + 3 \exp\left(\frac{-7J}{kT}\right) + 2 \exp\left(\frac{-12J}{kT}\right) + 3 \exp\left(\frac{-5J-2J'}{kT}\right)}$$

**Equation 1.4.** Bleaney-Bowers equation for the complex.

$$\chi_M = \frac{\chi}{1 - \chi\left(\frac{2zj'}{Ng^2\beta^2}\right)}$$

**Equation 1.5.** Expression for the  $\chi_m$  of the complex.

Oshio and Eto have reported a Cu(II) bisimpy complex [CuCl(bisimpy)EtOH]PF<sub>6</sub> (Figure 1.57) which exhibits interesting magnetic behaviour.

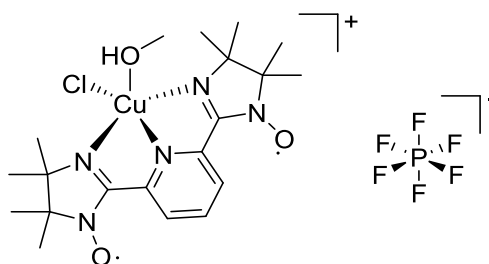


**Figure 1.57.** Structure of a Cu bisimpy complex.

The  $\chi_m T$  of [CuCl(bisimpy)EtOH]PF<sub>6</sub> at 300 K is 1.60 emu mol<sup>-1</sup> K, which is 0.475 emu mol<sup>-1</sup> K higher than predicted for three non-interacting spins. Upon cooling to 40

K the  $\chi_m T$  increases to 1.89 emu mol<sup>-1</sup> K, which has good agreement with the Curie constant for an  $S = 3/2$  state with  $g = 2.0$  (1.876 emu mol<sup>-1</sup> K), indicating ferromagnetic interactions dominate at low temperature. This is due to the unpaired d electron on the Cu(II) ion occupying the  $d_{x^2-y^2}$  orbital which is orthogonal to the  $p\pi$  orbitals on the ligand, and spin polarisation between the ligand radicals. The spin Hamiltonian is shown in **Equation 1.6**:<sup>[152]</sup>

$$\hat{H} = -2J_1(2S_{\text{Cu}} \cdot S_{\text{bisimpy}}) - 2J_2 S_{\text{bisimpy}} \cdot S_{\text{bisimpy}}$$

**Equation 1.6.** Spin Hamiltonian for the complex.

The authors also carried out DFT calculations on the complex and the free bisimpy ligand (with the methyl groups replaced by hydrogen atoms). The ligand radical spin density is located primarily on the imino nitroxyl groups, with positive spin populations present on the nitroxyl group and negative spin populations present on the  $sp^2$  hybridised carbon atoms.

A dinuclear Ag complex of bisimpy has also been reported by the same authors (**Figure 1.58**).

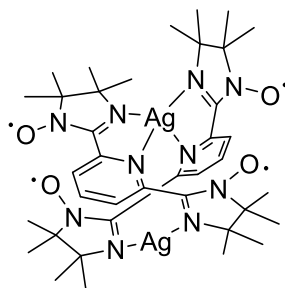


**Figure 1.58.** Structure of a helical {4 + 2} silver complex of bisimpy.

$[\text{Ag}_2(\text{bisimpy})_2]^{2+}$  forms a {4 + 2} helical structure. The complex contains two diamagnetic Ag(I) ions and four  $S = 1/2$  organic radical centres, and magnetic measurements show that at 300 K the  $\chi_m T = 1.50$  emu mol<sup>-1</sup> K, which is in agreement with what would be expected for four isolated spins. Upon cooling the complex, there is a gradual decrease in  $\chi_m T$  down to 40 K ( $\chi_m T = 0.75$  emu mol<sup>-1</sup> K), followed by a plateau in the region of 40-8 K, followed by a sharp decrease in  $\chi_m T$  down to 2 K (0.2

emu mol<sup>-1</sup> K). The observation of a plateau in the temperature of 40-8 K cannot be explained by a simplistic spin-polarization mechanism, and instead requires consideration of intermolecular interactions. Single crystal X-ray structural data shows that one of the oxygen atoms has a close contact (3.239 Å) with an oxygen atom of a neighbouring molecule, leading to SOMO-SOMO overlap which results in antiferromagnetic coupling and a consequent decrease in  $\chi_m T$ . The authors model this behaviour with two exchange coupling constants  $J_1$  and  $J_2$ , corresponding to intra- and inter-ligand interactions (**Equation 1.7** and **Figure 1.59**).<sup>[153]</sup>

$$\hat{H} = -2J_1(S_1 \cdot S_2 + S_3 \cdot S_4) - 2J_2(S_2 \cdot S_3)$$

**Equation 1.7.** Spin Hamiltonian for the helical silver complex of bisimpy.

Where  $J_1 = +17.4(8)$  cm<sup>-1</sup> and  $J_2 = -52.3(7)$  cm<sup>-1</sup>, and  $g$  was fixed to 2.0. Parallel SOMOs therefore lead to strong antiferromagnetism, which explains the behaviour.

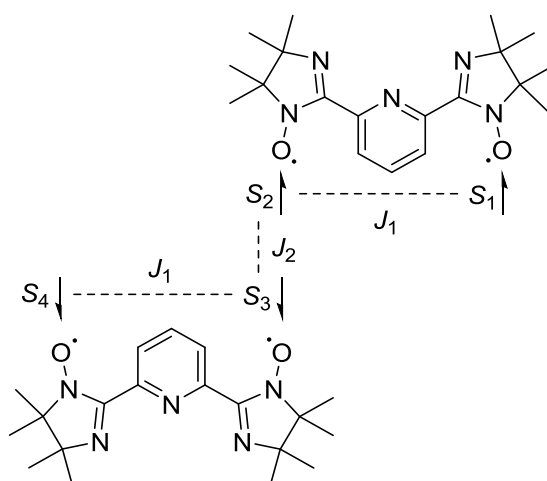


**Figure 1.58.** Simplified diagram (displaying only two ligands belonging to adjacent complexes) displaying the inter- and intramolecular radical coupling mechanism.

---

## 1.7 Project Aims

There are three main aims of the project. Firstly, catechol derivatives of triptycene will be synthesised and characterised crystallographically to elucidate their novel highly-porous supramolecular crystalline clathrates. These ligands will then be taken forward for the second aim, which is to produce novel mixed-valent multinuclear coordination complexes of triptycenes and related multi(dioxolenes). Efforts will be made towards the extension of this work to include coordination polymers and porous networks. The final section will involve the synthesis and magnetic characterisation of a variety of imino nitroxyl organic radical complexes of Cu(II).

### 1.7.1 Porous Crystalline Clathrates of Triptycene Derivatives

Triptycenes are well known as scaffolds for supramolecular architectures, being advantageous due to their rigid  $C_3$  symmetry which can produce cyclic or porous molecular assemblies. Triptycenes can be readily derivatised, which opens up their potential as polynucleating ligands which may in turn form interesting supramolecular structures. Several derivatives of triptycene will be prepared and crystallised from a range of organic solvents, and the resultant novel structures characterised. These ligands will then be taken forward into the following section, where they will be used to form mixed-valent coordination complexes.

### 1.7.2 Multinuclear Mixed-Valent Dioxolene Complexes

Mixed-valent dioxolene complexes are a well developed area of research, however complexes containing three or more dioxolene units are less prevalent. Most recently, the Halcrow group has investigated the dinuclear complex  $[(Pt(dppe))_2(thea)]$ , and the research presented in this section will use this as a starting point for the synthesis of related complexes. Multi-nuclear complexes which incorporate additional redox-active groups will be pursued, especially those which could form interesting supramolecular structures. Further to this, attempts will be made to produce polymeric metal-dioxolene complexes, which may adopt a variety of 1D, 2D or 3D structures. The complexes will be characterised by NMR, MS and single crystal X-ray

---

diffraction, and their electronic properties characterised by CV, EPR, UV/vis/NIR and IR.

### **1.7.3 Copper(II) Complexes of a Bis-Nitroxyl Chelate Ligand**

Continuing the theme of molecular magnetism, some *bis*(iminonitroxyl) complexes of Cu(II) will be synthesised, and their magnetic properties probed by SQUID magnetometry. The Jahn-Teller active nature of Cu(II) means that, by varying the steric bulk of the ligand, the axis of Jahn-Teller elongation should change, which in turn will affect the magnetic properties. Change in the  $\chi_m T$  as the temperature is varied is expected, with  $\chi_m T$  increasing as the temperature is decreased due to ferromagnetic coupling between the radical spins.

---

## 1.8 References

1. M. A. Halcrow, Spin-Crossover Materials. Properties and Applications. *Angew. Chem. Int. Ed.* 2013.
2. P. Gütlich, H. A. Goodwin, *Top. Curr. Chem.* **2004**, 233-235.
3. D. N. Hendrickson, C. G. Pierpont, Valence Tautomeric Transition Metal Complexes. In *Spin Crossover in Transition Metal Compounds II*, Springer Berlin Heidelberg: 2004; Vol. 234, pp 63-95.
4. A. Dei, D. Gatteschi, C. Sangregorio, L. Sorace, *Acc. Chem. Res.* **2004**, 37 (11), 827-835.
5. E. Evangelio, D. Ruiz-Molina, *Eur. J. Inorg. Chem.* **2005**, 2005 (15), 2957-2971.
6. E. Evangelio, D. Ruiz-Molina, *Comptes Rendus Chimie* **2008**, 11 (10), 1137-1154.
7. O. Sato, J. Tao, Y. Z. Zhang, *Angew. Chem. Int. Ed.* **2007**, 46 (13), 2152-2187.
8. O. Sato, A. Cui, R. Matsuda, S. H. J. Tao, *Acc. Chem. Res.* **2007**, 40 (5), 361-369.
9. A. Dei, L. Sorace, *App. Mag. Res.* **2010**, 38 (2), 139-153.
10. C. Boskovic, Valence Tautomeric Transitions in Cobalt-dioxolene Complexes. In *Spin-Crossover Materials*, John Wiley & Sons Ltd: 2013; pp 203-224.
11. M. D. Ward, J. A. McCleverty, *J. Chem. Soc. Dalton Trans.* **2002**, (3), 275-288.
12. C. K. Jørgensen, *Coord. Chem. Rev.* **1966**, 1 (1-2), 164-178.
13. W. I. Dzik, J. I. v. d. Vlugt, J. N. H. Reek, B. d. Bruin, *Angew. Chem. Int. Ed.* **2011**, 50 (15), 3356-3358.
14. W. Kaim, B. Schwederski, *Coord. Chem. Rev.* **2010**, 254 (13-14), 1580-1588.
15. I. Ratera, J. Veciana, *Chem. Soc. Rev.* **2012**, 41 (1), 303-349.
16. W. Kaim, W. Matheis, *J. Chem. Soc. Chem. Commun.* **1991**, 0, 597.
17. K. P. Butin, E. K. Beloglakina, N. V. Zyk, *Russ. Chem. Rev.* **2005**, 74, 531-553.

- 
18. Y. Yamamoto, Y. Hirata, M. Kodama, T. Yamaguchi, S. Matsukawa, K. Akiba, D. Hashizume, F. Iwasaki, A. Muranaka, M. Uchiyama, P. Chen, K. M. Kadish, N. Kobayashi, *J. Am. Chem. Soc.* **2010**, *132*, 12627.
  19. P. Chaudhuri, K. Wieghardt, Phenoxyl Radical Complexes. In *Progress in Inorganic Chemistry*, John Wiley & Sons, Inc.: 2002; pp 151-216.
  20. P. Day, N. S. Hush, R. J. H. Clark, *Phil. Trans. R. Soc. A* **2008**, *366*, 5-14.
  21. K. R. Dunbar, R. A. Heintz, Chemistry of Transition Metal Cyanide Compounds: Modern Perspectives. In *Prog. Inorg. Chem.*, John Wiley & Sons, Inc.: 2007; pp 283-391.
  22. C. Creutz, H. Taube, *J. Am. Chem. Soc.* **1969**, *91* (14), 3988-3989.
  23. J. R. Reimers, N. S. Hush, *Inorg. Chem.* **1990**, *29* (19), 3686-3697.
  24. M. B. Robin, P. Day, Mixed Valence Chemistry-A Survey and Classification. In *Adv. Inorg. Chem. Radiochem.*, Emeléus, H. J.; Sharpe, A. G., Eds. Academic Press: 1968; Vol. Volume 10, pp 247-422.
  25. M. Parthey, M. Kaupp, *Chem. Soc. Rev.* **2014**, *43*, 5067-5088.
  26. O. Carugo, C. B. Castellani, K. Djinovic, M. Rizzi, *J. Chem. Doc. Dalton Trans.* **1992**, 837-841.
  27. S. J. Lippard, J. M. Berg, Principles of bioinorganic chemistry, University Science Books: 1994.
  28. O. R. Luca, R. H. Crabtree, *Chem. Soc. Rev.* **2013**, *42*, 1440-1459.
  29. J. S. Miller, K. S. Min, *Angew. Chem. Int. Ed.* **2009**, *48* (2), 262-272.
  30. E. Konig, *Z. Naturforsch. A: Astrophys. Phys. Phys. Chem.* **1964**, *19a*, 1139.
  31. J. H. Waters, R. Williams, H. B. Gray, G. N. Schrauzer, H. W. Finck, *J. Am. Chem. Soc.* **1964**, *86*, 4198.
  32. M. E. Cass, N. R. Gordon, C. G. Pierpont, *Inorg. Chem.* **1986**, *25*, 3962.
  33. C. G. Pierpont, R. M. Buchanan, *Coord. Chem. Rev.* **1981**, *38*, 45-87.
  34. D. M. Arciero, J. D. Lipscomb, *J. Biol. Chem.* **1986**, *261*, 2170-2178.
  35. L. Que, J. D. Lipscomb, E. Munck, J. M. Wood, *Biochim. Biophys. Acta* **1977**, *486*, 60-74.
  36. L. Sommer, *Collect. Czech. Chem. Commun.* **1963**, *8* (28), 2102-2130.

- 
37. B. A. Borgias, S. R. Cooper, Y. B. Koh, K. N. Raymond, *Inorg. Chem.* **1984**, 23 (8), 1009-1016.
38. A. A. Vlcek, *J. Organometal. Chem.* **1984**, 297, 43.
39. J. M. Atkinson, P. B. Brindley, A. G. Davies, J. A. A. Hawari, *J. Organometal. Chem.* **1984**, 264, 253-261.
40. G. E. Freeman, K. N. Raymond, *Inorg. Chem.* **1985**, 24, 1410.
41. R. M. Buchanan, H. H. Downs, W. B. Shorthill, C. G. Pierpont, *J. Am. Chem. Soc.* **1983**, 104, 5092.
42. M. J. Smith, D. Kim, B. Horenstein, K. Nakanishi, K. Kustin, *Acc. Chem. Res.* **1991**, 24 (4), 117-124.
43. S. G. Brand, C. J. Hawkins, A. T. Marshall, G. W. Nette, D. L. Parry, *Comp. Biochem. Physiol.* **1989**, 93B, 425-436.
44. A. R. Bulls, C. G. Pippin, F. E. Hahn, K. N. Raymond, *J. Am. Chem. Soc.* **1990**, 112, 2627.
45. B. Galeffi, M. Postel, A. Grand, P. Rey, *Inorg. Chim. Acta* **1989**, 160 (1), 87-91.
46. M. E. Cass, D. L. Greene, R. M. Buchanan, C. G. Pierpont, *J. Am. Chem. Soc.* **1983**, 105, 2680-2680.
47. C. G. Pierpont, H. H. Downs, T. G. Rukavina, *J. Am. Chem. Soc.* **1974**, 96, 5573.
48. C. G. Pierpont, H. H. Downs, *J. Am. Chem. Soc.* **1975**, (97), 2123-2127.
49. L. A. DeLearie, R. C. Haltiwanger, C. G. Pierpont, *Inorg. Chem.* **1988**, 27 (10), 1736-1741.
50. M. E. Cass, C. G. Pierpont, *Inorg. Chem.* **1986**, 25 (15), 2552-2556.
51. R. M. Buchanan, S. L. Kessel, H. H. Downs, C. G. Pierpont, D. N. Hendrickson, *J. Am. Chem. Soc.* **1978**, 100 (25), 7894-7900.
52. K. Sarbasov, B. L. Tumanskii, A. I. Prokov'ev, V. B. Vol'eva, N. N. Bubnov, M. I. Kabachnik, *Isvest. Akad. Nauk SSSR Ser. Khim.* **1984**, 1789.
53. R. M. Buchanan, J. Claflin, C. G. Pierpont, *Inorg. Chem.* **1983**, 22 (18), 2552-2556.
54. R. M. Buchanan, C. G. Pierpont, *Inorg. Chem.* **1979**, 18 (6), 1616-1620.

- 
55. T. Matsumoto, M. W. H. Yano, A. Kobayashi, M. Kato, H. Chang, *Bull. Chem. Soc. Jpn.* **2015**, *88*, 74-83.
56. L. J. McCormick, B. F. Abrahams, B. A. Boughton, M. J. Grannas, T. A. Hudson, R. Robson, *Inorg. Chem.* **2014**, *53*, 1721-1728.
57. X. J. Xu, *J. Coord. Chem.* **2014**, *40* (1), 48-53.
58. C. Liu, P. Restorp, E. Nordlander, C. G. Pierpont, *Chem. Comm.* **2001**, 2686-2687.
59. M. E. Cass, C. G. Pierpont, *Inorg. Chem.* **1986**, *25* (2), 122-123.
60. F. A. Cotton, C. A. Murillo, D. Villagrán, R. Yu, *J. Am. Chem. Soc.* **2006**, *128*, 3281-3290.
61. A. Caneschi, A. Dei, *Angew. Chem. Int. Ed.* **1998**, *37* (21), 3005-3007.
62. L. A. DeLearie, R. C. Haltiwanger, C. G. Pierpont, *J. Am. Chem. Soc.* **1989**, *111*, 4324-4328.
63. D. H. Chin, D. T. Sawyer, W. P. Schaefer, C. J. Simmons, *Inorg. Chem.* **1983**, *22* (5), 752-758.
64. S. K. Larsen, C. G. Pierpont, G. DeMunno, G. Dolcetti, *Inorg. Chem.* **1986**, *25* (27), 4828-4831.
65. A. S. Attia, C. G. Pierpont, *Inorg. Chem.* **1995**, *34* (5), 1172-1179.
66. N. Shaikh, S. Goswami, A. Panja, H. L. Sun, F. Pan, S. Gao, P. Banerjee, *Inorg. Chem.* **2005**, *44* (26), 9714-9722.
67. N. Shaikh, S. Goswami, A. Panja, X. Y. Wang, S. Gao, R. J. Butcher, P. Banerjee, *Inorg. Chem.* **2004**, *43* (19), 5908-5918.
68. A. S. Attia, S. Bhattacharya, C. G. Pierpont, *Inorg. Chem.* **1995**, *34* (17), 4427-4433.
69. A. J. Simaan, M. L. Boillot, R. Carrasco, J. Cano, J. J. Girerd, T. A. Mattioli, J. Ensling, H. Spiering, P. Gütllich, *Chem. Eur. J.* **2005**, *11* (6), 1779-1793.
70. L. D. Loomis, K. N. Raymond, *Inorg. Chem.* **1991**, *30* (5), 906-911.
71. S. J. Rodgers, C. W. Lee, C. Y. Ng, K. N. Raymond, *Inorg. Chem.* **1987**, *26* (10), 1622-1625.
72. T. B. Karpishin, K. N. Raymond, *Angew. Chem. Int. Ed. Engl.* **1992**, *31*, 466-468.

- 
73. J. S. Lodge, T. Emery, *J. Bacteriol.* **1984**, *160* (2), 801-804.
74. T. D. P. Stack, T. B. Karpishin, K. N. Raymond, *J. Am. Chem. Soc.* **1992**, *114* (4), 1512-1514.
75. M. K. Biswas, S. C. Patra, A. N. Maity, S. C. Ke, N. D. Adhikary, P. Ghosh, *Inorg. Chem.* **2012**, *51* (12), 6687-6699.
76. M. K. Biswas, S. C. Patra, A. N. Maity, S. C. Ke, T. Weyhermuller, P. Ghosh, *Dalton Trans.* **2013**, *42* (18), 6538-6552.
77. I. Ando, T. Fukuishi, K. Ujimoto, H. Kurihara, *Inorg. Chim. Acta* **2012**, *390*, 47-52.
78. P. A. Wicklund, L. S. Beckmann, D. G. Brown, *Inorg. Chem.* **1976**, *15* (8), 1996-1997.
79. A. L. Balch, J. Catalano, M. M. Olmstead, *Inorg. Chem.* **1990**, *29* (9), 1638-1642.
80. N. S. Hush, A. T. Wong, G. B. Bacskay, J. R. Reimers, *J. Am. Chem. Soc.* **1990**, *112* (11), 4192-4197.
81. R. M. Buchanan, C. G. Pierpont, *J. Am. Chem. Soc.* **1980**, *102* (15), 4951-4957.
82. O. S. Jung, C. G. Pierpont, *J. Am. Chem. Soc.* **1994**, *116* (5), 2229-2230.
83. M. W. Lynch, R. M. Buchanan, C. G. Pierpont, D. N. Hendrickson, *Inorg. Chem.* **1981**, *20* (4), 1038-1046.
84. S. Goswami, A. Panja, R. J. Butcher, N. Shaikh, P. Banerjee, *Inorg. Chim. Acta* **2011**, *370* (1), 311-321.
85. A. Dei, A. Feis, G. Poneti, L. Sorace, *Inorg. Chim. Acta* **2008**, *361* (14-15), 3842-3846.
86. A. Beni, A. Dei, S. Laschi, M. Rizzitano, L. Sorace, *Chem. Eur. J.* **2008**, *14* (6), 1804-1813.
87. O. Sato, S. Miura, H. Maruyama, Y. Zhang, D. Wu, W. Zhang, H. Xu, R. Matsuda, H. Sun, J. Tao, *Inorg. Chim. Acta* **2008**, *361* (12-13), 3659-3662.
88. P. Dapporto, A. Dei, G. Poneti, L. Sorace, *Chem. Eur. J.* **2008**, *14* (35), 10915-10918.

- 
89. Y. Mulyana, G. Poneti, B. Moubaraki, K. S. Murray, B. F. Abrahams, L. Sorace, C. Boskovic, *Dalton Trans.* **2010**, 39 (20), 4757-4767.
90. O. S. Jung, D. H. Jo, Y. A. Lee, B. J. Conklin, C. G. Pierpont, *Inorg. Chem.* **1997**, 36 (1), 19-24.
91. R. D. Schmidt, D. A. Shultz, J. D. Martin, P. D. Boyle, *J. Am. Chem. Soc.* **2010**, 132 (17), 6261-6273.
92. R. D. Schmidt, D. A. Shultz, J. D. Martin, *Inorg. Chem.* **2010**, 49 (7), 3162-3168.
93. A. Bencini, A. Caneschi, C. Carbonera, A. Dei, D. Gatteschi, R. Righini, C. Sangregorio, J. V. Slageren, *J. Mol. Struct.* **2003**, 656 (1-3), 141-154.
94. F. Yu, B. Li, *Inorg. Chim. Acta* **2012**, 392 (0), 199-203.
95. A. Panja, *RSC Advances* **2013**, 3 (15), 4954-4963.
96. M. Graf, G. Wolmershäuser, H. Kelm, S. Demeschko, F. Meyer, H. Krüger, *Angew. Chem. Int. Ed.* **2010**, 49, (5), 950-953.
97. S. Bin-Salamon, S. H. Brewer, E. C. Depperman, S. Franzen, J. W. Kampf, M. L. Kirk, K. R. Kumar, S. Lappi, K. Peariso, K. E. Preuss, D. A. Shultz, *Inorg. Chem.* **2006**, 45 (11), 4461-4467.
98. N. G. R. Hearn, J. L. Korčok, M. M. Paquette, K. E. Preuss, *Inorg. Chem.* **2006**, 45 (22), 8817-8819.
99. A. Dei, D. Gatteschi, L. Pardi, U. Russo, *Inorg. Chem.* **1991**, 30 (12), 2589-2594.
100. K. G. Alley, G. Poneti, P. S. D. Robinson, A. Nafady, B. Moubaraki, J. B. Aitken, S. C. Drew, C. Ritchie, B. F. Abrahams, R. K. Hocking, K. S. Murray, A. M. Bond, H. H. Harris, L. Sorace, C. Boskovic, *J. Am. Chem. Soc.* **2013**, 135 (22), 8304-8323.
101. C. Carbonera, A. Dei, J. F. Létard, C. Sangregorio, L. Sorace, *Angew. Chem. Int. Ed.* **2004**, 43 (24), 3136-3138.
102. J. Tao, H. Maruyama, O. Sato, *J. Am. Chem. Soc.* **2006**, 128 (6), 1790-1791.
103. Y. Teki, M. Shirokoshi, S. Kanegawa, O. Sato, *Eur. J. Inorg. Chem.* **2011**, (25), 3761-3767.

- 
104. B. Li, J. Tao, H. L. Sun, O. Sato, R. B. Huang, L. S. Zheng, *Chem. Comm.* **2008**, (19), 2269-2271.
105. B. Li, L. Q. Chen, J. Tao, R. B. Huang, L. S. Zheng, *Inorg. Chem.* **2013**, *52* (8), 4136-4138.
106. K. S. Min, A. G. DiPasquale, J. A. Golen, A. L. Rheingold, J. S. Miller, *J. Amer. Chem. Soc.* **2007**, *129* (8), 2360-2368.
107. J. Overgaard, L. H. Møller, M. A. Borup, M. Tricoire, J. P. S. Walsh, E. Rentschler, *Dalton Trans.* **2016**, *45* (32), 12924-12932.
108. A. Panja, N. Jana, A. Bauzá, A. Frontera, C. Mathonière, *Inorg. Chem.* **2016**, *55* (17), 8331-8340.
109. S. Hayami, K. Hashiguchi, G. Juhász, M. Ohba, H. Ōkawa, Y. Maeda, K. Kato, K. Osaka, M. Takata, K. Inoue, *Inorg. Chem.* **2004**, *43* (14), 4124-4126.
110. O. S. Jung, C. G. Pierpont, *J. Amer. Chem. Soc.* **1994**, *116* (5), 2229-2230.
111. B. Li, L. Q. Chen, R. J. Wei, J. Tao, R. B. Huang, L. S. Zheng, Z. Zheng, *Inorg. Chem.* **2010**, *50* (2), 424-426.
112. F. Nador, F. Novio, D. Ruiz-Molina, *Chem. Comm.* **2014**, *50* (93), 14570-14572.
113. M. Affronte, A. Beni, A. Dei, L. Sorace, *Dalton Trans.* **2007**, *0* (45), 5253-5259.
114. M. Guardingo, F. Busqué, F. Novio, D. Ruiz-Molina, *Inorg. Chem.* **2015**, *54* (14), 6776-6781.
115. I. Imaz, D. Maspoch, C. Rodríguez-Blanco, J. Pérez-Falcón, *Angew. Chem. Int. Ed.* **2008**, *47* (10), 1857-1860.
116. F. Novio, J. Campo, D. Ruiz-Molina, *Inorg. Chem.* **2014**, *53* (13), 8742-8748.
117. P. González-Monje, F. Novio, D. Ruiz-Molina, *Chem. Eur. J.* **2015**, *21* (28), 10094-10099.
118. C. W. Lange, M. Foldeaki, V. I. Nevodchikov, V. K. Cherkasov, G. A. Abakumov, C. G. Pierpont, *J. Am. Chem. Soc.* **1992**, *114* (16), 6582-6583.
119. C. D. Hubbard, A. Gerhard, R. v. Eldik, *Inorg. Chem.* **1991**, *30* (26), 5023-5027.

- 
120. B. Szpoganicz, R. J. Motekaitis, A. E. Martell, *Inorg. Chem.* **1990**, *29* (8), 1467-1474.
121. P. Barbaro, C. Bianchini, P. Frediani, A. Meli, F. Vizza, *Inorg. Chem.* **1992**, *31* (8), 1523-1529.
122. P. Barbaro, C. Bianchini, C. Mealli, A. Meli, *J. Am. Chem. Soc.* **1991**, *113* (8), 3181-3183.
123. H. Ohtsu, K. Tanaka, *Angew. Chem. Int. Ed.* **2004**, *43* (46), 6301-6303.
124. H. Ohtsu, K. Tanaka, *Chem. Eur. J.* **2005**, *11* (11), 3420-3426.
125. J. J. Loughrey, S. Sproules, E. J. L. McInnes, M. J. Hardie, M. A. Halcrow, *Chem. Eur. J.* **2014**, *20* (21), 6272-6276.
126. G. A. Fox, C. G. Pierpont, *Inorg. Chem.* **1992**, *31* (18), 3718-3723.
127. W. Kaim, J. Rall, *Angew. Chem. Int. Ed.* **1996**, *35* (1), 43-60.
128. J. Rall, M. Wanner, M. Albrecht, F. M. Hornung, W. Kaim, *Chem. Eur. J.* **1999**, *5* (10), 2802-2809.
129. M. S. Dooley, M. A. McGuirl, D. E. Brown, P. N. Turowski, W. S. McIntire, P. F. Knowles, *Nature* **1991**, *349*, 262-264.
130. E. I. Solomon, M. J. Baldwin, M. D. Lowery, *Chem. Rev.* **1992**, *92* (4), 521-542.
131. M. Winkler, K. Lerch, E. I. Solomon, *J. Am. Chem. Soc.* **1981**, *103* (23), 7001-7003.
132. D. E. Wilcox, A. G. Porras, Y. Y. Hwang, K. Lerch, M. E. Winkler, E. I. Solomon, *J. Am. Chem. Soc.* **1985**, *107* (13), 4015-4027.
133. N. Kitajima, T. Koda, Y. Iwata, Y. Morooka, *J. Am. Chem. Soc.* **1990**, *112* (24), 8833-8839.
134. E. Gojon, J. M. Latour, J. Laugier, *Inorg. Chem.* **1987**, *26* (13), 2046-2052.
135. E. Gojon, J. M. Latour, S. J. Greaves, D. C. Povey, V. Ramdas, G. W. Smith, *J. Chem. Soc. Dalton Trans.* **1990**, *0* (7), 2043-2051.
136. E. Gojon, S. J. Greaves, J. M. Latour, D. C. Povey, G. W. Smith, *Inorg. Chem.* **1987**, *26* (9), 1457-1459.
137. S. Cho, T. Gadzikwa, M. Afshari, S. T. Nguyen, J. T. Hupp, *Eur. J. Inorg. Chem.* **2007**, (31), 4863-4867.

- 
138. M. I. Bodini, G. Copia, R. Robinson, D. T. Sawyer, *Inorg. Chem.* **1983**, 22 (1), 126-129.
139. A. I. Prokofev, N. A. Malysheva, N. N. Bubnov, S. P. Solodovnikov, M. I. Kabachnik, *Dokl. Akad. Nauk SSSR* **1980**, 252, 236.
140. V. A. Muraev, G. A. Abakumov, G. A. Razuvaev, *Isvest. Akad. Nauk SSSR Ser. Khim.* **1975**, 159.
141. B. L. Tumanskii, A. I. Prokofev, E. V. Maskaeva, V. V. Bashilov, V. I. Sokolov, S. P. Solodovnikov, N. N. Bubnov, O. A. Reutov, M. I. Kabachnik, *Metalloorg. Khim.* **1988**, 1, 407.
142. B. L. Tumanskii, V. T. Kampel, S. P. Solodovnikov, V. I. Bregadze, N. N. Godovikov, *Isvest. Akad. Nauk SSSR Ser. Khim.* **1985**, 2644.
143. A. Caneschi, D. Gatteschi, R. Sessoli, P. Rey, *Acc. Chem. Res.* **1989**, 22 (11), 392-398.
144. A. Caneschi, D. Gatteschi, P. Rey, *Prog. Inorg. Chem.* **1991**, 39, 331.
145. V. Ovcharenko, Copper(II) Nitroxide Molecular Spin-transition Complexes. In *Magnetism: Molecules to Materials IV*, Joel S. Miller, M. D., Ed. Wiley-VCH: 2002; pp 41-62.
146. R. Brière, H. Lemaire, A. Rassat, *Bull. Soc. Chim. France* **1965**, 3273.
147. A. Zheludev, V. Barone, M. Bonnet, B. Delley, A. Grand, E. Ressouche, R. Subra, P. Rey, J. Schweizer, *J. Am. Chem. Soc.* **1994**, 116 (5), 2019-2027.
148. M. H. Dickman, R. J. Doedens, *Inorg. Chem.* **1981**, 20 (8), 2677-2681.
149. L. C. Porter, M. H. Dickman, R. J. Doedens, *Inorg. Chem.* **1988**, 27 (9), 1548-1552.
150. N. Yoshioka, M. Irisawa, M. Abe, N. Aikawa, H. Inoue, *Mol. Cryst. Liq. Cryst.* **1997**, 306 (1), 403-408.
151. S. Y. Zhou, T. Li, Z. Li, Y. Q. Sun, Q. L. Wang, D. Z. Liao, L. Tian, *Inorg. Chim. Acta* **2016**, 444, 131-140.
152. H. Oshio, M. Yamamoto, H. Kawauchi, N. Koga, T. Ito, *J. Solid State Chem.* **2001**, 159 (2), 455-459.
153. H. Oshio, M. Yamamoto, T. Ito, *J. Chem. Soc. Dalton Trans.* **1999**, 0 (15), 2641-2643.

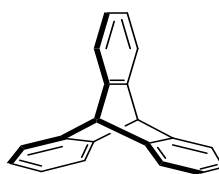
---

## Chapter 2

### Highly Porous Hydrogen-Bond Networks of a Triptycene Based *Tris-Dioxolene*

#### 2.1 Introduction

As discussed in Chapter 1, dioxolenes are of great interest as ligands which can provide mixed-valency, valence tautomerism, and bistability to coordination complexes. Monodioxolene complexes of cobalt are the most well explored systems reported in the literature, with the number of reported dioxolene complexes containing more than two metal atoms being comparatively small. Triptycene (**Figure 2.1**) derivatives have found use as supramolecular scaffolds,<sup>[1-10]</sup> polynucleating ligands for transition metal ions,<sup>[11-18]</sup> and polymeric materials.<sup>[19-22]</sup> Diamino phenylene derivatives of triptycene can be converted to extended arenes,<sup>[23]</sup> annelated heterocycles,<sup>[15-18]</sup> or polydentate metal binding domains<sup>[12-14]</sup> by Schiff base condensations. Triptycenes containing catechol functionalities have been used as components in hydrogen-bonded supramolecular assemblies, crown ether receptors,<sup>[1-8]</sup> or microporous polymer materials.<sup>[19-22]</sup>



triptycene

**Figure 2.1.** The structure of triptycene.

The Halcrow group has previously reported several redox-active metallo-supramolecular architectures composed of *bis*- and *tris*-dioxolene scaffolds,<sup>[24-26]</sup> and this chapter will build on this by exploring the synthesis and crystallography of *bis*- and *tris*-dioxolene ligands based on triptycene. There are a number of considerations that should be taken into account when designing such ligands. Firstly, the dioxolene rings should be in close proximity to one another in order to enhance the electronic

---

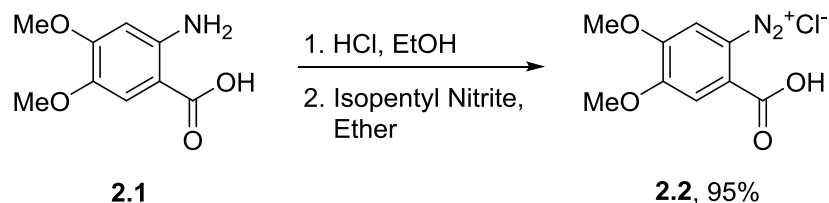
coupling between them.<sup>[27-28]</sup> It is also observed that there is a greater degree of communication and ferromagnetic coupling between semiquinone centres when they are not coplanar or formally conjugated to one another, so ideally a spacer should be used to skew the dioxolene rings away from a planar geometry.<sup>[29-34]</sup> It should also be ensured that the carbon atoms bonded directly to the dioxolene ring are quaternary centres, as the presence of CH or CH<sub>2</sub> groups in these positions provides a radical decomposition pathway that can lead to a very short lifetime of the complex once it has transitioned to the semiquinone state.<sup>[26]</sup> Finally, as the scope of this project also includes the possibility of supramolecular assemblies being formed from these ligands, it is therefore also important to design ligands which are likely to impart a desirable 2D or 3D network or coordination polymer structure. In this chapter, we report several novel highly porous hydrogen-bond network crystals of dioxolene derivatised triptycenes.

## 2.2 Results and Discussion

### 2.2.1 Synthesis

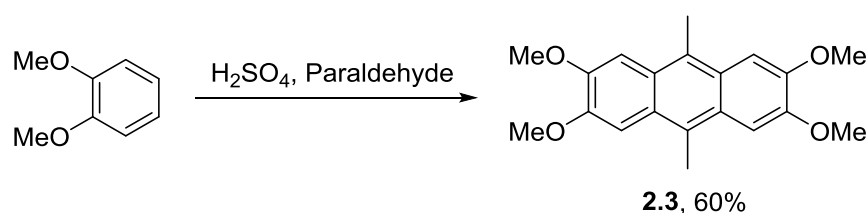
When synthesising triptycene based ligands, it is important to consider a synthetic strategy which allows for various moieties to be introduced to the final product so that structurally related ligands may be produced easily.<sup>[35]</sup>

The initial synthetic route that was employed involves the reaction of a functionalised *ortho*-aminobenzoic acid **2.1** with isopentyl nitrite to produce the corresponding diazonium salt, **2.2** (**Scheme 2.1**).



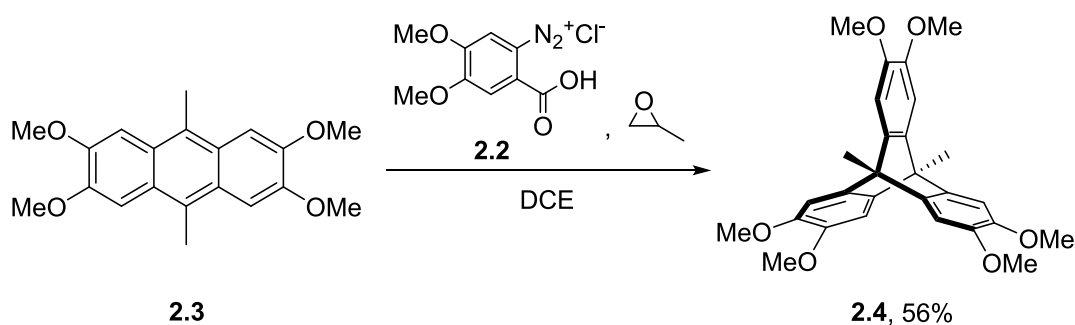
**Scheme 2.1.** Conversion of the *ortho*-aminobenzoic acid to the corresponding diazonium chloride.

This reaction has the advantage of allowing for ease of functionalisation of the desired triptycene by modification the initial *ortho*-aminobenzoic acid, many of which are commercially available. The next step requires the synthesis of a 9,10-dimethylantracene derivative **2.3**, which may be produced in one step from 1,2-dimethoxybenzene (**Scheme 2.2**). The presence of two phenylene methyl groups is important, as these will be the quarternary spacers in the final product.



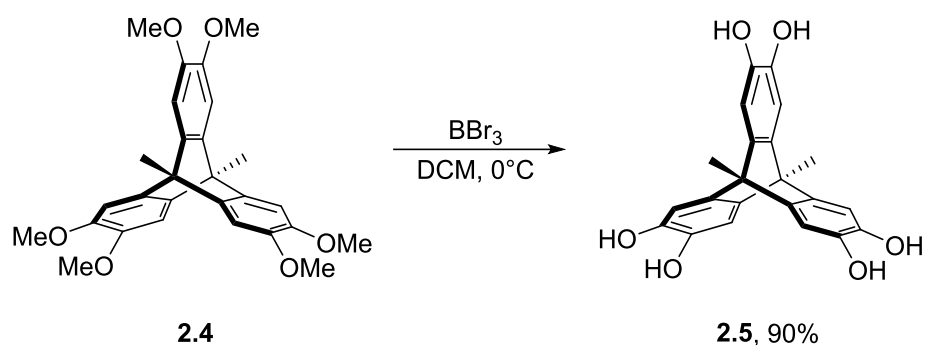
**Scheme 2.2.** Synthesis of the 9,10-dimethylantracene intermediate **2.3**.

The diazonium salt **2.2** is then reacted directly with the 9,10-dimethylantracene **2.3** to afford the hexamethoxy triptycene product **2.4** (**Scheme 2.3**).



**Scheme 2.3.** Synthesis of the hexamethoxy protected triptycene **2.4**.

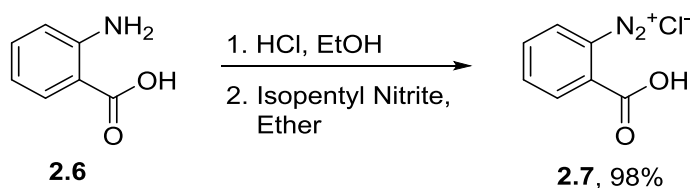
The final step is to remove the methoxy protecting groups from **2.4** with boron tribromide, a trivial procedure which invariably gives a high yield of the product **2.5** (**Scheme 2.4**). Compound **2.5** is stable and may be stored for later use without degradation.



**Scheme 2.4.** Deprotection to furnish the final *tris*(Cat) triptycene ligand, **2.5**.

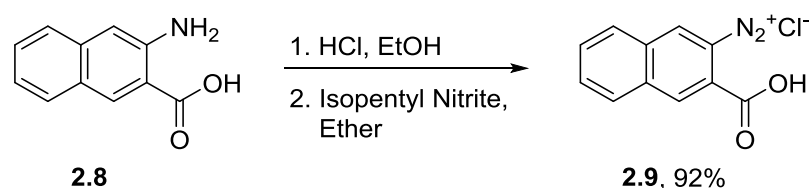
With this as a general procedure, the synthesis of several related triptycenes was attempted from commercially available *ortho*-aminobenzoic acids.

Another target ligand is the *bis*(Cat) version of triptycene, where one of the catechol moieties has been replaced by an unsubstituted benzene ring. The resultant triptycene can be thought of as a (*bis*)dentate form of the parent triptycene **2.5**. This product can be obtained by producing **2.7** in an analogous way to **2.2** (**Scheme 2.5**).



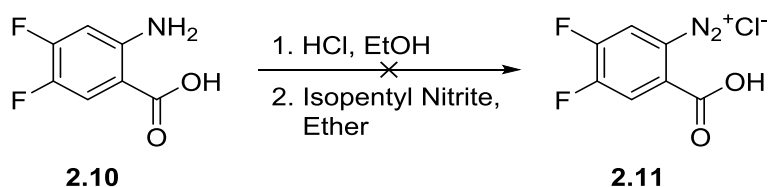
**Scheme 2.5.** Conversion of the *ortho*-aminobenzoic acid **2.6** to the corresponding diazonium chloride **2.7**.

Extending the aromatic rings may have an effect on crystal packing, and thus an *ortho*-aminobenzoic acid containing a naphthalene group in place of the benzene ring was synthesised (**Scheme 2.6**).



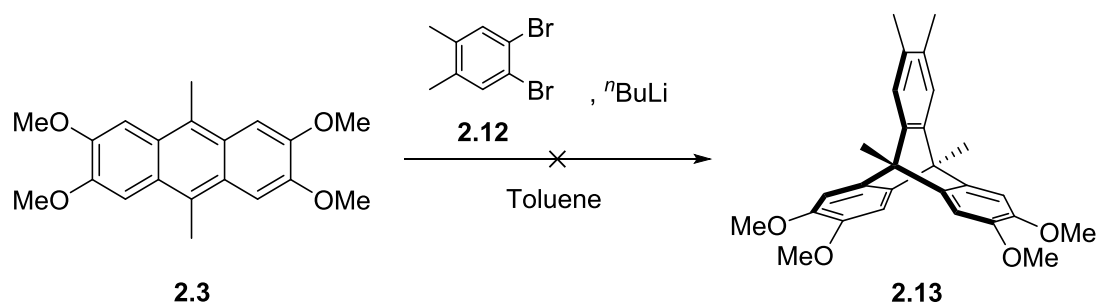
**Scheme 2.6.** Conversion of the *ortho*-aminobenzoic acid **2.8** to the corresponding diazonium chloride **2.9**.

Halogenation of one of the rings is another modification which may lead to differences in crystal packing, and the synthesis of the 1,2-difluoro derivative was attempted (**Scheme 2.7**). The reaction unfortunately did not proceed, with only starting materials being observed after 18 hours.



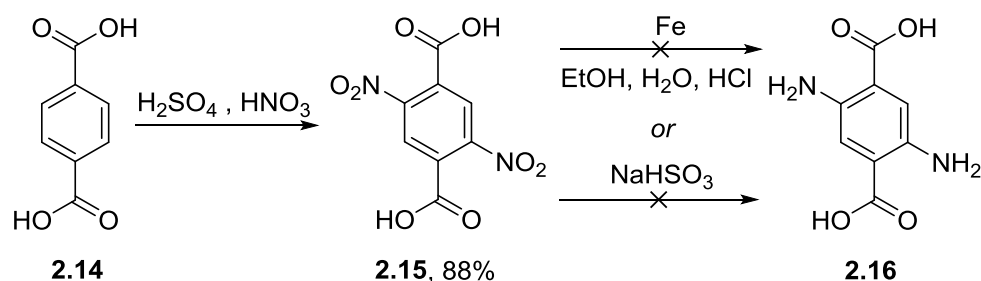
**Scheme 2.7.** Failed conversion of the *ortho*-aminobenzoic acid **2.10** to the corresponding diazonium chloride **2.11**.

The 4,5-dimethyl-2-amino-benzoic acid starting material is not commercially available, so another method for the synthesis of triptycenes<sup>[36]</sup> was employed in an effort to synthesise it (**Scheme 2.8**). This method uses an *ortho*-dibromo starting material instead of an *ortho*-aminobenzoic acid, in combination with <sup>n</sup>BuLi. Unfortunately, when this method was attempted the product was not obtained.



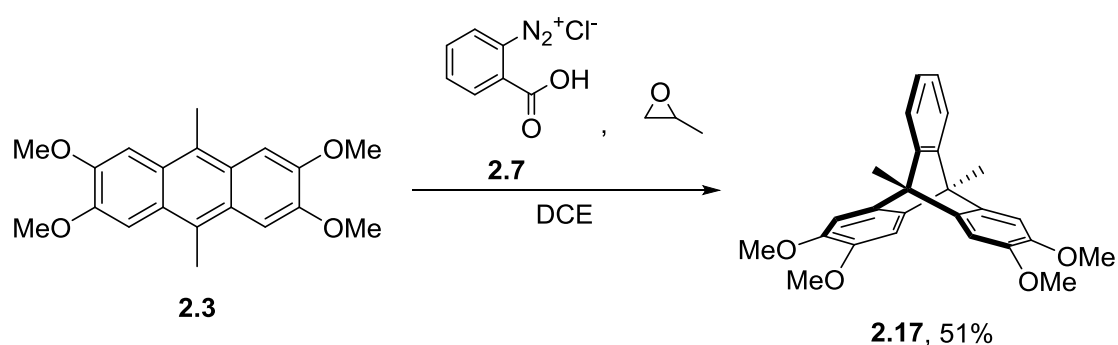
**Scheme 2.8.** Attempted alternative synthesis of triptycene **2.13** using *ortho*-dibromo starting material **2.12**.

Another potential target is the product obtained from the reaction of molecule of **2.3** with a single *bis(ortho-aminobenzoic acid)* molecule, **2.16**. Synthesis of the *bis(ortho-aminobenzoic acid)* compound is reported<sup>[37]</sup> by nitration of terephthalic acid to form **2.15**, followed by reduction (**Scheme 2.9**). Reductions with ethanolic HCl or  $\text{NaHSO}_3$  were attempted, however neither of these reactions yielded the product.



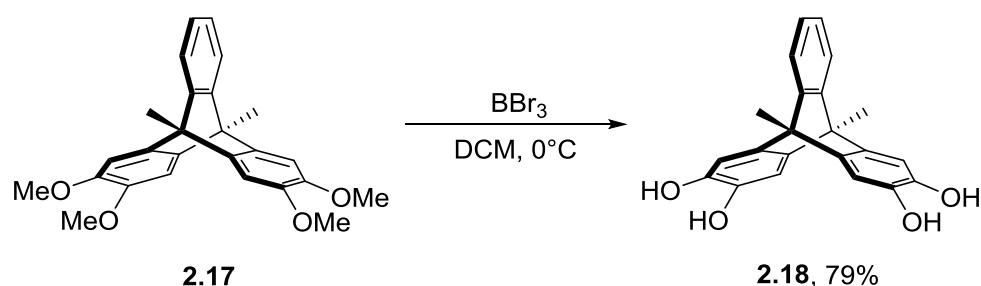
**Scheme 2.9.** Attempted synthesis of a *bis(ortho-aminobenzoic acid)* **2.16**.

Of the additional diazonium salts synthesised, only **2.7** was able to be successfully reacted to form a triptycene, **2.17** (**Scheme 2.10**). The reason for this poor reactivity is unclear, but is hypothesised to be a consequence of the electron withdrawing substituents on the diazonium salt inhibiting the reaction.



**Scheme 2.10.** Reaction of **2.7** with **2.3** to form **2.17**.

As with the synthesis of **2.5**, the final step involves deprotection of the methoxy groups with  $\text{BBr}_3$  (**Scheme 2.11**).



**Scheme 2.11.** Deprotection of **2.17** to form the *bis*(Cat) triptycene derivative **2.18**.

Given the lack of other commercially available *ortho*-aminobenzoic acids and the lack of reactivity when an EWG is present, the ligands **2.5** and **2.18** were selected to carry forward.

## 2.2.2 Single Crystal X-Ray Structural Determination of Crystalline Clathrates and Platinum Complexes of Triptycene

### Structure refinement of $2.5 \cdot 3\text{THF}$

The THF solvate of **2.5** was crystallised as brown needles by vapour diffusion of pentane into THF, and adopts the trigonal space group  $P3c1$  (**Figure 2.2**). The molecules of **2.5** hydrogen bond in a trigonal prismatic array to their 6 nearest neighbours in a  $4^9 \cdot 6^6$  (acs) net topology (**Figure 2.3**).<sup>[38-39]</sup> When viewed parallel to the (001) crystal vector, the structure can be seen to contain large open Y shaped  $C_3$ -symmetric channels (**Figure 2.4**). One THF molecule occupies each arm of the

---

channel, with an additional unresolved 0.4 equivalents of THF occupying the channel centre. When the crystalline solvent is ignored, the network has a void volume of 3089 Å<sup>3</sup> per unit cell which is 59.6% of the total unit cell volume.

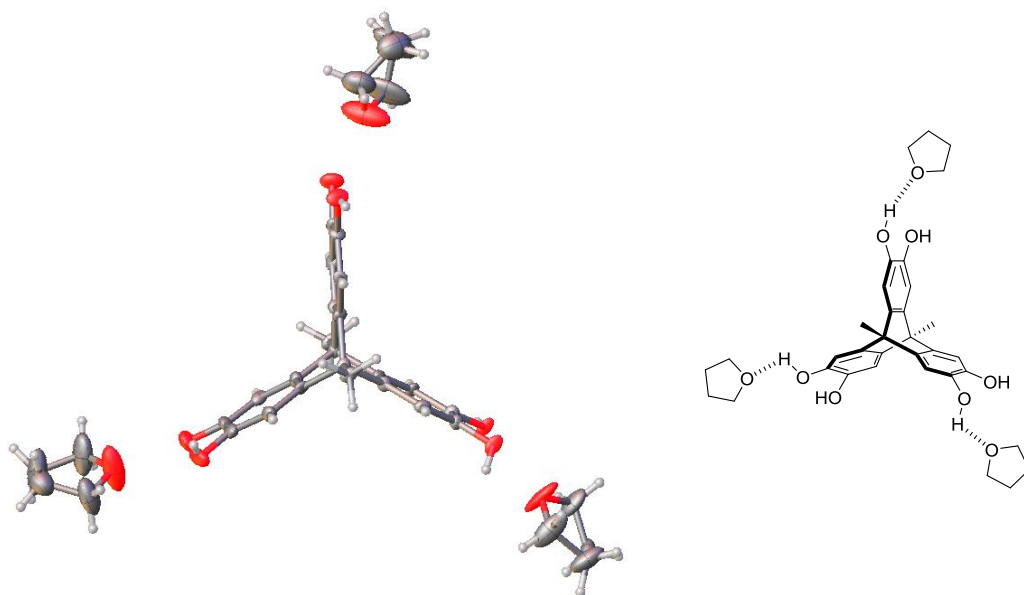


**Figure 2.2.** View of the asymmetric unit of **2.5·3.4THF**, showing hydrogen bond connected to three molecules of THF. Displacement ellipsoids are at the 50 % probability level, except for H atoms which have arbitrary radii.

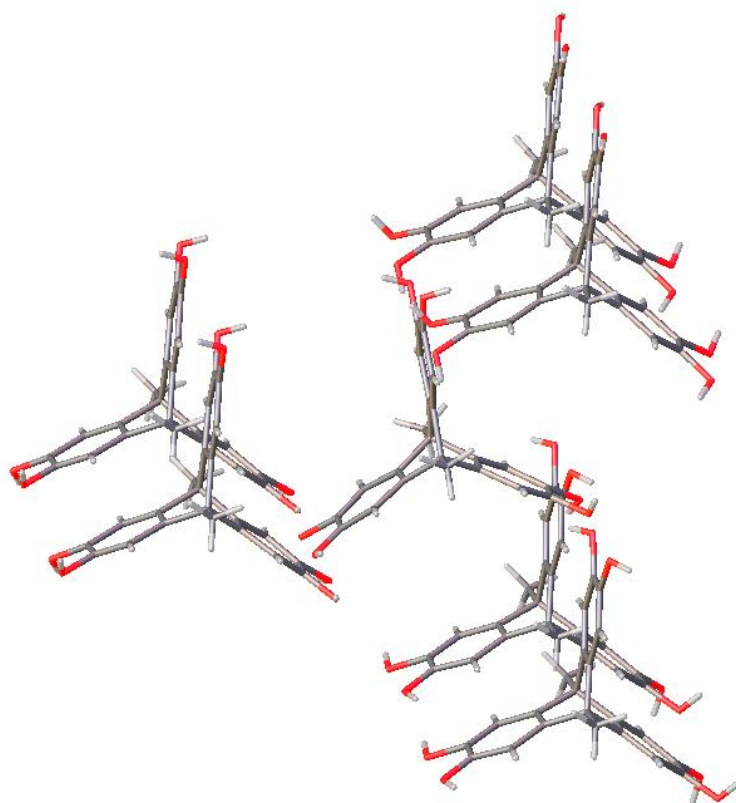


**Figure 2.3.** Packing diagram of **2.5·3.4THF** showing the hydrogen bonding connections to six nearest neighbours in an approximately trigonal prismatic geometry (THF molecules omitted for clarity).

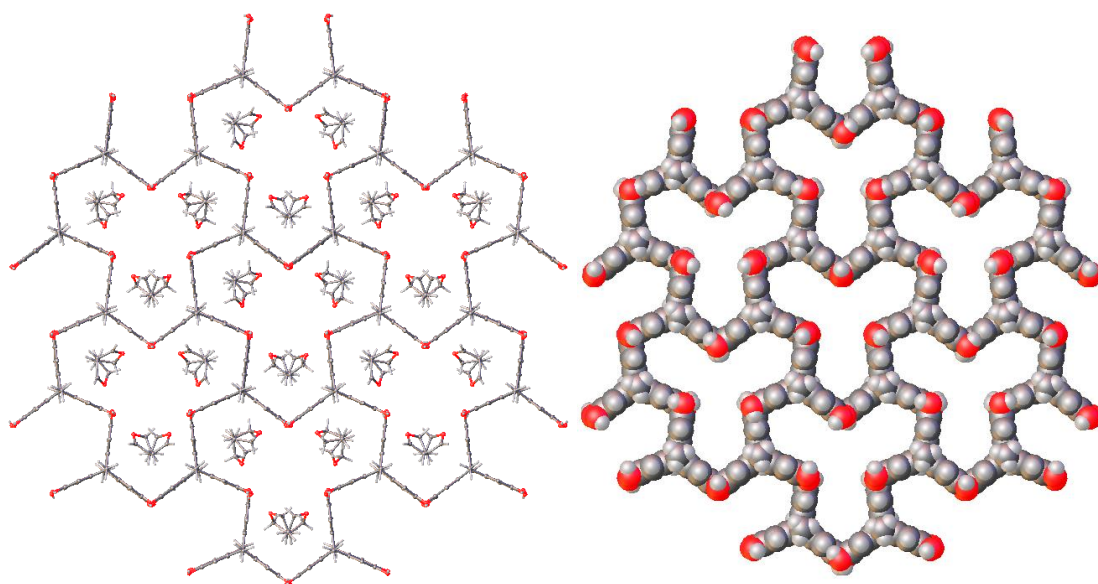


**Figure 2.4.** Packing diagram of **2.5·3.4THF** showing the view parallel to the (001) crystal vector. (Left) View showing the three resolved THF molecules in each channel and their hydrogen bonding. (Right) Space-filling representation of the structure with THF molecules omitted.

When removed from the mother liquor, the solvent rapidly evaporates from the open channels, causing the crystals to turn cloudy in colour and lose crystallinity. This was corroborated by powder X-ray diffraction studies, which showed good agreement with the simulated powder patterns (**Figure 2.5**) immediately after the crystals were removed from the mother liquor. However, when exposed to air over time, some of the peaks broaden or vanish while other grow in, indicating a transformation to a desolvated and amorphous phase **2.5'**. The channels are therefore solvent-supported and incapable of retaining their structure when the solvent leaves the channels.

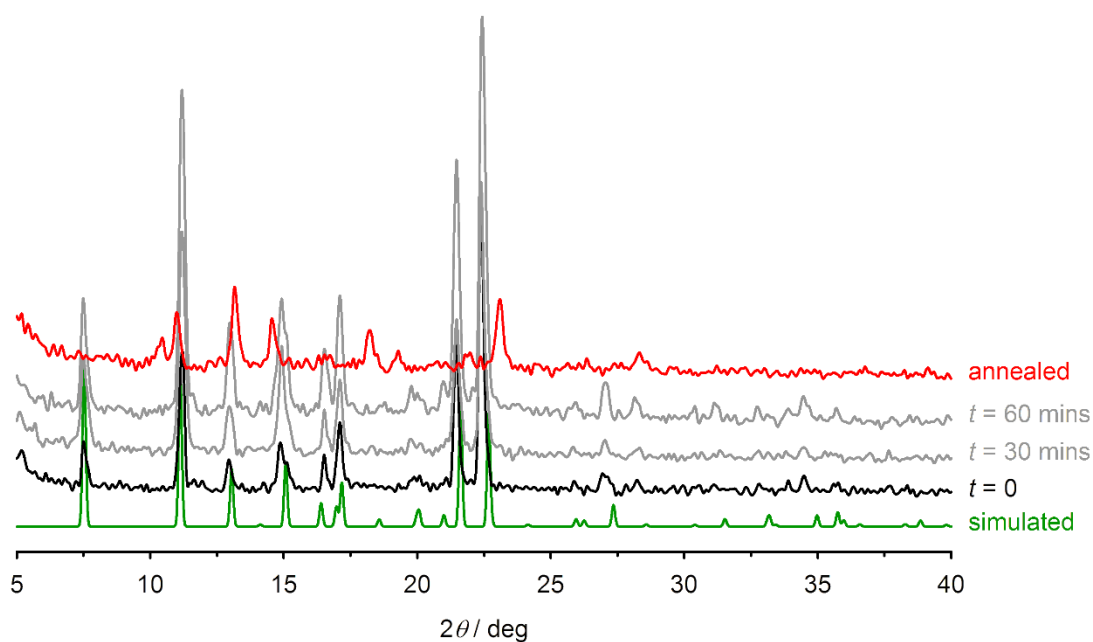


**Figure 2.5.** Powder X-ray diffraction patterns for **5·3.4THF** at 298 K, with the simulated powder pattern generated from the single crystal X-ray structure shown in green. Measurements were made on the same material after having been removed from the mother liquor for different durations, and finally after annealing at 370 K for 30 minutes.

### Structure refinement of **2.5·2.15CHCl<sub>3</sub>**

The  $\text{CHCl}_3$  solvate of **2.5** was crystallised as brown needles by vapour diffusion of pentane into  $\text{CHCl}_3$ . The structure of **2.5·2.15CHCl<sub>3</sub>** was solved in the monoclinic space group  $C2/c$ . The molecules of **2.5** contain O-H...O hydrogen bonds to their 7 nearest neighbours, forming a novel structure of the class of uninodal 7-connected topologies based on pillared stacks of  $4^4$  nets (**Figures 2.6** and **2.7**).<sup>[40-41]</sup> Viewed parallel to the (001) crystal vector, two types of channel are visible; small ones with a cross sectional area of  $4.5 \times 6.1 \text{ \AA}$  containing a single disordered molecule of  $\text{CHCl}_3$ , and large ones with a cross sectional area of  $5.5 \times 14.2 \text{ \AA}$  which likely also contain  $\text{CHCl}_3$ , but was unresolved (**Figure 2.8**). The total volume of both channels is  $2837 \text{ \AA}^3$  per unit cell which is 49.8% of the total unit cell volume.

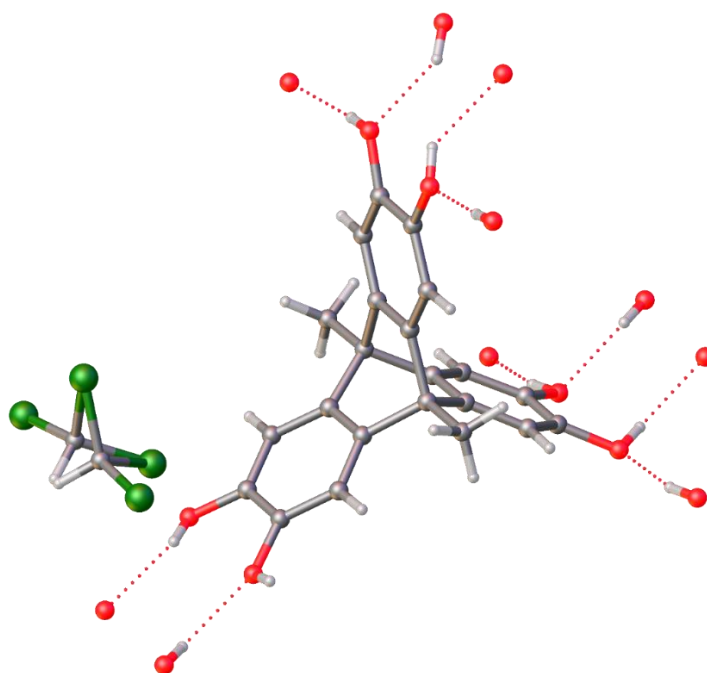


**Figure 2.6.** View of the asymmetric unit in the crystal structure of  $2.5 \cdot 2.15\text{CHCl}_3$ . Both equally occupied orientations of the disordered chloroform molecule are shown.

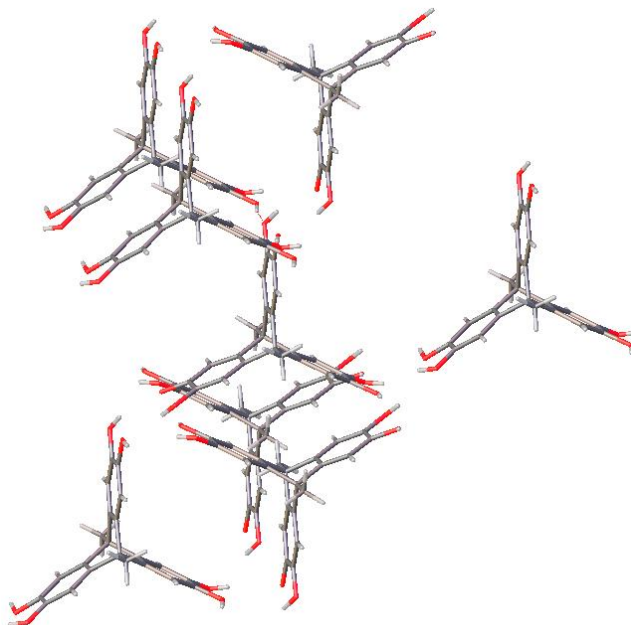


**Figure 2.7.** Packing diagram of  $2.5 \cdot 2.15\text{CHCl}_3$  showing the hydrogen bonding connections to seven nearest neighbours. The  $\text{CHCl}_3$  molecules do not hydrogen bond to the ligand and have been omitted for clarity.

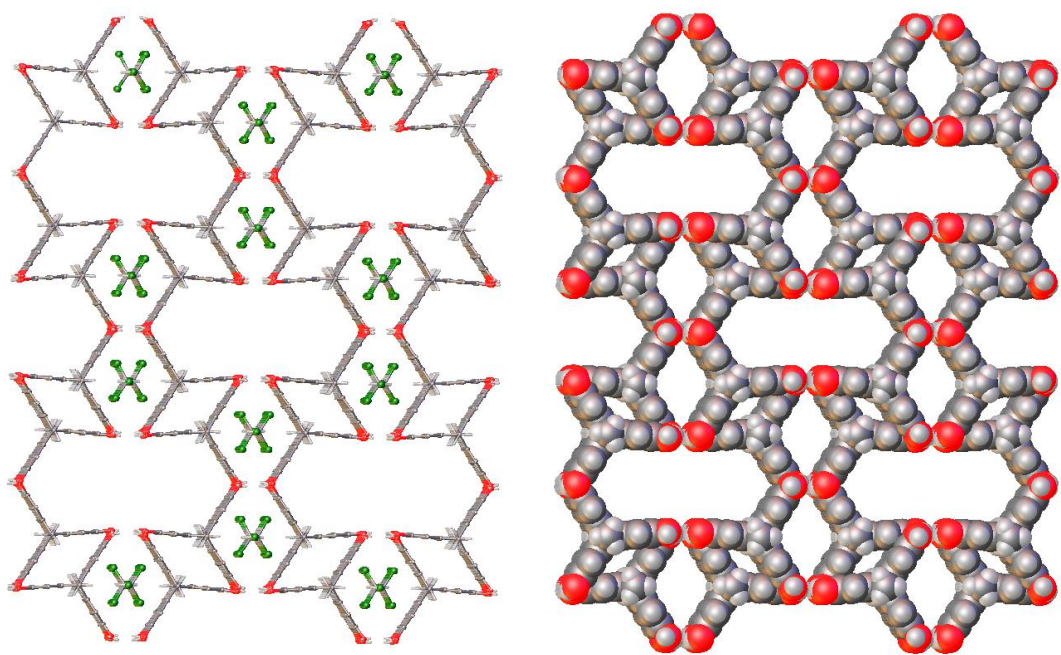


**Figure 2.8.** Packing diagram **2.5·2.15CHCl<sub>3</sub>** showing the view parallel to the (001) crystal vector. (Left) View showing the CHCl<sub>3</sub> molecules in the small channels. (Right) Space-filling representation of the structure with CHCl<sub>3</sub> omitted, showing large and small channels.

When removed from the mother liquor, the crystalline solvent rapidly evaporates from the open channels, causing the crystals to turn cloudy in colour and lose crystallinity. X-ray powder diffraction was carried out on **2.5·2.15CHCl<sub>3</sub>** immediately after removal from the mother liquor, and then after exposure to air for up to 60 minutes (**Figure 2.9**). Initially the powder pattern has good agreement with the simulation, except for the two peaks at  $2\theta = 15^\circ$ , which may arise from the unmodelled contents of the large channels. As the time exposed to air increases, there is a broadening of the peaks indicative of a gradual loss of crystallinity. After annealing the crystals at 370 K for 30 minutes, a new phase **2.5'** is formed, which has not been structurally characterised but corresponds to a solvent-free phase of **2.5**.

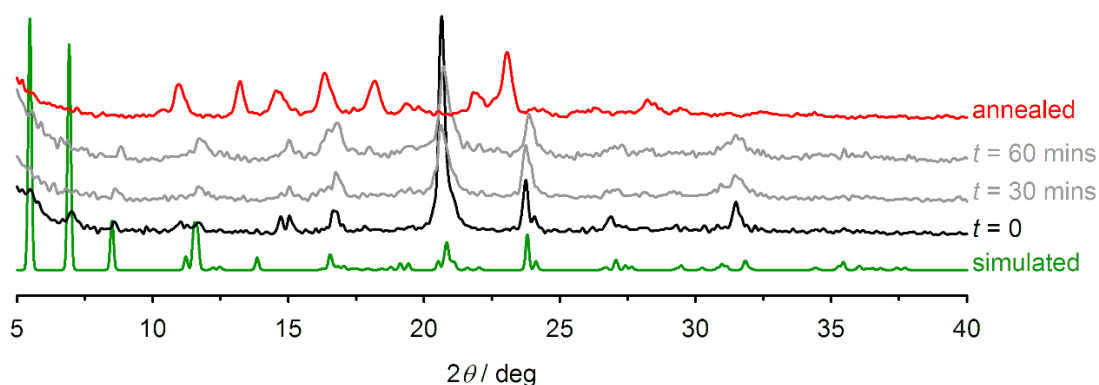


**Figure 2.9.** Powder X-ray diffraction patterns for **2.5**·2.15CHCl<sub>3</sub> at 298 K, with the simulated powder pattern generated from the single crystal X-ray structure shown in green.

### Structure refinement of **2.5**·2Et<sub>2</sub>O

The Et<sub>2</sub>O solvate of **2.5** was crystallised as brown needles by vapour diffusion of pentane into diethyl ether. The structure of **5**·2Et<sub>2</sub>O was solved in the tetragonal space group *I4<sub>1</sub>cd* using the *Olex2* program (**Figure 2.10**). Each molecule donates and accepts four O-H...O hydrogen bonds from its nearest neighbour and two from solvent sites. The triptycene is therefore described as being 8-connected to a distorted cubic array of neighbouring molecules, forming a CsCl (**bcu**) topology net with an elongated *c* axis.<sup>[38-39]</sup> The molecules form chequerboard layers in the [001] crystallographic plane, producing a 2D network of open interconnected channels along the {001} vector (**Figure 2.11**). These channels have a cross-section of 4.2 x 4.5 Å and contain two disordered molecules of Et<sub>2</sub>O per triptycene molecule. When the crystalline solvent is ignored, the network has a void volume of 2568.3 Å<sup>3</sup> per unit cell which is 46.6% of the total unit cell volume.

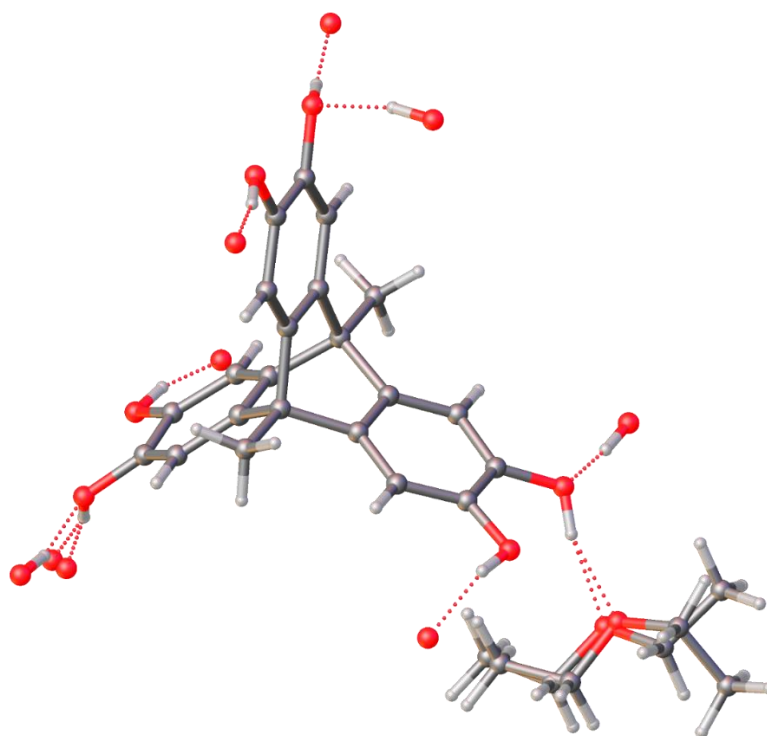


**Figure 2.10.** View of the unique molecules in the crystal structure of  $2.5 \cdot 2\text{Et}_2\text{O}$ . The molecule of **2.5** spans a crystallographic  $C_2$  axis. Both orientations of the disordered  $\text{Et}_2\text{O}$  molecule are shown.

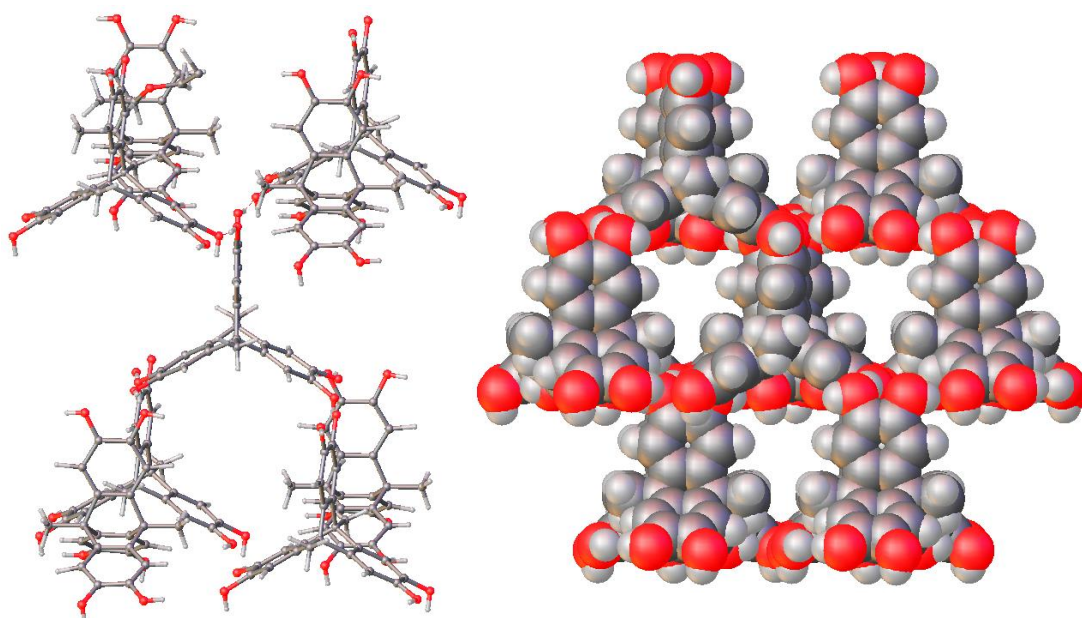


**Figure 2.11.** Packing diagrams of  $2.5 \cdot 2\text{Et}_2\text{O}$  viewed parallel to the (110) crystal vector. The structure adopts a CsCl (bcu) topology net.

---

Powder X-ray diffraction was carried out on **2.5**·2Et<sub>2</sub>O immediately after removal from the mother liquor, and then after exposure to air for up to 80 minutes (**Figure 2.12**). Initially the powder pattern has good agreement with the simulation, however as the time exposed to air increases there is a broadening of the peaks indicative of a gradual loss of crystallinity. After annealing the crystals at 370 K for 30 minutes, a new phase **2.5'** is formed, which has not been structurally characterised but corresponds to a solvent-free phase of **2.5**.

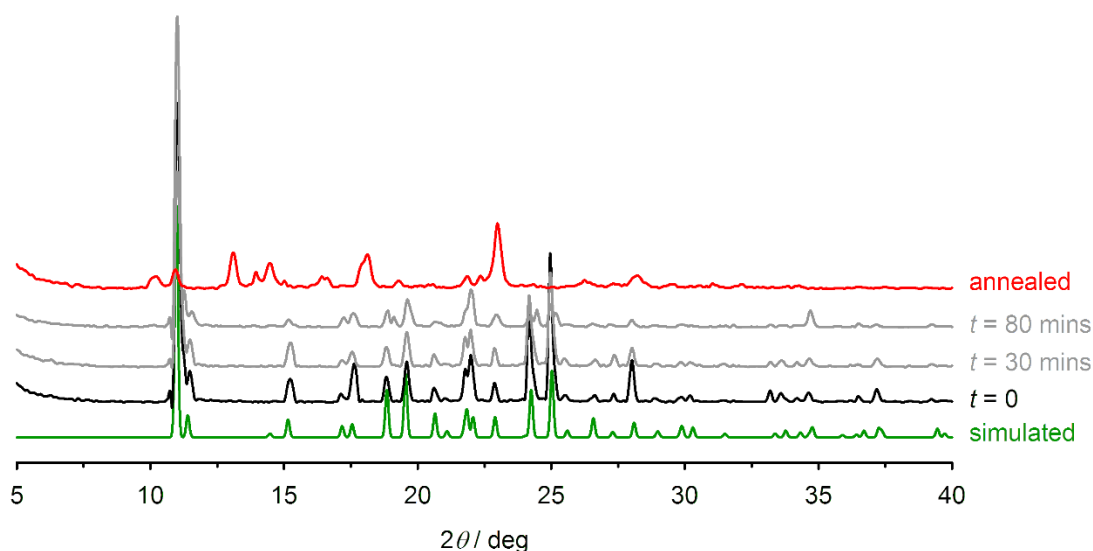


**Figure 2.12.** Powder X-ray diffraction patterns for **2.5**·2Et<sub>2</sub>O at 298 K, with the simulated powder pattern generated from the single crystal X-ray structure shown in green. Measurements were made on the same material after having been removed from the mother liquor for different durations, and finally after annealing at 370 K for 30 minutes.

### Structure refinement of **2.5**·EtOAc

The EtOAc solvate of **2.5** was crystallised as brown needles by vapour diffusion of pentane into EtOAc. The structure **2.5**·EtOAc was solved in the triclinic space group  $P\bar{1}$ . The structure is markedly different from the other solvates discussed in this chapter, as the hydrogen bond network is non-porous. One of the hydroxyl groups of **2.5** is disordered and donates half-occupied O-H...O hydrogen bond to two different acceptors. The three additional ordered hydrogen bonds lead to a 2D

---

puckered  $6^3$  topology in the  $[\bar{1}11]$  plane. There are also two additional hydrogen bond connections via the solvent to the disordered hydroxyl group, which form a hydrogen-bond network in the form of a racemic helical  $4^8.5^4.6^3$  (**bsn**) 3D net topology (**Figure 2.13**).<sup>[38-39]</sup>

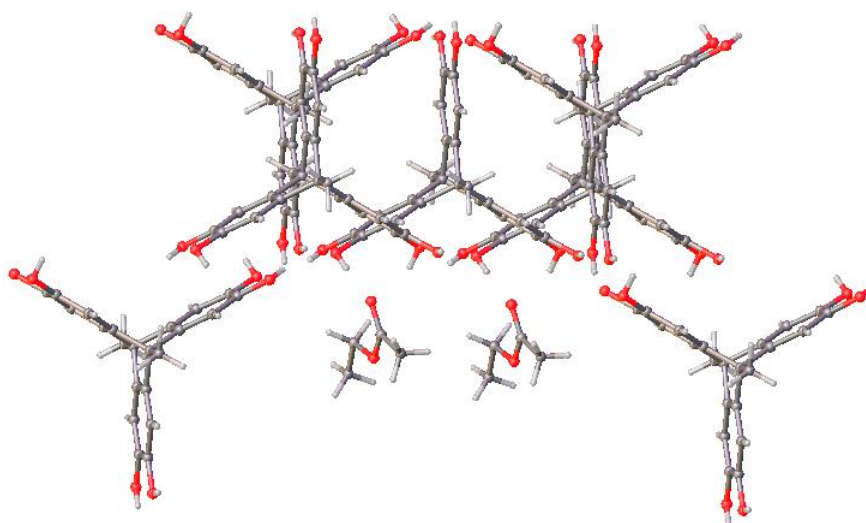


**Figure 2.13.** Packing diagram of **2.5**·EtOAc showing the hydrogen bonding connections to six nearest neighbours. The EtOAc molecules act as topological linkers in this structure, with three of the six network connections are disordered with an occupancy of  $\frac{1}{2}$ .

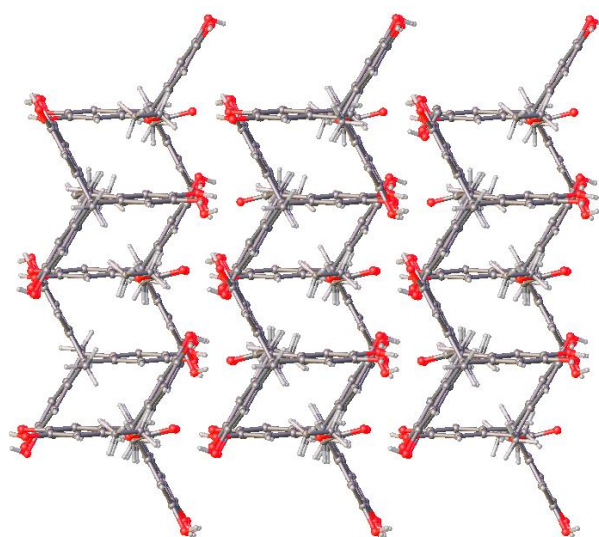


**Figure 2.14.** Packing diagram of the view parallel to the (011) crystal vector of **2.5**·EtOAc, showing solvent-containing pores. This structure forms a bsn topology net. Solvent molecules omitted for clarity.

The powder pattern (**Figure 2.15**) does not agree with the simulation for **2.5**·EtOAc, instead appearing to be pure **2.5'**, and it remains unchanged after annealing. This is possibly due to very fast solvent loss inside the diffractometer.

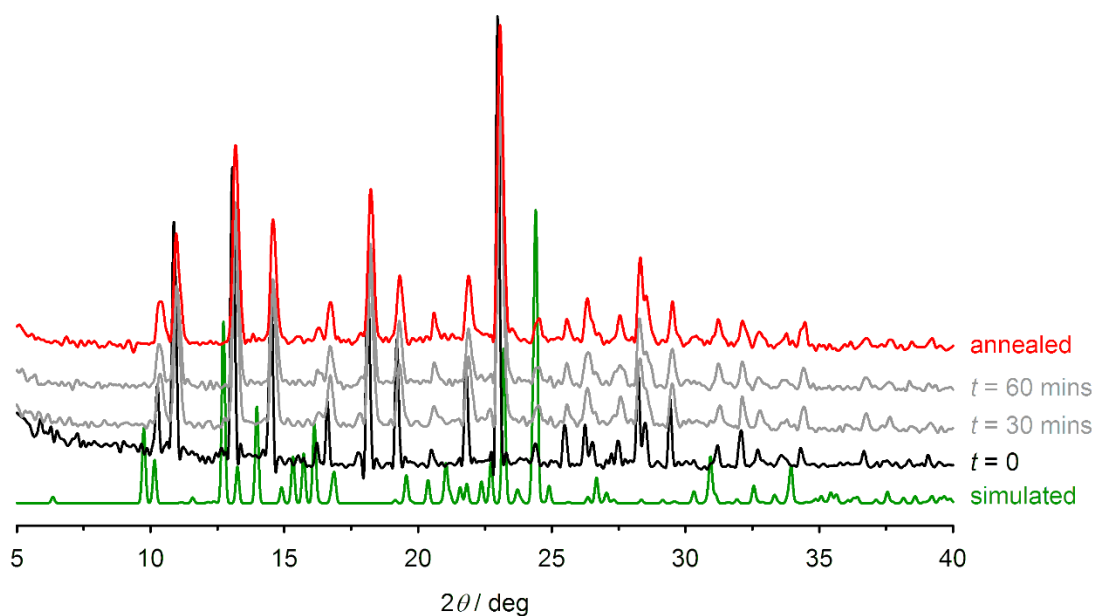


**Figure 2.15.** Powder X-ray diffraction patterns for **2.5**·EtOAc at 298 K, with the simulated powder pattern generated from the single crystal X-ray structure shown in green.

---

### Structure refinement of $2.18 \cdot \frac{1}{2}\text{Et}_2\text{O} \cdot \frac{1}{2}\text{H}_2\text{O}$

The  $\frac{1}{2}\text{Et}_2\text{O} \cdot \frac{1}{2}\text{H}_2\text{O}$  solvate of **2.18** was crystallised as brown needles by vapour diffusion of pentane into  $\text{Et}_2\text{O}$ . The structure  $2.18 \cdot \frac{1}{2}\text{Et}_2\text{O} \cdot \frac{1}{2}\text{H}_2\text{O}$  was solved in the monoclinic space group P21/c. The structure is non-porous with an asymmetric unit containing two formula units (**Figure 2.16**). The hydrogen bond network takes the form of a 2D bilayer parallel to the  $[10\bar{2}]$  crystal vector. The water molecule is disordered between a two- or three-connected sites, which alters the topology depending on which connections are considered. The ordered hydrogen bond connections in the structure form a bimodal 5-connected net with Schläfli notation of  $3.5.4.3.4^2$ ,  $3.4^2.5^2.4.6$ .<sup>[35]</sup> If the partially occupied hydrogen bonds to water are considered, the topology changes to a trinodal net with 3, 6 and 7-connected nodes when all connections are considered equivalently.

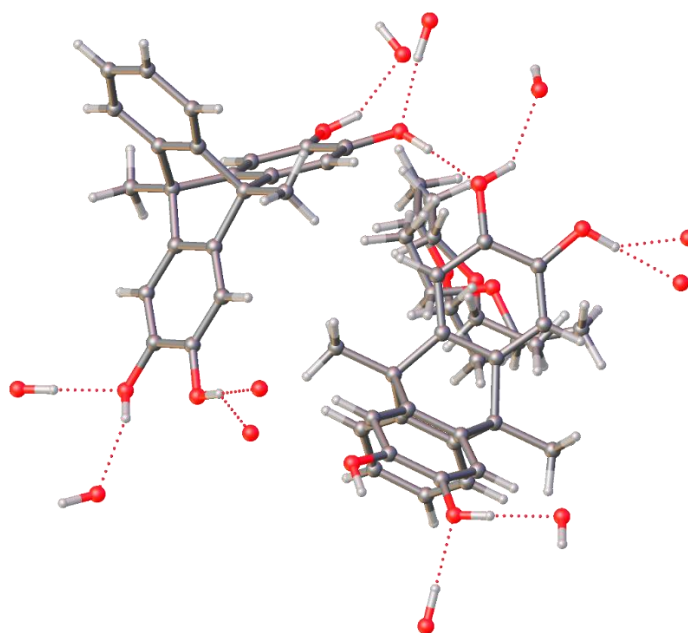


**Figure 2.16.** View of the asymmetric unit in the crystal structure of  $2.18 \cdot \frac{1}{2}\text{Et}_2\text{O} \cdot \frac{1}{2}\text{H}_2\text{O}$ . Both the major and minor orientations of the disordered diethyl ether molecule are included.

---

### Structure refinement of 2.18·dioxane

The dioxane solvate of **2.18** was crystallised as brown needles by vapour diffusion of pentane into dioxane. The non-porous structure **2.18**·dioxane was solved in the orthorhombic space group  $P2_12_12_1$ . Each molecule of **2.18** forms a hydrogen bond network to its 6 nearest neighbours, with two of these arising from linear connection through the dioxane molecule (**Figure 2.17**). The topology is based on a  $6^5.8$  (**dmp**) network modified by additional diagonal connections via the bridging dioxane molecules between adjacent 6-membered rings. The short Schläfli symbol for this net would be  $4^{12}.6^n$ , where  $n \geq 50$ .

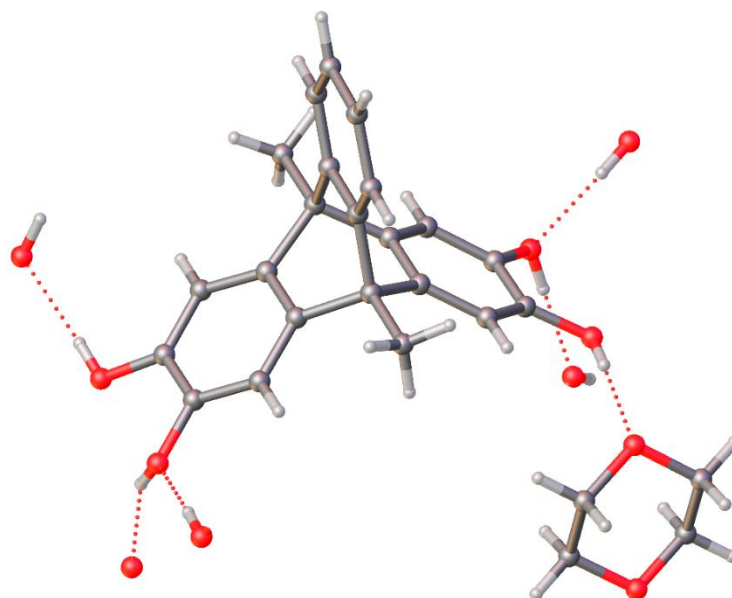


**Figure 2.17.** View of the asymmetric unit in the crystal structure of **2.18**·dioxane.

**Table 2.1.** Experimental data for the crystal structure determinations in this chapter. Flack parameters for the handed structures are not included, because they could not be determined meaningfully for these light-atom crystals.

	<b>2.5·2Et<sub>2</sub>O<sup>a</sup></b>	<b>2.5·3.4THF</b>	<b>2.5·2.15CHCl<sub>3</sub></b>	<b>2.5·EtOAc</b>	<b>2.18·½Et<sub>2</sub>O·½H<sub>2</sub>O<sup>a</sup></b>	<b>2.18·C<sub>4</sub>H<sub>8</sub>O<sub>2</sub></b>
Molecular formula	C <sub>30</sub> H <sub>38</sub> O <sub>8</sub>	C <sub>35.60</sub> H <sub>45.20</sub> O <sub>9.40</sub>	C <sub>24.15</sub> H <sub>20.15</sub> Cl <sub>6.44</sub> O <sub>6</sub>	C <sub>26</sub> H <sub>26</sub> O <sub>8</sub>	C <sub>24</sub> H <sub>23</sub> O <sub>5</sub>	C <sub>26</sub> H <sub>26</sub> O <sub>6</sub>
<i>M<sub>r</sub></i>	526.60	623.52	634.65	466.47	391.42	434.47
Crystal class	tetragonal	trigonal	monoclinic	triclinic	monoclinic	orthorhombic
Space group	<i>I4<sub>1</sub>cd</i>	<i>P3c1</i>	<i>C2/c</i>	<i>P1̄</i>	<i>P2<sub>1</sub>/c</i>	<i>P2<sub>1</sub>2<sub>1</sub>2<sub>1</sub></i>
<i>a</i> (Å)	13.3213(2)	23.519(4)	23.2178(16)	8.8058(5)	13.1161(4)	9.6831(2)
<i>b</i> (Å)	–	–	25.566(2)	9.1775(6)	11.8371(3)	11.9425(2)
<i>c</i> (Å)	31.0721(6)	10.8159(13)	10.7276(7)	14.0128(8)	24.8580(7)	18.3518(4)
<i>α</i> (°)	–	–	–	84.071(5)	–	–
<i>β</i> (°)	–	–	116.349(6)	85.136(4)	97.306(3)	–
<i>γ</i> (°)	–	–	–	82.927(5)	–	–
<i>V</i> (Å <sup>3</sup> )	5513.96(16)	5181.2(14)	5706.2(7)	1114.83(12)	3828.03(19)	2122.21(7)
<i>Z</i>	8	6	8	2	8	4
<i>T</i> (K)	120	120	120	120	120	120
<i>μ</i> (mm <sup>-1</sup> )	0.748 <sup>b</sup>	0.086 <sup>c</sup>	6.196 <sup>b</sup>	0.859 <sup>b</sup>	0.772 <sup>b</sup>	0.788 <sup>b</sup>
Measured reflections	4812	22120	8045	8449	15514	5791
Independent reflections	1377	4455	4795	4205	7501	2372
<i>R</i> <sub>int</sub>	0.044	0.082	0.043	0.057	0.054	0.043
<i>R</i> <sub>1</sub> , <i>I</i> > 2σ( <i>I</i> ) <sup>d</sup>	0.045	0.099	0.087	0.062	0.068	0.038
<i>wR</i> <sub>2</sub> , all data <sup>e</sup>	0.120	0.272	0.284	0.194	0.206	0.099
Goodness of fit	1.072	1.102	1.046	1.042	1.036	1.055

<sup>a</sup>See also ref. [35]. <sup>b</sup>Collected with Cu-*K<sub>α</sub>* radiation. <sup>c</sup>Collected with Mo-*K<sub>α</sub>* radiation. <sup>d</sup> $R = \Sigma[|F_o| - |F_c|] / \Sigma|F_o|$ . <sup>e</sup> $wR = [\Sigma w(F_o^2 - F_c^2) / \Sigma wF_o^4]^{1/2}$ .

---

### 2.2.3 Thermogravimetric Analysis (TGA) of Crystalline Clathrates of Triptycene

Thermogravimetric analysis of the crystalline clathrates obtained can give further insight into the extent of desolvation as a function of temperature. Pure solvent-free **2.5** has a high melting point ( $>300\text{ K}$ )<sup>[35]</sup>, and decomposes above this temperature. All samples were prepared by vapour diffusion, and the experiments were run directly after being removed from the mother liquor and quickly dried on a filter paper.

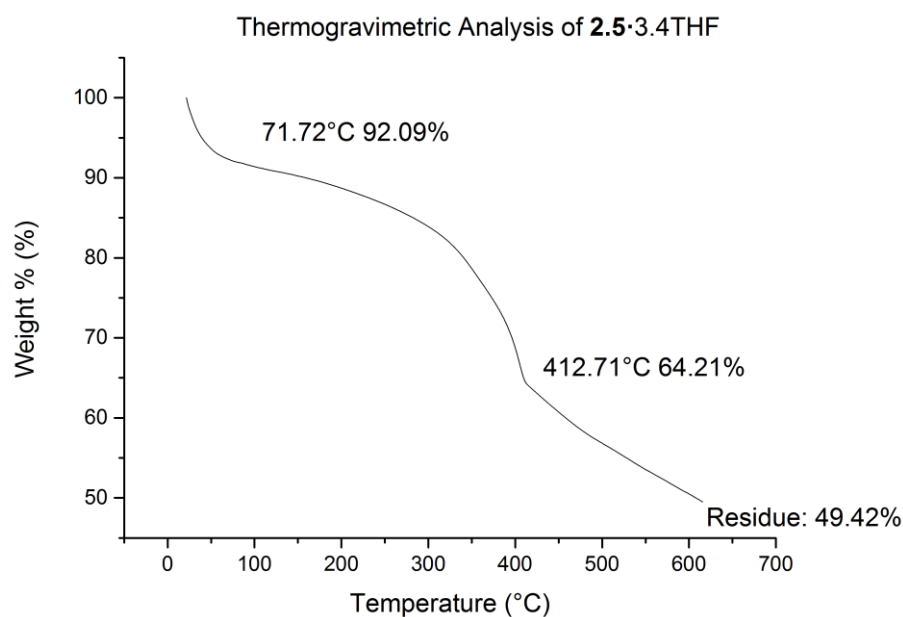


**Figure 2.18.** TGA for **2.5·3.4THF** showing crystalline solvent loss and decomposition.

For **2.5·3.4THF**, initially the mass drops from room temperature to  $71.72^{\circ}\text{C}$ , accounting for a mass loss of 7.91%. This drop arises from the loss of THF from the open channels. Less mass is lost than would be expected based on the crystal structure (which contains 39.3% THF by mass), which is likely due to the rapid evaporation of THF from the channels before the crystals were placed inside the analyser. After this, a single-stage decomposition curve can be seen with  $T_i$  of  $71.72^{\circ}\text{C}$  and  $T_f$  of  $412.71^{\circ}\text{C}$ . The mass continues to drop as the temperature is increased further, until a final residue of 49.42% remains at  $625^{\circ}\text{C}$ .

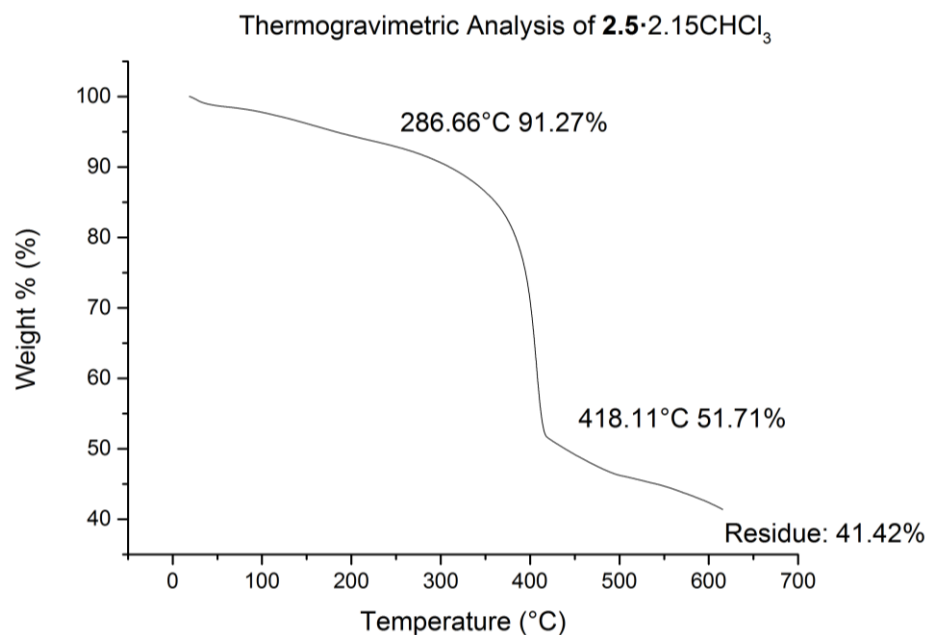


**Figure 2.19.** TGA for **2.5**·2.15CHCl<sub>3</sub> showing decomposition.

For **2.5**·2.15CHCl<sub>3</sub>, no crystalline solvent loss is observed, however there is a single-stage decomposition curve with  $T_i$  of 286.66°C and  $T_f$  of 418.11°C. The mass continues to drop as the temperature is increased further, until a final residue of 41.42% remains at 625°C.

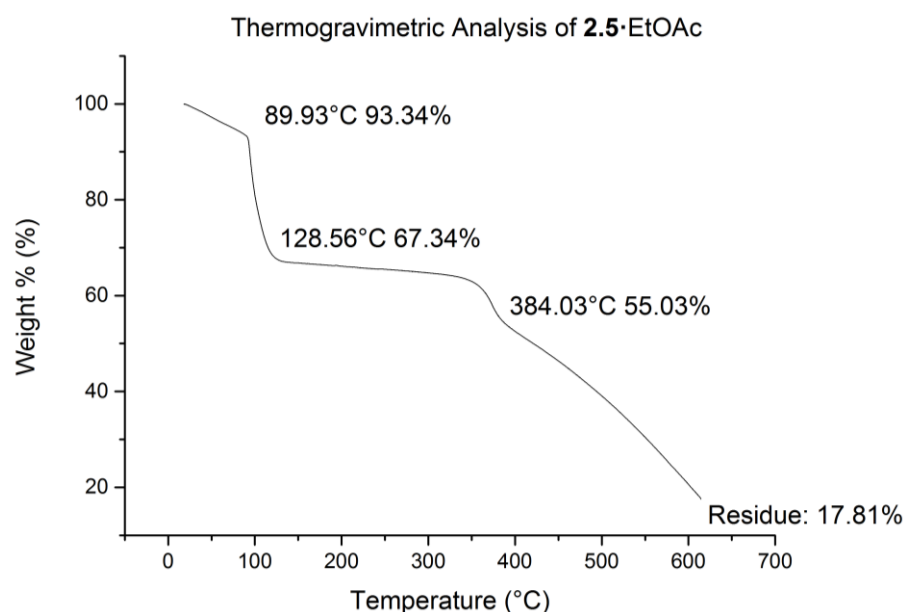


**Figure 2.20.** TGA for **2.5**·EtOAc showing crystalline solvent loss and decomposition.

---

For **2.5**·EtOAc, initially the mass drops linearly from room temperature to 89.93°C, accounting for a mass loss of 6.66%. This drop arises from the loss of excess EtOAc/pentane from the surface of the crystals. Between 89.93°C and 128.56°C the crystalline solvent is lost, accounting for 26.00% of the total mass. More mass is lost than would be expected based on the crystal structure (which contains 19% EtOAc by mass), which is likely due to some excess EtOAc/pentane on the surface of the crystals. After this, a single-stage decomposition curve can be seen with  $T_i$  of 340.64°C and  $T_f$  of 384.03°C. The mass continues to drop as the temperature is increased further, until a final residue of 17.81% remains at 625°C.

### 2.3 Conclusions and Future Work

It has been shown that **2.5** is a useful scaffold to support porosity in molecular assemblies or crystalline networks. Four novel solvent-supported assemblies have been characterised crystallographically, including a previously unreported 7-connected topological net. Loss of crystalline solvent from the lattice upon heating has been characterised by powder XRD and TGA.

The triptycenes discussed have shown promise as supramolecular components able to impart porosity. They are therefore good candidate ligands to use for the synthesis of metal-organic frameworks or other highly porous coordination polymers. In conjunction with this, the presence of two or three redox active catechol groups in the ligand should provide the potential for rich valence tautomeric behaviour.<sup>[42]</sup> Consequently, the following chapter will discuss coordination complexes containing **2.5** and related derivatives.

---

## 2.4 References

1. X. Z. Zhu, C. F. Chen, *J. Am. Chem. Soc.* **2005**, *127* (38), 13158-13159.
2. X. Z. Zhu, C. F. Chen, *Chem. Eur. J.* **2006**, *12* (21), 5603-5609.
3. C. Loholter, M. Brutschy, D. Lubczyk, S. R. Waldvogel, *Beilstein J. Org. Chem.* **2013**, *9*, 2821-2833.
4. Q. S. Zong, C. F. Chen, *Org. Lett.* **2006**, *9* (2), 211-214.
5. T. Han, C. F. Chen, *Org. Lett.* **2006**, *8* (6), 1069-1072.
6. J. M. Zhao, Q. S. Zong, C. F. Chen, *J. Org. Chem.* **2010**, *75* (15), 5092-5098.
7. Y. Han, H. Y. Lu, Q. S. Zong, J. B. Guo, C. F. Chen, *J. Org. Chem.* **2012**, *77* (5), 2422-2430.
8. Y. K. Gu, Y. Han, C. F. Chen, *Supramol. Chem.* **2015**, *27*, 357.
9. N. G. White, M. J. MacLachlan, *Chem. Sci.* **2015**, *6* (11), 6245-6249.
10. N. G. White, M. J. MacLachlan, *Cryst. Growth Des.* **2015**, *15* (11), 5629-5636.
11. J. H. Chong, M. J. MacLachlan, *Inorg. Chem.* **2006**, *45* (4), 1442-1444.
12. J. H. Chong, S. J. Ardakani, K. J. Smith, M. J. MacLachlan, *Chem. Eur. J.* **2009**, *15* (44), 11824-11828.
13. M. Mastalerz, S. Sieste, M. Ceni, I. M. Oppel, *J. Org. Chem.* **2011**, *76* (15), 6389-6393.
14. D. Anselmo, G. Salassa, E. C. Escudero-Adán, E. Martin, A. W. Kleij, *Dalton Trans.* **2013**, *42* (22), 7962-7970.
15. Y. Jiang, C. F. Chen, *SYNLETT* **2010**, (11), 1679-1681.
16. X. Roy, J. H. Chong, B. O. Patrick, M. J. MacLachlan, *Cryst. Growth Des.* **2011**, *11* (10), 4551-2558.
17. K. A. Williams, C. W. Bielawski, *Chem. Comm.* **2010**, *46* (28), 5166-5168.
18. S. Gonell, M. Poyatos, E. Peris, *Angew. Chem. Int. Ed.* **2013**, *52* (27), 7009-7013.
19. B. S. Ghanem, M. Hashem, K. D. M. Harris, K. J. Msayib, M. Xu, P. M. Budd, N. Chaukura, D. Book, S. Tedds, A. Walton, N. B. McKeown, *Macromolecules* **2010**, *43* (12), 5287-5294.
20. Y. C. Zhao, Q. Y. Cheng, D. Zhou, T. Wang, B. H. Han, *J. Mater. Chem.* **2012**, *22* (23), 11509-11514.
21. L. Liu, J. Zhang, *Macromol. Rapid Comm.* **2013**, *34* (23-24), 1833-1837.

- 
22. T. Y. Zhou, F. Lin, Z. T. Li, X. Zhao, *Macromolecules* **2013**, *46* (19), 7745-7752.
23. B. Kohl, F. Rominger, M. Mastalerz, *Org. Lett.* **2014**, *16* (3), 704-707.
24. J. J. Loughrey, C. A. Kilner, M. J. Hardie, M. A. Halcrow, *Supramol. Chem.* **2011**, *24* (1), 2-13.
25. J. J. Loughrey, S. Sproules, E. J. L. McInnes, M. J. Hardie, M. A. Halcrow, *Chem. Eur. J.* **2014**, *20* (21), 6272-6276.
26. J. J. Loughrey, N. J. Patmore, A. Baldansuren, A. J. Fielding, E. J. L. McInnes, M. J. Hardie, S. Sproules, M. A. Halcrow, *Chem. Sci.* **2015**, *6* (12), 6935-6948.
27. G. A. Abakumov, V. K. Cherkasov, V. I. Nevodchikov, V. A. Kuropatov, B. C. Noll, C. G. Pierpont, *Inorg. Chem.* **1998**, *37* (23), 6117-6119.
28. G. A. Abakumov, V. K. Cherkasov, V. I. Nevodchikov, V. A. Kuropatov, G. T. Yee, C. G. Pierpont, *Inorg. Chem* **2001**, *40* (10), 2434-2436.
29. D. A. Shultz, R. M. Fico, R. K. Kumar, K. E. Vostrikova, J. W. Kampf, P. D. Boyle, *J. Am. Chem. Soc.* **2003**, *125* (38), 11761-11771.
30. D. A. Shultz, A. K. Boal, H. Lee, G. T. Farmer, *J. Org. Chem.* **1998**, *63* (25), 9462-9469.
31. J. C. Sloop, D. A. Shultz, T. Coote, B. Shepler, U. Sullivan, J. W. Kampf, P. D. Boyle, *J. Phys. Org. Chem.* **2012**, *25* (4), 314-321.
32. D. A. Shultz, S. H. Bodnar, H. Lee, J. W. Kampf, C. D. Incarvito, A. L. Rheingold, *J. Am. Chem. Soc.* **2002**, *124* (34), 10054-10061.
33. R. Jain, M. B. Sponsler, F. D. Coms, D. A. Dougherty, *J. Am. Chem. Soc.* **1988**, *110* (5), 1356-1366.
34. A. Rajca, S. Utamapanya, J. Xu, *J. Am. Chem. Soc.* **1991**, *113* (24), 9235-9241.
35. Y. Han, Y. Jiang, C. F. Chen, *Chin. Chem. Lett.* **2013**, *24* (6), 475-478.
36. K. J. Gould, N. P. Hacker, J. F. W. McOmie, D. H. Perry, *J. Chem. Soc. Perkin Trans. 1 Org. Bio-Org. Chem.* **1980**, *8* (0), 1834-1840.
37. M. Ghaemy, H. Mighani, *Chin. Chem. Lett.* **2009**, *20* (7), 800-804.
38. L. Öhrström, K. Larsson, *Molecule-Based Materials - the Structural Network Approach*, Elsevier: Amsterdam, 2005.

- 
39. M. O'Keeffe, M. A. Preskov, S. J. Ramsden, O. M. Yaghi, **2008**, *41* (12), 1782-1989.
40. D. L. Long, A. J. Blake, N. R. Champness, C. Wilson, M. Schröder, *Angew. Chem. Int. Ed.* **2001**, *40* (13), 2443-2447.
41. J. J. Morris, B. C. Noll, K. W. Henderson, *Chem. Comm.* **2007**, *0* (48), 5191.
42. L. Sun, M. G. Campbell, M. Dincă, *Angew. Chem. Int. Ed.* **2016**, *55* (11), 3566-3579.

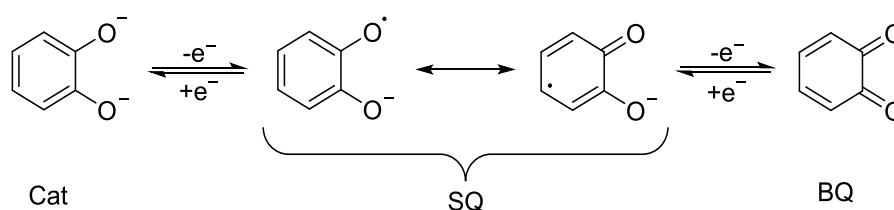
---

## Chapter 3

### Synthesis, Structure and Valence Tautomerism of Triptycene Based Dioxolene Complexes of Pt(II)

#### 3.1 Introduction

Building upon the previous chapter, this chapter will explore the coordination chemistry and redox activity (**Scheme 3.1**) of the multinuclear platinum coordination complexes of these ligands. Their redox chemistry, valence tautomeric transitions and potential for supramolecular structures will be investigated by cyclic voltammetry (CV), electron paramagnetic resonance (EPR), ultraviolet-visible/near-infrared (UV-vis/NIR) spectroscopy, and spectroelectrochemistry (SEC).



**Scheme 3.1.** Catechol, semiquinone and benzoquinone forms of catechol.

As mixed-valent complexes of the Robin-Day class II type are of most interest, the complexes that have been synthesised were designed with several structural features designed to promote the likelihood of possessing this property;<sup>[1]</sup> in particular a large dihedral angle between the dioxolene groups and short through-space dioxolene-dioxolene distances. Platinum is an ideal metal for coordination through the two oxygen atoms of the dioxolene, as it is redox stable and able to accommodate ligand-based oxidation state changes. As Pt(II) adopts a square planar coordination geometry, some care has to be taken to also introduce an appropriate ancillary (capping) ligand to occupy the remaining two *cis* coordination sites. Several options are available for this, including chelating diphosphines such as diphenylphosphinoethane (dppe) and diphenylphosphinobenzene (dppb), or chelating bipyridines such as bipyridine (bipy) or *bis*-4,4'-di-*tert*-butyl-2,2'-bipyridine (<sup>t</sup>Bu<sub>2</sub>bipy). The degree of  $\sigma$  or  $\pi$  donating/accepting character of the ancillary ligand can modulate the redox properties of the resulting complex. As bipyridines are themselves redox active, and early trials syntheses of these complexes have proven to lead to highly insoluble products, it was

decided that chelating diphosphines are the optimal choice to carry forward for full analysis.

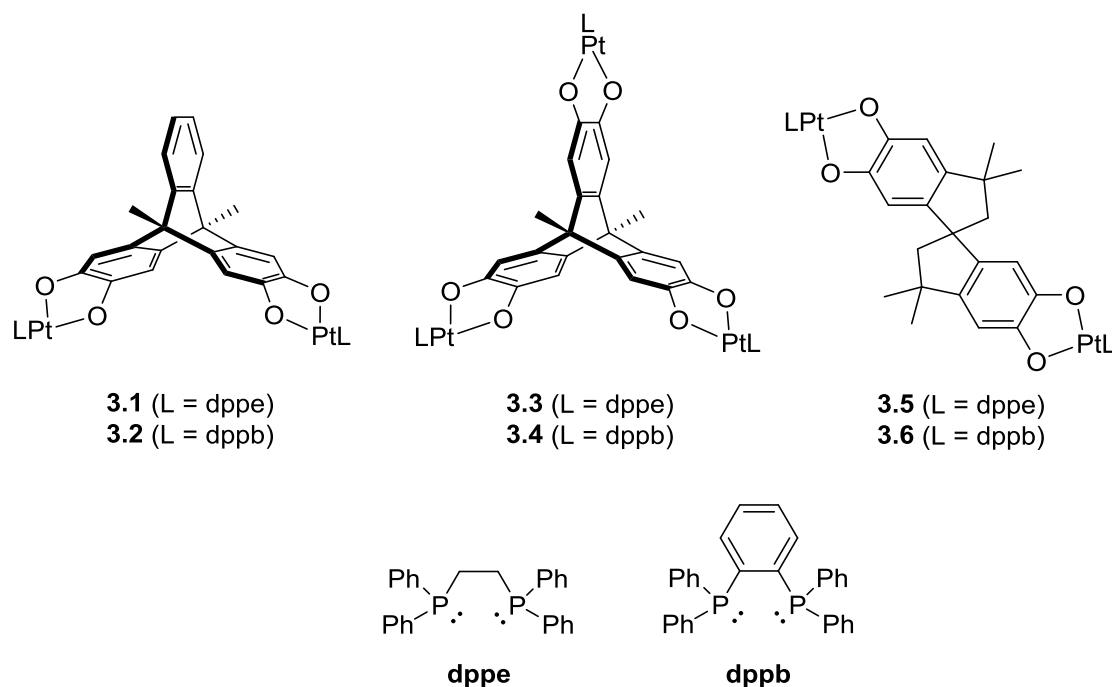


**Figure 3.1.** The Pt coordination complexes discussed in this chapter.

The complexes **3.1-3.6** (**Figure 3.1**) have been characterised by proton nuclear magnetic resonance ( $^1\text{H}$  NMR), high resolution mass spectrometry (HRMS), X-ray crystallography, and elemental microanalysis (CHN). Preliminary experiments were carried out using CV and differential pulse voltammetry (DPV) to determine the oxidation potentials of successive catechol  $\rightarrow$  semiquinone redox transitions. In several cases these transitions are reversible, allowing the neutral starting material to be regenerated on the electrode surface. Some of the redox transitions (particularly on semiquinone  $\rightarrow$  quinone level) have proven to be irreversible, indicating in these cases that there is likely rapid decomposition of the cation once it is formed.

Herein, the results of these studies will be discussed in detail to fully characterise the electrochemically generated radical species obtained from these complexes, with the aim of shedding light onto the degree of electron delocalisation/coupling between the dioxolene rings. EPR has been used to elucidate the extent of hyperfine coupling to  $^{195}\text{Pt}$  and  $^{31}\text{P}$  nuclei, which can demonstrate that the radical electron is able to hop between the two/three dioxolene sites in the solution phase. The presence of a low energy intervalence charge transfer (IVCT) band in the UV-vis/NIR spectrum of the

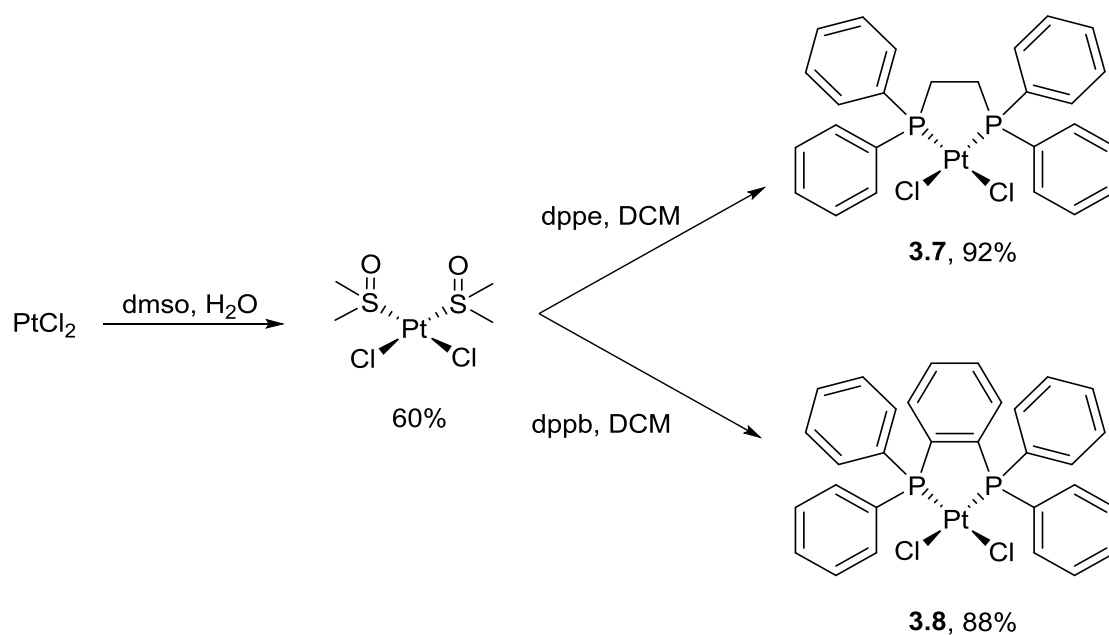
electrochemically generated species also provides further evidence of delocalisation as well as being able to give an estimation of the electron coupling energy  $H_{ab}$ . SEC measurements should be able to show if the oxidised complexes are able to be reversibly regenerated the neutral *bis/tris* catechol state, a process which should be accompanied by a concomitant loss of the IVCT.

## 3.2 Results and Discussion

### 3.2.1 [{"(dppe)Pt}<sub>2</sub>(2.18)] (3.1) and [{"(dppb)Pt}<sub>2</sub>(2.18)] (3.2)

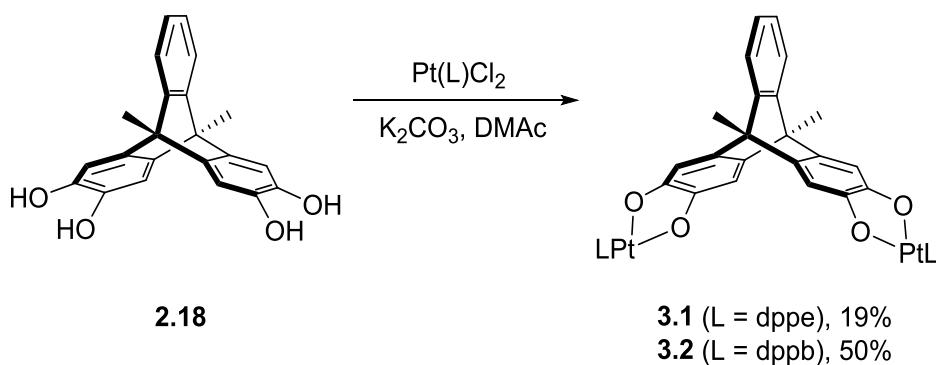
#### 3.2.1.1 Synthesis and Characterisation

The synthesis of the platinum diphosphene precursor is achieved by conversion of PtCl<sub>2</sub> to the *cis-bis*(dmsO) adduct, which may then undergo ligand exchange with the desired diphosphine (Scheme 3.2).



**Scheme 3.2.** Addition of a dppe or dppb ancillary ligand to the PtCl<sub>2</sub> starting material to form **3.7** and **3.8**.

The dinuclear triptycene complexes **3.1** and **3.2** were synthesised (Scheme 3.3) by addition of **2.18** to **3.7** or **3.8**. Both complexes are yellow in colour and rapidly decompose upon exposure to air or moisture.<sup>[2]</sup>



**Scheme 3.3.** Complexation of **2.18** with **3.7** and **3.8** to form the dinuclear complexes **3.1** and **3.2**.

The  $^1\text{H}$  NMR spectrum of **3.1** (**Figure 3.2**) has paramagnetically broadened because of the presence of a small impurity of  $[\mathbf{3.1}]^+$  in the sample due to aerial oxidation, which makes precise assignment difficult. Nevertheless, the multiplet at 7.90 ppm corresponds to 16 protons located at the *ortho* position of the dppe phenyl rings, and the multiplet at 7.34 ppm corresponds to the 24 protons located at the *para* and *meta* positions. The peaks at 7.01, 6.73 and 6.40 ppm correspond to the aromatic triptycene protons in good agreement with the  $^1\text{H}$  NMR spectrum of the free ligand.

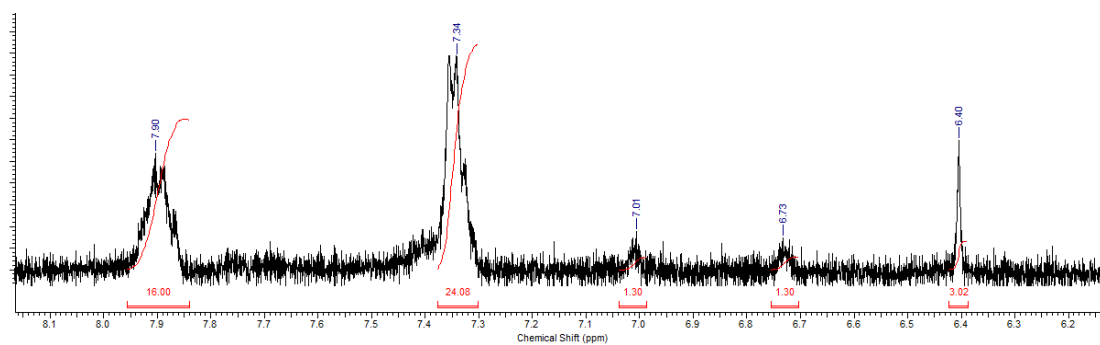


**Figure 3.2.**  $^1\text{H}$  NMR (500 MHz,  $\text{CDCl}_3$ ) spectrum of **3.1**, showing a representative example of broadened peaks.

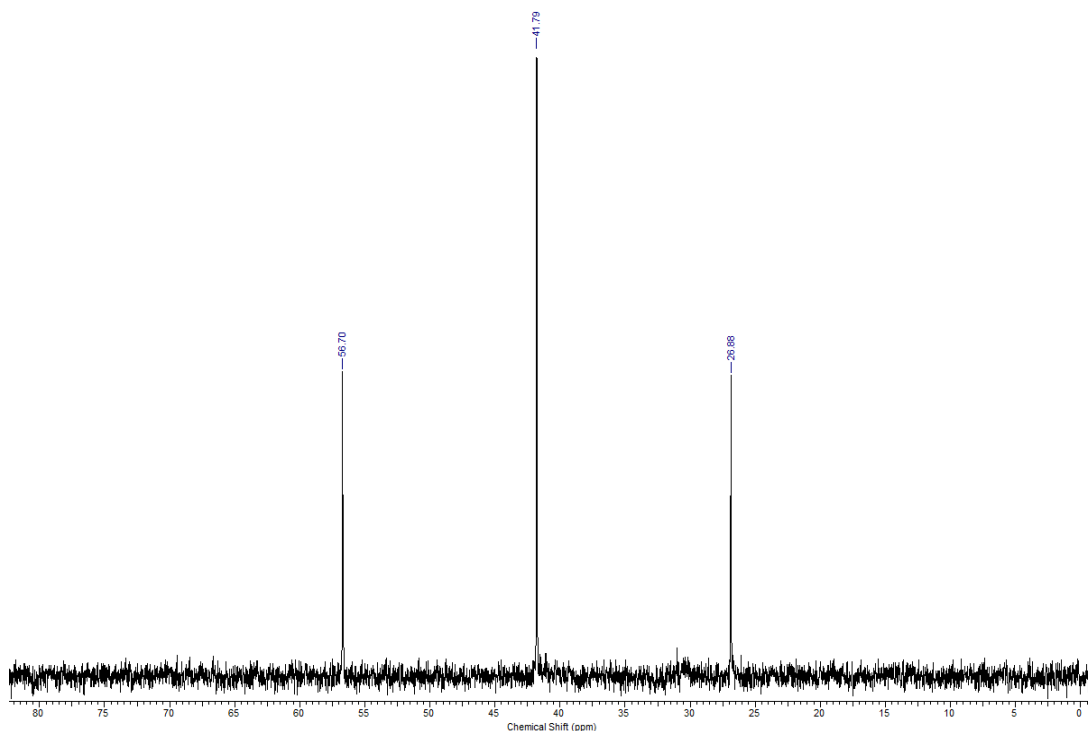


**Figure 3.3.**  $^{31}\text{P}\{^1\text{H}\}$  NMR (300 MHz,  $\text{CDCl}_3$ ) spectrum of **3.1**, showing  $^{195}\text{Pt}$  satellites.

The  $^{31}\text{P}\{^1\text{H}\}$  NMR spectrum shows a single phosphorus environment at 41.79 ppm, which is to be expected given the  $C_2$  symmetry of the complex. Platinum satellite peaks with a coupling constant of 1811.99 Hz are also observed due to the coupling of the  $^{31}\text{P}$  nuclei to a  $^{195}\text{Pt}$  ( $S = 1/2$ ) nucleus.<sup>[3]</sup>

The high resolution mass spectra for **3.1** and **3.2** (**Figure 3.4** and **Figure 3.5**) have good agreement with the simulated isotopic distribution expected for the molecular ions  $[\text{C}_{74}\text{H}_{62}\text{O}_4\text{P}_4\text{Pt}_2]^+$  (1528.29 g mol<sup>-1</sup>) and  $[\text{C}_{82}\text{H}_{62}\text{O}_4\text{P}_4\text{Pt}_2]^+$  (1624.29 g mol<sup>-1</sup>) respectively. For both spectra, a second set of peaks corresponding to  $[(\mathbf{3.1})_2(\text{H})]^{2+}$  and  $[(\mathbf{3.2})_2(\text{H})]^{2+}$  are also observed.

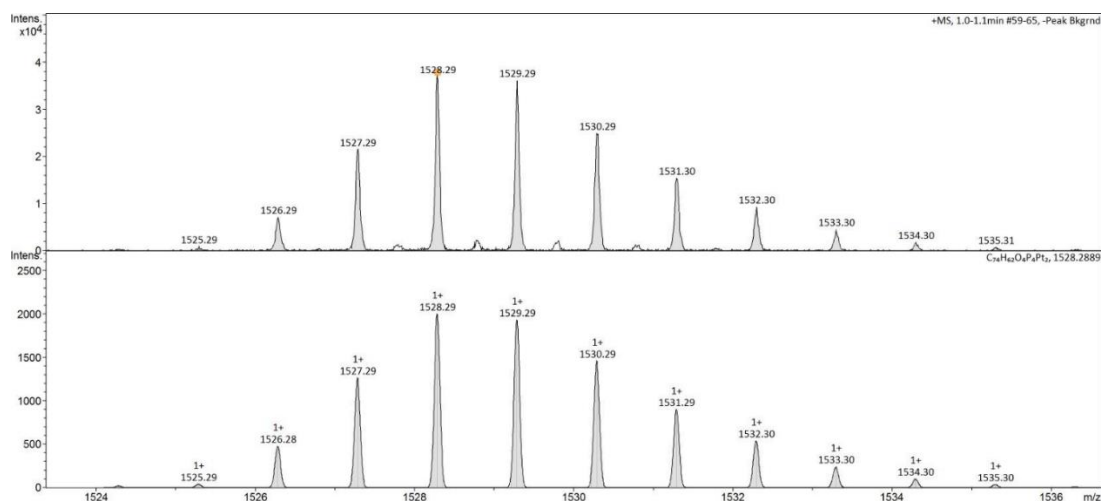


**Figure 3.4.** Experimental (top) and simulated (bottom) molecular ion of **3.1**. There is good agreement between the spectrum and simulation, with the characteristic isotopic distribution for a complex containing two Pt ions.

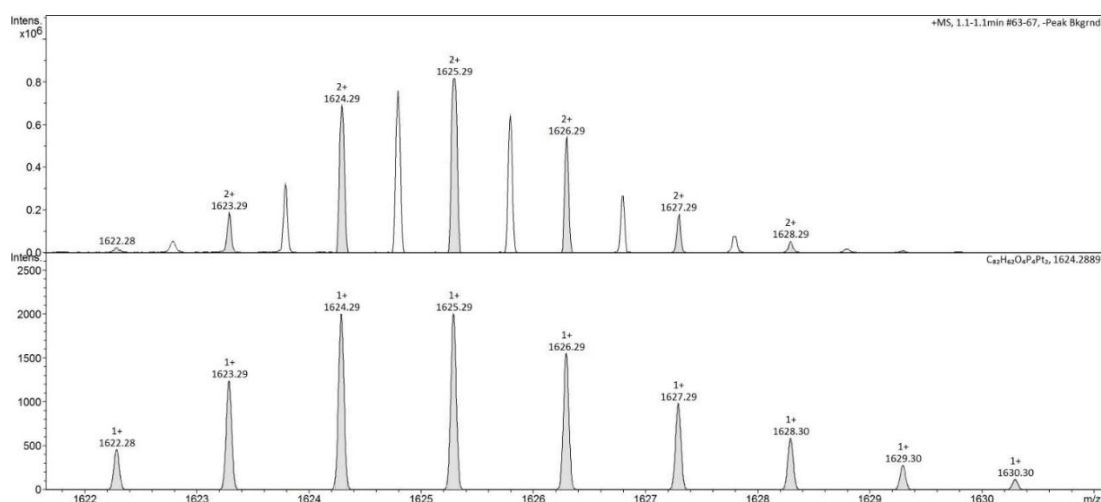


**Figure 3.5.** Experimental (top) and simulated (bottom) molecular ion of **3.2**. There is good agreement between the spectrum and simulation, with the characteristic isotopic distribution for a complex containing two Pt ions.

### 3.2.1.2 X-ray Crystal Structure Refinement of **3.2**

The air sensitivity of **3.2** made obtaining a suitable monocrystalline sample challenging, as crystallinity is lost very rapidly after removal of the crystal from the mother liquor. **3.2** was crystallised as orange plates by vapour diffusion of hexane into

---

dichloromethane. The structure of **3.2** was solved in the monoclinic space group *Ia* using the *Olex2* program (**Figure 3.6**).

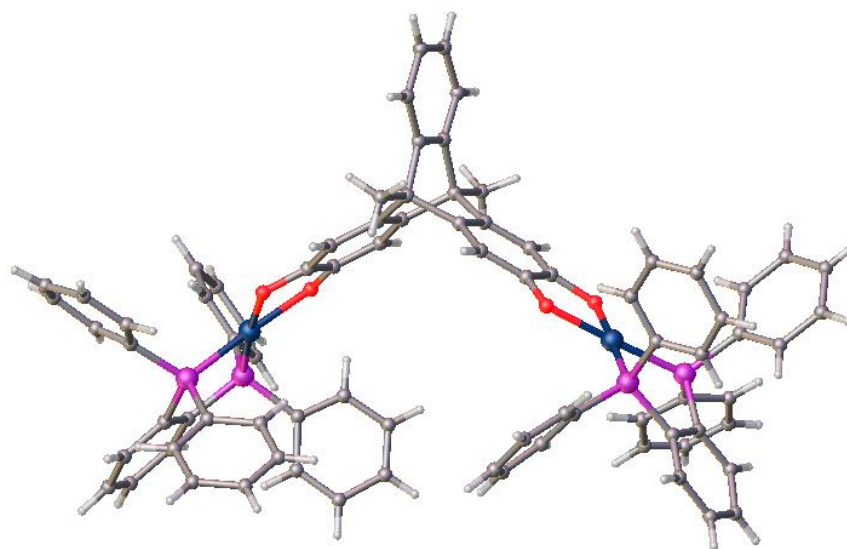


**Figure 3.6.** Single crystal X-ray structure of a single molecule of **3.2**, showing the desired structural features have been maintained after complexation.

The desired structural features are shown to be preserved in the complex, with an average Pt-Pt distance of 10.68 Å. The average C-O bond length in this complex is 1.344 Å, which is close to the C-O bond lengths of 1.37 Å for free **2.18**. The typical C-O bond length for catecholates is 1.35 Å, for semiquinonates is 1.29 Å, and for benzoquinones is 1.23 Å.<sup>[4-5]</sup> Combining this with the fact that the free triptycene **2.18** in its catechol form has C-O bond lengths of 1.37 Å, it can be inferred that the **3.2** represents the bis(Cat) form of the complex. The dihedral angle between the dioxolene groups is 116.3°, which is close to the values for the free **2.18** (117.4°), providing additional evidence that this complex exists in bis(Cat) form.

It is not sufficient to use only the crystallographic C-O bond lengths to assign which valence tautomer the complex adopts, because the C-C bond lengths within the dioxolene ring are also subject to changes due to coordination, chelation and steric effects. A method for more precisely correlating dioxolene oxidation state with crystallographic data while taking into account these effects has been developed by Carugo *et al.*<sup>[6]</sup> This method takes into account the experimental observation that benzoquinones have distinct C-C and C=C bond lengths, whereas in catecholates all the C-C bond lengths are equal. The parameter  $\Delta$  is defined in such a way that free

---

dianionic catecholate has a value of -2.0, and free neutral 1,2-benzoquinone has a value of 0.0, with values  $-2.0 \leq \Delta \leq 0.0$  being indicative of semiquinone character.

$$\Delta_i = \frac{-2(d_i - d_{\text{III}i})}{d_{\text{I}i} - d_{\text{III}i}} \quad \text{(Equation 3.1)}^{[6]}$$

$$w_i = \frac{d_i}{\sigma(d_{\text{I}i}) + \sigma(d_{\text{III}i}) + \sigma(d_i)} \quad \text{(Equation 3.2)}^{[6]}$$

$$\Delta = \frac{\sum w_i \Delta_i}{\sum w_i} \quad \text{(Equation 3.3)}^{[6]}$$

Where  $d_i$  is the  $i$ th bond length in the dioxolene ring, and  $d_{\text{I}i}$  and  $d_{\text{III}i}$  are the analogous  $i$ th bond lengths for free catechol (**I**)<sup>[7]</sup> and 1,2-benzoquinone (**III**),<sup>[8]</sup> and  $w_i$  is a weighting value which takes into consideration the standard uncertainty ( $\sigma$ ) of the bond lengths.<sup>[6]</sup> Using the formula above for complex **3.2** gives a value of  $\Delta = -1.96$ , confirming that the complex is in the bis(Cat) form in this crystal structure.

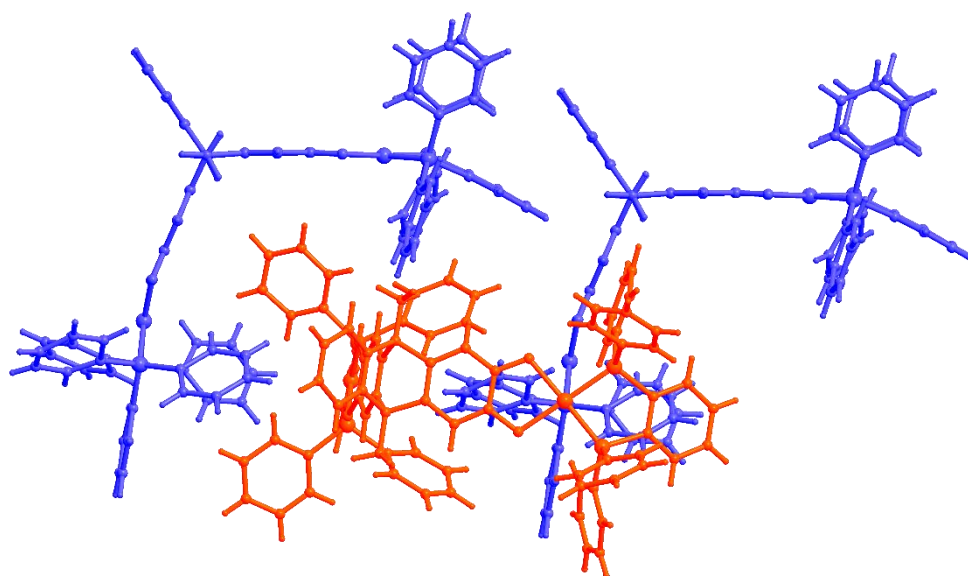


**Figure 3.7.** Crystal packing of **3.2**.

The crystal packing of **3.2** is noticeably different to the structurally related complex [Pt<sub>2</sub>(thea)(dppe)<sub>2</sub>] previously reported by Halcrow *et al.*<sup>[9]</sup> (**Figure 3.7**). The complexes do not adopt the nested dimer crystal packing as seen in [Pt<sub>2</sub>(thea)(dppe)<sub>2</sub>] but instead pack in such a way that the bulky dppb ancilliary ligands occupy the cavity created by the triptycene moieties.

### 3.2.1.3 Electrochemical Analysis of Complexes **3.1** and **3.2**

The redox chemistry of complexes **3.1** and **3.2** was investigated by CV and DPV. All experiments were carried out at 298 K in a 0.1 M solution of <sup>n</sup>Bu<sub>4</sub>NPF<sub>6</sub> in dry, degassed dichloromethane under argon atmosphere. The analysis (**Figures 3.8-3.11**) showed that both **3.1** and **3.2** contained two chemically reversible one-electron oxidation processes in the  $-0.5 \leq E_{1/2} \leq 0.0$  V (*vs.* Fc/Fc<sup>+</sup>) region, attributed to sequential Cat → SQ transitions as displayed in **Scheme 3.3**. The shoulder on the second oxidation of **3.1** (ca -0.027 V) is likely present due to a daughter product resulting from the decomposition of [3.1<sup>••</sup>]<sup>2+</sup>. Furthermore, complexes **3.1** and **3.2** also exhibit one (**3.1**) or two (**3.2**) further chemically irreversible oxidation occurring at a higher potential (+0.75 V), which can be assigned to subsequent SQ → q transitions, as displayed in **Scheme 3.4**.

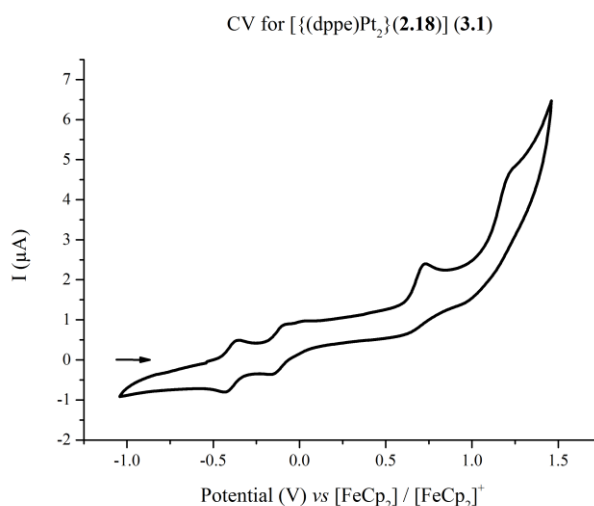


**Figure 3.8.** CV for **3.1** in 0.1 M solution of <sup>n</sup>Bu<sub>4</sub>NPF<sub>6</sub> in dry degassed dichloromethane at 298 K under argon atmosphere *vs.* [FeCp<sub>2</sub>] / [FeCp<sub>2</sub>]<sup>+</sup>. The first two chemically reversible Cat → SQ oxidations are shown, as well as two further chemically irreversible SQ → BQ oxidations.

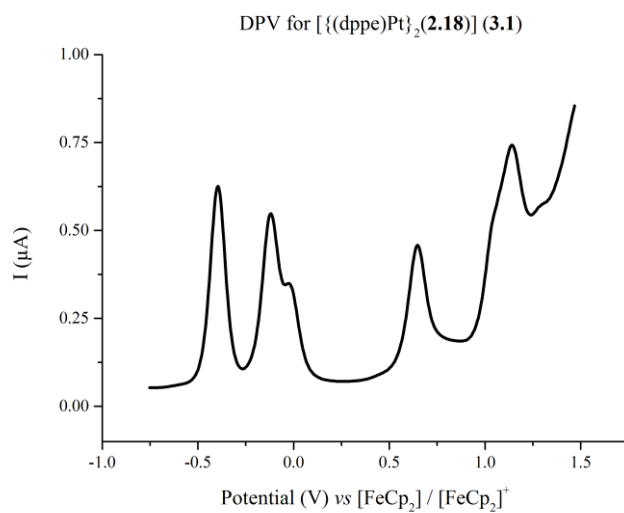


**Figure 3.9.** DPV of **3.1** in 0.1 M solution of  $n\text{Bu}_4\text{NPF}_6$  in dry degassed dichloromethane at 298 K under argon atmosphere vs  $[\text{FeCp}_2] / [\text{FeCp}_2]^+$ .

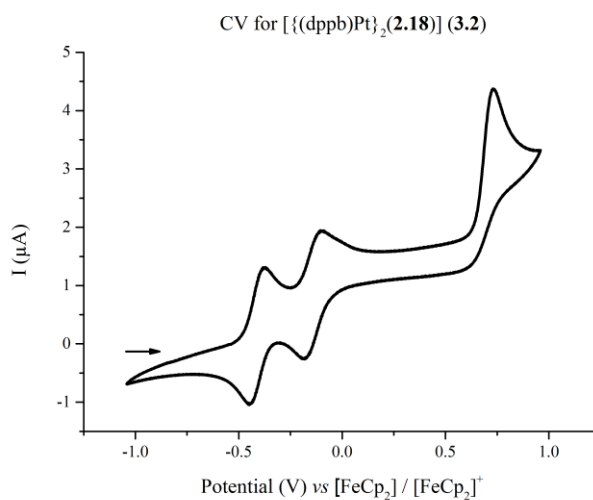


**Figure 3.10.** CV of **3.2** in 0.1 M solution of  $n\text{Bu}_4\text{NPF}_6$  in dry degassed dichloromethane at 298 K under argon atmosphere vs  $[\text{FeCp}_2] / [\text{FeCp}_2]^+$ . The first two chemically reversible Cat  $\rightarrow$  SQ oxidations are shown, as well as one irreversible SQ  $\rightarrow$  BQ oxidation.

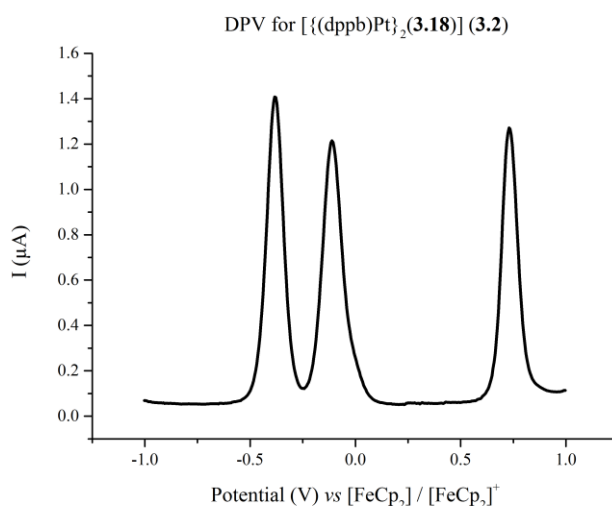


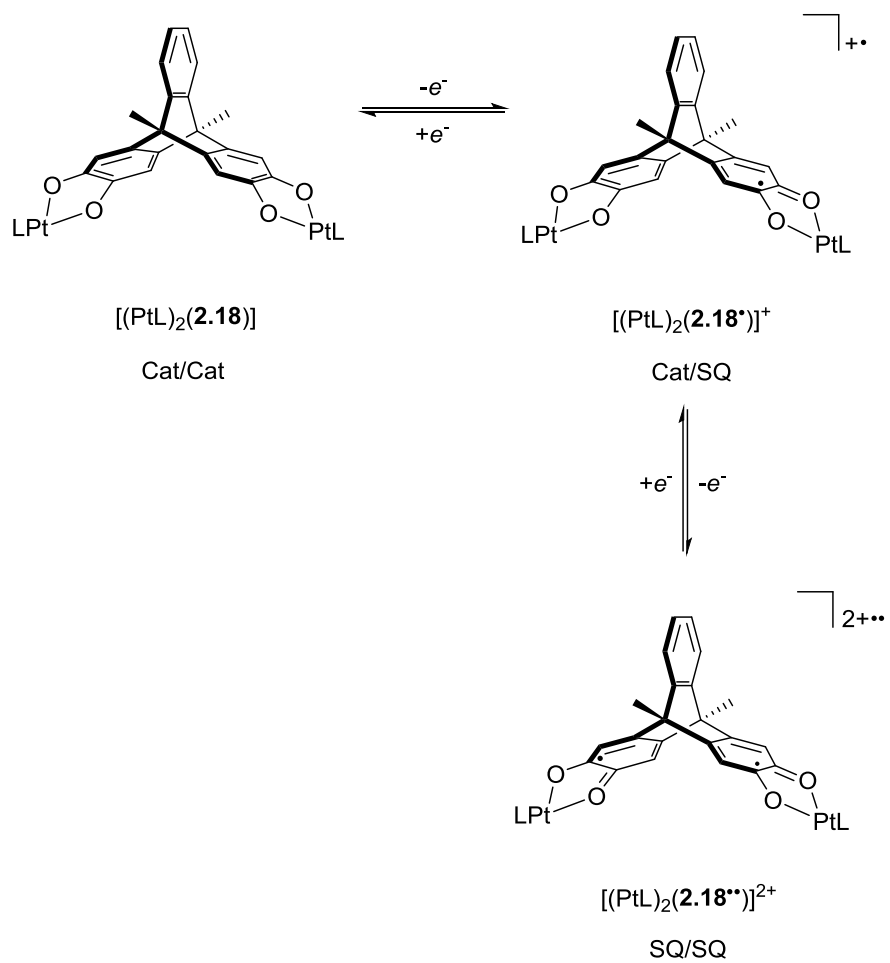
**Figure 3.11.** DPV of **3.2** in 0.1 M solution of  $n\text{Bu}_4\text{NPF}_6$  in dry degassed dichloromethane at 298 K under argon atmosphere vs  $[\text{FeCp}_2] / [\text{FeCp}_2]^+$ .

**Table 3.1.** Cyclic voltammetric data for complexes **3.1** and **3.2** in 0.1 M solution of  $n\text{Bu}_4\text{NPF}_6$  in dry degassed  $\text{CH}_2\text{Cl}_2$  at 298 K under argon atmosphere. Potentials (V) are referenced to a  $[\text{FeCp}_2] / [\text{FeCp}_2]^+$  internal standard, measured at a scan rate of 0.1  $\text{Vs}^{-1}$ .

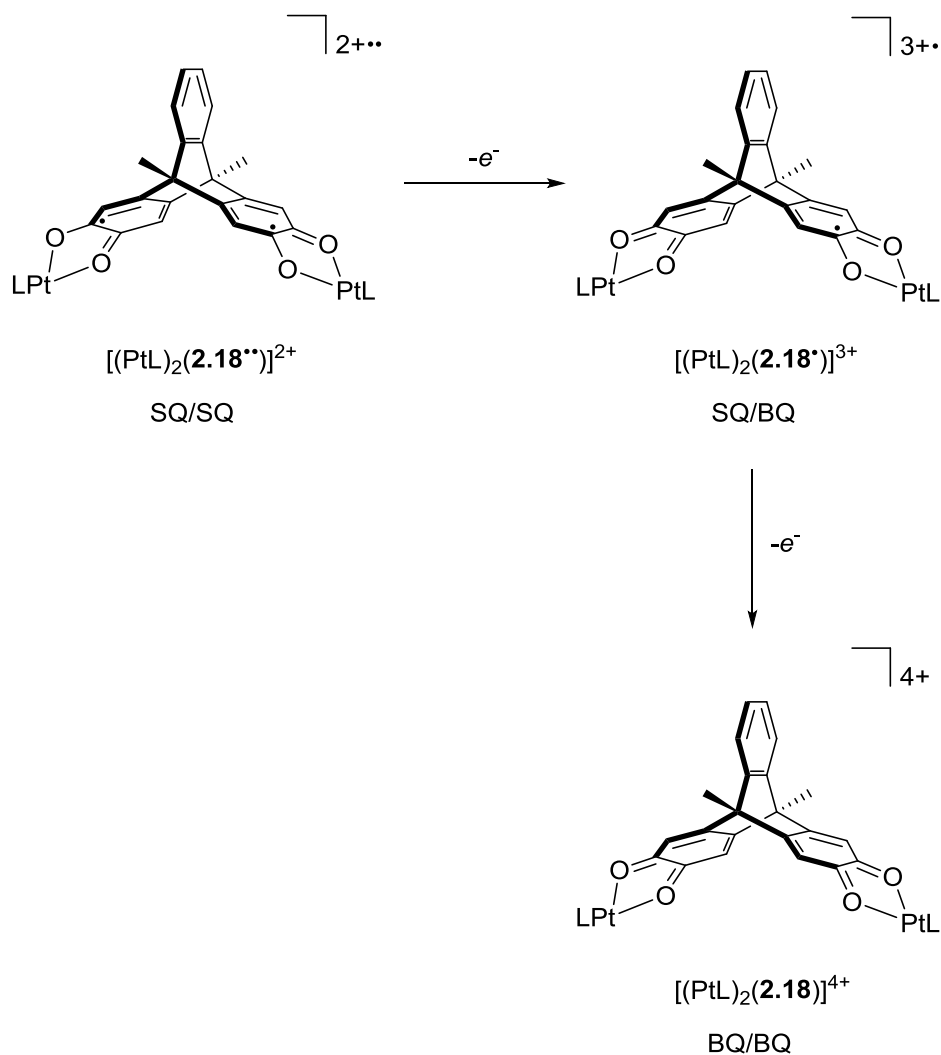
Transition (V)	( <b>3.1</b> )	( <b>3.2</b> )
$E_{1/2}$ Cat/Cat $\rightarrow$ Cat/BQ	-0.393	-0.403
$E_{1/2}$ Cat/SQ $\rightarrow$ BQ/BQ	-0.113	-0.117

**Table 3.2.** Differential pulse voltammetric data for complexes **3.1** and **3.2** in 0.1 M solution of  $n\text{Bu}_4\text{NPF}_6$  in dry degassed  $\text{CH}_2\text{Cl}_2$  at 298 K under argon atmosphere. Potentials (V) are referenced to a  $[\text{FeCp}_2] / [\text{FeCp}_2]^+$  internal standard, measured at a scan rate of 0.1  $\text{Vs}^{-1}$ .

Transition (V)	$E_p$ ( <b>3.1</b> )	$E_p$ ( <b>3.2</b> )
$E_{1/2}$ Cat/Cat $\rightarrow$ Cat/SQ	-0.395	-0.383
$E_{1/2}$ Cat/SQ $\rightarrow$ SQ/SQ	-0.118	-0.111
$E_{1/2}$ SQ/SQ $\rightarrow$ SQ/BQ	0.647	0.730
$E_{1/2}$ BQ/BQ $\rightarrow$ BQ/BQ	1.141	-



**Scheme 3.4.** Ligand based redox series for the Cat  $\rightarrow$  SQ transitions for **3.1** and **3.2**.



**Scheme 3.5.** Ligand based redox series of the SQ  $\rightarrow$  BQ transitions for **3.1** and **3.2**. Only the first oxidation is observed in the CV/DPV of **3.1**.

The peak-to-peak and  $E_{1/2}$  separations for the oxidation processes provide a measure of the degree of communication between the dioxolene rings, with a larger separation being indicative of a lesser degree of communication.

For the Cat  $\rightarrow$  SQ transitions, complex **3.1** has a peak-to-peak  $E_{1/2}$  separation of  $E_p = 0.277$  V, and for the SQ  $\rightarrow$  BQ transitions  $E_p = 0.493$  V. Complex **3.2** is comparable with an  $E_p$  0.272 V for the Cat  $\rightarrow$  SQ transitions, however the presence of only a single SQ  $\rightarrow$  BQ peak precludes determination of the SQ  $\rightarrow$  BQ  $E_p$ . The structurally related complexes  $[(Pt(L))_2\text{thea}]$  (L = dppe or dppb) previously studied by Halcrow *et al.*<sup>[9]</sup> have similar peak-to-peak  $E_{1/2}$  separations of 0.270 and 0.230 V respectively.

### 3.2.1.4 UV-vis-NIR Oxidative Titrations

As the CV measurements discussed in the previous section showed the Cat  $\rightarrow$  SQ transitions for complexes **3.1** and **3.2** all occurred at an oxidation potential more negative than that of the  $[\text{FeCp}_2] / [\text{FeCp}_2]^+$  couple, it is therefore appropriate to use  $[\text{FeCp}_2]\text{PF}_6$  as a chemical oxidant to generate the SQ radicals in solution by titration of stoichiometric amounts of the oxidant. In principle, the *mono*- and *bi*- and radicals should be accessible by the addition of one or two molar equivalents of the oxidant. Consequently, oxidative titrations of complexes **3.1** and **3.2** in aliquots of 0.25 eq of  $[\text{FeCp}_2]\text{PF}_6$  were carried out in nitrogen-degassed  $\text{CH}_2\text{Cl}_2$  at 298 K, and the UV-vis/NIR spectra of these solutions were recorded immediately after addition of the oxidant.

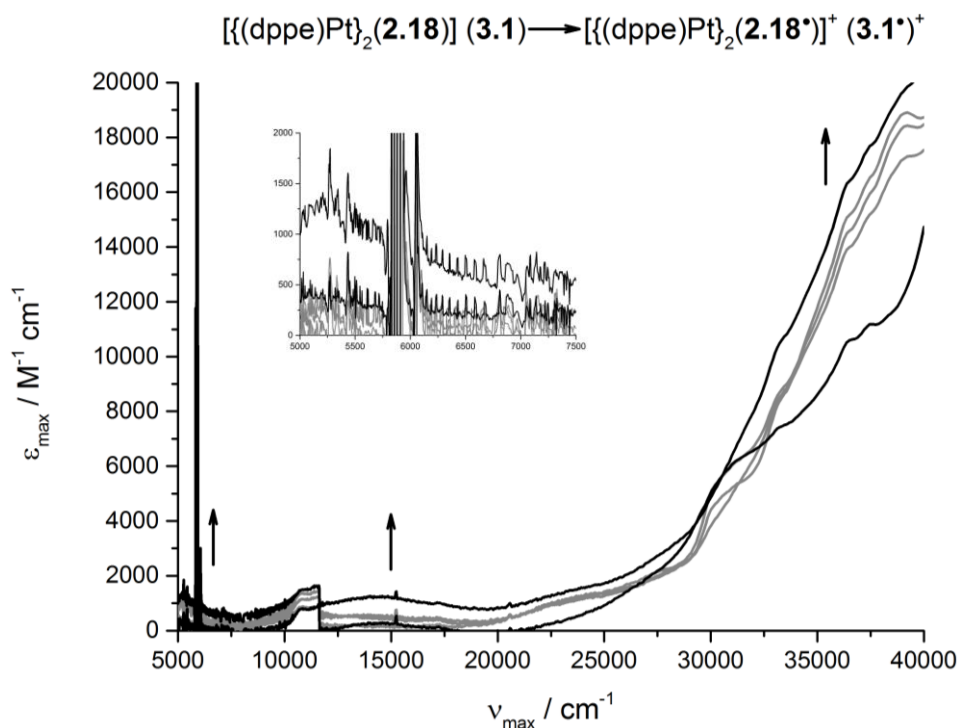


**Figure 3.12.** UV-vis/NIR oxidative titration of **3.1** to  $[\mathbf{3.1}']^+$  by sequential addition of 0.25 eq of  $[\text{FeCp}_2]\text{PF}_6$ . The spectra of pure **3.1** and  $[\mathbf{3.1}']^+$  are displayed in black, with intermediate spectra displayed in grey.

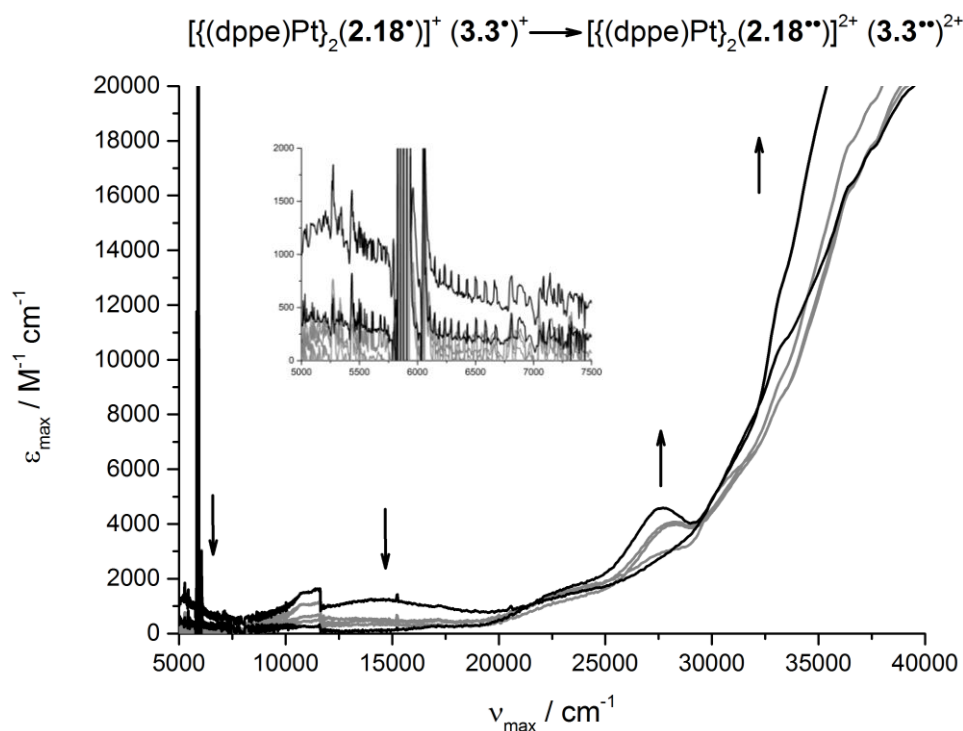
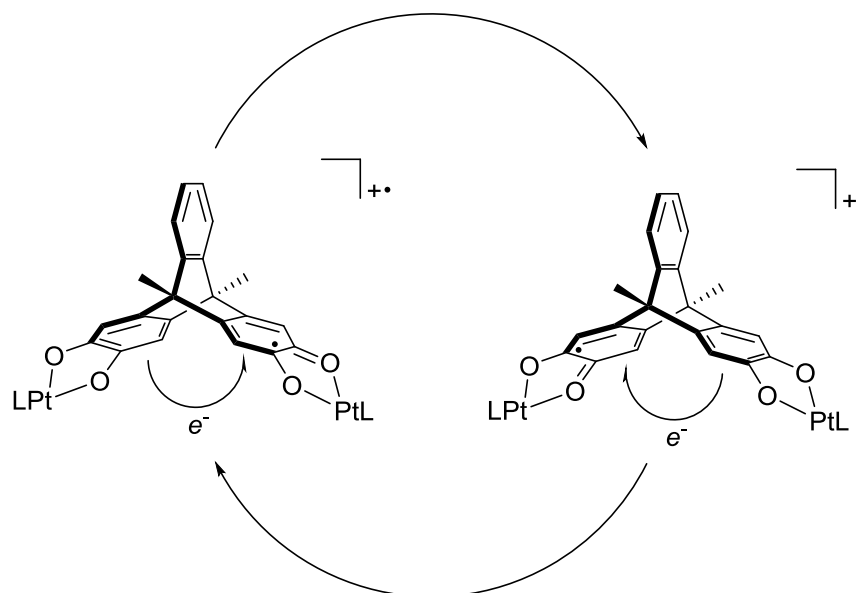


**Figure 3.13.** UV-vis/NIR oxidative titration of  $[\mathbf{3.1}^*]^+$  to  $[\mathbf{3.1}^{**}]^{2+}$  by sequential addition of 0.25 eq of  $[\text{FeCp}_2]\text{PF}_6$ . The spectra of pure  $[\mathbf{3.1}^*]^+$  and  $[\mathbf{3.1}^{**}]^{2+}$  are displayed in black, with intermediate spectra displayed in grey.

As the first equivalent  $[\text{FeCp}_2]^+$  is added (**Figure 3.12**), a low energy IVCT grows in at a  $\nu_{\text{max}}$  of 5277  $\text{cm}^{-1}$ . This IVCT arises due to intramolecular electron transfer from the unoxidised catecholate to the semiquinone. The electron is therefore delocalised and the dioxolene rings are able to communicate with one another (**Scheme 3.6**). Addition of the first equivalent of  $[\text{FeCp}_2]^+$  proceeds non-isosbesticly, indicating that there is fast decomposition of the radical cation.

As the second equivalent of  $[\text{FeCp}_2]^+$  is added (**Figure 3.13**), the IVCT decreases in intensity until it vanishes upon the generation of pure  $[\mathbf{3.1}^{**}]^{2+}$ . This can be rationalised by noting that once the  $(\text{SQ})_2$  tautomer is formed there is no longer any available catecholate moiety for electron transfer to take place from. Similarly to the addition of the first equivalent of the oxidant, there is a similar lack of isosbesticity due to fast decomposition of the biradical.



**Scheme 3.6.** Representation of the electronic delocalisation in  $[3.1^*]^+$  and  $[3.2^*]^+$ .

An estimation of the degree of electron delocalisation can be obtained by finding the width at half height ( $\Delta\nu_{1/2}$ ) of the IVCT peak.<sup>[10]</sup> A large  $\Delta\nu_{1/2}$  is indicative of a broad transition and therefore class II behaviour, whereas a small  $\Delta\nu_{1/2}$  and narrow transition implies class III behaviour.<sup>[11]</sup> The IVCT has a tail which extends to a lower energy than could be measured ( $<5000\text{ cm}^{-1}$ ), however it is still possible to estimate  $\Delta\nu_{1/2}$  by assuming the peak is symmetrical either side of its maximum. An expression which predicts  $\Delta\nu_{1/2}$  for class II mixed-valent complexes at an energy  $E$  is:

$$\Delta\nu_{\frac{1}{2}} = (2310E)^{\frac{1}{2}} \quad \text{(Equation 1.4)}^{[10]}$$

Noting that the IVCT for  $[3.1^*]^+$  has a  $\Delta\nu_{1/2}$  of  $2380\text{ cm}^{-1}$ , and that **Equation 1.4** predicts a  $\Delta\nu_{1/2}$  of  $3480\text{ cm}^{-1}$  for an IVCT with a  $\nu_{\text{max}}$  of  $5277\text{ cm}^{-1}$ , it can be concluded that the valent electron in  $[3.1^*]^+$  is more delocalised than a strictly class II system, placing it more towards the class II/III border.

In the class III limit, the electron coupling energy ( $H_{ab}$ ) is given by the following expression:

$$H_{ab} = \frac{1}{2}\Delta\nu_{\frac{1}{2}} \quad \text{(Equation 1.5)}^{[10]}$$

By applying this equation for the IVCT in the spectrum of  $[3.1^*]^+$ , a coupling energy in the class III limit of  $1190\text{ cm}^{-1}$  is obtained. This value is comparable to cyclophane

radical anions which show through-space electron transfer between stacked aromatic rings.<sup>[12]</sup>

The remaining higher energy absorptions are phosphine based, with the peak at 14493  $\text{cm}^{-1}$  being assigned to a Pt  $\rightarrow$  SQ MLCT, and the peak at 27700  $\text{cm}^{-1}$  corresponding to phosphine interligand charge absorptions.

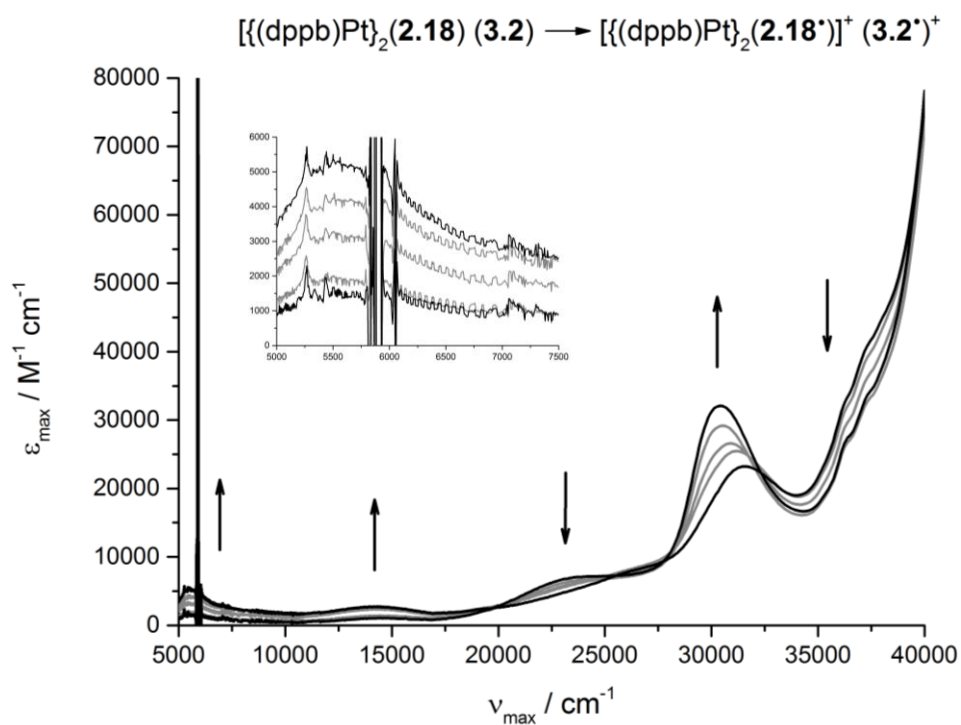


**Figure 3.14.** UV-vis/NIR oxidative titration of **3.2** to  $[\mathbf{3.2}^+]^+$  by sequential addition of 0.25 eq of  $[\text{FeCp}_2]\text{PF}_6$ . The spectra of pure **3.2** and  $[\mathbf{3.2}^+]^+$  are displayed in black, with intermediate spectra displayed in grey.

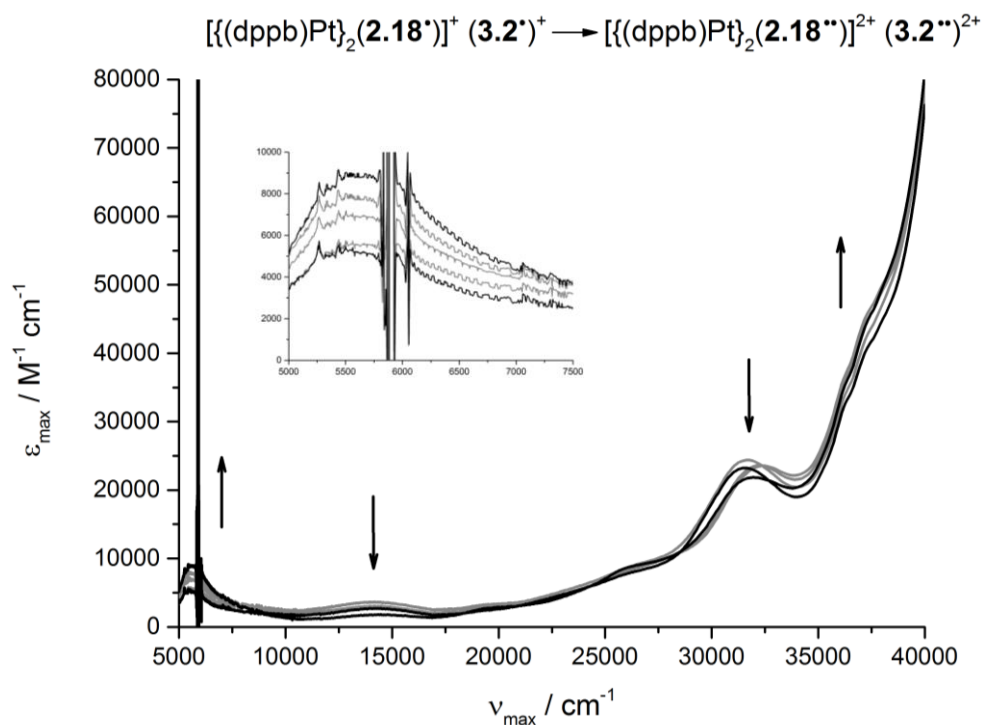


**Figure 3.15.** UV-vis/NIR oxidative titration of  $[\mathbf{3.2}^{\bullet}]^+$  to  $[\mathbf{3.2}^{\bullet\bullet}]^{2+}$  by sequential addition of 0.25 eq of  $[\text{FeCp}_2]\text{PF}_6$ . The spectra of pure  $[\mathbf{3.2}^{\bullet}]^+$  and  $[\mathbf{3.2}^{\bullet\bullet}]^{2+}$  are displayed in black, with intermediate spectra displayed in grey.

As the first equivalent  $[\text{FeCp}_2]^+$  is added to **3.2** (**Figure 3.14**), a low energy IVCT grows in at a  $\nu_{\text{max}}$  of 5618  $\text{cm}^{-1}$ . As with **3.1**, this IVCT arises due to intramolecular electron transfer from the unoxidised catecholate to the semiquinone. There is a low intensity residual peak at this wavenumber prior to any  $[\text{FeCp}_2]^+$  being added, which is present due to a small impurity of aeri ally oxidised  $[\mathbf{3.2}^{\bullet}]^+$ . Addition of the first equivalent of  $[\text{FeCp}_2]^+$  proceeds isosbesticly, indicating that there is no decomposition of the radical cation over the course of the measurement.

As the second equivalent of  $[\text{FeCp}_2]^+$  is added to **3.2** (**Figure 3.15**), the IVCT continues to increase in intensity, and there is a loss of isosbesticity due to fast decomposition of the  $(\text{SQ})_2$  tautomer.

An estimation of the degree of electron delocalisation can be obtained by the same method described above. Noting that the IVCT for  $[\mathbf{3.2}^{\bullet}]^+$  has a  $\Delta\nu_{1/2}$  of 2695  $\text{cm}^{-1}$ , and that **Equation 1.4** predicts a  $\Delta\nu_{1/2}$  of 3602  $\text{cm}^{-1}$  for an IVCT with a  $\nu_{\text{max}}$  of 5618  $\text{cm}^{-1}$ , it can be concluded that the valent electron in  $[\mathbf{3.2}^{\bullet}]^+$  is more delocalised than a strictly class II system, placing it towards the class II/III border. By applying

**Equation 1.2** to the IVCT in the spectrum of  $[3.2]^+$ , a coupling energy in the class III limit of  $1348\text{ cm}^{-1}$  is obtained.

The remaining higher energy absorptions are phosphine based, with the peak at  $14,265\text{ cm}^{-1}$  being assigned to a  $\text{Pt} \rightarrow \text{SQ MLCT}$ , and the peak at  $30,395\text{ cm}^{-1}$  corresponding to phosphine interligand charge absorptions.

### 3.2.1.5 Spectroelectrochemical analysis of 3.1

As discussed previously, the UV-vis/NIR oxidation titrations of **3.1** with  $[\text{FeCp}_2]\text{PF}_6$  did not produce isosbestic points. Therefore, it was decided to carry out spectroelectrochemical measurements to obtain the spectra of the oxidised complex. The experimental setup uses an optically transparent electrode (OTTLE) cell containing a solution of **3.1** and  $0.1\text{ M } n\text{-Bu}_4\text{NPF}_6$  in  $\text{CH}_2\text{Cl}_2$  at  $298\text{ K}$ . By observing the oxidation potentials elucidated by the CV measurements, it is possible to electrochemically generate the semiquinone radical by passing a current through the solution. **Figure 3.20** shows the spectral changes upon oxidation of **3.1** to  $[3.1]^+$ .

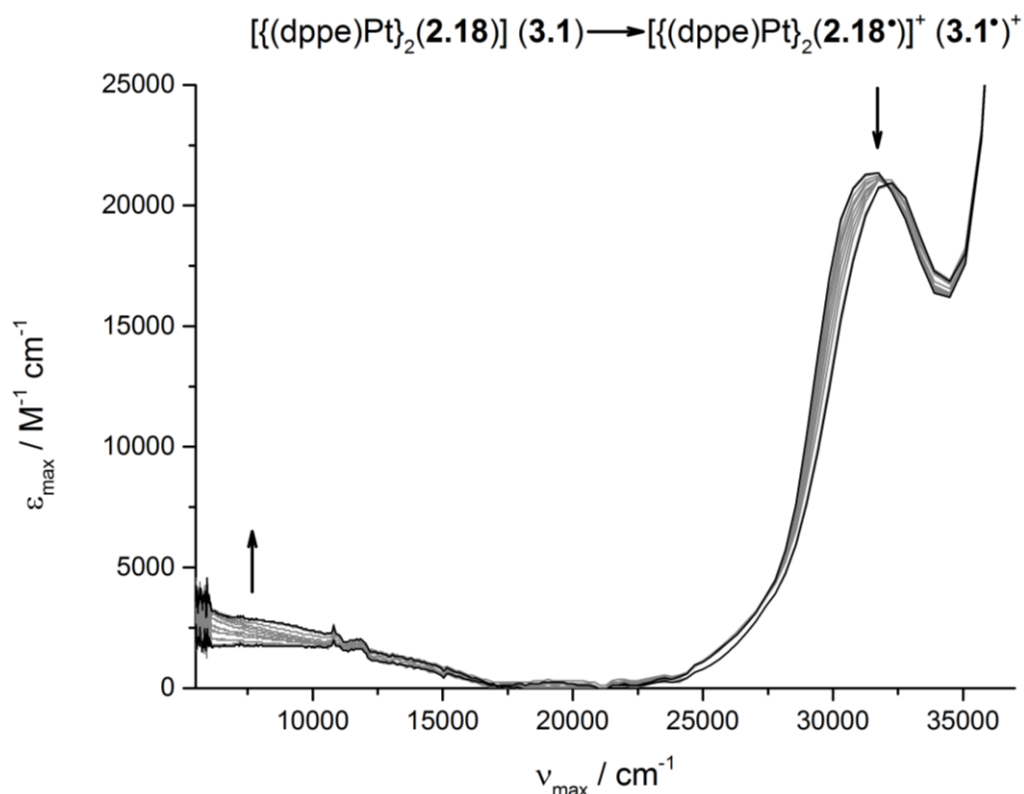


**Figure 3.20.** UV-vis/NIR spectroelectrochemical data for the first oxidation of a **3.1** to  $[3.1]^+$  in a  $0.1\text{ M } n\text{-Bu}_4\text{NPF}_6$  solution in  $\text{CH}_2\text{Cl}_2$  at  $298\text{ K}$ . The spectra of pure **3.1** and  $[3.1]^+$  are displayed in black, with intermediate spectra displayed in grey.

---

As in **Figure 3.14**, the shoulder of a low energy IVCT grows in at ca.  $5000\text{ cm}^{-1}$ , however the peak maximum appears to be outside of the wavelength window permitted by the setup, and is coincident with noise arising from the solvent vibrational structure. Encouragingly, the spectra have well defined isosbesticity. Attempts were made to regenerate the starting material **3.1** by cycling back the applied potential, however the resultant decrease in intensity of the IVCT was only very small.

### **3.2.1.6 EPR Measurements of Chemically Oxidised Mixed-Valent Radical Cations of 3.1 and 3.2**

EPR can give valuable information about the local environment of the semiquinone radical. For example, the degree of electron delocalisation is reflected in the hyperfine coupling constants, because each  $S = \frac{1}{2}$  nucleus that the electron interacts with will split the signal into  $(2nI+1)$  peaks. Thus, if the molecular orbital which the radical occupies has a large amount of Pt or P character, this should manifest as a large hyperfine coupling to each of these atoms respectively. EPR also sheds light on the degree of electron transfer between Pt centres, as hyperfine coupling to two or more  $^{195}\text{Pt}$  nuclei is only observed if electron transfer occurs rapidly (i.e. shorter than the timescale of the EPR experiment).

The following S and X band EPR measurements were carried out at the University of Manchester with the aid of Dr. Amgalanbataar Baldansuren. The singly oxidised samples were prepared by addition of a  $\text{CH}_2\text{Cl}_2$  solution of one equivalent of  $[\text{FeCp}_2]\text{PF}_6$  to a  $\text{CH}_2\text{Cl}_2$  solution of the complex in question, followed by (in the case of the frozen solution spectra) the immediate cooling of the sample in liquid nitrogen. The data was collected as soon as possible after the addition of the oxidant to try to minimise decomposition of the radical cation.

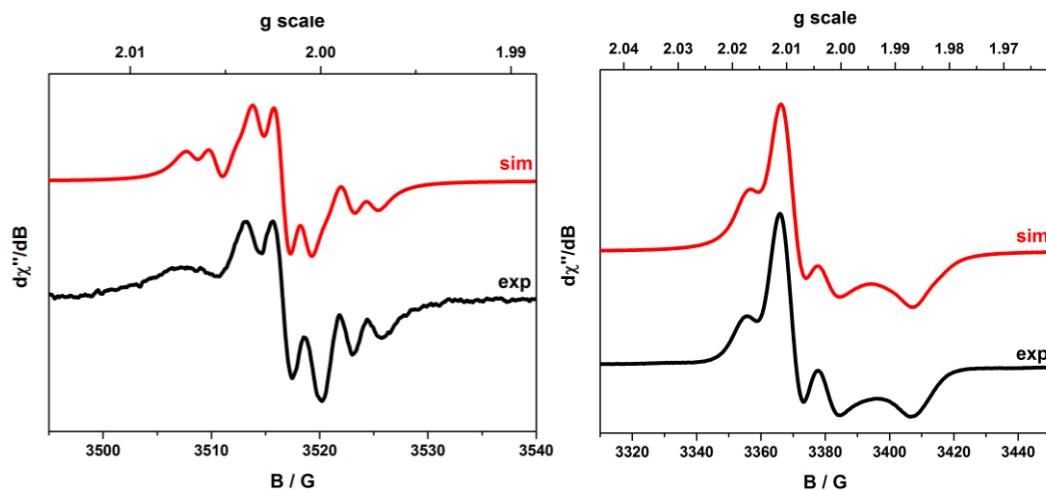


**Figure 3.16.** X-band EPR spectra of  $[(dppe)Pt]_2(2.18')^+ [3.1']^+$  in  $CH_2Cl_2$  at (left) 300 K and (right) 150 K (frozen solution). Experimental data displayed in black, simulation displayed in red.

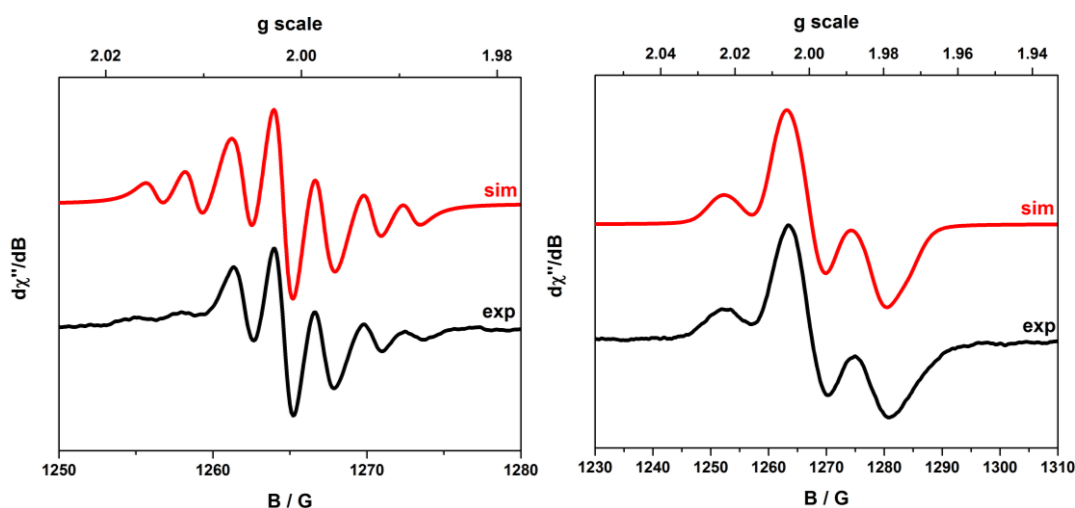


**Figure 3.17.** S-band EPR spectra of  $[(dppe)Pt]_2(2.18')^+ [3.1']^+$  in  $CH_2Cl_2$  at (left) 300 K and (right) 150 K (frozen solution). Experimental data displayed in black, simulation displayed in red.

The X and S band spectra of  $[3.1']^+$  (**Figures 3.16** and **3.17**) at 300 K show an isotropic signal with the classic splitting pattern expected for an organic radical with large hyperfine coupling to one  $S = \frac{1}{2}$   $^{195}Pt$  nucleus and smaller superhyperfine couplings to two  $S = \frac{1}{2}$   $^{31}P$  atoms. The spectrum is simulated with a g factor of 2.0019, which is close in value to  $g_e$ , indicating that the molecular orbital that the radical occupies is

largely organic in character. The  $^{195}\text{Pt}$  hyperfine coupling is large,  $A(^{195}\text{Pt}) = 34 \times 10^{-4} \text{ cm}^{-1}$ , which implies a significant amount of delocalisation of the radical onto the metal. The  $^{31}\text{P}$  superhyperfine coupling is smaller but not insignificant,  $A(^{31}\text{P}) = 7 \times 10^{-4} \text{ cm}^{-1}$ , therefore the radical is also slightly localised on the phosphine. When  $[\mathbf{3.1}^+]^+$  is cooled to 150 K, a rhombic signal is observed with an increased hyperfine coupling to  $^{195}\text{Pt}$  of  $60 \times 10^{-4} \text{ cm}^{-1}$ . In contrast to the 300 K measurements, there appears to be no contribution from  $^{31}\text{P}$  hyperfine coupling at 150 K.

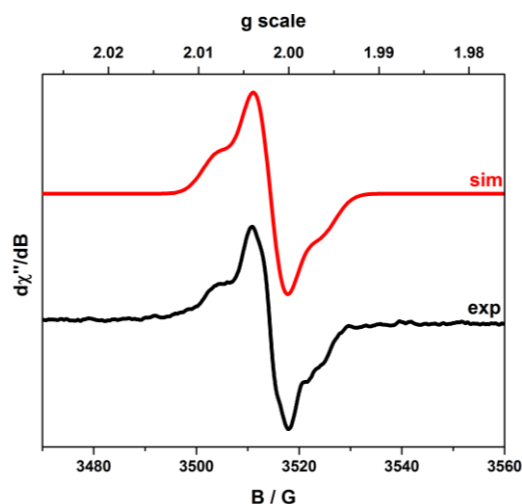


**Figure 3.18.** X-band EPR spectra of  $[(\text{dppbPt})_2(\mathbf{2.18}')^+]^+ [\mathbf{3.2}']^+$  in  $\text{CH}_2\text{Cl}_2$  at 300 K. Experimental data displayed in black, simulation displayed in red.

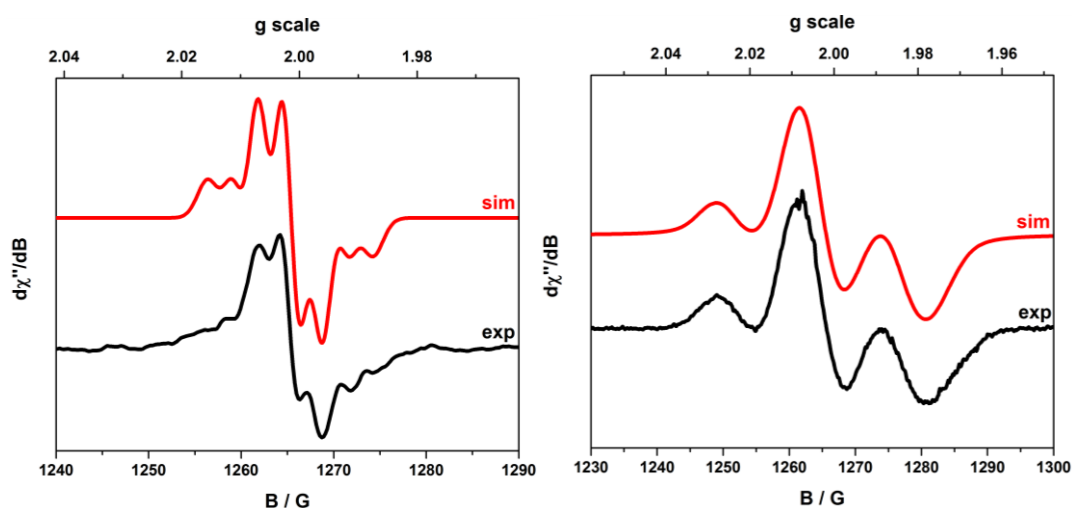


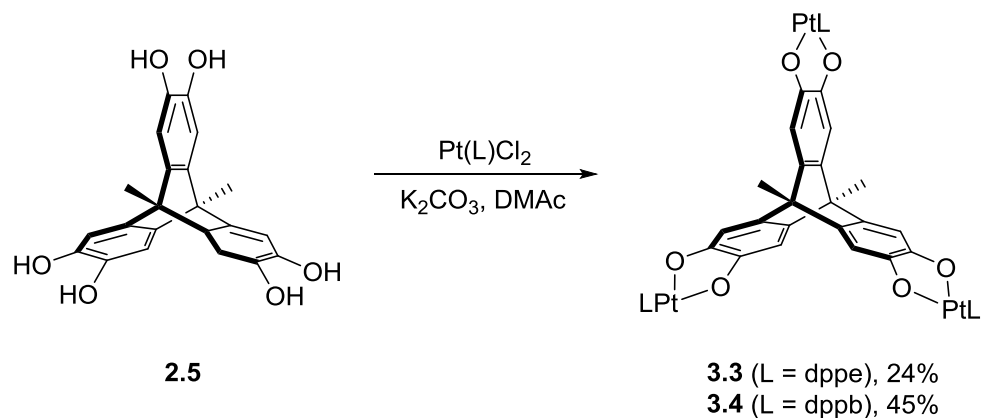
**Figure 3.19.** S-band EPR spectra of  $[(\text{dppbPt})_2(\mathbf{2.18}')^+]^+ [\mathbf{3.2}']^+$  in  $\text{CH}_2\text{Cl}_2$  at (top) 300 K and (bottom) 100 K (frozen solution). Experimental data displayed in black, simulation displayed in red.

The S band spectrum of  $[3.2']^+$  at 300 K (**Figure 3.9**) shows an isotropic signal very similar to that of  $[3.1']^+$ , with large hyperfine coupling to one  $S = \frac{1}{2}$   $^{195}\text{Pt}$  nucleus, and a smaller hyperfine coupling to two  $S = \frac{1}{2}$   $^{31}\text{P}$  atoms. The spectrum is simulated with a g factor of 2.0017, which is also consistent with  $[3.1']^+$ . The  $^{195}\text{Pt}$  hyperfine coupling  $A(^{195}\text{Pt}) = 30 \times 10^{-4} \text{ cm}^{-1}$  is large, but slightly smaller than  $[3.1']^+$ , suggesting the radical is slightly less delocalised onto the  $^{195}\text{Pt}$  atom. The  $A(^{31}\text{P}) = 7 \times 10^{-4} \text{ cm}^{-1}$ , identical to that of  $[3.1']^+$ . When  $[3.2']^+$  is cooled to 150 K, the S band spectrum takes on the same rhombic lineshape as  $[3.1']^+$ , and a loss of  $^{31}\text{P}$  superhyperfine coupling is also observed. A weak X band signal which only contained hyperfine coupling to one  $^{195}\text{Pt}$  nucleus was obtained at 300 K, however no X band spectrum was able to be collected at 150 K.

### 3.2.2 $[\{(\text{dppe})\text{Pt}\}_3(2.5)]$ (**3.3**) and $[\{(\text{dppb})\text{Pt}\}_3(2.5)]$ (**3.4**)

#### 3.2.2.1 Synthesis and Characterisation

Reaction of the *tris*(catechol) ligand **2.5** with **3.7** and **3.8** were carried out under air and moisture free conditions to produce the complexes **3.3** and **3.4** (**Scheme 3.7**).



**Scheme 3.7.** Complexation of **2.5** with **3.7** and **3.8** to form the trinuclear complexes **3.3** and **3.4**.

The green complexes **3.3** and **3.4** are highly air and moisture sensitive and must be synthesised and stored under rigorously air and moisture free conditions. The  $^1\text{H}$  NMR spectrum of **3.3** confirms the identity of the complex (**Figure 3.21**).

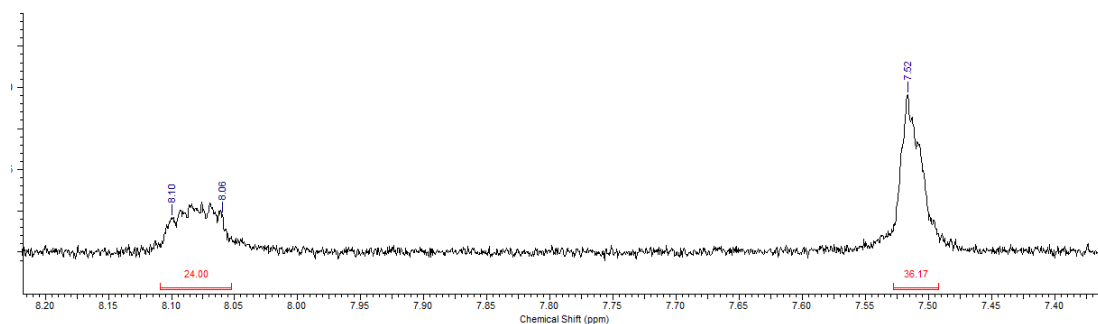


**Figure 3.21.**  $^1\text{H}$  NMR (500 MHz,  $\text{CDCl}_3$ ) spectrum of **3.3** showing a representative example of paramagnetically broadened aromatic peaks.

The peaks between 8.10-8.06 ppm correspond to 24 protons located at the *ortho* position of the dppe phenyl rings, and the peaks at 7.52 ppm correspond to the 36 protons located at the *para* and *meta* positions. Exposure of **3.3** or **3.4** to air causes an immediate colour change from green to blue, accompanied by progressively more paramagnetic broadening of the aromatic peaks in the  $^1\text{H}$  NMR spectrum.

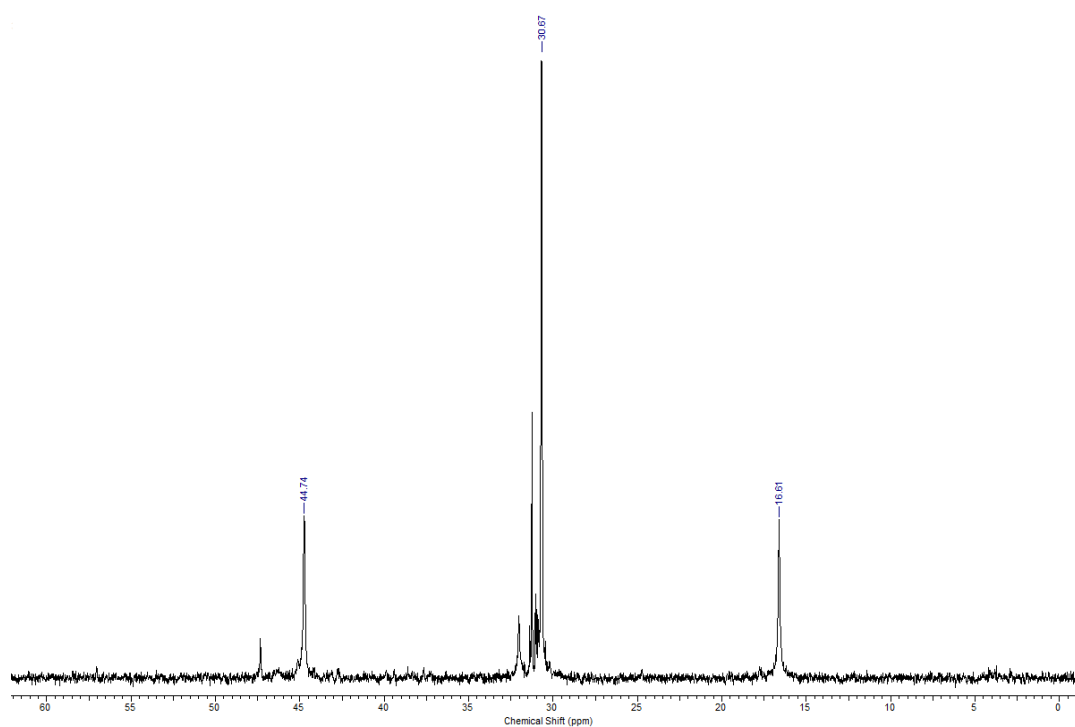


**Figure 3.22.**  $^{31}\text{P}\{^1\text{H}\}$  NMR (300 MHz,  $\text{CDCl}_3$ ) spectrum of **3.3**, showing  $^{195}\text{Pt}$  satellites.

The  $^{31}\text{P}\{^1\text{H}\}$  NMR spectrum (**Figure 3.22**) shows a phosphorus environment at 30.67 ppm, which is to be expected given the  $C_3$  symmetry of the complex. Platinum satellite peaks with a coupling constant of 1708.7 Hz are also observed due to the coupling of

the  $^{31}\text{P}$  nuclei to a  $^{195}\text{Pt}$  ( $S = 1/2$ ) nucleus.<sup>[3]</sup> Some slight impurity due to the presence of a small amount of starting material is also observed.

The high resolution mass spectra for **3.3** (Figure 3.23) has good agreement with the simulated isotopic distribution expected for the molecular ions  $[\text{C}_{100}\text{H}_{84}\text{O}_6\text{P}_6\text{Pt}_3]^+$  (2151.36 g mol<sup>-1</sup>) and  $[\text{C}_{112}\text{H}_{84}\text{O}_6\text{P}_6\text{Pt}_3]^+$  (2295.36 g mol<sup>-1</sup>) respectively. For both spectra, a second smaller set of peaks corresponding to  $[(\mathbf{3.3})_2(\text{H})]^{2+}$  and  $[(\mathbf{3.4})_2(\text{H})]^{2+}$  are also observed.

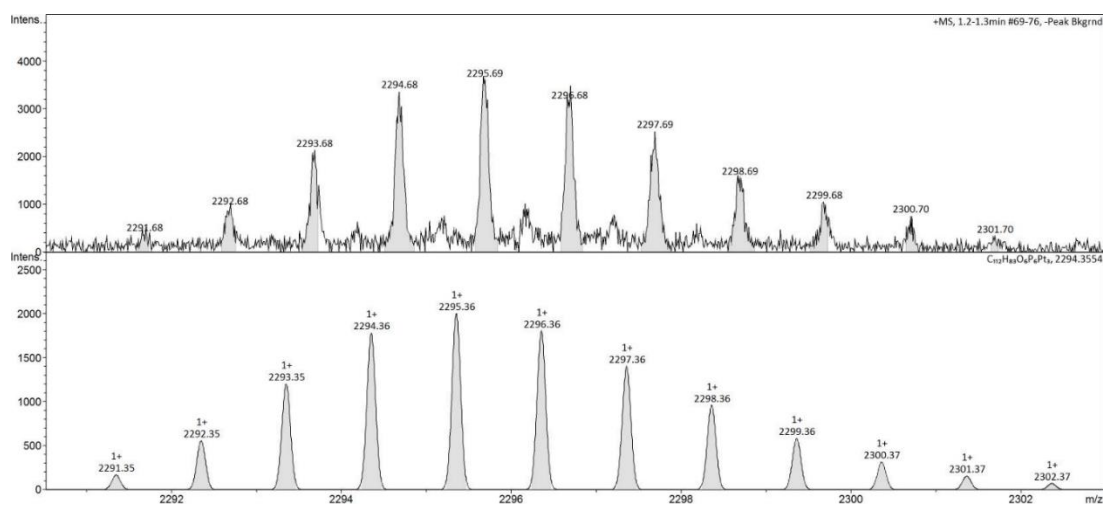


**Figure 3.23.** Experimental (top) and simulated (bottom)  $[\text{M}]^+$  ion of **3.4**. There is good agreement between the spectrum and simulation, with the characteristic isotopic distribution for a complex containing three Pt ions.

### 3.2.2.2 X-ray Crystal Structure Refinement of **3.3**

The air sensitivity of **3.3** made obtaining a suitable monocrystalline sample challenging, but small twinned green blocks were obtained by vapour diffusion of pentane into chloroform. The crystals rapidly change colour from green to blue upon their removal from the mother liquor, losing crystallinity in the process. The small twinned crystals which were obtained were unsuitable for use on the in-house diffractometer, and consequently X-ray diffraction experiments were carried out at the Diamond Light Source synchrotron. The higher intensity X-rays produced by this facility were sufficient to resolve the structure of the complex. The structure of **3.3**

---

was solved in the monoclinic space group  $C2/c$  using the *Olex2* program (**Figure 3.24**).

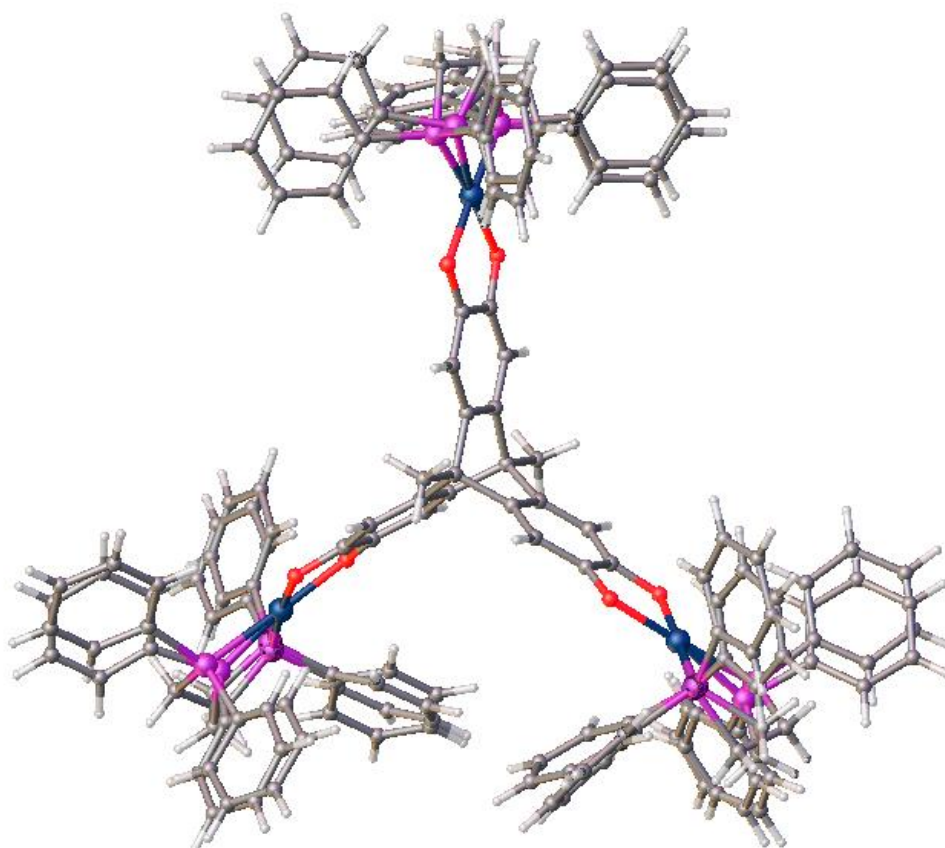


**Figure 3.24.** Crystal structure of a single molecule of **3.3**, showing the desired structural features are present in the complex. Each phenyl group on the dppe ligand is disordered over two crystallographic sites.

The desired trigonal shape is clearly apparent in the structure, with an average Pt-Pt distance of 11.30 Å. The phenyl groups of the dppe ligand are each disordered 50% over two crystallographic sites. The average C-O bond length in this complex is 1.372 Å, which is identical (within experimental error) to the C-O bond lengths of the free triptycene **2.5** (1.372 and 1.370 Å respectively for the crystal structures obtained). As the free triptycene **2.5** is in the *tris*(catechol) form, it can be inferred that **3.3** also occupies the *tris*(Cat) form of the complex, as the SQ or BQ forms of this complex would be expected to show a contraction of the C-O bond lengths. The dihedral angle between the dioxolene groups is 118.13°, which is close to the values for the free

---

tritycene (118.49), providing additional evidence that this complex exists in the tris(Cat) form.

Using the **Equations 3.1-3.3** for complex **3.3** gives a value of  $\Delta = -1.98$ , indicating that the complex is in the (Cat)<sub>3</sub> form in this crystal structure.

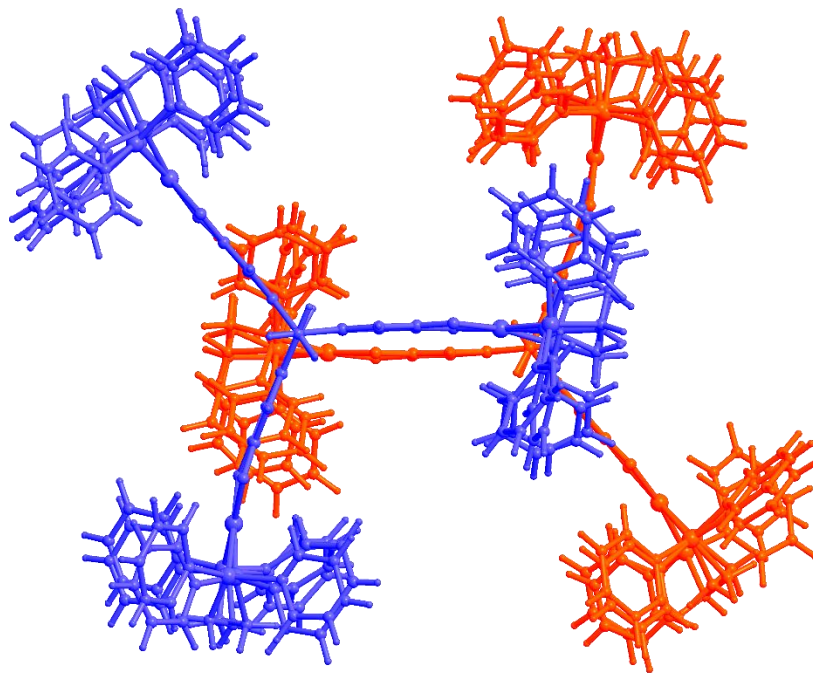


**Figure 3.25.** Crystal packing of **3.3**.

The bulk crystal packing consists of pillared complex molecules offset from one another and rotated by 180°.

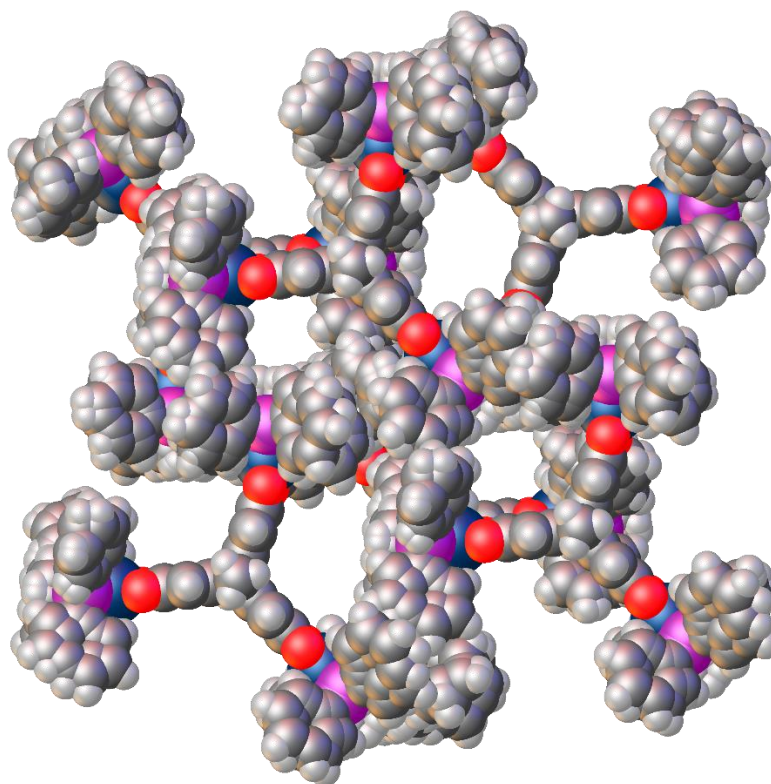


**Figure 3.26.** Crystal packing (spacefilling view) of **3.3** showing void space.

### 3.2.2.3 Electrochemical Analysis of Complexes **3.3** and **3.4**

The redox chemistry of complexes **3.3** and **3.4** was investigated by CV and DPV (**Figures 3.27-3.30**). The measurements were carried out at 298 K in a 0.1 M solution of  $n\text{Bu}_4\text{NPF}_6$  in dry, degassed dichloromethane under argon atmosphere. The analysis showed that both complexes **3.3** and **3.4** contained three chemically reversible one-electron oxidation processes in the  $-0.70 \leq E_{1/2} \leq +0.10$  V (vs.  $\text{Fc}/\text{Fc}^+$ ) region, attributed to sequential  $\text{Cat} \rightarrow \text{SQ}$  transitions as displayed in **Scheme 3.8**. Furthermore, complexes **3.3** and **3.4** also show one (**3.3**) or three (**3.4**) further oxidations occurring in the 0.0-1.0 V region, which can be assigned as subsequent  $\text{SQ} \rightarrow \text{BQ}$  transitions, as displayed in **Scheme 3.9**. The shoulder on the sixth oxidation of **3.4** (0.871 V) is likely present due to a daughter product resulting from the decomposition of  $[\mathbf{3.4}]^{6+}$ .

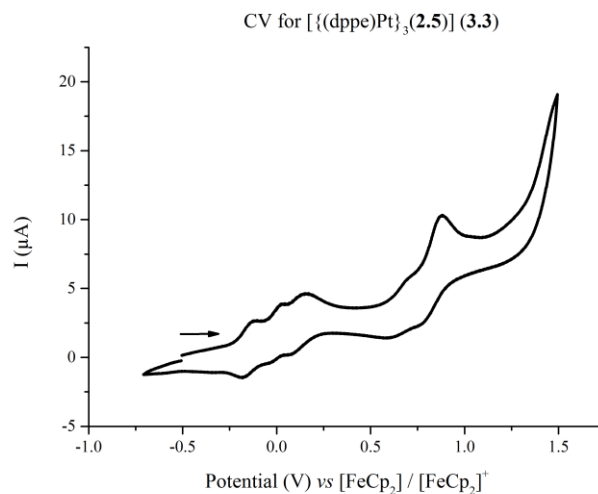


**Figure 3.27.** CV for **3.3** in 0.1 M solution of  $n\text{Bu}_4\text{NPF}_6$  in dry degassed dichloromethane at 298 K under argon atmosphere. The first three chemically reversible Cat  $\rightarrow$  SQ transitions are shown, as well as a further chemically irreversible SQ  $\rightarrow$  BQ transition.

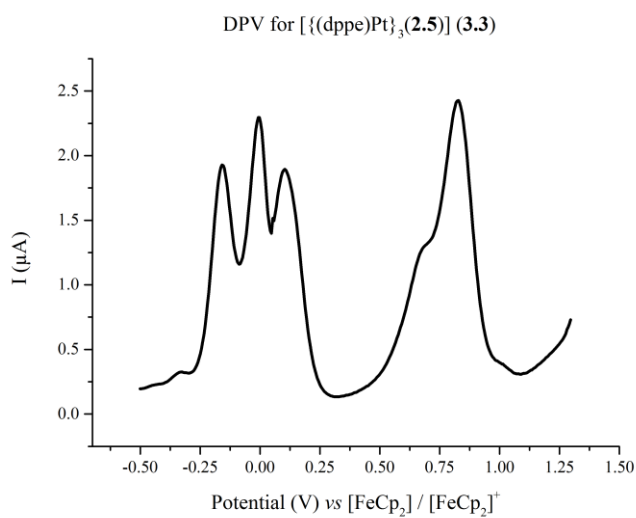


**Figure 3.28.** DPV for **3.3** in 0.1 M solution of  $n\text{Bu}_4\text{NPF}_6$  in dry degassed dichloromethane at 298 K under argon atmosphere.

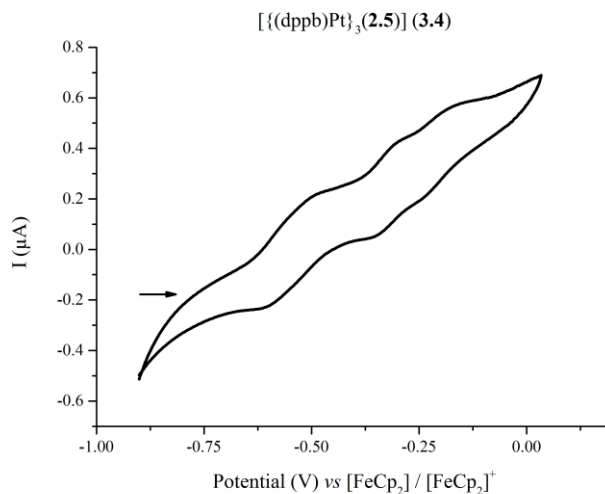


**Figure 3.29.** CV for **3.4** in 0.1 M solution of  $n\text{Bu}_4\text{NPF}_6$  in dry degassed dichloromethane at 298 K under argon atmosphere. The first three chemically reversible Cat  $\rightarrow$  SQ transitions are shown.

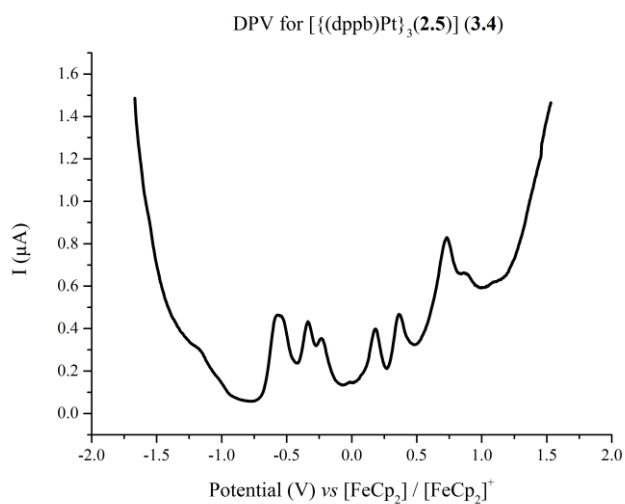


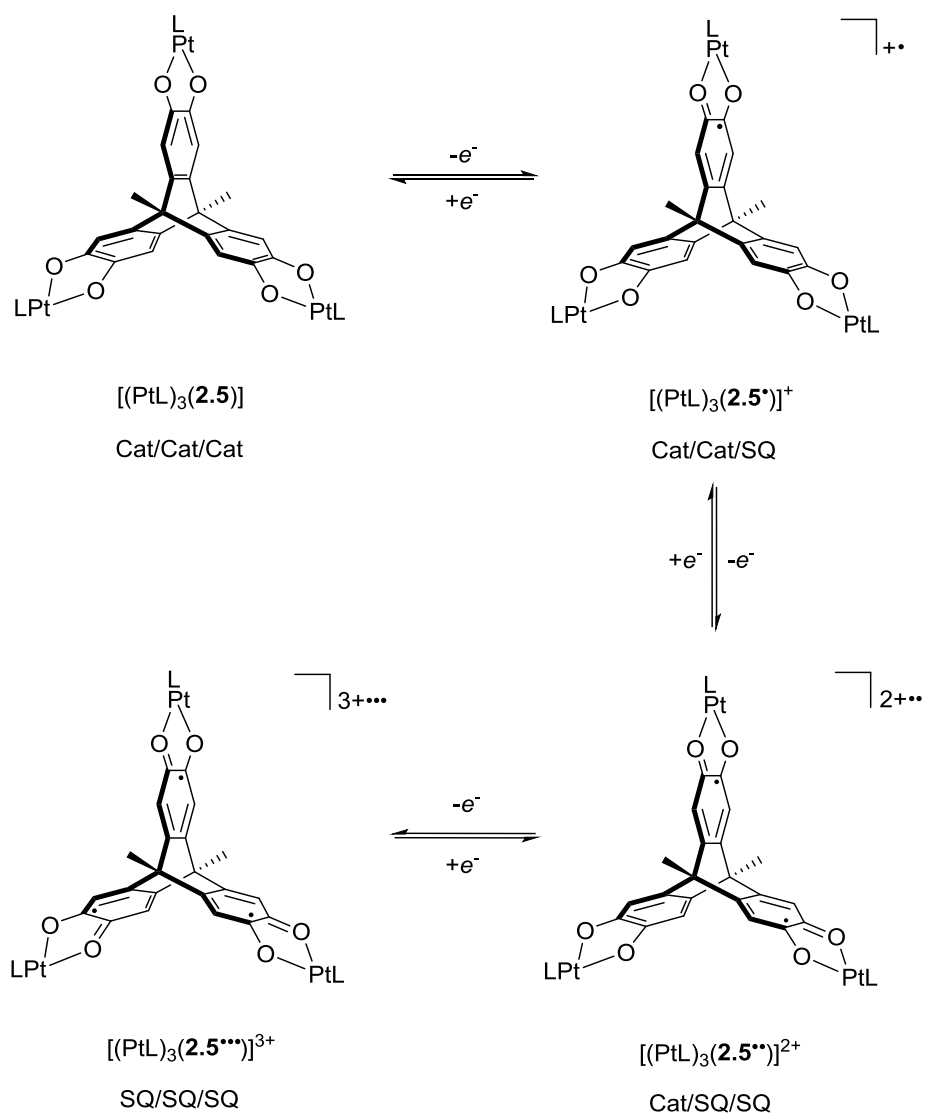
**Figure 3.30.** DPV for **3.4** in 0.1 M solution of  $n\text{Bu}_4\text{NPF}_6$  in dry degassed dichloromethane at 298 K under argon atmosphere. The first three chemically reversible Cat  $\rightarrow$  SQ transitions are shown, as well as three further SQ  $\rightarrow$  BQ transitions.

**Table 3.3.** Cyclic voltammetric data for complexes **3.3** and **3.4** in 0.1 M solution of  $t\text{Bu}_4\text{NPF}_6$  in dry degassed  $\text{CH}_2\text{Cl}_2$  at 298 K under argon atmosphere. Potentials (V) are referenced to a  $[\text{FeCp}_2] / [\text{FeCp}_2]^+$  internal standard, measured at a scan rate of  $0.1 \text{ Vs}^{-1}$ .

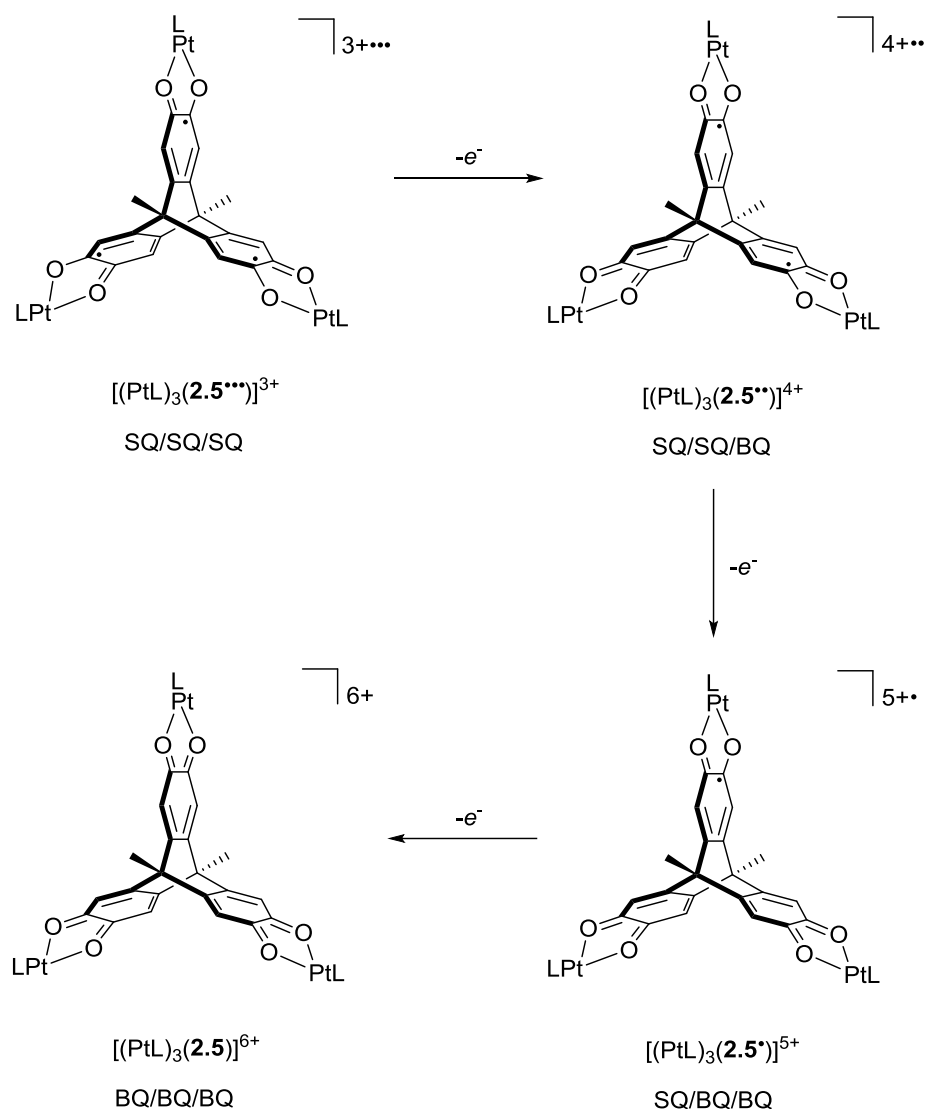
Transition (V)	$E_p$ ( <b>3.3</b> )	$E_p$ ( <b>3.4</b> )
$E_{1/2}$ Cat/Cat/Cat $\rightarrow$ Cat/Cat/SQ	-0.151	-0.350
$E_{1/2}$ Cat/Cat/SQ $\rightarrow$ Cat/SQ/SQ	-0.210	-0.316
$E_{1/2}$ Cat/SQ/SQ $\rightarrow$ SQ/SQ/SQ	0.115	-0.193

**Table 3.4.** Differential pulse voltammetric data for complexes **3.3** and **3.4** in 0.1 M solution of  $t\text{Bu}_4\text{NPF}_6$  in dry degassed  $\text{CH}_2\text{Cl}_2$  at 298 K under argon atmosphere. Potentials (V) are referenced to a  $[\text{FeCp}_2] / [\text{FeCp}_2]^+$  internal standard, measured at a scan rate of  $0.1 \text{ Vs}^{-1}$ .

Transition (V)	$E_p$ ( <b>3.3</b> )	$E_p$ ( <b>3.4</b> )
$E_{1/2}$ Cat/Cat/Cat $\rightarrow$ Cat/Cat/SQ	-0.159	-0.544
$E_{1/2}$ Cat/Cat/SQ $\rightarrow$ Cat/SQ/SQ	-0.003	-0.337
$E_{1/2}$ Cat/SQ/SQ $\rightarrow$ SQ/SQ/SQ	0.103	-0.232
$E_{1/2}$ SQ/SQ/SQ $\rightarrow$ SQ/SQ/BQ	0.828	0.181
$E_{1/2}$ SQ/SQ/BQ $\rightarrow$ SQ/BQ/BQ	-	0.363
$E_{1/2}$ SQ/BQ/BQ $\rightarrow$ BQ/BQ/BQ	-	0.830



**Scheme 3.8.** Ligand based redox series of the observed Cat  $\rightarrow$  SQ transitions for **3.3** and **3.4**.



**Scheme 3.9.** Ligand based redox series of the observed Cat  $\rightarrow$  BQ transitions for **3.3** and **3.4**. **3.3** is only observed to undergo the first oxidation shown.

For the **3.3**  $\rightarrow$  [**3.3** $\cdot^+$ ] transition, the peak-to-peak  $E_{1/2}$  separation is  $E_p = 0.156$  V, and the subsequent [**3.3** $\cdot^+$ ]  $\rightarrow$  [**3.3** $\cdot\cdot^{2+}$ ] transition has a smaller separation of  $E_p = 0.106$  V. For the **3.4**  $\rightarrow$  [**3.4** $\cdot^+$ ] transition, the peak-to-peak  $E_{1/2}$  separation is  $E_p = 0.206$  V and for the subsequent [**3.4** $\cdot^+$ ]  $\rightarrow$  [**3.4** $\cdot\cdot^{2+}$ ] transition the  $E_p = 0.106$  V. Both complexes have smaller  $E_p$  values than has been observed for the structurally related [(Pt(dppb) $_2$ thea)] complex investigated by Halcrow *et al.*,<sup>[9]</sup> which has an  $E_p$  of 0.25 V. This would suggest that the inclusion of a third dioxolene group into the complex imparts a higher degree of communication between the dioxolene rings, placing it closer to the class III formalism.

### 3.2.2.4 UV-vis/NIR Oxidative Titrations with $[\text{FeCp}_2]\text{PF}_6$

The CV measurements discussed in the previous section showed the first two Cat  $\rightarrow$  SQ transitions for complexes **3.3** and **3.4** occurred at an oxidation potential more negative than that of the  $[\text{FeCp}_2] / [\text{FeCp}_2]^+$  couple, with the third Cat  $\rightarrow$  SQ transition occurring at 0.115 or -0.193 V respectively. It is therefore reasonable to assume that at least the first two oxidations (and possibly the third) can be achieved by titration of stoichiometric amounts of  $[\text{FeCp}_2]\text{PF}_6$ . In principle, the *mono*-, *bi*-, and possibly *tri*-radicals should be accessible by the addition of one, two or three molar equivalents of the oxidant. Consequently, oxidative titrations of complexes **3.3** and **3.4** with  $[\text{FeCp}_2]\text{PF}_6$  were carried out in dry degassed  $\text{CH}_2\text{Cl}_2$  at 298 K, and the UV-vis/NIR spectra of these solutions were recorded immediately after addition of the oxidant (Figures 3.31-3.33).

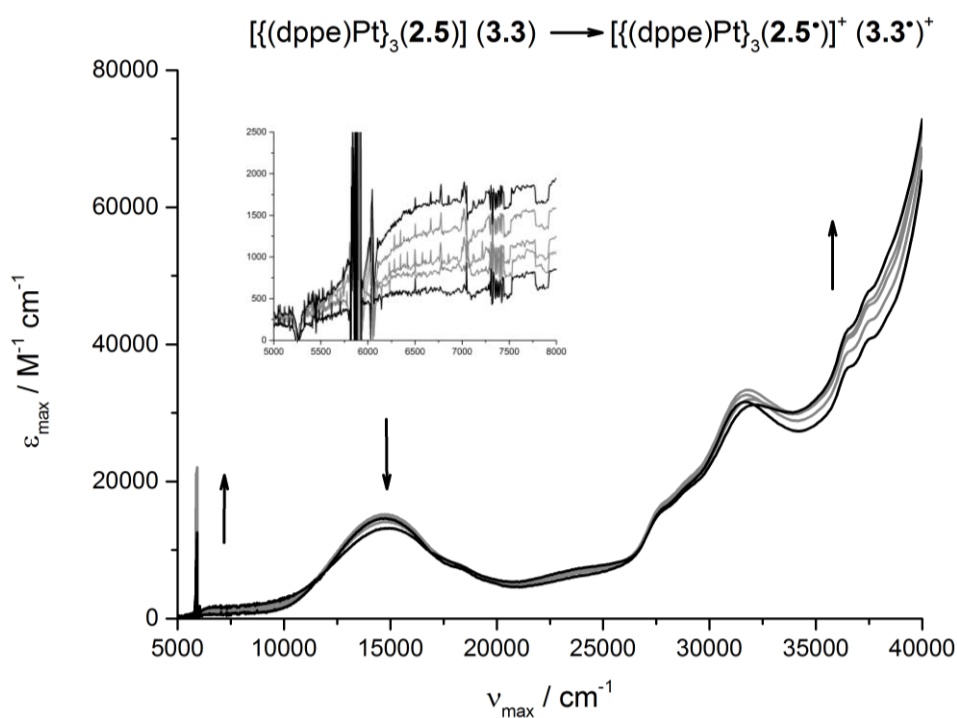


**Figure 3.31.** UV-vis/NIR oxidative titration of **3.3** to **3.3\*+** by sequential addition of 0.25 eq of  $[\text{FeCp}_2]\text{PF}_6$ . The spectra of pure **3.3** and **3.3\*+** are displayed in black, with intermediate spectra displayed in grey.

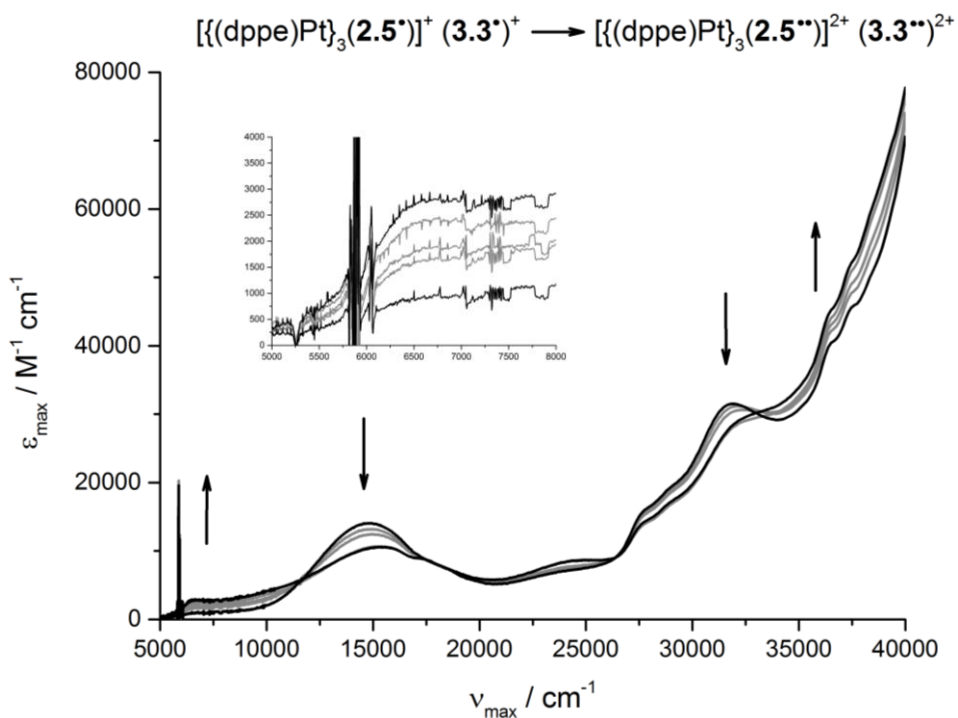


**Figure 3.32.** UV-vis/NIR oxidative titration of  $[3.3^{\bullet}]^+$  to  $[3.3^{\bullet\bullet}]^{2+}$  by sequential addition of 0.25 eq of  $[\text{FeCp}_2]\text{PF}_6$ . The spectra of pure  $[3.3^{\bullet}]^+$  and  $[3.3^{\bullet\bullet}]^{2+}$  are displayed in black, with intermediate spectra displayed in grey.

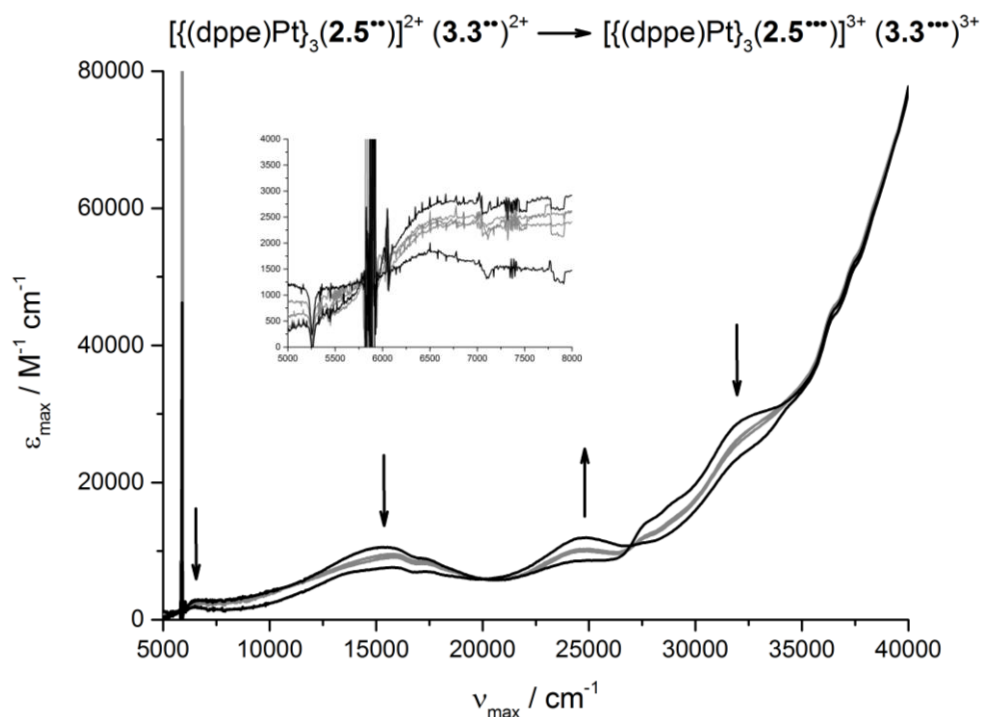


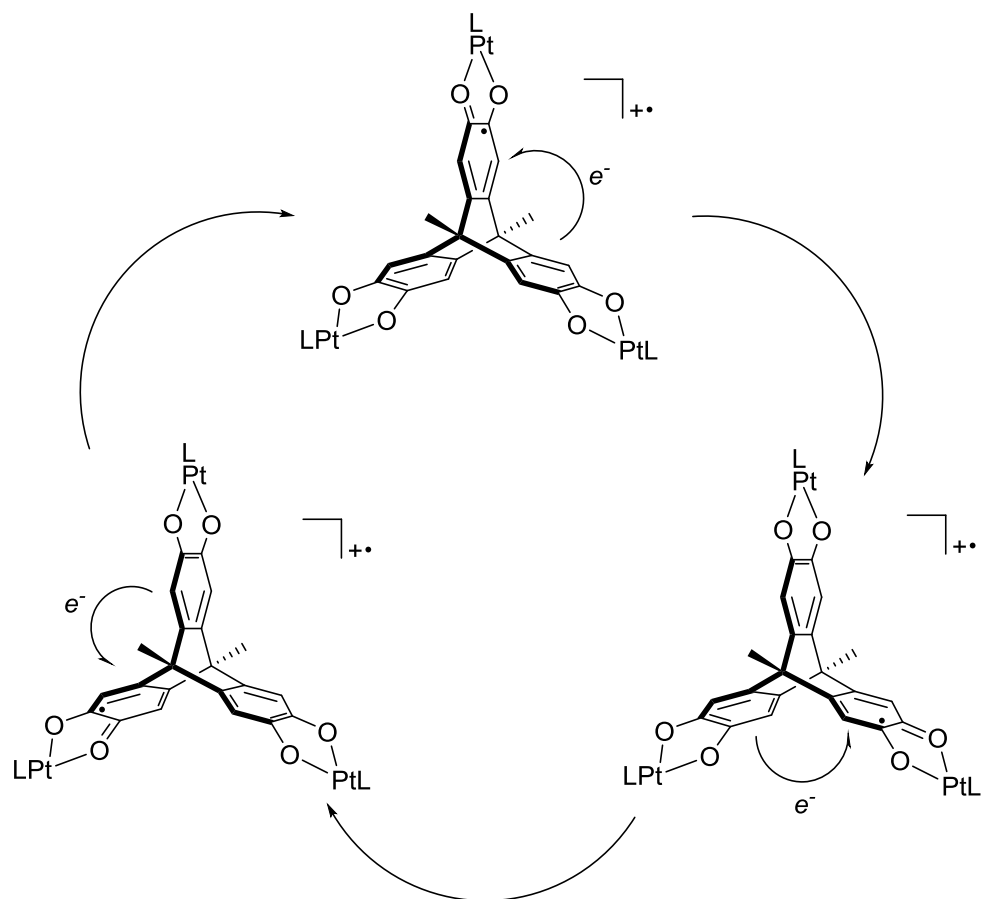
**Figure 3.33.** UV-vis/NIR oxidative titration of  $[3.3^{\bullet\bullet}]^{2+}$  to  $[3.3^{\bullet\bullet\bullet}]^{3+}$  by sequential addition of 0.25 eq of  $[\text{FeCp}_2]\text{PF}_6$ . The spectra of pure  $[3.3^{\bullet\bullet}]^{2+}$  and  $[3.3^{\bullet\bullet\bullet}]^{3+}$  are displayed in black, with intermediate spectra displayed in grey.

---

As the first equivalent  $[\text{FeCp}_2]^+$  is added (**Figure 3.30**), a low energy IVCT grows in at a  $\nu_{\text{max}}$  of  $6725 \text{ cm}^{-1}$ . This IVCT arises due to intramolecular electron transfer from an unoxidised catecholate to the semiquinone. The unpaired electron is therefore delocalised and the dioxolene rings are able to communicate with one another (**Scheme 3.10**). Addition of the first equivalent of  $[\text{FeCp}_2]^+$  proceeds non-isosbesticly, indicating that there is fast decomposition of the radical cation.

As the second equivalent of  $[\text{FeCp}_2]^+$  is added (**Figure 3.31**), the IVCT continues to increase in intensity upon the generation of pure  $[\mathbf{3.3}^{\bullet}]^{2+}$ . The spectra contain isosbestic points, suggesting increased stability.

Upon addition of the third equivalent of  $[\text{FeCp}_2]^+$ , the IVCT reduces in intensity, as would be expected for  $[\mathbf{3.3}^{\bullet}]^{3+}$ , due to the  $(\text{SQ})_3$  form no longer containing any catecholate groups for electron transfer to take place from. The IVCT does not completely disappear, which is likely due to the  $[\mathbf{3.3}^{\bullet}]^{3+}$  state having on a marginally more negative oxidation potential vs  $[\text{FeCp}_2]\text{PF}_6$ . Interestingly, this final transition proceeds isosbesticly.



**Scheme 3.10.** Representation of the electronic delocalisation in  $[3.1\cdot]^+$  and  $[3.2\cdot]^+$ .

An estimation of the degree of electron delocalisation can be obtained by the same method described above. Noting that the IVCT for  $[3.3^{2+}]^{2+}$  has a  $\Delta\nu_{1/2}$  of  $1306\text{ cm}^{-1}$ , and that **Equation 1.4** predicts a  $\Delta\nu_{1/2}$  of  $3941\text{ cm}^{-1}$  for an IVCT with a  $\nu_{\text{max}}$  of  $6725\text{ cm}^{-1}$ , it can be concluded that the valent electron in  $[3.2\cdot]^+$  is more delocalised than a strictly class II system, placing it towards the class II/III border. By applying **Equation 3.5** to the IVCT in the spectrum of  $[3.2\cdot]^+$ , a coupling energy in the class III limit of  $653\text{ cm}^{-1}$  is obtained.

The remaining higher energy absorptions are phosphine based, with the peak at  $14837\text{ cm}^{-1}$  being assigned to a  $\text{Pt} \rightarrow \text{SQ MLCT}$ , and the peak at  $31947\text{ cm}^{-1}$  corresponding to phosphine interligand charge absorptions.

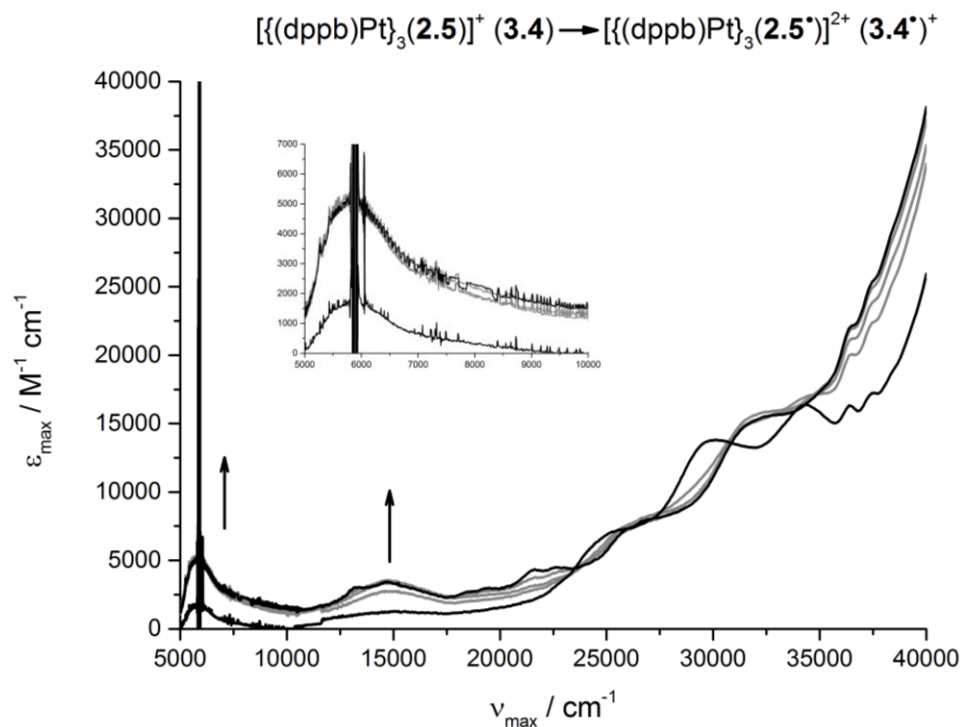


**Figure 3.34.** UV-vis/NIR oxidative titration of **3.4** to **[3.4']<sup>+</sup>** by sequential addition of 0.25 eq of  $[\text{FeCp}_2]\text{PF}_6$ . The spectra of pure **3.4** and **[3.4']<sup>+</sup>** are displayed in black, with intermediate spectra displayed in grey.

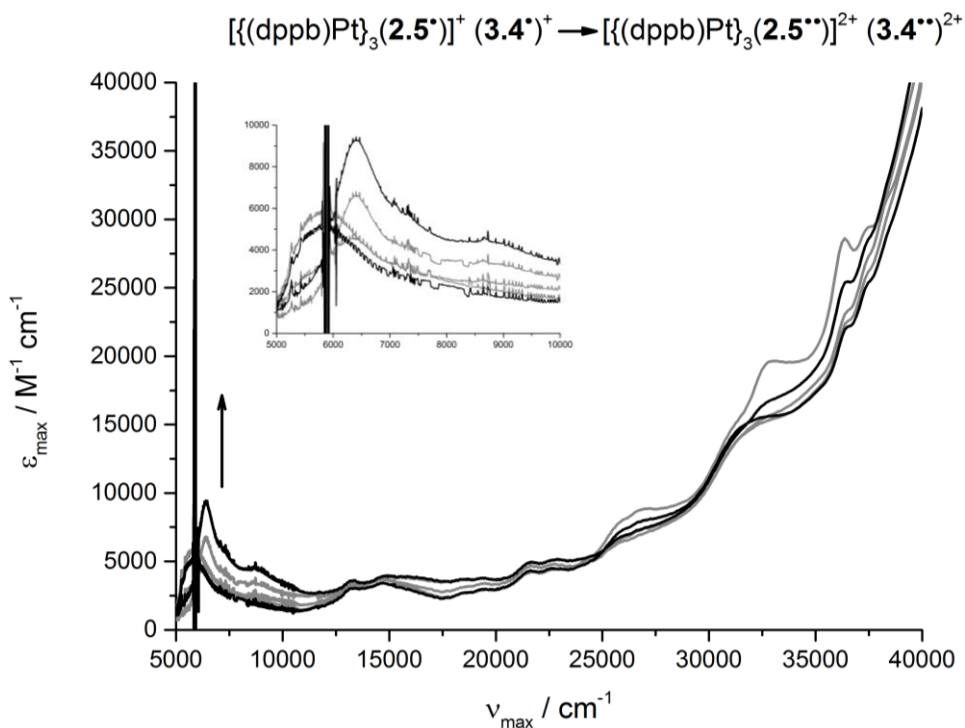


**Figure 3.35.** UV-vis/NIR oxidative titration of **[3.4']<sup>+</sup>** to **[3.4'']<sup>2+</sup>** by sequential addition of 0.25 eq of  $[\text{FeCp}_2]\text{PF}_6$ . The spectra of pure **[3.4']<sup>+</sup>** and **[3.4'']<sup>2+</sup>** are displayed in black, with intermediate spectra displayed in grey.

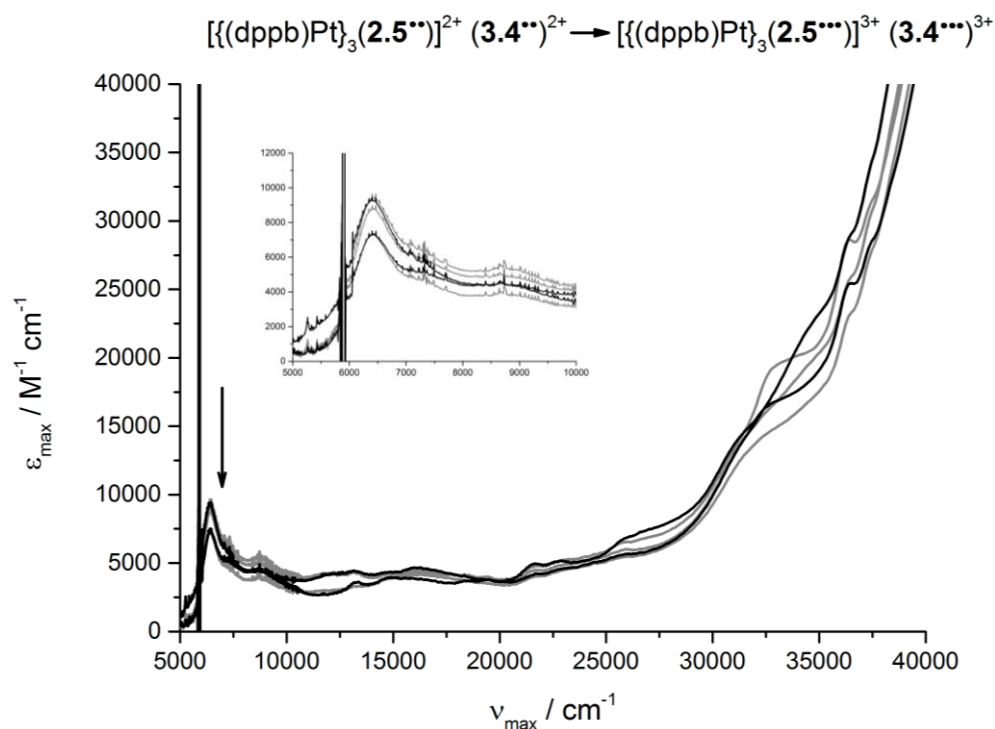


**Figure 3.36.** UV-vis/NIR oxidative titration of  $[\mathbf{3.4}^{\bullet\bullet}]^{2+}$  to  $[\mathbf{3.4}^{\bullet\bullet\bullet}]^{3+}$  by sequential addition of 0.25 eq of  $[\text{FeCp}_2]\text{PF}_6$ . The spectra of pure  $[\mathbf{3.4}^{\bullet\bullet}]^{2+}$  and  $[\mathbf{3.4}^{\bullet\bullet\bullet}]^{3+}$  are displayed in black, with intermediate spectra displayed in grey.

As the first equivalent  $[\text{FeCp}_2]^+$  is added to **3.4** (**Figure 3.34**), a low energy IVCT grows in at a  $\nu_{\text{max}}$  of  $5790 \text{ cm}^{-1}$ . There is a low intensity residual peak at this wavelength prior to any oxidant being added, because of the presence of a small amount of  $[\mathbf{3.4}^{\bullet}]^+$  due to aerial oxidation. Addition of the first equivalent of oxidant proceeds non-isosbesticly, indicating that there is decomposition of the radical cation.

As the second equivalent of oxidant is added (**Figure 3.35**), the IVCT continues to grow, and is blueshifted by  $650 \text{ cm}^{-1}$  to a  $\nu_{\text{max}}$  of  $6410 \text{ cm}^{-1}$ . The IVCT also grows in a shoulder at  $8700 \text{ cm}^{-1}$ . As the third equivalent of oxidant is added (**Figure 3.36**) the intensity of the IVCT decreases, which is consistent with the SQ/SQ/SQ form being generated and thus leaving no remaining catechol groups for the valent electron to transfer to. The IVCT does not completely vanish however, indicating that some  $[\mathbf{3.4}^{\bullet\bullet}]^{2+}$  remains in solution. One explanation for this is that the oxidation potential for the reaction  $[\mathbf{3.4}^{\bullet\bullet}]^{2+} \rightarrow [\mathbf{3.4}^{\bullet\bullet\bullet}]^{3+}$  is close to 0 V vs  $[\text{Fc}] / [\text{Fc}]^+$ , therefore stronger oxidant may be required for full conversion to the  $[\mathbf{3.4}^{\bullet\bullet\bullet}]^{3+}$  state.

---

Using **Equation 3.4**, a class II system would be predicted to have a  $\Delta v_{1/2}$  of  $3657\text{ cm}^{-1}$ , whereas experimentally the value is  $2380\text{ cm}^{-1}$ . Therefore, as with complexes **3.1-3.3**, this complex has a larger amount of electron delocalisation and is closer to the class II/III border. **Equation 3.5** gives an electron coupling energy in the class III limit of  $1090\text{ cm}^{-1}$ .

The remaining higher energy absorptions are phosphine based, with the peak at  $14,800\text{ cm}^{-1}$  being assigned to a Pt  $\rightarrow$  SQ MLCT, and the peak at  $30,000\text{ cm}^{-1}$  corresponding to a phosphine interligand charge absorption.

#### 3.2.2.5 Spectroelectrochemical Analysis of **3.4**

As discussed previously, the UV-vis/NIR oxidation titrations of **3.4** with  $[\text{FeCp}_2]\text{PF}_6$  did not produce isosbestic points. Therefore, as with complex **3.1**, spectroelectrochemical oxidation was attempted using an optically transparent electrode (OTTLE) cell containing a solution of **3.4** and  $0.1\text{ M } n\text{Bu}_4\text{NPF}_6$  in  $\text{CH}_2\text{Cl}_2$  at  $298\text{ K}$ . By observing the oxidation potentials elucidated by the CV measurements, it is possible to electrochemically generate  $[\mathbf{3.4}^+]^+$ , as shown in **Figure 3.40**.

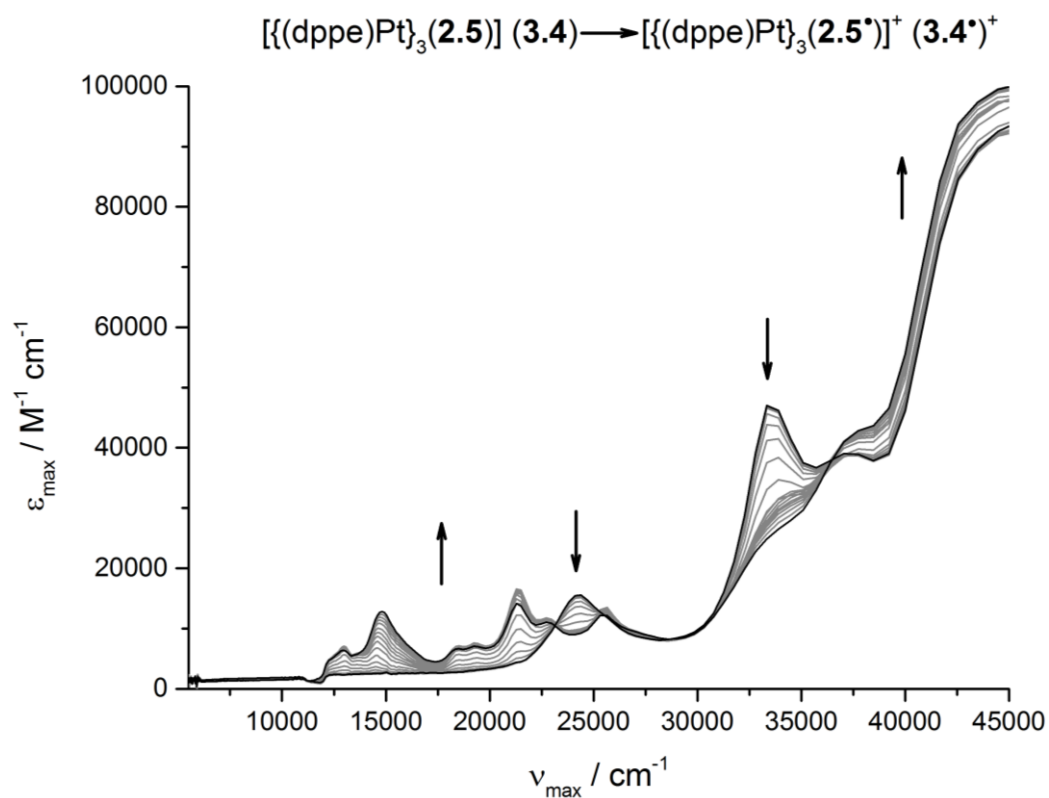


**Figure 3.40.** UV-vis/NIR spectroelectrochemical data for the first oxidation of a **3.4** to **[3.4']<sup>+</sup>** in a 0.1 M <sup>n</sup>Bu<sub>4</sub>NPF<sub>6</sub> solution in CH<sub>2</sub>Cl<sub>2</sub> at 298 K. The spectra of pure **3.4** and **[3.4']<sup>+</sup>** are displayed in black, with intermediate spectra displayed in grey.

Unexpectedly, the spectrum of pure **[3.4']<sup>+</sup>** does not show the appearance of an IVCT as was observed in the chemical titrations. Despite this, the other higher energy peaks are retained with good isosbesticity. The lack of IVCT may be attributed to the fact that the solution contains a high concentration of <sup>n</sup>Bu<sub>4</sub>NPF<sub>6</sub> electrolyte unlike the oxidative titrations, and these charged species in solution may be leading to a loss of intramolecular electron transfer. The inability to observe any IVCT in the SEC proved to be a consistent problem with several of the other complexes.

### 3.2.2.6 EPR Measurements of Chemically Oxidised Mixed-Valent Radical Cations of 3.3 and 3.4

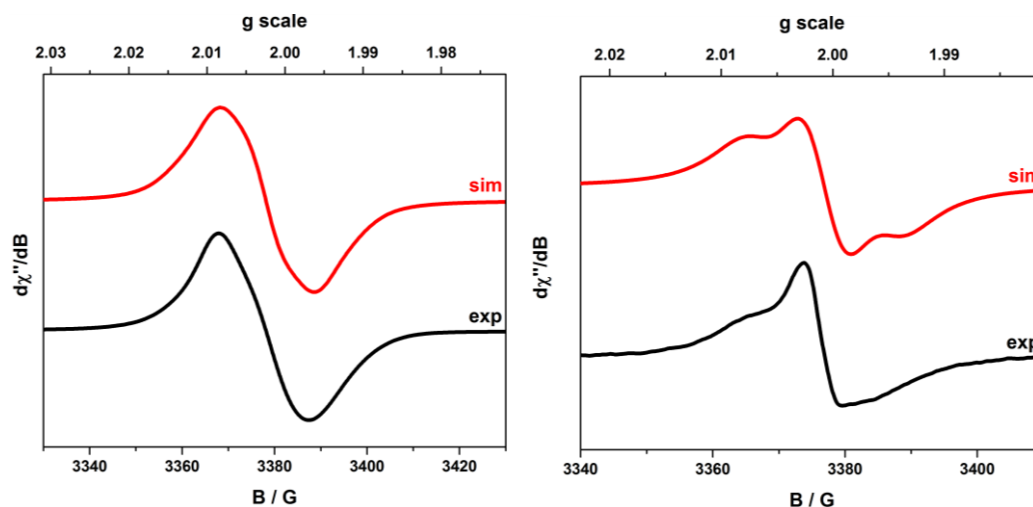


**Figure 3.37.** X-band EPR spectra of  $[(dppe)Pt]_3(2.5)^+ [3.3]^+$  in  $CH_2Cl_2$  at (top) 300 K (top) and (bottom) 140 K (frozen solution). Experimental data displayed in black, simulation displayed in red.

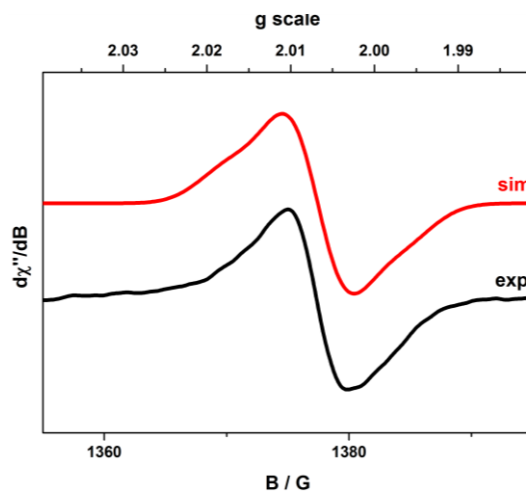


**Figure 3.38.** S-band EPR spectra of  $[(dppe)Pt]_3(2.5)^+ [3.3]^+$  in  $CH_2Cl_2$  at 45 K (frozen solution). Experimental data displayed in black, simulation displayed in red.

The X band spectrum of  $[3.3]^+$  obtained at 300 K shows  $g = 2.0045$  and  $A(^{195}Pt) = 45 \times 10^{-4} \text{ cm}^{-1}$  and  $A(^{195}P) = 20 \times 10^{-4} \text{ cm}^{-1}$  (**Figure 3.37**). An S band spectrum at 300 K was not able to be collected. Upon cooling to 140 K, the X band spectrum showed rhombic signal with hyperfine coupling to  $^{195}Pt$  but no  $^{31}P$  coupling. A weak rhombic signal was able to be obtained on the S band by cooling the sample to 45 K (**Figure 3.38**).

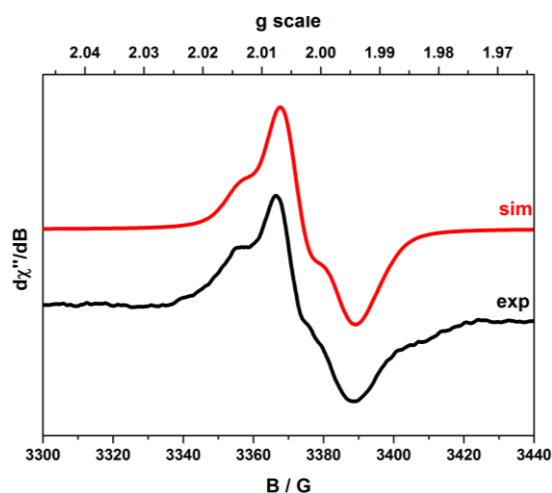


**Figure 3.39.** X-band EPR spectra of  $[(\text{dppbPt})_3(\mathbf{2.5})]^+ [\mathbf{3.4}]^+$  in  $\text{CH}_2\text{Cl}_2$  at 150 K (frozen solution). Experimental data displayed in black, simulation displayed in red.

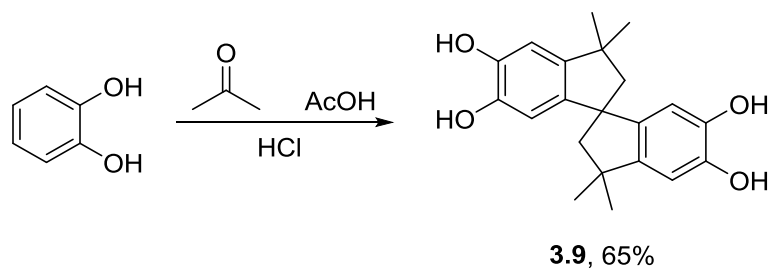
The X band spectrum of  $[\mathbf{3.4}]^+$  obtained at 150 K shows that  $g = 2.0047$ , and the hyperfine coupling to  $^{195}\text{Pt}$  is  $A(^{195}\text{P}) = 32 \times 10^{-4} \text{ cm}^{-1}$  (**Figure 3.39**). No 300 K measurements were able to be obtained, and it was found that the S band measurements also did not produce a signal at any temperature.

EPR characterisation of both **3.3** and **3.4** was hindered due to rapid precipitation and bleaching upon addition of the  $[\text{FeCp}_2]\text{PF}_6$ .

### 3.2.3 $[(\text{dppePt})_2(\mathbf{3.9})]$ and $[(\text{dppbPt})_2(\mathbf{3.9})]$

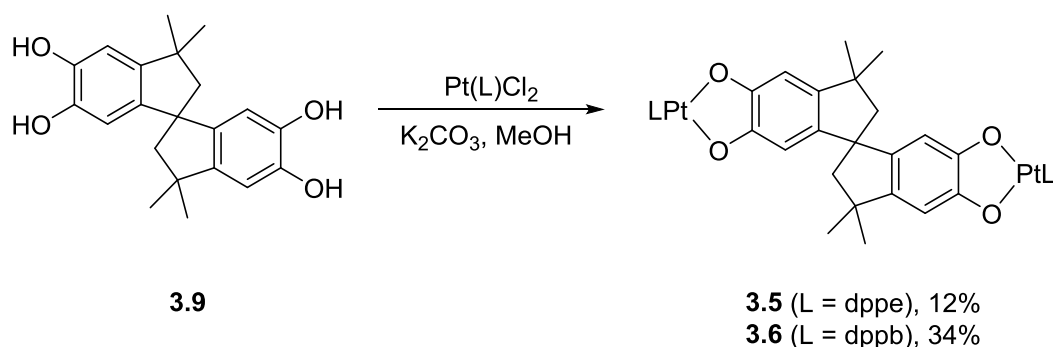
#### 3.2.3.1 Synthesis of Complexes **3.5** and **3.6**.

In addition to triptycene derivatives, another bis(catechol) ligand of interest is the spiroconjugated ligand **3.9**. While not structurally related to triptycene, it is an attractive target for similar reasons such as a  $90^\circ$  angle between the catechol rings, short dioxolene-dioxolene distance, and ease of synthesis. This ligand was synthesised from catechol and acetone in good yield without the need for protecting groups (**Scheme 3.11**).



**Scheme 3.11.** One-step synthesis of a spirobis(Cat) ligand **3.9**.

Complexes containing the ligand **3.9** have also been synthesised and characterised by  $^1\text{H}$  NMR and HRMS using the same conditions as **3.1-3.4** (Scheme 3.12).



**Scheme 3.12.** Complexation of **3.9** with **3.7** or **3.8** to form the dinuclear complexes **3.5** and **3.6**.

The  $^1\text{H}$  NMR spectrum of **3.5** displays many of the same characteristics of the previous complexes (Figure 3.41).

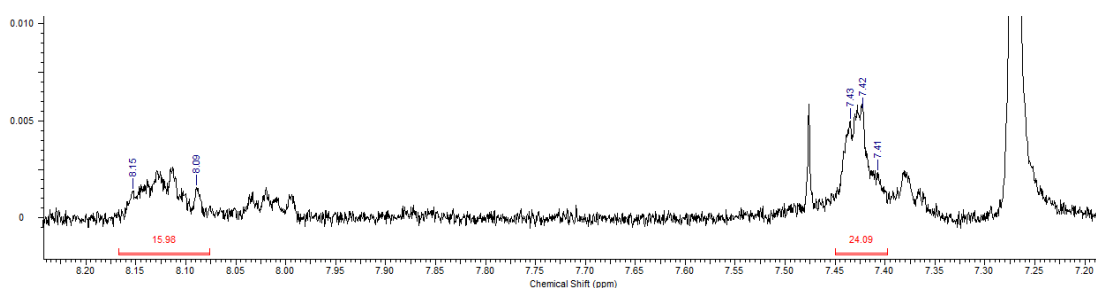


**Figure 3.41.** Interpreted  $^1\text{H}$  NMR (500 MHz,  $\text{CDCl}_3$ ) spectrum of **3.5** showing the multiple aromatic resonances and their splitting patterns. The peak at  $\delta = 7.26$  ppm belongs to  $\text{CHCl}_3$ .

The peaks between 8.15-8.09 ppm correspond to 16 protons located at the *ortho* position of the dppe phenyl rings, and the peaks at 7.43-7.41 ppm correspond to the

24 protons located at the *para* and *meta* positions. Exposure of **3.5** or **3.6** to air causes broadening of the aromatic peaks in the  $^1\text{H}$  NMR spectrum.

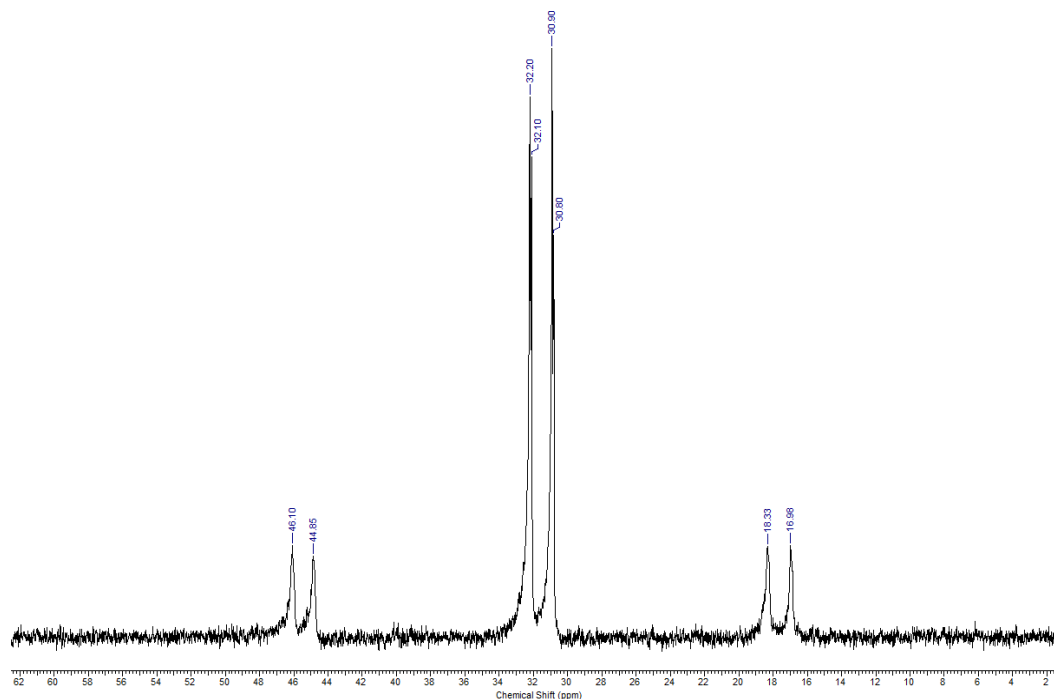


**Figure 3.42.**  $^{31}\text{P}\{^1\text{H}\}$  NMR (300 MHz,  $\text{CDCl}_3$ ) spectrum of **3.5**, showing  $^{195}\text{Pt}$  satellites.

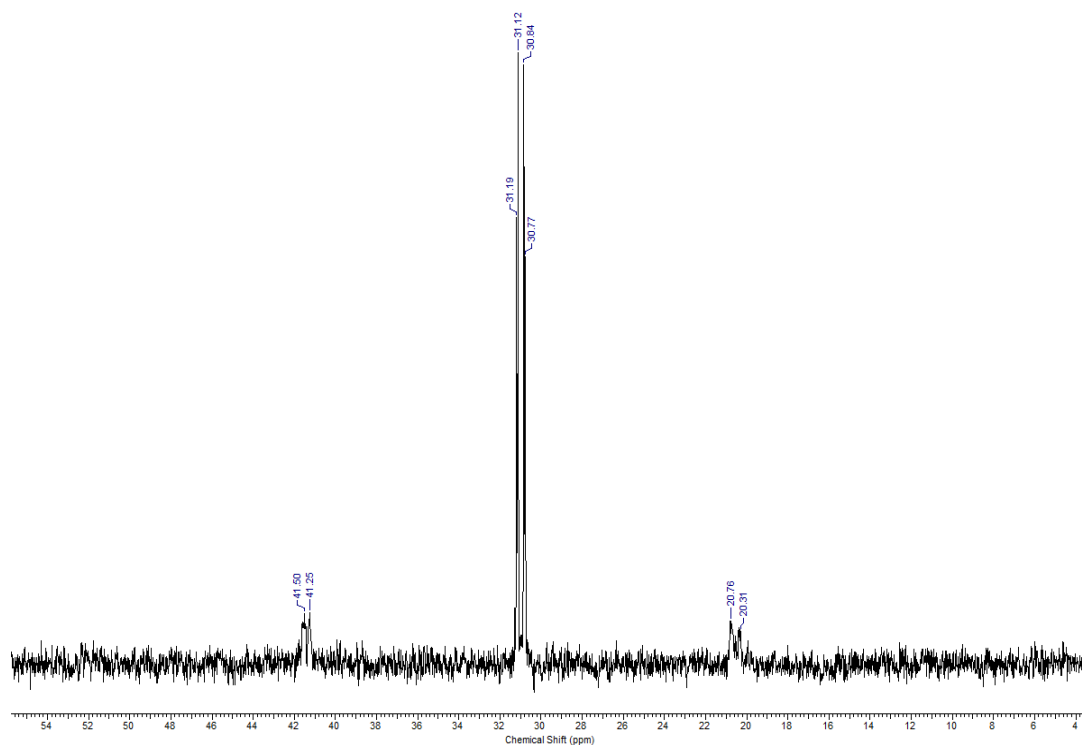


**Figure 3.43.**  $^{31}\text{P}\{^1\text{H}\}$  NMR (300 MHz,  $\text{CDCl}_3$ ) spectrum of **3.6**, showing  $^{195}\text{Pt}$  satellites.

The  $^{31}\text{P}\{^1\text{H}\}$  NMR spectra of **3.5** and **3.6** show two peaks at 30.6 and 32.2 ppm for **3.5** (Figure 3.42) and 30.77 and 31.19 ppm for **3.6** (Figure 3.43). Both spectra contain platinum satellite peaks with a coupling constant of 1692.37 and 1687.82 Hz respectively due to the coupling of the  $^{31}\text{P}$  nuclei to a  $^{195}\text{Pt}$  ( $S = 1/2$ ) nucleus.<sup>[3]</sup>

The high resolution mass spectra for **3.5** and **3.6** have good agreement with the simulated isotopic distribution expected for the molecular ions  $[\text{C}_{73}\text{H}_{68}\text{O}_4\text{P}_4\text{Pt}_2]^+$  (1522.34 g mol $^{-1}$ ) and  $[\text{C}_{81}\text{H}_{68}\text{O}_4\text{P}_4\text{Pt}_2]^+$  (1618.34 g mol $^{-1}$ ) respectively (Figures 3.44 and 3.45). For both spectra, a second smaller set of peaks corresponding to  $[(\mathbf{3.5})_2(\text{H})]^{2+}$  and  $[(\mathbf{3.6})_2(\text{H})]^{2+}$  are also observed.

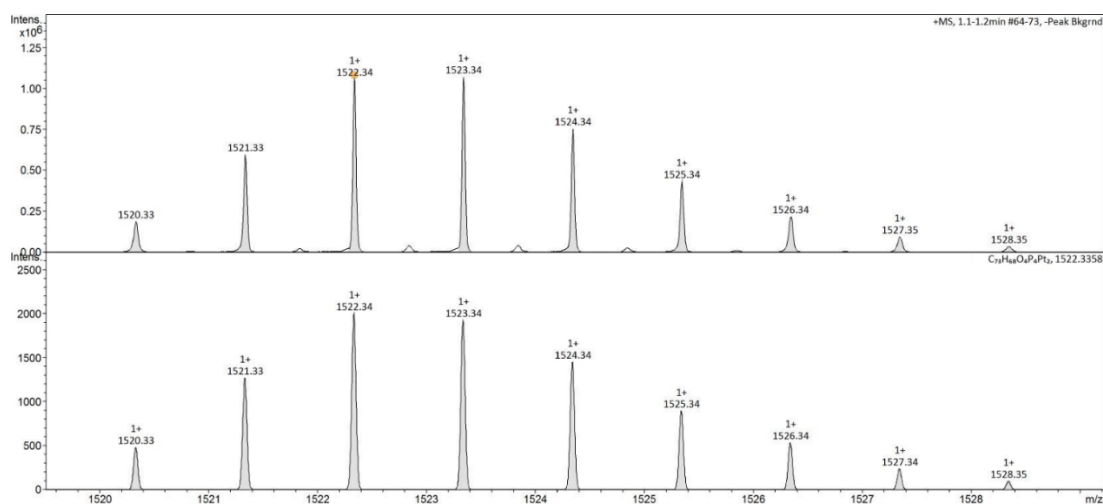


**Figure 3.44.** Experimental (top) and simulated (bottom) molecular ion of **3.5**. There is good agreement between the spectrum and simulation, with the characteristic isotopic distribution for a complex containing two Pt ions.

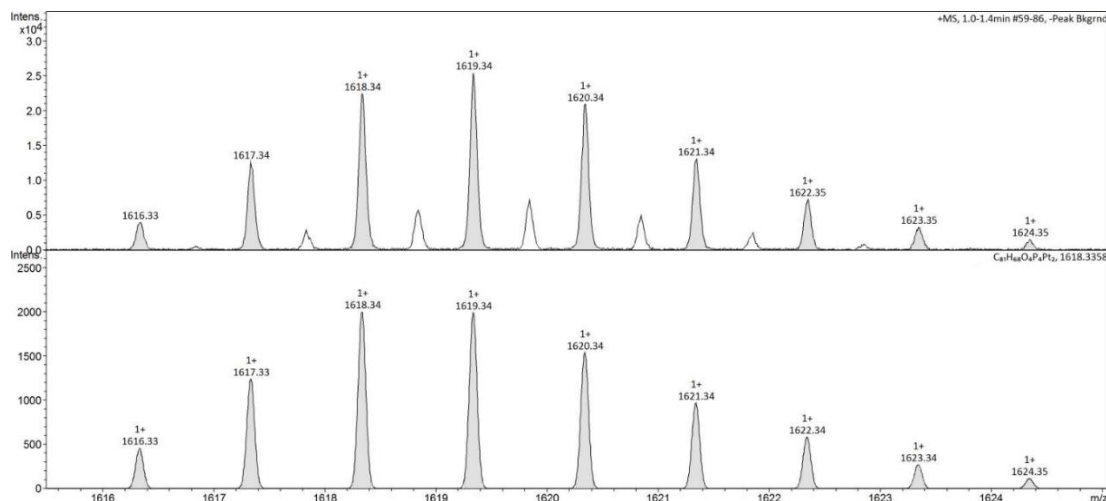


**Figure 3.45.** Experimental (top) and simulated (bottom) molecular ion of **3.6**. There is good agreement between the spectrum and simulation, with the characteristic isotopic distribution for a complex containing two Pt ions.

### 3.2.3.2 X-ray Crystal Structure Refinement of **3.6**

The air sensitivity of **3.6** made obtaining a suitable monocrystalline sample challenging, as crystallinity is lost very rapidly after removal of the crystal from the mother liquor. Complex **3.6** was crystallised as yellow plates by vapour diffusion of pentane into dichloromethane. The structure of **3.2** was solved in the triclinic space group  $P\bar{1}$  using the *Olex2* program (**Figure 3.46**).

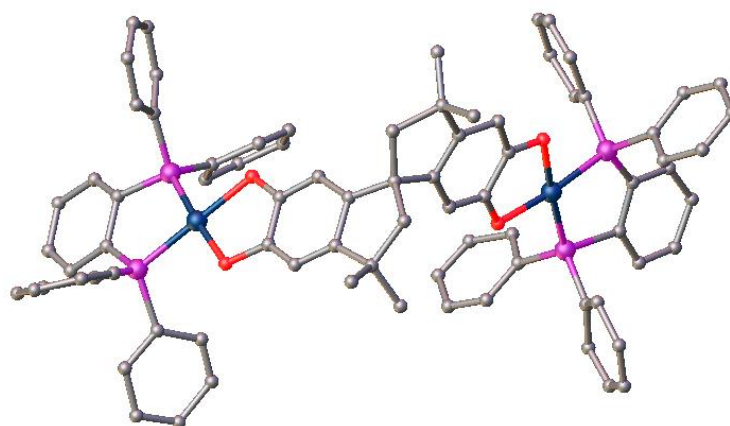


**Figure 3.46.** Single crystal X-ray structure of a single molecule of **3.6**, showing the desired structural features have been maintained after complexation.

The desired structural features are shown to be preserved in the complex, with an average Pt-Pt distance of 10.09 Å. Using the **Equations 3.1-3.3** for complex **3.6** gives

---

a value of  $\Delta = -1.89$ , indicating that the complex is in the Cat/Cat form in this crystal structure.

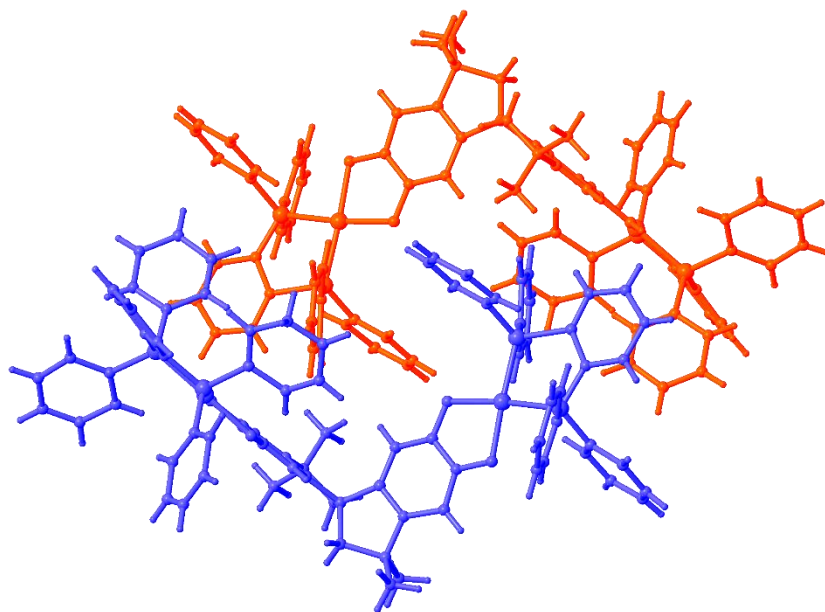


**Figure 3.47.** Crystal packing of **3.6**.

The bulk crystal packing consists of a staircase shaped motif with coplanar neighboring dioxolene groups.

### 3.2.3.3 Electrochemical Analysis of Complexes **3.5** and **3.6**

The redox chemistry of complexes **3.5** and **3.6** was investigated by CV and DPV. All experiments were carried out at 298 K in a 0.1 M solution of  $n\text{Bu}_4\text{NPF}_6$  in dry, degassed dichloromethane under argon atmosphere. The analysis (**Figures 3.48-3.51**) showed that both **3.5** and **3.6** contained two chemically reversible one-electron oxidation processes in the  $-0.5 \leq E_{1/2} \leq 0.0$  V (*vs.*  $\text{Fc}/\text{Fc}^+$ ) region, attributed to sequential Cat  $\rightarrow$  SQ transitions as displayed in **Scheme 3.13**. Furthermore, complexes **3.5** and **3.6** also exhibit one two further chemically irreversible oxidation occurring at a higher potential (+0.7 and +1.2 V), which can be assigned to subsequent SQ  $\rightarrow$  BQ transitions, as displayed in **Scheme 3.14**. The shoulder on the fourth oxidation of **3.5** (ca 0.896 V) is likely present due to a daughter product resulting from the decomposition of  $[\mathbf{3.5}]^{4+}$ .

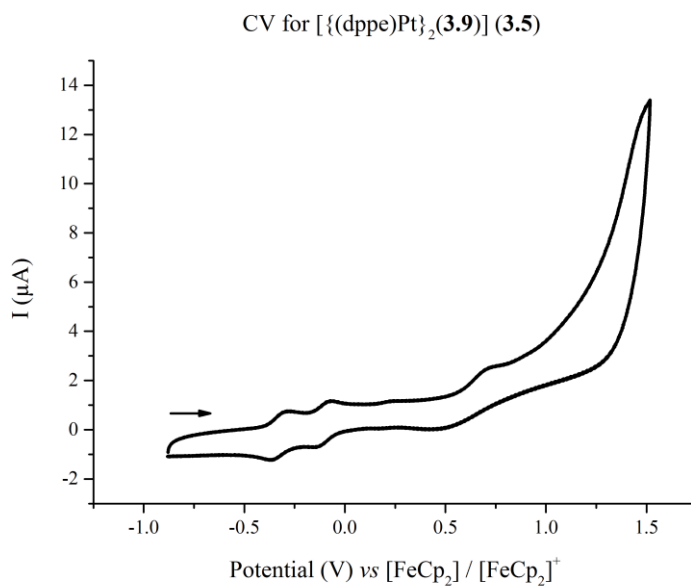


**Figure 3.48.** Cyclic voltammogram of **3.5** in 0.1 M solution of <sup>n</sup>Bu<sub>4</sub>NPF<sub>6</sub> in dry degassed dichloromethane at 298 K. The first two chemically reversible Cat → SQ oxidations are shown, as well as one SQ → BQ oxidation.

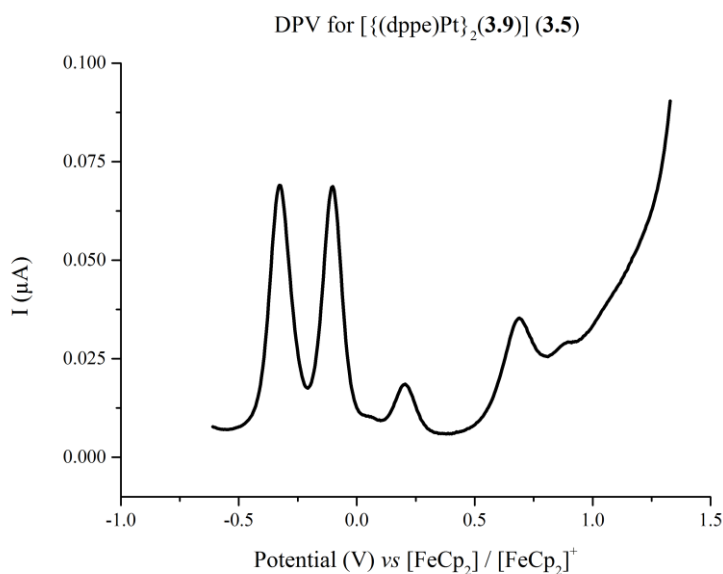


**Figure 3.49.** DPV of **3.5** in 0.1 M solution of <sup>n</sup>Bu<sub>4</sub>NPF<sub>6</sub> in dry degassed dichloromethane at 298 K. The first two chemically reversible Cat → SQ oxidations are shown, as well as two SQ → BQ oxidations.

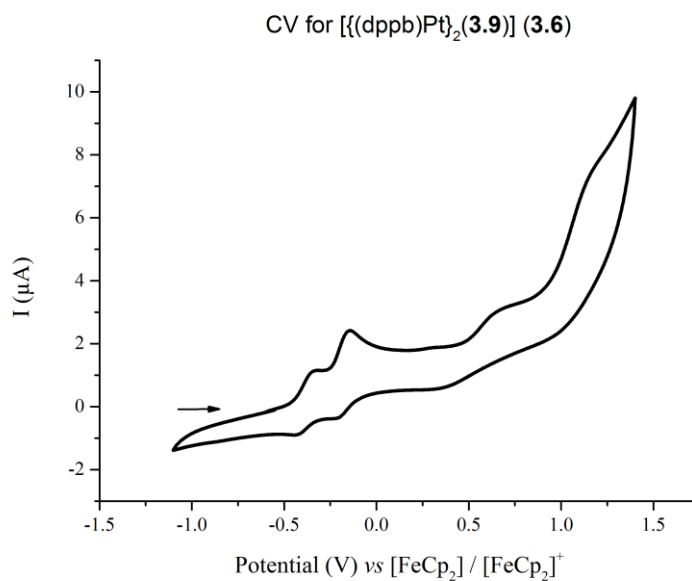


**Figure 3.50.** Cyclic voltammogram of **3.6** in 0.1 M solution of <sup>n</sup>Bu<sub>4</sub>NPF<sub>6</sub> in dry degassed dichloromethane at 298 K. The first two chemically reversible Cat → SQ oxidations are shown, as well as two SQ → BQ oxidations which occur at a more positive potential.

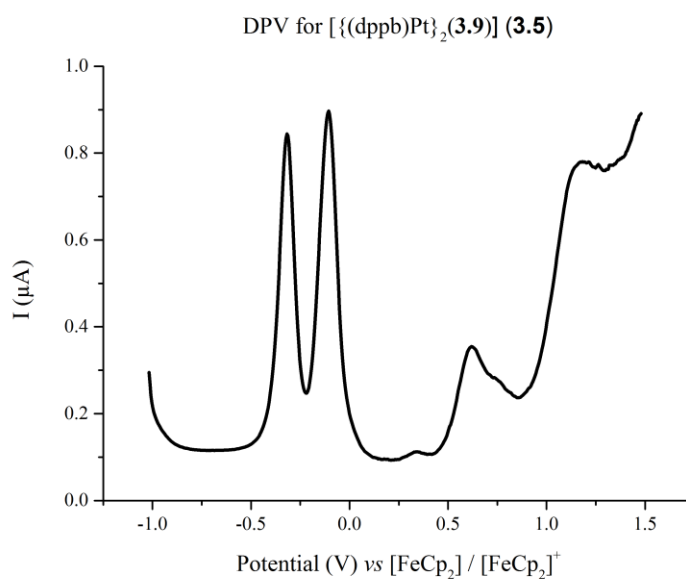


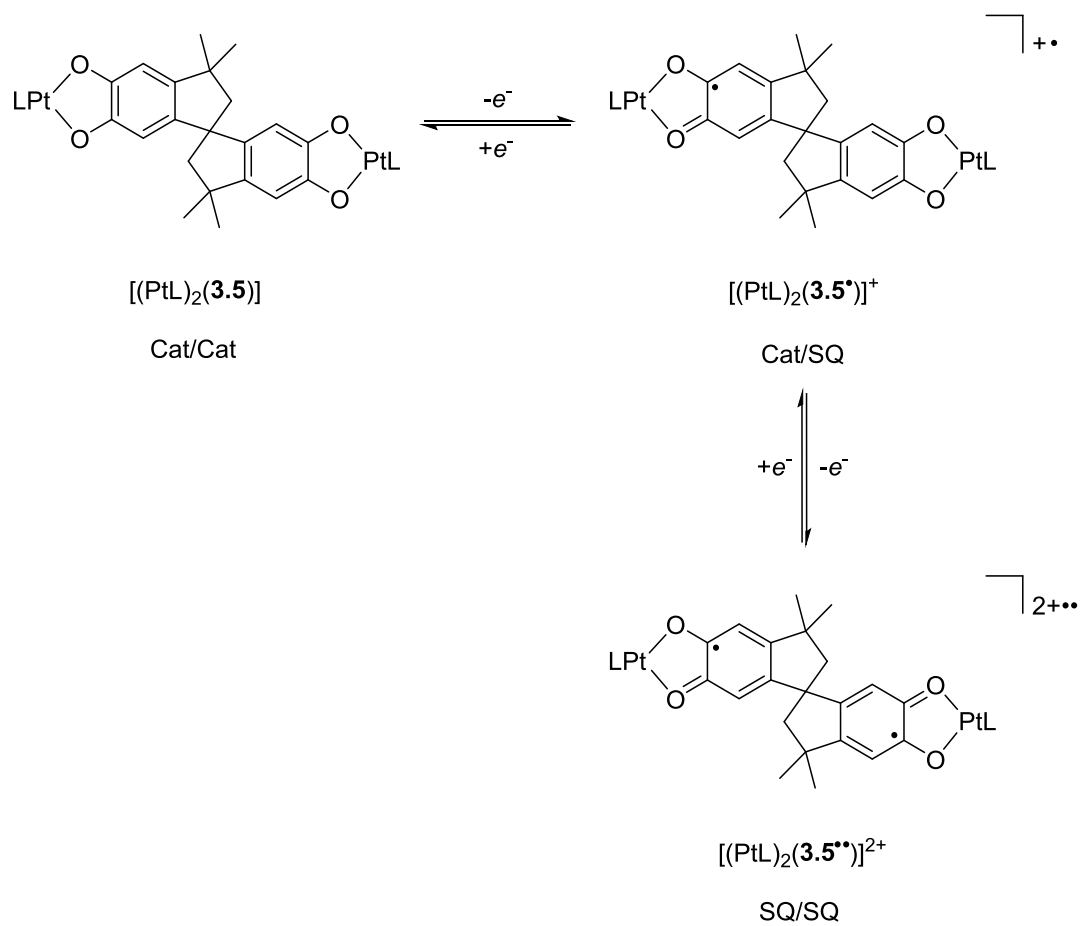
**Figure 3.51.** Differential pulse voltammogram of **3.5** in 0.1 M solution of <sup>n</sup>Bu<sub>4</sub>NPF<sub>6</sub> in dry degassed dichloromethane at 298 K.

**Table 3.5.** Cyclic voltammetric data for complexes **3.1** and **3.2** in 0.1 M solution of  $t\text{Bu}_4\text{NPF}_6$  in dry degassed  $\text{CH}_2\text{Cl}_2$  at 298 K under argon atmosphere. Potentials (V) are referenced to a  $[\text{FeCp}_2] / [\text{FeCp}_2]^+$  internal standard, measured at a scan rate of  $0.1 \text{ V s}^{-1}$ .

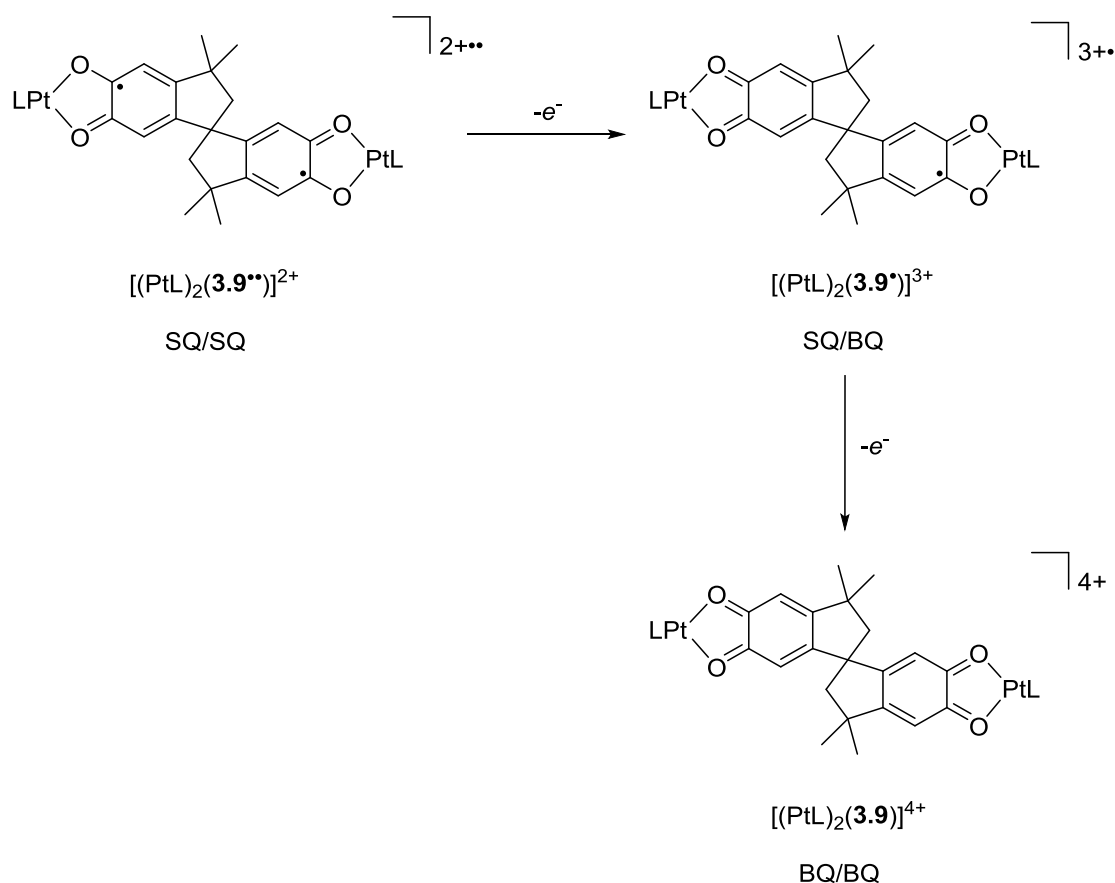
Peak	$E_{1/2}(\mathbf{3.5})$	$E_{1/2}(\mathbf{3.6})$
$E_{1/2} \text{ Cat/Cat} \rightarrow \text{Cat/SQ}$	-0.330	-0.383
$E_{1/2} \text{ Cat/SQ} \rightarrow \text{SQ/SQ}$	-0.116	-0.182

**Table 3.6.** Differential pulse voltammetric data for complexes **3.1** and **3.2** in 0.1 M solution of  $t\text{Bu}_4\text{NPF}_6$  in dry degassed  $\text{CH}_2\text{Cl}_2$  at 298 K under argon atmosphere. Potentials (V) are referenced to a  $[\text{FeCp}_2] / [\text{FeCp}_2]^+$  internal standard, measured at a scan rate of  $0.1 \text{ V s}^{-1}$ .

Transition	$E_p(\mathbf{3.5})$	$E_p(\mathbf{3.6})$
$E_{1/2} \text{ Cat/Cat} \rightarrow \text{Cat/SQ}$	-0.328	-0.318
$E_{1/2} \text{ Cat/SQ} \rightarrow \text{SQ/SQ}$	-0.101	-0.106
$E_{1/2} \text{ Cat/Cat} \rightarrow \text{Cat/SQ}$	0.206	0.619
$E_{1/2} \text{ Cat/SQ} \rightarrow \text{SQ/SQ}$	0.689	1.194



**Scheme 3.13.** Ligand based redox series of the observed Cat  $\rightarrow$  SQ transitions for **3.5** and **3.6**.



**Scheme 3.14.** Ligand based redox series of the observed SQ  $\rightarrow$  BQ transitions for **3.5** and **3.6**.

The first two chemically reversible redox processes undergone by **3.5** and **3.6** have peak-to-peak and  $E_{1/2}$  separations of 0.227 and 0.211 V respectively, which is higher than for the [Co-**3.9**-tpa] complexes previously investigated by Boskovic,<sup>[13]</sup> who observed a 0.15 V separation. The  $E_{1/2}$  separations of the SQ  $\rightarrow$  BQ transitions for **3.5** and **3.6** are 0.483 and 0.574 V respectively.

### 3.2.3.4 UV-vis/NIR Oxidative Titrations of **3.5** and **3.6**

As the CV measurements discussed in the previous section showed the Cat  $\rightarrow$  SQ transitions for complexes **3.5** and **3.6** all occurred at an oxidation potential more negative than that of the [FeCp<sub>2</sub>] / [FeCp<sub>2</sub>]<sup>+</sup> couple, it is therefore appropriate to use [FeCp<sub>2</sub>]PF<sub>6</sub> as a chemical oxidant to generate the SQ radicals in solution by titration of stoichiometric amounts of the oxidant. In principle, the *mono*- and *bi*- and radicals should be accessible by the addition of one or two molar equivalents of the oxidant.

Consequently, oxidative titrations of complexes **3.5** and **3.6** in aliquots of 0.25 eq of  $[\text{FeCp}_2]\text{PF}_6$  were carried out in nitrogen-degassed  $\text{CH}_2\text{Cl}_2$  at 298 K, and the UV-vis/NIR spectra of these solutions were recorded immediately after addition of the oxidant (**Figures 3.52** and **3.53**).

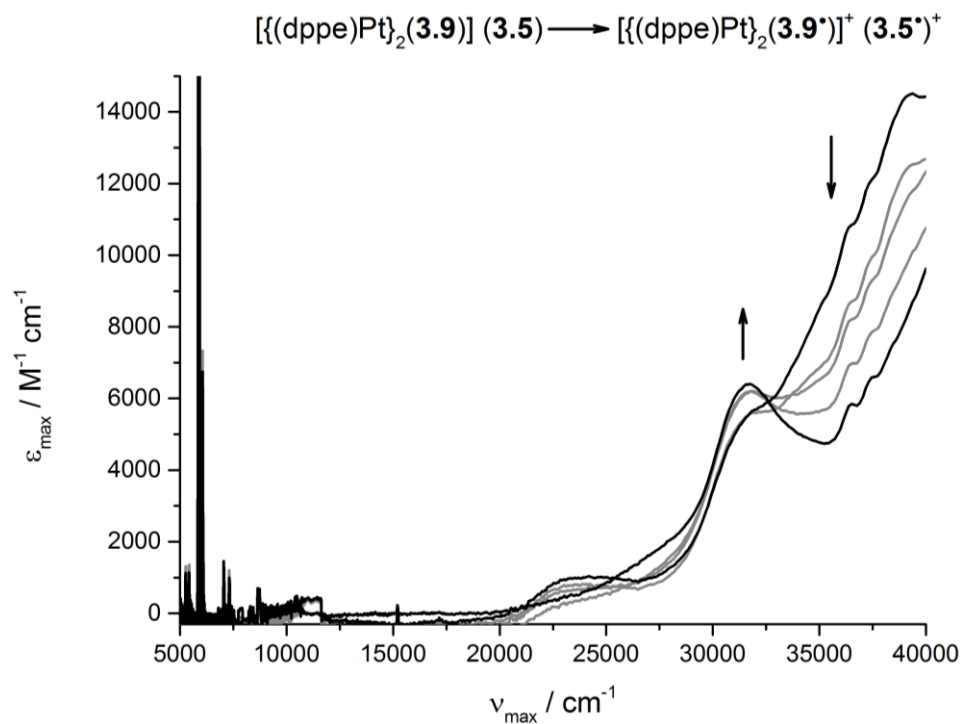


**Figure 3.52.** UV-vis/NIR oxidative titration of **[3.5]** to **[3.5\*]<sup>+</sup>** by sequential addition of 0.25 eq of  $[\text{FeCp}_2]\text{PF}_6$ . The spectra of pure **[3.5]** and **[3.5\*]<sup>+</sup>** are displayed in black, with intermediate spectra displayed in grey.

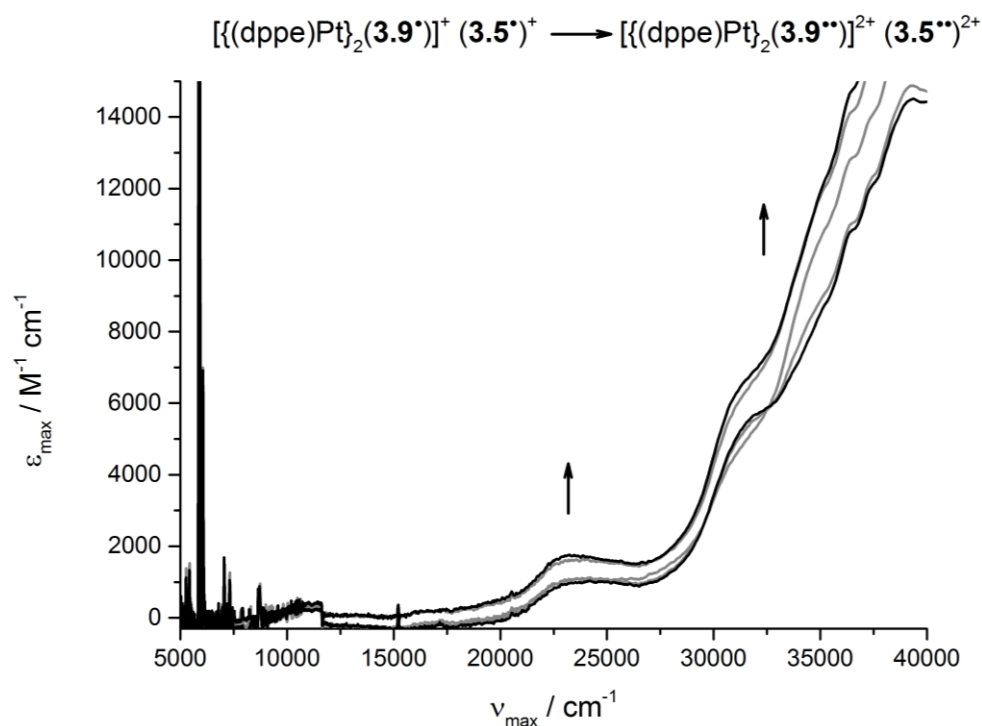


**Figure 3.53.** UV-vis/NIR oxidative titration of  $[3.5^{\bullet}]^+$  to  $[3.5^{\bullet\bullet}]^{2+}$  by sequential addition of 0.25 eq of  $[\text{FeCp}_2]\text{PF}_6$ . The spectra of pure  $[3.5^{\bullet}]^+$  and  $[3.5^{\bullet\bullet}]^{2+}$  are displayed in black, with intermediate spectra displayed in grey.

As the first equivalent  $[\text{FeCp}_2]^+$  is added (**Figure 3.52**), the spectrum undergoes changes however no IVCT peak is present. The complex therefore does not undergo intramolecular electron transfer in the Cat/SQ state, and the radical can be considered fully localised on one dioxolene ring in contrast to complexes **3.1-3.4**. This places **3.5** in the strictly class I category. The spectral changes proceed non-isosbesticly for both oxidations, indicating that there is also fast decomposition of the radical cations  $[3.5^{\bullet}]^+$  and  $[3.5^{\bullet\bullet}]^{2+}$ .

The remaining higher energy absorptions are phosphine based, with the peak at 23,420  $\text{cm}^{-1}$  being assigned to a  $\text{Pt} \rightarrow \text{SQ}$  MLCT, and the peak at 31,746  $\text{cm}^{-1}$  corresponding to phosphine interligand charge absorptions.

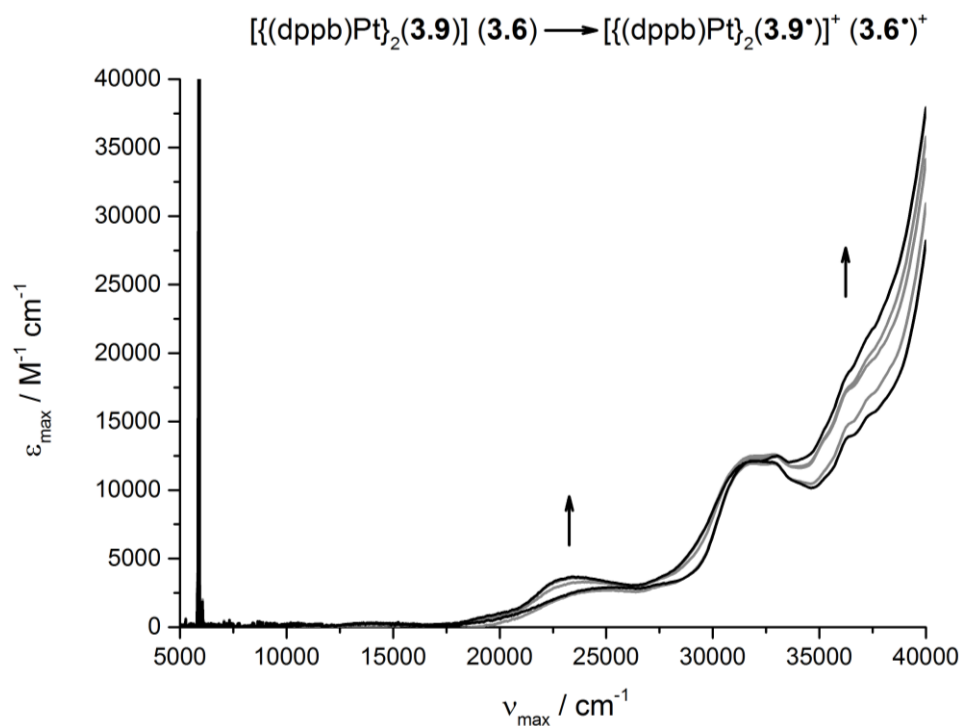


**Figure 3.54.** Oxidative titration  $[\mathbf{3.6}]$  to  $[\mathbf{3.6}^+]$  by sequential addition of 0.25 equivalents of  $[\text{Fc}]\text{PF}_6$ . The spectra of  $[\mathbf{3.6}]$  and  $[\mathbf{3.6}^+]$  are displayed as black lines, with intermediate oxidation displayed as grey lines.

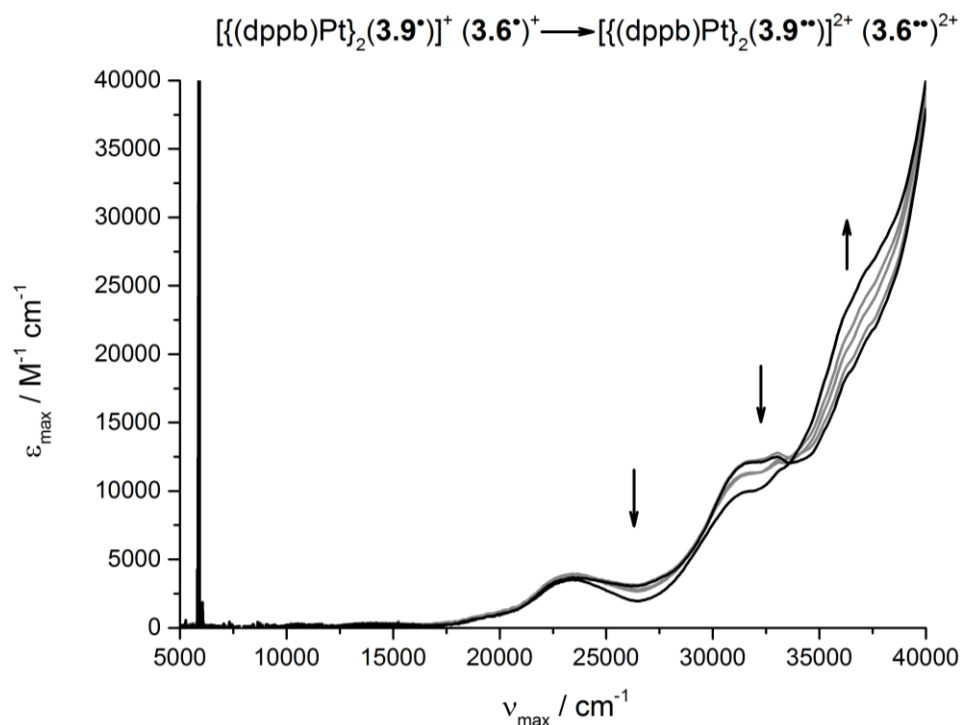


**Figure 3.55.** Oxidative titration of  $[\mathbf{3.6}^+]$  to  $[\mathbf{3.6}^{2+}]$  by sequential addition of 0.25 equivalents of  $[\text{Fc}]\text{PF}_6$ . The spectra of  $[\mathbf{3.6}^+]$  and  $[\mathbf{3.6}^{2+}]$  are displayed as black lines, with intermediate oxidation displayed as grey lines.

The oxidative titrations of **3.6** (Figures 3.54 and 3.55) are comparable to those of **3.5**, with no IVCT peak being present and thus class I behaviour. An isosbestic point is observed upon addition of the second equivalent of oxidant (Figure 3.55), indicating that the biradical is more stable and able to be formed without significant decomposition over the timescale of the experiment. The peak at 23,474  $\text{cm}^{-1}$  corresponds to a Pt  $\rightarrow$  SQ MLCT, and the peak at 31,847  $\text{cm}^{-1}$  corresponds phosphine interligand charge absorptions.

### 3.2.3.5 Spectroelectrochemical Analysis of 3.6

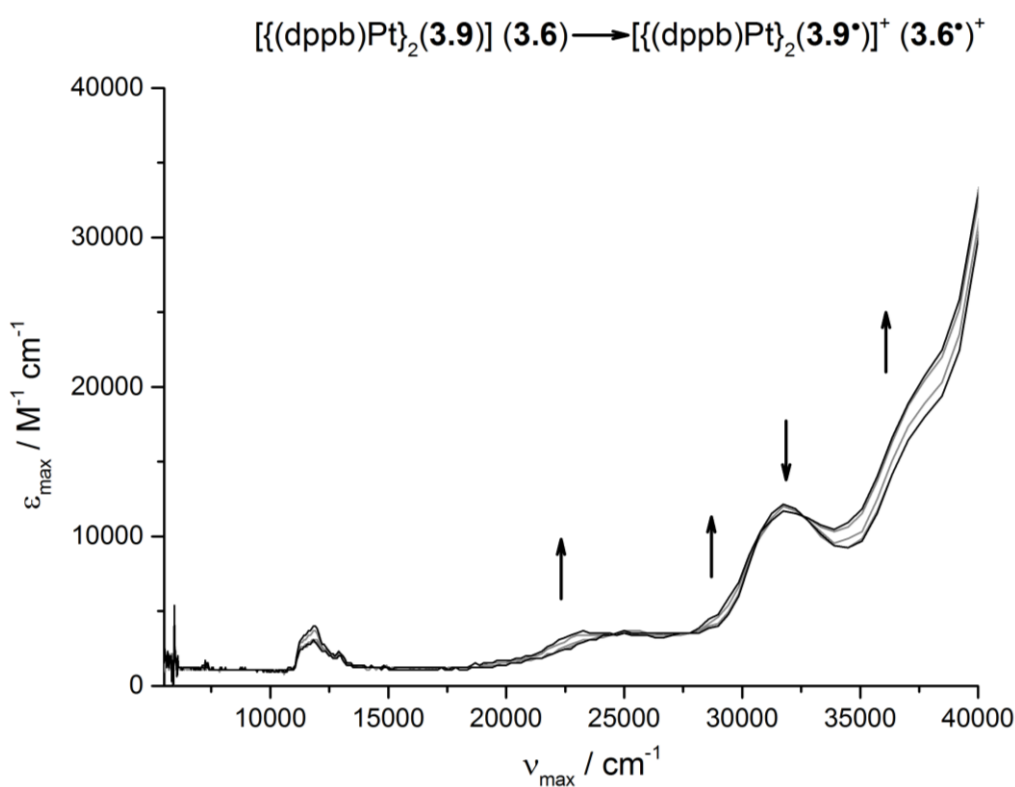


**Figure 3.56.** UV-vis/NIR spectroelectrochemical data for the first oxidation of a **3.6** to  $[\mathbf{3.6}^{\bullet}]^+$  in a 0.1 M  $n\text{Bu}_4\text{NPF}_6$  solution in  $\text{CH}_2\text{Cl}_2$  at 298 K. The spectra of pure **3.6** and  $[\mathbf{3.6}^{\bullet}]^+$  are displayed in black, with intermediate spectra displayed in grey.

The spectrum of  $[\mathbf{3.4}^{\bullet}]^+$  (Figure 5.56) does not show the appearance of an IVCT, which is to be expected. The spectral features are comparable to the UV/vis oxidative titrations, with the same peaks and isosbestic points being present. The peak at ca. 12,000  $\text{cm}^{-1}$  is an artefact resulting from the diffraction grating change.

### 3.2.3.6 EPR Measurements of Chemically Oxidised Mixed-Valent Radical Cations of 3.5 and 3.6

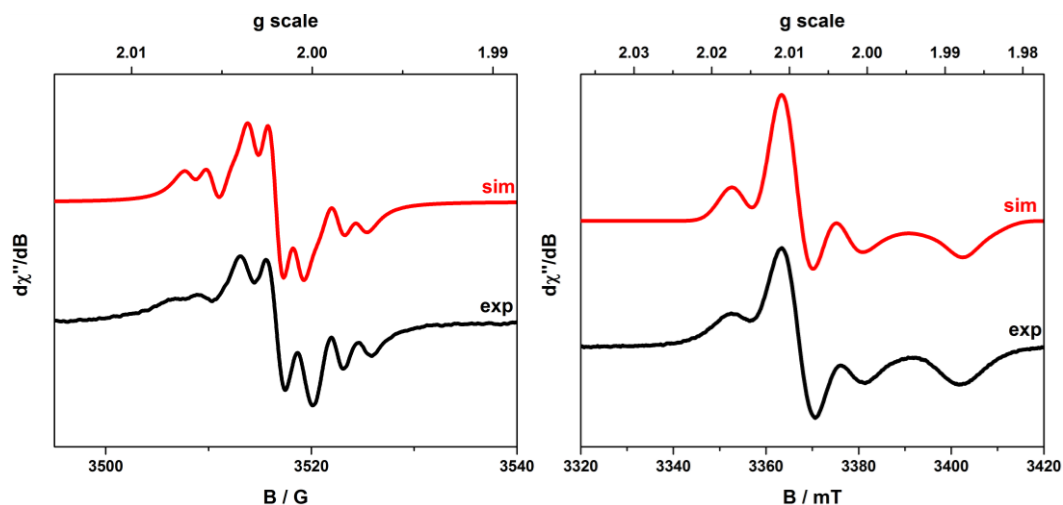


**Figure 3.57.** X-band EPR spectra of  $[(dppe)Pt]_2(3.9)^+ [3.5]^+$  in  $CH_2Cl_2$  at (top) 300 K and (bottom) 150 K (frozen solution). Experimental data displayed in black, simulation displayed in red.

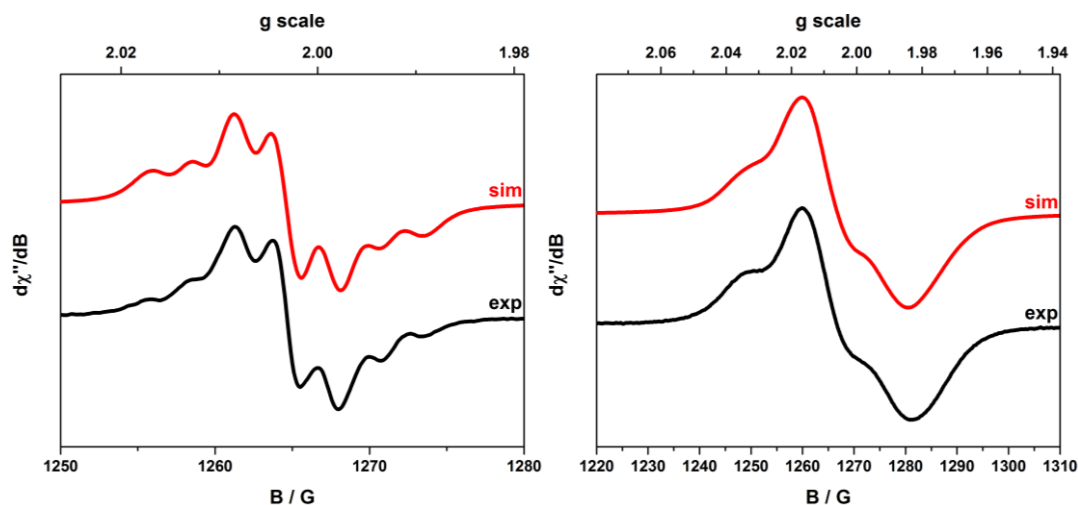


**Figure 3.58.** S-band EPR spectra of  $[(dppe)Pt]_2(3.9)^+ [3.5]^+$  in  $CH_2Cl_2$  at (top) 300 K and (bottom) 100 K (frozen solution). Experimental data displayed in black, simulation displayed in red.

The X and S band spectra of  $[3.5]^+$  obtained at 300 K (Figures 3.57 and 3.58) show a well-defined hyperfine coupling to  $^{195}Pt$ , with  $A(^{195}Pt) = 28 \times 10^{-4} \text{ cm}^{-1}$  and  $A(^{195}P) = 7 \times 10^{-4} \text{ cm}^{-1}$ , with  $g = 2.0018$ . Upon cooling to 100 K, a rhombic spectrum is observed in both the S and X band, with hyperfine coupling to  $^{195}Pt$ , but no  $^{31}P$  coupling.

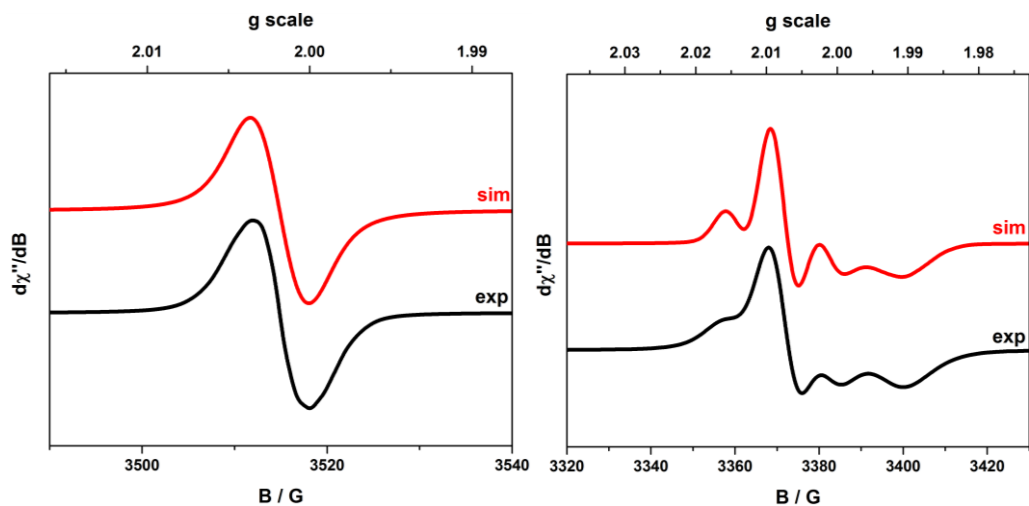


**Figure 3.59.** X-band EPR spectra of  $[\{(\text{dppb})\text{Pt}\}_2(\mathbf{3.9}')\}^+ [\mathbf{3.6}')^+$  in  $\text{CH}_2\text{Cl}_2$  at (top) 300 K and (bottom) 150 K (frozen solution). Experimental data displayed in black, simulation displayed in red.

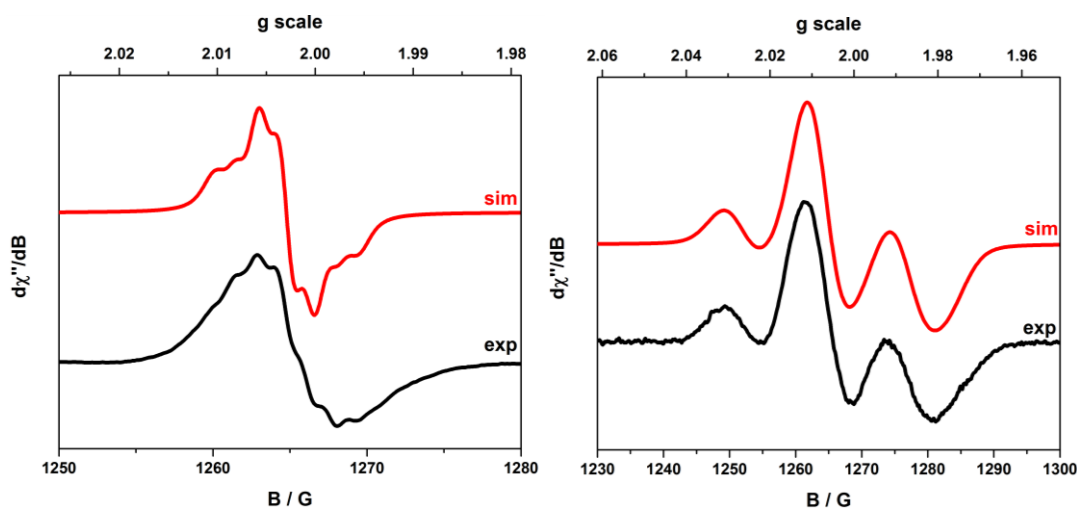


**Figure 3.60.** S-band EPR spectra of  $[\{(\text{dppb})\text{Pt}\}_2(\mathbf{3.9}')\}^+ [\mathbf{3.6}')^+$  in  $\text{CH}_2\text{Cl}_2$  at (top) 300 K and (bottom) 100 K (frozen solution). Experimental data displayed in black, simulation displayed in red.

The X band spectrum of  $[\mathbf{3.6}')^+$  obtained at 300 K shows a normal isotropic lineshape with  $g = 2.0017$  and no discernible hyperfine coupling (**Figure 3.59**). Switching to the S band at this temperature reveals hyperfine coupling to both  $^{195}\text{Pt}$  ( $A(^{195}\text{Pt}) = 20 \times 10^{-4} \text{ cm}^{-1}$ ) and  $^{31}\text{P}$  ( $A(^{31}\text{P}) = 4.5 \times 10^{-4} \text{ cm}^{-1}$ ) albeit with a very broadened signal (**Figure 3.60**). Upon cooling to 100 K, a rhombic spectrum is observed in both the S and X band, with hyperfine coupling to  $^{195}\text{Pt}$ .

### 3.3 Summary, Trends and Conclusions

**Table 3.7.** Cyclic voltammetric data for complexes **3.1-3.6**, showing  $E_{1/2}$  values recorded in 0.1 M solution of  ${}^n\text{Bu}_4\text{NPF}_6$  in dry degassed  $\text{CH}_2\text{Cl}_2$  at 298 K. All measurements were taken at a scan rate of  $0.1 \text{ V s}^{-1}$ , with potentials (V) referenced against the internal  $[\text{FeCp}_2] / [\text{FeCp}_2]^+$  standard.

Peak	$E_{1/2}$ (3.1)	$E_{1/2}$ (3.2)	$E_{1/2}$ (3.3)	$E_{1/2}$ (3.4)	$E_{1/2}$ (3.5)	$E_{1/2}$ (3.6)
1	-0.393	-0.403	-0.151	-0.350	-0.330	-0.383
2	-0.298	-0.118	-0.210	-0.316	-0.116	-0.182
3	-	-	0.115	-0.193	-	-

**Table 3.8.** Differential pulse voltammetric data for complexes **3.1-3.6**, showing  $E_p$  values recorded in 0.1 M solution of  ${}^n\text{Bu}_4\text{NPF}_6$  in dry degassed  $\text{CH}_2\text{Cl}_2$  at 298 K. All measurements were taken at a scan rate of  $0.1 \text{ V s}^{-1}$ , with potentials (V) referenced against the internal  $[\text{FeCp}_2] / [\text{FeCp}_2]^+$  standard.

Region	Peak	$E_p$ (3.1)	$E_p$ (3.2)	$E_p$ (3.3)	$E_p$ (3.4)	$E_p$ (3.5)	$E_p$ (3.6)
Cat – SQ	1	-0.395	-0.383	-0.159	-0.544	-0.328	-0.318
	2	-0.118	-0.111	-0.003	-0.337	-0.101	-0.106
	3	-	-	0.103	-0.232	-	-
SQ - BQ	1	0.647	0.730	0.828	0.181	0.206	0.619
	2	1.141	-	-	0.363	0.689	1.193
	3	-	-	-	0.830	-	-

**Table 3.9.**  $\Delta E_p$  values for the peaks listed in **Table 3.8**.

Complex	Cat / SQ		SQ / BQ	
	[3.1]	0.277	-	0.494
[3.2]	0.272	-	-	-
[3.3]	0.156	0.106	-	-
[3.4]	0.207	0.106	0.181	0.467
[3.5]	0.227	-	0.483	-
[3.6]	0.212	-	0.574	-

**Table 3.10.** UV/vis/NIR data for the different redox states of **3.1-3.6** in CH<sub>2</sub>Cl<sub>2</sub> at 298 K.

Complex	$\nu_{\max}$ ( $10^3 \text{ cm}^{-1}$ ) ( $\epsilon_{\max}$ ( $10^3 \text{ M}^{-1} \text{ cm}^{-1}$ ))
<b>3.1</b>	37.4 (11.2), 36.6 (10.6), 33.3 (7.5), 27.4 (2.1), 14.6 (0.3), 5.3 (0.2)
[ <b>3.1</b> ] <sup>+</sup>	37.4 (17.7), 36.5 (16.4), 33.3 (10.6), 14.5 (1.3), 5.3 (1.3)
[ <b>3.1</b> ] <sup>2+</sup>	27.7 (4.6), 5.3 (0.4)
<b>3.2</b>	37.4 (34.2), 36.3 (27.3), 30.4 (32.0), 24.2 (7.2), 14.3 (1.1), 5.6 (1.6)
[ <b>3.2</b> ] <sup>+</sup>	37.3 (40.9), 36.4 (33.3), 31.5 (23.2), 14.3 (2.7), 5.6 (5.2)
[ <b>3.2</b> ] <sup>2+</sup>	31.5 (23.2), 14.2 (1.8), 5.7 (9.0)
<b>3.3</b>	37.6 (40.9), 36.6 (36.8), 31.6 (31.6), 27.9 (16.3), 14.7 (14.6)
[ <b>3.3</b> ] <sup>+</sup>	37.6 (48.1), 36.6 (24.5), 32.2 (31.2), 27.9 (16.0), 15.0 (13.2), 6.7 (1.8)
[ <b>3.3</b> ] <sup>2+</sup>	37.6 (52.8), 36.6 (45.7), 32.7 (30.0), 27.8 (14.3), 15.4 (10.5), 6.7 (2.8)
[ <b>3.3</b> ] <sup>3+</sup>	24.9 (12.0), 15.7 (7.6), 6.6 (1.8)
<b>3.4</b>	37.5 (17.2), 36.4 (16.3), 34.4 (16.4), 30.1 (13.8), 25.6 (7.2), 15.1 (1.3), 5.8 (1.8)
[ <b>3.4</b> ] <sup>+</sup>	37.5 (25.3), 36.5 (22.2), 32.5 (15.5), 26.8 (7.9), 22.6 (4.5), 21.6 (4.3), 14.7 (3.4), 5.8 (3.1)
[ <b>3.4</b> ] <sup>2+</sup>	36.5 (24.5), 33.2 (17.0), 22.9 (5.2), 21.7 (5.0), 14.9 (4.0), 13.4 (3.6), 8.7 (4.4), 6.5 (9.4)
[ <b>3.4</b> ] <sup>3+</sup>	16.1 (4.7), 13.3 (4.4), 8.6 (4.4), 6.5 (7.2)
<b>3.5</b>	39.3 (14.5), 37.5 (12.1), 36.5 (10.8), 32.1 (5.7), 24.2 (1.0)
[ <b>3.5</b> ] <sup>+</sup>	37.6 (6.6), 36.5 (5.8), 31.7 (6.4)
[ <b>3.5</b> ] <sup>2+</sup>	31.6 (6.7), 23.3 (1.8)
<b>3.6</b>	37.5 (15.6), 36.5 (14.0), 32.1 (12.1), 25.1 (2.9)
[ <b>3.6</b> ] <sup>+</sup>	37.5 (21.7), 36.4 (18.6), 31.9 (12.1), 23.4 (3.7)
[ <b>3.6</b> ] <sup>2+</sup>	33.2 (11.6), 31.6 (10.0), 23.5 (3.5)

**Table 3.11.** Spectroelectrochemical UV/vis/NIR data for the different redox states of **3.1, 3.4** and **3.6** in CH<sub>2</sub>Cl<sub>2</sub> at 298 K.

Complex	$\nu_{\max}$ ( $10^3 \text{ cm}^{-1}$ ) ( $\epsilon_{\max}$ ( $10^3 \text{ M}^{-1} \text{ cm}^{-1}$ ))
[ <b>3.1</b> ]	31.4 (21.2)
[ <b>3.1</b> ] <sup>+</sup>	32.5 (20.9), 6.6 (3.1)(sh)
[ <b>3.4</b> ]	37.4 (38.8), 33.3 (46.8), 24.2 (15.4) 37.7 (42.8)(sh), 33.9 (26.5)(sh), 25.5 (12.2), 22.7 (11.0), 21.3 (14.2), 19.2 (7.1), 18.5 (6.6), 14.8 (12.8), 13.0 (6.4)
[ <b>3.4</b> ] <sup>+</sup>	37.7 (18.0)(sh), 31.7 (12.1), 25.5 (3.7)
[ <b>3.6</b> ]	38.0 (22.5)(sh), 31.7 (11.7), 23.5 (3.7)
[ <b>3.6</b> ] <sup>+</sup>	

**Table 3.12.** Extracted X-band EPR g values for complexes **[3.1]<sup>+</sup>**-**[3.6]<sup>+</sup>** in CH<sub>2</sub>Cl<sub>2</sub> in units of 10<sup>-4</sup> cm<sup>-1</sup>.

Complex	300 K	150 K		
	g <sub>iso</sub>	g <sub>1</sub>	g <sub>2</sub>	g <sub>3</sub>
<b>[3.1]<sup>+</sup></b>	2.002	2.009	2.009	1.986
<b>[3.2]<sup>+</sup></b>	2.002	2.005	1.997	1.997
<b>[3.3]<sup>+</sup></b>	2.005	2.002	2.002	2.002
<b>[3.4]<sup>+</sup></b>	2.005	2.005	2.005	2.005
<b>[3.5]<sup>+</sup></b>	2.002	2.009	2.010	1.987
<b>[3.6]<sup>+</sup></b>	2.002	2.009	2.007	1.990

Average g values ( $g_{av} = 1/3(g_1+g_2+g_3)$ ) were very similar to g<sub>iso</sub>, suggesting that the decrease in temperature did not perturb the complex substantially.

**Table 3.13.** Extracted X-band EPR hyperfine and superhyperfine coupling constants to one <sup>195</sup>Pt nucleus and two <sup>31</sup>P nuclei for complexes **[3.1]<sup>+</sup>**-**[3.6]<sup>+</sup>** in CH<sub>2</sub>Cl<sub>2</sub> in units of 10<sup>-4</sup> cm<sup>-1</sup>.

Complex	300 K	150 K		
	{A <sub>iso</sub> ( <sup>195</sup> Pt)} {A <sub>iso</sub> ( <sup>35</sup> P)}	{A <sub>1</sub> ( <sup>195</sup> Pt)} {A <sub>1</sub> ( <sup>35</sup> P)}	{A <sub>2</sub> ( <sup>195</sup> Pt)} {A <sub>2</sub> ( <sup>35</sup> P)}	{A <sub>3</sub> ( <sup>195</sup> Pt)} {A <sub>3</sub> ( <sup>35</sup> P)}
<b>[3.1]<sup>+</sup></b>	{34} {7}	{60} {7}	{60} {7}	{60} {7}
<b>[3.2]<sup>+</sup></b>	{30} {7} <sup>[a]</sup>	{50} {8} <sup>[a]</sup>	{50} {8} <sup>[a]</sup>	{50} {8} <sup>[a]</sup>
<b>[3.3]<sup>+</sup></b>	{45} {20}	{45} {20}	{45} {20}	{45} {20}
<b>[3.4]<sup>+</sup></b>	{32}	{80} {20}	{80} {20}	{-35} {20}
<b>[3.5]<sup>+</sup></b>	{28} {7}	{60} {1}	{60} {1}	{-35} {-12}
<b>[3.6]<sup>+</sup></b>	{20} {4.5}	{60} {1}	{60} {1}	{-35} {-12}

[a] Hyperfine coupling extracted from S band measurements.

To summarise, the results presented in this chapter detail the spectroscopic characterisation by EPR, UV/vis and SEC of four *bis*- and two *tris*-dioxlene complexes of Pt(II).

The UV-vis/NIR oxidative titrations and SEC establish a clear trend – the ligands based around the triptycene functionality (**3.1**, **3.2**, **3.3** and **3.4**) exhibit intramolecular electron transfer behaviour on the class II/III borderline, which is consistent with complexes of the H<sub>4</sub>thea ligand studied previously in the Halcrow group.<sup>[9]</sup> The other complexes **3.5** and **3.6** show strictly class I behaviour with localised semiquinone radicals. The difference in electron transfer class for **3.5** and **3.6** is due to the 90°

---

dihedral angle of the dioxolene rings, which leads to poor orbital overlap between the rings.

[**3.3**]<sup>+</sup> has the lowest  $\Delta v_{1/2}$  value of 1306 cm<sup>-1</sup>, indicating that its radical is the most delocalised of the complexes studied. Following this are [**3.1**]<sup>+</sup> and [**3.4**]<sup>+</sup> with a  $\Delta v_{1/2}$  values of 2380 cm<sup>-1</sup>, which are very close to value that of [(Pt(dpppe))<sub>2</sub>thea], which is 2300 cm<sup>-1</sup>. The largest  $\Delta v_{1/2}$  value is that of [**3.2**]<sup>+</sup>, which is 2695 cm<sup>-1</sup>, making this the least delocalised of the complexes studied. For comparison, the previously studied H<sub>6</sub>CTC complex has an experimental  $\Delta v_{1/2}$  of >5000 cm<sup>-1</sup>, indicating that this is far more towards the class III formalism than any of the triptycenes studied here. The electron coupling energies naturally follow the same trend described above.

Complexes **3.1**, **3.2**, **3.5** and **3.6** show fairly good stability at room temperature when protected from air and moisture, however **3.3** and **3.4** defy this trend by being highly prone to decomposition even when much care is taken to protect them, as seen in both non-isobesticity of the UV-vis/NIR spectra and the very weak or non-existent signals observed by EPR.

The EPR measurements undertaken confirm that each complex generates a radical cation after addition of [FeCp<sub>2</sub>]PF<sub>6</sub>. The *bis*-dioxolene complexes **3.1**, **3.2**, **3.5** and **3.6** have g values very similar to each other, in the region of 2.0017-2.0019. The *tris*-dioxolene complexes **3.3** and **3.4** have higher g values, in the range of 2.0031-2.0060. Hyperfine couplings, when observed, were of very similar values between all of the complexes, typically in the region of 30 x10<sup>-4</sup> cm<sup>-1</sup> for the <sup>195</sup>Pt coupling, and 7 x10<sup>-4</sup> cm<sup>-1</sup> for the <sup>31</sup>P coupling. Interestingly, the <sup>31</sup>P hyperfine coupling is always lost upon freezing of the solution.

---

### 3.4 References

1. A. Heckmann, C. Lambert, *Angew. Chem. Int. Ed.* **2012**, (51), 326-392.
2. Y. Han, Y. Jiang, C. F. Chen, *Chin. Chem. Lett.* **2013**, 24, 475.
3. J. Best, I. V. Sazanovich, H. Adams, R. D. Bennett, E. S. Davies, A. J. H. M. Meijer, M. Towrie, S. A. Tikhomirov, O. V. Bouganov, M. D. Ward, J. A. Weinstein, *Inorg. Chem.* **2010**, (49), 10041-10056.
4. C. G. Pierpont, R. M. Buchanan, *Coord. Chem. Rev.* **1981**, 38, 45.
5. S. Bhattacharya, S. R. Boone, G. A. Fox, C. G. Pierpont, *J. Am. Chem. Soc.* **1990**, (112), 1088-1096.
6. O. Carugo, C. B. Castellani, K. Djinovic, M. Rizzi, *Journal of the Chemical Society, Dalton Transactions* **1992**, (5), 837-841.
7. H. Wunderlich, D. Mootz, *Acta Cryst. Sect. B* **1971**, (27), 1684-1686.
8. A. L. Macdonald, J. Trotter, *J. Chem. Soc. Perkin Trans.* **1973**, (2), 476-480.
9. J. J. Loughrey, S. Sproules, E. J. L. McInnes, M. J. Hardie, M. A. Halcrow, *Chem. Eur. J.* **2014**, 20 (21), 6272-6276.
10. K. D. Demadis, C. M. Hartshorn, T. J. Meyer, *Chem. Rev.* **2001**, (101), 2655-2685.
11. M. B. Robin, P. Day, *Advan. Inorg. Chem. Radiochem.* **1967**, (10), 247-422.
12. D. Sun, S. V. Rosokha, J. K. Kochi, *J. Am. Chem. Soc.* **2004**, 126, 1388-1401.
13. C. Boskovic, Valence Tautomeric Transitions in Cobalt-dioxolene Complexes. In *Spin-Crossover Materials*, John Wiley & Sons Ltd: 2013; pp 203-224.

---

## Chapter 4

### Synthesis, Structure and Metallation of a *Tris*-Dioxolene Based Tribenzotriquinacene

#### 4.1 Introduction

Cyclotricatechylene (CTC) (**Figure 4.1**) is an important *tris*(catechol) ligand which has attracted much attention in recent years for its role as a supramolecular host molecule and cage tecton.<sup>[1-2]</sup> Its  $C_{3v}$  symmetry<sup>[3]</sup> and strong electron donating ability makes it desirable as a trigonal building block for cryptophanes,<sup>[4]</sup> cavitands<sup>[5]</sup> and tentacular<sup>[6]</sup> molecules, particularly those incorporating an electron accepting metal ion. Many CTC derivatives have been reported in the literature however the bulk of these have involved modifying the outer ring positions, with alterations to the inner core of the molecule presenting a significantly harder synthetic challenge.<sup>[7-8]</sup>

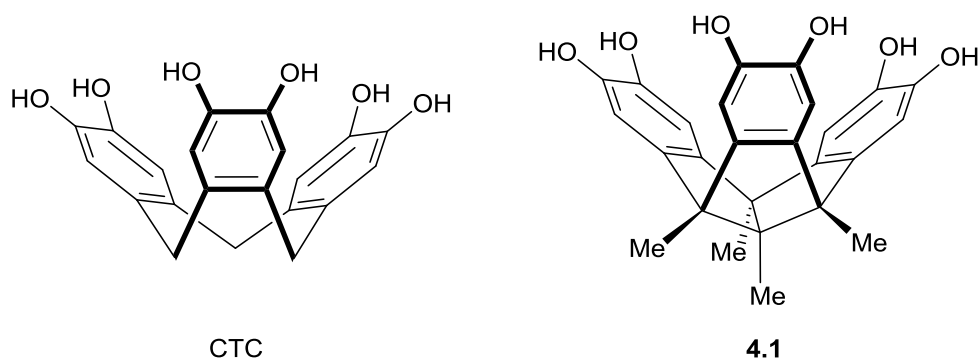


**Figure 4.1.** CTC and the target tribenzotriquinacene (tbtq) ligand **4.1**.

CTC has been recognised as having the potential for rich electrochemistry due to the presence of “non-innocent” catechol functionalities,<sup>[9-10]</sup> and the potential for electron transfer between the three redox sites. Bohle and Stasko first reported two complexes of CTC coordinated with Pt and an ancillary diphosphine,<sup>[11]</sup> and while their electrochemistry was studied, no further characterisation of their semiquinone radicals was carried out. Complexes of this type are expected to show intense charge transfer absorptions in visible or near-infrared region.<sup>[12]</sup> To this end, work has been done previously in the Halcrow group to investigate Pt, Pd and Cu complexes of CTC.<sup>[10]</sup> This line of research has been complicated by the fact that the presence of unsaturated C-H bonds adjacent to the catechol functionalities render CTC unstable to oxidation via a semiquinone radical decomposition pathway, limiting its applications. One

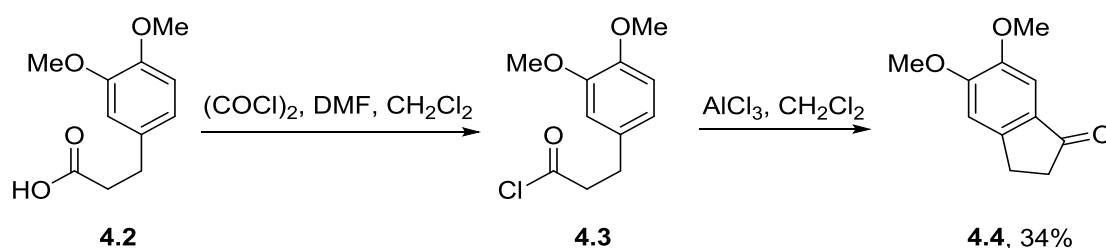
hypothesised strategy to circumvent this decomposition is to prepare a rigid form of CTC, **4.1**<sup>[8]</sup> (**Figure 4.1**), wherein the alkyl C-H groups are replaced by quaternary methyl groups to afford greater steric protection. This modification, however, comes at the cost of increasing the total number of synthetic steps required to prepare this compound from 2 to 10. Crystalline clathrates and donor:acceptor assemblies of CTC have been reported previously,<sup>[9]</sup> and it will be interesting to see if similar phenomena are observed with this tribenzotriquinacene.

## 4.2 Results and Discussion

### 4.2.1 Synthesis of the ligand

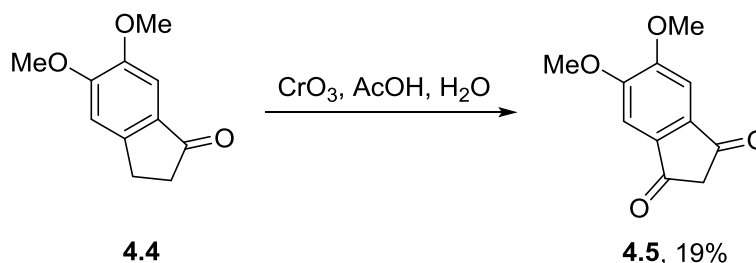
Synthesis of the hexamethoxy version of the target tribenzotriquinacene (**4.13**) has been reported by Kuck *et al.*,<sup>[8]</sup> and the same general method will be followed here with slight alterations and/or optimisations when necessary. It is important throughout this synthesis to take precautions to protect certain reactive functional groups that are susceptible to undergoing unwanted side-reactions during intermediate steps. The main concern relating to this is the presence of hydroxyl groups, hence all dioxolene hydroxyl groups will be initially introduced in their protected methoxy form, to be deprotected in the final step. Yield is also an important consideration, as even relatively high yields for each individual step will result in a substantial decrease in the amount of product retained over the 10 synthetic steps.

The synthetic approach is to first produce the indane-1,3-dione (**4.5**) and bis(3,4-dimethoxymethyl)methanol (**4.8**) fragments. **4.5** can be made in three steps, first by conversion of **4.2** to the acid chloride **4.3** *in situ* before reaction with AlCl<sub>3</sub> to promote cyclisation into **4.4** (**Scheme 4.1**).



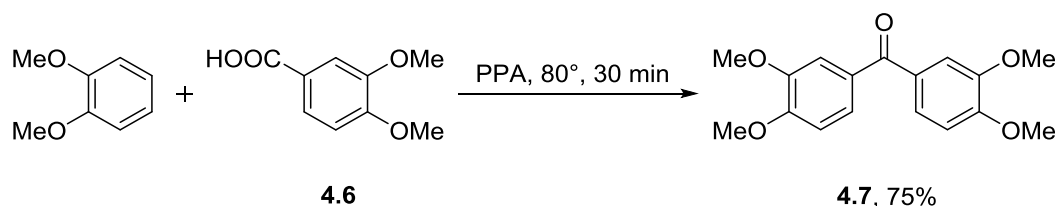
**Scheme 4.1.** Cyclisation of the acid chloride **4.3** to produce **4.4**, an indanone intermediate.

**4.4** is then oxidised with  $\text{CrO}_3$  (**Scheme 4.2**). It should be noted that while these reaction conditions can lead to oxidation of benzylic methylene groups, the reaction is sensitive to how electron rich the benzene ring is, with less electron rich analogues failing to undergo reaction.



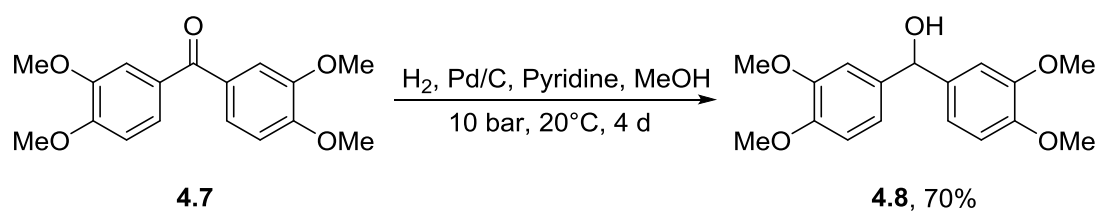
**Scheme 4.2.** Oxidation to form an indane-1,3-dione **4.5**.

Kulkarni's method<sup>[13]</sup> for the synthesis of the next intermediate fragment **4.7** was followed, which furnished the product in high yield (**Scheme 4.3**).



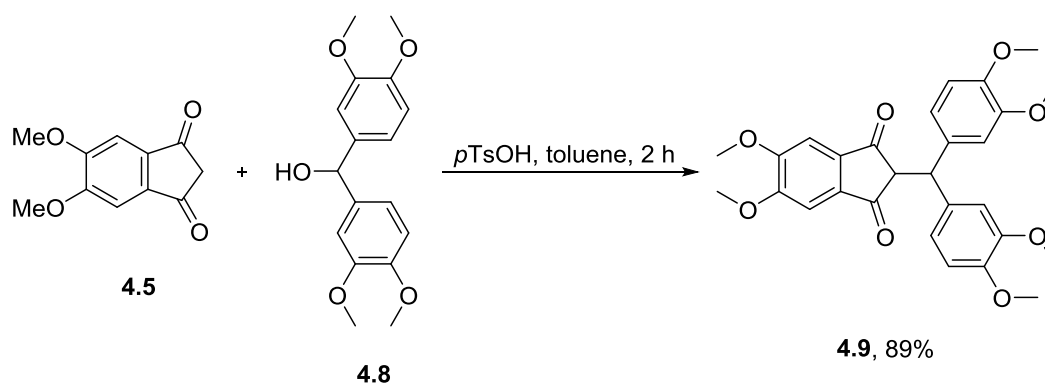
**Scheme 4.3.** Synthesis of the methanone intermediate **4.7**.

The next step is to reduce the ketone to an alcohol (**4.8**). While this appears to be a relatively straightforward reduction, in practice many simple/mild reducing conditions fail to produce the desired product.<sup>[8]</sup> Kuck reports that use of Zn in alkaline ethanol, Meerwein-Ponndorf-Verley,  $\text{LiAlH}_4$  and  $\text{NaBH}_4$  all result in the formation of over-reduced ethers rather than the desired product.<sup>[8]</sup> The optimised reaction conditions that were reported involve hydrogenation with Pd/C and hydrogen gas at 10 bar for 4 days (**Scheme 4.4**). This reaction can be accomplished in a pressurised Parr reactor with mechanical stirring, and it was observed by monitoring hydrogen uptake that after 4 days the reaction was complete as it had ceased absorbing any more hydrogen. It should be noted that it is important to remove any traces of acid prior to the reaction by filtering the starting materials through basic alumina and adding a trace amount of pyridine.



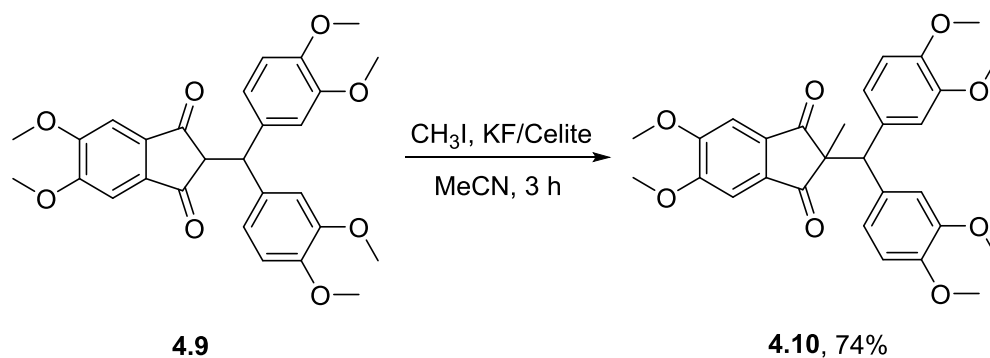
**Scheme 4.4.** Reduction of ketone **4.7** with H<sub>2</sub> and Pd/C to afford **4.8**.

With fragments **4.5** and **4.8** successfully produced, these can now be reacted together to produce **4.9**. **4.8** was converted to the tosylate *in situ* to promote an S<sub>N</sub>2 reaction with **4.5** to produce **4.9**. Care must be taken to keep the reaction completely water free, so it was carried out in a Thiele-Pape extractor containing 4 Å molecular sieves. The reaction may produce unwanted side products if precautions are not taken, but this can be mitigated by adding **4.8** slowly to **4.5** to ensure a low stationary concentration of the reactive benzhydryl cationic intermediate. The crude product must be purified by flash column chromatography regardless, as a small amount of side-product is invariably produced (**Scheme 4.5**).



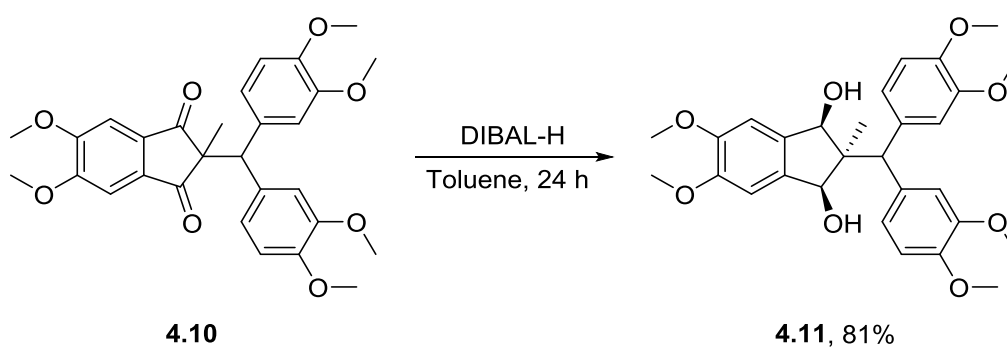
**Scheme 4.5.** Condensation of the two previously synthesised intermediates **4.5** and **4.8**, to form **4.9**.

For the next step, it is required that a methyl group is introduced to the carbon atom that will become the base of the tbq bowl. This is accomplished by another S<sub>N</sub>2 reaction, this time with methyl iodide catalysed by KF on Celite (**Scheme 4.6**).



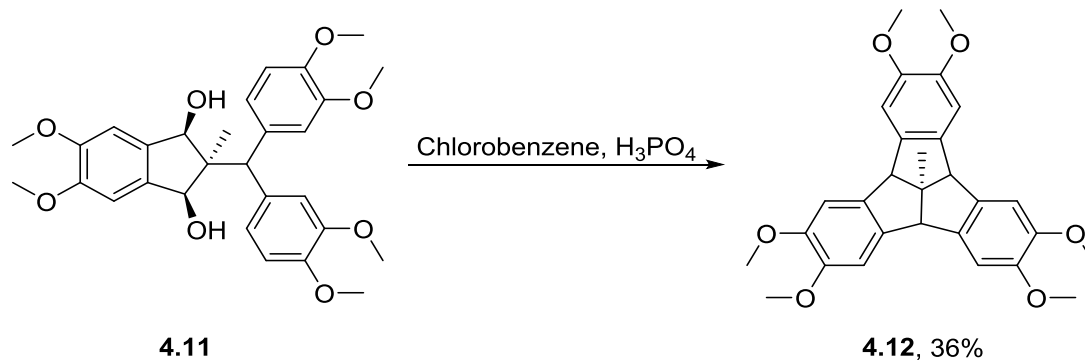
**Scheme 4.6.** Methylation of **4.9** with methyl iodide to produce **4.10**.

At this stage it is now important to introduce the desired stereochemistry into the molecule. This is due to the requirement that the final product should adopt the “bowl” rather than “saddle” conformation of CTC, and hence the central methyl group must be made to point in the opposite direction to the two reduced ketones. The asymmetric reducing agent DIBAL-H is ideal for this reaction, and leads to the formation of a single diastereomeric product of  $C_s$  symmetry, as confirmed by the  $^1\text{H}$  NMR spectrum (**Scheme 4.7**).



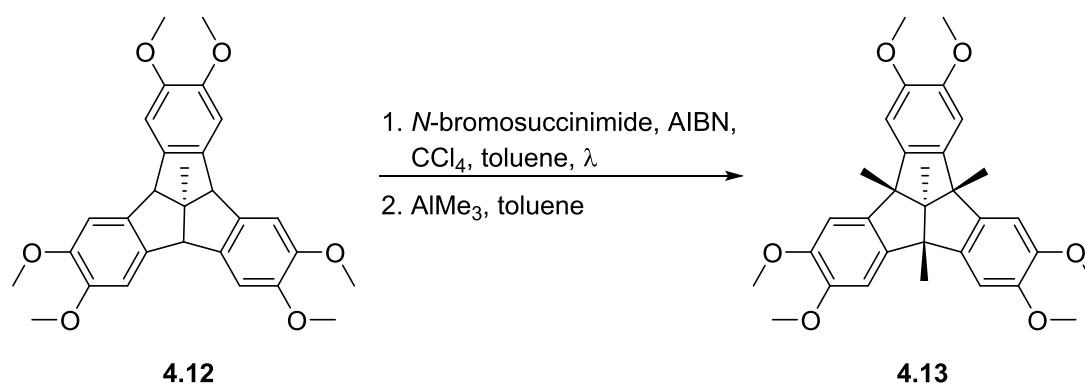
**Scheme 4.7.** Asymmetric reduction of **4.10** to form **4.11**.

A cyclodehydration reaction was then carried out by refluxing the enantiopure **4.11** in orthophosphoric acid in a Thiele-Pape extractor containing 4 Å molecular sieves, to produce **4.12** (**Scheme 4.8**).



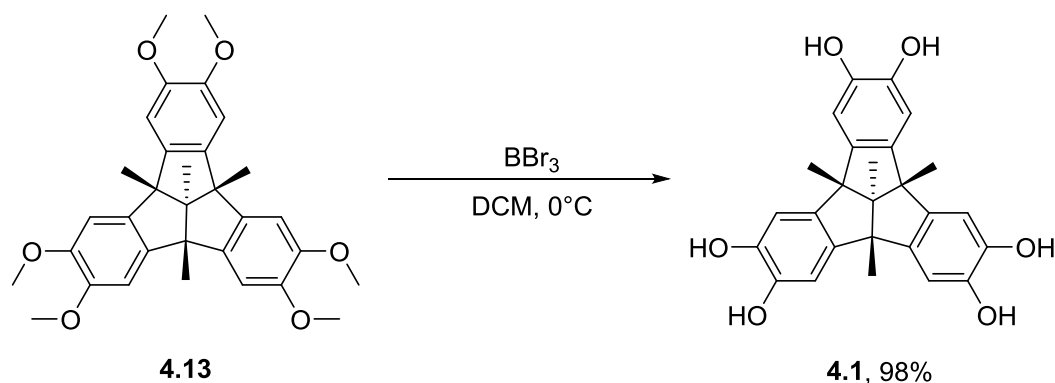
**Scheme 4.8.** Cyclisation of **4.11** to form the rigid backbone of **4.12**.

The next step involves a radical reaction under UV irradiation, first to substitute 3 bromine atoms onto the bridgehead positions, then to substitute these in turn with methyl groups with  $\text{AlMe}_3$  in a one-pot manner (**Scheme 4.9**). No isolation or purification of the tribromo intermediate was required.



**Scheme 4.9.** One-pot radical bromination followed by substitution of bromine for methyl.

The final step was to remove the methoxy protecting groups with boron tribromide (**Scheme 4.10**).



**Scheme 4.10.** Deprotection of the methoxy groups of **4.13** with  $\text{BBr}_3$  to form **4.1**.

#### 4.2.2 Characterisation of **4.1**, $[\{(\text{dppe})\text{Pt}\}_3(\text{4.1})]$ (**4.14**) and $[\{(\text{dppb})\text{Pt}\}_3(\text{4.1})]$ (**4.15**)

**4.1** was crystallised as pale yellow plates by vapour diffusion of pentane into THF. The structure of **4.1** was solved in the triclinic space group  $P\bar{1}$  using the *Olex2* program (**Figure 4.2**).

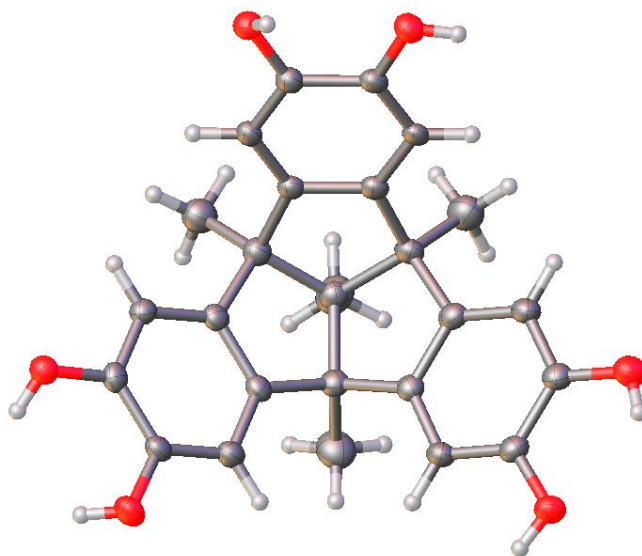


**Figure 4.2.** View into the bowl shaped cavity of **4.1**.

There is one THF molecule per molecule of **4.1** in the structure which sits inside the cavity of the bowl, with the oxygen atoms of the THF molecule pointing away from the hydrophobic cavity and hydrogen bonding to an OH group on an adjacent molecule of **4.1**. This forms a crystalline clathrate composed of hydrogen-bonded bilayers with alternative upwards and downwards facing molecules of **4.1** (**Figure 4.3**). This highly resembles a previously reported CTC clathrate by Halcrow *et al.*,<sup>[9]</sup>

---

and similar solvent incorporation in the cavity has been reported for a variety of different solvents of underivatized CTC.<sup>[14-16]</sup> The average dihedral angle between the catechol rings is 117.3°.

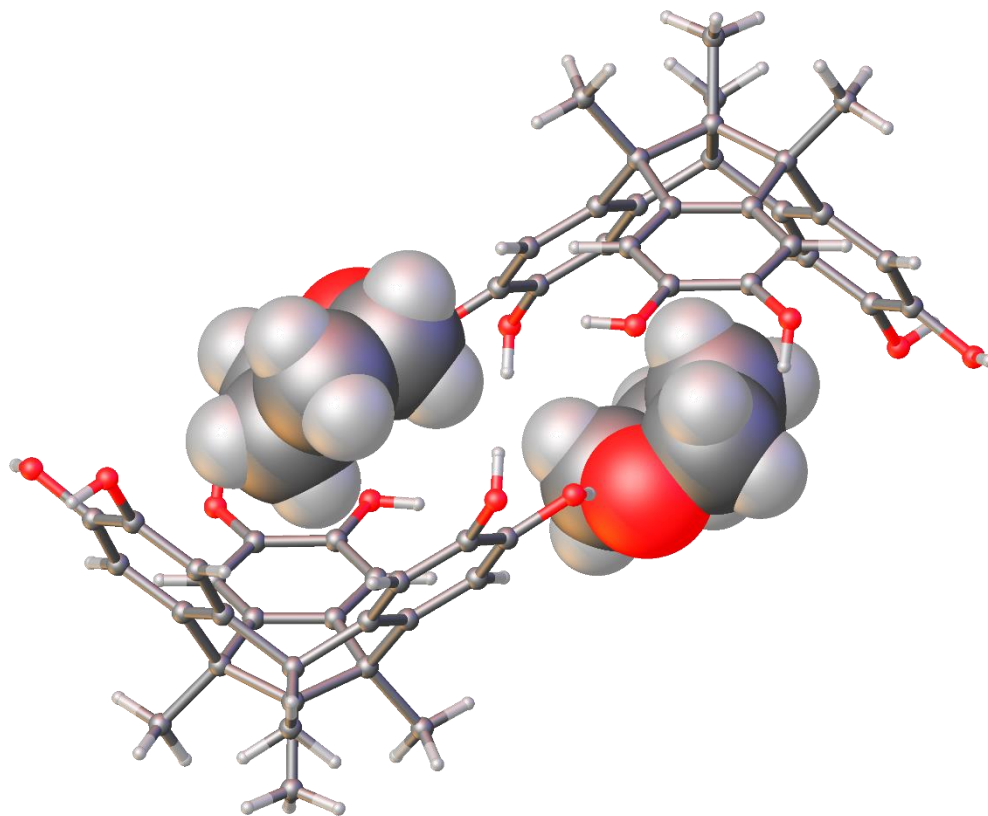


**Figure 4.3.** One molecule of THF sits inside each molecule of **4.1**, with adjacent layers of **4.1** being translated by half a molecule and alternating between opposite orientations.

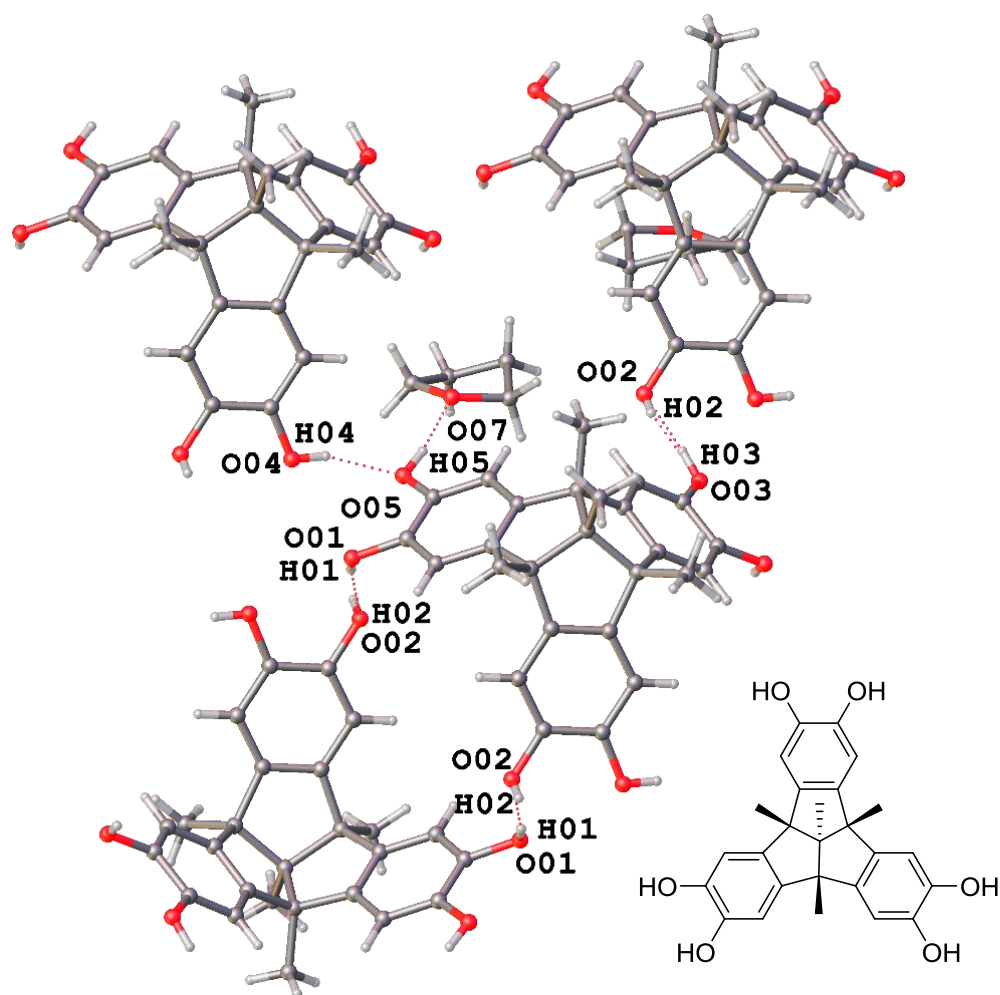


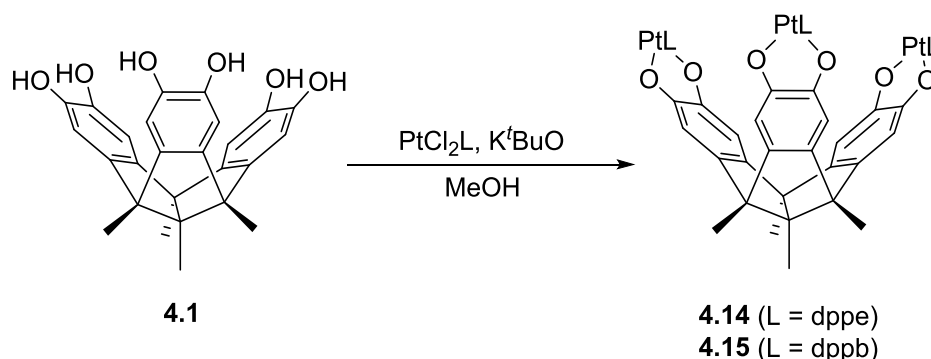
**Figure 4.4.** Hydrogen bond connectivity between nearest-neighbour molecules of **4.1**.

As shown in **Figure 4.4**, there is a significant amount of hydrogen bonding between both **4.1** and the THF molecules in the structure. Each molecule of **4.1** participates in 5 hydrogen bonds, 4 of which are to its 3 nearest neighbours, and one to the THF molecule. The parameters for these hydrogen bonds are listed in **Table 4.1**.

**Table 4.1.** Hydrogen bond parameters for the crystal structure of **4.1** (Å, °). See **Figure 4.4** for the atom numbering scheme.

	H...A	D-H	D...A	D-H...A
O01-H01...O02	1.9857(3)	0.81997(13)	2.7743(4)	161.123(4)
O02-H02...O03	2.0794(2)	0.81996(13)	2.7757(3)	142.587(9)
O03-H03...O02	2.0178(3)	0.82000(8)	2.7757(3)	153.467(5)
O04-H04...O05	1.9083(4)	0.81999(17)	2.6955(5)	160.595(4)
O05-H05...O07	1.7889(3)	0.81995(14)	2.5963(4)	167.874(3)

Having confirmed that the ligand synthesis was successful, the next step was to carry out similar complexation reactions to those discussed in the previous chapter. **4.1** was reacted with  $\text{PtCl}_2(\text{dppe})_2$  and  $\text{PtCl}_2(\text{dppb})_2$  under aerobic conditions (**Scheme 4.11**).



**Scheme 4.11.** Complexation with  $\text{PtCl}_2(\text{dppe})_2$  and  $\text{PtCl}_2(\text{dppb})_2$ .

The HRMS for **4.14** did not contain a molecular ion peak, however a peak corresponding to the ligand coordinated with two  $\text{Pt}(\text{dppe})$  fragments and two potassium ions ( $[\text{C}_{78}\text{H}_{68}\text{K}_2\text{O}_6\text{P}_4\text{Pt}_2][\text{K}]_2^+$ ,  $1693.25 \text{ g mol}^{-1}$ ) was observed (**Figure 4.5**).

The HRMS for **4.15** has good agreement with the simulated isotopic distribution expected for the molecular ion  $[\text{C}_{116}\text{H}_{89}\text{O}_6\text{P}_6\text{Pt}_3]^+$  ( $2350.41 \text{ g mol}^{-1}$ ), showing the characteristic isotopic distribution for a molecular containing three platinum nuclei (**Figure 4.6**). For both spectra, a second set of peaks corresponding to the protonated +2 charge state were also present.

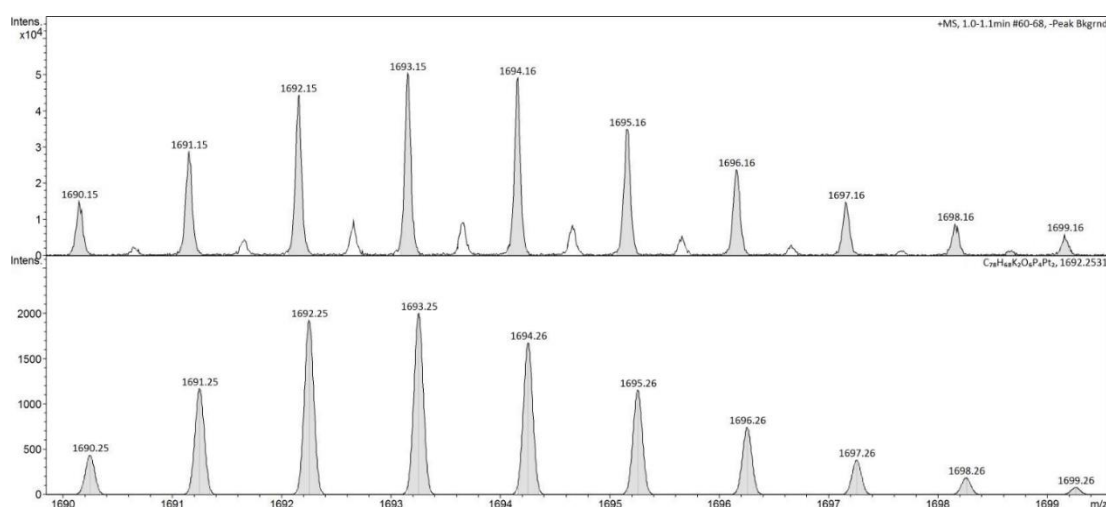


**Figure 4.5.** Experimental and simulated high resolution mass spectra of a fragment of **4.14** with two  $\text{Pt}(\text{dppe})$  groups and two  $\text{K}^+$  ions coordinated.

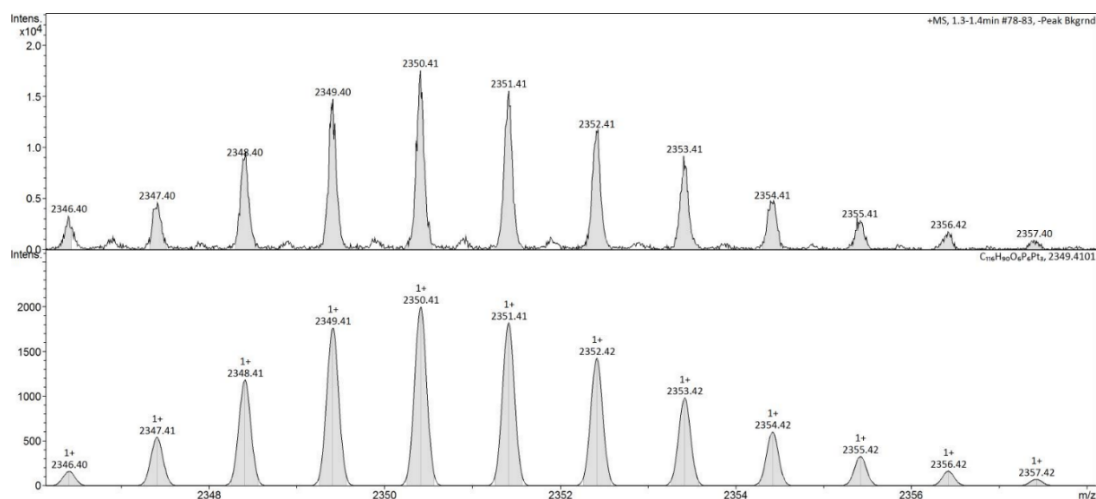


**Figure 4.6.** Experimental and simulated high resolution mass spectra of **4.15**.

The  $^{31}\text{P}\{^1\text{H}\}$  NMR spectra for the complexes show a single phosphorus environment at 40.74 ppm for **4.14** (**Figure 4.7**), and 28.85 ppm for **4.15** (**Figure 4.8**), which is to be expected given the  $C_{3v}$  symmetry of the complexes. Platinum satellite peaks with a coupling constant of 1803.23 Hz (**4.14**) and 1682.43 Hz (**4.15**) are also observed due to the coupling of the  $^{31}\text{P}$  nuclei to a  $^{195}\text{Pt}$  ( $S = 1/2$ ) nucleus.<sup>[17]</sup>

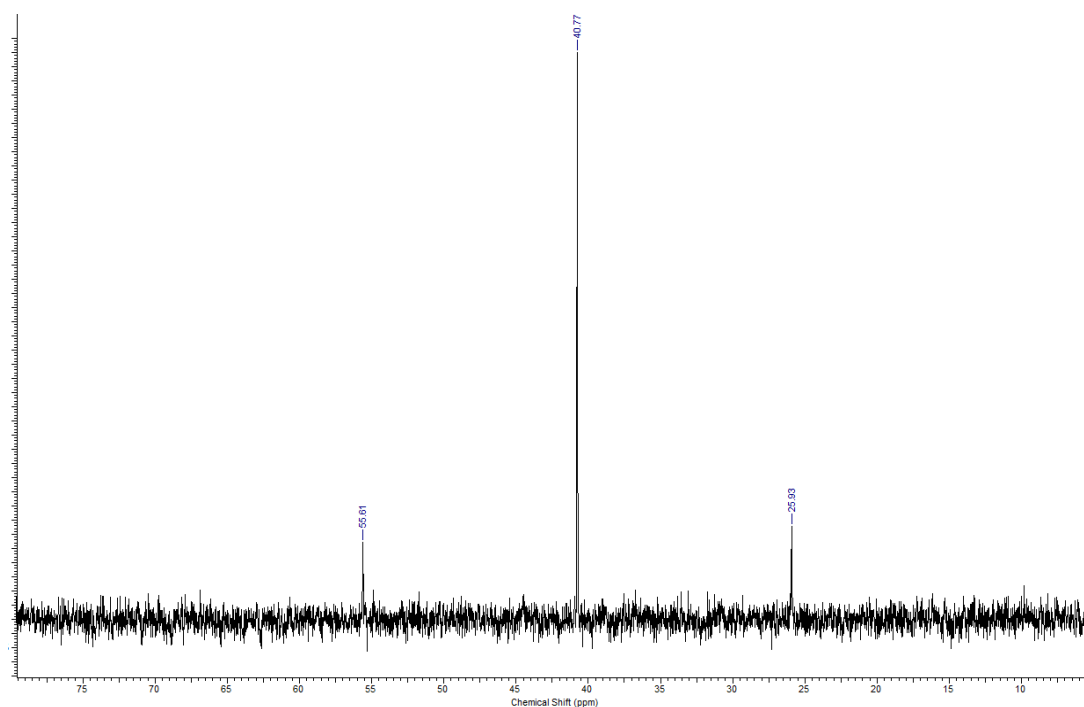


**Figure 4.7.**  $^{31}\text{P}\{^1\text{H}\}$  NMR (300 MHz,  $\text{CD}_2\text{Cl}_2$ ) spectrum of **4.14**, showing  $^{195}\text{Pt}$  satellites.

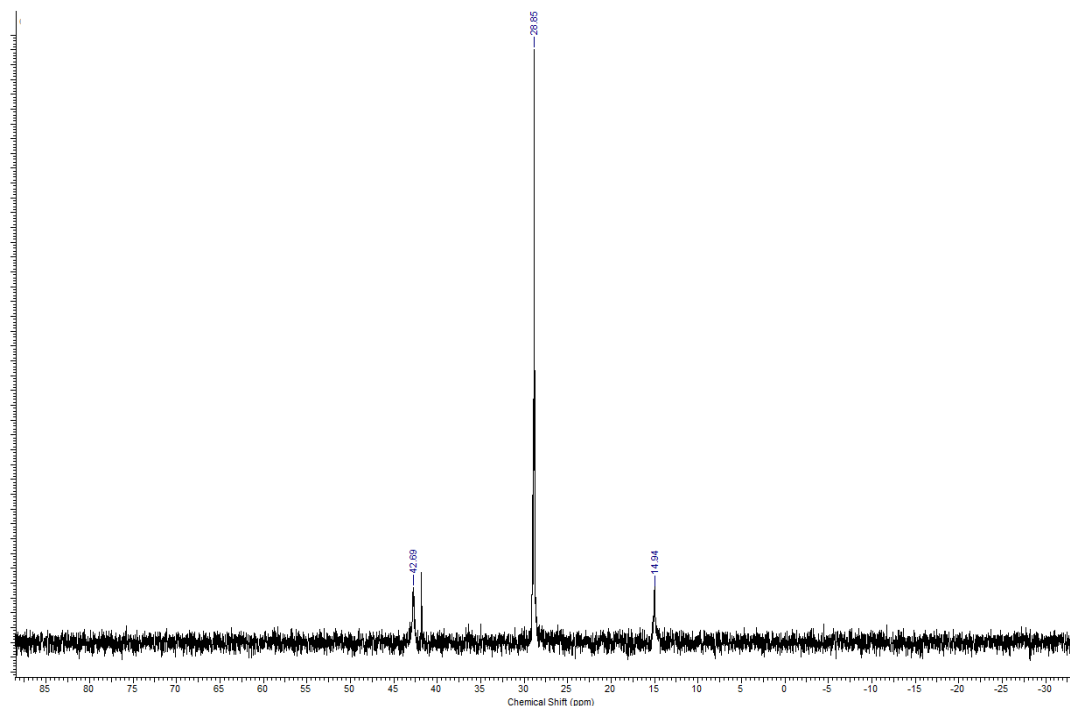


**Figure 4.8.**  $^1\text{P}\{^1\text{H}\}$  NMR (300 MHz,  $\text{CD}_2\text{Cl}_2$ ) spectrum of **4.15**, showing  $^{195}\text{Pt}$  satellites.

### 4.2.3 Electrochemical Analysis of **4.14** and **4.15**.

The redox chemistry of complexes **4.14** and **4.15** was investigated by CV and DPV. All experiments were carried out at 298 K in a 0.1 M solution of  $n\text{Bu}_4\text{NPF}_6$  in dry, degassed dichloromethane under argon atmosphere. The voltammetry (**Figures 4.9-4.13**) showed that both **4.14** and **4.15** exhibit three chemically reversible one-electron processes in the  $-0.5 \leq E_{1/2} \leq 0.1$  V (*vs*  $\text{Fc}/\text{Fc}^+$ ) region, attributed to sequential  $\text{Cat} \rightarrow \text{SQ}$  transitions as displayed in **Scheme 4.12**.

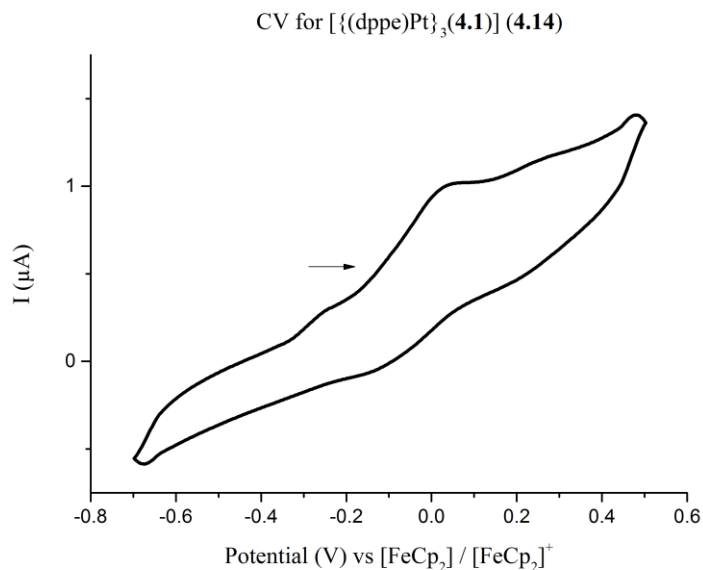


**Figure 4.9.** CV for **4.14** in 0.1 M solution of  $n\text{Bu}_4\text{NPF}_6$  in dry degassed dichloromethane at 298 K under argon atmosphere vs  $[\text{FeCp}_2] / [\text{FeCp}_2]^+$ . The first three chemically reversible Cat  $\rightarrow$  SQ oxidations are shown.

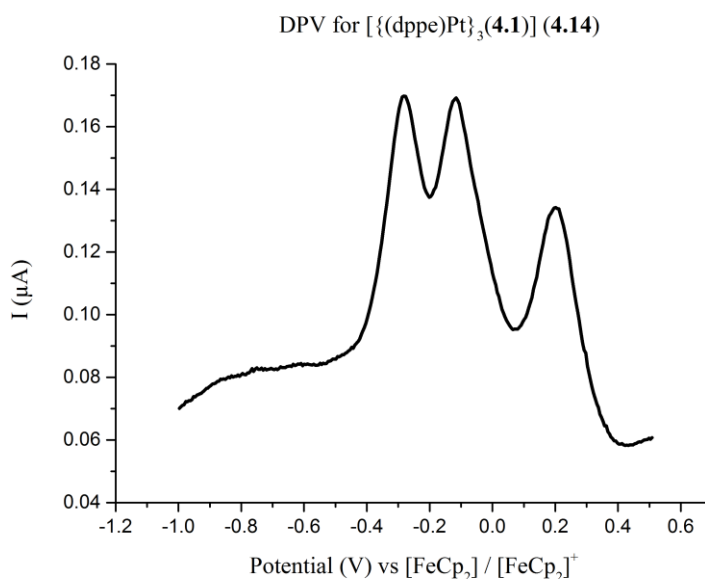


**Figure 4.10.** DPV of **4.14** in 0.1 M solution of  $n\text{Bu}_4\text{NPF}_6$  in dry degassed dichloromethane at 298 K under argon atmosphere vs  $[\text{FeCp}_2] / [\text{FeCp}_2]^+$ .

Complex **4.14** did not display exhibit any SQ  $\rightarrow$  BQ processes (even when scanning up to +2.0 V) and the Cat  $\rightarrow$  SQ oxidations that were present were extremely weak, and only easily identifiable in the DPV (**Figure 4.10**). Generally speaking, this complex was the least well-behaved complex of those studied (by several analytical

techniques) due to a combination of poor solubility, stability, and rapid precipitation/bleaching of its oxidised forms.

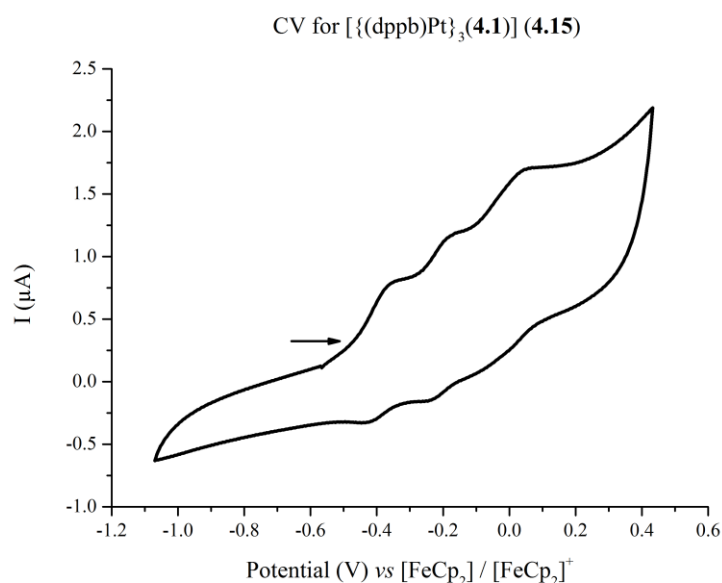


**Figure 4.11.** CV for **4.15** in 0.1 M solution of  $n\text{Bu}_4\text{NPF}_6$  in dry degassed dichloromethane at 298 K under argon atmosphere vs  $[\text{FeCp}_2] / [\text{FeCp}_2]^+$ . The first three chemically reversible Cat  $\rightarrow$  SQ oxidations are shown.

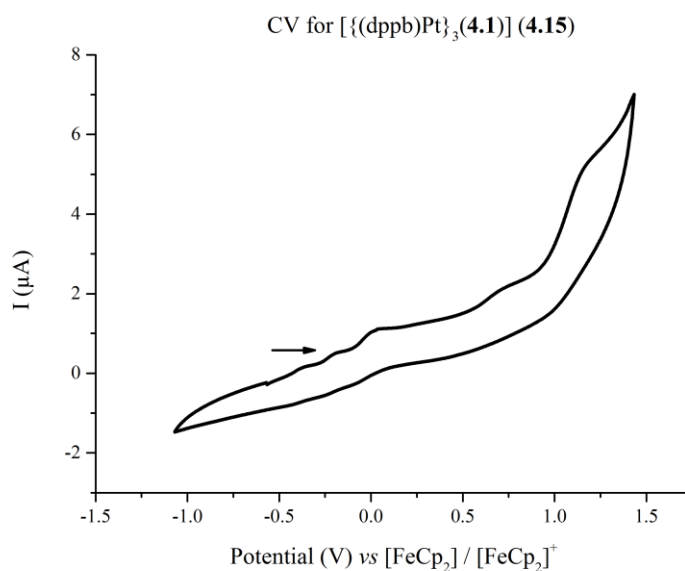


**Figure 4.12.** CV for **4.15** in 0.1 M solution of  $n\text{Bu}_4\text{NPF}_6$  in dry degassed dichloromethane at 298 K under argon atmosphere vs  $[\text{FeCp}_2] / [\text{FeCp}_2]^+$ . The first three chemically reversible Cat  $\rightarrow$  SQ oxidations are shown, as well as two further chemically irreversible SQ  $\rightarrow$  BQ oxidations.

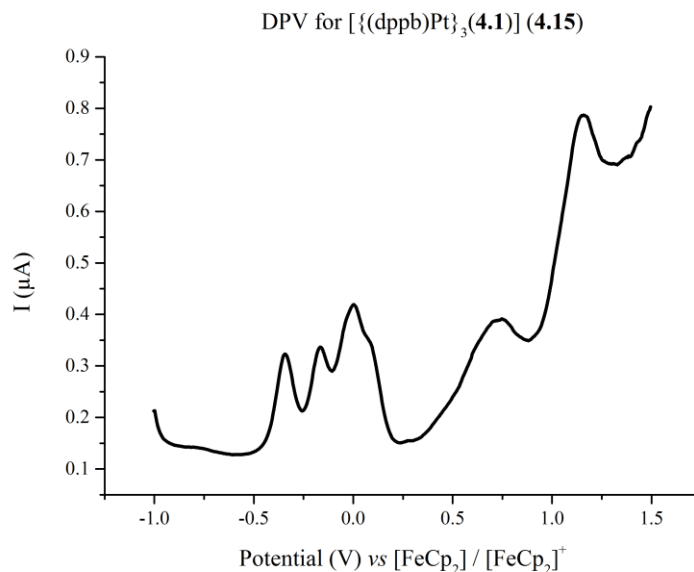


**Figure 4.13.** Differential pulse voltammogram of **4.15** in 0.1 M solution of <sup>n</sup>Bu<sub>4</sub>NPF<sub>6</sub> in dry degassed dichloromethane at 298 K. The first three chemically reversible Cat → SQ oxidations are shown, as well as two irreversible SQ → BQ oxidations which occur at a more positive potential.

The first three chemically reversible redox processes undergone by **4.15** are comparable to that of the [(Pt(dppb))<sub>3</sub>CTC] complex studied previously in the Halcrow group,<sup>[9]</sup> although the transitions occur at a slightly more negative potential vs [FeCp<sub>2</sub>] (between 0.04-0.09 V more negative) in **4.15**. The peak-to-peak and *E*<sub>1/2</sub> separations of these complexes are almost identical to the [(Pt(dppb))<sub>3</sub>CTC] complex at 0.18 V.

The shoulder on the second oxidation of **4.15** (ca 0.1 V) is likely present due to a daughter product resulting from the decomposition of [**4.15**<sup>••</sup>]<sup>2+</sup>. Furthermore, complex **4.15** also exhibits two further chemically irreversible oxidation occurring at a higher potential (0.74 and 1.30 V), which can be assigned to subsequent SQ → BQ processes, as displayed in **Scheme 4.13**.

**Table 4.2.** Cyclic voltammetric data for complexes **4.14** and **4.15** in 0.1 M solution of  $n\text{Bu}_4\text{NPF}_6$  in dry degassed  $\text{CH}_2\text{Cl}_2$  at 298 K under argon atmosphere. Potentials (V) are referenced to a  $[\text{FeCp}_2] / [\text{FeCp}_2]^+$  internal standard, measured at a scan rate of  $0.1 \text{ Vs}^{-1}$ .

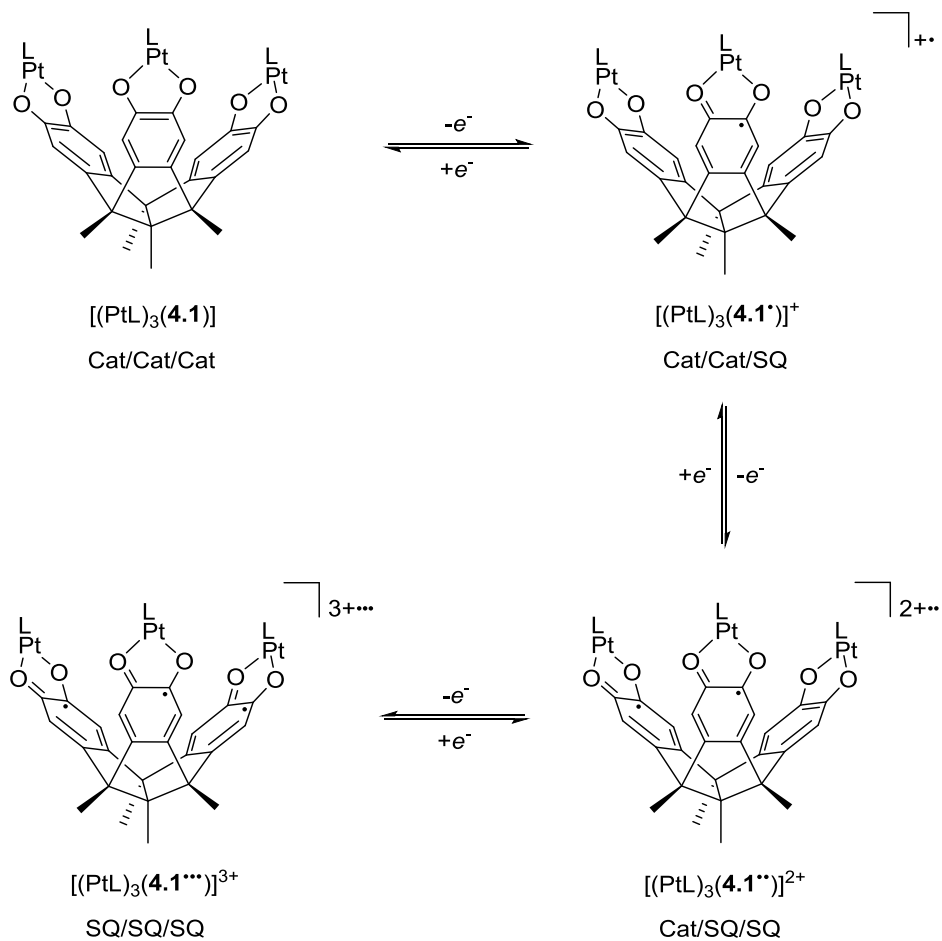
Transition (V)	( <b>4.14</b> )	( <b>4.15</b> )
$E_{1/2} \text{ Cat/Cat} \rightarrow \text{Cat/Cat/SQ}$	-0.183	-0.386
$E_{1/2} \text{ Cat/SQ} \rightarrow \text{SQ/SQ/Cat}$	0.127	-0.200
$E_{1/2} \text{ Cat/SQ} \rightarrow \text{SQ/SQ/SQ}$	0.348	0.031

**Table 4.3.** Differential pulse voltammetric data for complexes **4.14** and **4.15** in 0.1 M solution of  $n\text{Bu}_4\text{NPF}_6$  in dry degassed  $\text{CH}_2\text{Cl}_2$  at 298 K under argon atmosphere. Potentials (V) are referenced to a  $[\text{FeCp}_2] / [\text{FeCp}_2]^+$  internal standard, measured at a scan rate of  $0.1 \text{ Vs}^{-1}$ .

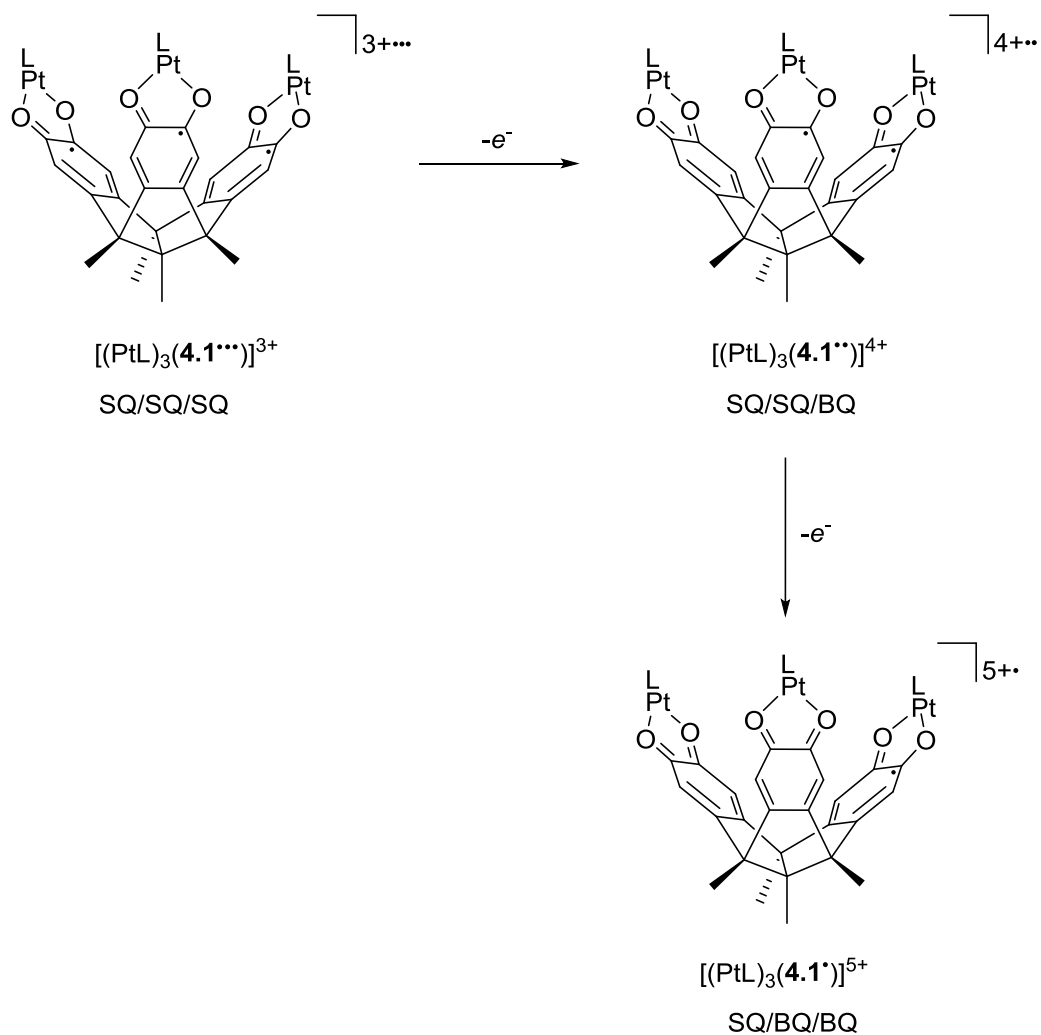
Transition (V)	$E_p$ ( <b>4.14</b> )	$E_p$ ( <b>4.15</b> )
$E_p \text{ Cat/Cat} \rightarrow \text{Cat/Cat/SQ}$	-0.282	-0.343
$E_p \text{ Cat/SQ} \rightarrow \text{Cat/SQ/SQ}$	-0.116	-0.167
$E_p \text{ Cat/SQ} \rightarrow \text{SQ/SQ/SQ}$	0.201	0.004
$E_p \text{ SQ/SQ} \rightarrow \text{SQ/SQ/BQ}$	-	0.745
$E_p \text{ SQ/BQ} \rightarrow \text{SQ/BQ/BQ}$	-	1.158

**Table 4.4.**  $\Delta E_p$  (V) values for the peaks listed in **Table 4.3**.

Complex	Cat / SQ		SQ / BQ	
	[ <b>4.14</b> ]	0.116	0.317	-
[ <b>4.15</b> ]	0.176	0.171	0.413	-



**Scheme 4.12.** Ligand based redox series of the observed Cat  $\rightarrow$  SQ transitions for 4.14 and 4.15.



**Scheme 4.13.** Ligand based redox series of the observed Cat  $\rightarrow$  BQ transitions for **4.15**.

The peak-to-peak and  $E_{1/2}$  separations for the oxidation processes provide a measure of the degree of communication between the dioxolene rings, with a larger separation being indicative of a greater degree of communication.<sup>[18]</sup>

For the Cat  $\rightarrow$  SQ transitions, complex **4.15** has  $\Delta E_p$  separations of  $\Delta E_p = 0.176$  V and 0.171 V, and a peak-to-peak  $E_{1/2}$  separation of 0.413 V for the SQ  $\rightarrow$  BQ transition. Complex **4.15** has a  $\Delta E_p = 0.166$  V and 0.317 V for the Cat  $\rightarrow$  SQ transitions. The structurally related complex  $[(Pt(dppe))_3CTC]$  previously studied by Halcrow *et al.*<sup>[10]</sup> has similar peak-to-peak  $E_{1/2}$  separation between the first two oxidations (0.18 V), and 0.40 V between the second and third oxidations.

---

#### 4.2.4 UV-vis-NIR Oxidative Titrations

As the CV measurements discussed in the previous section showed that the first two Cat  $\rightarrow$  SQ transitions for complexes **4.14** and **4.15** occurred at an oxidation potential more negative than that of the  $[\text{FeCp}_2] / [\text{FeCp}_2]^+$  couple, it is therefore appropriate to use  $[\text{FeCp}_2]\text{PF}_6$  as a chemical oxidant to generate the SQ radicals in solution by titration of stoichiometric amounts of the oxidant. For both complexes, the third Cat  $\rightarrow$  SQ oxidation occurred at a potential more positive than the  $[\text{FeCp}_2] / [\text{FeCp}_2]^+$  (+0.201 V, and +0.004 V for **4.14** and **4.15** respectively), therefore the  $(\text{SQ})_3$  form may not be generated by addition of three equivalents of the oxidant, especially in the case of **4.14**. Despite this, the *mono*- and *bi*- radicals should be accessible by the addition of one or two molar equivalents of the oxidant. Consequently, oxidative titrations of complexes **4.14** and **4.15** in aliquots of 0.25 eq of  $[\text{FeCp}_2]\text{PF}_6$  were carried out in nitrogen-degassed  $\text{CH}_2\text{Cl}_2$  at 298 K, and the UV-vis/NIR spectra of these solutions were recorded immediately after addition of the oxidant.

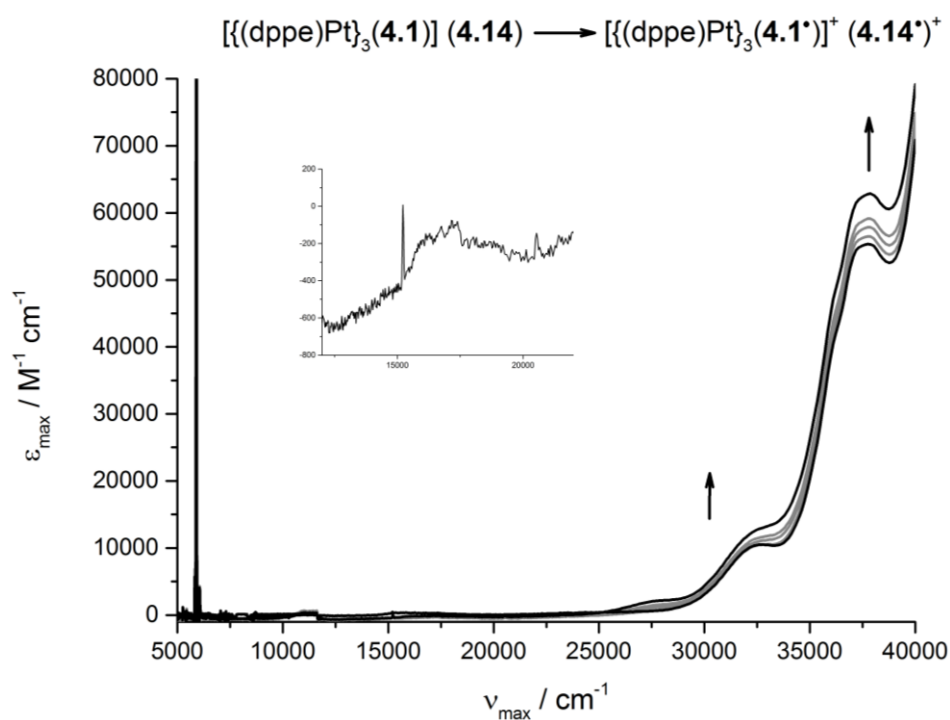


**Figure 4.14.** UV-vis/NIR oxidative titration of **4.14** to **[4.14]<sup>+</sup>** by addition of 1 equivalent of  $[FeCp_2]PF_6$  in 0.25 eq increments. The spectra of pure **4.14** and **[4.14]<sup>+</sup>** are displayed in black, with intermediate spectra displayed in grey.

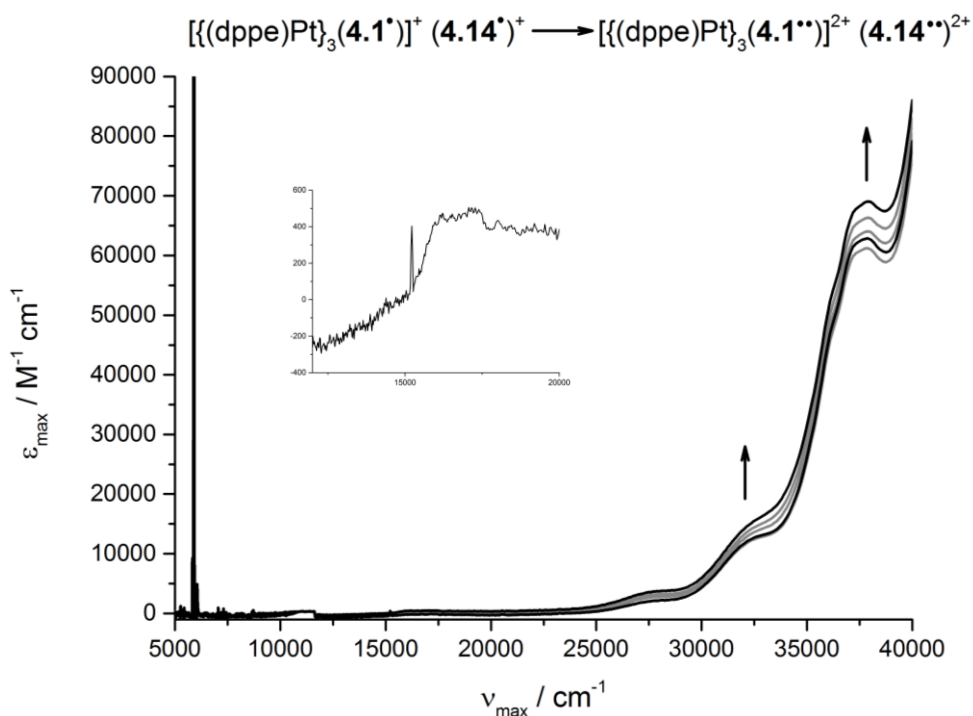


**Figure 4.15.** UV-vis/NIR oxidative titration of **[4.14]<sup>+</sup>** to **[4.14]<sup>2+</sup>** by addition of 1-2 equivalents of  $[FeCp_2]PF_6$  in 0.25 eq increments. The spectra of pure of **[4.14]<sup>+</sup>** and **[4.14]<sup>2+</sup>** are displayed in black, with intermediate spectra displayed in grey.

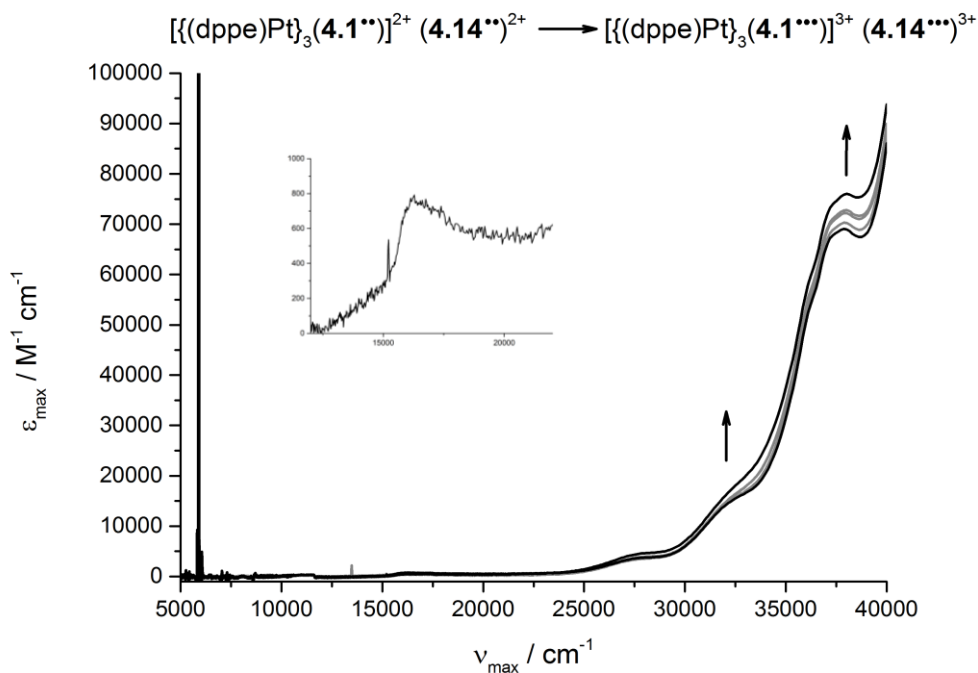


**Figure 4.16.** UV-vis/NIR oxidative titration of  $[4.14^{**}]^{2+}$  to  $[4.14^{***}]^{3+}$  by addition of 2-3 equivalents of  $[\text{FeCp}_2]\text{PF}_6$  in 0.25 eq increments. The spectra of pure of  $[4.14^{**}]^{2+}$  and  $[4.14^{***}]^{3+}$  are displayed in black, with intermediate spectra displayed in grey.

The high intensity narrow peak at  $5907 \text{ cm}^{-1}$  arises from the vibrational structure of the  $\text{CH}_2\text{Cl}_2$  solvent used. **Figure 4.14** shows that **4.14** does not produce an IVCT when  $[4.14]^+$  is generated, and no isosbestic point is observed, suggesting fast decomposition of the radical cation. This therefore suggests that **4.14** is a class I type complex with no electron transfer between the dioxolene rings, and the radical cation is highly unstable.

There is a very weak absorbance at  $16,300 \text{ cm}^{-1}$  (see inserts in **Figures 4.14-4.16**) which grows in intensity during all three Cat  $\rightarrow$  SQ oxidations, and has been assigned in structurally related complexes as a  $\text{Pt}(d\sigma) \rightarrow \text{SQ MLCT}$  band.<sup>[17]</sup>

Upon the first oxidation, the absorptions at  $33,000 \text{ cm}^{-1}$  and  $37,000 \text{ cm}^{-1}$  both grow. An absorbance at  $32,700 \text{ cm}^{-1}$  has been reported as an intraligand charge absorption in the  $\text{Pt}(\text{dppb})\text{Cl}_2$  starting material,<sup>[19]</sup> and this band is absent in related complexes which do not contain diphosphine ancilliary ligands.<sup>[17]</sup> Further addition of the second and third equivalents of oxidant in **Figures 4.15** and **4.16** show a continued increase in the intensity of the existing absorptions, however no isosbestic points were present in these spectra either.

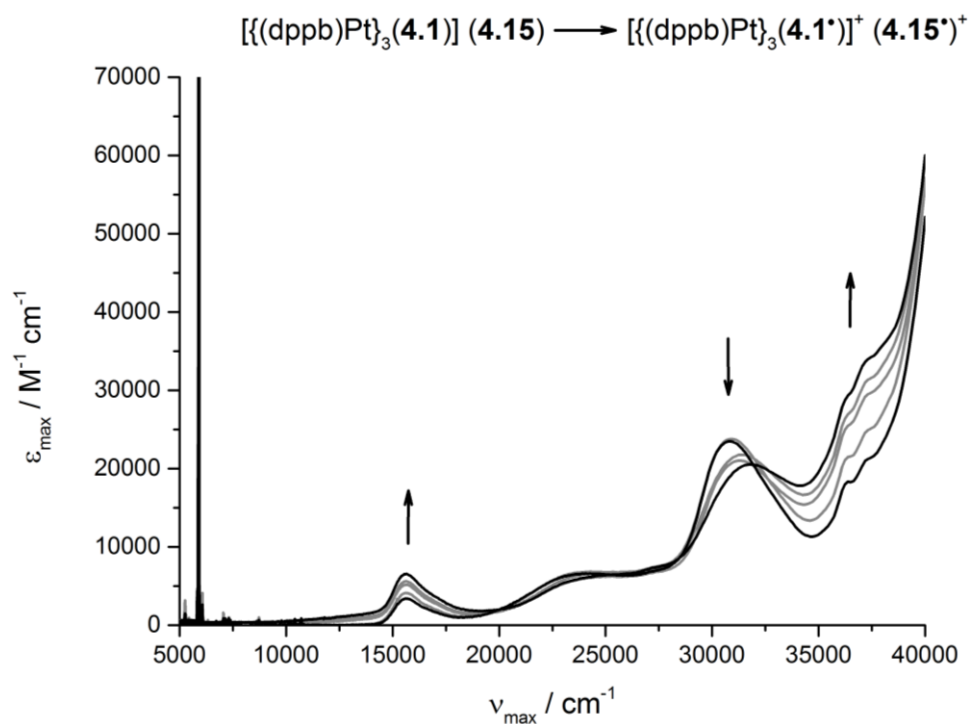


**Figure 4.17.** Oxidative titration of **4.15** to  $[\mathbf{4.15}^+]^+$  by addition of 1 equivalent of  $[\text{FeCp}_2]\text{PF}_6$  in 0.25 eq increments. The spectra of pure **4.15** and  $[\mathbf{4.15}^+]^+$  are displayed as black lines, with intermediate oxidations displayed as grey lines.

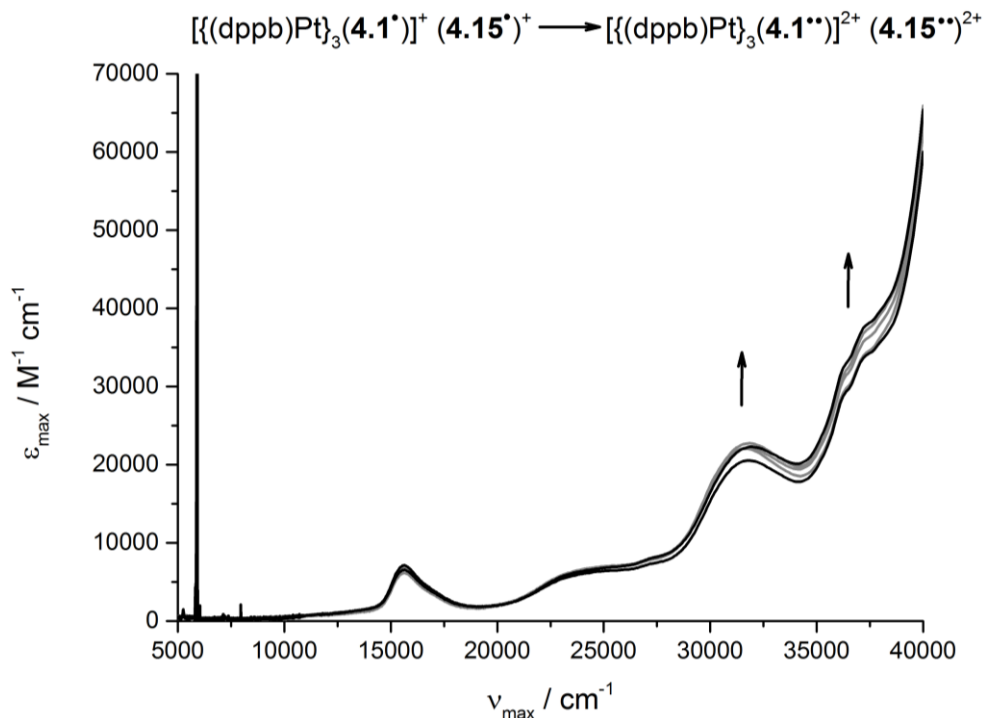


**Figure 4.18.** Oxidative titration of  $[\mathbf{4.15}^+]^+$  to  $[\mathbf{4.15}^{2+}]^{2+}$  by addition of 1-2 equivalents of  $[\text{FeCp}_2]\text{PF}_6$  in 0.25 eq increments. The spectra of pure  $[\mathbf{4.15}^+]^+$  and  $[\mathbf{4.15}^{2+}]^{2+}$  are displayed as black lines, with intermediate oxidations displayed as grey lines.

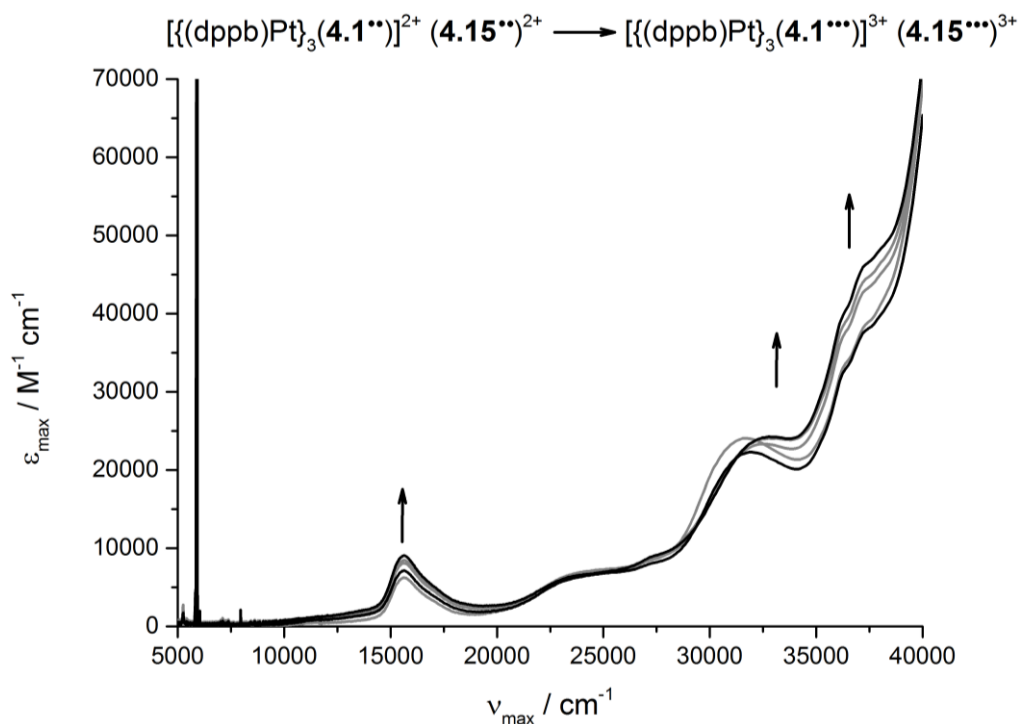


**Figure 4.19.** Oxidative titration of  $[4.15^{**}]^{2+}$  to  $[4.15^{***}]^{3+}$  by addition of 2-3 equivalents of  $[FeCp_2]PF_6$  in 0.25 eq increments. The spectra of  $[4.15^{**}]^{2+}$  and  $[4.15^{***}]^{3+}$  are displayed as black lines, with intermediate oxidation displayed as grey lines.

The high intensity narrow peak at  $5907\text{ cm}^{-1}$  arises from the vibrational structure of the  $CH_2Cl_2$  solvent used. **Figure 4.17** shows that **4.15** does not produce an IVCT when  $[4.15^*]^+$  is generated, however an isosbestic point is observed for this oxidation, indicating that no decomposition is taking place.

Further addition of the second and third equivalents of oxidant in **Figures 4.18** and **4.19** show a continued increase in the intensity of the existing absorptions, however no isosbestic point is present in these spectra. This therefore suggests that **4.15** is a class I complex with no electron transfer between the dioxolene rings, and there is likely rapid decomposition of the complex it is oxidised beyond the Cat/Cat/SQ form.

The intensity of the absorbance at  $15,673\text{ cm}^{-1}$  grows during all three Cat  $\rightarrow$  SQ oxidations, and has been previously been assigned in structurally related complexes as a  $Pt(d\sigma) \rightarrow SQ$  MLCT band.<sup>[17]</sup>

Upon the first oxidation, the absorption at 32,000 cm<sup>-1</sup> decays while the absorbance at 34,000 cm<sup>-1</sup> grows. An absorbance at 32,700 cm<sup>-1</sup> has been reported as an intraligand charge absorption in the Pt(dppb)Cl<sub>2</sub> starting material,<sup>[19]</sup> and this band is absent in related complexes which do not contain diphosphine ancilliary ligands.<sup>[17]</sup>

The new band which grows in at 34,000 cm<sup>-1</sup> is likely to be assigned to a SQ → diphosphine LL'CT as this has been previously reported in homologous mononuclear complexes.<sup>[17, 20]</sup>

**Table 4.5.** UV/vis/NIR data for the different redox states of **4.14** and **4.15** in CH<sub>2</sub>Cl<sub>2</sub> at 298 K.

Complex	$\nu_{\max}$ [10 <sup>3</sup> cm <sup>-1</sup> ] ( $\epsilon_{\max}$ [10 <sup>3</sup> M <sup>-1</sup> cm <sup>-1</sup> ])
<b>4.14</b>	37.7 (55.3), 32.6 (10.5)
[ <b>4.14</b> <sup>•+</sup>	37.9 (62.9), 32.6 (12.8), 27.9 (2.1)
[ <b>4.14</b> <sup>••2+</sup>	37.9 (69.0), 32.7 (15.9), 28.0 (3.7)
[ <b>4.14</b> <sup>•••3+</sup>	38.0 (76.0), 32.6 (18.3), 28.0 (4.6)
<b>4.15</b>	37.3 (21.2), 36.4 (18.3), 30.9 (23.5), 24.0 (6.6), 15.7 (3.4)
[ <b>4.15</b> <sup>•+</sup>	37.4 (34.2), 36.4 (29.3), 31.8 (20.5), 24.9 (6.4), 15.7 (6.5)
[ <b>4.15</b> <sup>••2+</sup>	37.3 (37.8), 36.4 (32.9), 31.9 (22.3), 24.0 (6.3), 15.7 (7.1)
[ <b>4.15</b> <sup>•••3+</sup>	37.3 (46.3), 36.4 (40.3), 32.8 (24.2), 24.0 (6.3), 15.6 (9.0)

#### 4.2.5 Spectroelectrochemical Analysis of 4.14

Spectroelectrochemical oxidation was carried out using an optically transparent electrode (OTTLE) cell containing a solution of **4.14** and 0.1 M <sup>n</sup>Bu<sub>4</sub>NPF<sub>6</sub> in CH<sub>2</sub>Cl<sub>2</sub> at 298 K. By observing the oxidation potentials elucidated by the CV measurements, it is possible to electrochemically generate [**4.14**<sup>•+</sup>, as shown in **Figure 4.20**.

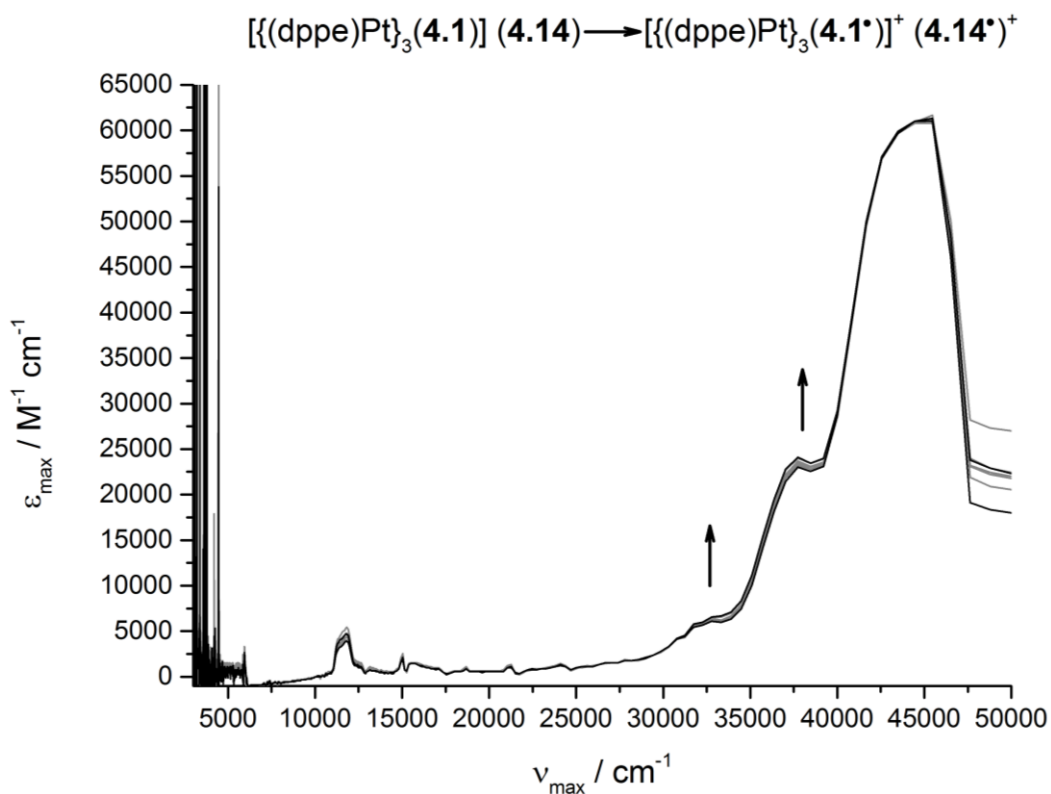


**Figure 4.20.** UV-vis/NIR spectroelectrochemical data for the first oxidation of a **4.14** to **[4.14]<sup>+</sup>** in a 0.1 M <sup>n</sup>Bu<sub>4</sub>NPF<sub>6</sub> solution in CH<sub>2</sub>Cl<sub>2</sub> at 298 K. The spectra of pure **4.14** and **[4.14]<sup>+</sup>** are displayed in black, with intermediate spectra displayed in grey.

The SEC of **[4.14]<sup>+</sup>** does not show the appearance of an IVCT, corroborating what was observed in the chemical titrations. Despite this, the other higher energy peaks are retained, showing a gradual increase in absorbance as the oxidised species is generated. The peak at 12,000  $\text{cm}^{-1}$  is an artefact produced by a change of diffraction grating.

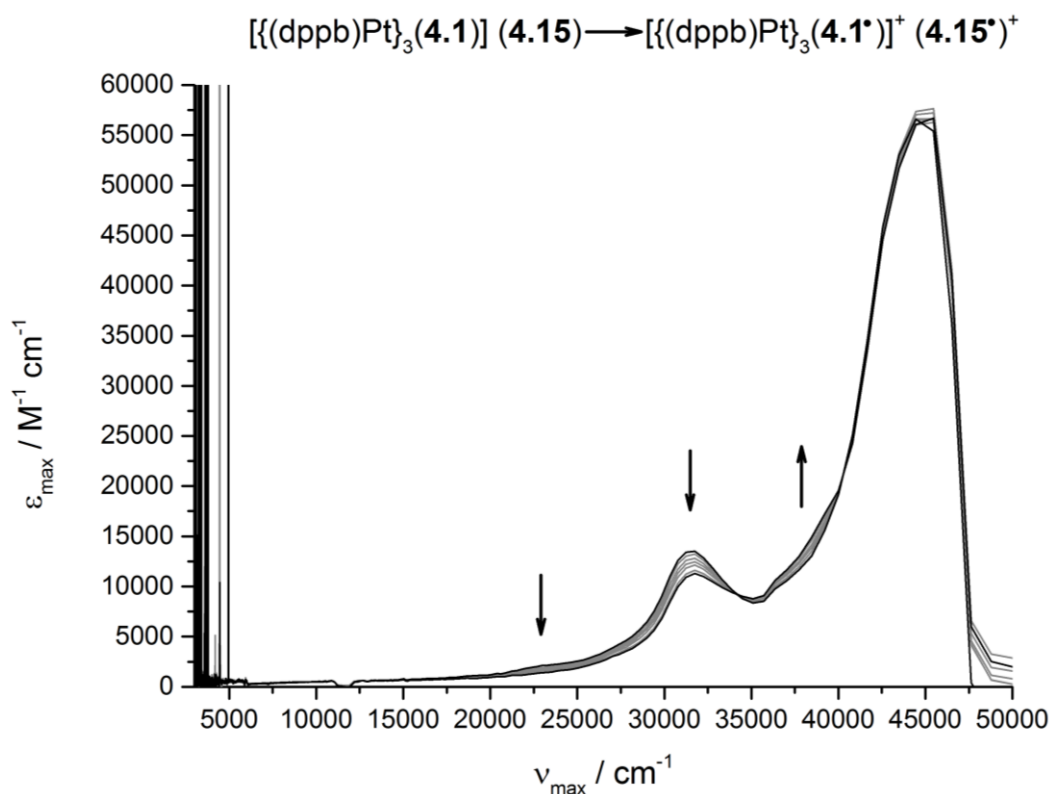


**Figure 4.21.** UV-vis/NIR spectroelectrochemical data for the first oxidation of a **4.15** to  $[4.15^*]^+$  in a 0.1 M  $n\text{Bu}_4\text{NPF}_6$  solution in  $\text{CH}_2\text{Cl}_2$  at 298 K. The spectra of pure **4.15** and  $[4.15^*]^+$  are displayed in black, with intermediate spectra displayed in grey.

As with the SEC measurements of **4.14**, the SEC of  $[4.15^*]^+$  does not show the appearance of an IVCT, however the other higher energy peaks are retained with good isosbesticity (**Figure 4.21**). The dip in absorbance at  $12,000\text{ cm}^{-1}$  is an artefact produced by the change of diffraction grating.

**Table 4.6.** Spectroelectrochemical UV/vis/NIR data for the different redox states of **4.14** and **4.15** in  $\text{CH}_2\text{Cl}_2$  at 298 K.

Complex	$\nu_{\text{max}} (10^3\text{ cm}^{-1})$ ( $\epsilon_{\text{max}} (10^3\text{ M}^{-1}\text{ cm}^{-1})$ )
<b>[4.14]</b>	44.4 (60.1), 37.7 (23.2), 32.8 (6.2)
<b>[4.14]<sup>+</sup></b>	44.4 (61.0), 37.7 (24.0), 32.8 (6.6)
<b>[4.15]</b>	45.5 (57.2), 36.4 (10.0)(sh), 31.5 (13.2), 23.0 (1.9)
<b>[4.15]<sup>+</sup></b>	44.4 (56.0), 37.0 (11.6)(sh), 31.7 (11.3)

---

#### 4.2.6 EPR Measurements of Chemically Oxidised Mixed-Valent Radical Cations of 4.14 and 4.15

The following S and X band EPR measurements were carried out at the University of Manchester with the aid of Dr. Amgalanbataar Baldansuren. The singly oxidised samples were prepared by addition of a CH<sub>2</sub>Cl<sub>2</sub> solution of one equivalent of [FeCp<sub>2</sub>]PF<sub>6</sub> to a CH<sub>2</sub>Cl<sub>2</sub> solution of the complex in question, followed by (in the case of the frozen solution spectra) the immediate cooling of the sample in liquid nitrogen. The data was collected as soon as possible after the addition of the oxidant to try to minimise decomposition of the radical cation.

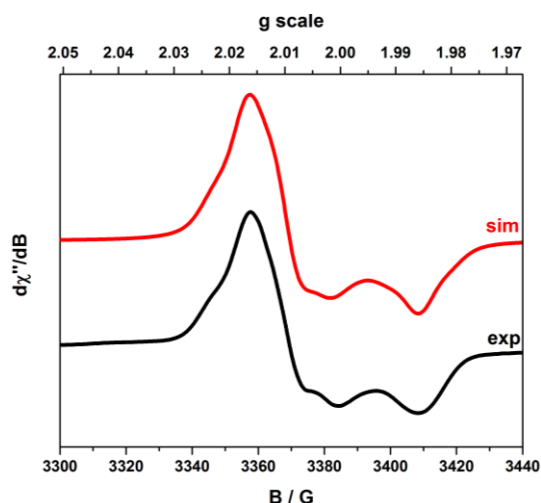


**Figure 4.22.** X-band EPR spectra of  $[\{(dppe)Pt\}_3(4.1')^+] [4.14']^+$  in CH<sub>2</sub>Cl<sub>2</sub> at 150 K (frozen solution). Experimental data displayed in black, simulation displayed in red.

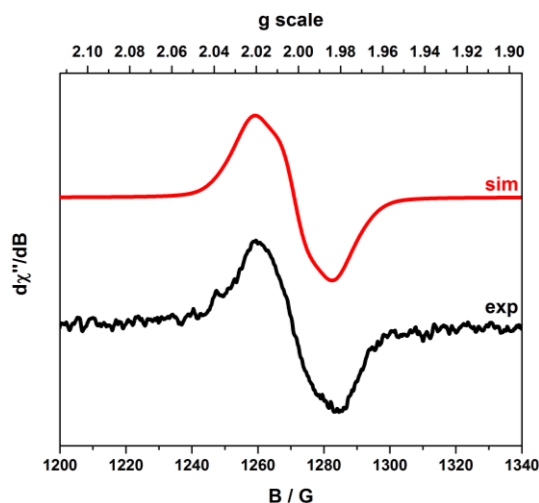


**Figure 4.23.** S-band EPR spectra of  $[(dppe)Pt]_3(4.1')^+ [4.14']^+$  in  $CH_2Cl_2$  at 45 K (frozen solution). Experimental data displayed in black, simulation displayed in red.

The S and X band spectra of  $[4.14']^+$  could not be obtained at 300 K, likely due to rapid decomposition of the radical cation at this temperature. Upon cooling to 150 K, a rhombic spectrum with  $g_1 = 2.009$ ,  $g_2 = 2.0155$ , and  $g_3 = 1.9850$  and hyperfine coupling  $A(^{195}Pt) = 60 \times 10^{-4} \text{ cm}^{-1}$  and  $^{31}P$  hyperfine coupling of  $A(^{31}P) = 8 \times 10^{-4} \text{ cm}^{-1}$  was extracted from the simulation (**Figure 4.22**), marginally higher figures than  $[4.15']^+$ . No S band signal was observed at 150 K, however reducing the temperature to 45 K allowed a weak signal to be detected due to the apparent increased stability of the radical at low temperature (**Figure 4.23**).

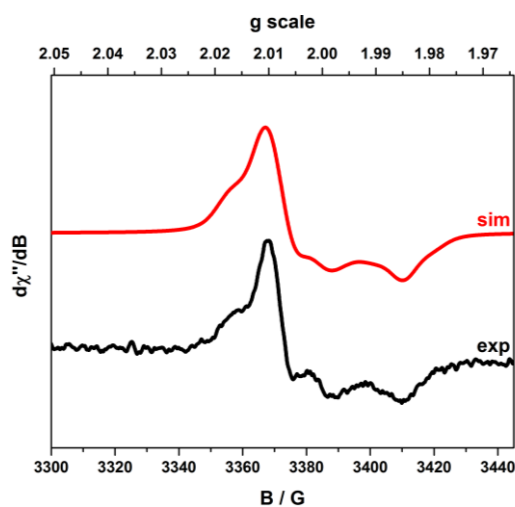


**Figure 4.24.** X-band EPR spectra of  $[(dppb)Pt]_3(4.1')^+ [4.15']^+$  in  $CH_2Cl_2$  at 150 K (frozen solution). Experimental data displayed in black, simulation displayed in red.

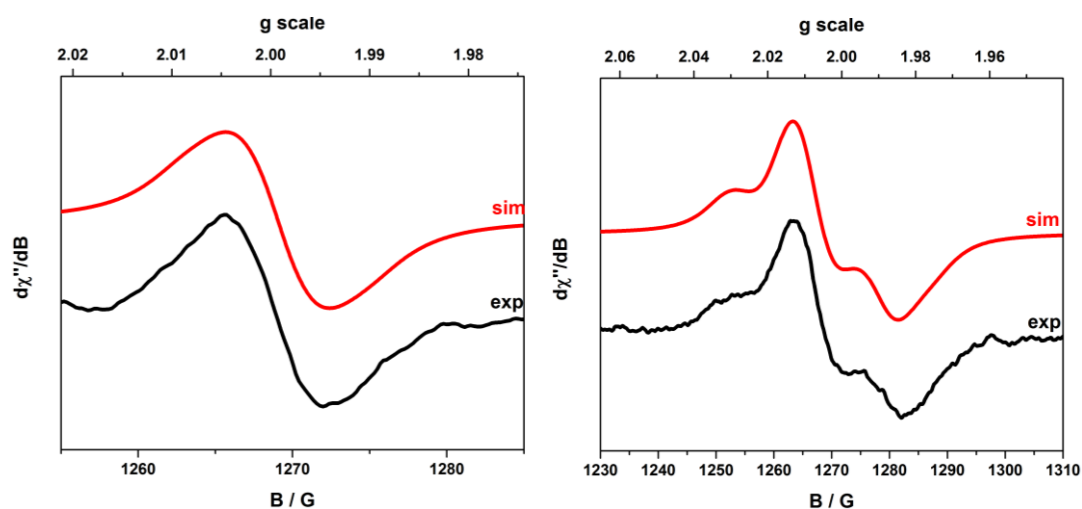


**Figure 4.25.** S-band EPR spectra of  $[(\text{dppbPt})_3(\mathbf{4.1}')^+] [\mathbf{4.15}'^+]^+$  in  $\text{CH}_2\text{Cl}_2$  at (left) 300 K and (right) 45 K (frozen solution). Experimental data displayed in black, simulation displayed in red.

The S band spectrum of  $[\mathbf{4.15}'^+]^+$  at 300 K shows an isotropic signal with  $g = 2.006$ , and hyperfine coupling of  $A(^{195}\text{Pt}) = 20 \times 10^{-4} \text{ cm}^{-1}$  and  $A(^{31}\text{P}) = 5 \times 10^{-4} \text{ cm}^{-1}$  (**Figure 4.25**). Upon cooling to 45 K, a rhombic spectrum with hyperfine coupling to  $^{195}\text{Pt}$  is observed.  $A(^{195}\text{Pt}) = 60 \times 10^{-4} \text{ cm}^{-1}$ , a similar figure to  $[\mathbf{4.14}'^+]^+$ . A spectrum could not be obtained on the X band at 300 K, however a signal was obtained when the sample was cooled to 150 K (**Figure 4.24**).  $^{31}\text{P}$  hyperfine coupling ( $A(^{31}\text{P}) = 7 \times 10^{-4} \text{ cm}^{-1}$ ) was extracted from the X-band simulation.

**Table 4.7.** Extracted X-band EPR  $g$  values for complexes  $[\mathbf{4.14}'^+]^+$  and  $[\mathbf{4.15}'^+]^+$  in  $\text{CH}_2\text{Cl}_2$  in units of  $10^{-4} \text{ cm}^{-1}$ .

Complex	300 K	150 K		
	$g_{\text{iso}}$	$g_1$	$g_2$	$g_3$
$[\mathbf{4.14}'^+]^+$	-	2.0090 <sup>†</sup>	2.0155 <sup>†</sup>	1.9850 <sup>†</sup>
$[\mathbf{4.15}'^+]^+$	-	2.0060	2.0100	1.9840

<sup>†</sup> Spectrum recorded at 45 K rather than 150 K.

**Table 4.8.** Extracted X-band EPR hyperfine and superhyperfine coupling constants to one  $^{195}\text{Pt}$  nucleus and two  $^{31}\text{P}$  nuclei for complexes  $[\mathbf{4.14}^{\bullet}]^+$ - $[\mathbf{4.15}^{\bullet}]^+$  in  $\text{CH}_2\text{Cl}_2$  in units of  $10^{-4} \text{ cm}^{-1}$ .

Complex	300 K	150 K		
	$\{A_{\text{iso}}(^{195}\text{Pt})\}$ $\{A_{\text{iso}}(^{35}\text{P})\}$	$\{A_1(^{195}\text{Pt})\}$ $\{A_1(^{35}\text{P})\}$	$\{A_2(^{195}\text{Pt})\}$ $\{A_2(^{35}\text{P})\}$	$\{A_3(^{195}\text{Pt})\}$ $\{A_3(^{35}\text{P})\}$
$[\mathbf{4.14}^{\bullet}]^+$		(60) (8) <sup>†</sup>	(60) (8) <sup>†</sup>	(60) (8) <sup>†</sup>
$[\mathbf{4.15}^{\bullet}]^+$	(20) (5) <sup>[a]</sup>	(62) (7)	(62) (7)	(62) (7)

<sup>†</sup> Spectrum recorded at 45 K rather than 150 K.

[a] Hyperfine coupling extracted from S band measurements.

### 4.3 Summary, Trends, Conclusions and Future Work

To summarise, the results presented in this section detail the spectroscopic characterisation by CV, EPR, UV/vis of two *tris*-dioxolene CTC derivative complexes of Pt(II).

The UV-vis/NIR oxidative titrations do not show the expected low energy IVCT band indicative of electron transfer between the dioxolene rings for the oxidised forms. This was not predicted, as structurally similar complexes which have been previously investigated in the group exhibited class II/III electron transfer behaviour.<sup>[10]</sup> It can therefore be concluded that **4.14** and **4.15** are strictly class I complexes with localised semiquinone radicals, similar to the spiroconjugated complexes **3.5** and **3.6**. Although no crystal structure of the complexes were obtained, the crystal structure of the free ligand shows that the bowl-shaped cavity of **4.1** has an average dihedral angle of  $117.3^\circ$ , which is wider than the  $110.3^\circ$  angle present in underivatized CTC. This geometry is not expected to change substantially upon complexation with Pt. The increase in dihedral angle places the dioxolene  $\pi$  orbitals further away from each other, reducing orbital overlap and thus preventing electron transfer.

Both complexes **4.14** and **4.15** show poor stability when not protected from air and moisture. Upon oxidation to  $[\mathbf{4.14}^{\bullet}]^+$  rapid decomposition occurs, as seen in both in non-isobesticity of the UV-vis/NIR spectra and the very weak or non-existent signals observed by EPR, which made analysis of this species difficult.  $[\mathbf{4.15}^{\bullet}]^+$  is rather more stable however, indicating that the steric protection provided by the ligand had the

---

desired effect of preventing the fast decomposition which hindered characterisation of the homologous CTC complex.<sup>[10]</sup>

The EPR measurements undertaken confirm that each complex generates a radical cation after addition of  $[\text{FeCp}_2]\text{PF}_6$ . The complexes have similar  $g$  values to each other,  $g_{\text{av}} = 2.003$  for  $[\mathbf{4.14}^{\bullet+}]^+$  and  $g_{\text{av}} = 2.000$  for  $[\mathbf{4.15}^{\bullet+}]^+$ . Hyperfine couplings, when observed, were of very similar values between all of the complexes,  $60 \times 10^{-4} \text{ cm}^{-1}$  for the  $^{195}\text{Pt}$  coupling, and  $8 \times 10^{-4} \text{ cm}^{-1}$  for the  $^{31}\text{P}$  coupling in  $[\mathbf{4.14}^{\bullet+}]^+$ , and  $62 \times 10^{-4} \text{ cm}^{-1}$  for the  $^{195}\text{Pt}$  coupling, and  $7 \times 10^{-4} \text{ cm}^{-1}$  for the  $^{31}\text{P}$  coupling in  $[\mathbf{4.15}^{\bullet+}]^+$ . Hyperfine coupling is only seen to one  $^{195}\text{Pt}$  nucleus, which is understandable given the localised nature of the radical.

## 4.4 Towards Coordination Polymers

### 4.4.1 Introduction

There are relatively few examples of coordination polymers containing a redox active dioxolene unit for which single crystal X-ray structures have been obtained. Of these, three are either linear or zig-zag 1D chains (**Figure 4.26**), and only one is 2D. No 3D coordination polymers of this type have been reported in the literature.<sup>[21]</sup>

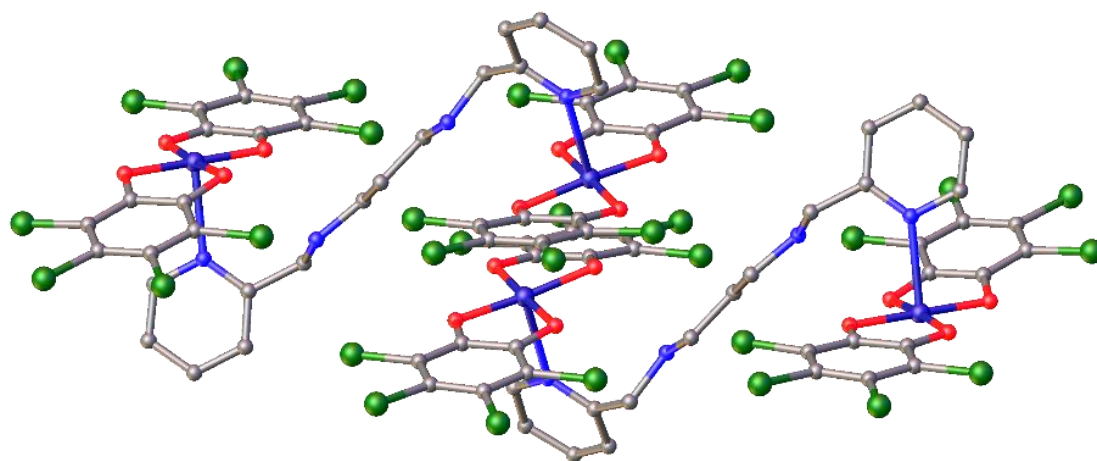


**Figure 4.26.** Single crystal X-ray structure of  $[\text{Mn}_2(\text{NLN})(\text{Cl}_4\text{-diox})_2]_n$  at 180 K. Image reproduced from Banerjee *et al.*<sup>[22]</sup>

This 1D coordination polymer also undergoes thermal VT transition in the temperature range of 298-338 K, described by **Scheme 4.14**.



**Scheme 4.14.** Thermal VT transition of  $[\text{Mn}^{\text{III}}(\text{Cat})_2]_2$ .

The first reported 1D VT coordination polymer of Co was  $[\text{Co}(\text{pyz})(3,6\text{-DBSQ})(3,6\text{-DBdiox})]_n$  which is formed out of individual chains of repeating metal-pyrazine units, with the dioxolene functionalities coordinated in an equatorial fashion (**Figure 4.27**).<sup>[23]</sup>

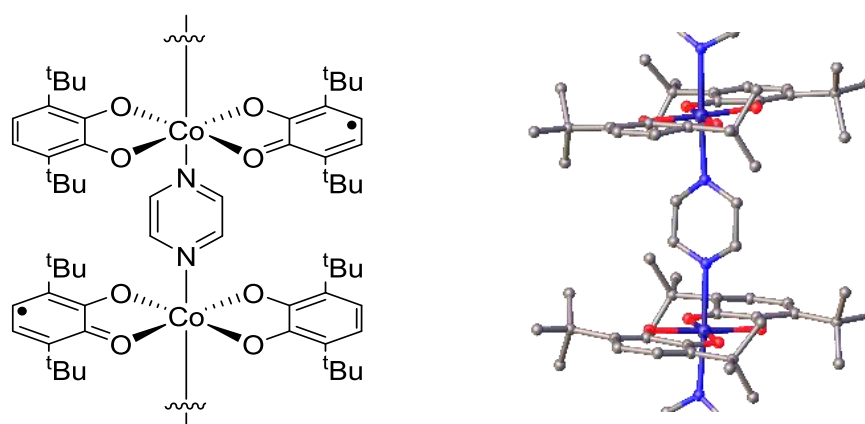


**Figure 4.27.** A section of repeating structure of  $[\text{Co}(\text{pyz})(3,6\text{-DBSQ})(3,6\text{-DBdiox})]_n$ .

This polymer undergoes VT transition from HS-Co(II)-SQ to LS-Co(III)-Cat between 350-5 K. Coordination polymers of this type (variations typically involve placement of the tertiary butyl groups on the dioxolene ring) undergo thermal VT transition between  $(\text{LS-Co(III)-Cat})_n$  and  $(\text{HS-Co(II)-SQ})_n$  without hysteresis. Upon irradiation with light a reversible photomechanical distortion occurs as a consequence of VT transition, leading to a 6% change in polymer length as a consequence of change in Co-N bond length.

Following this, subsequent 1D coordination polymers were found using similar synthetic methods and replacing the pyrazine linker with one of a variety of ditopic *bis*(pyridyl) ligands. These all display thermal VT transition above 100 K. Linear pyridyl linkers lead to straight 1D chains, whereas bent linkers such as dpq (1,2-di-4-pyridinyl-1,2-ethanediol) lead to 1D zig-zag chains (**Figure 4.28**).

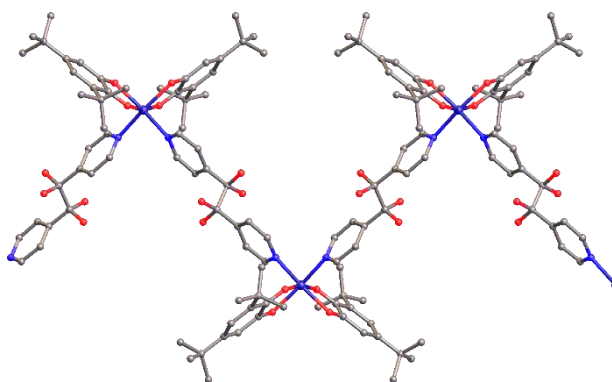


**Figure 4.28.** 1D zig-zag coordination polymer reported by Boskovic.<sup>[23]</sup>

Only one example of a 2D VT coordination polymer has been reported, that being  $[\text{Co}(\text{tpom})(3,5\text{-DBSQ})(3,5\text{-DBdiox})]_n$  (**Figure 4.29**).<sup>[24]</sup>

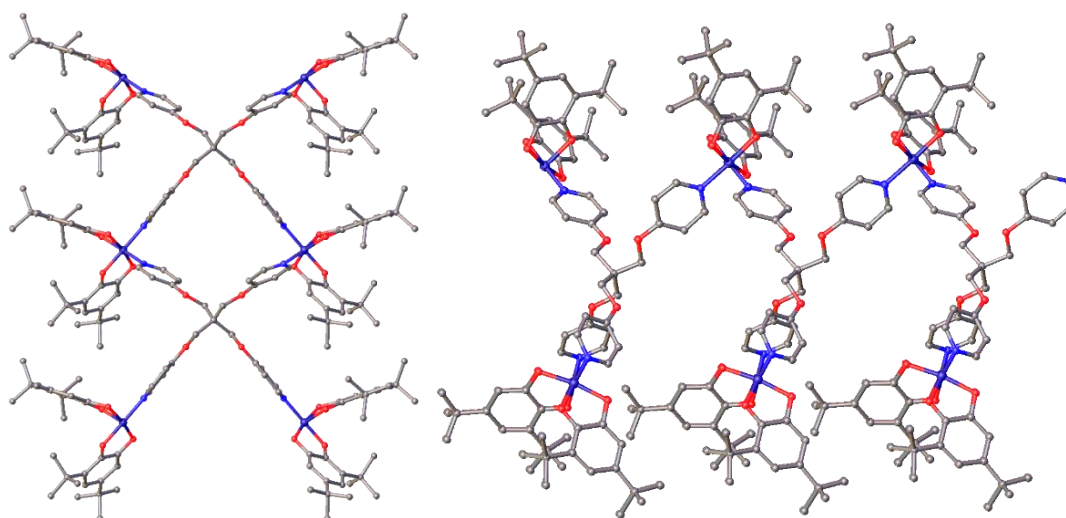


**Figure 4.29.** Two views of  $[\text{Co}(\text{tpom})(3,5\text{-DBSQ})(3,5\text{-DBdiox})]_n$  showing its two dimensional structure.<sup>[24]</sup>

This complex may undergo a thermal and photo-induced VT transition, although in the thermal case it is observed that solvent molecules incorporated within the structure are lost upon heating, leading to a very gradual transition. The ancillary ligand is flexible about the ether moiety, and hence there is little evidence of intramolecular cooperativity.

It is useful when describing metal-organic supramolecular assemblies to classify ligands as either linkers or capping groups. A linker will bridge two or more metal atoms, whereas a capping ligand will occupy vacant coordination sites without

increasing the interconnectivity of the structure. 4,4'-bipyridine is an example of a linear linker, whereas pyridine is an example of a capping group, both of which coordinate through pyridyl nitrogen atom(s).

In the field of valence tautomeric coordination polymers, almost all reported compounds contain some combination of aromatic N-donor ligands and catecholates. A simplified way of visualising the possibilities that arise is shown in **Figure 4.30**.

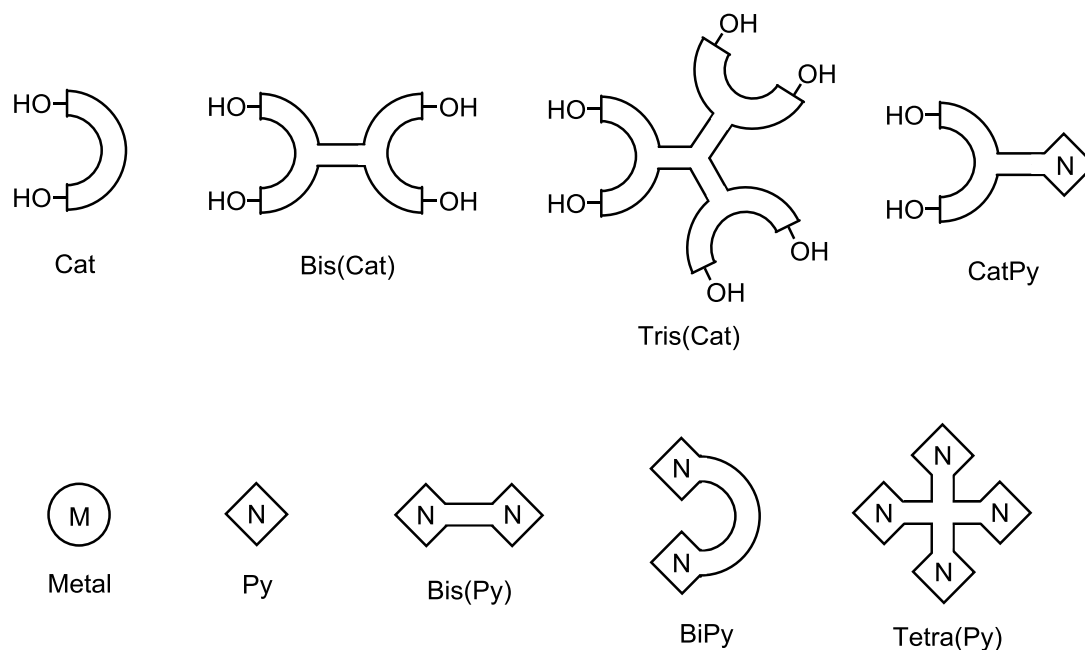


**Figure 4.30.** Simplified cartoon representations of the types of dioxolene and N-donor ligands which have been employed in the synthesis of metal-dioxolene coordination polymers.

Using this simplified depiction, the 1D coordination polymers reported by both Pierpont and Banerjee would be described as  $[M_2\{(Bis(Py))(Cat)_2\}]$ , as the repeat unit contains one metal ion, two mono-catecholates, and a *bis*pyridyl crosslinking ligand. The 2D coordination polymer reported by Zheng would be described as  $[M(Tetra(Py))(Cat)_2]$  in this notation. It is noteworthy that these reported coordination polymers have several structural similarities. In particular, they all contain pendant mono-dioxolene groups coordinated to the metal, while the linking group is a di-, or tetra-dentate aromatic N-donor.<sup>[25]</sup>

---

Attempts have been made by other researchers to incorporate catechol linking groups (e.g. ligands of “Bis(Cat)” class),<sup>[26]</sup> or mixed-functionality ligands such as “CatPy” (see **Figure 4.31**).<sup>[27]</sup>

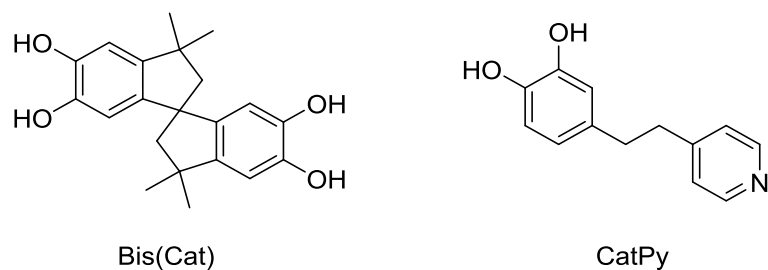


**Figure 4.31.** Bis(Cat) and CatPy type linking groups that have been used to form valence tautomeric coordination polymers.

Several coordination polymers containing these ligands have been reported, however their crystal structures remain elusive.<sup>[21]</sup> The polymers obtained are generally darkly coloured, highly insoluble, and amorphous or nanoparticulate in structure. Without single crystal or solution phase data, full characterisation of these products is difficult, and this remains a significant challenge to the further investigation of such compounds.

Triptycenes and spiro derivatives possess intrinsic geometry that can in principle lead to a large number of polymeric structures, such as simple linear 1D zig-zag chains, planar/rippled 2D sheets, or hollow 2D honeycomb networks formed from alternating triangular nodes. Assemblies of this type should show redox activity similar to that of discrete complexes, with the potential for the manifestation of additional phenomena such as intramolecular cooperativity. When low valent metal ions are incorporated into such frameworks, the accumulation of negative charge may be prevented by the introduction of neutral co-ligands. While many of these networks are expected to oxidise upon exposure to air, electrochemical oxidation and chemical doping are also expected to yield interesting mixed-valent forms exhibiting spin-mobility. The host:guest chemistry of these complexes is likely to be different from their redox-inactive analogues, with charge-transfer assemblies being favoured.

The catechol ligands that were discussed in Chapters 2, 3 and 4 can be classified according to the above naming system (**Figure 4.31**). Ligands **2.18** and **3.9** are of Bis(Cat) type, whereas **2.5** and **4.1** are of Tris(Cat) type. The spiroconjugated ligand

**2.18** has previously been used to produce valence tautomeric coordination polymers,<sup>[18]</sup> **2.5** and **3.9** have thus far not been investigated for this application. As these ligands have been determined to have class II/III electron transfer character in their oxidised forms, and they possess geometries which should favour polymeric crosslinking, this following section will discuss attempted syntheses of coordination polymers incorporating them.

#### 4.4.2 Synthesis

Given that triptycene **2.5** possesses a trigonal geometry, it could theoretically coordinate in a 1:1 ratio with a trigonal antiprismatic metal ion to produce a 2D coordination polymer adopting a “honeycomb” structure ( $[M(\text{Tris}(\text{Cat}))]$  by the aforementioned naming scheme) (**Figure 4.32**). Mo(IV) exhibits trigonal antiprismatic geometry, therefore this metal was used in the first synthetic attempts to produce such a polymer.

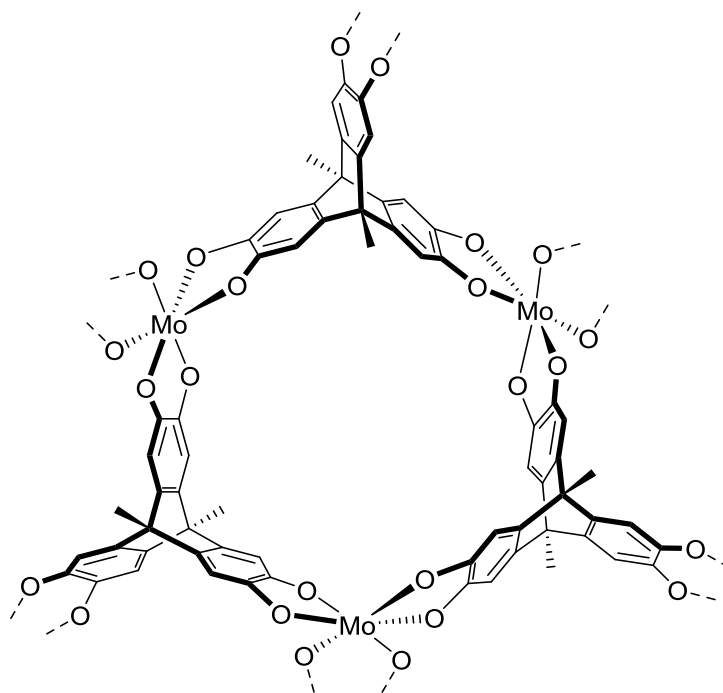
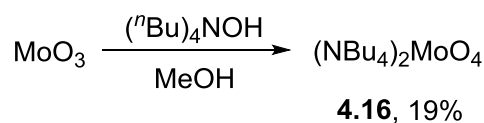


**Figure 4.32.** Proposed 2D honeycomb structure formed from the reaction of **2.5** and Mo(VI).

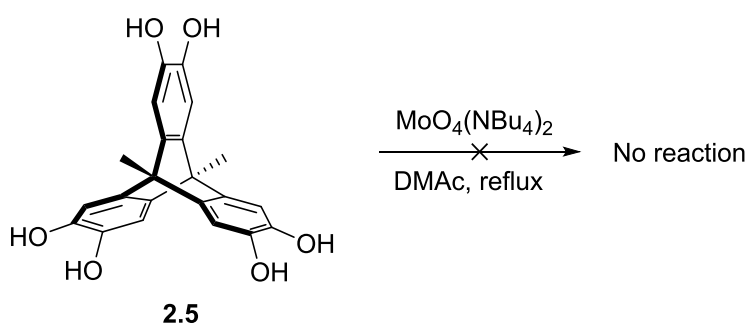
There are two possible synthetic routes to this product (**Schemes 4.16** and **4.19**). The first is to react the tris(catechol) form of triptycene **2.5** with an oxidised form of Mo,

such as  $(\text{NBu}_4)_2\text{MoO}_4$ .  $(\text{NBu}_4)_2\text{MoO}_4$  was synthesised from  $\text{MoO}_3$  via the following reaction (**Scheme 4.15**).



**Scheme 4.15.** Synthesis of tetrabutylammonium molybdate **4.16**.

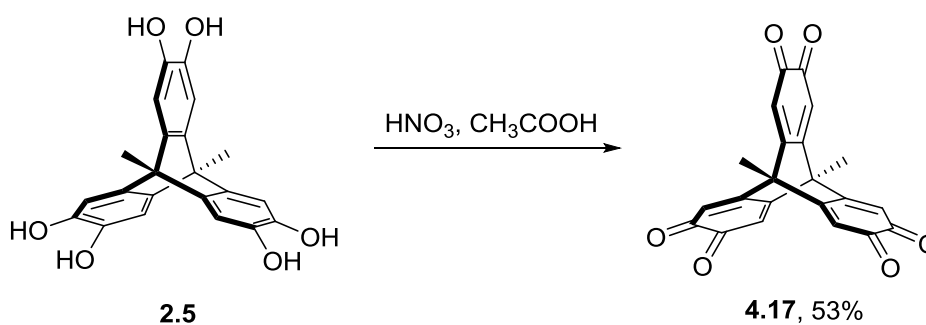
This reaction between the **2.5** and tetrabutylammonium molybdate did not proceed, and only starting material was observed after refluxing the mixture for 18 hours (**Scheme 4.16**).



**Scheme 4.16.** Unsuccessful reaction between **2.5** and tetrabutylammonium molybdate.

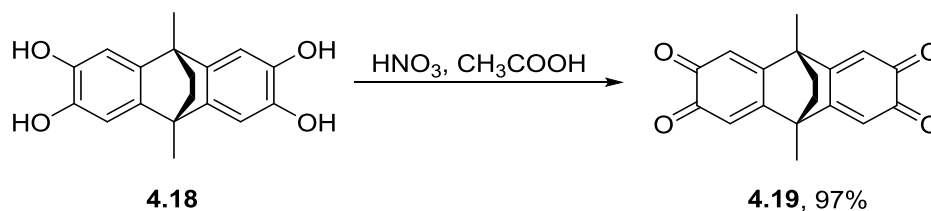
Consequently, the alternative route was attempted. This involves reaction the oxidised tris(BQ) form of **2.5** with a reduced compound of Mo, such as  $\text{Mo}(\text{CO})_6$ .

Chemical oxidation of catechols can be achieved by reaction with a mixture of nitric acid and acetic acid<sup>[28]</sup> (**Scheme 4.17**).



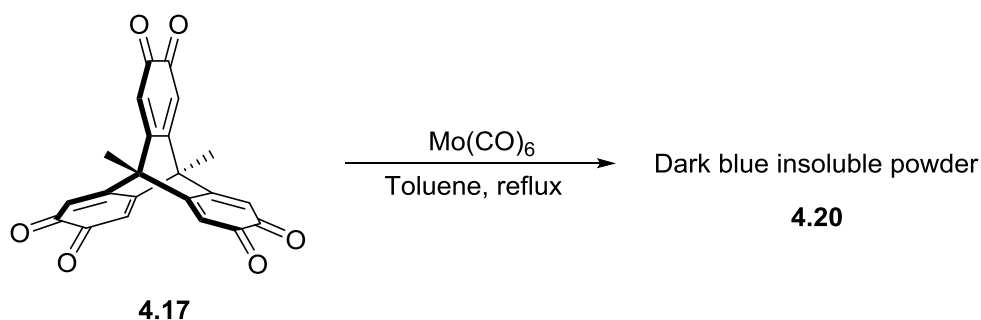
**Scheme 4.17.** Oxidation of **2.5** to afford the tris(BQ) form, **4.17**.

The bis(BQ) form of H<sub>2</sub>thea, a class II ligand similar to **2.18** that has been reported in previous work in the Halcrow group,<sup>[29]</sup> was also synthesised using the same procedure (**Scheme 4.18**).



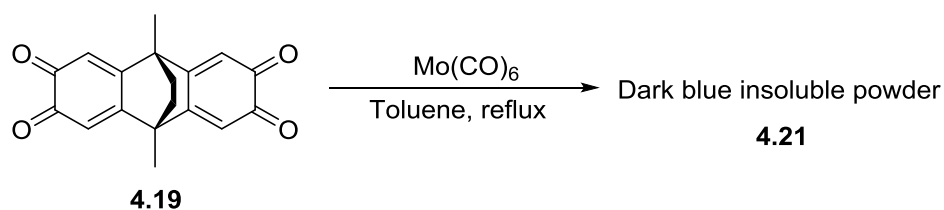
**Scheme 4.18.** Oxidation of H<sub>4</sub>thea to afford the bis(BQ) form, **4.19**.

**4.17** was then reacted with Mo(CO)<sub>6</sub>, which precipitated a dark blue insoluble powder **4.20** after 18 hours (**Scheme 4.19**).



**Scheme 4.19.** Reaction of the tris(BQ) ligand **4.17** with molybdenum hexacarbonyl.

The analogous reaction was also carried out with ligand **4.19** (**Scheme 4.20**).



**Scheme 4.20.** Reaction of the bis(BQ) ligand **4.19** with molybdenum hexacarbonyl.

The products of these reactions, **4.20** and **4.21**, have proven difficult to characterise, as they are insoluble in all commonly available solvents. This is not entirely unexpected, as an extended network would need to break up into smaller monomeric or oligomeric units to become solubilised. Unfortunately, the precipitates formed directly from the reactions are not monocrystalline, and hence single-crystal X-ray

---

diffraction studies could not be carried out to elucidate their structures. The powder X-ray pattern for **4.20** was obtained, which confirms that the product is amorphous (**Figure 4.33**).

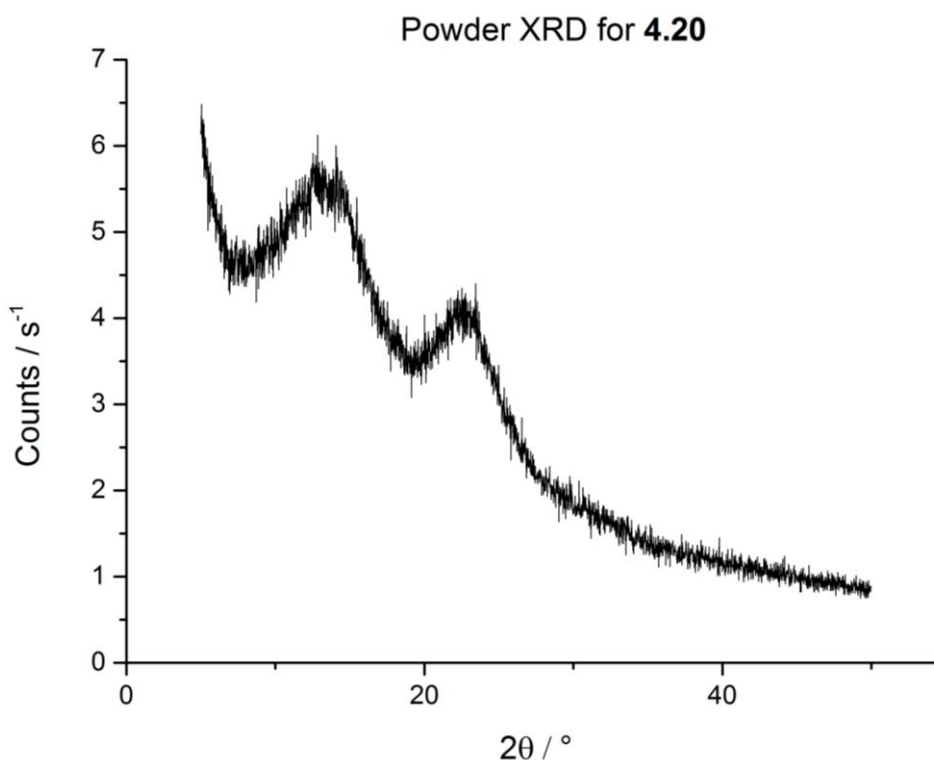


**Figure 4.33.** Powder X-ray pattern for **4.20**.

Single crystals of **4.20** and **4.21** could not be obtained by recrystallization, vapour diffusion, layering or sublimation methods as these all invariably produced similar amorphous powders or films unsuitable for single crystal X-ray diffraction. Elemental analysis of **4.20** and **4.21** showed that they contain 52.60% C and 5.60% H (**4.20**) and 48.40 % C and 4.20 % H (**4.21**) respectively. These ratios which cannot be fitted to any reasonable single stoichiometric product, as a one-to-one ratio of metal and ligand would be expected to contain 56.43 % C 2.58 % H (**4.20**) and 55.40 % C and 3.62 % H (**4.21**) respectively.

Concerns over the possibility of some quantity of starting material being present in the product were investigated by obtaining the IR spectra of **4.17** and **4.20**. If starting material were present, a very broad carbonyl stretching frequency would be observed in the product, corresponding to Mo(CO)<sub>6</sub> (**Figure 4.36**).

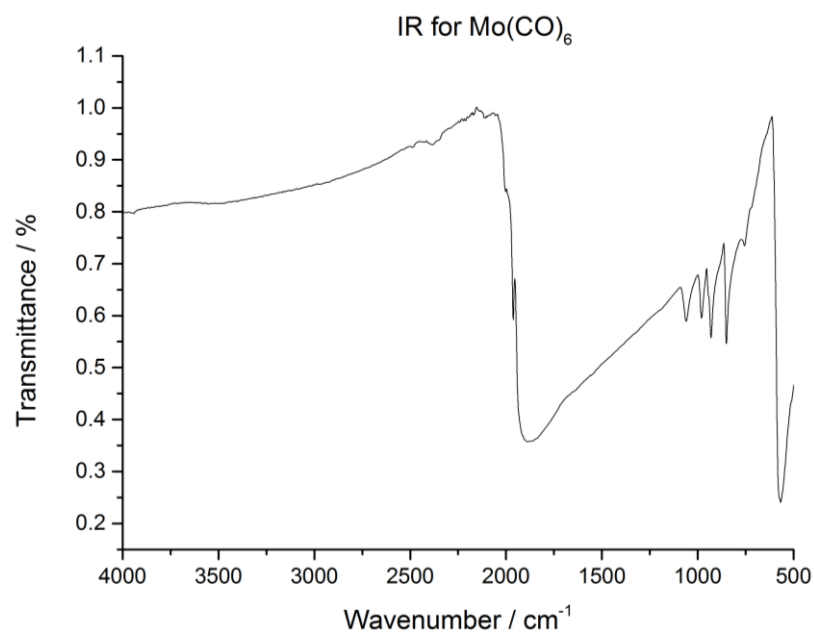


**Figure 4.34.** IR spectrum (solid state) of Mo(CO)<sub>6</sub>.

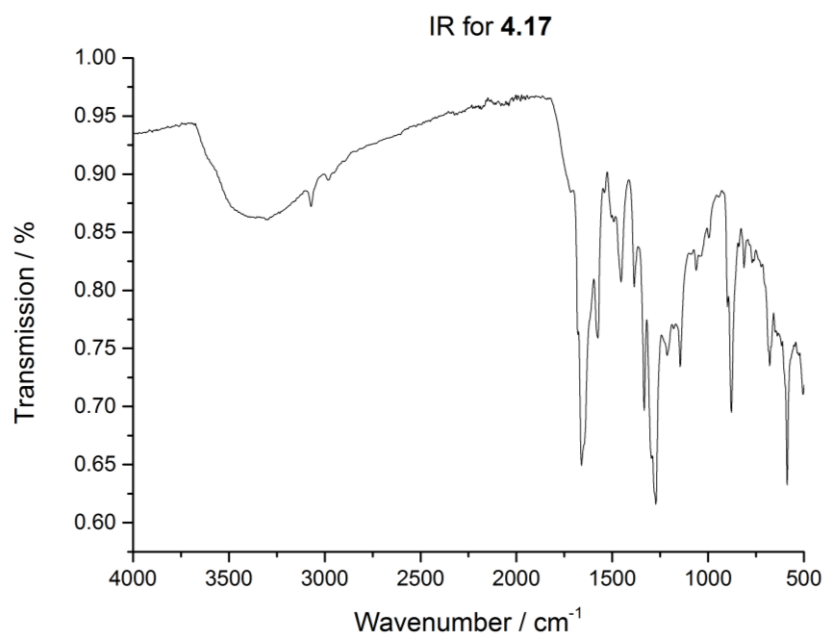


**Figure 4.35.** IR spectrum of 4.17.

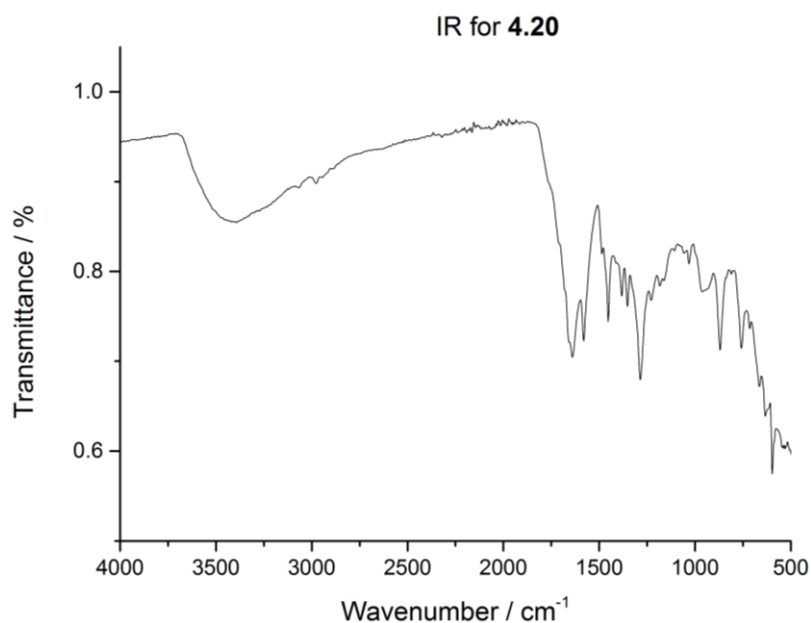
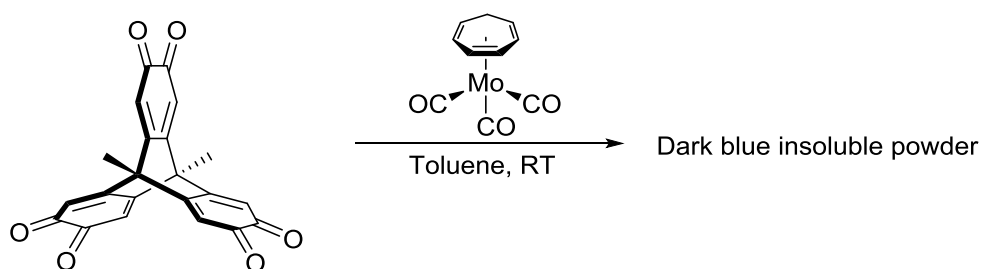


**Figure 4.36.** IR spectrum for **4.20**.

The IR spectrum for **4.20** (**Figure 4.36**) shows no indication that excess  $\text{Mo}(\text{CO})_6$  is present, and has a different set of peaks to the pure ligand **4.17**. It is difficult to provide any definitive determination of the structure based purely on the IR spectrum however.

In a final attempt to produce a monocrystalline product, a more reactive Mo(VI) source, cycloheptatrienyl molybdenum tricarbonyl was used (**Scheme 4.21**). The increased reactivity of this compound allows the reaction to be undertaken at room temperature rather than reflux.



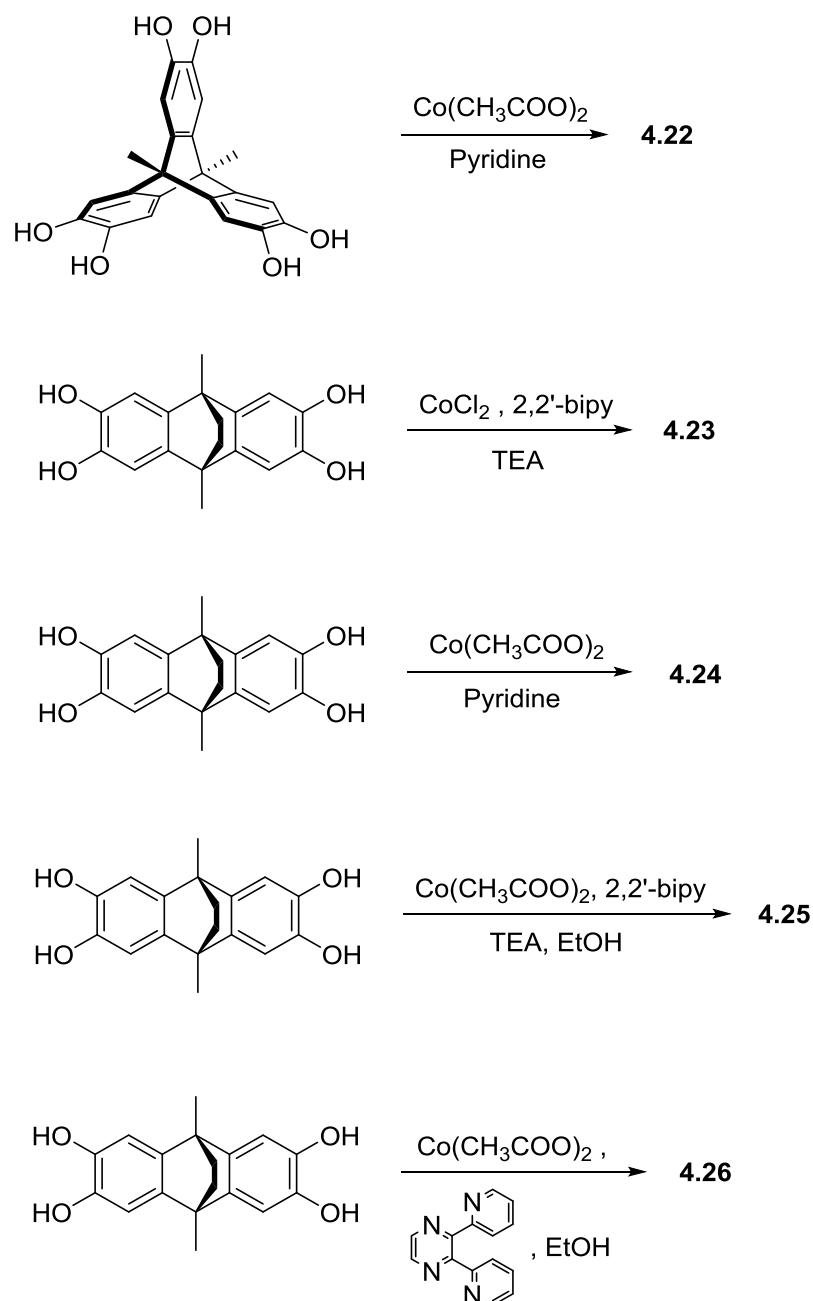
**Scheme 4.21.** Reaction between **4.17** and cycloheptatrienyl molybdenum tricarbonyl.

Unfortunately, the product obtained was comparable to the previous reactions, precluding characterisation.

---

One conclusion that may be drawn from these attempts at characterisation is that there may be multiple products being formed. Molybdenum may adopt several bridging or terminal oxo forms<sup>[30]</sup>, and Pierpont has observed multiple examples of these possibilities being formed in similar reactions involving other benzoquinone ligands<sup>[31]</sup>, with the obtained products being highly dependent on the amount of oxygen or water the reaction is exposed to. Consequently, attempts to synthesise the molybdenum polymer were abandoned in favour of different metals.

Cobalt is by far the most commonly used metal across all valence tautomeric catecholate complexes, and only cobalt and manganese have ever been reported for single-crystallographically characterised polymers. It was therefore decided that cobalt was the most likely to successfully form crystalline products, and reactions were attempted following similar conditions to those used by Boskovic<sup>[23]</sup>, Ruiz-Molina<sup>[27, 32]</sup>, and Zheng<sup>[24]</sup> (products **4.22**, **4.24**, **4.25**, **4.26**) and Sorace and Dei<sup>[26]</sup> (**4.23**) (**Scheme 4.22**).



**Scheme 4.22.** Reactions to form **4.22-4.26**.

The products obtained were comparable to **4.20**, being darkly coloured, totally insoluble, and structurally amorphous. IR spectra were obtained for the various products (**Figure 4.37**), however full characterisation was not possible.

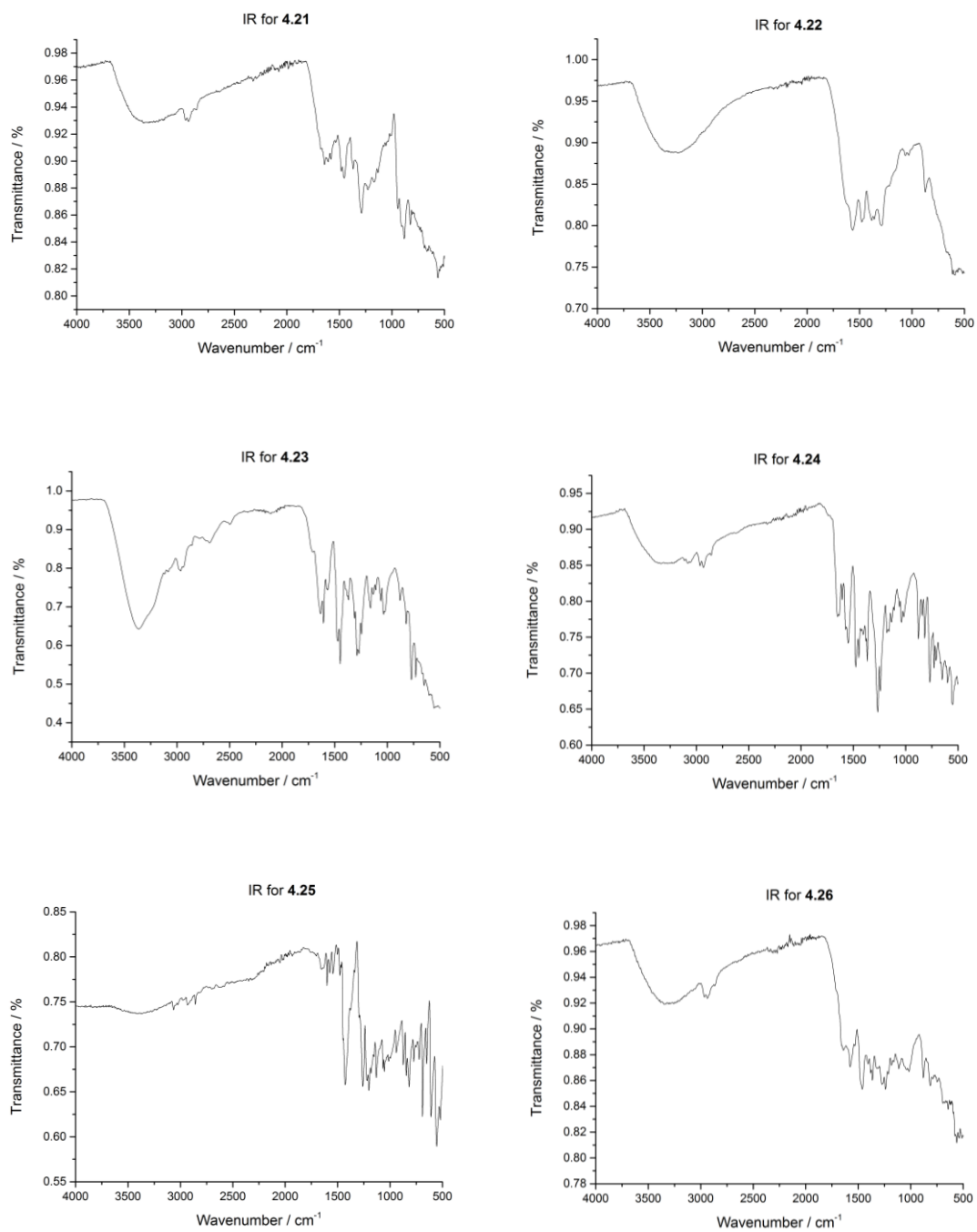


**Figure 4.37.** IR spectra for 4.21-4.26.

---

#### **4.4.3 Coordination Polymers – Conclusions and Future Work**

The difficult nature of these products is perhaps to be expected, as this has been a commonly recognised problem which has been recently discussed by other researchers in the field.<sup>[21]</sup> In general, characterisation of these types of polymers is limited to only elemental analysis,<sup>[26-27, 32-36]</sup> and this represents significant challenge to researchers and is an area of active ongoing research. Given the intractability of the products, it was decided to abandon the attempted synthesis of valence tautomeric coordination polymers within the scope of this project. This does however represent an ideal topic for future research.

---

## 4.5 References

1. D. J. Cram, J. Weiss, R. C. Helgeson, C. B. Knobler, A. E. Dorigo, K. N. Houk, *J. Chem. Soc. Chem. Commun.* **1988**, 0 (6), 407-409.
2. J. A. Wytko, J. Weiss, *Tet. Lett.* **1991**, 32 (49), 7261-7264.
3. C. Moberg, *Angew. Chem.* **1998**, 110 (3), 260-281.
4. T. Brotin, J.-P. Dutasta, *Chem. Rev.* **2009**, 109 (1), 88-130.
5. M. J. Hardie, *Chem. Soc. Rev.* **2010**, 39 (2), 516-527.
6. A. Collet, *Tetrahedron* **1987**, 43 (24), 5725-5759.
7. C. Schmuck, W. Wienand, *Synthesis* **2002**, (5), 655-663.
8. M. Harig, B. Neumann, H. G. Stammler, D. Kuck, *Eur. J. Org. Chem.* **2004**, (11), 2381-2397.
9. J. J. Loughrey, C. A. Kilner, M. J. Hardie, M. A. Halcrow, *Supramol. Chem.* **2011**, 24 (1), 2-13.
10. J. J. Loughrey, N. J. Patmore, A. Baldansuren, A. J. Fielding, E. J. L. McInnes, M. J. Hardie, S. Sproules, M. A. Halcrow, *Chem. Sci.* **2015**, 6 (12), 6935-6948.
11. D. S. Bohle, D. Stasko, *Chem. Comm.* **1998**, 0 (5), 567.
12. S. Archer, J. A. Weinstein, *Coord. Chem. Rev.* **2012**, 256 (21-22), 2530-2561.
13. A. B. Diwadkar, H. D. Shroff, A. B. Kulkarni, *Curr. Sci. (India)* **1962**, 31 (4), 149-150.
14. A. Chakrabarti, H. M. Chawla, G. Hundal, N. Pant, *Tetrahedron* **2005**, 61 (52), 12323-12329.
15. J. A. Hyatt, E. N. Duesler, D. Y. Curtin, I. C. Paul, *J. Org. Chem.* **1980**, 45 (25), 5074-5079.
16. C. J. Sumby, M. J. Hardie, *Acta Cryst. Sect. E* **2007**, E63 (4), 1537.
17. J. Best, I. V. Sazanovich, H. Adams, R. D. Bennett, E. S. Davies, A. J. H. M. Meijer, M. Towrie, S. A. Tikhomirov, O. V. Bouganov, M. D. Ward, J. A. Weinstein, *Inorg. Chem.* **2010**, 49 (21), 10041-10056.
18. K. G. Alley, G. Poneti, P. S. D. Robinson, A. Nafady, B. Moubaraki, J. B. Aitken, S. C. Drew, C. Ritchie, B. F. Abrahams, R. K. Hocking, K. S. Murray, A. M. Bond, H. H. Harris, L. Sorace, C. Boskovic, *J. Am. Chem. Soc.* **2013**, 135 (22), 8304-8323.

- 
19. W. Levason, C. A. McAuliffe, *Inorg. Chim. Acta* **1976**, *16*, 167-172.
  20. F. Hartl, A. Vlček, *Inorg. Chem* **1996**, *35* (5), 1257-1265.
  21. O. Drath, C. Boskovic, *Coord. Chem. Rev.* **2018**, *in press*.
  22. N. Shaikh, S. Goswami, A. Panja, H. L. Sun, F. Pan, S. Gao, P. Banerjee, *Inorg. Chem.* **2005**, *44* (26), 9714-9722.
  23. O. Drath, R. W. Gable, B. Moubaraki, K. S. Murray, G. Poneti, L. Sorace, C. Boskovic, *Inorg. Chem* **2016**, *55* (9), 4141-4151.
  24. B. Li, L. Q. Chen, R. J. Wei, J. Tao, R. B. Huang, L. S. Zheng, Z. Zheng, *Inorg. Chem.* **2010**, *50* (2), 424-426.
  25. C. Boskovic, Valence Tautomeric Transitions in Cobalt-dioxolene Complexes. In *Spin-Crossover Materials*, John Wiley & Sons Ltd: 2013; pp 203-224.
  26. M. Affronte, A. Beni, A. Dei, L. Sorace, *Dalton Trans.* **2007**, *0* (45), 5253-5259.
  27. M. Guardingo, F. Busqué, F. Novio, D. Ruiz-Molina, *Inorg. Chem.* **2015**, *54* (14), 6776-6781.
  28. A. R. Pournali, A. Goli, *J. Chem. Sci.* **2011**, *123* (1), 63-67.
  29. J. J. Loughrey, S. Sproules, E. J. L. McInnes, M. J. Hardie, M. A. Halcrow, *Chem. Eur. J.* **2014**, *20* (21), 6272-6276.
  30. M. E. Cass, C. G. Pierpont, *Inorg. Chem.* **1986**, *25* (2), 123-125.
  31. C. Liu, P. Restorp, E. Nordlander, C. G. Pierpont, *Chem. Comm.* **2001**, *0* (24), 2686-2687.
  32. F. Nador, F. Novio, D. Ruiz-Molina, *Chem. Comm.* **2014**, *50* (93), 14570-14572.
  33. S. Cho, T. Gadzikwa, M. Afshari, S. T. Nguyen, J. T. Hupp, *Eur. J. Inorg. Chem.* **2007**, (31), 4863-4867.
  34. F. Novio, J. Campo, D. Ruiz-Molina, *Inorg. Chem.* **2014**, *53* (13), 8742-8748.
  35. I. Imaz, D. MasPOCH, C. Rodríguez-Blanco, J. Pérez-Falcón, *Angew. Chem. Int. Ed.* **2008**, *47* (10), 1857-1860.
  36. P. González-Monje, F. Novio, D. Ruiz-Molina, *Chem. Eur. J.* **2015**, *21* (28), 10094-10099.

---

## Chapter 5

### Copper(II) Complexes of a Bis-Nitroxyl Chelate Ligand

#### 5.1 Introduction

Molecular magnetic materials are a rapidly growing area of research interest, due to their ability to exhibit spontaneous magnetisation below a critical temperature.<sup>[1]</sup> There are many advantages of molecular magnets over conventional bulk magnets, such as being lightweight, soluble in organic solvents, and optically transparent.<sup>[2-3]</sup> Unpaired spins may align in either parallel (ferromagnetism) or antiparallel (antiferromagnetism or ferrimagnetism) to one another, giving rise to a variety of possible magnetic behaviours (**Figure 5.1**).

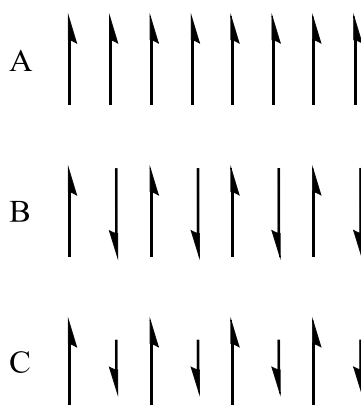


**Figure 5.1.** Spin alignment in A) ferromagnets, B) antiferromagnets, and C) ferrimagnets.

The interaction between two spins  $S_i$  and  $S_j$  has a coupling constant (energy gap between the singlet and triplet states) given by the spin Hamiltonian  $\hat{H} = -2J(S_i \cdot S_j)$ .<sup>[4]</sup> A negative  $J$  therefore implies antiferromagnetism, whereas a positive  $J$  implies ferromagnetism. If two magnetic orbitals in a molecule are orthogonal, their spins will align parallel to each other as per Hund's rule, giving a ferromagnetic interaction. If there is nonzero overlap between the magnetic orbitals, antiferromagnetism will be favoured instead (**Figure 5.3**). The spins need not be especially close to one another provided that the interaction can be transmitted through the space between them (for example by conjugation).

---

Copper(II) nitroxide complexes have attracted a substantial amount of interest in recent years as magnetic materials.<sup>[5-9]</sup> In an octahedral ligand field,  $d^9$  Cu(II) has a single unpaired electron ( $S = 1/2$ ), and each coordinated nitroxyl radical adds another  $S = 1/2$  organic radical to the molecule, which may couple in a ferro- or antiferromagnetic fashion. The nitroxyl radical occupies a half filled antibonding orbital, as shown in **Figure 5.2**.

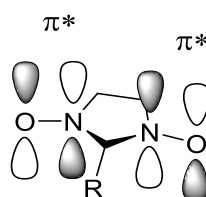


**Figure 5.2.** Magnetic orbital in nitroxides. The nitrogen and oxygen atoms carry large positive spin densities,  $sp^2$  carbon atom carries negative spin density.

### 5.1.1 Coordination through the oxygen atom

Orbital overlap between the nitroxyl magnetic orbital and the metal magnetic orbital(s) is highly dependent on the number of unpaired electrons present on the metal. In the case of Cu(II) nitroxyl complexes, the single unpaired d electron occupies a half filled d-orbital and thus different coordination geometries can lead to substantially variable orbital overlap between the metal and ligand (**Figure 5.3**). Transition metals with several half-filled d orbitals are more flexible due to the multitude of potential magnetic orbital overlaps available.

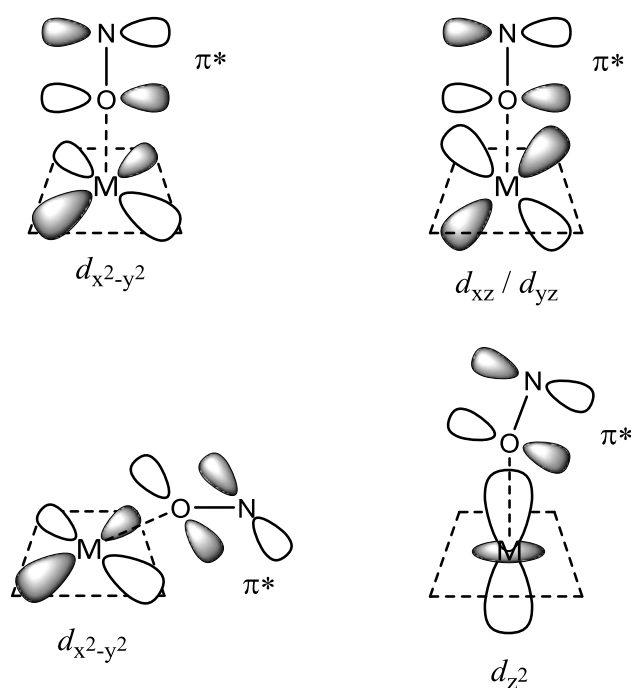


**Figure 5.3.** Possible orbital interactions between a nitroxyl and metal ion.

Antiferromagnetic coupling is observed when the orbital overlap takes place along the M-O bond, whereas ferromagnetic coupling is observed in the case of Cu(II) complexes where the nitroxyl is bound axially, due to the orthogonality of the ligand  $\pi^*$  and metal  $d_{x^2-y^2}$  orbitals.<sup>[1]</sup> The magnitude of the interaction varies from  $100\text{ cm}^{-1}$  in rigorously octahedral complexes, to smaller values of  $10\text{-}30\text{ cm}^{-1}$  in distorted octahedral complexes.<sup>[5]</sup>

### 5.1.2 Coordination through the nitrogen atom

The nitrogen lone pair that is donated to the metal is orthogonal to the  $\pi^*$  magnetic orbital. Orbital overlap is disfavoured and coupling is therefore ferromagnetic. For Cu(II) and Ni(II) complexes, the interaction is in the region of  $300\text{-}400\text{ cm}^{-1}$  and  $>100\text{ cm}^{-1}$  respectively.<sup>[5]</sup>

### 5.1.3 Geometry of the nitroxyl

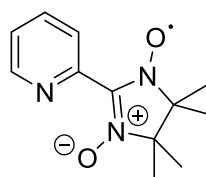
There is no method of predicting whether the nitroxyl will bond in an axial or equatorial geometry with absolute certainty, due to the subtle interplay of steric and

---

electronic factors. However, some general trends have been observed. In octahedral complexes, bulky nitroxyls favour axial coordination due to the concomitant reduction in steric clashing. This observation is magnified in Jahn-Teller elongated complexes due to the increased axial bond lengths providing additional space to accommodate the ligand. Conversely, nitroxyls which contain only a single coordinating group and a small steric bulk tend to favour the equatorial coordination mode. Careful consideration of the structural design of the nitroxyl (and ancillary ligands if present) can be used to influence which coordination geometry will ultimately be obtained.

#### 5.1.4 Effect of the counter-ion

The choice of co-ligand in Cu nitroxyl complexes can have a marked effect on magnetic behaviour. Inoue *et al.* synthesised a family of bidentate nitronyl nitroxide and imino nitroxyl ligands functionalised with either pyridyl or pyrazolyl moieties.<sup>[10]</sup>



Py-NN

**Figure 5.4.** Nitroxyl ligand reported by Inoue *et al.*<sup>[10]</sup>

When Py-NN (**Figure 5.4**) is coordinated with Cu using a chloride counter-ion, the resultant Jahn-Teller elongated complex has the chloride ions coordinated in the axial positions. At 300 K the complex shows magnetic behaviour indicative of three non-interacting spins (1.16 emu), however the value of  $\chi_m T$  rises below 75 K due to ferromagnetic coupling (**Figure 5.5**). In contrast, when the same complex is formed with perchlorate counter-ions, they coordinate equatorially and the  $\chi_m T$  at 300 K is lower (0.65 emu), and it continues to drop as the complex is cooled, indicative of antiferromagnetic coupling (**Figure 5.5**).

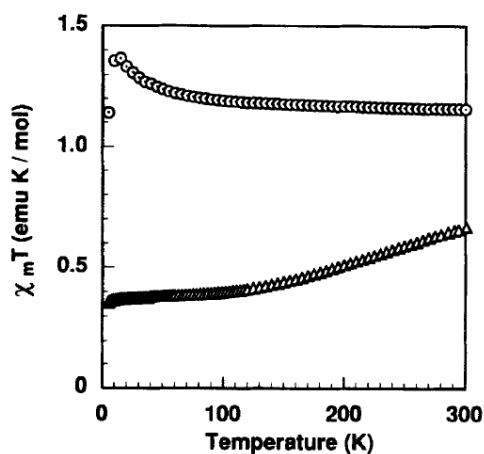


**Figure 5.5.** Magnetic susceptibility for Cu complexes of Py-NN<sup>[10]</sup>

This demonstrates that a small variation in the counter ion can lead to a markedly different magnetic behaviour.

### 5.1.5 The bisimpy ligand

The bisimpy ligand has been the subject of some recent studies in the literature. Tian *et al.* synthesised a variety of complexes where the bisimpy was present as a biradical complexed to manganese and cobalt with hfac co-ligands (**Figures 5.6 and 5.7**).<sup>[11]</sup>

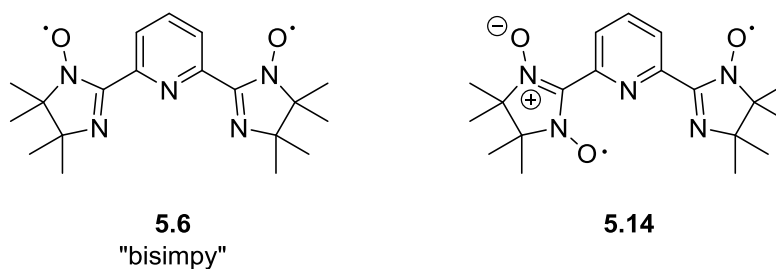


**Figure 5.6.** Structures of biradical nitroxyl ligands **5.6** (bisimpy) and **5.14**.

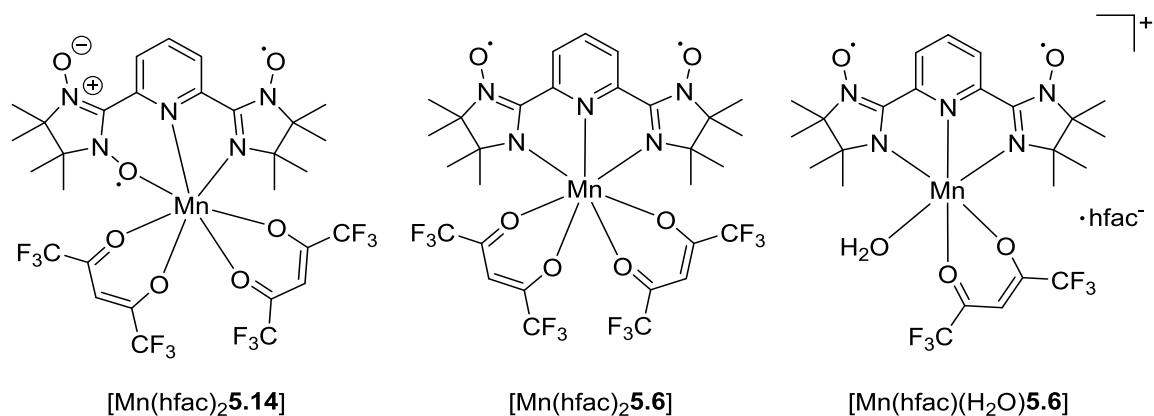


**Figure 5.7.** Three bisimpy derived Mn complexes reported by Zhou *et al.*<sup>[11]</sup>

At room temperature all of the complexes show antiferromagnetic coupling, however several different magnetic behaviours are exhibited upon cooling. [Mn(hfac)<sub>2</sub>5.14] has a room temperature  $\chi_m T$  of  $3.27 \text{ cm}^3 \text{ K mol}^{-1}$ , which is less than the theoretical value for a totally uncorrelated spin system. The  $\chi_m T$  decreases linearly upon cooling, until a temperature of 15 K is reached, at which point the  $\chi_m T$  rapidly drops until reaching a minimum of  $0.84 \text{ cm}^3 \text{ K mol}^{-1}$ , indicating strong antiferromagnetism.

The authors have characterised the complexes by X-ray diffraction, which provides insight into the geometry of the nitroxyl relative to the manganese centre. The metal ion and nitroxyl groups form a scalene triangle in [Mn(hfac)<sub>2</sub>5.14], and hence the magnetic exchange was modelled as a scalene triangle of three spins (one spin  $S = 5/2$  Mn(II) ion and two  $S = 1/2$  ligands, **Figure 5.8**), which has the following spin Hamiltonian:

$$\hat{H} = -2J_1 \hat{S}_{\text{Mn}} \hat{S}_{\text{rad1}} - 2J_2 \hat{S}_{\text{Mn}} \hat{S}_{\text{rad2}} \quad \text{(Equation 5.1)}$$



**Figure 5.8.** Model of the magnetic exchange in [Mn(hfac)<sub>2</sub>5.14].

[Mn(hfac)(H<sub>2</sub>O)**5.6**·hfac] has a room temperature  $\chi_m T$  of 3.96 cm<sup>3</sup> K mol<sup>-1</sup>, which is lower than the predicted value of 5.12 cm<sup>3</sup> K mol<sup>-1</sup>, indicating some degree of antiferromagnetism. The  $\chi_m T$  decreases linearly as the temperature is reduced to 35 K, reaching a minimum of 2.10 cm<sup>3</sup> K mol<sup>-1</sup>. Upon cooling below this temperature to 2 K the  $\chi_m T$  rises to a maximum of 2.87 cm<sup>3</sup> K mol<sup>-1</sup>, due to intermolecular radical-radical ferromagnetic coupling.

In contrast to [Mn(hfac)<sub>2</sub>**5.14**], [Mn(hfac)<sub>2</sub>**5.6**] and [Mn(hfac)(H<sub>2</sub>O)**5.6**·hfac] have a geometry such that the metal and nitroxyl groups form an isosceles triangle. The magnetic susceptibility these complexes was modelled as an isosceles triangle of spins (**Figure 5.9**) with the following spin Hamiltonian:

$$\hat{H} = -2J(\hat{S}_{Mn}\hat{S}_{rad1} + \hat{S}_{Mn}\hat{S}_{rad2}) - 2J' \hat{S}_{rad1}\hat{S}_{rad2} \quad \text{(Equation 5.2)}$$

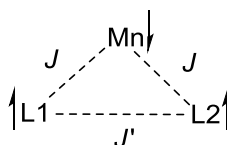


**Figure 5.9.** Model of the magnetic exchange in [Mn(hfac)<sub>2</sub>**5.6**] and [Mn(hfac)(H<sub>2</sub>O)**5.6**].

$$\chi = \frac{N\beta^2 g^2}{4kT} \frac{84 + 35 \exp\left(\frac{-7J}{kT}\right) + 10 \exp\left(\frac{-12J}{kT}\right) + 35 \exp\left(\frac{-5J-2J'}{kT}\right)}{4 + 3 \exp\left(\frac{-7J}{kT}\right) + 2 \exp\left(\frac{-12J}{kT}\right) + 3 \exp\left(\frac{-5J-2J'}{kT}\right)} \quad \text{(Equation 5.2)}$$

These results represent the most extensive study of the bisimpy ligand in molecular magnetism that has been undertaken so far.

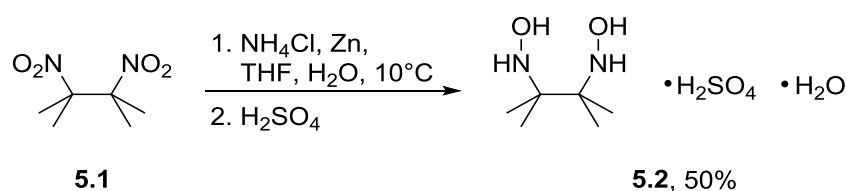
The results presented in the following sections were obtained in collaboration with Prof. Ovcharenko and the International Tomography Centre (ITC), Novosibirsk.



Ovcharenko *et al.* have subsequently developed an improved synthetic method employing THF as the solvent. Ammonium chloride is highly soluble in aqueous ethanol, whereas the dinitro starting material **5.1** is only sparingly soluble. This situation is reversed when aqueous THF is used, which helps to reduce the amount of side product formation. The original Lamchem-Mittag route uses 2 equivalents of ammonium chloride, stemming from the incorrect belief that its only role is as a buffer. Increasing the number of equivalents of ammonium chloride to 8 significantly improves the yield, and provides the correct stoichiometry to form  $[\text{Zn}(\text{NH}_3)_2\text{Cl}_2]$  as a by-product.<sup>[16]</sup>

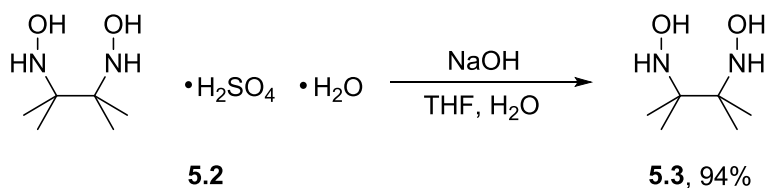
Addition of the zinc in a portionwise manner is another source of irreproducibility, as this creates localised areas of higher temperature within the reaction which may be warmer than the ideal temperature of  $<10^\circ\text{C}$ . Zinc may also coordinate **5.2** to form the complex  $[\text{Zn}(\mathbf{5.2})\text{Cl}_2]$ , effectively sequestering the product before it can be isolated.

With these caveats in mind, an optimised synthetic method was carried out to produce **5.2** in good yield (**Scheme 5.3**).<sup>[16]</sup>



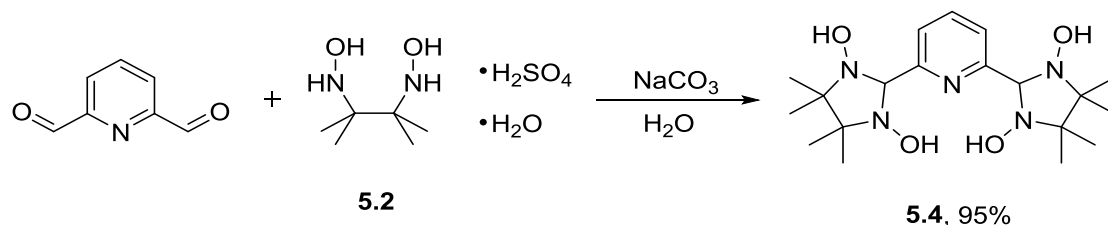
**Scheme 5.3.** Successful optimised synthesis of *bis*(hydroxylamine) compound **5.2**.

This sulphate hydrate may be reacted as-is with the pyridylcarbaldehyde, however it slowly decomposes over the course of several months, so for long term storage is it preferable to convert it to the free base form. This conversion is trivially performed by reaction with sodium hydroxide to afford the free base **5.3** in high yield (**Scheme 5.4**).



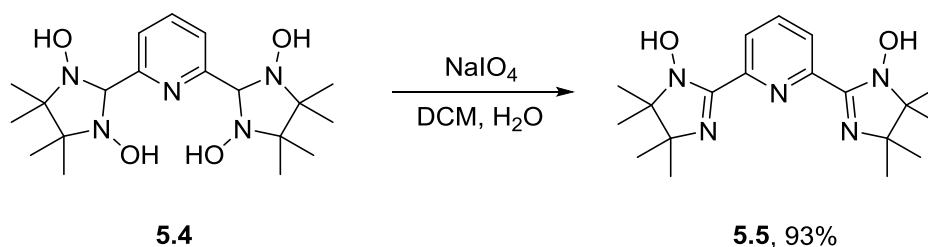
**Scheme 5.4.** Conversion of the sulphate salt **5.2** to the free base **5.3**.

The dihydroxylamine and pyridinedicarbaldehyde are reacted in the presence of sodium carbonate, to complete the dicyclisation to form the *bis*(imidazoline) **5.4** (Scheme 5.5).<sup>[18]</sup>



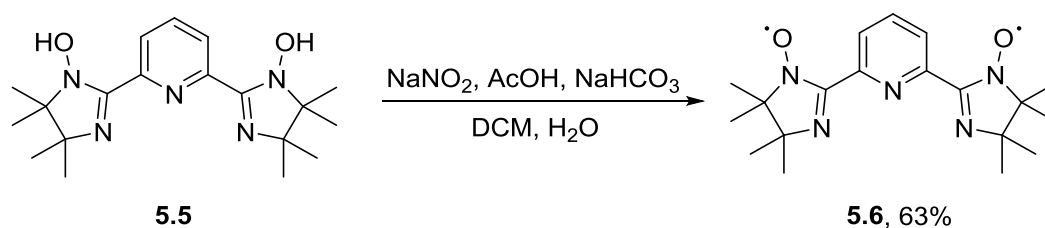
**Scheme 5.5.** Synthesis of the *bis*(imidazoline) **5.4**.

The next step involves mild reduction with sodium periodate to form the *bis*(imidazole) **5.5** (Scheme 5.6).<sup>[18]</sup>



**Scheme 5.6.** Reduction of **5.4** with sodium periodate to produce **5.5**.

The final step to oxidise the product to biradical ligand **5.6** is carried out with sodium nitrite in the presence of acetic acid (Scheme 5.7).<sup>[18]</sup>



**Scheme 5.7.** Oxidation of **5.5** to produce the biradical **5.6**, bisimpy.

**5.6** was allowed to crystallise by slow evaporation from a CH<sub>2</sub>Cl<sub>2</sub> solution. The ligand crystallised as orange needles, and the crystal structure was obtained (Figure 5.10).

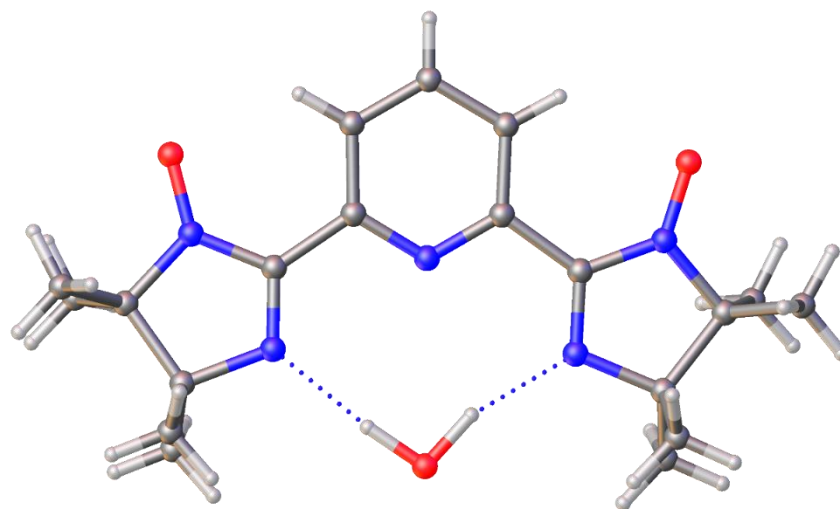
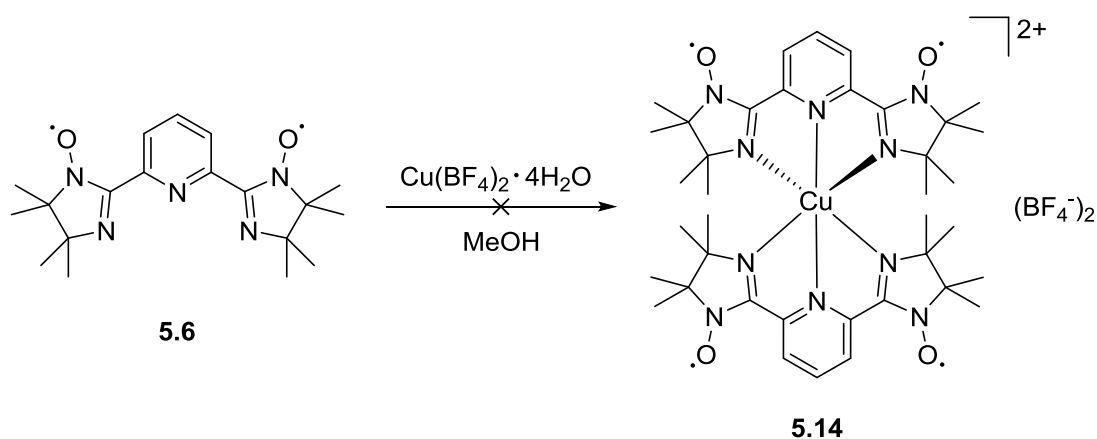


**Figure 5.10.** X-ray crystal structure of **5.6**.

**5.6** crystallised in the monoclinic space group  $P2_1/n$ , with the asymmetric unit containing one molecule of **5.6** and one molecule of water. The water molecule forms two N...H-O hydrogen bonds with the ligand, such that the water molecule occupies the space between the three coordinating nitrogen atoms.

Initially, attempts were made to synthesise the homoleptic complex consisting of two bisimpy ligands coordinated to a Cu(II) centre (**Scheme 5.8**).

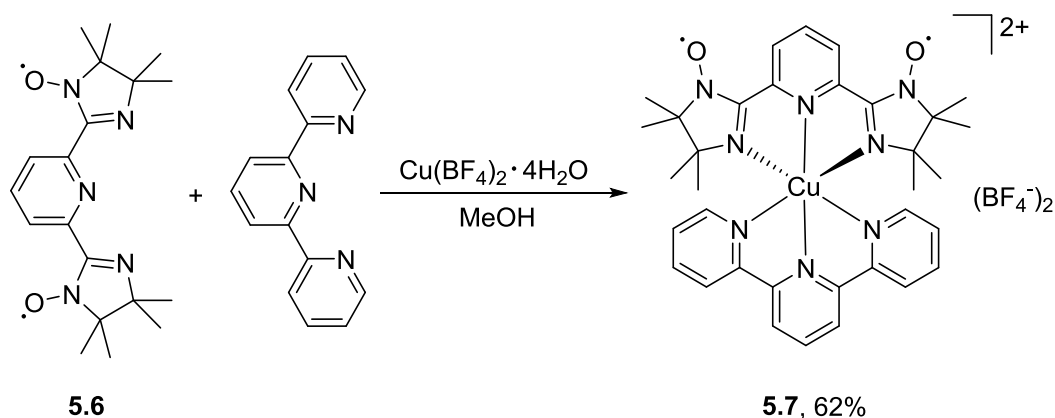


**Scheme 5.8.** Attempted complexation of two **5.6** ligands with Cu(II).

The reaction did not produce the product, which is likely due to steric clashing between the (*bis*)dimethyl groups of the bisimpy. A subsequent synthetic strategy was

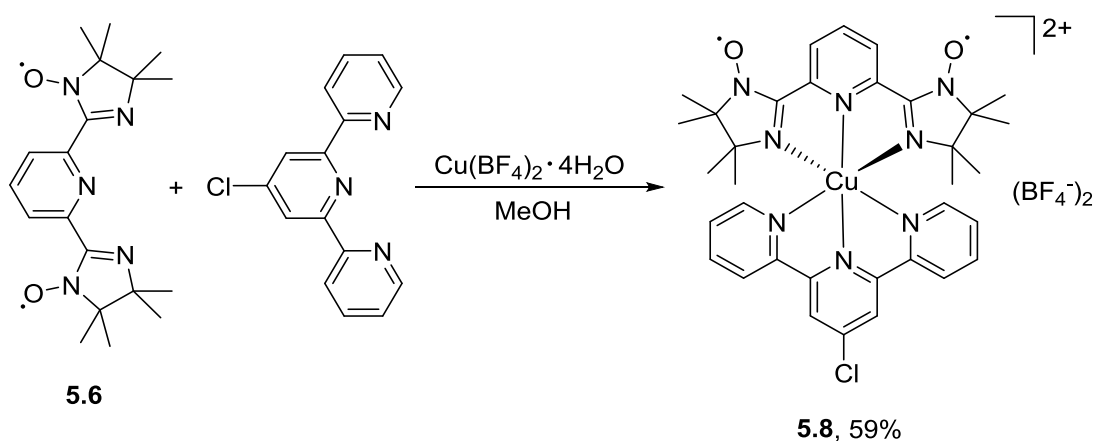
devised, wherein the syntheses of heteroleptic products containing one bisimpy ligand and a variety of less sterically bulky tridentate N-donor ligands were attempted.

The simplest and therefore most logical starting point is to replace one equivalent of **5.6** with 2,2';6',2''-terpyridine (terpy) to produce **5.7** (**Scheme 5.8**).



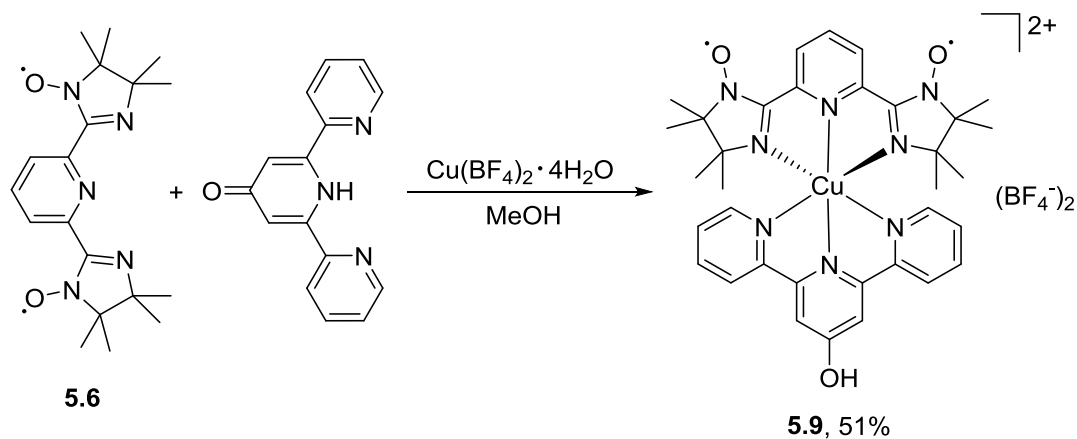
**Scheme 5.9.** Complexation of **5.6** and terpy with Cu(II) to form the heteroleptic complex **5.7**.

The 4-chloro and 4-hydroxyl derivatives of terpy are also commercially available, so these were used to synthesise analogous complexes with more electron withdrawing or donating terpy ligands respectively (**Schemes 5.10** and **5.11**).



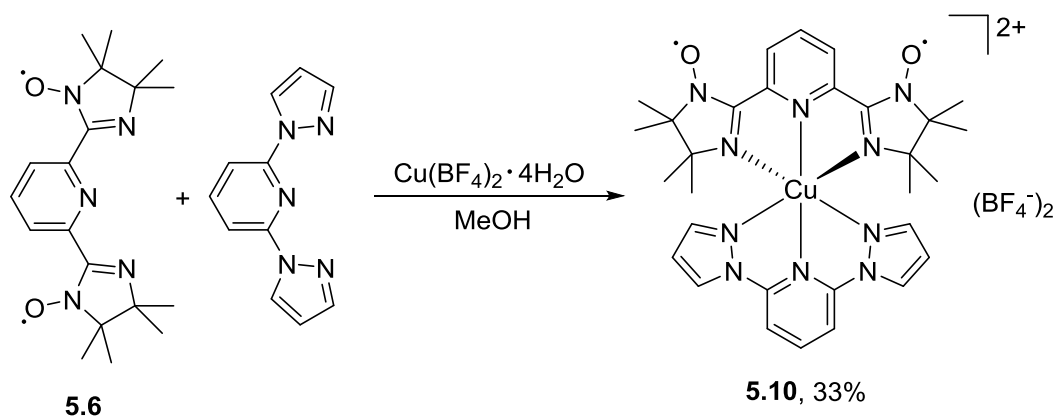
**Scheme 5.10.** Complexation of **5.6** and 4'-chloro(terpy) with Cu(II) to form the heteroleptic complex **5.8**.

The 4-hydroxyl(terpy) derivative can be synthesised by *in situ* tautomerisation of 6-bis(2-pyridyl)-4(1*H*)-pyridone to form the heteroleptic complex **5.9** (Scheme 5.11).<sup>[19]</sup>



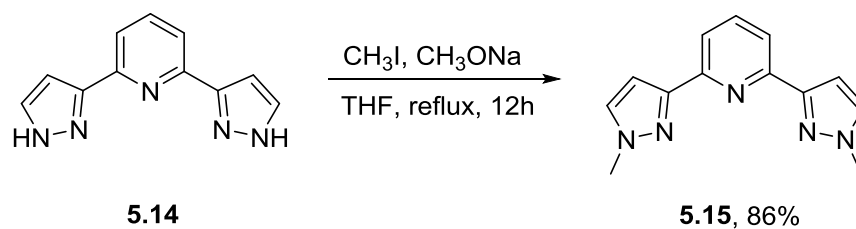
**Scheme 5.11.** Complexation of **5.6** and 4-hydroxyl(terpy) with Cu(II) to form the heteroleptic complex **5.9**.

*Bis*(pyrazolyl)pyridines are also suitable ligands to use for these complexes as they allow easy functionalisation of the 3 position of the pyrazolyl rings, which may sterically force the Jahn-Teller axis to adopt a different orientation. 1-bpp, bismpy and  $\text{Cu}(\text{BF}_4)_2$  were reacted to synthesise **5.10** (Scheme 5.12).



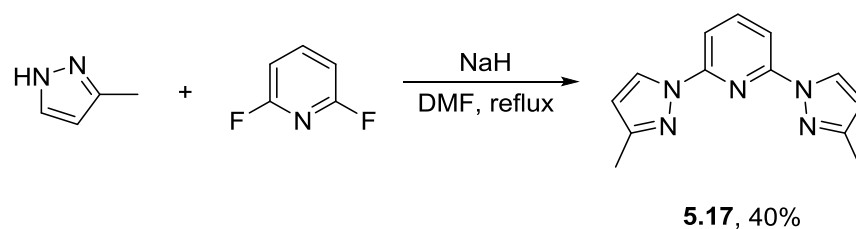
**Scheme 5.12.** Complexation of **5.6** and 1-bpp with Cu(II) to form the heteroleptic complex **5.10**.

N-methylation of the pyrazolyl rings in **5.14** (3-bpp) can be readily achieved by refluxing with iodomethane (Scheme 5.13).<sup>[20]</sup>



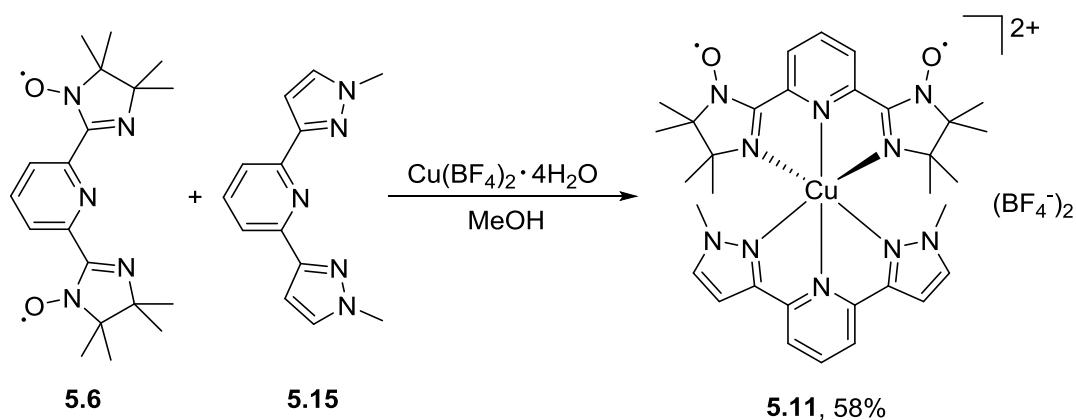
**Scheme 5.13.** N-methylation of **5.14** (3-bpp) to produce **5.15**.

The synthesis of **5.17** has been developed previously in the Halcrow group, and involves refluxing 3-methylpyrazole with 2,6-difluoropyridine in the presence of sodium hydride (**Scheme 5.14**).<sup>[21]</sup> The yield of the desired product is low due to the formation of multiple isomers which must be separated by flash column chromatography.



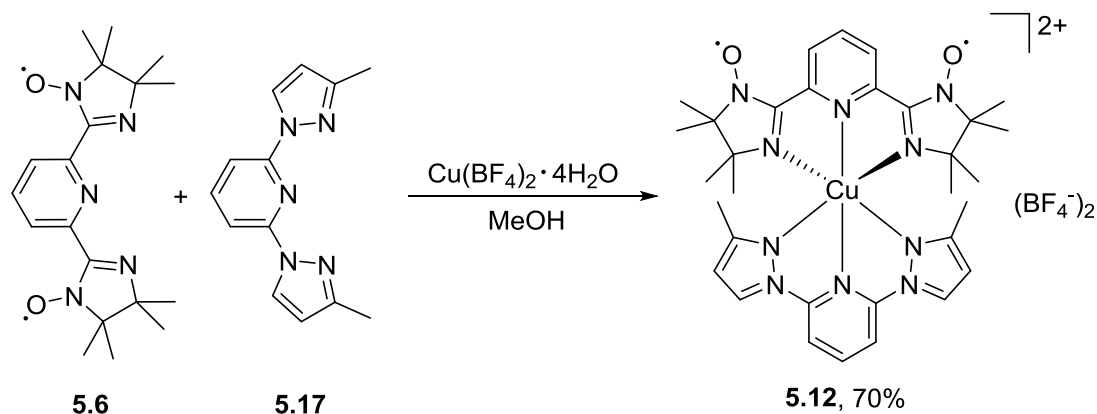
**Scheme 5.14.** Reaction of 3-methylpyrazole and 2,6-difluoropyridine to produce **5.17**.

**5.15** was then reacted with bisimpy and  $\text{Cu}(\text{BF}_4)_2$  to form complex **5.11** (**Scheme 5.15**).



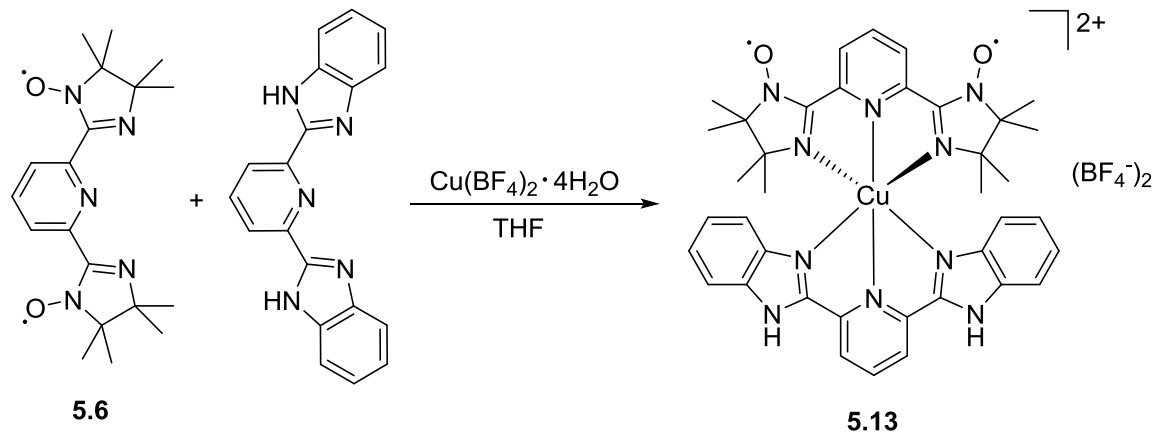
**Scheme 5.15.** Complexation of **5.6** and **5.15** with  $\text{Cu}(\text{II})$  to form the heteroleptic complex **5.11**.

**5.17** was also reacted with bisimpy and Cu(BF<sub>4</sub>)<sub>2</sub> to form complex **5.12** (Scheme 5.15).



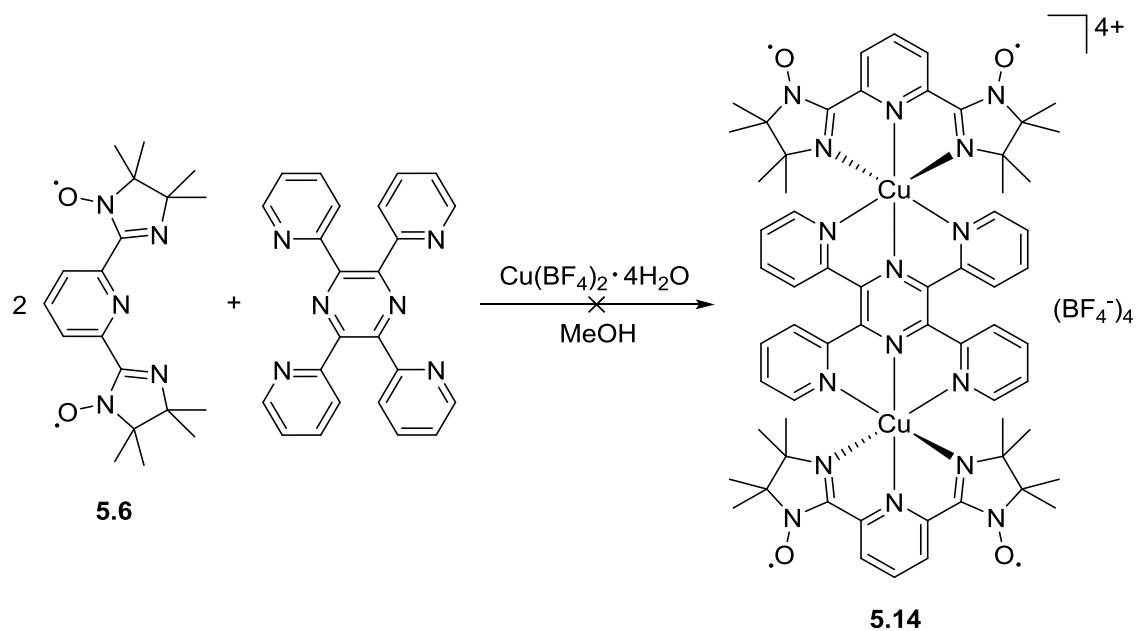
**Scheme 5.16.** Complexation of **5.6** and **5.17** with Cu(II) to form the heteroleptic complex **5.12**.

Additionally, a final complex, **5.13**, bearing a 2,6-*bis*(2-benzimidazolyl)pyridine was also synthesised (**Scheme 5.17**).



**Scheme 5.17.** Complexation of **5.6** and 2,6-*bis*(2-benzimidazolyl)pyridine with Cu(II) to form the heteroleptic complex **5.13**.

The synthesis of complex **5.14** was also attempted (**Scheme 5.17**). This complex is interesting because it contains two Cu(II) ions and two bisimpy ligands, bridged by the *bis*(tridentate) ligand 2,3,5,6-tetra-2-pyridinylpyrazine which may be considered a “double sided” form of terpyridine (**Scheme 5.18**).



**Scheme 5.18.** Attempted synthesis of **5.14** from **5.6** and 2,3,5,6-tetra-2-pyridinylpyrazine.

Unfortunately the product was not isolated from this reaction. This is hypothesised to be due to the fact that 2,3,5,6-tetra-2-pyridinylpyrazine is not a planar molecule due to a steric clash between the protons on the pyridine rings.<sup>[22]</sup> This twists the pyridyl rings out of the plane, leading to an unfavourable conformation for octahedral coordination to a copper ion.

### 5.3 Crystallography

While crystal structures were obtained for **5.7**, **5.8**, **5.11**, and **5.12**, all but **5.8** suffered from low resolution data. This problem arose from the tendencies of the crystals to become oily and lose crystallinity rapidly upon removal from the mother liquor, and diffraction was generally poor even when suitable crystals were obtained. Higher resolution crystal structures would be desirable for future work, to provide a more accurate measure of the Cu-N bond lengths and the steric influence of the ligand on the Jahn-Teller elongation axis.

**5.7** was crystallised as orange needles by vapour diffusion of diethyl ether into acetonitrile. The structure was solved in the triclinic space group  $P\bar{1}$  using *ShelXT* in the *Olex2* program (**Figure 5.11**).

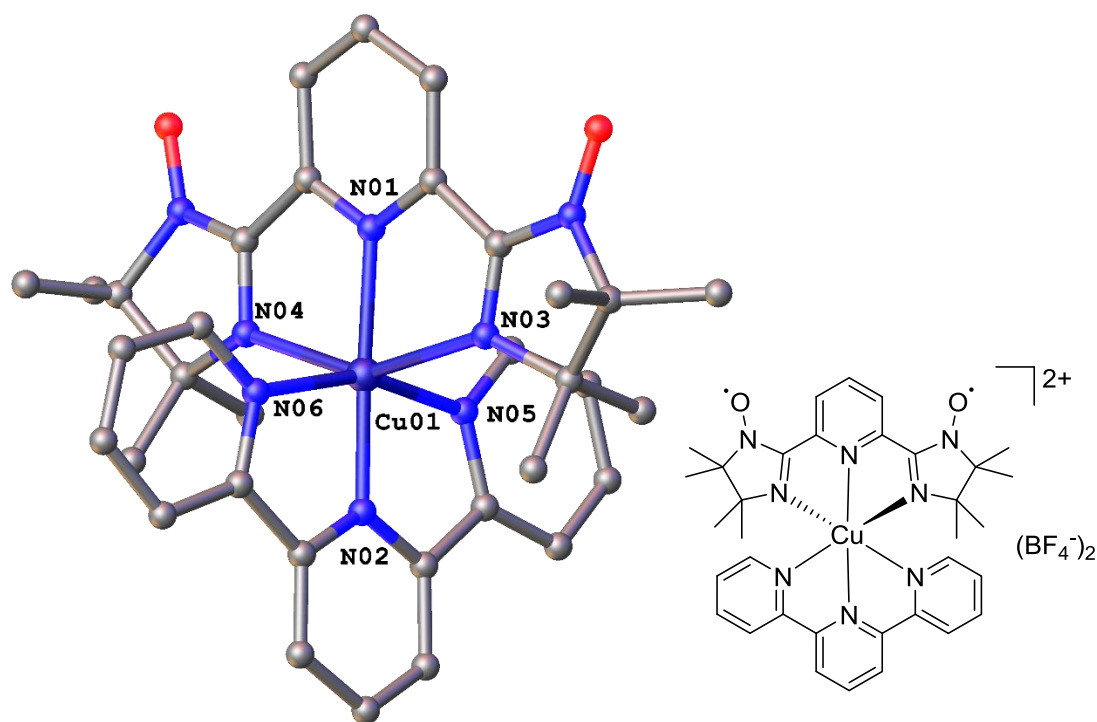


**Figure 5.11.** X-ray structure for **5.7**.

The complex adopts a Jahn-Teller distorted octahedral geometry, with the elongated axis along the N03-Cu01-N04 bonds (**Table 5.1**).

**Table 5.1.** Selected bond lengths and angles for **5.7** [ $\text{\AA}$  /  $^\circ$ ].

**5.7**

Bond	Length / Angle
Cu01-N01	2.053(2)
Cu01-N02	1.923(2)
Cu01-N03	2.302(3)
Cu01-N04	2.281(3)
Cu01-N05	2.091(15)
Cu01-N06	2.084(19)
N03-Cu01-N04	151.40(4)
N05-Cu01-N06	158.95(13)
N01-Cu01-N02	176.17(6)

**5.8** was crystallised as orange needles by vapour diffusion of diethyl ether into acetonitrile. The structure was solved in the monoclinic space group  $P2_1/n$  using *ShelXT* in the *Olex2* program (**Figure 5.12**).

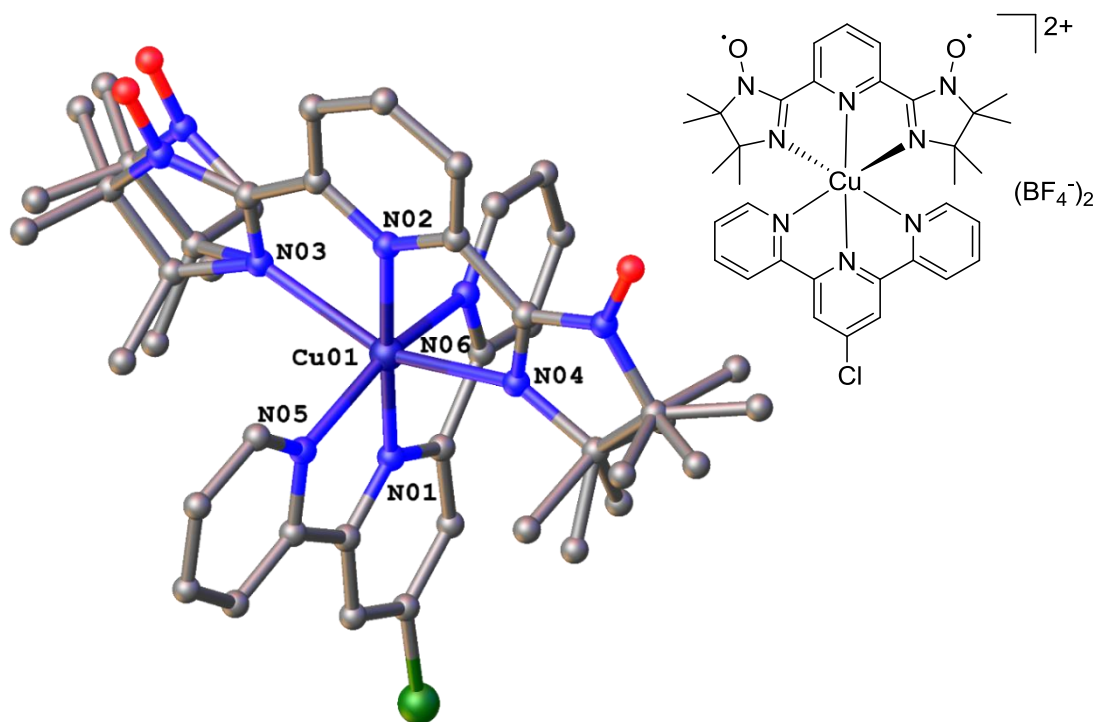


**Figure 5.12.** X-ray structure for **5.8**.

The complex adopts a Jahn-Teller distorted octahedral geometry, with the elongated axis along the N03-Cu01-N04 bonds (**Table 5.2**). One of the imino nitroxyl rings is disordered over two positions, and the BF<sub>4</sub> counter-ions are disordered over 5 positions.

**Table 5.2.** Selected bond lengths and angles for **5.8** [ $\text{\AA}$  /  $^\circ$ ].

**5.8**

Bond	Length / Angle
Cu01-N01	1.943(4)
Cu01-N02	2.052(5)
Cu01-N03	2.289(5)
Cu01-N04	2.323(4)
Cu01-N05	2.063(5)
Cu01-N06	2.062(5)
N01-Cu01-N02	177.97(19)
N03-Cu01-N04	150.81(17)
N05-Cu01-N06	158.74(18)

**5.11** was crystallised as orange needles by vapour diffusion of diethyl ether into acetonitrile. The structure was solved in the triclinic space group  $P\bar{1}$  using *ShelXT* in the *Olex2* program (**Figure 5.13**).

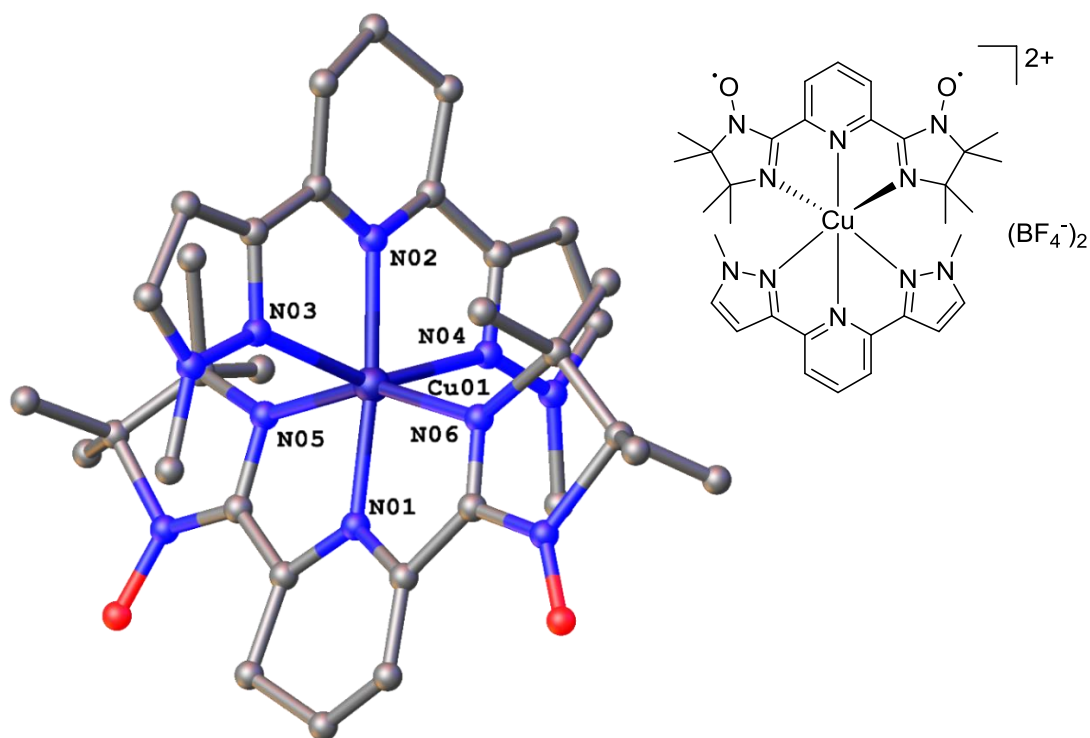


**Figure 5.13.** X-ray structure for **5.11**.

---

The crystal structure obtained is unfortunately of rather poor quality, owing to the previously mentioned difficulties with carrying out crystallography on these compounds. Despite this, some information can be gleaned from the structure, namely that the complex adopts a Jahn-Teller distorted octahedral geometry, with the elongated axis along the N03-Cu01-N04 bonds (**Table 5.3**). This differs from the previously described structures, as the Jahn-Teller axis of elongation is now associated with the bpp ligand rather than the nitroxyl.

**Table 5.3.** Selected bond lengths and angles for **5.11** [ $\text{\AA}$  /  $^\circ$ ].

### 5.11

Bond	Length / Angle
Cu01-N01	1.927(18)
Cu01-N02	1.977(17)
Cu01-N03	2.300(17)
Cu01-N04	2.253(16)
Cu01-N05	2.05(2)
Cu01-N06	2.09(2)
N01-Cu01-N02	154.48(3)
N05-Cu01-N06	152.51(5)
N03-Cu01-N04	172.43(16)

**5.12** was crystallised as orange needles by vapour diffusion of diethyl ether into acetonitrile. The structure was solved in the tetragonal space group  $I\bar{4}2d$  using *ShelXT* in the *Olex2* program (**Figure 5.14**).

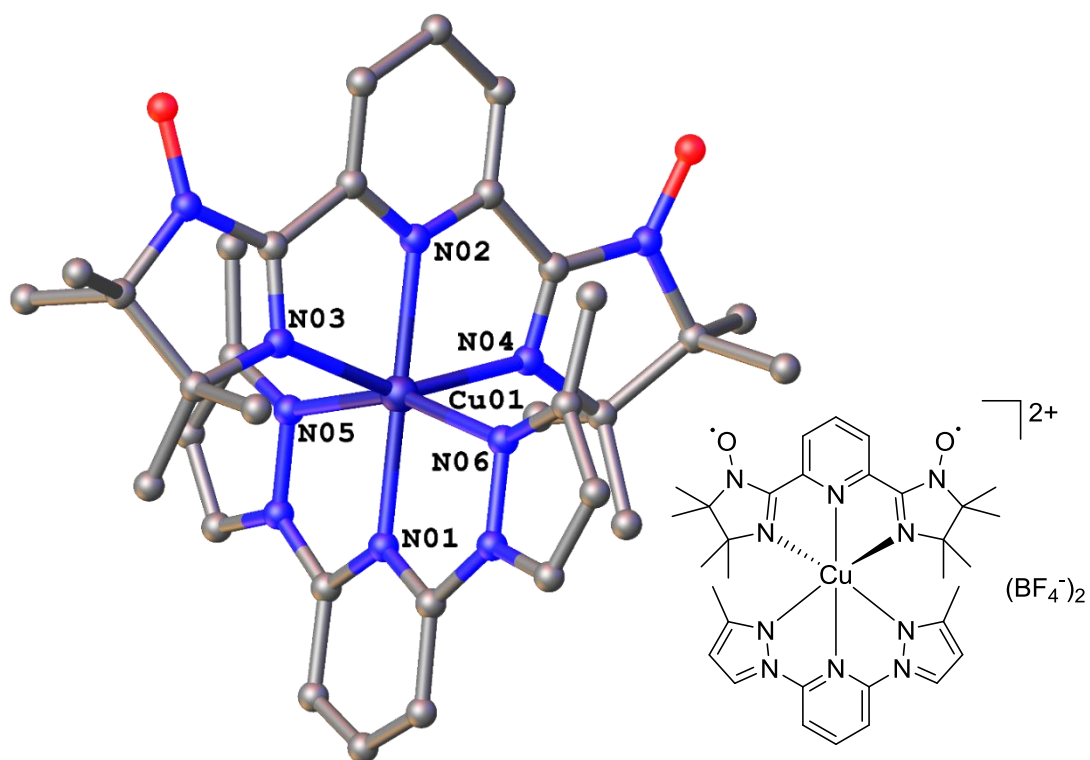


**Figure 5.14.** X-ray structure for **5.12**.

The complex adopts a Jahn-Teller distorted octahedral geometry, with the elongated axis along the N03-Cu01-N04 bonds (**Table 5.4**).

**Table 5.4.** Selected bond lengths and angles for **5.12** [ $\text{\AA}$  /  $^\circ$ ].

### 5.12

Bond	Length / Angle
Cu01-N01	1.98(2)
Cu01-N02	2.00(2)
Cu01-N03	2.224(17)
Cu01-N04	2.224(17)
Cu01-N05	2.092(17)
Cu01-N06	2.092(17)
N01-Cu01-N02	180
N05-Cu01-N06	151.5(9)
N03-Cu01-N04	157.5(9)

## 5.4 Magnetic Measurements

The spin-only magnetic moment is given by **Equation 5.3**.

$$\mu_{eff} = \sqrt{n(n+2)}\mu_B \quad \text{(Equation 5.3)}$$

The spin-only magnetic moment may be converted to  $\chi_m T$  by the expression in **Equation 5.4**.

$$\mu_{eff} = \sqrt{\frac{3kT\chi}{N\mu_B^2}} \approx 2.828\sqrt{\chi_m T} \quad \text{(Equation 5.4)}$$

Based on the crystallographic data, the magnetic susceptibility for complexes **5.7-5.13** can be modelled as an isosceles triangle of three spins. There are three spin  $\frac{1}{2}$  centres and two inequivalent exchange interactions  $J$  and  $J'$ , depicted in the simplified diagram in **Figure 5.15**.

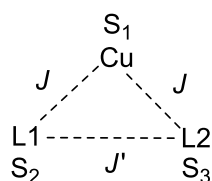


**Figure 5.15.** Model of the magnetic exchange in complexes **5.7-5.13**.

When three paramagnetic centres are arranged in a trinuclear cluster of this geometry, the spin Hamiltonian is given by **Equation 5.5**.

$$\hat{H} = -2J(\hat{S}_1 \cdot \hat{S}_2 + \hat{S}_1 \cdot \hat{S}_3) - 2J'(\hat{S}_2 \cdot \hat{S}_3) \quad \text{(Equation 5.5)}^{[23]}$$

Using the Kambe vector coupling method:

$$\text{Let } \hat{S}^* = \hat{S}_2 + \hat{S}_3$$

$$\therefore \hat{S}^{*2} = \hat{S}_2^2 + 2\hat{S}_2 \cdot \hat{S}_3 + \hat{S}_3^2$$

$$\therefore 2\hat{S}_2 \cdot \hat{S}_3 = \hat{S}^{*2} - \hat{S}_2^2 - \hat{S}_3^2 \quad \text{(Equation 5.6)}$$

Let  $\widehat{\mathbf{S}}_T = \mathbf{S}^* + \widehat{\mathbf{S}}_1$

$$\therefore \widehat{\mathbf{S}}_T^2 = \widehat{\mathbf{S}}_1^2 + \mathbf{S}^{*2} + 2\widehat{\mathbf{S}}_1 \cdot \widehat{\mathbf{S}}^*$$

$$= \widehat{\mathbf{S}}_1^2 + \mathbf{S}^{*2} + 2\widehat{\mathbf{S}}_1(\widehat{\mathbf{S}}_2 + \widehat{\mathbf{S}}_3)$$

$$= \widehat{\mathbf{S}}_1^2 + \mathbf{S}^{*2} + 2\widehat{\mathbf{S}}_1\widehat{\mathbf{S}}_2 + 2\widehat{\mathbf{S}}_1\widehat{\mathbf{S}}_3$$

$$\therefore 2(\widehat{\mathbf{S}}_1\widehat{\mathbf{S}}_2 + \widehat{\mathbf{S}}_1\widehat{\mathbf{S}}_3) = \widehat{\mathbf{S}}_T^2 - \mathbf{S}^{*2} - \widehat{\mathbf{S}}_1^2 \quad \text{(Equation 5.7)}$$

Substituting **Equations 5.5** and **5.6** into **Equation 5.7**:

$$\widehat{H} = -J(\widehat{\mathbf{S}}_T^2 - \widehat{\mathbf{S}}^{*2} - \widehat{\mathbf{S}}_1^2) - J'(\widehat{\mathbf{S}}^{*2} - \widehat{\mathbf{S}}_2^2 - \widehat{\mathbf{S}}_3^2)$$

As  $\widehat{\mathbf{S}}_1^2, \widehat{\mathbf{S}}_2^2, \widehat{\mathbf{S}}_3^2 = \text{constant}$

$$= -J(\widehat{\mathbf{S}}_T^2 - \widehat{\mathbf{S}}^{*2}) - J'(\widehat{\mathbf{S}}^{*2})$$

When  $\widehat{H} = \widehat{\mathbf{S}}^2, E = S(S + 1)$

$$\therefore E_{(S_T)} = -J(S_T(S_T + 1) - \mathbf{S}^*(\mathbf{S}^* + 1) - \mathbf{S}_1(\mathbf{S}_1 + 1)) - J'(\mathbf{S}^*(\mathbf{S}^* + 1) - \mathbf{S}_2(\mathbf{S}_2 + 1) - \mathbf{S}_3(\mathbf{S}_3 + 1)) \quad \text{(Equation 5.8)}$$

The above may be used for any  $M_3$  system.

$$\mathbf{S}^* = 1, 0$$

$$\mathbf{S}_T = \frac{3}{2}, \frac{1}{2} \quad \text{for } \mathbf{S}^* = 1$$

$$\mathbf{S}_T = \frac{1}{2} \quad \text{for } \mathbf{S}^* = 0$$

$\therefore$  three states are possible.

The spins in **5.7-5.13** may arrange in one of three possible orientations, with a visual representation of this being shown in **Figure 5.16**.

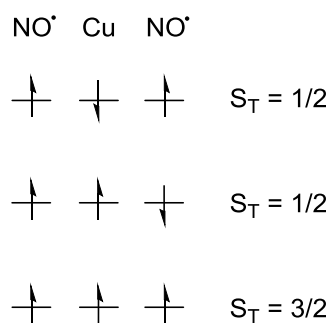


**Figure 5.16.** Possible spin orientations in complexes **5.7-5.13**.

$E_{S_T}$  may be calculated from these values and substituted into the van Vleck equation (**Equation 5.7**).

$$\chi_m = \frac{Ng^2\beta^2}{3kT} \frac{\sum \widehat{S}_T(\widehat{S}_T + 1)(2\widehat{S}_T + 1) e^{-\frac{E(\widehat{S}_T)}{kT}}}{\sum (2\widehat{S}_T + 1) e^{-\frac{E(\widehat{S}_T)}{kT}}}$$

$$= \frac{Ng^2\beta^2}{4kT} \frac{1 + e^{-\frac{-2J+2J'}{kT}} + 10e^{-\frac{J+2J'}{kT}}}{1 + e^{-\frac{-2J+2J'}{kT}} + 2e^{-\frac{J+2J'}{kT}}}$$

**(Equation 5.9)**

By fitting the experimental magnetic susceptibility data to this equation, the magnitude of exchange  $J$  and  $J'$  can be obtained, along with the  $g$  factor.

Magnetic measurements were run on the 7 complexes obtained, of which 6 provided suitable data for interpretation.

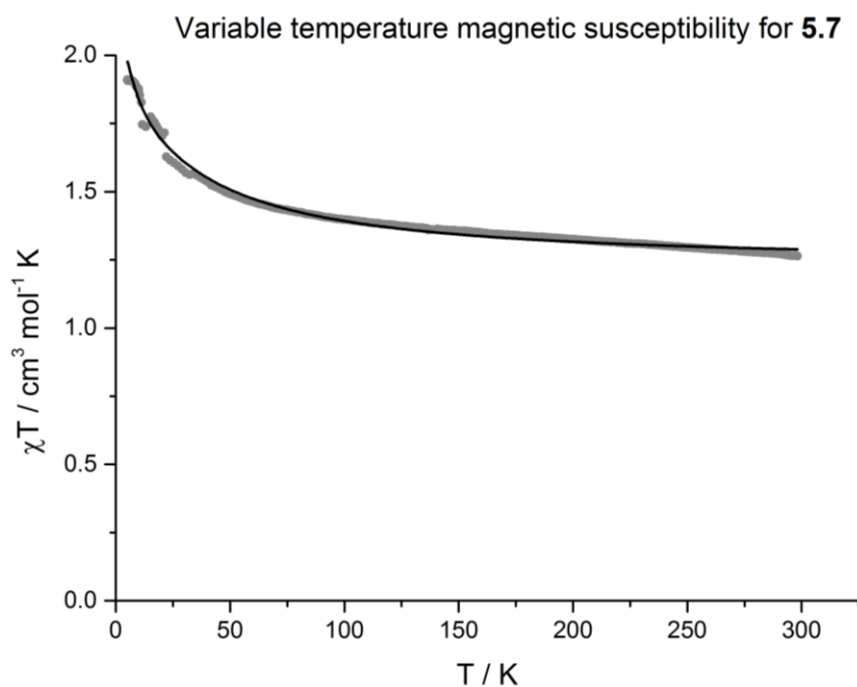


**Figure 5.17.** Magnetic susceptibility curve for **5.7** between 5 and 300 K.

In **5.7** (**Figure 5.17**), the  $\chi T$  undergoes a small linear increase from a value of 1.26 to 1.40  $\text{cm}^3 \text{mol}^{-1} \text{K}$  as the sample is decreased in temperature from 300 to 95 K, as would be expected for a system containing three non-interacting spins. As **5.7** is cooled below this point, the  $\chi T$  grows exponentially to a maximum of 1.91  $\text{cm}^3 \text{mol}^{-1} \text{K}$  at 5 K. The exchange between the spins is therefore ferromagnetic, and this is corroborated by the crystallographic observation that the nitroxyl magnetic orbitals are orthogonal to the half-filled metal orbital.

The curve was fit to **Equation 5.8** ( $R^2 = 0.995$ ) with  $J = 18.7(6)$ ,  $J' = -5.04(2)$  and  $g = 2.086(2)$ .

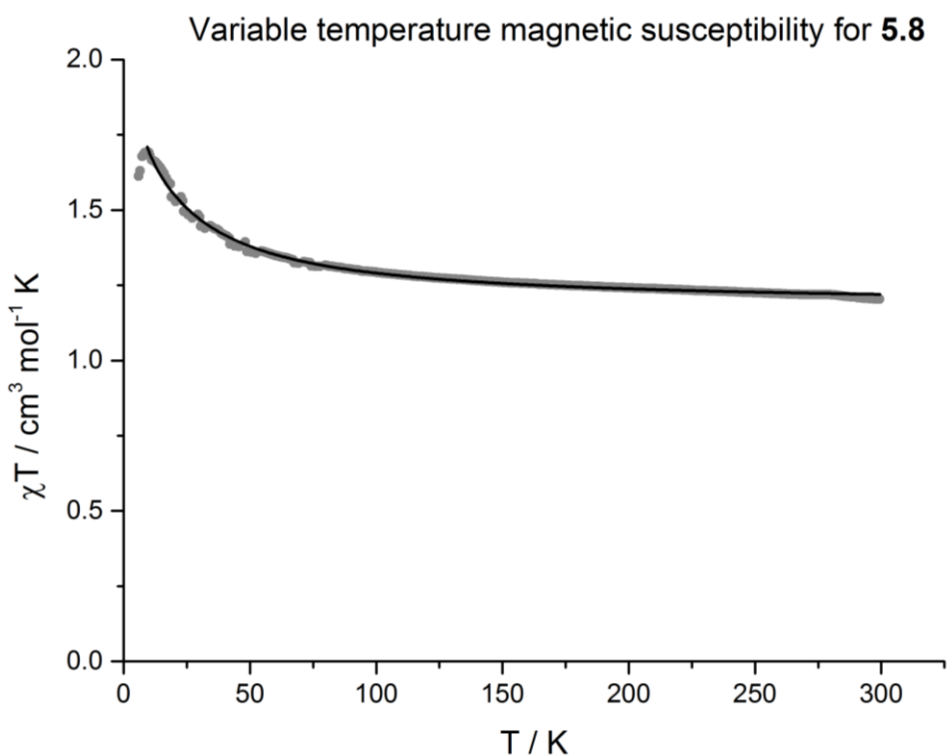


**Figure 5.18.** Magnetic susceptibility curve for **5.8** between 6 and 300 K.

In **5.8** (**Figure 5.18**), the  $\chi T$  undergoes a small linear increase from a value of 1.22 to 1.29  $\text{cm}^3 \text{mol}^{-1} \text{K}$  as the sample is decreased in temperature from 300 to 105 K, as would be expected for a system containing three non-interacting spins. As **5.8** is cooled below this point, the  $\chi T$  grows exponentially to a maximum of 1.69  $\text{cm}^3 \text{mol}^{-1} \text{K}$  at 10 K. The exchange between the spins is therefore ferromagnetic, and this is corroborated by the crystallographic observation that the nitroxyl magnetic orbitals are orthogonal to the half-filled metal orbital. Below this temperature, weak intermolecular antiferromagnetic coupling begins to occur and the  $\chi T$  decreases slightly.

The curve was fit to **Equation 5.8** ( $R^2 = 0.996$ ) with  $J = 11.96(18)$ ,  $J' = -2.95(9)$  and  $g = 2.047(1)$ .

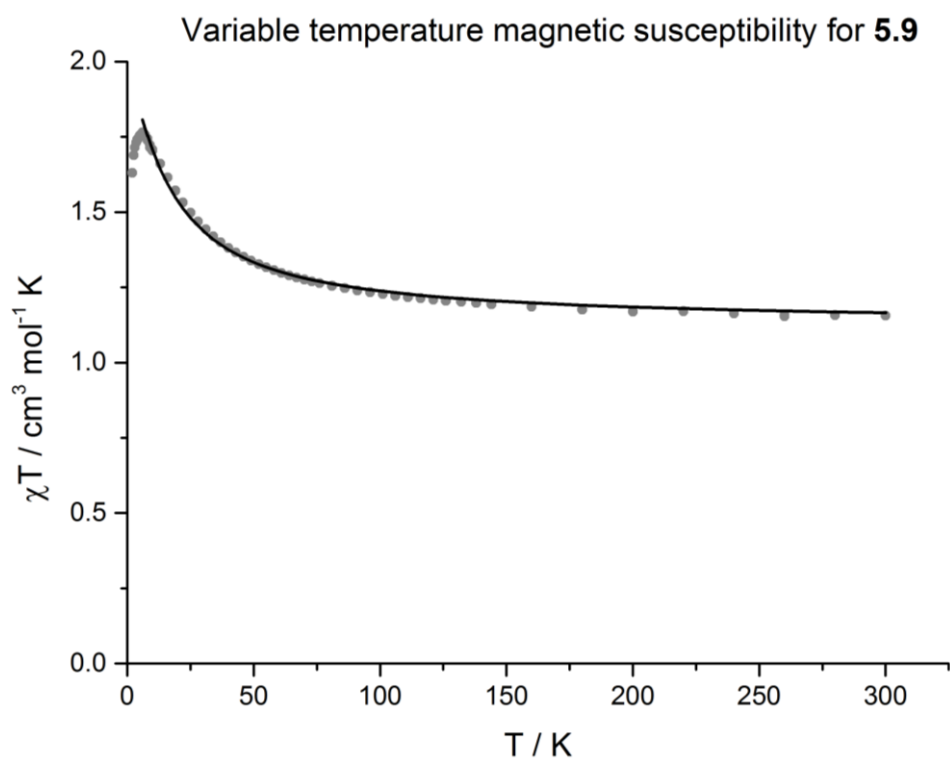


**Figure 5.19.** Magnetic susceptibility curve for **5.9** between 6 and 300 K.

In **5.9** (**Figure 5.19**), the  $\chi T$  undergoes a small linear increase from a value of  $1.15$  to  $1.22 \text{ cm}^3 \text{ mol}^{-1} \text{ K}$  as the sample is decreased in temperature from  $300$  to  $111 \text{ K}$ , as would be expected for a system containing three non-interacting spins. As **5.9** is cooled below this point, the  $\chi T$  grows exponentially to a maximum of  $1.76 \text{ cm}^3 \text{ mol}^{-1} \text{ K}$  at  $6 \text{ K}$ . The exchange between the spins is therefore ferromagnetic, and this is corroborated by the crystallographic observation that the nitroxyl magnetic orbitals are orthogonal to the half-filled metal orbital. Below this temperature, weak intermolecular antiferromagnetic coupling begins to occur and the  $\chi T$  decreases slightly.

The curve was fit to **Equation 5.8** ( $R^2 = 0.995$ ) with  $J = 11.2(2)$ ,  $J' = -0.84(16)$  and  $g = 2.00$  (fixed).

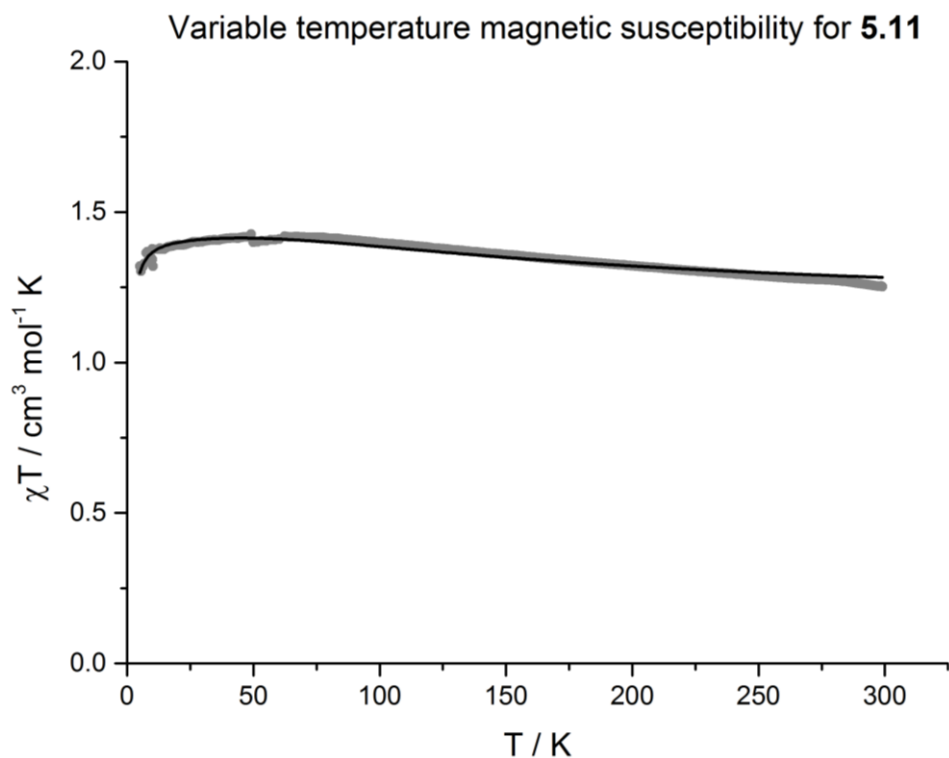


**Figure 5.20.** Magnetic susceptibility curve for **5.11** between 6 and 300 K.

In **5.11** (**Figure 5.20**), the  $\chi T$  undergoes a small linear increase from a value of 1.27 to 1.42  $\text{cm}^3 \text{mol}^{-1} \text{K}$  as the sample is decreased in temperature from 300 to 65 K, as would be expected for a system containing three non-interacting spins. As **5.11** is cooled below this point, the  $\chi T$  decreases to a minimum of 1.30  $\text{cm}^3 \text{mol}^{-1} \text{K}$  at 5 K. The  $\chi T$  magnetic behaviour is marked different in this complex, with the  $\chi T$  increasing much less. This can be rationalised by observing that both the  $J$  and  $J'$  values are larger, and a more negative  $J'$  prevents the low temperature increase in  $\chi T$ . This effect is corroborated by the crystallographic observation that the nitroxyl magnetic orbitals are non-orthogonal to the half-filled metal orbital, in contrast to the other complexes.

The curve was fit to **Equation 5.8** ( $R^2 = 0.947$ ) with  $J = 49.4(11)$ ,  $J' = -25.3(5)$  and  $g = 2.037(2)$ .

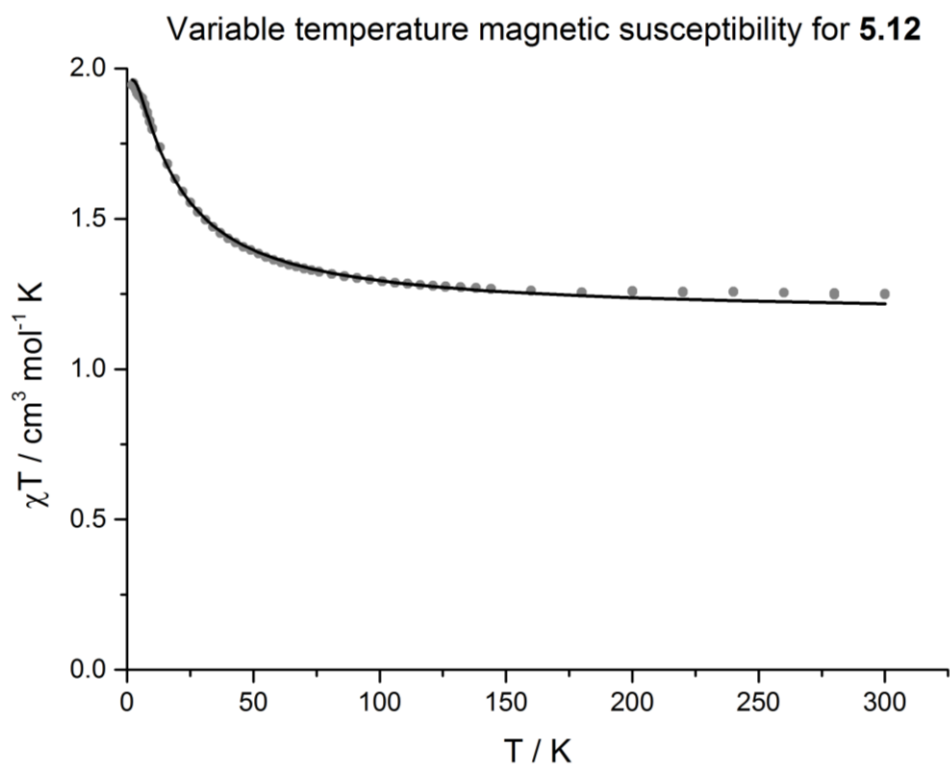


**Figure 5.21.** Magnetic susceptibility curve for **5.12** between 6 and 300 K.

In **5.12** (**Figure 5.21**), the  $\chi T$  undergoes a small linear increase from a value of 1.25 to 1.28  $\text{cm}^3 \text{mol}^{-1} \text{K}$  as the sample is decreased in temperature from 300 to 116 K, as would be expected for a system containing three non-interacting spins. As **5.12** is cooled below this point, the  $\chi T$  grows exponentially to a maximum of 1.95  $\text{cm}^3 \text{mol}^{-1} \text{K}$  at 2.5 K. The exchange between the spins is therefore ferromagnetic, and this is corroborated by the crystallographic observation that the nitroxyl magnetic orbitals are orthogonal to the half-filled metal orbital.

The curve was fit to **Equation 5.8** ( $R^2 = 0.997$ ) with  $J = 11.2(2)$ ,  $J' = -0.53(14)$  and  $g = 2.043(2)$

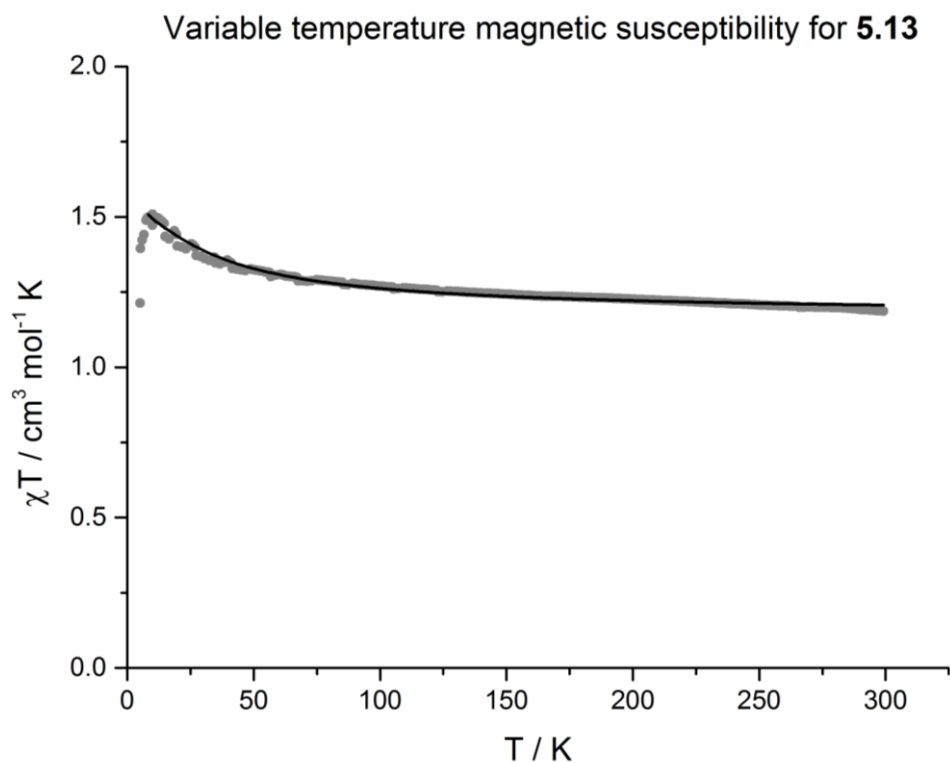


**Figure 5.22.** Magnetic susceptibility curve for **5.13** between 6 and 300 K.

In **5.13** (**Figure 5.22**), the  $\chi T$  undergoes a small linear increase from a value of 1.19 to 1.27  $\text{cm}^3 \text{mol}^{-1} \text{K}$  as the sample is decreased in temperature from 300 to 87 K, as would be expected for a system containing three non-interacting spins. As **5.13** is cooled below this point, the  $\chi T$  grows exponentially to a maximum of 1.5  $\text{cm}^3 \text{mol}^{-1} \text{K}$  at 10 K. The exchange between the spins is therefore ferromagnetic, and this is corroborated by the crystallographic observation that the nitroxyl magnetic orbitals are orthogonal to the half-filled metal orbital. Below this temperature, weak intermolecular antiferromagnetic coupling begins to occur and the  $\chi T$  decreases.

The curve was fit to **Equation 5.8** ( $R^2 = 0.985$ ) with  $J = 11.1(2)$ ,  $J' = -4.92(12)$  and  $g = 2.042(1)$ .

---

## 5.5 Conclusions and Future Work

In conclusion 7 Cu(II) complexes containing the biradical ligand **5.6** were synthesised. Their crystal structures and variable temperature magnetic susceptibilities have been investigated. Of the complexes studied, **5.7**, **5.8**, **5.9**, **5.12** and **5.13** displayed an increase in  $\chi T$  at low temperatures (<75 K), due to ferromagnetic coupling between the unpaired electrons. For **5.11**, the low temperature  $\chi T$  does not rise significantly due to both  $J$  and  $J'$  being are larger, the latter of which prevents the increase. This difference can be rationalised by the observation that the axis of Jahn-Teller elongation spans the N<sub>bisimpy</sub>-Cu-N<sub>bisimpy</sub> bonds in **5.7**, **5.8**, **5.9**, **5.12** and **5.13**, where it spans the N<sub>bpp</sub>-Cu-N<sub>bpp</sub> bonds in the **5.11** complex.

This result is comparable to those obtained by Inoue *et al.*<sup>[10]</sup>, which were discussed in detail in the introduction.

**Table 5.5.** Magnetic parameters calculated for complexes **5.8**, **5.9**, **5.11**, **5.12**, and **5.13**.

Complex	J	J'	g
<b>5.7</b>	18.7(6)	-5.04(2)	2.086(2)
<b>5.8</b>	11.96(18)	-2.95(9)	2.047(1)
<b>5.9</b>	11.2(2)	-0.84(16)	2.00 <sup>[a]</sup>
<b>5.11</b>	49.4(11)	-25.3(5)	2.037(2)
<b>5.12</b>	11.2(2)	-0.53(14)	2.043(2)
<b>5.13</b>	11.1(2)	-4.92(12)	2.042(1)

[a] g value fixed to 2.00

There was some difficulty in obtaining magnetic data for complex **5.10**, and due to time constraints their SQUID curves were not obtained. This presents a good topic for future work in this area, as they would expand the breadth of complexes studied.

With regard to the design of additional complexes to add to the series discussed in this chapter, several options are available. Increasing steric bulk on the 3-position of pyrazole as in complex **5.11** has the desired effect of changing the orientation of the Jahn-Teller axis, so other bpp ligand derivatives with heteroatoms such as Cl, Br and

---

I bonded to this position would appear likely to promote the same effect. Successful extension of the project to encompass di- or multi- nuclear complexes as in the attempted synthesis of **5.14** are also desirable, as richer magnetic properties may be observed for such systems.

---

## 5.6 References

1. A. Caneschi, D. Gatteschi, R. Sessoli, P. Rey, *Acc. Chem. Res.* **1989**, 22 (11), 392-398.
2. J. S. Miller, A. J. Epstein, W. R. Reiff, *Acc. Chem. Res.* **1988**, 21 (3), 114-120.
3. O. Kahn, *O. Angew. Chem., Int. Ed. Engl.* **1985**, 24 (10), 834-850.
4. D. C. Mattis, Springer-Verlag: The Theory of Magnetism, New York, 1981; Vol. 1.
5. V. Ovcharenko, Copper(II) Nitroxide Molecular Spin-transition Complexes. In *Magnetism: Molecules to Materials IV*, Joel S. Miller, M. D., Ed. Wiley-VCH: 2002; pp 41-62.
6. V. I. Ovcharenko, R. Z. Sagdeev, *Russ. Chem. Rev.* **1999**, 5 (68), 345-364.
7. O. Kahn, Magnetism: A Supramolecular Function, Kluwer Academic, Dordrecht: 1996.
8. K. Itoh, J. S. Miller, T. Takui, *Mol. Cryst. Liq. Cryst.* **1997**, 306 (1), ix-xi.
9. O. Kahn, *Mol. Cryst. Liq. Cryst.* **1999**, 334 (1), 69-79.
10. N. Yoshioka, M. Irisawa, M. Abe, T. Aoki, N. Aizawa, H. Inoue, *Mol. Cryst. Liq. Cryst.* **1997**, 306 (1), 397-402.
11. S. Y. Zhou, T. Li, Z. Li, Y. Q. Sun, Q. L. Wang, D. Z. Liao, L. Tian, *Inorg. Chim. Acta* **2016**, 444, 131-140.
12. G. Ulrich, R. Ziessel, D. Luneau, P. Rey, *Tet. Lett.* **1994**, 35 (8), 1211-1214.
13. G. Ulrich, R. Ziessel, *Tet. Lett.* **1994**, 35 (8), 1215-1218.
14. E. F. Ullman, L. Call, J. H. Osiecki, *J. Org. Chem.* **1970**, 35 (11), 3623-3631.
15. J. H. Osiecki, E. F. Ullman, *J. Am. Chem. Soc.* **1968**, 90 (4), 1078-1079.
16. C. Hirel, K. E. Vostrikova, J. Pécaut, V. I. Ovcharenko, *Chem. Eur. J.* **2001**, 7 (9), 2007.
17. M. Lamchen, T. W. Mittag, *J. Chem. Soc. (C)* **1966**, (0), 2300-2303.
18. H. Oshio, M. Yamamoto, H. Kawauchi, N. Koga, T. Ito, *J. Solid State Chem.* **2001**, 159 (2), 455-459.
19. P. Misra, C.-Y. Liao, H.-H. Wei, S. Mohanta, *Polyhedron* **2008**, 27 (4), 1185-1192.
20. C.-M. Che, C.-F. Chow, M.-Y. Yuen, V. A. L. Roy, W. Lu, Y. Chen, S. S.-Y. Chui, N. Zhu, *Chem. Sci.* **2011**, 2 (2), 216-220.

- 
21. J. Elhaik, C. A. Kilner, M. A. Halcrow, *Dalton Trans.* **2006**, 0 (6), 823-830.
  22. J. P. Gazda, B. Machura, R. Kruszynski, T. Grancha, N. Moliner, F. Lloret, M. Julve, *Inorg. Chem.* **2017**, 56 (11), 6281-6296.
  23. C. J. O'Connor, John Wiley & Sons: 1982; Vol. 29.

---

## Chapter 6

### Experimental

#### 6.1 Methods and Instrumentation

##### 6.1.1 NMR Spectroscopy

NMR spectra were recorded using a DPX 300 MHz or Avance 500 MHz (Bruker Corp.) spectrometer using automated procedures. All deuterated solvents were purchased from Sigma Aldrich and used as received.

##### 6.1.2 Mass Spectrometry

High resolution electrospray (ES) mass spectra were recorded on a MicroTOF mass spectrometer (Bruker Corp.) in either positive or negative ion mode by the University of Leeds mass spectrometry service. Samples were injected directly from feed solutions diluted to 10  $\mu\text{g cm}^{-1}$  and acquired over the  $m/z$  range 50 – 4000. Low resolution electrospray mass spectra were recorded on an open access Micromass LCT (Bruker Corp.) after passing through a short HPLC column. All spectra were recorded using an acetonitrile / water mix as an eluent and sodium formate calibrant.

##### 6.1.3 Elemental Analysis

The elemental composition of samples were determined by Stephen Boyer of London Metropolitan University Microanalytical Service.

##### 6.1.4 X-ray Crystallography

Crystals were mounted under Fomblin onto a nylon loop then diffraction data was collected using an in-house Agilent Supernova dual-source diffractometer using monochromated Cu- $K_{\alpha}$  radiation ( $\lambda = 1.54184 \text{ \AA}$ ) or Mo- $K_{\alpha}$  radiation ( $\lambda = 0.71073 \text{ \AA}$ ). Data collected using synchrotron radiation was acquired at Diamond Light Source ( $\lambda = 0.6889$ ) using a Rigaku Saturn 724 CCD diffractometer. Crystals were held at 120 K throughout the data capture using an Oxford Cryostream (Oxford Cryosystems) low temperature device. Reflections were measured from a hemisphere of data collected of frames, each covering  $\omega = 0.5^{\circ}$  as standard. Datasets were corrected for absorption, Lorentz and polarisation effects by semiempirical methods based upon symmetry-equivalent and multi-scan methods. Structures were solved by direct

---

methods using *ShelXL* through *Olex2*. All hydrogen atoms were refined anisotropically and hydrogen atoms included as invariants at geometrically estimated positions unless otherwise stated.

### **6.1.5 Infrared Spectroscopy**

FTIR spectra were recorded using a Spectrum One spectrophotometer (PerkinElmer) fitted with a diffuse reflectance probe with a zinc-selenide window. Eight scans were recorded for each averaged spectrum with a new background recorded after each sample. IR spectra were analysed using the spectroscopy software package *OPUS* (V 6.5 Bruker Optik GmbH).

### **6.1.6 Electronic Absorbance (UV/vis/NIR) Spectroscopy**

UV/vis/NIR spectra were recorded using a Lambda900 UV/vis/NIR spectrophotometer (PerkinElmer) in 1 cm quartz cuvettes. Spectra were recorded over a 200-2000 nm range using tungsten-halogen and deuterium lamps where appropriate and R6872 photomultiplier detector for UV/vis radiation and cooled PbS detector for NIR radiation. All data was normalized and tabulated using Origin (OriginLab Corporation).

### **6.1.7 Electrochemical Analysis**

Electrochemical analysis was carried out using a PGstat 204 (Metrohm Autolab). The working electrode was a platinum disk, the counter electrode a platinum electrode, and the reference electrode an Ag<sup>+</sup>/AgCl electrode. Data was processed using *Nova 2.0*. In all cases, solutions containing 0.1 M [<sup>n</sup>Bu<sub>4</sub>N]PF<sub>6</sub> were used as a supporting electrolyte and all peaks referenced to a ferrocene internal standard.

### **6.1.8 Magnetic Susceptibility Measurements**

Magnetic susceptibility measurements for complexes **5.8**, **5.11** and **5.13** were performed by Dr. Rafal Kulmaczewski on a Quantum Design SQUID magnetometer, in an applied field of 1000 Oe. Magnetic susceptibility measurements for complexes **5.9** and **5.12** were carried out a Quantum Design SQUID magnetometer, in an applied field of 5000 Oe. A diamagnetic correction for the sample was estimated from Pascal's constants, and a diamagnetic correction for the sample holder was also applied to the data.

---

### 6.1.9 Thermogravimetric Analysis

Thermogravimetric analyses were performed by Dr. Algy Kazlauciusas at the University of Leeds using a TA instruments TGA 2050 analyser.

### 6.1.10 Electron Paramagnetic Resonance

The continuous wave EPR spectra were recorded with help from Dr. Amgalanbataar Baldensuren on a Bruker EMX spectrometer operating at X-band with a microwave frequency of ~9.4 GHz and S-band with a microwave frequency of ~3.0 GHz. The microwave frequency and magnetic field were measured using the Bruker internal frequency counter and field controller, respectively. In order to avoid a saturation of signals, an optimized microwave power of 0.8 and 1 mW (23 and 24 dB) was applied for all measurements. Modulation amplitude of 2 – 4 G was applied to prevent an artificial signal broadening, combined with a fixed modulation frequency of 100 KHz applying a receiver gain of  $3.2 \times 10^3$  depending upon the signal-to-noise ratio. The Bruker SHQE (ER 4122) resonator was used for measurements at variable temperatures. The ESR900 helium-flow cryostat was applied for low temperature measurements. The applied magnetic field was calibrated using a Bruker standard sample with a well-known *g*-value, and all the measurements were performed at 3400 G. Simulated EPR spectra were produced with *EasySpin*.

### 6.1.11 Spectroelectrochemical Analysis

UV/vis/NIR spectroelectrochemical spectra were recorded in collaboration with Dr. Nathan Patmore and with help from Dr. Kevin Vincent of The University of Huddersfield, using an optically transparent thin layer electrode (OTTLE) cell and Cary 5000 spectrophotometer controlled by a PC running *WinUV Scan 3.0* (Agilent Technologies). The working electrode was a platinum gauze in the path of the beam, and platinum wire was used as the reference electrode. The complexes were dissolved in a solution of 0.1 M tetrabutylammonium hexafluorophosphate in dry dichloromethane.

---

## 6.2 Experimental Details

### General Procedure 1.

To a stirred solution of *ortho*-aminobenzoic acid (10 mmol) in ethanol (53 mL) in an ice bath was added concentrated hydrochloric acid (1 mL). To this was added isopentyl nitrite (2.4 mL, 18.72 mmol) and the mixture was stirred vigorously for 30 minutes. To the resulting solution was added diethyl ether (53 mL) and the mixture was stirred for 15 minutes, leading to the formation of a precipitate. The mixture was filtered and washed with diethyl ether (3 x 5 mL) to afford the diazonium salt product.

### General Procedure 2.

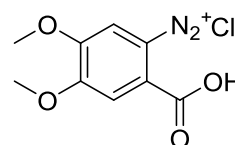
To 2,3,6,7-tetramethoxy-9,10-dimethylantracene (1.0 g, 3.07 mmol) and *ortho*-diazoniumbenzoic acid (2.3 mmol) in dichloromethane (90 mL) was added propylene oxide (20 mL, 291 mmol) and the mixture was refluxed for 18 hours. The mixture was cooled to room temperature, concentrated *in vacuo*, filtered and washed with acetone (2 x 10 mL). The resulting powder was recrystallized from acetone to afford the product.

### General Procedure 3.

To a stirred solution of methylarylether (0.13 mmol) in dry dichloromethane (6.5 mL) in an ice bath under nitrogen atmosphere was added boron tribromide (0.1 mL, 1.06 mmol). After 6 hours the reaction mixture was poured onto ice (40 g), stirred at room temperature until the ice completely melted, and was then filtered, washed with water (3 x 5 mL) and dried in a vacuum desiccator to afford the product.

### Preparation of 4,5-dimethoxybenzenediazonium-2-carboxylate (2.2).<sup>[1]</sup>

The product was prepared according to general procedure 1. To a stirred solution of 2-amino-4,5-dimethoxybenzoic acid (2.002 g, 10.16 mmol) in ethanol (53 mL) in an ice bath was added concentrated hydrochloric acid (1 mL) and the brown solution formed a brick red precipitate. To this was added isopentyl nitrite (2.4 mL, 18.72 mmol) and the mixture was stirred vigorously for 30 minutes. To the resulting dark brown solution was added diethyl ether (53 mL) and the mixture was stirred for 15 minutes, forming a tan

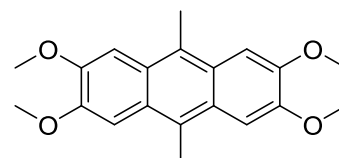


precipitate. The mixture was filtered and washed with diethyl ether (3 x 5 mL) to afford the product as a tan powder weighing 1.9515 g, 78%.

$^1\text{H}$  NMR ( $\text{CD}_3\text{OD}$ , 500 MHz) :  $\delta$  = 8.39 (s, 1H, {CH}), 7.94 (s, 1H, {CH}), 4.21 (s, 3H,  $\text{CH}_3$ ), 4.09 (s, 3H,  $\text{CH}_3$ ) ppm.  $^{13}\text{C}\{^1\text{H}\}$  NMR ( $\text{CD}_3\text{OD}$ , 75 MHz) :  $\delta$  = 163.57, 161.02, 154.17, 131.47, 116.15, 104.63, 58.53 ppm. High resolution mass spectrum (ES+)  $m/z$ : 242.2845 [ $\text{C}_9\text{H}_7\text{ClN}_2\text{O}_4$ ] $^+$ .

### Preparation of 2,3,6,7-tetramethoxy-9,10-dimethylantracene (2.3).<sup>[1]</sup>

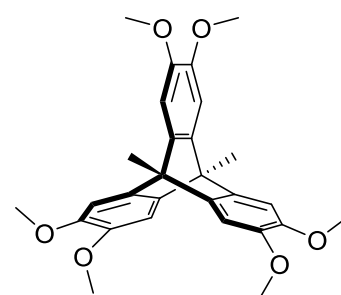
Veratrol (10 g, 72.5 mmol) was stirred in 70% sulfuric acid (20 mL) at 0°C for 15 minutes. Paraldehyde (5.5 mL, 41.4 mmol) was added dropwise very slowly with vigorous stirring, and the mixture turned red over the course of an hour. After being left to react overnight, the resulting mixture was diluted with ethanol (300 mL) and then stored in a freezer for 2 days. The mixture was filtered and washed with ethanol (10 mL) to afford a white solid weighing 11.16 g, 94.4%.



$^1\text{H}$  NMR (Chloroform-*d*, 500 MHz) :  $\delta$  = 7.34 (s, 4H, {CH}), 4.01 (s, 12H, {OCH<sub>3</sub>}), 2.88 (s, 6H, {CH<sub>3</sub>}) ppm.  $^{13}\text{C}\{^1\text{H}\}$  NMR (Chloroform-*d*, 125 MHz) :  $\delta$  = 148.74, 125.82, 102.64, 55.69, 14.76 ppm. Mass spectrum (ES+)  $m/z$ : 324.9 [ $\text{C}_{20}\text{H}_{22}\text{O}_4$ ] $^+$ .

### Preparation of 9,10-dimethyl-2,3,6,7,14,15-hexamethoxy-9,10-[1',2']benzenoanthracene (2.4).<sup>[1]</sup>

The product was prepared according to general procedure 2. To 2,3,6,7-tetramethoxy-9,10-dimethylantracene (1.0 g, 27.6 mmol) and 4,5-dimethoxybenzenediazonium-2-carboxylate (3.0 g, 12.1 mmol) in dichloromethane (90 mL) was added propylene oxide (20 mL, 30 mmol) and the mixture was refluxed for 18 hours. The mixture was cooled to room temperature, concentrated *in vacuo*, filtered and washed with ice cold acetone (2 x 10 mL). The resulting powder was recrystallized from acetone to afford white crystals weighing 3.036 g, 59%.



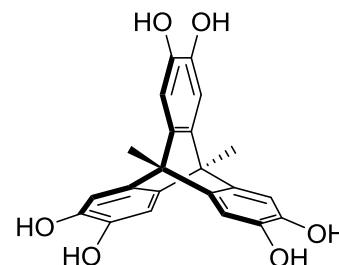
$^1\text{H}$  NMR (Chloroform-*d*, 500 MHz):  $\delta$  = 6.86 (s, 6H, {ArH}), 3.77 (s, 18H, {OCH<sub>3</sub>}), 2.31 (s, 6H, {CH<sub>3</sub>}) ppm.  $^{13}\text{C}\{^1\text{H}\}$  NMR (Chloroform-*d*, 125 MHz) :  $\delta$  = 145.69,

142.01, 105.89, 56.41, 47.72, 14.00 ppm. Mass spectrum (ES+)  $m/z$ : 463.7  $\{[C_{28}H_{30}O_6][H]\}^+$ , 947.7  $\{[C_{28}H_{30}O_6]_2[Na]\}^+$ .

### Preparation of 9,10-dimethyl-2,3,6,7,14,15-hexahydroxy-9,10-[1',2']benzenoanthracene (2.5).<sup>[1]</sup>

The product was prepared according to general procedure 3. To a stirred solution of 9,10-dimethyl-2,3,6,7,14,15-hexamethoxy-9,10-

[1',2']benzenoanthracene (0.0605 g, 0.13 mmol) in dry dichloromethane (6.5 mL) in an ice bath under nitrogen atmosphere was added boron tribromide (0.1 mL, 1.06

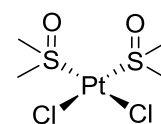


mmol). After 6 hours the reaction mixture was poured onto ice (40 g), stirred at room temperature until the ice completely melted, then filtered, washed with water (3 x 5 mL) and dried in a vacuum desiccator to afford a red powder weighing 0.0411 g, 92%.

$^1H$  NMR (Chloroform-*d*, 500 MHz) :  $\delta$  = 2.31 (s, 6H,  $\{CH_3\}$ ), 3.77 (s, 18H,  $\{OCH_3\}$ ), 6.86 (s, 6H,  $\{ArH\}$ ) ppm.  $^{13}C\{^1H\}$  NMR (Chloroform-*d*, 125 MHz) :  $\delta$  = 145.78, 114.11, 51.18, 18.92 ppm. Mass spectrum (ES+)  $m/z$ : 379.0  $\{[C_{22}H_{18}O_8][H]\}^+$ .

### Preparation of *cis*-bis(dimethylsulfoxide)platinum (II) chloride.

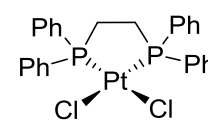
Platinum(II) chloride (0.808g, 3.04 mmol) dissolved in a 50:50 mixture of water and dimethyl sulfoxide (40 mL) was stirred for 18 hours. The mixture was filtered and dried in a vacuum desiccator to afford a cream powder weighing 1.00 g, 78%.



$^1H$  NMR ( $CD_2Cl_2$ , 500 MHz) :  $\delta$  = 1.6 (s, 12H,  $\{CH_3\}$ ) ppm.  $^{13}C\{^1H\}$  NMR (Chloroform-*d*, 125 MHz) :  $\delta$  = 41.45 ppm. Mass spectrum (ES+)  $m/z$ : 295.7  $\{[C_2H_6OSPt][Na]\}^+$ .

### Preparation of diphenylphosphinoethaneplatinum (II) chloride (3.7).

*cis*-bis(dimethylsulfoxide)platinum (II) chloride (0.771 g, 1.8 mmol) was dissolved in dichloromethane (20 mL) and added dropwise to a stirred solution of 1,2-bis(diphenylphosphino)ethane



(0.75 g, 1.9 mmol) dissolved in dichloromethane (20 mL). The mixture was heated to 40°C and stirred for 18 hours. The white precipitate that formed was filtered, washed

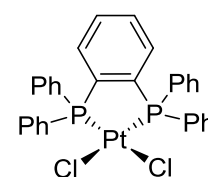
---

with chloroform (2 x 10 mL) and dried in a vacuum desiccator to afford a white powder weighing 1.1045 g, 92%.

$^1\text{H}$  NMR (dms $o$ - $d_6$ , 500 MHz) :  $\delta$  = 7.95-7.77 (m, 8H, { $\text{CH}^{2,6}$ }), 7.66-7.48 (m, 12H, { $\text{CH}^{3,4,5}$ }), 2.68-2.56 (m, 2H, { $\text{CH}_2$ }) ppm.  $^{13}\text{C}\{^1\text{H}\}$  NMR (dms $o$ - $d_6$ , 125 MHz) : 133.38, 133.23, 131.90, 128.90, 128.75.  $^{31}\text{P}\{^1\text{H}\}$  NMR (dms $o$ - $d_6$ , 121 MHz) :  $\delta$  = 42.55 (s, 2P, {P}). Mass spectrum (ES+)  $m/z$ : 495.6  $\{[(\text{C}_{24}\text{H}_{26}\text{P}_2)_2\text{Pt}]\}^{2+}$ .

### Preparation of diphenylphosphinobenzeneplatinum (II) chloride (3.8).

*cis*-bis(dimethylsulphoxide)platinum (II) chloride (0.771 g, 1.8 mmol) was dissolved in dichloromethane (20 mL) and added dropwise to a stirred solution of 1,2-bis(diphenylphosphino)ethane (0.75 g, 1.9 mmol) dissolved in dichloromethane (20 mL). The



mixture was heated to 40°C and stirred for 18 hours. The white precipitate that formed was filtered, washed with chloroform (2 x 10 mL) and dried in a vacuum desiccator to afford a white powder weighing 1.1045 g, 92%.

$^1\text{H}$  NMR (dms $o$ - $d_6$ , 300 MHz) :  $\delta$  = 7.89-7.81 (m, 2H, {ArH}), 7.80-7.69 (m, 10H, {ArH}), 7.66-7.54 (m, 12H, {ArH}) ppm.  $^{13}\text{C}\{^1\text{H}\}$  NMR (methanol- $d_4$ , 75 MHz) : 209.96, 30.56 ppm.  $^{31}\text{P}\{^1\text{H}\}$  NMR (dms $o$ - $d_6$ , 121 MHz) :  $\delta$  = 40.78 (s, 2P, {P}). High resolution mass spectrum (ES+)  $m/z$ : 752.8617  $\{[\text{C}_{30}\text{H}_{24}\text{Cl}_2\text{P}_2\text{Pt}][\text{CH}_3\text{CN}]\}^+$ , 719.1743  $\{[\text{C}_{30}\text{H}_{24}\text{Cl}_2\text{P}_2\text{Pt}][\text{Li}]\}^+$ , 677.8588  $\{[\text{C}_{30}\text{H}_{24}\text{ClP}_2\text{Pt}][\text{CH}_3\text{CN}]\}^+$ .

---

**Preparation of [(Pt(diphenylphosphinoethane))<sub>3</sub>(9,10-dimethyl-2,3,6,7,14,15-hexahydroxy-9,10-[1',2']benzenoanthracene)] (3.3).**

A mixture of 9,10-dimethyl-2,3,6,7,14,15-hexahydroxy-9,10-

[1',2']benzenoanthracene

(0.05 g, 0.13 mmol) and

diphenylphosphinoethaneplatinum(II)

chloride (0.16 g, 0.403 mmol) in dry

deoxygenated dimethylacetamide (30 mL)

was stirred for 30 minutes under nitrogen atmosphere before potassium carbonate

(0.126 g, 0.91 mmol) in dry deoxygenated methanol (12 mL) was added dropwise.

The mixture turned from yellow to green and was stirred for 18 hours. Dry

deoxygenated ether (50 mL) was added, and the mixture was cooled in an ice bath for

30 minutes before being filtered by cannula to afford a green powder. The product

was recrystallized from hot dry deoxygenated dichloromethane and filtered by cannula to afford a green powder weighing 0.067 g, 24%. Single crystals of the

product were obtained by vapour diffusion of pentane into dichloromethane.

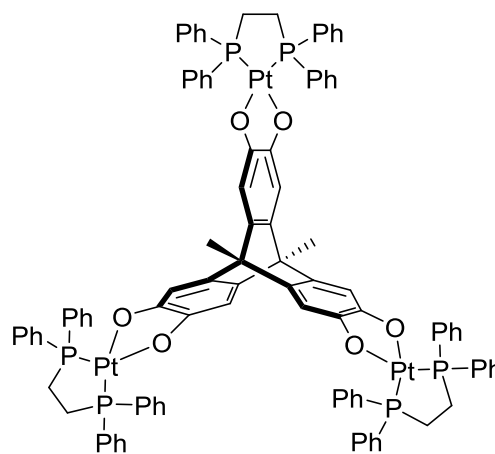
<sup>1</sup>H NMR (dms-*d*<sub>6</sub>, 500 MHz) : δ = 8.03-8.11 (m, 24H, {CH<sup>3,4,5</sup>}), 7.48-7.54 (m, 36H, {CH<sup>2,6</sup>}), 6.5 (s, 6H, {OCCH}), 1.77 (qd, 12H, (PCH<sub>2</sub>)), 1.25 (s, 6H, {CH<sub>3</sub>}) ppm.

<sup>31</sup>C{<sup>1</sup>H} NMR (CDCl<sub>3</sub>, 75 MHz) : δ = 170.60, 38.00, 35.14, 21.55 ppm. <sup>31</sup>P{<sup>1</sup>H}

NMR (CD<sub>2</sub>Cl<sub>2</sub>, 121 MHz) : δ = 30.67 (s, 6P) ppm. High resolution mass spectrum

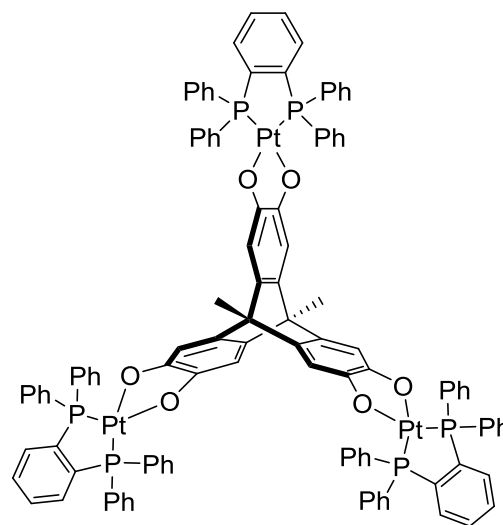
(ES<sup>+</sup>) *m/z*: 1159.2690 {[C<sub>74</sub>H<sub>61</sub>O<sub>6</sub>P<sub>4</sub>Pt<sub>2</sub>]}<sup>+</sup>, 1087.1239 {[C<sub>100</sub>H<sub>84</sub>O<sub>6</sub>P<sub>6</sub>Pt<sub>3</sub>][Na]}<sup>2+</sup>.

Found %; C 46.17, H 3.20, N 0.00 %. Calculated for Pt<sub>3</sub>P<sub>6</sub>O<sub>6</sub>C<sub>100</sub>H<sub>84</sub>(CHCl<sub>3</sub>)<sub>5</sub>; C 45.87, H 3.26, N 0.00 %.



### Preparation of [(Pt(diphenylphosphinobenzene))<sub>3</sub>(9,10-dimethyl-2,3,6,7,14,15-hexahydroxy-9,10-[1',2']benzenoanthracene)] (3.4).

A mixture of diphenylphosphinobenzeneplatinum(II) chloride (0.284 g, 0.4 mmol) and 9,10-dimethyl-2,3,6,7,14,15-hexahydroxy-9,10-[1',2']benzenoanthracene (0.05 g, 0.13 mmol) in 30 mL of dry deoxygenated dimethylacetamide was stirred for 30 minutes under nitrogen atmosphere before potassium carbonate (0.126 g, 0.91 mmol) in dry deoxygenated methanol (12 mL) was

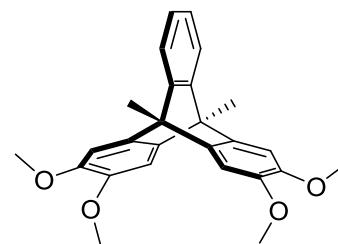


added dropwise. The mixture turned from yellow to green and was stirred for 18 hours. Dry deoxygenated ether (50 mL) was added, and the mixture was cooled in an ice bath for 30 minutes before being filtered by cannula to afford a green powder. The product was recrystallized from hot dry deoxygenated dichloromethane and filtered by cannula to afford a green powder weighing 0.146 g, 49%. Single crystals of the product were obtained by vapour diffusion of pentane into dichloromethane.

<sup>1</sup>H NMR (dms-*d*<sub>6</sub>, 500 MHz) :  $\delta$  = 7.76-7.47 (m, 78H, {ArH}), 1.99 (s, 3H, {CH<sub>3</sub>}), 1.91 (s, 3H, {CH<sub>3</sub>}) ppm. <sup>13</sup>C{<sup>1</sup>H} NMR (CD<sub>2</sub>Cl<sub>2</sub>, 75 MHz) :  $\delta$  = 134.33, 129.43, 129.29, 129.12 ppm. <sup>31</sup>P{<sup>1</sup>H} NMR (CD<sub>2</sub>Cl<sub>2</sub>, 121 MHz) :  $\delta$  = 40.74 (s, 6P) ppm. High resolution mass spectrum (ES<sup>+</sup>) *m/z*: 1655.2556 {[C<sub>82</sub>H<sub>61</sub>O<sub>6</sub>P<sub>4</sub>Pt<sub>2</sub>]}<sup>+</sup>, 2295.6864 {[C<sub>112</sub>H<sub>84</sub>O<sub>6</sub>P<sub>6</sub>Pt<sub>3</sub>]}<sup>+</sup>, 2368.3133 {[C<sub>112</sub>H<sub>84</sub>O<sub>6</sub>P<sub>6</sub>Pt<sub>3</sub>][C<sub>3</sub>H<sub>7</sub>NO]}<sup>+</sup>. Found %; C 49.00, H 3.40, N 0.00 %. Calculated for Pt<sub>3</sub>P<sub>6</sub>O<sub>6</sub>C<sub>112</sub>H<sub>84</sub>(CHCl<sub>3</sub>)<sub>4</sub>(H<sub>2</sub>O)<sub>4</sub>; C 48.95, H 3.40, N 0.00 %.

### Preparation of 9,10-dimethyl-2,3,6,7-tetramethoxy-9,10-[1',2']benzenoanthracene (2.17).<sup>[1]</sup>

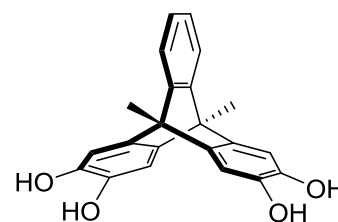
9,10-dimethyl-2,3,6,7-tetramethoxy-9,10-[1',2']benzenoanthracene was prepared according to general procedure 2 to afford a yellow powder weighing 0.3787 g, 51%.



$^1\text{H}$  NMR (Chloroform-*d*, 500 MHz) :  $\delta$  = 7.48 (t, 2H, {ArH}), 6.87 (t, 2H, {ArH}), 6.71 (s, 4H, {OCCH}), 3.77 (s, 12H, {OCH<sub>3</sub>}), 2.34 (s, 6H, {CH<sub>3</sub>}) ppm.  $^{13}\text{C}\{^1\text{H}\}$  NMR (dms-*d*<sub>6</sub>, 125 MHz) :  $\delta$  = 149.04, 145.28, 141.28, 124.18, 119.87, 106.65, 56.00, 47.60, 41.46, 13.46 ppm. Mass spectrum (ES+) *m/z*: 402.5 {[C<sub>26</sub>H<sub>26</sub>O<sub>4</sub>]}<sup>+</sup>, 425.5 {[C<sub>26</sub>H<sub>26</sub>O<sub>4</sub>][Na]}<sup>+</sup>, 827.6 {[C<sub>26</sub>H<sub>26</sub>O<sub>4</sub>]<sub>2</sub>[Na]}<sup>+</sup>.

**Preparation of 9,10-dimethyl-2,3,6,7-tetrahydroxy-9,10-[1',2']benzenoanthracene (2.18).<sup>[1]</sup>**

9,10-dimethyl-2,3,6,7-tetrahydroxy-9,10-[1',2']benzenoanthracene was prepared according to general procedure 3 to afford a red powder weighing 0.2173 g, 79%

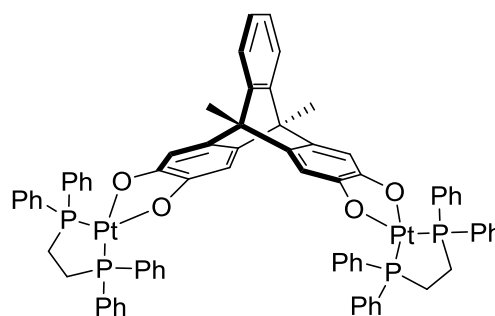


$^1\text{H}$  NMR (Chloroform-*d*, 500 MHz) :  $\delta$  = 7.28 (t, 2H, {ArH}), 6.95 (t, 2H, {ArH}), 6.87 (s, 4H, {OCCH}), 2.25 (s, 6H, {CH<sub>3</sub>}) ppm.  $^{13}\text{C}\{^1\text{H}\}$  NMR (dms-*d*<sub>6</sub>, 75 MHz) :  $\delta$  = 149.49, 140.94, 139.82, 123.98, 119.47, 109.24, 46.71, 13.55 ppm. High resolution mass spectrum (ES+) *m/z*: 367.0944 {[C<sub>22</sub>H<sub>16</sub>O<sub>4</sub>][Na]}<sup>+</sup>.

**Preparation of [(Pt(diphenylphosphinoethane))<sub>2</sub>(9,10-dimethyl-2,3,6,7-tetrahydroxy-9,10-[1',2']benzenoanthracene)] (3.1).**

9,10-dimethyl-2,3,6,7-tetrahydroxy-9,10-[1',2']benzenoanthracene (0.05 g, 0.144 mmol) and

diphenylphosphinoethaneplatinum(II) chloride (0.193 g, 0.288 mmol) in 30 mL of dry deoxygenated dimethylacetamide was



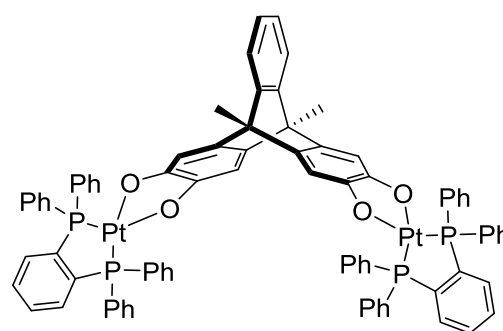
stirred for 30 minutes under nitrogen atmosphere before potassium carbonate (0.126 g, 0.91 mmol) in dry deoxygenated methanol (12 mL) was added dropwise. The mixture turned from yellow to brown and was stirred for 18 hours. Dry deoxygenated ether (50 mL) was added, and the mixture was cooled in an ice bath for 30 minutes before being filtered by cannula to leave an orange powder. The product was recrystallised from hot dry deoxygenated dichloromethane and filtered by cannula to afford an orange powder weighing 0.042 g, 19%. Single crystals of the product were obtained by vapour diffusion of pentane into dichloromethane.

$^1\text{H}$  NMR (dms- $d_6$ , 500 MHz) :  $\delta$  = 8.60-8.58 (m, 16H,  $\{\text{CH}^{3,4,5}\}$ ), 7.52-7.50 (m, 24H,  $\{\text{CH}^{2,6}\}$ ), 6.57 (s, 6H,  $\{\text{OCCH}\}$ ), 1.79 (qd, 8H,  $\{\text{PCH}_2\}$ ), 2.14 (s, 6H,  $\{\text{CH}_3\}$ ) ppm.  $^{13}\text{C}\{^1\text{H}\}$  NMR ( $\text{CD}_2\text{Cl}_2$ , 75 MHz) :  $\delta$  = 134.22, 134.04, 133.88, 132.48, 129.40, 129.24 ppm.  $^{31}\text{P}\{^1\text{H}\}$  NMR ( $\text{CD}_2\text{Cl}_2$ , 121 MHz) :  $\delta$  = 41.79 (s, 4P) ppm. High resolution mass spectrum (ES+)  $m/z$ : 1528.2907  $\{[\text{C}_{74}\text{H}_{61}\text{O}_4\text{P}_4\text{Pt}_2]\}^+$ . Found %; C 48.45, H 3.47, N 0.00 %. Calculated for  $[(\text{C}_{74}\text{H}_{62}\text{O}_4\text{P}_4\text{Pt}_2)(\text{CHCl}_3)_3]$ ; C 49.00, H 3.47, N 0.00 %.

**Preparation of  $[(\text{Pt}(\text{diphenylphosphinobenzene}))_2(9,10\text{-dimethyl-2,3,6,7-tetrahydroxy-9,10-[1',2']\text{benzenoanthracene})]$  (3.2).**

9,10-dimethyl-2,3,6,7-tetrahydroxy-9,10-[1',2']benzenoanthracene (0.05 g, 0.144 mmol) and

diphenylphosphinobenzeneplatinum(II) chloride (0.21 g, 0.29 mmol) in 30 mL of dry deoxygenated dimethylacetamide was stirred for 30 minutes under nitrogen

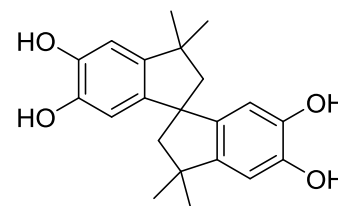


atmosphere before potassium carbonate (0.126 g, 0.91 mmol) in dry deoxygenated methanol (12 mL) was added dropwise. The mixture turned from yellow to brown and was stirred for 18 hours. Dry deoxygenated ether (50 mL) was added, and the mixture was cooled in an ice bath for 30 minutes before being filtered by cannula to leave a yellow powder. The product was recrystallised from hot dry deoxygenated dichloromethane and filtered by cannula to afford a yellow powder weighing 0.050 g, 27%. Single crystals of the product were obtained by vapour diffusion of pentane into dichloromethane.

$^1\text{H}$  NMR ( $\text{CD}_2\text{Cl}_2$ , 300 MHz) :  $\delta$  = 7.76-7.10 (m, 50H,  $\{\text{ArH}\}$ ), 6.80-6.67 (m, 4H,  $\{\text{ArH}\}$ ), 6.07 (s, 2H,  $\{\text{ArH}\}$ ), 1.62 (s, 6H,  $\{\text{CH}_3\}$ ) ppm.  $^{13}\text{C}\{^1\text{H}\}$  NMR ( $\text{CD}_2\text{Cl}_2$ , 75 MHz) :  $\delta$  = 134.43-133.90, 132.42, 129.69-129.29 ppm.  $^{31}\text{P}\{^1\text{H}\}$  NMR ( $\text{CD}_2\text{Cl}_2$ , 121 MHz) :  $\delta$  = 31.14 (s, 4P) ppm. High resolution mass spectrum (ES+)  $m/z$ : 1625.2923  $\{[\text{C}_{82}\text{H}_{63}\text{O}_4\text{P}_4\text{Pt}_2]\}^+$ . Found %; C 48.68, H 3.05, N 0.00 %. Calculated for  $\text{Pt}_2\text{P}_4\text{O}_4\text{C}_{82}\text{H}_{62}(\text{CHCl}_3)_4$ ; C 49.12, H 3.16, N 0.00 %.

### Preparation of 3,3,3',3'-tetramethyl-5,5',6,6'-tetrahydroxy-1,1'-spirobis(indane).<sup>[2]</sup>

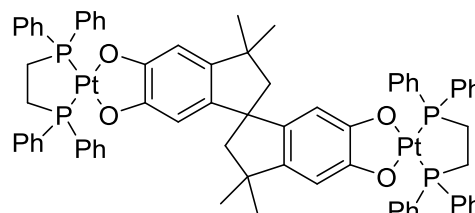
Catechol (1 g, 9.1 mmol), acetone (1.1 mL, 15 mmol), acetic acid (2.3 mL, 40.2 mmol), and concentrated hydrochloric acid (1.8 mL) were heated at reflux for 48 hours. The crystalline product was filtered, washed with ice cold acetic acid (2 x 10 mL), then water (3 x 10 mL), and dried in a vacuum desiccator to afford white crystals weighing 0.84 g, 57%.



<sup>1</sup>H NMR (Chloroform-*d*, 500 MHz) :  $\delta$  = 6.65 (s, 2H, {ArH}), 6.24 (s, 2H, {ArH}), 2.26-2.31 (d, <sup>3</sup>J<sub>H,H</sub> = 1.9 Hz, 2H, {CH<sub>2</sub>}), 2.10-2.15 (d, <sup>3</sup>J<sub>H,H</sub> = 1.9 Hz, 2H, {CH<sub>2</sub>}), 1.35 (s, 6H, {CH<sub>3</sub>}), 1.25 (s, 6H, {CH<sub>3</sub>}) ppm. <sup>13</sup>C{<sup>1</sup>H} NMR (Chloroform-*d*, 125 MHz) :  $\delta$  = 144.59, 142.12, 140.80, 110.12, 108.29, 59.55, 56.30, 42.33, 31.53, 30.48 ppm. Mass spectrum (ES+) *m/z*: 361.7 {[C<sub>21</sub>H<sub>23</sub>O<sub>4</sub>][Na]}<sup>+</sup>, 699.8 {[C<sub>21</sub>H<sub>24</sub>O<sub>4</sub>]<sub>2</sub>[H<sub>2</sub>O][H]}<sup>+</sup>.

### Preparation of [(diphenylphosphinoethaneplatinum)(3,3,3',3'-tetramethyl-5,5',6,6'-tetrahydroxy-1,1'-spirobis(indane))] (3.5).

A mixture of 3,3,3',3'-tetramethyl-5,5',6,6'-tetrahydroxy-1,1'-spirobis(indane) (0.1 g, 0.29 mmol) and diphenylphosphinoethaneplatinum(II)



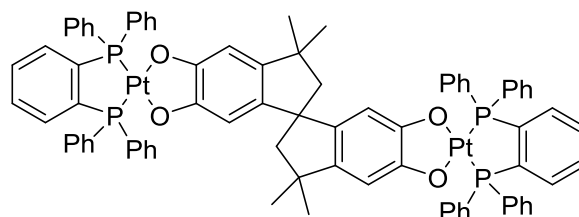
chloride (0.39 g, 0.59 mmol) in 20 mL of dry deoxygenated dimethylacetamide were stirred for 30 minutes under nitrogen atmosphere before potassium carbonate (0.01 g, 0.725 mmol) in dry deoxygenated methanol (5 mL) was added dropwise. The mixture was stirred for 18 hours. Dry deoxygenated ether (30 mL) was added, and the mixture was cooled in an ice bath for 30 minutes before being filtered by cannula to afford a yellow powder. The yellow powder was recrystallised from hot dry deoxygenated dichloromethane and filtered by cannula to afford a yellow powder weighing 0.053 g, 12%. Single crystals of the product were obtained by vapour diffusion of pentane into dichloromethane.

<sup>1</sup>H NMR (Chloroform-*d*, 500 MHz) :  $\delta$  = 8.06-7.78 (m, 16H, {ArH}), 7.48-7.29 (m, 24H, {ArH}), 6.62 (s, 2H, {ArH}), 6.47 (s, 2H, {ArH}), 2.25 (d, <sup>3</sup>J<sub>H,H</sub> = 1.9 Hz, 2H,

{CH<sub>2</sub>}), 2.10 (s, 2H, {CH<sub>2</sub>}), 1.29 (s, 6H, {CH<sub>3</sub>}), 1.26 (s, 6H, {CH<sub>3</sub>}) ppm. <sup>13</sup>C{<sup>1</sup>H} NMR (CD<sub>2</sub>Cl<sub>2</sub>, 75 MHz): δ = 225.78, 170.62, 133.61, 131.88, 129.41 ppm. <sup>31</sup>P{<sup>1</sup>H} NMR (CD<sub>2</sub>Cl<sub>2</sub>, 121 MHz) : δ = 32.20-32.10 (d, 2P), 30.90-30.80 (d, 2P) ppm. High resolution mass spectrum (ES+) *m/z*: 1523.3384 {[C<sub>73</sub>H<sub>69</sub>O<sub>4</sub>P<sub>4</sub>Pt<sub>2</sub>]}<sup>+</sup>. Found %; C 57.61, H 4.68, N 0.00 %. Calculated for Pt<sub>2</sub>P<sub>4</sub>O<sub>4</sub>C<sub>81</sub>H<sub>68</sub>(CHCl<sub>3</sub>)<sub>5</sub>; C 57.56, H 4.50, N 0.00 %.

**Preparation of [(Pt(diphenylphosphinobenzene))<sub>2</sub>(3,3,3',3'-tetramethyl-5,5',6,6'-tetrahydroxy-1,1'-spirobis(indane))] (3.6).**

A mixture of 3,3,3',3'-tetramethyl-5,5',6,6'-tetrahydroxy-1,1'-spirobis(indane) (0.1 g, 0.29 mmol) and

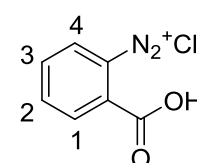


diphenylphosphinobenzeneplatinum(II) chloride (0.42 g, 0.59 mmol) in 20 mL of dry deoxygenated dimethylacetamide were stirred for 30 minutes under nitrogen atmosphere before potassium carbonate (0.01 g, 0.725 mmol) in dry deoxygenated methanol (5 mL) was added dropwise. The mixture was stirred for 18 hours. Dry deoxygenated ether (30 mL) was added, and the mixture was cooled in an ice bath for 30 minutes before being filtered by cannula to leave a yellow powder. The yellow powder was recrystallised from hot dry deoxygenated dichloromethane and filtered by cannula to afford a yellow powder weighing 0.164 g, 35%. Single crystals of the product were obtained by vapour diffusion of pentane into dichloromethane.

<sup>1</sup>H NMR (CD<sub>2</sub>Cl<sub>2</sub>, 300 MHz) : δ = 8.81-7.49 (m, 24H, {ArH}), 6.35 (s, 1H, {ArH}), 6.03 (s, 1H, {ArH}), 2.16-1.25 (t, 16H, {AlkH}) ppm. <sup>13</sup>C{<sup>1</sup>H} NMR (dms-*d*<sub>6</sub>, 125 MHz) : δ = 149.22, 140.67, 139.34, 123.70, 119.20, 108.97, 106.97, 46.44, 13.28 ppm. <sup>31</sup>P{<sup>1</sup>H} NMR (CD<sub>2</sub>Cl<sub>2</sub>, 121 MHz) : δ = 31.05 (s, 4P) ppm. High resolution mass spectrum (ES+) *m/z*: 1619.3395 {[C<sub>81</sub>H<sub>69</sub>O<sub>4</sub>P<sub>4</sub>Pt<sub>2</sub>]}<sup>+</sup>. Found %; C 46.48, H 3.30, N 0.00 %. Calculated for Pt<sub>2</sub>P<sub>4</sub>O<sub>4</sub>C<sub>81</sub>H<sub>68</sub>(CHCl<sub>3</sub>)<sub>5</sub>; C 46.61, H 3.32, N 0.00 %.

**Preparation of benzenediazonium-2-carboxylate (2.7).<sup>[1]</sup>**

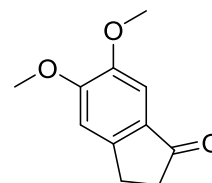
Benzenediazonium-2-carboxylate was prepared according to general procedure 1 to afford a tan powder weighing 2.1024 g, 78%.



$^1\text{H}$  NMR (Chloroform-*d*, 500 MHz) :  $\delta$  = 8.60 (d,  $^3J_{\text{H,H}} = 1.9$  Hz, 1H, {ArH<sup>1</sup>}), 8.33 (d,  $^3J_{\text{H,H}} = 1.9$  Hz, 1H, {ArH<sup>4</sup>}), 8.24 (t,  $^3J_{\text{H,H}} = 1.8$  Hz, 1H, {ArH<sup>2</sup>}), 8.00 (t,  $^3J_{\text{H,H}} = 1.8$  Hz, 1H, {ArH<sup>3</sup>}) ppm.  $^{13}\text{C}\{^1\text{H}\}$  NMR (Chloroform-*d*, 125 MHz) :  $\delta$  = 165.55, 142.37, 136.41, 136.09, 134.37, 133.94, 117.00 ppm. Mass spectrum (ES+) *m/z*: 121.0 {[C<sub>7</sub>H<sub>5</sub>O<sub>2</sub>]}<sup>+</sup>, 197.0 {[C<sub>7</sub>H<sub>5</sub>ClN<sub>2</sub>O<sub>2</sub>]<sub>2</sub>[Na][H]}<sup>2+</sup>.

#### Preparation of 5,6-dimethoxy-1-indanone (4.4).<sup>[3]</sup>

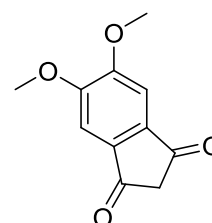
To a solution of 3-(3,4-dimethoxyphenyl)propionic acid (1 g, 4.76 mmol) in dry dichloromethane (14.3 mL) and dimethylformamide (0.05 mL) was added oxalyl chloride (0.83 mL, 9.52 mmol) dropwise over 30 minutes. The mixture was stirred at room temperature for 18 hours. The resulting mixture was concentrated under reduced pressure and the crude product was redissolved in dry dichloromethane (15 mL) at 0°C. To this solution was added portionwise aluminium (III) chloride (0.953 g, 7.14 mmol) and the reaction mixture was stirred at room temperature for 2 hours. Ice (0.5 g) was added slowly at 0°C followed by ice water (7.5 mL). The organic phase was separated, and the aqueous phase extracted with dichloromethane (2 x 7.5 mL). The combined organic phases were washed with brine (1 x 10 mL), dried over sodium sulphate, decolourised with activated carbon, then filtered and concentrated *in vacuo*. The product was purified by flash column chromatography (hexane : ethyl acetate = 4 : 1) on silica gel to afford a pale yellow powder weighing 0.3063g, 34%.



$^1\text{H}$  NMR (Chloroform-*d*, 500 MHz) :  $\delta$  = 7.16 (s, 1H, {ArH}), 6.89 (s, 1H, {ArH}), 3.98 (s, 3H, {OCH<sub>3</sub>}), 3.91 (s, 3H, {OCH<sub>3</sub>}), 3.03 (s, 2H, {CH<sub>2</sub>}), 2.65 (s, 2H, {CH<sub>2</sub>}) ppm.  $^{13}\text{C}\{^1\text{H}\}$  NMR (Chloroform-*d*, 125 MHz) :  $\delta$  = 205.50, 155.26, 150.32, 149.22, 129.75, 107.38, 104.00, 56.11, 55.95, 36.39, 25.42 ppm. Mass spectrum (ES+) *m/z*: 192.1 {[C<sub>11</sub>H<sub>12</sub>O<sub>3</sub>]}<sup>+</sup>.

#### Preparation of 2,3-dihydro-5,6-dimethoxy-1H-indene-1,3-dione (4.5).<sup>[3]</sup>

A solution of 5,6-dimethoxy-1-indanone (1.977 g, 10.3 mmol) in acetic acid (3 mL) and water (0.6 mL) was stirred and cooled in an ice bath while chromium (VI) oxide (0.78 g, 7.8 mmol) was added in portions over a period of 2 hours. The temperature of the reaction was kept below 15°C initially before being allowed to return to ambient

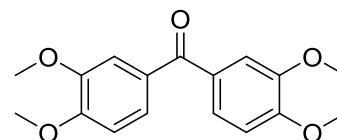


temperature where it was stirred for 3 days. After addition of 2-propanol (0.6 mL) and stirring for an hour, the solvent was removed *in vacuo* in a water bath of temperature <50°C. The residue was dissolved in water (5 mL) and extracted with dichloromethane (1 x 5 mL and 5 x 2.5 mL). The extracts were washed with water (4.5 mL), dried with sodium sulphate and concentrated *in vacuo*. The crude product was precipitated by addition of *n*-hexane (1.1 mL), separated by filtration and dried in a vacuum desiccator to afford the product as a yellow solid weighing 0.403 g, 19%.

$^1\text{H}$  NMR (Chloroform-*d*, 500 MHz) :  $\delta$  = 7.30 (s, 2H, {ArH}), 4.05 (s, 6H, {CH<sub>3</sub>}), 3.20 (s, 2H, {CH<sub>2</sub>}) ppm.  $^{13}\text{C}\{^1\text{H}\}$  NMR (Chloroform-*d*, 125 MHz) :  $\delta$  = 196.61, 155.88, 138.43, 103.23, 56.71, 44.70 ppm. Mass spectrum (ES+) *m/z*: 207.5 {[C<sub>11</sub>H<sub>10</sub>O<sub>4</sub>][H]}<sup>+</sup>, 432.5 {[C<sub>11</sub>H<sub>10</sub>O<sub>4</sub>]<sub>2</sub>[H<sub>2</sub>O][H]}<sup>+</sup>.

### Preparation of bis(3,4-dimethoxyphenyl)methanone (4.7).<sup>[3]</sup>

Polyphosphoric acid (11.6 g) was heated to 80°C and then veratrol (1 g, 7.26 mmol) and 3,4-dimethoxybenzoic acid (1.32 g, 7.25 mmol) were added and the mixture was stirred at 80°C. After stirring for 30

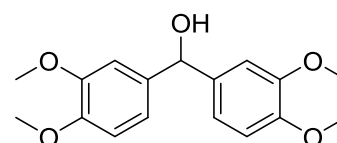


minutes, the reaction mixture was poured onto ice (60 g) while still hot, then the brown precipitate was collected by vacuum filtration, dried in a vacuum desiccator, then recrystallized twice from ethanol to afford a light brown solid weighing 1.64 g, 75%.

$^1\text{H}$  NMR (Chloroform-*d*, 500 MHz) :  $\delta$  = 7.46 (d,  $^4J_{\text{H,H}}$  = 1.9 Hz, 2H, {ArH}), 7.42-7.40 (dd,  $^3J_{\text{H,H}}$  = 8.2 Hz,  $^4J_{\text{H,H}}$  = 1.9 Hz, 2H, ArH), 6.94 (d,  $^4J_{\text{H,H}}$  = 8.1 Hz, 2H, {ArH}), 4.00 (s, 6H, {OCH<sub>3</sub>}), 3.98 (s, 6H, {OCH<sub>3</sub>}) ppm.  $^{13}\text{C}\{^1\text{H}\}$  NMR (Chloroform-*d*, 125 MHz) :  $\delta$  = 194.50, 152.63, 148.90, 130.81, 124.78, 112.34, 109.77, 56.08, 56.07 ppm. Mass spectrum (ES+) *m/z*: 302.1 {[C<sub>17</sub>H<sub>18</sub>O<sub>5</sub>]}<sup>+</sup>.

### Preparation of bis(3,4-dimethoxyphenyl)methane monohydrate (4.8).<sup>[3]</sup>

bis(3,4-dimethoxyphenyl)methanone (17.0 g, 56.29 mmol) was suspended in methanol (280 mL) which had been deacidified by passing it through basic alumina.



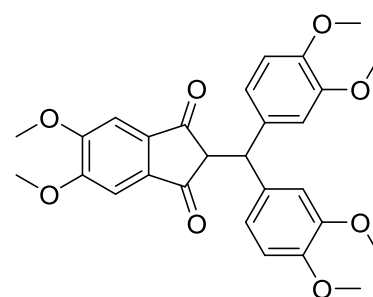
Pyridine (0.35 mL) and palladium on charcoal (0.1 g, 10% Pd, oxidic form) were then added and the mixture was mechanically stirred under hydrogen in a Parr apparatus

(10.0 bar, 20°C). The absorption of hydrogen was monitored over time, and after 4 days the rate of absorption fell to zero. The suspension was then filtered through Celite 545 and then washed with deacidified methanol (20 mL). The solvent was removed under reduced pressure to give a residue which was recrystallized from toluene to afford the monohydrate as a light yellow sticky solid weighing 12.0 g, 70%.

$^1\text{H}$  NMR (Chloroform-*d*, 500 MHz) :  $\delta$  = 6.96 (d,  $^4J_{\text{H,H}} = 1.9$  Hz, 2H, {ArH}), 6.91 (dd,  $^3J_{\text{H,H}} = 8.2$  Hz,  $^4J_{\text{H,H}} = 1.9$  Hz, 2H, {ArH}), 6.86 (d,  $^3J_{\text{H,H}} = 8.2$  Hz, 2H, {ArH}), 5.79 (s, 1H, {CH}), 3.89 (s, 6H, {OCH<sub>3</sub>}), 3.90 (s, 6H, {OCH<sub>3</sub>}), 2.20 (b, 1H, {OH}) ppm.  $^{13}\text{C}\{^1\text{H}\}$  NMR (Chloroform-*d*, 125 MHz) :  $\delta$  = 149.03, 148.47, 136.59, 118.89, 110.94, 109.76, 75.75, 55.93-55.88 ppm. Mass spectrum (ES+) *m/z*: 287.4 {[C<sub>17</sub>H<sub>19</sub>O<sub>4</sub>]}<sup>+</sup>, 303.4 {[C<sub>17</sub>H<sub>20</sub>O<sub>5</sub>]}<sup>+</sup>, 631.2 {[C<sub>17</sub>H<sub>20</sub>O<sub>5</sub>]<sub>2</sub>[Na]}<sup>+</sup>.

#### Preparation of 2-[bis(3,4-dimethoxyphenyl)methyl]-5,6-dimethoxy-1*H*-indene-1,3(2*H*)-dione (4.9).<sup>[3]</sup>

A solution of **4.8** (0.109 g, 0.53 mmol) and *para*-toluenesulfonic acid monohydrate (0.0115 g, 0.06 mmol) in toluene (30 mL) was heated to reflux in a flask equipped with a Thiele-Pape extractor containing 4 Å molecular sieves. A solution of **4.5** (0.1836 g, 0.60 mmol) in dichloroethane (24 mL) was



added slowly to the reaction mixture. Initially, addition caused a purple colouration to appear, which then rapidly vanished with vigorous stirring. After the addition was complete, the reaction had changed colour from yellow to red, and was left to reflux for 18 hours. The reaction was cooled, washed with water and the combined organics dried with sodium sulfate and concentrated to dryness. The residue was purified by column chromatography (ethyl acetate) and then recrystallized from methanol to afford the product as a light yellow solid weighing 0.232 g, 89 %.

$^1\text{H}$  NMR (Chloroform-*d*, 500 MHz) :  $\delta$  = 7.14 (s, 2H, {ArH}), 6.88 (d,  $^4J_{\text{H,H}} = 1.9$  Hz, 2H, {ArH}), 6.81 (d,  $^4J_{\text{H,H}} = 1.9$  Hz, 2H, {ArH}), 6.66 (d,  $^3J_{\text{H,H}} = 8.2$  Hz, 2H, {ArH}), 4.91 (d,  $^3J_{\text{H,H}} = 2.0$  Hz, 1H, {CH}), 3.91 (s, 6H, {OCH<sub>3</sub>}), 3.74 (s, 6H, {OCH<sub>3</sub>}), 3.71 (m, 7H, {OCH<sub>3</sub>, CH}) ppm.  $^{13}\text{C}\{^1\text{H}\}$  NMR (Chloroform-*d*, 125 MHz) :  $\delta$  = 203.63,

---

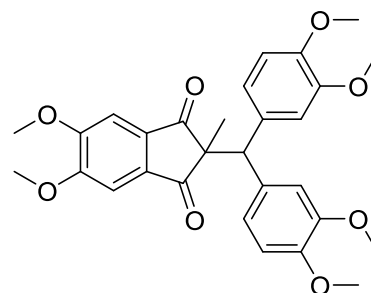
156.15, 147.56, 135.25, 133.00, 121.86, 112.82, 110.84, 103.60, 56.70, 55.70, 49.50 ppm. Mass spectrum (ES+)  $m/z$ : 287.5 {[C<sub>17</sub>H<sub>19</sub>O<sub>4</sub>]}<sup>+</sup>, 529.5 {[C<sub>28</sub>H<sub>28</sub>O<sub>8</sub>][K]}<sup>+</sup>.

#### Preparation of potassium fluoride on celite 545.

Celite 545 (20 g) was mixed with potassium fluoride (20 g) in water (500 mL), and the water was removed at 60°C by rotary evaporator. The solid obtained was shaken in acetonitrile (100 mL), filtered, washed with acetonitrile (2 x 50 mL) then dried in a vacuum desiccator for 18 hours.

#### Preparation of 2-[bis(3,4-dimethoxyphenyl)methyl]-5,6-dimethoxy-2-methyl-1H-indene-1,3(2H)-dione (4.10).<sup>[3]</sup>

A solution of 2-[bis(3,4-dimethoxyphenyl)methyl]-5,6-dimethoxy-1H-indene-1,3(2H)-dione (0.200 g, 0.407 mmol) in acetonitrile (0.61 mL) was stirred while iodomethane (0.087 g, 0.617 mmol) and potassium fluoride on Celite 545 (0.12 g) were added.



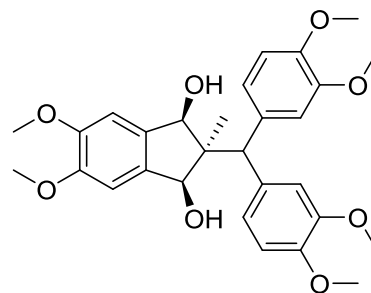
The suspension was heated to reflux for 18 hours then allowed to cool before being filtered. The solid residue was washed with acetonitrile (3 x 1 mL) until its colour had faded. The combined organics were concentrated to dryness and the residue was recrystallised from methanol to afford the product as a yellow solid weighing 0.152 g, 74 %.

<sup>1</sup>H NMR (Chloroform-*d*, 500 MHz) :  $\delta$  = 7.19 (d, <sup>4</sup>J<sub>H,H</sub> = 1.9 Hz, 2H, {ArH}), 7.11 (d, 2H, {ArH}), 6.88 (dd, <sup>3</sup>J<sub>H,H</sub> = 8.2 Hz, <sup>4</sup>J<sub>H,H</sub> = 1.9 Hz, 2H, {ArH}), 6.60 (d, <sup>3</sup>J<sub>H,H</sub> = 8.2 Hz, 2H, {ArH}), 4.41 (s, 1H, {CH}), 3.90 (s, 6H, {OCH<sub>3</sub>}), 3.79 (s, 6H, {OCH<sub>3</sub>}), 3.71 (s, 6H, {OCH<sub>3</sub>}), 1.21 (s, 3H, {CH<sub>3</sub>}) ppm. <sup>13</sup>C{<sup>1</sup>H} NMR (Chloroform-*d*, 125 MHz) :  $\delta$  = 203.53, 155.90, 148.35, 147.57, 136.46, 132.98, 121.82, 110.74, 102.37, 58.29, 56.63, 56.55, 55.69, 55.64, 55.63, 20.22 ppm. Mass spectrum (ES+)  $m/z$ : 506.2 {[C<sub>29</sub>H<sub>30</sub>O<sub>8</sub>]}<sup>+</sup>.

---

**Preparation of all-*cis*-2-[bis(3,4-dimethoxyphenyl)methyl]-5,6-dimethoxy-2-methyl-1,3-indanediol (4.11).**<sup>[3]</sup>

A solution of 2-[bis(3,4-dimethoxyphenyl)methyl]-5,6-dimethoxy-2-methyl-1*H*-indene-1,3(2*H*)-dione (0.0386 g, 0.076 mmol) in toluene (1 mL) was stirred under nitrogen atmosphere and cooled in an ice bath. A 1.0 M solution of diisobutylaluminium hydride in toluene (0.2 mL, 0.2 mmol) was added dropwise and

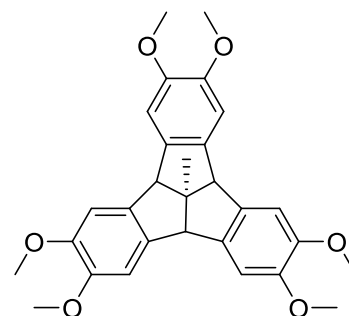


the mixture was then stirred at ambient temperature for 18 hours. After the slow addition of saturated ammonium chloride (0.2 mL), the precipitate was collected by Buchner filtration and washed with dichloromethane (4 x 0.2 mL). The organic layer was separated, and the aqueous layer was extracted with dichloromethane (1 mL). The combined organics were washed with water (5 mL), dried with sodium sulfate and concentrated to dryness. The solid residue was recrystallized from toluene to afford the product as a white solid weighing 31 mg, 80 %.

<sup>1</sup>H NMR (Chloroform-*d*, 500 MHz) :  $\delta$  = 7.11-7.10 (d, <sup>4</sup>J<sub>H,H</sub> = 1.9 Hz, 2H, {ArH}), 7.01 (d, <sup>4</sup>J<sub>H,H</sub> = 1.9 Hz, 2H, {ArH}), 6.91 (s, 2H, {ArH}), 6.80-6.78 (d, <sup>3</sup>J<sub>H,H</sub> = 8.7 Hz, 2H, {ArH}), 5.02 (s, 1H, {CH}), 4.45-4.43 (d, <sup>3</sup>J<sub>H,H</sub> = 5.7 Hz, 2H), 3.82 (s, 18H, {CH<sub>3</sub>}), 2.14-2.13 (d, <sup>3</sup>J<sub>H,H</sub> = 6.2 Hz, 2H), 0.79 (s, 3H, {CH<sub>3</sub>}) ppm. <sup>13</sup>C{<sup>1</sup>H} NMR (Chloroform-*d*, 125 MHz) :  $\delta$  = 150.21, 148.95, 147.80, 136.79, 134.46, 121.57, 113.40, 111.13, 108.58, 82.38, 56.01, 55.93, 55.88, 54.45, 47.17, 20.70 ppm. Mass spectrum (ES+) *m/z*: 287.4 {[C<sub>17</sub>H<sub>19</sub>O<sub>4</sub>]}<sup>+</sup>, 533.5 {[C<sub>29</sub>H<sub>34</sub>O<sub>8</sub>][Na]}<sup>+</sup>, 1043.7 {[C<sub>29</sub>H<sub>34</sub>O<sub>8</sub>]<sub>2</sub>[Na]}<sup>+</sup>.

**Preparation of 2,3,6,7,10,11-Hexamethoxy-12*d*-methyl-4*b*,8*b*,12*b*,12*d*-tetrahydrodibenzo[2,3:4,5]pentaleno[1,6-*ab*]indene(4.12).**<sup>[3]</sup>

Chlorobenzene (13 mL) and orthophosphoric acid (0.17 mL), were mixed together and heated at reflux under nitrogen atmosphere for 30 minutes. A solution of all-*cis*-2-[bis(3,4-dimethoxyphenyl)methyl]-5,6-dimethoxy-2-methyl-



1,3-indanediol (0.5 g, 0.98 mmol) in 8 mL of chlorobenzene was then added dropwise. After the addition was complete, reflux was

continued for 1 hour. The mixture was cooled to ambient temperature and washed with 2 M aqueous sodium hydroxide (2 mL x 2) and with water (5 mL), dried over sodium sulfate and concentrated to dryness *in vacuo* to afford the produce as a yellow powder weighing 0.167 g, 36 %.

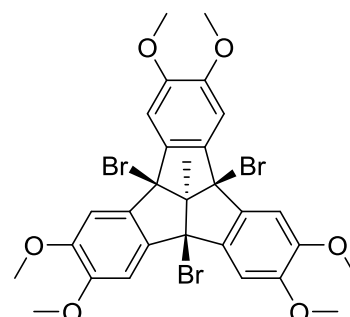
$^1\text{H}$  NMR (Chloroform-*d*, 500 MHz) :  $\delta$  = 6.82 (s, 6H, {ArH}), 4.22 (s, 3H, {CH}), 3.80 (s, 18H, {OCH<sub>3</sub>}), 1.60 (s, 3H, CH<sub>3</sub>) ppm.  $^{13}\text{C}\{^1\text{H}\}$  NMR (Chloroform-*d*, 125 MHz) :  $\delta$  = 149.25, 137.35, 107.45, 63.31, 63.26, 56.28, 27.45 ppm. Mass spectrum (ES+) *m/z*: 475.7 {[C<sub>29</sub>H<sub>30</sub>O<sub>6</sub>][H]}<sup>+</sup>, 971.8 {[C<sub>29</sub>H<sub>30</sub>O<sub>6</sub>]<sub>2</sub>[Na]}<sup>+</sup>.

### Preparation of 4b,8b,12b-Tribromo-2,3,6,7,10,11-hexamethoxy-12d-methyl-4b,8b,12b,12d-tetrahydrodibenzo[2,3:4,5]pentaleno[1,6-*ab*]indene.<sup>[3]</sup>

*N*-Bromosuccinimide (1.312 g, 8 mol) and a small amount of 2,2'-azobis(isobutyronitrile) (5 mg) were added to a solution of 2,3,6,7,10,11-Hexamethoxy-12d-methyl-4b,8b,12b,12d-

tetrahydrodibenzo[2,3:4,5]pentaleno[1,6-*ab*]indene (0.8752 g, 1.85 mmol) in anhydrous benzene (92 mL)

under nitrogen atmosphere, and the mixture was irradiated with a UV photolamp at room temperature for 45 min. The reaction mixture was used directly in the next step without isolating the product.

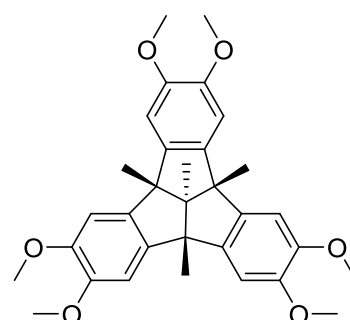


### Preparation of 2,3,6,7,10,11-Hexamethoxy-4b,8b,12b,12d-tetramethyl-4b,8b,12b,12d-tetrahydrodibenzo[2,3:4,5]pentaleno[1,6-*ab*]indene (4.13).<sup>[3]</sup>

The solution of 4b,8b,12b-Tribromo-2,3,6,7,10,11-hexamethoxy-12d-methyl-4b,8b,12b,12d-tetrahydrodibenzo[2,3:4,5]pentaleno[1,6-*ab*]indene.

(92 mL in benzene) was stirred under nitrogen while a solution of trimethylaluminium (7.4 mL, 14.8 mmol) in toluene (2.0 M) was added dropwise. Stirring was

continued whilst heating at 50 °C for 1 h. The mixture was cooled in an ice bath and then hydrolysed by careful addition of 100 mL of water. The organic later was separated and the aqueous one extracted with dichloromethane (3 x 50 mL). The combined organic solutions were washed with water, dried with sodium sulfate and



---

concentrated to dryness. The residue was recrystallized from methanol to afford the product as colourless crystals weighing 234 mg, 25 %.

$^1\text{H}$  NMR (Chloroform-*d*, 500 MHz) :  $\delta$  = 6.81 (s, 6H, {ArH}), 3.86 (s, 18H, {OCH<sub>3</sub>}), 1.62 (s, 9H, {CH<sub>3</sub>}), 1.35 (s, 3H, {CH<sub>3</sub>}) ppm.  $^{13}\text{C}\{^1\text{H}\}$  NMR (Chloroform-*d*, 125 MHz) :  $\delta$  = 147.80, 135.82, 105.93, 61.73, 54.77 ppm. High resolution mass spectrum (ES+) *m/z*: 515.2045 {[C<sub>32</sub>H<sub>35</sub>O<sub>6</sub>]}<sup>+</sup>.

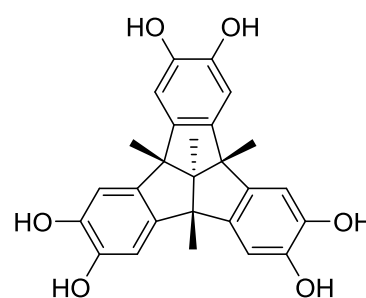
**Preparation of 2,3,6,7,10,11-Hexahydroxy-4b,8b,12b,12d-tetramethyl-4b,8b,12b,12d-tetrahydrodibenzo[2,3:4,5]pentaleno[1,6-*ab*]indene (4.1).**

2,3,6,7,10,11-Hexamethoxy-4b,8b,12b,12d-

tetramethyl-4b,8b,

12b,12d-tetrahydrodibenzo[2,3:4,5]pentaleno[1,6-

*ab*]indene was prepared according to general procedure 3 to afford a red powder weighing 94 mg, 98 %.

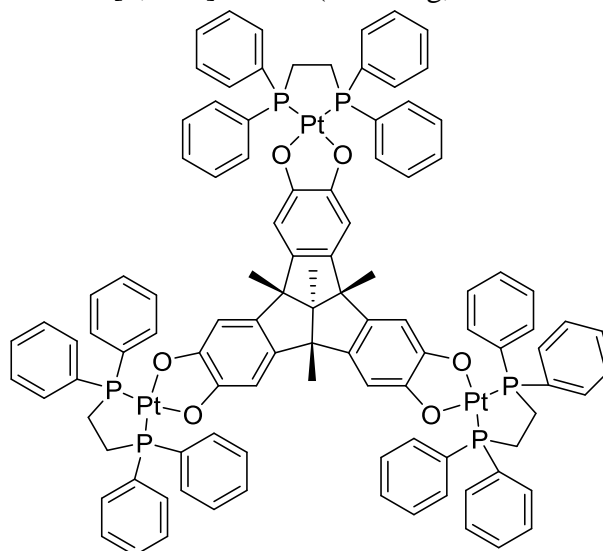


$^1\text{H}$  NMR (Chloroform-*d*, 500 MHz) :  $\delta$  = 6.63 (s, 6H, {ArH}), 1.34 (s, 9H, {CH<sub>3</sub>}), 1.23 (s, 3H, {CH<sub>3</sub>}) ppm. High resolution mass spectrum (ES+) *m/z*: 453.1265 {[C<sub>26</sub>H<sub>22</sub>O<sub>6</sub>][Na]}<sup>+</sup>.

**Preparation of [(Pt(diphenylphosphinoethane))<sub>3</sub>(2,3,6,7,10,11-hexahydroxy-4b,8b,12b,12d-tetramethyl-4b,8b,12b,12d-tetrahydrodibenzo[2,3:4,5]pentaleno[1,6-*ab*]indene)] (4.14).**

A mixture of 2,3,6,7,10,11-Hexahydroxy-4b,8b,12b,12d-tetramethyl-4b,8b,12b,12d-tetrahydrodibenzo[2,3:4,5]pentaleno[1,6-*ab*]indene (0.0171 g, 0.04 mmol) and

diphenylphosphinoethaneplatinum (II) chloride (0.1 g, 0.14 mmol) in 10 mL of dry deoxygenated dimethylacetamide was stirred for 30 minutes under nitrogen atmosphere before potassium *tert*-butoxide (0.04 g, 0.36 mmol) in dry deoxygenated methanol (5 mL) was added dropwise. The mixture

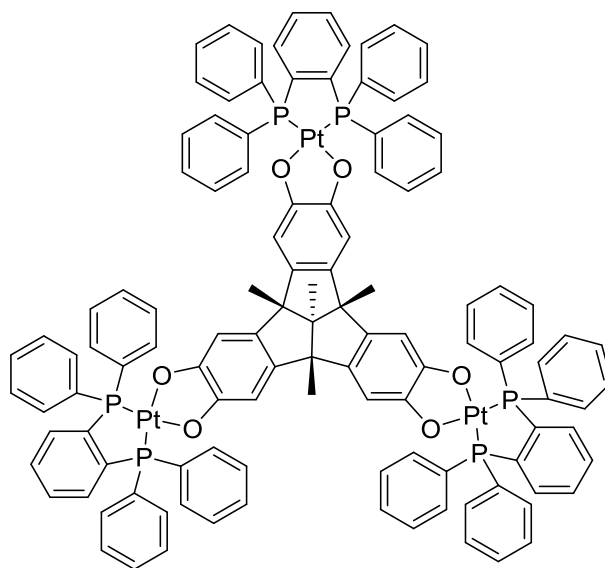


turned from yellow to green and was stirred for 18 hours. Dry deoxygenated ether (20 mL) was added, and the mixture was cooled in an ice bath for 30 minutes before being filtered by cannula to afford a pale green powder weighing 44 mg, 50%.

<sup>1</sup>H NMR (CD<sub>2</sub>Cl<sub>2</sub>, 300 MHz) : δ = 1.27 (s, 3H, {CH<sub>3</sub>}), 7.47-7.78 (m, 66H, {ArH}) ppm. <sup>13</sup>C{<sup>1</sup>H} NMR (CD<sub>2</sub>Cl<sub>2</sub>, 75 MHz) : δ = 134.31, 134.17, 132.35, 129.29, 129.12 ppm. <sup>31</sup>P{<sup>1</sup>H} NMR (CD<sub>2</sub>Cl<sub>2</sub>, 121 MHz) : δ = 40.74 (s, 6P) ppm. High resolution mass spectrum (ES+) *m/z*: 1693.1538 {[C<sub>78</sub>H<sub>68</sub>O<sub>6</sub>P<sub>4</sub>Pt<sub>2</sub>][K]<sub>2</sub>}<sup>+</sup>. Found %; C 48.43, H 3.15, N 0.00 %. Calculated for [(C<sub>104</sub>H<sub>90</sub>O<sub>6</sub>P<sub>6</sub>Pt<sub>3</sub>)(CHCl<sub>3</sub>)<sub>4</sub>]; C 48.32, H 3.52, N 0.00 %.

**Preparation of (Pt(diphenylphosphinobenzene))<sub>3</sub>(2,3,6,7,10,11-hexahydroxy-4b,8b,12b,12d-tetramethyl-4b,8b,12b,12d-tetrahydrodibenzo[2,3:4,5]pentaleno[1,6-*ab*]indene) (4.15).**

A mixture of 2,3,6,7,10,11-Hexahydroxy-4b,8b,12b,12d-tetramethyl-4b,8b,12b,12d-tetrahydrodibenzo[2,3:4,5]pentaleno[1,6-*ab*]indene (0.0171 g, 0.04 mmol) and diphenylphosphinobenzeneplatinum (II) chloride (0.1 g, 0.14 mmol) in 10 mL of dry deoxygenated dimethylacetamide

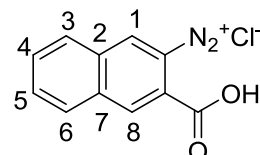


was stirred for 30 minutes under nitrogen atmosphere before potassium *tert*-butoxide (0.04 g, 0.36 mmol) in dry deoxygenated methanol (5 mL) was added dropwise. The mixture turned from yellow to green and was stirred for 18 hours. Dry deoxygenated ether (20 mL) was added, and the mixture was cooled in an ice bath for 30 minutes before being filtered by cannula to afford a pale green powder weighing 59 mg, 63%.

<sup>1</sup>H NMR (CD<sub>2</sub>Cl<sub>2</sub>, 500 MHz) : δ = 1.12 (s, 3H, {CH<sub>3</sub>}), 1.36 (s, 9H, {CH<sub>3</sub>}), 6.47 (s, 6H, {ArH<sup>TBTQ</sup>}), 7.40-7.85 (m, 72H, {ArH<sup>dppb</sup>}). <sup>13</sup>C{<sup>1</sup>H} NMR (methanol-*d*<sub>4</sub>, 125 MHz) : δ = 79.22, 78.96, 78.70 ppm. <sup>31</sup>P{<sup>1</sup>H} NMR (methanol-*d*<sub>4</sub>, 121 MHz) : δ = 30.67 (s, 6P) ppm. High resolution mass spectrum (ES+) *m/z*: 2350.4058 {[C<sub>116</sub>H<sub>89</sub>O<sub>6</sub>P<sub>6</sub>Pt<sub>3</sub>]}<sup>+</sup>.

**Preparation of naphthalene-3-diazonium-2-carboxylate (2.9).<sup>[1]</sup>**

**9** was prepared according to general procedure 1 to afford a tan powder weighing 0.2237 g, 89%.

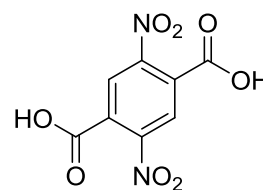


<sup>1</sup>H NMR (Chloroform-*d*, 500 MHz) : δ = 9.38 (s, 1H, {CH<sup>1</sup>}), 8.74 (s, 1H, {CH<sup>8</sup>}), 8.21 (d, <sup>3</sup>J<sub>H,H</sub> = 1.9 Hz, 1H, {CH<sup>3</sup>}), 8.17 (d, <sup>3</sup>J<sub>H,H</sub> = 1.9 Hz, 1H, {CH<sup>6</sup>}), 8.02 (t, <sup>3</sup>J<sub>H,H</sub> = 1.9 Hz, 1H, {CH<sup>4</sup>}), 7.92 (t, <sup>3</sup>J<sub>H,H</sub> = 1.9 Hz, 1H, {CH<sup>5</sup>}) ppm. Mass spectrum (ES+) *m/z*: 251.8 {[C<sub>11</sub>H<sub>7</sub>ClN<sub>2</sub>O<sub>2</sub>].[H<sub>2</sub>O]}<sup>+</sup>.

---

### Preparation of 2,5-dinitrobenzene-1,4-dicarboxylic acid (2.15).<sup>[4]</sup>

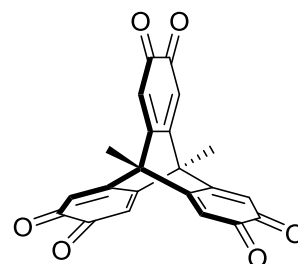
To terephthalic acid (2 g, 12.0 mmol) was added a concentrated sulfuric acid (2.42 mL) and concentrated nitric acid (7.25 mL) dropwise and the mixture was stirred with a condenser at 100°C for 3 hours. To the suspension, another mixture of concentrated sulfuric acid (2.42 mL) and concentrated nitric acid (9.7 mL) was added drop wise while the temperature remained at 100°C. After the complete addition, the reaction continued at 80°C for 12 h. The reaction mixture was then poured onto ice (100 g). The precipitate was filtered and the filtrate was recrystallized from water. The product was filtered and dried in a vacuum desiccator to produce yellow crystals weighing 1.5 g, 88%.



<sup>1</sup>H NMR (Chloroform-*d*, 500 MHz) :  $\delta$  = 8.05 (s, 2H, {ArH}), 3.34 (b, 2H, COOH) ppm.

### Preparation of 9,10-dimethyltritycene-2,3,6,7,12,13-hexone (4.17).<sup>[5]</sup>

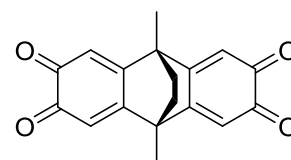
A suspension of **5** (50 mg, 0.13 mmol) was cooled on ice, and then a mixture of concentrated nitric acid (0.5 mL) and glacial acetic acid (0.5 mL) was added dropwise. The mixture was stirred at ambient temperature for 18 hours. The solids were collected by Buchner filtration, washed with water (2 x 3 mL) and ethanol (2 x 3 mL) and dried in a vacuum desiccator to afford a brown solid weighing 25 mg, 53%.



<sup>1</sup>H NMR (*d*<sub>6</sub>-DMSO, 500 MHz) :  $\delta$  = 6.27 (s, 6H, {ArH}), 1.93 (s, 6H, {CH<sub>3</sub>}) ppm. High resolution mass spectrum (ES+) *m/z*: 371.0121 {[C<sub>22</sub>H<sub>11</sub>O<sub>6</sub>]}<sup>+</sup>.

### Preparation of 2,3,6,7-tetraone-9,10-dimethyl-9,10-dihydroethanoanthracene (4.19).<sup>[5]</sup>

A suspension of H<sub>4</sub>thea (0.1445 g, 0.48 mmol) was cooled on ice, and then a mixture of concentrated nitric acid (2 mL) and glacial acetic acid (2 mL) was added dropwise. The mixture was stirred at ambient temperature for 18 hours. The solids were collected by Buchner filtration, washed



---

with water (2 x 10 mL) and ethanol (2 x 10 mL) and dried in a vacuum desiccator to afford a brown solid weighing 0.138 g, 97%.

$^1\text{H}$  NMR ( $d_6$ -DMSO, 500 MHz) :  $\delta$  = 6.31 (s, 4H,  $\text{CH}_{\text{Ar}}$ ), 2.07 (s, 4H,  $\text{CH}_2$ ), 1.56 (s, 6H,  $\text{CH}_3$ ).  $^{13}\text{C}\{^1\text{H}\}$  NMR ( $d_6$ -DMSO, 125 MHz):  $\delta$  = 6.27 (s, 4H,  $\{\text{ArH}\}$ ), 1.94 (d, 4H,  $\{\text{CH}_2\}$ ), 1.46 (s, 6H,  $\{\text{CH}_3\}$ ). Mass spectrum (ES+)  $m/z$ : 316.9  $\{[\text{C}_{18}\text{H}_{14}\text{O}_4][\text{Na}]\}^+$ , 610.9  $\{[\text{C}_{18}\text{H}_{14}\text{O}_4]_2[\text{Na}]_2\}^+$ .

#### **Preparation of tetrabutylammonium molybdate (4.16).**

$\text{MoO}_3$  (1.3 g, 9.0 mmol) was added to a solution of tetrabutylammonium hydroxide (18 mL, 18.0 mmol) in ethanol (30 mL) for 6 hours at room temperature. The mixture was filtered and then the solvent was removed *in vacuo* to afford a viscous yellow oil weighing 0.7 g, 19 %.

$^1\text{H}$  NMR (Chloroform- $d$ , 500 MHz) :  $\delta$  = 3.29-3.26 (dd,  $^3J_{\text{H,H}} = 11.5$  Hz,  $^4J_{\text{H,H}} = 6.0$  Hz 2H,  $\text{CH}_2$ ), 1.65-1.59 (quint,  $^3J_{\text{H,H}} = 7.0$  Hz, 2H,  $\text{CH}_2$ ), 1.45-1.38 (h,  $^3J_{\text{H,H}} = 7.5$  Hz, 2H,  $\text{CH}_2$ ), 0.96-0.93 (t,  $^3J_{\text{H,H}} = 7.5$  Hz, 3H,  $\text{CH}_3$ ) ppm.  $^{13}\text{C}\{^1\text{H}\}$  NMR (Chloroform- $d$ , 125 MHz):  $\delta$  = 58.51, 23.92, 19.64, 13.68 ppm. Mass spectrum (ES+)  $m/z$ : 242.0  $\{[\text{N}(\text{C}_4\text{H}_9)_4]\}^+$ .

#### **Preparation of unknown molybdenum complex of 5 (4.20).**

Molybdenum hexacarbonyl (8 mg, 0.03 mmol) and 9,10-dimethyltriptycene-2,3,6,7,12,13-hexone (11 mg, 0.03 mmol) were dissolved in toluene (10 mL) under a nitrogen atmosphere and heated at reflux for 18 hours. The orange solution turned dark blue. The reaction mixture was filtered and washed with ice cold acetone (1 x 5 mL) to afford a dark blue solid weighing 3 mg.

Found %; C 52.43, H 5.60 %. Calculated for  $\text{MoC}_{22}\text{H}_{12}\text{O}_6$ ; C 56.43, H 2.58 %.

#### **Preparation of unknown molybdenum complex of 28 (4.21).**

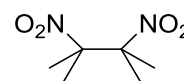
Molybdenum hexacarbonyl (36 mg, 0.14 mmol) and 9,10-dimethyltriptycene-2,3,6,7,12,13-hexone (40 mg, 0.14 mmol) were dissolved in toluene (50 mL) under a nitrogen atmosphere and heated at reflux for 18 hours. The orange solution turned dark blue. The reaction mixture was filtered and washed with ice cold acetone (1 x 5 mL) to afford a dark blue solid weighing 43 mg.

---

Found %; C 43.60, H 3.60 %. Calculated for  $\text{MoC}_{18}\text{H}_{16}\text{O}_4$ ; C 55.11, H 4.11 %.

### Preparation of 2,3-dimethyl-2,3-dinitrobutane (5.1).<sup>[6]</sup>

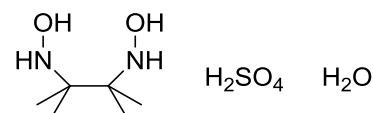
Sodium hydroxide (43.52 g) was dissolved in water (170 mL) and the solution was cooled on ice. 2-nitropropane (95 mL, 1.05 mol) was added at 0°C, and then bromine (27 mL, 1.05 mol) was added dropwise to the mixture, which was then stirred until the brown coloration disappeared. Ethanol (200 mL) was added and the mixture was then refluxed for 3 hours. The reaction mixture was then poured onto a water/ice mixture (500 mL), causing a white precipitate to immediately form. The mixture was stirred for an additional 10 minutes then filtered. The solids collected were washed twice with water, then dried in a vacuum desiccator. The white crystalline solid was then recrystallized from methanol to afford large colourless crystals weighing 66.53 g, 72%.



$^1\text{H}$  NMR (Chloroform-*d*, 500 MHz) :  $\delta = 1.74$  (s, 12H,  $\text{CH}_3$ ) ppm.  $^{13}\text{C}\{^1\text{H}\}$  NMR (Chloroform-*d*, 125 MHz):  $\delta = 24.23, 92.27$  ppm. High resolution mass spectrum (ES<sup>+</sup>) *m/z*: 198.1274  $\{[\text{C}_6\text{H}_{11}\text{N}_2\text{O}_4][\text{Na}]\}^+$ , 391.2840  $\{[\text{C}_6\text{H}_{12}\text{N}_2\text{O}_4]_2[\text{K}]\}^+$ , 413.2663  $\{[\text{C}_6\text{H}_{11}\text{N}_2\text{O}_4]_2[\text{Na}][\text{K}]\}^+$ .

### Preparation of 2,3-dimethyl-2,3-dihydroxyaminobutane sulphate hydrate (5.2).<sup>[6]</sup>

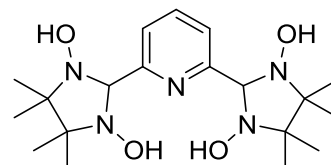
2,3-dimethyl-2,3-dinitrobutane (20 g, 0.114 mol) was dissolved in THF (300 mL) and water (10 mL) and cooled to 10°C. Ammonium chloride (25 g, 0.467 mol) was dissolved in water (150 mL) and then added to the solution. Zinc powder (27 g, 0.413 mol) was slowly added to the mixture in small portions with mechanical stirring, and the reaction was left stirring for 17 hours. The mixture initially turned light blue, before turning pale yellow. The mixture was filtered and the solids were washed with THF (3 x 100 mL). The THF was removed at room temperature in vacuo. Ethanol (200 mL) was added, the solution was filtered to remove unreacted starting material, and then to the filtrate was added dropwise 10% sulphuric acid until it was pH 3 (thymol blue). The white precipitate that formed was filtered off, washed with ethanol, and the solvent removed in vacuo to afford white crystals weighing 15.0 g, 50%.



$^1\text{H}$  NMR (Chloroform-*d*, 500 MHz) :  $\delta$  = 1.55 (s, 12H, *CH*<sub>3</sub>), 5.31 (s, 2H, *NH*), 6.92 (s, 2H, *OH*) ppm.  $^{13}\text{C}\{^1\text{H}\}$  NMR (Chloroform-*d*, 125 MHz):  $\delta$  = 30.59, 93.03 ppm. High resolution mass spectrum (ES+) *m/z*: 149.0228 {[C<sub>6</sub>H<sub>16</sub>N<sub>2</sub>O<sub>2</sub>][H]}<sup>+</sup>, 171.0922 {[C<sub>6</sub>H<sub>16</sub>N<sub>2</sub>O<sub>2</sub>][Na]}<sup>+</sup>, 186.2213 {[C<sub>6</sub>H<sub>15</sub>N<sub>2</sub>O<sub>2</sub>][K]}<sup>+</sup>, 302.1903 {[C<sub>6</sub>H<sub>15</sub>N<sub>2</sub>O<sub>2</sub>]<sub>2</sub>[Li]}<sup>+</sup>.

### Preparation of 2,6-bis(1,3-dihydroxy-4,4,5,5-tetramethyl-2-imidazolidinyl)pyridine (5.4).<sup>[7]</sup>

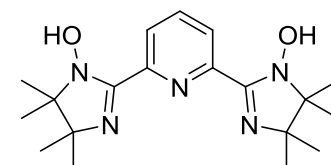
Pyridine-2,5-dicarbaldehyde (0.6 g, 4.44 mmol) and 2,3-dimethyl-2,3-dihydroxyaminobutane sulphate hydrate (4.5 g, 17.0 mmol) were dissolved in water and the solution was stirred for 2 hours. Sodium carbonate was added until no more effervescence was observed, after which the reaction mixture was filtered to afford a white powder weighing 1.66 g, 95%.



$^1\text{H}$  NMR (Chloroform-*d*, 500 MHz) :  $\delta$  = 1.12 (s, 12H, *CH*<sub>3</sub>), 1.17 (s, 12H, *CH*<sub>3</sub>), 4.92 (s, 2H, *NCH*), 6.44 (b, 4H, *OH*), 6.92 (t, 1H, *ArH*), 7.44 (d, 2H, *ArH*) ppm.  $^{13}\text{C}\{^1\text{H}\}$  NMR (Chloroform-*d*, 125 MHz):  $\delta$  = 18.3, 24.6, 67.4, 92.5, 121.3, 161.7 ppm. High resolution mass spectrum (ES+) *m/z*: 396.2628 {[C<sub>19</sub>H<sub>33</sub>N<sub>5</sub>O<sub>4</sub>][H]}<sup>+</sup>, 418.2425 {[C<sub>19</sub>H<sub>33</sub>N<sub>5</sub>O<sub>4</sub>][Na]}<sup>+</sup>, 791.5138 {[C<sub>19</sub>H<sub>33</sub>N<sub>5</sub>O<sub>4</sub>]<sub>2</sub>[H]}<sup>+</sup>, 813.4957 {[C<sub>19</sub>H<sub>33</sub>N<sub>5</sub>O<sub>4</sub>]<sub>2</sub>[Na]}<sup>+</sup>.

### Preparation of 2,6-bis(4,5-dihydro-1-hydroxy-4,4,5,5-tetramethyl-1H-imidazol-2-yl)pyridine (5.5).<sup>[8]</sup>

**5.4** (1.5 g, 3.79 mmol) and sodium metaperiodate (2.61 g, 12.2 mmol) were added to dichloromethane (150 mL) and to this was added water (22 mL) to initiate the reaction.



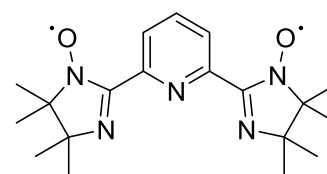
The mixture turned dark purple, and after 2 hours the two-phase mixture was separated, and the organics were dried with sodium sulphate, filtered, and the solvent removed in vacuo. The crude purple product was collected, hexane was added, and the solution was filtered. This afforded **5.5** as a blue solid weighing 1.29 g, 95%.

$^1\text{H}$  NMR (Chloroform-*d*, 500 MHz) :  $\delta$  = 1.71 (s, 12H, *CH*<sub>3</sub>), 1.81 (s, 12H, *CH*<sub>3</sub>), 8.10 (t, 1H, *ArH*), 8.42 (d, 2H, *ArH*) ppm. High resolution mass spectrum (ES+) *m/z*: 359.2316 {[C<sub>19</sub>H<sub>29</sub>N<sub>5</sub>O<sub>2</sub>]}<sup>+</sup>, 717.4523 {[C<sub>19</sub>H<sub>28</sub>N<sub>5</sub>O<sub>2</sub>]<sub>2</sub>}<sup>+</sup>.

---

**Preparation of 2,2'-(2,6-pyridinediyl)bis[4,5-dihydro-4,4,5,5-tetramethyl]-1H-imidazol-1-yloxy (5.6).<sup>[8]</sup>**

5.5 (1.389 g, 3.86 mmol) and sodium nitrite (0.6 g, 8.7 mmol) were added to a mixture of dichloromethane (50 mL) and water (10 mL). Acetic acid (0.5 mL, 8.74 mmol) was added dropwise. The solution turned brown and then

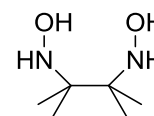


orange. After the colour remained constant, the mixture was neutralized with sodium hydrogencarbonate until no more effervescence was observed. The mixture was separated, the organics collected (with care not to collect any of the white solid precipitate), and dried with sodium sulphate. The mixture was filtered through alumina to remove trace impurities to afford an orange solution which was left to slowly evaporate at room temperature, to afford orange crystals of the product weighing 0.875 g, 63%.

High resolution mass spectrum (ES+)  $m/z$ : 156.9091  $\{[C_{19}H_{27}N_5O_2]\}^+$ , 356.9091  $\{[C_{19}H_{26}N_5O_2]_2\}^{2+}$ , 418.8795  $\{[C_{19}H_{27}N_5O_2][Na][K]\}^+$ , 434.8894  $\{[C_{19}H_{27}N_5O_2][K]_2\}^+$ .

**Preparation of 2,3-dimethyl-2,3-dihydroxyaminobutane (freebase) (5.3).<sup>[9]</sup>**

2,3-dimethyl-2,3-dihydroxyaminobutane sulphate hydrate (10 g, 37.84 mmol) was dissolved in THF (150 mL) and cooled on ice. Sodium



hydroxide (3 g, 75 mmol) was dissolved in the minimum amount of

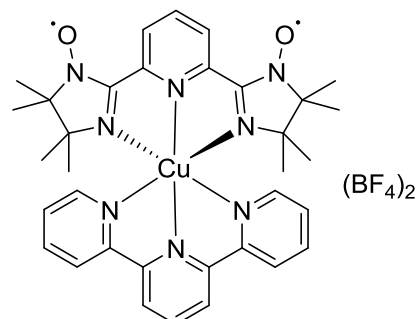
water (10 mL) and cooled on ice. The sodium hydroxide solution was added dropwise to the sulphate solution until the mixture became neutral (care must be taken not to add too much base). The organics were collected, dried with sodium sulphate, filtered and the solvent was reduced to a small volume in vacuo. Acetone (20 mL) was added, the mixture was filtered, the solids were collected, and the organics were again reduced to a small volume in vacuo. Acetone (20 mL) was again added, and the solution was filtered. The solids were washed with a small amount of cold acetone to afford a white crystalline product weighing 3.018 g, 54%.

$^1H$  NMR (Chloroform-*d*, 500 MHz) :  $\delta$  = 1.55 (s, 12H,  $CH_3$ ), 5.31 (s, 2H, NH), 6.92 (s, 2H, OH) ppm.  $^{13}C\{^1H\}$  NMR (Chloroform-*d*, 125 MHz):  $\delta$  = 30.59, 93.03 ppm.

High resolution mass spectrum (ES+)  $m/z$ : 149.0228  $\{[C_6H_{16}N_2O_2][H]\}^+$ , 171.0922  $\{[C_6H_{16}N_2O_2][Na]\}^+$ , 186.2213  $\{[C_6H_{15}N_2O_2][K]\}^+$ , 302.1903  $\{[C_6H_{15}N_2O_2]_2[Li]\}^+$ .

### Preparation of 5.7.

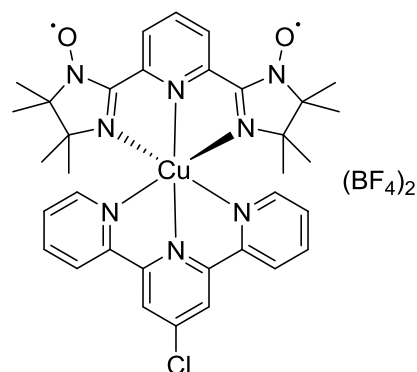
Bisimpy (30 mg, 0.084 mmol) and 2,2':6',2''-terpyridine (19.6 mg, 0.084 mmol) were dissolved in methanol (5 mL) and stirred in a round bottom flask. Copper(II) tetrafluoroborate (20 mg, 0.084 mmol) was dissolved in methanol (2 mL) and was then added dropwise to the solution. The solution turned from orange to red, and a red powder precipitated over the course of 18 hours. The reaction mixture was filtered, washed with ice cold methanol (1 mL) and the solid collected to afford 43 mg of the product, 62%.



High resolution mass spectrum (ES+)  $m/z$ : 296.0241  $\{[C_{15}H_{10}CuN_3]\}^+$ , 655.1697  $\{[C_{34}H_{38}CuN_8O_2][H]_2\}^+$ . Found %; C 49.14, H 4.53, N 13.41 %. Calculated for  $C_{34}H_{38}B_2CuF_8N_8O_2$ ; C 49.33, H 4.63, N 13.54 %.

### Preparation of 5.8.

Bisimpy (30 mg, 0.084 mmol) and 4'-chloro-2,2':6',2''-terpyridine (23 mg, 0.084 mmol) were dissolved in methanol (5 mL) and stirred in a round bottom flask. Copper(II) tetrafluoroborate (20 mg, 0.084 mmol) was dissolved in methanol (2 mL) and was then added dropwise to the solution. The solution turned from orange to red, and a red powder precipitated over the course of 18 hours. The reaction mixture was filtered, washed with ice cold methanol (1 mL) and the solid collected to afford 42.7 mg of the product, 59%.

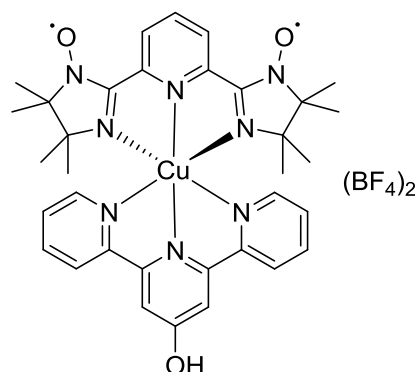


High resolution mass spectrum (ES+)  $m/z$ : 343.6004  $\{[C_{34}H_{37}ClCuN_8O_2]\}^{2+}$ . Found %; C 47.22, H 4.30, N 12.84 %. Calculated for  $C_{34}H_{37}B_2ClCuF_8N_8O_2$ ; C 47.36, H 4.33, N 12.99 %.

### Preparation of 5.9.

Bisimpy (30 mg, 0.084 mmol) and 2,6-bis(2-pyridyl)-4-(1H)-pyridone (21 mg, 0.084 mmol) were dissolved in methanol (5 mL) and stirred in a round bottom flask. Copper(II) tetrafluoroborate (20 mg, 0.084 mmol) was dissolved in methanol (2 mL) and was then added dropwise to the solution.

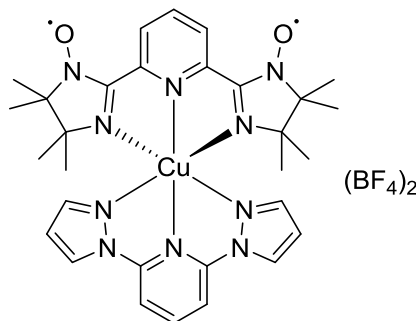
The solution turned from orange to red, and a red powder precipitated over the course of 18 hours. The reaction mixture was filtered, washed with ice cold methanol (1 mL) and the solid collected to afford 36.2 mg of the product, 51%.



High resolution mass spectrum (ES+)  $m/z$ : 668.2280  $\{[\text{C}_{34}\text{H}_{37}\text{CuN}_8\text{O}_3]\}^+$ . Found %; C 46.73, H 4.52, N 12.39 %. Calculated for  $[(\text{C}_{34}\text{H}_{38}\text{B}_2\text{CuF}_8\text{N}_8\text{O}_3)(\text{H}_2\text{O})_2]$ ; C 46.41, H 4.81, N 12.73 %.

### Preparation of 5.10.

Bisimpy (30 mg, 0.084 mmol) and 1,6-bis(pyrazol-1-yl)pyridine (17.7 mg, 0.084 mmol) were dissolved in methanol (5 mL) and stirred in a round bottom flask. Copper(II) tetrafluoroborate (20 mg, 0.084 mmol) was dissolved in methanol (2 mL) and was then added dropwise to the solution. The



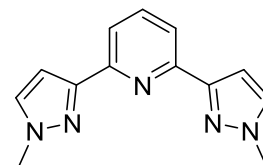
The solution turned from orange to red, and a red powder precipitated over the course of 18 hours. The reaction mixture was filtered, washed with ice cold methanol (1 mL) and the solid collected to afford 22.3 mg of the product, 33%.

High resolution mass spectrum (ES+)  $m/z$ : 359.2313  $\{[\text{C}_{30}\text{H}_{36}\text{BCuF}_4\text{N}_{10}\text{O}_2]\}^{2+}$ .

Found %; C 48.73, H 5.02, N 19.26 %. Calculated for  $[(\text{C}_{30}\text{H}_{36}\text{B}_2\text{CuF}_8\text{N}_{10}\text{O}_2)]$ ; C 44.71, H 4.50, N 17.38 %.

### Preparation of 2,6-bis(1-methyl-1H-pyrazol-3-yl)pyridine (5.15).<sup>[10]</sup>

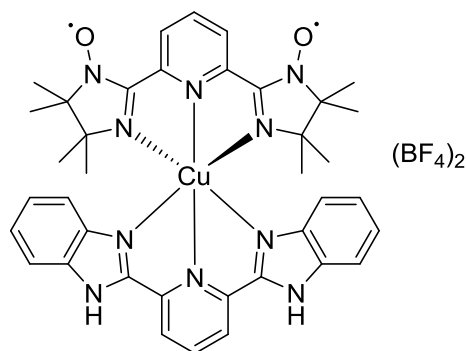
A mixture of 3-bis(pyrazolyl)pyridine (0.8 g, 3.8 mmol), iodomethane (0.41 mL, 3.8 mmol) and sodium methoxide (0.41 g, 12 mmol) in anhydrous tetrahydrofuran (50 mL) was refluxed under nitrogen atmosphere for 12 hours. The mixture was cooled on ice and a pale yellow precipitate formed. The precipitate was filtered off, washed with ice cold THF (10 mL) and then recrystallized from chloroform to afford pale yellow crystals weighing 0.782 g, 86%.



<sup>1</sup>H NMR (300 MHz, CDCl<sub>3</sub>) δ = 7.89 (t, 8.0 Hz, 1H), 7.62 (d, 8.0 Hz, 2H), 7.46 (d, 2.5 Hz, 2H), 6.72 (d, 2.3 Hz, 2H), 3.43 (s, 6H) ppm. <sup>13</sup>C NMR (75 MHz, CDCl<sub>3</sub>) δ = 150.88, 150.25, 138.85, 132.62, 119.04, 104.25, 38.83 ppm.

### Preparation of 5.13.

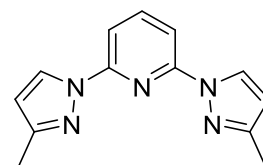
Bisimpy (30 mg, 0.084 mmol) and 2,6-bis(benzimidazole)pyridine (26 mg, 0.084 mmol) were dissolved in methanol (5 mL) and stirred in a round bottom flask. Copper(II) tetrafluoroborate (20 mg, 0.084 mmol) was dissolved in methanol (2 mL) and was then added dropwise to the solution. The solution turned from orange to red, and a red powder precipitated over the course of 18 hours. The reaction mixture was filtered, washed with ice cold methanol (1 mL) and the solid collected to afford 48 mg of the product, 63%.



High resolution mass spectrum (ES<sup>+</sup>) *m/z*: 365.6312 {[C<sub>38</sub>H<sub>40</sub>CuN<sub>10</sub>O<sub>2</sub>]<sup>2+</sup>, 730.2546 {[C<sub>38</sub>H<sub>39</sub>CuN<sub>10</sub>O<sub>2</sub>]<sup>+</sup>. Found %; C 49.43, H 4.61, N 15.08 %. Calculated for [(C<sub>38</sub>H<sub>40</sub>CuB<sub>2</sub>F<sub>8</sub>N<sub>10</sub>O<sub>2</sub>)(H<sub>2</sub>O)]; C 49.40, H 4.58, N 15.16 %.

### Preparation of 2,6-di(3-methylpyrazol-1-yl)pyridine (5.17).

A mixture of 3-methylpyrazole (3.7 g, 460 mmol) and sodium hydride (1.8 g, 460 mmol) in dimethylformamide under nitrogen atmosphere was stirred for 1 h, affording a white suspension. 2,6-difluoropyridine (5.32 g, 220 mmol) was

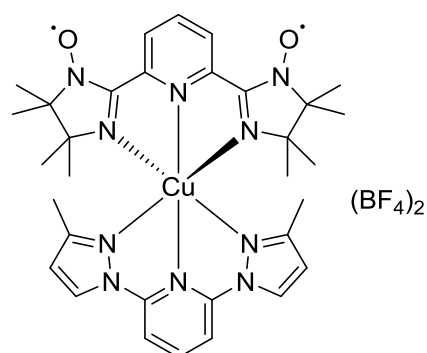


added to the mixture and when then refluxed for 5 days. The mixture was cooled, and quenched with excess water (300 mL) to afford a white precipitate which was dried over phosphorus pentoxide in a vacuum desiccator. The product was purified by flash column chromatography (eluent 3 : 1 pentane / diethyl ether) to afford the pure product as a white powder weighing 0.84 g, 16%.

$^1\text{H}$  NMR (300 MHz,  $\text{CDCl}_3$ )  $\delta$  = 8.45 (d, 2.5 Hz, 2H,  $\text{PzH}^5$ ), 7.88 (dd, 7.1 Hz, 1H,  $\text{PyH}^4$ ), 7.74 (d, 7.9 Hz, 2H,  $\text{PyH}^{3,5}$ ), 6.26 (d, 2.5 Hz, 2H,  $\text{PzH}^4$ ), 2.40 (s, 6H,  $\text{CH}_3$ ) ppm. High resolution mass spectrum (ES+)  $m/z$ : 240  $\{[\text{C}_{13}\text{H}_{13}\text{N}_5][\text{H}]\}^+$ .

### Preparation of 5.12.

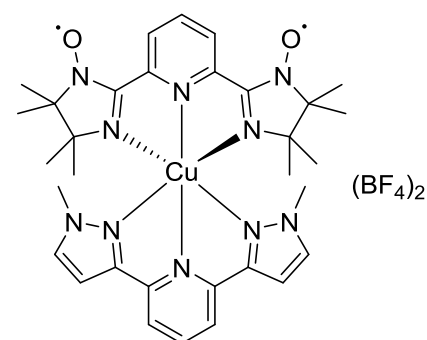
Bisimpy (30 mg, 0.084 mmol) and 2,6-di(3-methylpyrazol-1-yl)pyridine (20 mg, 0.084 mmol) were dissolved in methanol (5 mL) and stirred in a round bottom flask. Copper(II) tetrafluoroborate (20 mg, 0.084 mmol) was dissolved in methanol (2 mL) and was then added dropwise to the solution. The solution turned from orange to red, and a red powder precipitated over the course of 18 hours. The reaction mixture was filtered, washed with ice cold methanol (1 mL) and the solid collected to afford 49.0 mg of the product, 70%.



High resolution mass spectrum (ES+)  $m/z$ : 659.2654  $\{[\text{C}_{32}\text{H}_{40}\text{CuB}_2\text{F}_8\text{N}_{10}\text{O}_2]\}^+$ . Found %; C 45.93, H 4.80, N 16.68 %. Calculated for  $\text{C}_{32}\text{H}_{40}\text{B}_2\text{CuF}_8\text{N}_{10}\text{O}_2$ ; C 46.09, H 4.84, N 16.80 %.

### Preparation of 5.11.

Bisimpy (30 mg, 0.084 mmol) and 2,6-bis(1-methyl-1H-pyrazol-3-yl)pyridine (20.1 mg, 0.084 mmol) were dissolved in methanol (5 mL) and stirred in a round bottomed flask. Copper(II) tetrafluoroborate (20 mg, 0.084 mmol) was dissolved in methanol (2 mL) and was then added dropwise to the solution. The solution turned from orange to red, and a red powder precipitated over the course of a few hours. The



---

reaction mixture was filtered, washed with ice cold methanol (1 mL) and the solid collected to afford 40.6 mg of the product, 58%.

High resolution mass spectrum (ES+)  $m/z$ : 329.6309  $\{[C_{32}H_{40}CuN_{10}O_2]^{2+}$ , 659.2626  $\{[C_{32}H_{40}CuN_{10}O_2]^+$ . Found %; C 44.05, H 5.03, N 15.78 %. Calculated for  $[(C_{32}H_{40}B_2CuF_8N_{10}O_2)(H_2O)_2]$ ; C 44.18, H 5.10, N 16.10 %.

### 6.3 Crystallographic Data Tables

	<b>2.5·dioxane</b>	<b>2.5·Et<sub>2</sub>O</b>	<b>2.5·EtOAc</b>
Empirical formula	C <sub>20</sub> H <sub>20</sub> O <sub>4</sub>	C <sub>12</sub> H <sub>12</sub> O <sub>4</sub>	C <sub>26</sub> H <sub>26</sub> O <sub>8</sub>
Formula weight	347.59	205.87	466.47
Temperature/K	120.01(11)	120.02(16)	120.01(11)
Crystal system	orthorhombic	monoclinic	triclinic
Space group	P2 <sub>1</sub> 2 <sub>1</sub> 2 <sub>1</sub>	P2 <sub>1</sub> /c	P-1
a/Å	9.68307(19)	13.1161(4)	8.8043(5)
b/Å	11.9425(2)	11.8371(3)	9.1744(6)
c/Å	18.3518(4)	24.8580(7)	13.9988(8)
α/°	90	90	84.050(5)
β/°	90	97.306(3)	85.160(4)
γ/°	90	90	83.030(5)
Volume/Å <sup>3</sup>	2122.20(8)	3828.02(19)	1113.39(11)
Z	5	14	2
ρ <sub>calc</sub> /cm <sup>3</sup>	1.3598	1.2501	1.391
μ/mm <sup>-1</sup>	0.788	0.737	0.86
2θ range for data collection/°	8.84 to 147.12	6.8 to 146.84	6.36 to 134.14
Index ranges	-11 ≤ h ≤ 8, -10 ≤ k ≤ 14, -17 ≤ l ≤ 22	-16 ≤ h ≤ 11, -14 ≤ k ≤ 13, -30 ≤ l ≤ 30	-10 ≤ h ≤ 8, -10 ≤ k ≤ 10, -16 ≤ l ≤ 16
Reflections collected	5791	15514	7926
Independent reflections	3763 [R <sub>int</sub> = 0.0392, R <sub>sigma</sub> = 0.0500]	7501 [R <sub>int</sub> = 0.0539, R <sub>sigma</sub> = 0.0709]	3833 [R <sub>int</sub> = 0.0564, R <sub>sigma</sub> = 0.0633]
Data/restraints/parameters	3763/0/392	7501/0/513	3833/0/317
Goodness-of-fit on F <sup>2</sup>	0.894	1.522	1.061
Largest diff. peak/hole / e Å <sup>-3</sup>	0.24/-0.24	6.08/-0.95	0.45/-0.33

	<b>2.5·THF</b>	<b>2.5·CHCl<sub>3</sub></b>	<b>4.1·THF</b>
Empirical formula	C <sub>22</sub> H <sub>18</sub> O <sub>6</sub>	C <sub>24.15</sub> H <sub>20.15</sub> Cl <sub>6.44</sub> O <sub>6</sub>	C <sub>15</sub> H <sub>15</sub> O <sub>6</sub>
Formula weight	378.38	634.65	291.27
Temperature/K	120.01(11)	120(2)	119.97(15)
Crystal system	trigonal	monoclinic	triclinic
Space group	P3c1	C2/c	P-1
a/Å	23.511(4)	23.2178(16)	11.1115(13)
b/Å	23.511(4)	25.566(2)	11.3585(16)
c/Å	10.8154(13)	10.7276(7)	12.7308(15)
α/°	90	90	67.602(12)
β/°	90	116.349(6)	67.891(11)
γ/°	120	90	62.042(13)
Volume/Å <sup>3</sup>	5177.6(13)	5706.2(7)	1273.1(3)
Z	6	8	3
ρ <sub>calc</sub> /cm <sup>3</sup>	0.7281	1.478	1.14
μ/mm <sup>-1</sup>	0.053	6.196	0.75
2θ range for data collection/°	6.5 to 59.46	6.92 to 146.94	9.1 to 147.1
Index ranges	-31 ≤ h ≤ 29, - 16 ≤ k ≤ 30, - 10 ≤ l ≤ 14	-28 ≤ h ≤ 27, -31 ≤ k ≤ 28, -13 ≤ l ≤ 11	-13 ≤ h ≤ 13, -13 ≤ k ≤ 8, - 15 ≤ l ≤ 15
Reflections collected	22107	8045	9545
Independent reflections	7610 [R <sub>int</sub> = 0.0796, R <sub>sigma</sub> = 0.1153]	4795 [R <sub>int</sub> = 0.0431]	4773 [R <sub>int</sub> = 0.0603, R <sub>sigma</sub> = 0.0738]
Data/restraints/parameters	7610/0/260	4795/1/315	4773/0/344
Goodness-of-fit on F <sup>2</sup>	0.975	1.046	1.548
Largest diff. peak/hole / e Å <sup>-3</sup>	0.44/-0.51	0.58/-0.58	1.38/-0.58

	<b>3.6</b>	<b>3.2</b>	<b>3.3</b>
Empirical formula	C <sub>81</sub> H <sub>68</sub> O <sub>4</sub> P <sub>4</sub> Pt <sub>2</sub>	C <sub>100</sub> H <sub>100</sub> O <sub>4</sub> P <sub>4</sub> Pt <sub>2</sub>	C <sub>107</sub> H <sub>98</sub> Cl <sub>14</sub> O <sub>6</sub> P <sub>6</sub> Pt <sub>3</sub>
Formula weight	1619.41	1879.86	2747.24
Temperature/K	120(2)	120(2)	120(2)
Crystal system	triclinic	monoclinic	monoclinic
Space group	P-1	Ia	C2/c
a/Å	15.844(3)	15.6742(5)	18.3091(3)
b/Å	16.4328(17)	34.5723(6)	32.3693(7)
c/Å	16.981(3)	15.7445(4)	38.9108(7)
α/°	106.845(12)	90	90
β/°	115.370(17)	117.678(4)	90.470(2)
γ/°	92.932(11)	90	90
Volume/Å <sup>3</sup>	3744.0(10)	7555.6(3)	23059.8(8)
Z	16	8	8
ρ <sub>calc</sub> /cm <sup>3</sup>	11.492	3.305	1.583
μ/mm <sup>-1</sup>	30.916	16.157	4.088
F(000)	12832	7584	10800
Radiation	MoKα (λ = 0.71073)	CuKα (λ = 1.54184)	synchrotron (λ = 0.69980)
2θ range for data collection/°	5.66 to 59.54	6.84 to 147.5	3.18 to 63.32
Index ranges	-22 ≤ h ≤ 21, - 22 ≤ k ≤ 22, - 18 ≤ l ≤ 23	-18 ≤ h ≤ 18, - 39 ≤ k ≤ 40, -19 ≤ l ≤ 18	-27 ≤ h ≤ 27, - 48 ≤ k ≤ 48, - 50 ≤ l ≤ 58
Reflections collected	51525	13191	148438
Independent reflections	18345 [R <sub>int</sub> = 0.2748, R <sub>sigma</sub> = = 0.4597]	10027 [R <sub>int</sub> = 0.0227, R <sub>sigma</sub> = 0.0355]	39033 [R <sub>int</sub> = 0.0633, R <sub>sigma</sub> = = N/A]
Data/restraints/parameters	18345/3/372	10027/2/888	39033/42/717
Goodness-of-fit on F <sup>2</sup>	1.335	1.095	0.895
Final R indexes [I ≥ 2σ (I)]	R <sub>1</sub> = 0.2112, wR <sub>2</sub> = 0.3948	R <sub>1</sub> = 0.0434, wR <sub>2</sub> = 0.1240	R <sub>1</sub> = 0.0619, wR <sub>2</sub> = 0.1557
Final R indexes [all data]	R <sub>1</sub> = 0.3846, wR <sub>2</sub> = 0.4665	R <sub>1</sub> = 0.0447, wR <sub>2</sub> = 0.1257	R <sub>1</sub> = 0.1213, wR <sub>2</sub> = 0.1770
Largest diff. peak/hole / e Å <sup>-3</sup>	10.70/-10.72	1.67/-1.20	3.06/-1.23

	5.8	5.12	5.7
Empirical formula	C <sub>36.1</sub> H <sub>43.3</sub> B <sub>2</sub> Cl CuF <sub>8</sub> N <sub>10.1</sub> O <sub>6.2</sub>	C <sub>32</sub> H <sub>40</sub> B <sub>2</sub> CuF <sub>8</sub> N 10O <sub>2</sub>	C <sub>34</sub> H <sub>38</sub> B <sub>2</sub> CuF <sub>8</sub> N <sub>8</sub> O <sub>2</sub>
Formula weight	990.52	833.89	827.89
Temperature/K	120(2)	120(2)	120(2)
Crystal system	triclinic	tetragonal	monoclinic
Space group	P-1	I-42d	P2 <sub>1</sub> /n
a/Å	10.7430(6)	27.463(5)	22.0383(17)
b/Å	11.4495(6)	27.463(5)	12.865(2)
c/Å	18.538(1)	10.467(3)	39.688(5)
α/°	87.426(4)	90	90
β/°	86.138(4)	90	90.787(8)
γ/°	79.679(4)	90	90
Volume/Å <sup>3</sup>	2237.0(2)	7894(3)	11251(2)
Z	2	34	49
ρ <sub>calc</sub> /cm <sup>3</sup>	1.471	1.251	1.259
μ/mm <sup>-1</sup>	2.028	0.71	0.695
F(000)	1016	3137	4502
Radiation	CuKα (λ = 1.54184)	CuKα (λ = 1.54184)	CuKα (λ = 1.54184)
2θ range for data collection/°	7.86 to 148.34	6.44 to 147.66	7.22 to 147.58
Index ranges	-13 ≤ h ≤ 12, - 14 ≤ k ≤ 13, - 15 ≤ l ≤ 21	-31 ≤ h ≤ 22, - 19 ≤ k ≤ 30, -10 ≤ l ≤ 8	-26 ≤ h ≤ 26, - 12 ≤ k ≤ 15, - 45 ≤ l ≤ 33
Reflections collected	17401	3654	31876
Independent reflections	8423 [R <sub>int</sub> = 0.0500, R <sub>sigma</sub> = N/A]	2268 [R <sub>int</sub> = 0.0416, R <sub>sigma</sub> = 0.0666]	18083 [R <sub>int</sub> = 0.1363, R <sub>sigma</sub> = 0.2279]
Data/restraints/parameters	8423/104/665	2268/0/91	18083/0/496
Goodness-of-fit on F <sup>2</sup>	1.013	3.101	3.508
Final R indexes [I ≥ 2σ (I)]	R <sub>1</sub> = 0.0900, wR <sub>2</sub> = 0.2309	R <sub>1</sub> = 0.2306, wR <sub>2</sub> = 0.5103	R <sub>1</sub> = 0.5911, wR <sub>2</sub> = 0.8458
Final R indexes [all data]	R <sub>1</sub> = 0.1261, wR <sub>2</sub> = 0.2608	R <sub>1</sub> = 0.2614, wR <sub>2</sub> = 0.5347	R <sub>1</sub> = 0.6538, wR <sub>2</sub> = 0.8784
Largest diff. peak/hole / e Å <sup>-3</sup>	0.86/-0.78	2.62/-1.35	5.99/-1.35

---

**5.11**

---

Empirical formula	C <sub>32</sub> H <sub>40</sub> B <sub>2</sub> CuF <sub>8</sub> N <sub>10</sub> O <sub>2</sub>
Formula weight	833.89
Temperature/K	120(2)
Crystal system	triclinic
Space group	P-1
a/Å	18.1836(17)
b/Å	19.3336(18)
c/Å	21.5565(16)
α/°	87.751(7)
β/°	66.588(8)
γ/°	62.145(9)
Volume/Å <sup>3</sup>	6047.7(12)
Z	26
ρ <sub>calc</sub> /cm <sup>3</sup>	1.344
μ/mm <sup>-1</sup>	1.4
F(000)	2411.3
Radiation	Cu Kα (λ = 1.54184)
2θ range for data collection/°	6.3 to 147.34
Index ranges	-22 ≤ h ≤ 20, -22 ≤ k ≤ 24, -24 ≤ l ≤ 26
Reflections collected	30436
Independent reflections	17558 [R <sub>int</sub> = 0.0822, R <sub>sigma</sub> = 0.0757]
Data/restraints/parameters	17558/0/696
Goodness-of-fit on F <sup>2</sup>	3.164
Final R indexes [I >= 2σ (I)]	R <sub>1</sub> = 0.3348, wR <sub>2</sub> = 0.6407
Final R indexes [all data]	R <sub>1</sub> = 0.3808, wR <sub>2</sub> = 0.6722
Largest diff. peak/hole / e Å <sup>-3</sup>	4.93/-2.43

---

	<b>5.11</b>	<b>5.6</b>
Empirical formula	C <sub>32</sub> H <sub>40</sub> B <sub>2</sub> CuF <sub>8</sub> N <sub>10</sub> O <sub>2</sub>	C <sub>19</sub> H <sub>29</sub> N <sub>5</sub> O <sub>3</sub>
Formula weight	833.89	375.47
Temperature/K	120(2)	120
Crystal system	triclinic	monoclinic
Space group	P-1	P2 <sub>1</sub> /n
a/Å	18.1836(17)	9.366(3)
b/Å	19.3336(18)	12.539(3)
c/Å	21.5565(16)	17.864(4)
α/°	87.751(7)	90
β/°	66.588(8)	92.916(17)
γ/°	62.145(9)	90
Volume/Å <sup>3</sup>	6047.7(12)	2095.2(10)
Z	26	4
ρ <sub>calc</sub> /cm <sup>3</sup>	1.344	1.19
μ/mm <sup>-1</sup>	1.4	0.669
F(000)	2411.3	808
Radiation	Cu Kα (λ = 1.54184)	CuKα (λ = 1.54178)
2θ range for data collection/°	6.3 to 147.34	8.62 to 119.98
Index ranges	-22 ≤ h ≤ 20, -22 ≤ k ≤ 24, -24 ≤ l ≤ 26	-10 ≤ h ≤ 10, -14 ≤ k ≤ 14, -20 ≤ l ≤ 20
Reflections collected	30436	15417
Independent reflections	17558 [R <sub>int</sub> = 0.0822, R <sub>sigma</sub> = 0.0757]	3117 [R <sub>int</sub> = 0.2582, R <sub>sigma</sub> = 0.1345]
Data/restraints/parameters	17558/0/696	3117/3/251
Goodness-of-fit on F <sup>2</sup>	3.164	0.932
Final R indexes [I ≥ 2σ (I)]	R <sub>1</sub> = 0.3348, wR <sub>2</sub> = 0.6407	R <sub>1</sub> = 0.1053, wR <sub>2</sub> = 0.2851
Final R indexes [all data]	R <sub>1</sub> = 0.3808, wR <sub>2</sub> = 0.6722	R <sub>1</sub> = 0.1356, wR <sub>2</sub> = 0.3329
Largest diff. peak/hole / e Å <sup>-3</sup>	4.93/-2.43	0.47/-0.27

---

## 6.4 References

1. Y. Han, Y. Jiang, C. F. Chen, *Chin. Chem. Lett.* **2013**, *24* (6), 475-478.
2. A. Dei, L. Sorace, *Dalton Trans.* **2003**, *0* (17), 3382-3386.
3. M. Harig, B. Neumann, H. G. Stammeler, D. Kuck, *Eur. J. Org. Chem.* **2004**, (11), 2381-2397.
4. M. Ghaemy, H. Mighani, *Chin. Chem. Lett.* **2009**, *20* (7), 800-804.
5. A. R. Pourali, A. Goli, *J. Chem. Sci.* **2011**, *123* (1), 63-67.
6. E. F. Ullman, L. Call, J. H. Osiecki, *J. Org. Chem.* **1970**, *35* (11), 3623-3631.
7. G. Ulrich, R. Ziessel, *Tet. Lett.* **1994**, *35* (8), 1215-1218.
8. G. Ulrich, R. Ziessel, D. Luneau, P. Rey, *Tet. Lett.* **1994**, *35* (8), 1211-1214.
9. J. H. Osiecki, E. F. Ullman, *J. Am. Chem. Soc.* **1968**, *90* (4), 1078-1079.
10. C.-M. Che, C.-F. Chow, M.-Y. Yuen, V. A. L. Roy, W. Lu, Y. Chen, S. S.-Y. Chui, N. Zhu, *Chem. Sci.* **2011**, *2* (2), 216-220.